T.C.
ISTANBUL UNIVERSITY
INSTITUTE OF HEALTH SCIENCES

(DOCTORAL THESIS)

STUDIES ON NOVEL 4-THIAZOLINE-CONTAINING BENZENESULFONAMIDE DERIVATIVES TARGETING THE TUMOUR-ASSOCIATED HUMAN CARBONIC ANHYDRASE IX AND XII ENZYMES FOR CANCER THERAPY

MUHAMMED TRAWALLY

SUPERVISOR
PROF. DR. ÖZLEN GÜZEL-AKDEMİR
PROF. DR. ATİLLA AKDEMİR

DEPARTMENT OF PHARMACEUTICAL CHEMISTRY
PHARMACEUTICAL CHEMISTRY PROGRAMME

ISTANBUL-2023

DECLARATION

I hereby declare that this thesis is my original work and that it does not contain any material that has been, or is currently being submitted, in whole or in part, for any other degree or qualification, to the best of my knowledge. I attest that no ethical misconduct occurred at any stage of this thesis work, that all data and results presented are accurate and reliable to the best of my knowledge, that all sources and references have been duly acknowledged, and that no patent and copyright infringement occurred at any stage of this thesis work.

Part of the work presented herein has been submitted to the Scientific and Technological Research Council of Türkiye (TÜBİTAK) in the final report of project 118S580.

Muhammed Trawally

EXPLANATION:

At the meeting of the Personal Data Protection Board dated 24/09/2020 and numbered 2020/722, the application of uploading theses without personal has been initiated upon the decision of "Updating the application of publishing wet-signed documents in the Open Access System without including wet-signed documents belonging to the relevant persons".

DEDICATION

I dedicate this thesis to;
The memory of my late grandma, Lu, and aunt Nuimi
My great mother, Queen
My father, Abdourahman
My wife, Fatima
My daughter, Rayhanah
My brothers and sisters
All my teachers

ACKNOWLEDGMENTS

First and foremost, I am grateful to Allah for granting me health, patience and strength throughout this arduous journey. Indeed, there is no success except that it comes from Him.

I would like to express my sincere and utmost gratitude to my caring supervisors Prof. Dr. Özlen Güzel Akdemir and Prof. Dr. Atilla Akdemir for their immeasurable support, guidance and constant encouragement. This journey would not have been a success without their relentless assistance. They have been there for me in the shifting sands of my academic odyssey, and the altruistic knowledge and experience they imparted on me will remain an inspiration to me.

I would like to convey my appreciation to Prof. Dr. Nilgün Karalı and Prof. Dr. Bedia Kaymakçıoğlu for their guidance and invaluable contribution as members of my thesis monitoring committee. I also profoundly owe many thanks to my colleague, Research Assistant, Kübra Demir-Yazıcı for her remarkable support. I would like to thank Prof. Dr. Nuray Güzeldemirci for her support during her tenure as the head of our department.

I would further like to assert my earnest acknowledgement of Prof. Dr. Hakan Göker for performing the NMR analyses and for his kind support during this period. Additionally, I would like to thank Prof. Dr. Claudiu T. Supuran and his team for performing the carbonic anhydrase inhibition studies. I am grateful to Pinar Aksoy Sağirli and Research Assistant Gamze Arcan for conducting the cytotoxicity experiment. I am also thankful to Dr. Kerem Kaya for performing the single X-ray diffraction analyses.

I owe many thanks to all my colleagues in our department for their erudite discussions and exchange of information and ideas. Special thanks to Lale, Research Assistant, Merve and Asu for the chats and monitoring my reactions and TLC. I would like to recognize the help of Research Assistant, Ipek and Fatih at the CADD lab at Bezmialem University for their support. I cannot forget the assistance of our secretary, Sevgi and the coffee and nuts of our laborants, Özden and Cennet. I would like to express my gratitude to my friends, Momodou Jang, Ali Ertuğrul, Pharmacist Emre,

Masanneh, Fatih Turan, Gueye, Omar and Mustapha, who supported me in many ways in these trying times.

I am deeply grateful to my best friend, my wife, Fatima, for her continuous support, encouragement and unwavering faith in me, and to my beautiful daughter, Rayhanah, whose broad smiles served as my inspirational pillar during my thesis writing.

Lastly, I would like to thank my parents and siblings for their endless support and encouragement, especially my mum, without whom my dreams of attaining a higher education would not have come to reality.

This project has been funded by the Scientific and Technological Research Council of Türkiye (TÜBİTAK). Project No: 118S580

TABLE OF CONTENTS

DECLARATION ..... İİ
DEDICATION ..... İİİ
ACKNOWLEDGMENTS ..... İV
TABLE OF CONTENTS ..... Vİ
LIST OF TABLES ..... Xİİİ
LIST OF FIGURES ..... XVİ
TABLE OF SCHEMES ..... XXXİİ
LIST OF SYMBOLS / ABBREVIATIONS ..... XXXİV
ABSTRACT ..... XXXVİİ
ÖZET ..... XXXVİİİ
1. INTRODUCTION AND AIM 1
2. GENERAL INFORMATION/LITERATURE REVIEW 4
2.1. Computer-Aided Drug Design 4
2.1.1. Ligand-Based Design 6
2.1.2. Structure-Based Design 6
2.1.2.1. Molecular Docking 7
2.1.2.2. Ensemble Docking 8
2.1.3. Molecular Mechanics with Generalised Born and Surface Area Solvation (MM-GBSA) Calculations 9
2.1.4. Molecular Dynamic Simulations and post-MM-GBSA Evaluation 11
2.1.5. *In silico* prediction of ADME properties 12
2.2. Cancer 13
2.2.1. The microenvironment of tumour cells 15
2.2.2. Hypoxia and Hypoxia-Inducible Factor 17
2.2.3. Warburg Effect and Acidosis 19
2.3. Carbonic anhydrase enzymes 23
2.3.1. CA Superfamily and Expression Profile 24
2.3.2. Catalytic Mechanism and Physiological Importance 30
2.3.3. Structure and functions of hCAIX and XII 37
2.3.4. (Over)expression of hCAIX and hCAXII and their implications as diagnostic, prognostic and therapeutic targets in Cancer 40

2.3.5. Inhibition Mechanism of CA Inhibitors....43
2.3.5.1. Binding to the active site metal....43
2.3.5.2. Anchoring to the zinc-coordinated water/hydroxide....44
2.3.5.3. Blockage of the active site entrance....45
2.3.5.4. Binding outside the active site (Allosteric site)....46
2.3.5.5. Unknown Mechanism....47
2.3.6. Tail-Approach in designing CAIs....48
2.4. Sulfonamides....50
2.4.1. Chemistry of Sulfonamides....50
2.4.2. CA inhibitory properties of sulfonamide-containing compounds....53
2.5. Synthesis of Isothiocyanates....60
2.6. Thiosemicarbazides....63
2.6.1. Synthesis of thiosemicarbazides....63
2.7. Thiosemicarbazones....64
2.7.1. Synthesis and biological activities of thiosemicarbazones....65
2.8. Biological activities azine-containing molecules....69
2.9. Thiazole and Thiazolines....73
2.9.1. Chemistry of Thiazole and Thiazolines....73
2.9.2. General synthesis of thiazole and 4-thiazoline derivatives....75
2.9.2.1. Hantzsch's Synthesis....76
2.9.2.2. Cook- Heilborn's Synthesis....79
2.9.2.3. Gabriel Synthesis....80
2.9.2.4. Erlenmeyer Synthesis....80
2.9.2.5. Tcherniac's Synthesis....81
2.9.3. Biological Activities of thiazole derivatives....81
2.9.4. Anticancer activities of thiazole derivatives....90
2.9.5. CA inhibitory properties of 4-thiazoline derivatives....94
3. EXPERIMENTAL....96
3.1. Materials and Instruments....96
3.1.1. Chemicals....96
3.1.2. Analytical instruments....96
3.1.3. Chromatography....96
3.1.4. *In silico* studies....97

3.2. Synthetic Procedures.....97
3.2.1. General Synthesis of 3/4-isothiocyanatobenzenesulfonamide (B) 98
3.2.2. General Synthesis of *N*-(3/4-sulfamoylphenyl)hydrazinecarbothioamide (C) .98
3.2.3. General Synthesis of 2-(Alkylidene/arylidene)-*N*-(3/4-sulfamoylphenyl)hydrazine-1-carbothioamide derivatives (E) 98
3.2.4. General Synthesis of ω-Bromoacetophenone derivatives (3) 99
3.2.5. General synthesis of 3/4-[4-(Non)substitutedphenyl-2-(alkylidene/arylidenehydrazinylidene)-1,3-thiazol-3(*2H*)-yl]benzenesulfonamide derivatives (4a-4v) 99
3.3. Single X-ray Diffraction Analyses.....99
3.4. *In Silico* ADME Predictions and Molecular Modelling Studies.....100
3.4.1. *In Silico* ADME Predictions 100
3.4.2. Preparation of Ligands 100
3.4.3. Preparation of Protein Structures 100
3.4.4. Receptor Grid Generation 101
3.4.5. Reverse Ensemble Docking and Rescoring with MM-GBSA 102
3.4.6. Molecular Dynamics Simulations 102
3.5. Biological activity 103
3.5.1. CA Inhibition assay.....103
3.5.2. Anticancer Assay (In vitro cytotoxicity Assay against some cancer cells) 104
3.5.2.1. Cell Culture 104
3.5.2.2. Cell Viability Assay 104
4. RESULTS 106
4.1. Preliminary Molecular Modelling studies 106
4.1.1. Retrospective Docking Studies 106
4.1.2. Library Screening with SP Docking and Suggestion of compounds for Synthesis 106
4.2. *In Silico* ADME Prediction.....112
4.3. Chemistry 114
4.3.1. Synthesis of 2-(Alkylidene/arylidene)-*N*-(3/4-sulfamoylphenyl)hydrazine-1-carbothioamide derivatives (E) 114
4.3.1.1. (*E*)-N-(3-sulfamoylphenyl)-2-(thiophen-2-ylmethylene)hydrazine-1-carbothioamide (E1).....114

4.3.1.2. (*E*)-2-((5-bromothiophen-2-yl)methylene)-*N*-(3-sulfamoylphenyl)hydrazine-1-carbothioamide (E2) 118

4.3.1.3. (*E*)-2-((1*H*-pyrrol-2-yl)methylene)-*N*-(3-sulfamoylphenyl)hydrazine-1-carbothioamide (E3).....121

4.3.1.4. (*E*)-2-((1-methyl-1*H*-pyrrol-2-yl)methylene)-*N*-(3-sulfamoylphenyl)hydrazine-1-carbothioamide (E4) 126

4.3.1.5. (*E*)-2-(furan-2-ylmethylene)-*N*-(3-sulfamoylphenyl)hydrazine-1-carbothioamide (E5).....130

4.3.1.6. (*E*)-2-((1*H*-pyrrol-2-yl)methylene)-*N*-(4-sulfamoylphenyl)hydrazine-1-carbothioamide (E6).....136

4.3.1.7. (*E*)-2-(furan-2-ylmethylene)-*N*-(4-sulfamoylphenyl)hydrazine-1-carbothioamide (E7).....139

4.3.1.8. 2-(propan-2-ylidene)-*N*-(3-sulfamoylphenyl)hydrazine-1-carbothioamide (E8).....142

4.3.1.9. 2-(pentan-3-ylidene)-*N*-(3-sulfamoylphenyl)hydrazine-1-carbothioamide (E9).....149

4.3.1.10. 2-(propan-2-ylidene)-*N*-(4-sulfamoylphenyl)hydrazine-1-carbothioamide (E10).....153

4.3.1.11. 2-(pentan-3-ylidene)-*N*-(4-sulfamoylphenyl)hydrazine-1-carbothioamide (E11).....159

4.3.1.12. (E)-2-(pentan-2-ylidene)-*N*-(4-sulfamoylphenyl)hydrazine-1-carbothioamide (E12).....163

4.3.1.13. 2-cyclopentylidene-N-(4-sulfamoylphenyl)hydrazine-1-carbothioamide (E13).....166

4.3.2. Synthesis of Targeted Compounds 3/4-[4-(Non)substitutedphenyl-2-(alkylidene/arylidenehydrazinylidene)-1,3-thiazol-3(*2H*)-yl]benzenesulfonamide Derivatives (4a-4v) 170

4.3.2.1. 3-((*Z*)-4-phenyl-2-(((*E*)-thiophen-2-ylmethylene)hydrazineylidene)thiazol-3(2*H*)-yl)benzenesulfonamide (4a) 170

4.3.2.2. 3-((Z)-2-(((E)-(5-bromothiophen-2-yl)methylene)hydrazineylidene)-4-phenylthiazol-3(2H)-yl)benzenesulfonamide (4b).....175

4.3.2.3. 3-((*Z*)-2-(((*E*)-(1*H*-pyrrol-2-yl)methylene)hydrazineylidene)-4-phenylthiazol-3(2*H*)-yl)benzenesulfonamide (4c) 182

4.3.2.4. 3-((*Z*)-2-(((*E*)-(1-methyl-1*H*-pyrrol-2-yl)methylene)hydrazineylidene)-4-phenylthiazol-3(2*H*)-yl)benzenesulfonamide (4d).....187

4.3.2.5. 3-((*Z*)-2-(((*E*)-furan-2-ylmethylene)hydrazineylidene)-4-phenylthiazol-3(2*H*)-yl)benzenesulfonamide (4e) 191

4.3.2.6. 4-((*Z*)-2-(((*E*)-(1*H*-pyrrol-2-yl)methylene)hydrazineylidene)-4-phenylthiazol-3(2*H*)-yl)benzenesulfonamide (4f) 197

4.3.2.7. 4-((*Z*)-2-(((*E*)-(1*H*-pyrrol-2-yl)methylene)hydrazineylidene)-4-(4-bromophenyl)thiazol-3(2*H*)-yl)benzenesulfonamide (4g) 204

4.3.2.8. 4-((*Z*)-2-(((*E*)-(1*H*-pyrrol-2-yl)methylene)hydrazineylidene)-4-(4-hydroxyphenyl)thiazol-3(2*H*)-yl)benzenesulfonamide (4h) 207

4.3.2.9. 4-((*Z*)-2-(((*E*)-furan-2-ylmethylene)hydrazineylidene)-4-phenylthiazol-3(2*H*)-yl)benzenesulfonamide (4i) 211

4.3.2.10. 4-((*Z*)-4-(4-bromophenyl)-2-(((*E*)-furan-2-ylmethylene)hydrazineylidene)thiazol-3(2*H*)-yl)benzenesulfonamide (4j).....216

4.3.2.11. (*Z*)-3-(2-(pentan-3-ylidenehydrazineylidene)-4-phenylthiazol-3(2*H*)-yl)benzenesulfonamide (4k).....221

4.3.2.12. (*Z*)-4-(4-(4-bromophenyl)-2-(propan-2-ylidenehydrazineylidene)thiazol-3(2*H*)-yl)benzenesulfonamide (4l).....226

4.3.2.13. (*Z*)-4-(2-(propan-2-ylidenehydrazineylidene)-4-(4-(trifluoromethyl)phenyl)thiazol-3(2*H*)-yl)benzenesulfonamide (4m) 230

4.3.2.14. (*Z*)-4-(2-(propan-2-ylidenehydrazineylidene)-4-(4-(trifluoromethoxy)phenyl)thiazol-3(2*H*)-yl)benzenesulfonamide (4n) 235

4.3.2.15. (*Z*)-4-(4-(4-fluorophenyl)-2-(propan-2-ylidenehydrazineylidene)thiazol-3(2*H*)-yl)benzenesulfonamide (4o).....239

4.3.2.16. (*Z*)-4-(2-(propan-2-ylidenehydrazineylidene)-4-(3-(trifluoromethyl)phenyl)thiazol-3(2*H*)-yl)benzenesulfonamide (4p) 243

4.3.2.17. (*Z*)-4-(2-(pentan-3-ylidenehydrazineylidene)-4-(4-methylphenyl)thiazol-3(2*H*)-yl)benzenesulfonamide (4q).....245

4.3.2.18. (*Z*)-4-(4-(4-fluorophenyl)-2-(pentan-3-ylidenehydrazineylidene)thiazol-3(2*H*)-yl)benzenesulfonamide (4r).....249

4.3.2.19. 4-((*Z*)-2-(((*E*)-pentan-2-ylidene)hydrazineylidene)-4-phenylthiazol-3(2*H*)-yl)benzenesulfonamide (4s) 252

4.3.2.20. (*Z*)-4-(2-(cyclopentylidenehydrazineylidene)-4-phenylthiazol-3(2*H*)-yl)benzenesulfonamide (4t).....257

4.3.2.21. (*Z*)-4-(4-(4-bromophenyl)-2-(cyclopentylidenehydrazineylidene)thiazol-3(2*H*)-yl)benzenesulfonamide (4u).....262

4.3.2.22. (*Z*)-4-(2-(cyclopentylidenehydrazineylidene)-4-(4-hydroxyphenyl)thiazol-3(2*H*)-yl)benzenesulfonamide (4v) 269
4.4. Single X-ray Diffraction Analyses 273
4.4.1. Crystal data of compound E3 273
4.4.2. Crystal data of compound E8 277
4.4.3. Crystal data of compound 4e 282
4.5. Biological Activity 287
4.5.1. CA Inhibition assay 287
4.5.2. Cytotoxicty of 3/4-[2-(alkylidene/arylidenehydrazinylidene)-4-(non)substitutedphenyl-1,3-thiazol-3(*2H*)-yl]benzenesulfonamide derivatives (4a – 4v) 289
4.6. Molecular Modelling Studies 290
4.6.1. The binding pose of 3,5-diphenylbenzenesulfonamide, the cocrystallised ligand, in hCAIX (PDB:6TL5) 290
4.6.2. The binding pose of 4-chloro-2-cyclohexylsulfanyl-*N*-(2-hydroxyethyl)-5-sulfamoylbenzamide, the cocrystallised ligand, in hCAXII (PDB:6R6Y) 292
4.6.3. The docked pose of compound 4f in hCAIX (PDB: 5FL6 & 6TL5) 294
4.6.4. The docked pose of compound 4f in hCAXII (PDB:6R6Y) 298
4.6.5. The docked pose of compound 4i in hCAIX (PDB:6TL5) 300
4.6.6. Docked pose of compound 4i in hCAXII (PDB: 1JD0) 302
4.6.7. Docked pose of compound 4o in hCAIX (PDB: 6TL5) 304
4.6.8. Docked pose of compound 4o in hCAXII (PDB: 5LL5 & 6R6Y) 305
4.6.9. Docked pose of compound 4t in hCAIX (PDB: 6TL5) 309
4.6.10. Docked pose of compound 4t in hCAXII (PDB: 6R6Y) 311
4.6.11. Docked pose of compound 4u in hCAIX (PDB: 6TL5) 313
4.6.12. Docked pose of compound 4u in hCAXII (PDB: 6R6Y) 315
5. DISCUSSION 318
5.1. Chemistry 318
5.1.1. 3/4-Isothiocyanatobenzenesulfonamide (B) 319
5.1.2. *N*-(3/4-sulfamoylphenyl)hydrazinecarbothioamide (C) 322
5.1.3. 2-(Alkylidene/arylidene)-*N*-(3/4-sulfamoylphenyl)hydrazine-1-carbothioamide derivatives (E) 325
5.1.3.1. IR Spectral Analysis 328

5.1.3.2. ^{1}H-NMR Spectral Analysis 334
5.1.3.3. ^{13}C-NMR Spectral Analysis 344
5.1.3.4. Mass Spectral Analysis 350
5.1.4. 3/4-[4-(Non)substitutedphenyl-2-(alkylidene/arylidenehydrazinylidene)-1,3-thiazol-3(2*H*)-yl]benzenesulfonamide derivatives (4a-4v) 354
5.1.4.1. IR Spectral Analysis 361
5.1.4.2. ^{1}H-NMR Spectral Analysis 367
5.1.4.3. ^{13}C-NMR Spectral Analysis 378
5.1.4.4. Mass Spectral Analysis 395
5.2. Single X-ray Diffraction Analyses 396
5.3. Biological Activity 398
5.3.1. CA inhibition assay for 2-(alkylidene/arylidene)-*N*-(3/4-sulfamoylphenyl)hydrazine-1-carbothioamide derivatives (E) 398
5.3.2. CA inhibition assay for 3/4-[4-(non)substitutedphenyl-2-(alkylidene/arylidenehydrazinylidene)-1,3-thiazol-3(2*H*)-yl]benzenesulfonamide derivatives (4a – 4v) 399
5.3.3. Cytotoxicity of 3/4-[4-(Non)substitutedphenyl-2-(alkylidene/arylidenehydrazinylidene)-1,3-thiazol-3(2*H*)-yl]benzenesulfonamide derivatives (4a – 4v) 403
5.4. In silico ADME prediction 407
5.5. Molecular modelling studies 408
BIBLIOGRAPHY 412
PLAGIARISM REPORT 460

LIST OF TABLES

Table 2-1: Percentage sequence similarity between hCA isoenzymes, adapted from (Imtaiyaz Hassan et al. 2013) 27
Table 2-2 Kinetic properties, subcellular localization, and tissue/organ distribution of hCA isoenzymes. Adapted from (Carta et al. 2014; Supuran and Mugelli 2019; Chegwidden 2021) 29
Table 2-3: Primary physiological functions and related pathological conditions of hCA enzymes (Imtaiyaz Hassan et al. 2013; Chegwidden 2021) 32
Table 2-4: Residues forming the binding pockets of hCAI, II, IX and XII. (Akdemir et al. 2015) 49
Table 2-5 Bond lengths and bond angles of thiazole ring (Gupta et al. 1999) 74
Table 3-1: Crystal Structures of hCAIX and hCAXII used in molecular modelling studies 101
Table 4-1: Preliminary SP docking scores of the designed ligands 107
Table 4-2: ADME properties of compounds 4a – 4v 113
Table 4-3: Crystal data and structure refinement for E3 273
Table 4-4: Fractional Atomic Coordinates ($\times 10^4$) and Equivalent Isotropic Displacement Parameters ($Å^2 \times 10^3$) for E3. U_{eq} is defined as 1/3 of the trace of the orthogonalised U_{IJ} tensor 274
Table 4-5: Bond Lengths for E3 275
Table 4-6: Bond Angles for E3 275
Table 4-7: Anisotropic Displacement Parameters ($Å^2 \times 10^3$) for E3. The Anisotropic displacement factor exponent takes the form: $-2\pi^2[h^2a^{*2}U_{11}+2hka^*b^*U_{12}+\ldots]$. 276
Table 4-8: Hydrogen Atom Coordinates ($Å \times 10^4$) and Isotropic Displacement Parameters ($Å^2 \times 10^3$) for E3. 277
Table 4-9: Sample and crystal data for E8 278
Table 4-10: Atomic coordinates and equivalent isotropic atomic displacement parameters ($Å^2$) for E8. U(eq) is defined as 1/3 of the trace of the orthogonalized U_{ij} tensor. 279
Table 4-11: Bond lengths (Å) for E8. 279
Table 4-12: Bond angles (°) for E8. 280

Table 4-13: Anisotropic atomic displacement parameters ($Å^2$) for E8. The anisotropic atomic displacement factor exponent takes the form: $-2\pi^2[h^2 a^{*2} U_{11} + ... + 2 h k a^* b^* U_{12}]$ 281
Table 4-14: Hydrogen atomic coordinates and isotropic atomic displacement parameters (Å2) for E8. 281
Table 4-15: Crystal data and structure refinement for 4e. 283
Table 4-16: Fractional Atomic Coordinates ($\times 10^4$) and Equivalent Isotropic Displacement Parameters ($Å^2 \times 10^3$) for 4e. U_{eq} is defined as 1/3 of the trace of the orthogonalised U_{IJ} tensor. 284
Table 4-17: Bond Lengths for 4e. 285
Table 4-18: Angles for 4e. 285
Table 4-19: Hydrogen Atom Coordinates ($Å \times 10^4$) and Isotropic Displacement Parameters ($Å^2 \times 10^3$) for 4e. 286
Table 4-20: The hCAI, hCAII, hCAIX and hCAXII enzyme inhibition values of the intermediate thiosemicarbazone derivatives (E1 – E13) 287
Table 4-21: The hCAI, hCAII, hCAIX and hCAXII enzyme inhibition values of 3/4-[2-(alkylidene/arylidenehydrazinylidene)-4-(non)substitutedphenyl-1,3-thiazol-3(2*H*)-yl]benzenesulfonamide derivatives 288
Table 4-22: Cytotoxic effects of 3/4-[2-(alkylidene/arylidenehydrazinylidene)-4-(non)substitutedphenyl-1,3-thiazol-3(2*H*)-yl]benzenesulfonamide derivatives (4a – 4v) on ECC-1, MCF-7, A549, HT-29, U118-MG, Caco-2 and HUVEC cell lines 289
Table 5-1: Physical properties of 3/4-Isothiocyanatobenzenesulfonamide (B) 320
Table 5-2: IR data of 3/4-Isothiocyanatobenzenesulfonamide (B) 321
Table 5-3: Physical properties of *N*-(3/4-sulfamoylphenyl)hydrazinecarbothioamide (C) 323
Table 5-4: IR data of *N*-(3/4-sulfamoylphenyl)hydrazinecarbothioamide (C) 323
Table 5-5: Physical properties and elemental analysis data of 2-(Alkylidene/arylidene)-*N*-(3/4-sulfamoylphenyl)hydrazine-1-carbothioamide derivatives (E) 326
Table 5-6: IR data of 2-(Alkylidene/arylidene)-*N*-(3/4-sulfamoylphenyl)hydrazine-1-carbothioamide derivatives (E1 – E13) 332
Table 5-7: ^1H NMR data of 2-(Alkylidene/arylidene)-*N*-(3/4-sulfamoylphenyl)hydrazine-1-carbothioamide derivatives (E1 – E13) 341

Table 5-8: ^{13}C NMR data of 2-(Alkylidene/arylidene)-*N*-(3/4-sulfamoylphenyl)hydrazine-1-carbothioamide derivatives (E1 – E13)..... 345
Table 5-9: Elemental analysis data and physical properties of 3/4-[4-(Non)substitutedphenyl-2-(alkylidene/arylidenehydrazinylidene)-1,3-thiazol-3(*2H*)-yl]benzenesulfonamide derivatives (4a-4v)..... 358
Table 5-10: IR data of 3/4-[4-(Non)substitutedphenyl-2-(alkylidene/arylidenehydrazinylidene)-1,3-thiazol-3(*2H*)-yl]benzenesulfonamide derivatives (4a-4v)..... 363
Table 5-11: ^{1}H NMR data of 3/4-[4-(Non)substitutedphenyl-2-(alkylidene/arylidenehydrazinylidene)-1,3-thiazol-3(*2H*)-yl]benzenesulfonamide derivatives (4a-4v)..... 373
Table 5-12: Chemical shifts and the ^{13}C – F couplings constants of fluorobenzene..... 383
Table 5-13: ^{13}C NMR data of 3/4-[4-(Non)substitutedphenyl-2-(alkylidene/arylidenehydrazinylidene)-1,3-thiazol-3(*2H*)-yl]benzenesulfonamide derivatives (4a-4v)..... 388
Table 5-14: Selectivity ratios for the inhibition of hCAIX and hCAXII over hCAI and hCAII for E1 – E13..... 399
Table 5-15: Selectivity ratios for the inhibition of hCAIX and hCAXII over hCAI and hCAII for 4a – 4v..... 402
Table 5-16: Cytotoxicity on endometrium cancer cell line (ECC-1)..... 403
Table 5-17: Cytotoxicity on breast cancer cell line (MCF-7)..... 404
Table 5-18: Cytotoxicity on lung cancer cell line (A549)..... 405
Table 5-19: Cytotoxicity on colon cancer cell lines (HT-29 and Caco-2)..... 406
Table 5-20: Cytotoxicity on glioblastoma cancer cell line (U118-MG)..... 407
Table 5-21: Summary of molecular modelling studies compounds 4f, 4i, 4o, 4t and 4u 411

LIST OF FIGURES

Figure 1-1: Lead Molecule 3
Figure 2-1: Drug discovery pipeline 4
Figure 2-2: Application of CADD in drug discovery pipeline 5
Figure 2-3: General workflow of CADD 6
Figure 2-4: Global map of cancer as the major cause of death before age 70 (ages 30–69), with rankings and numbers of countries in parenthesis. (Stewart et al. 2020) 14
Figure 2-5: Hallmarks of Cancer (Hanahan 2022; Hanahan and Weinberg 2011) 15
Figure 2-6: Regulation of angiogenesis by angiogenic factors induced by HIF. (Krock et al. 2011) 17
Figure 2-7: HIF orchestrates the upregulation of glycolysis, angiogenesis, erythropoiesis, and pH-regulating proteins in hypoxic (Supuran 2017b) 19
Figure 2-8: Differences between oxidative phosphorylation, anaerobic glycolysis, and aerobic glycolysis (Warburg effect) (Vander Heiden et al. 2009) 20
Figure 2-9: Proteins involved in pH regulation within a tumour cell (Neri and Supuran 2011) 22
Figure 2-10 A) Turquoise represents β-sheets, red represents α-helixes B) Coloured regions represent the active site; green represents the hydrophobic region and turquoise represents the hydrophilic region. 25
Figure 2-11 Overlay of some hCA isoenzymes. PDB IDs: 3LXE for hCAI (green), 4E3D for hCAII (blue), 1Z93 for hCAIII (yellow), 1ZNC for hCAIV (red), 3FE4 for hCAVI (teal), 6SDT for hCAVII (violet), 3IAI for hCAIX (orange), 1JD0 for hCAXII (magenta), 4KNM for hCAXIII (grey), 5CJF for hCAXIV (black). 26
Figure 2-12 Localization of human CA isoforms in the cell. Proteins are marked as horseshoe shaped figures with their colour being proportional to the enzymatic activity. The acatalytic isoforms are shown in white. The zinc ions in the active sites of CAs are shown as small purple spheres (Baranauskienė and Matulis 2019) 28
Figure 2-13: A) Active site of hACII (PDB: 4E3D) showing the cone-shaped cavity and the Zn^{2+} coordination with His94, His96, and His119. The grey sphere represents Zn^{2+}. B) Ribbon diagram; turquoise represents β-strands and grey represents α-helices. 35

Figure 2-14: Catalytic (for the physiological reaction), inhibition (with zinc binders) and activation mechanisms of α-CAs (hCAI amino acid numbering of the zinc ligands (Supuran 2016b) 36
Figure 2-15 Schematic and structural models of CA IX and XII. (A) Domains of CAIX: PG (violet), CD (teal), TM (red), CT (blue). (B) Homodimeric membrane-bound CAIX (C) Domains of CAXII: CD (wheat), TM (gold), CT (black). (D) Homodimeric membrane-bound CAXII (Y. Mboge et al. 2016) 38
Figure 2-16: A dimeric structure of hCAIX (PDB: 3IAI) showing the intermolecular disulfide bond. 39
Figure 2-17: VHL protein binds to HIF-1 in normoxia, causing its degradation. Hypoxia inactivates VHL and increases cytoplasmic HIF-1 which triggers CAIX transcription (Aldera and Govender 2021) 41
Figure 2-18: ZBG-containing CAIs 43
Figure 2-19: Binding mechanism of zinc-binding CAIs 44
Figure 2-20: CAIs that anchor to the zinc-coordinated water/hydroxide 44
Figure 2-21: A) Binding mechanism of CAIs that anchor to the Zn(II)-coordinated water molecule/hydroxide ion B) Binding of phenol, the first CAI that anchors to zinc-coordinated water. 45
Figure 2-22: CAIs that block the active site entrance of CAs and their hydrolysed product 45
Figure 2-23: Binding mechanism of CAI that blocks the entrance to the active site. SG is a sticky group of the phenol, carboxylic acid, or amide type. 46
Figure 2-24: (A) 2-(2-phenylacetyl)benzoic acid (B) Binding of 2-(2-phenylacetyl)benzoic acid to the allosteric site of CA. (C) hCAII complexed with 2-(2-phenylacetyl)benzoic acid 47
Figure 2-25: CAIs with the unknown binding mode 48
Figure 2-26: Comparison of hCAII (green) and hCAIX (yellow). Catalytic Zn^{2+} is shown as a sphere (grey) 49
Figure 2-27: Diagrammatic representation of the tail approach for ZBG-containing CAIs. A) Single tail B) Dual-tail C) Three tails (Bonardi et al. 2020). 50
Figure 2-28: General structures of primary, secondary and tertiary sulfonamides 51
Figure 2-29: Commercially available compounds containing a cyclic sulfonamide 52
Figure 2-30: Structures of clinically approved CAIs containing a sulfonamide 54

Figure 2-31: General structures of TSC 64
Figure 2-32: Structure of azine 69
Figure 2-33: Azines as conjugation switches: a planar conformation (left) and twisted conformation (right). p-orbitals of C=N bonds (grey), lone pairs on N (black) (McLoughlin et al. 2007). 70
Figure 2-34: Structure of thiazole 73
Figure 2-35: Isosteres of thiazole 73
Figure 2-36: Resonance structures of thiazole 74
Figure 2-37: Calculated π-electron density of thiazole ring 75
Figure 2-38: Structures of partially and fully saturated thiazoles 75
Figure 2-39 Fragments generated by retrosynthetic (Katritzky 2008) 76
Figure 2-40: Thiazole-containing natural compounds 82
Figure 2-41: Thiazole-containing commercially available drugs 83
Figure 4-1 A) Retrospective docked pose of 5-(1-(4-Methylphenyl)-1*H*-1,2,3-triazol-4-yl)thiophene-2- sulfonamide in hCAIX (PDB:5FL6) B) Retrospective docked pose of AAZ in hCAXII (PDB:1JD0). The grey sphere represents the Zn^{2+}. Pink dashed lines represent metal coordination. Yellow dashed lines represent hydrogen bonding. Turquoise dashed lines represent π-π stackings. 106
Figure 4-2: A) The SP docked pose of 4s in the active site of hCAIX (3IAI). B) The SP docked pose of 4s in the active site of hCAXII (1JD0). The grey sphere represents the Zn^{2+}. Pink dashed lines represent metal coordination. Yellow dashed lines represent hydrogen bonding. Turquoise dashed lines represent π-π stackings 111
Figure 4-3: A) The SP docked pose of 4d in the active site of hCAIX (3IAI). B) The SP docked pose of 4v in the active site of hCAXII (1JD0). The grey sphere represents the Zn^{2+}. Pink dashed lines represent metal coordination. Yellow dashed lines represent hydrogen bonding. Turquoise dashed lines represent π-π stackings. 112
Figure 4-4: IR spectrum of compound E1 115
Figure 4-5: ^{1}H-NMR Spectrum of compound E1 115
Figure 4-6: ^{13}C-NMR Spectrum of compound E1 116
Figure 4-7: HSQC Spectrum of compound E1 117
Figure 4-8: Mass Spectrum of compound E1 117
Figure 4-9: IR spectrum of compound E2 119
Figure 4-10: ^{1}H-NMR Spectrum of compound E2 (0 – 12 ppm) 119

Figure 4-11: ^{1}H-NMR Spectrum of compound E2 (7.2 – 8.4 ppm) 120
Figure 4-12: Mass Spectrum of compound E2 120
Figure 4-13: IR spectrum of compound E3 122
Figure 4-14: ^{1}H-NMR spectrum of compound E3 (0 – 12 ppm) 122
Figure 4-15: ^{1}H-NMR spectrum of compound E3 (6.0 – 8.1 ppm) 123
Figure 4-16: ^{13}C-NMR spectrum of compound E3 (0 – 200 ppm) 123
Figure 4-17: ^{13}C-NMR spectrum of compound E3 (110 – 145 ppm) 124
Figure 4-18: HSQC spectrum of compound E3 125
Figure 4-19: HSQC spectrum of compound E3 (6 – 8.2 ppm; 105 – 140 ppm) 125
Figure 4-20: Mass spectrum of compound E3 126
Figure 4-21: IR spectrum of compound E4 127
Figure 4-22: ^{1}H-NMR spectrum of compound E4 (0 – 12 ppm) 128
Figure 4-23: ^{1}H-NMR spectrum of compound E4 (6.0 – 8.2 ppm) 129
Figure 4-24: Mass spectrum of compound E4 129
Figure 4-25: IR spectrum of compound E5 131
Figure 4-26: ^{1}H-NMR spectrum of compound E5 (0 – 12 ppm) 132
Figure 4-27: ^{1}H-NMR spectrum of compound E5 (6.6 – 8.3 ppm) 132
Figure 4-28: ^{13}C-NMR spectrum of compound E5 (0 – 180 ppm) 133
Figure 4-29: ^{13}C-NMR spectrum of compound E5 (110 – 1175 ppm) 133
Figure 4-30: HSQC spectrum of compound E5 (0 – 10 ppm; 0 – 140 ppm) 134
Figure 4-31: HSQC spectrum of compound E5 (6.5 – 8.5 ppm; 110 – 150 ppm) 135
Figure 4-32: Mass spectrum of compound E5 135
Figure 4-33: IR spectrum of compound E6 137
Figure 4-34: ^{1}H-NMR spectrum of compound E6 (0 – 14 ppm) 137
Figure 4-35: ^{1}H-NMR spectrum of E6 compound (6.5 – 12 ppm) 138
Figure 4-36: ^{1}H-NMR spectrum of compound E6 (6.0 – 8.2 ppm) 138
Figure 4-37: Mass spectrum of compound E6 139
Figure 4-38: IR spectrum of compound E7 140
Figure 4-39: ^{1}H-NMR spectrum of compound E7 (0 – 14 ppm) 141
Figure 4-40: ^{1}H-NMR spectrum of compound E7 (6.5 – 12.5 ppm) 141
Figure 4-41: ^{1}H-NMR spectrum of compound E7 (6.5 – 12 ppm) 141
Figure 4-42: Mass spectrum of compound E7 142
Figure 4-43: IR spectrum of compound E8 143

Figure 4-44: ^{1}H-NMR spectrum of E8 (0 – 14 ppm) 144
Figure 4-45: ^{1}H-NMR spectrum of compound E8 (1 – 11 ppm) 144
Figure 4-46: ^{1}H-NMR spectrum of compound E8 (2 – 3.6 ppm) 145
Figure 4-47: ^{1}H-NMR spectrum of compound E8 (7.3 – 10.5 ppm) 145
Figure 4-48: ^{13}C-NMR spectrum of compound E8 (0 – 190 ppm) 146
Figure 4-49: ^{13}C-NMR spectrum of compound E8 (17 – 175 ppm) 146
Figure 4-50: ^{13}C-NMR spectrum of compound E8 (120 – 177 ppm) 146
Figure 4-51: HSQC spectrum of compound E8 (1.9 – 8.5 ppm; 0 – 130 ppm) 147
Figure 4-52: HSQC spectrum of compound E8 (7.3 – 8.2 ppm; 114 – 133 ppm) 148
Figure 4-53: HSQC spectrum of compound E8 (1.9 – 2.6 ppm; 0 – 44 ppm) 148
Figure 4-54: Mass spectrum of compound E8 149
Figure 4-55: IR spectrum of compound E9 150
Figure 4-56: ^{1}H-NMR spectrum of compound E9 (0 – 11 ppm) 151
Figure 4-57: ^{1}H-NMR spectrum of compound E9 (0 – 2.9 ppm) 151
Figure 4-58: ^{1}H-NMR spectrum of compound E9 (6.6 – 8.5 ppm) 152
Figure 4-59: Mass spectrum of compound E9 152
Figure 4-60: IR spectrum of compound E10 154
Figure 4-61: ^{1}H-NMR spectrum of compound E10 (0 – 14 ppm) 154
Figure 4-62: ^{1}H-NMR spectrum of compound E10 (0 – 10.6 ppm) 155
Figure 4-63: ^{1}H-NMR spectrum of compound E10 (0 – 3.4 ppm) 155
Figure 4-64: ^{1}H-NMR spectrum of E9 (7.4 – 10.6 ppm) 155
Figure 4-65: ^{13}C-NMR spectrum of compound E10 (0 – 200 ppm) 156
Figure 4-66: ^{13}C-NMR spectrum of compound E10 (16 – 44 ppm) 156
Figure 4-67: ^{13}C-NMR spectrum of compound E10 (123 – 177 ppm) 157
Figure 4-68: HSQC spectrum of compound E10 (0 – 10 ppm; 0 – 140 ppm) 157
Figure 4-69: HSQC spectrum of compound E10 (7.2 – 8.3 ppm; 114 – 140 ppm) 158
Figure 4-70: HSQC spectrum of compound E10 (1.6 – 2.9 ppm; 15 – 45 ppm) 158
Figure 4-71: Mass spectrum of compound E10 159
Figure 4-72: IR spectrum of compound E11 160
Figure 4-73: ^{1}H NMR spectrum of compound E11 (0 – 14 ppm) 161
Figure 4-74: ^{1}H NMR spectrum of compound E11 (1 – 10.5 ppm) 161
Figure 4-75^{1}H NMR spectrum of compound E11 (0.9 – 3.6 ppm) 162
Figure 4-76: ^{1}H NMR spectrum of compound E11 (7.2 – 10.8 ppm) 162

Figure 4-77: Mass spectrum of compound E11 163
Figure 4-78: IR spectrum of compound E12 164
Figure 4-79: ^{1}H-NMR spectrum of compound E12 (0 – 14 ppm) 165
Figure 4-80: ^{1}H-NMR spectrum of compound E12 (0.8 – 3.6 ppm) 165
Figure 4-81: ^{1}H-NMR spectrum of compound E12 (1 – 11 ppm) 165
Figure 4-82: Mass spectrum of compound E12 166
Figure 4-83: IR spectrum of compound E13 167
Figure 4-84: ^{1}H NMR spectrum of compound E13 (0 – 14 ppm) 168
Figure 4-85: ^{1}H NMR spectrum of compound E13 (2.6 – 10.6 ppm) 168
Figure 4-86: ^{1}H NMR spectrum of compound E13 (1.2 – 4 ppm) 169
Figure 4-87: ^{1}H NMR spectrum of compound E13 (7 – 10.5 ppm) 169
Figure 4-88: Mass spectrum of compound E13 170
Figure 4-89: IR spectrum of compound 4a 171
Figure 4-90: ^{1}H-NMR spectrum of compound 4a (0 – 9 ppm) 172
Figure 4-91: ^{1}H-NMR spectrum of compound 4a (6.8 – 8.4 ppm) 172
Figure 4-92: ^{13}C-NMR spectrum of compound 4a (0 – 200 ppm) 173
Figure 4-93: HSQC spectrum of compound 4a (2.2 – 8.6 ppm; 0 – 150 ppm) 174
Figure 4-94: HSQC spectrum of compound 4a (7.1 – 7.8 ppm; 124 – 133 ppm) 174
Figure 4-95: Mass spectrum of compound 4a 175
Figure 4-96: IR spectrum of compound 4b 176
Figure 4-97: ^{1}H-NMR spectrum of compound 4b (0 – 9 ppm) 177
Figure 4-98: ^{1}H-NMR spectrum of compound 4b (6.7 – 8.3 ppm) 178
Figure 4-99: APT spectrum of compound 4b (0 – 200 ppm) 179
Figure 4-100: APT spectrum of compound 4b (100 – 170 ppm) 179
Figure 4-101: HSQC spectrum of compound 4b 180
Figure 4-102: HSQC spectrum of compound 4b (6.7 – 8.5 ppm; 100 – 150 ppm) 181
Figure 4-103: Mass spectrum of compound 4b 181
Figure 4-104: IR spectrum of compound 4c 183
Figure 4-105: ^{1}H-NMR spectrum of compound 4c (0 – 11.5 ppm) 184
Figure 4-106: ^{1}H-NMR spectrum of compound 4c (5.4 – 8.2 ppm) 184
Figure 4-107: ^{13}C-NMR spectrum of compound 4c (0 – 200 ppm) 185
Figure 4-108: HSQC spectrum of compound 4c (-1 – 11 ppm; 0 – 140 ppm) 186
Figure 4-109: Mass spectrum of compound 4c 186

Figure 4-110: IR spectrum of compound 4d 188
Figure 4-111: ^{1}H-NMR spectrum of compound 4d (0 – 8.5 ppm) 189
Figure 4-112: ^{1}H-NMR spectrum of compound 4d (6.2 – 8.2 ppm) 189
Figure 4-113: ^{13}C-NMR spectrum of compound 4d (0 – 200 ppm) 190
Figure 4-114: Mass spectrum of compound 4d 190
Figure 4-115: IR spectrum of compound 4e 192
Figure 4-116: ^{1}H-NMR spectrum of compound 4e (0 – 8.5 ppm) 193
Figure 4-117: ^{1}H-NMR spectrum of compound 4e (6.5 – 8.1 ppm) 193
Figure 4-118: ^{13}C-NMR spectrum of compound 4e (0 – 200 ppm) 194
Figure 4-119: ^{13}C-NMR spectrum of compound 4e (103 – 170 ppm) 194
Figure 4-120: HSQC spectrum of compound 4e (2.5 – 8.5; 30 – 150 ppm) 195
Figure 4-121: HSQC spectrum of compound 4e (6.6 – 8.2; 100 – 145 ppm) 196
Figure 4-122: Mass spectrum of compound 4e 196
Figure 4-123: IR spectrum of compound 4f 198
Figure 4-124: ^{1}H-NMR spectrum of compound 4f (0 – 14 ppm) 198
Figure 4-125: ^{1}H-NMR spectrum of compound 4f (5.8 – 8.4 ppm) 199
Figure 4-126: ^{13}C-NMR spectrum of compound 4f (0 – 200 ppm) 199
Figure 4-127: ^{13}C-NMR spectrum of compound 4f (95 – 125 ppm) 200
Figure 4-128: ^{13}C-NMR spectrum of compound 4f (127 – 141 ppm) 200
Figure 4-129: ^{13}C-NMR spectrum of compound 4f (144 – 168 ppm) 201
Figure 4-130: HSQC spectrum of compound 4f (2 – 12; 0 – 140 ppm) 202
Figure 4-131: HSQC spectrum of compound 4f (6 – 8; 104 – 124 ppm) 202
Figure 4-132: HSQC spectrum of compound 4f (6 – 8; 104 – 124 ppm) 203
Figure 4-133: Mass spectrum of compound 4f 203
Figure 4-134: IR spectrum of compound 4g 205
Figure 4-135: ^{1}H-NMR spectrum of compound 4g (0 – 14 ppm) 206
Figure 4-136: ^{13}C-NMR spectrum of compound 4g (0 – 200 ppm) 206
Figure 4-137: Mass spectrum of compound 4g 207
Figure 4-138: IR spectrum of compound 4h 208
Figure 4-139: ^{1}H-NMR spectrum of compound 4h (0 – 14 ppm) 209
Figure 4-140: APT spectrum of compound 4h (0 – 200 ppm) 210
Figure 4-141: APT spectrum of compound 4h 210
Figure 4-142: IR spectrum of compound 4i 212

Figure 4-143: ^{1}H-NMR spectrum of compound 4i (0 – 14 ppm) 212
Figure 4-144: ^{1}H-NMR spectrum of compound 4i (0 – 200 ppm) 213
Figure 4-145: HSQC spectrum of compound 4i (0 – 12; 0 – 140 ppm) 214
Figure 4-146: HSQC spectrum of compound 4i (6.3 – 6.9; 98 – 118 ppm) 214
Figure 4-147: HSQC spectrum of compound 4i (6.7 – 8.1; 116 – 134 ppm) 215
Figure 4-148: HSQC spectrum of compound 4i (7.4 – 8.3; 137 – 148 ppm) 215
Figure 4-149: Mass spectrum of compound 4i 216
Figure 4-150: IR spectrum of compound 4j 217
Figure 4-151: ^{1}H-NMR spectrum of compound 4j (0 – 14 ppm) 218
Figure 4-152: ^{13}C-NMR spectrum of compound 4j (0 – 200 ppm) 219
Figure 4-153: HSQC spectrum of compound 4j (0 – 9; 0 – 140 ppm) 220
Figure 4-154: Mass spectrum of compound 4j 220
Figure 4-155: IR spectrum of compound 4k 222
Figure 4-156: ^{1}H-NMR spectrum of compound 4k (0 – 14 ppm) 223
Figure 4-157: ^{1}H-NMR spectrum of compound 4k (0 – 1.3 ppm) 223
Figure 4-158: ^{1}H-NMR spectrum of compound 4k (2.0 – 3.5 ppm) 224
Figure 4-159: ^{1}H-NMR spectrum of compound 4k (7.15 – 7.80 ppm) 224
Figure 4-160: ^{13}C-NMR spectrum of compound 4k (0 – 220 ppm) 225
Figure 4-161: ^{13}C-NMR spectrum of compound 4k (123 – 170 ppm) 225
Figure 4-162: IR spectrum of compound 4l 227
Figure 4-163: ^{1}H-NMR spectrum of compound 4l (0 – 14 ppm) 227
Figure 4-164: ^{13}C-NMR spectrum of compound 4l (0 – 220 ppm) 228
Figure 4-165: HSQC spectrum of compound 4l (0 – 14; 0 – 140 ppm) 229
Figure 4-166: Mass spectrum of compound 4l 229
Figure 4-167: IR spectrum of compound 4m 231
Figure 4-168: ^{1}H-NMR spectrum of compound 4m (0 – 14 ppm) 232
Figure 4-169: ^{13}C-NMR spectrum of compound 4m (0 – 220 ppm) 233
Figure 4-170: HSQC spectrum of compound 4m (0 – 8; 0 – 140 ppm) 234
Figure 4-171: Mass spectrum of compound 4m 234
Figure 4-172: IR spectrum of compound 4n 236
Figure 4-173: ^{1}H-NMR spectrum of compound 4n (0 – 14 ppm) 237
Figure 4-174: ^{13}C-NMR spectrum of compound 4n (0 – 200 ppm) 237
Figure 4-175: HSQC spectrum of compound 4n (0 – 8.5; 0 – 140 ppm) 238

Figure 4-176: Mass spectrum of compound 4n 239
Figure 4-177: IR spectrum of compound 4o 240
Figure 4-178: ^{1}H-NMR spectrum of compound 4o (0 – 14 ppm) 241
Figure 4-179: ^{13}C-NMR spectrum of compound 4o (0 – 200 ppm) 242
Figure 4-180: Mass spectrum of compound 4o 242
Figure 4-181: IR spectrum of compound 4p 244
Figure 4-182: ^{1}H-NMR spectrum of compound 4p (0 – 14 ppm) 244
Figure 4-183: ^{1}H-NMR spectrum of compound 4p (1 – 8 ppm) 245
Figure 4-184: ^{1}H-NMR spectrum of compound 4p (1.5 – 8 ppm) 245
Figure 4-185: IR spectrum of compound 4q 247
Figure 4-186: ^{1}H-NMR spectrum of compound 4q (0 – 14 ppm) 247
Figure 4-187: ^{1}H-NMR spectrum of compound 4q (0 – 14 ppm) 248
Figure 4-188: ^{13}C-NMR spectrum of compound 4q (0 – 200 ppm) 248
Figure 4-189: Mass spectrum of compound 4q 249
Figure 4-190: IR spectrum of compound 4r 250
Figure 4-191: ^{1}H-NMR spectrum of compound 4r (0 – 14 ppm) 251
Figure 4-192: ^{13}C-NMR spectrum of compound 4r (0 – 180 ppm) 252
Figure 4-193: IR spectrum of compound 4s 253
Figure 4-194: ^{1}H-NMR spectrum of compound 4s (0 – 14 ppm) 254
Figure 4-195: ^{13}C-NMR spectrum of compound 4s (0 – 220 ppm) 255
Figure 4-196: HSQC spectrum of compound 4s (1 – 8; 0 – 140 ppm) 256
Figure 4-197: Mass spectrum of compound 4s 256
Figure 4-198: IR spectrum of compound 4t 258
Figure 4-199: ^{1}H-NMR spectrum of compound 4t (0 – 14 ppm) 258
Figure 4-200: ^{1}H-NMR spectrum of compound 4t (1.5 – 5 ppm) 259
Figure 4-201: ^{1}H-NMR spectrum of compound 4t (6.5 – 8 ppm) 259
Figure 4-202: ^{13}C-NMR spectrum of compound 4t (0 – 220 ppm) 260
Figure 4-203: ^{13}C-NMR spectrum of compound 4t (20 – 110 ppm) 260
Figure 4-204: ^{13}C-NMR spectrum of compound 4t (125 – 175 ppm) 261
Figure 4-205: Mass spectrum of compound 4t 261
Figure 4-206: IR spectrum of compound 4u 263
Figure 4-207: ^{1}H-NMR spectrum of compound 4u (0 – 13 ppm) 264
Figure 4-208: ^{1}H-NMR spectrum of compound 4u (1 – 5 ppm) 264

Figure 4-209: ^{1}H-NMR spectrum of compound 4u (6.4 – 7.8 ppm) 264
Figure 4-210: ^{13}C-NMR spectrum of compound 4u (0 – 200 ppm) 265
Figure 4-211: ^{13}C-NMR spectrum of compound 4u (20 – 104 ppm) 265
Figure 4-212: ^{13}C-NMR spectrum of compound 4u (120 – 175 ppm) 266
Figure 4-213: HSQC spectrum of compound 4u (2 – 8; 0 – 140 ppm) 267
Figure 4-214: HSQC spectrum of compound 4u (6 – 7.3; 85 – 125 ppm) 267
Figure 4-215: HSQC spectrum of compound 4u (7.1 – 7.9; 123 – 133 ppm) 268
Figure 4-216: Mass spectrum of compound 4u 268
Figure 4-217: IR spectrum of compound 4v 270
Figure 4-218: ^{1}H-NMR spectrum of compound 4v (0 – 14 ppm) 271
Figure 4-219: APT spectrum of compound 4v (0 – 200 ppm) 272
Figure 4-220: Mass spectrum of compound 4v 272
Figure 4-221: A) Crystal structure of compound E3 illustrated with thermal ellipsoids drawn at 50% probability to show the spatial arrangement of atoms. B) Molecular packing showing intermolecular hydrogen bondings. 273
Figure 4-222: A) Crystal structure of compound E8 illustrated with thermal ellipsoids drawn at 50% probability to show the spatial arrangement of atoms. B) Molecular packing showing intermolecular hydrogen bonding. 277
Figure 4-223: Crystal packing of compound E8 showing probable π – π interactions between the benzenesulfonamide rings. 278
Figure 4-224: A) Crystal structure of compound 4e illustrated with thermal ellipsoids drawn at 50% probability to show the spatial arrangement of atoms. B) Molecular packing showing intermolecular hydrogen bondings. 282
Figure 4-225: Crystal packing of compound 4e 283
Figure 4-226: (A) The binding pose of 3,5-diphenylbenzenesulfonamide (green) in the active site of hCAIX (6TL5). The grey sphere represents the Zn^{2+}. Pink dashed lines represent metal coordination. Yellow dashed lines represent hydrogen bond. (B) Binding interactions observed for at least 30% of the 250 ns MD simulation. Green represents hydrophobic amino acid (aa), blue represents polar aa, red represents negatively charged aa. (C) Histogram of protein-ligand contacts, with green indicating hydrogen bonds, blue indicating water-bridged hydrogen bonds, red indicating ionic bonds and grey indicating hydrophobic interactions. (D) RMSD plot of the protein Cα-

atoms (blue) and ligand (red). (E) Protein-ligand interaction energy (kcal/mol) throughout the MD simulation. 291
Figure 4-227: (A) The binding pose of 4-chloro-2-cyclohexylsulfanyl-*N*-(2-hydroxyethyl)-5-sulfamoylbenzamide (green) in the active site of hCAXII (6R6Y). The grey sphere represents the Zn^{2+}. Pink dashed lines represent metal coordination. Yellow dashed lines represent hydrogen bond. (B) Binding interactions observed for at least 30% of the 250 ns MD simulation. Green represents hydrophobic amino acid (aa), blue represents polar aa, red represents negatively charged aa. (C) Histogram of protein-ligand contacts, with green indicating hydrogen bonds, blue indicating water-bridged hydrogen bonds, red indicating ionic bonds and grey indicating hydrophobic interactions. (D) RMSD plot of the protein Cα-atoms (blue) and ligand (red). (E) Protein-ligand interaction energy (kcal/mol) throughout the MD simulation. 293
Figure 4-228: (A) The docked pose of compound 4f (green) in the active site of hCAIX (5FL6). The grey sphere represents the Zn^{2+}. Pink dashed lines represent metal coordination. Yellow dashed lines represent hydrogen bonds. Turquoise dashed lines represent π-π stacking. (B) Binding interactions observed for at least 30% of the 250 ns MD simulation. Green represents hydrophobic amino acid (aa), blue represents polar aa, red represents negatively charged aa. (C) Histogram of protein-ligand contacts, with green indicating hydrogen bonds, blue indicating water-bridged hydrogen bonds, red indicating ionic bonds and grey indicating hydrophobic interactions. (D) RMSD plot of the protein Cα-atoms (blue) and ligand (red). (E) Protein-ligand interaction energy (kcal/mol) throughout the MD simulation. 295
Figure 4-229: (A) The docked pose of compound 4f (green) in the active site of hCAIX (6TL5). The grey sphere represents the Zn^{2+}. Pink dashed lines represent metal coordination. Yellow dashed lines represent hydrogen bonds. Turquoise dashed lines represent π-π stacking. (B) Binding interactions observed for at least 30% of the 250 ns MD simulation. Green represents hydrophobic amino acid (aa), blue represents polar aa, and red represents negatively charged aa. (C) Histogram of protein-ligand contacts, with green indicating hydrogen bonds, blue indicating water-bridged hydrogen bonds, red indicating ionic bonds and grey indicating hydrophobic interactions. (D) RMSD plot of the protein Cα-atoms (blue) and ligand (red). (E) Protein-ligand interaction energy (kcal/mol) throughout the MD simulation. 297

Figure 4-230: (A) The docked pose of compound 4f (green) in the active site of hCAXII (6R6Y). The grey sphere represents the Zn^{2+}. Pink dashed lines represent metal coordination. Yellow dashed lines represent hydrogen bonds. Turquoise dashed lines represent π-π stacking. (B) Binding interactions observed for at least 30% of the 250 ns MD simulation. Green represents hydrophobic amino acid (aa), blue represents polar aa, red represents negatively charged aa. (C) Histogram of protein-ligand contacts, with green indicating hydrogen bonds, blue indicating water-bridged hydrogen bonds, red indicating ionic bonds and grey indicating hydrophobic interactions. (D) RMSD plot of the protein Cα-atoms (blue) and ligand (red). (E) Protein-ligand interaction energy (kcal/mol) throughout the MD simulation. 299
Figure 4-231: (A) The docked pose of compound 4i (green) in the active site of hCAIX (6TL5). The grey sphere represents the Zn^{2+}. Pink dashed lines represent metal coordination. Yellow dashed lines represent hydrogen bond. (B) Binding interactions observed for at least 30% of the 250 ns MD simulation. Green represents hydrophobic amino acid (aa), blue represents polar aa, red represents negatively charged aa. (C) Histogram of protein-ligand contacts, with green indicating hydrogen bonds, blue indicating water-bridged hydrogen bonds, red indicating ionic bond and grey indicating hydrophobic interactions. (D) RMSD plot of the protein Cα-atoms (blue) and ligand (red). (E) Protein-ligand interaction energy (kcal/mol) throughout the MD simulation. 301
Figure 4-232: (A) The docked pose of compound 4i (green) in the active site of hCAXII (1JD0). The grey sphere represents the Zn^{2+}. Pink dashed lines represent metal coordination. Yellow dashed lines represent hydrogen bonds. Turquoise dashed lines represent π-π stacking. Green dashed lines represent cation – π interaction (B) Binding interactions observed for at least 30% of the 250 ns MD simulation. Green represents hydrophobic amino acid (aa), blue represents polar aa, red represents negatively charged aa. (C) Histogram of protein-ligand contacts, with green indicating hydrogen bonds, blue indicating water-bridged hydrogen bonds, red indicating ionic bonds and grey indicating hydrophobic interactions. (D) RMSD plot of the protein Cα-atoms (blue) and ligand (red). (E) Protein-ligand interaction energy (kcal/mol) throughout the MD simulation. 303
Figure 4-233: The docked pose of compound 4o (green) in the active site of hCAXI (6TL5). The grey sphere represents the Zn^{2+}. Pink dashed lines represent metal

coordination. Yellow dashed lines represent hydrogen bonds. Turquoise dashed lines represent π-π stacking. (B) Binding interactions observed for at least 30% of the 250 ns MD simulation. Green represents hydrophobic amino acid (aa), blue represents polar aa, red represents negatively charged aa. (C) Histogram of protein-ligand contacts, with green indicating hydrogen bonds, blue indicating water-bridged hydrogen bonds, red indicating ionic bonds and grey indicating hydrophobic interactions. (D) RMSD plot of the protein Cα-atoms (blue) and ligand (red). (E) Protein-ligand interaction energy (kcal/mol) throughout the MD simulation. 305
Figure 4-234: The docked pose of compound 4o (green) in the active site of hCAXII (5LL5). The grey sphere represents the Zn^{2+}. Pink dashed lines represent metal coordination. Yellow dashed lines represent hydrogen bonds. Turquoise dashed lines represent π-π stacking. (B) Binding interactions observed for at least 30% of the 250 ns MD simulation. Green represents hydrophobic amino acid (aa), blue represents polar aa, red represents negatively charged aa. (C) Histogram of protein-ligand contacts, with green indicating hydrogen bonds, blue indicating water-bridged hydrogen bonds, red indicating ionic bonds and grey indicating hydrophobic interactions. (D) A timeline representation of the interactions and contacts (0 – 250 ns). (E) RMSD plot of the protein Cα-atoms (blue) and ligand (red). (F) Protein-ligand interaction energy (kcal/mol) throughout the MD simulation. 307
Figure 4-235: The docked pose of compound 4o (green) in the active site of hCAXII (6R6Y). The grey sphere represents the Zn^{2+}. Pink dashed lines represent metal coordination. Yellow dashed lines represent hydrogen bonds. Turquoise dashed lines represent π-π stacking. (B) Binding interactions observed for at least 30% of the 250 ns MD simulation. Green represents hydrophobic amino acid (aa), blue represents polar aa, red represents negatively charged aa. (C) Histogram of protein-ligand contacts, with green indicating hydrogen bonds, blue indicating water-bridged hydrogen bonds, red indicating ionic bonds and grey indicating hydrophobic interactions. (D) RMSD plot of the protein Cα-atoms (blue) and ligand (red). (E) Protein-ligand interaction energy (kcal/mol) throughout the MD simulation. 308
Figure 4-236: The docked pose of compound 4t (green) in the active site of hCAIX (6TL5). The grey sphere represents the Zn^{2+}. Pink dashed lines represent metal coordination. Yellow dashed lines represent hydrogen bond. Turquoise dashed lines represent π-π stacking. (B) Binding interactions observed for at least 30% of the 250 ns

MD simulation. (C) Binding interactions observed for at least 30% of the last 70 ns of the MD simulation. Green represents hydrophobic amino acid (aa), blue represents polar aa, red represents negatively charged aa. (D) Histogram of protein-ligand contacts, with green indicating hydrogen bonds, blue indicating water-bridged hydrogen bonds, red indicating ionic bond and grey indicating hydrophobic interactions. (E) A timeline representation of the interactions and contacts (180 – 250 ns). (F) RMSD plot of the protein Cα-atoms (blue) and ligand (red). (G) Protein-ligand interaction energy (kcal/mol) throughout the MD simulation. 311

Figure 4-237: The docked pose of compound 4t (green) in the active site of hCAXII (6R6Y). The grey sphere represents the Zn^{2+}. Pink dashed lines represent metal coordination. Yellow dashed lines represent hydrogen bonds. Turquoise dashed lines represent π-π stacking. (B) Binding interactions observed for at least 30% of the 250 ns MD simulation. (C) Binding interactions observed for at least 30% of the last 50 ns of the MD simulation. Green represents hydrophobic amino acid (aa), blue represents polar aa, red represents negatively charged aa. (D) Histogram of protein-ligand contacts, with green indicating hydrogen bonds, blue indicating water-bridged hydrogen bonds, red indicating ionic bonds and grey indicating hydrophobic interactions. (E) A timeline representation of the interactions and contacts (180 – 250 ns). (F) RMSD plot of the protein Cα-atoms (blue) and ligand (red). (G) Protein-ligand interaction energy (kcal/mol) throughout the MD simulation. 313

Figure 4-238: The docked pose of compound 4u (green) in the active site of hCAIX (6TL5). The grey sphere represents the Zn^{2+}. Pink dashed lines represent metal coordination. Yellow dashed lines represent hydrogen bonds. (B) Binding interactions observed for at least 30% of the 250 ns MD simulation. Green represents hydrophobic amino acid (aa), blue represents polar aa, red represents negatively charged aa. (C) Histogram of protein-ligand contacts, with green indicating hydrogen bonds, blue indicating water-bridged hydrogen bonds, red indicating ionic bonds and grey indicating hydrophobic interactions. (D) The Ligand Root Mean Square Fluctuation. (E) RMSD plot of the protein Cα-atoms (blue) and ligand (red). (F) Protein-ligand interaction energy (kcal/mol) throughout the MD simulation. 315

Figure 4-239: A) The docked pose of compound 4u (green) in the active site of hCAXII (6R6Y). The grey sphere represents the Zn^{2+}. Pink dashed lines represent metal coordination. Yellow dashed lines represent hydrogen bonds. Purple dashed lines

represent halogen bond (B) Binding interactions observed for at least 30% of the 250 ns MD simulation. Green represents hydrophobic amino acid (aa), blue represents polar aa, red represents negatively charged aa. (C) Histogram of protein-ligand contacts, with green indicating hydrogen bonds, blue indicating water-bridged hydrogen bonds, red indicating ionic bonds and grey indicating hydrophobic interactions. (D) RMSD plot of the protein Cα-atoms (blue) and ligand (red). (E) Protein-ligand interaction energy (kcal/mol) throughout the MD simulation. 316
Figure 5-1: IR spectrum of compound B1 321
Figure 5-2: IR spectrum of compound B2 321
Figure 5-3: Comparative IR spectrum of compounds of A2 and B2. Red represents A2 and black represents B2. 322
Figure 5-4: IR spectrum of compound C1 324
Figure 5-5: IR spectrum of compound C2 324
Figure 5-6: IR spectra of D1, D3 and D9 obtained from SDBS 329
Figure 5-7: ^{1}H NMR Spectrum of compound E7. 337
Figure 5-8: ^{1}H NMR Spectrum of compound E8. 338
Figure 5-9: ^{1}H NMR spectrum of A) anethole (6.676 – 7.32 ppm). B) *p*-chloronitrobenzene (7.48 – 8.20 ppm) 340
Figure 5-10: ^{13}C NMR spectrum of E1 (122 – 176 ppm) 349
Figure 5-11: HSQC spectrum of compound E1 350
Figure 5-12: Mass spectrum of compound E2 351
Figure 5-13: Mass spectrum of compound E6 352
Figure 5-14: Mass spectrum of compound E8 353
Figure 5-15: Desulfurization pathways of compound E8 353
Figure 5-16: Mass spectrum of compound E13 354
Figure 5-17: Comparative IR spectrum of compounds of E1 and 4a. Green represents E1 and black represents 4a. 361
Figure 5-18: ^{1}H-NMR spectrum of compound 4o (6.7 – 8 ppm) 369
Figure 5-19: ^{1}H-NMR spectrum of compound 4r (6.6 – 7.85 ppm) 370
Figure 5-20: ^{1}H-NMR spectrum of compound 4r (0.9 – 2.3 ppm) 371
Figure 5-21: ^{1}H-NMR spectrum of compound 4j (6.3 – 8.3 ppm) 372
Figure 5-22: ^{13}C NMR spectrum of compound 4a 380
Figure 5-23: HSQC spectrum of compound 4a 382

Figure 5-24: APT spectrum of compound 4b 383
Figure 5-25: ^{13}C-NMR spectrum of compound 4o 385
Figure 5-26: ^{13}C-NMR spectrum of compound 4m 386
Figure 5-27: HSQC spectrum of compound 4m 387
Figure 5-28: Mass spectrum of compound 4b 395
Figure 5-29: Mass spectrum of compound 4g 396
Figure 5-30: Docked pose of compound 4h in A) hCAIX (PDB: 3IAI). B) hCAIX (PDB: 6TL5) 409

TABLE OF SCHEMES

Scheme 2-1: The reversible hydration of CO_2 to HCO_3^- 30
Scheme 2-2: Reactions catalyzed by CAs (Supuran 2016b) 31
Scheme 2-3: Conversion of Prontosil to sulfanilamide 51
Scheme 2-4: General synthesis of sulfonamides 52
Scheme 2-5: Synthesis of isothiocyanate derivatives from amines and thiophosgene ... 61
Scheme 2-6: Synthesis of isothiocyanatobenzene from aniline and DPT 61
Scheme 2-7: Synthesis of DPT 61
Scheme 2-8: Synthesis of isothiocyanates from azides 62
Scheme 2-9: Synthesis of 4-isothiocyanatobenzenesulfonamide from CS_2 and TEA 62
Scheme 2-10: Synthesis of isothiocyanates from amines and CS_2 using DMT/NMM/TsO^- catalyst. 63
Scheme 2-11: General synthesis of thiosemicarbazides from isothiocyanates and hydrazine 63
Scheme 2-12: General synthesis of thiosemicarbazides starting from alkylamines using KOH and CS_2 64
Scheme 2-13: General synthesis of thiosemicarbazides starting from arylamines using KOH and CS_2 64
Scheme 2-14: Thione-thiol tautomerism of TSCs 65
Scheme 2-15: General synthesis of TSC 67
Scheme 2-16: Hydrazone-azine tautomerism 71
Scheme 2-17: Some aromatic nucleophilic and electrophilic substitutions of thiazole . 75
Scheme 2-18: The general synthesis scheme of Hantzsch's synthesis 77
Scheme 2-19: Thiazole synthesis from the condensation of chloroacetaldehyde with thioformamide 77
Scheme 2-20: The general synthesis of 2-aminothiazole derivatives 78
Scheme 2-21: General synthesis of 2-imino-4-thiazoline derivatives from thioureas and α-haloketones 78
Scheme 2-22: General synthesis of 2-phenylamino-4-thiazole derivatives from aniline and α-haloketones using sodium/potassium thiocyanate 78
Scheme 2-23: General synthesis of 2-imino-4-thiazoline and 2-hydrazino-4-thiazoline derivatives 79

Scheme 2-24: General synthesis of 2-azino/hydrazino-4-thiazoline derivatives..... 79
Scheme 2-25: The general synthesis scheme of the Cook-Heilbron synthesis..... 80
Scheme 2-26: The general synthesis scheme of the Gabriel synthesis..... 80
Scheme 2-27: The general synthesis scheme of the Erlenmeyer synthesis 81
Scheme 2-28: The general synthesis scheme of the 2.9.2.5. Tcherniac's Synthesis..... 81
Scheme 3-1: General Synthesis Scheme of 3/4-[4-(Non)substitutedphenyl-2-(alkylidene/arylidenehydrazinylidene)-1,3-thiazol-3(*2H*)-yl]benzenesulfonamide derivatives (4a – 4v) 98
Scheme 5-1: Genera synthesis pathway of 3/4-[4-(Non)substitutedphenyl-2-(alkylidene/arylidenehydrazinylidene)-1,3-thiazol-3(2*H*)-yl]benzenesulfonamide derivatives (4a-4v) starting from 3/4-aminobenzenesulfonamide 319
Scheme 5-2: Synthesis mechanism of 3/4-Isothiocyanatobenzenesulfonamide (B) 320
Scheme 5-3: Synthesis mechanism of *N*-(3/4-sulfamoylphenyl)hydrazinecarbothioamide (C) 323
Scheme 5-4: Synthesis of 2-(Alkylidene/arylidene)-*N*-(3/4-sulfamoylphenyl)hydrazine-1-carbothioamide derivatives (E)..... 325
Scheme 5-5: Proposed synthesis mechanism of 2-(Alkylidene/arylidene)-*N*-(3/4-sulfamoylphenyl)hydrazine-1-carbothioamide derivatives (E) 328
Scheme 5-6: Synthesis of 3/4-[4-(Non)substitutedphenyl-2-(alkylidene/arylidenehydrazinylidene)-1,3-thiazol-3(*2H*)-yl]benzenesulfonamide derivatives (4a-4v) showing possible hydrazo/azine tautomerism 355
Scheme 5-7: Proposed synthesis mechanism of 3/4-[4-(Non)substitutedphenyl-2-(alkylidene/arylidenehydrazinylidene)-1,3-thiazol-3(*2H*)-yl]benzenesulfonamide derivatives (4a-4v) 356
Scheme 5-8: Synthesis of 3/4-[4-(Non)substitutedphenyl-2-(alkylidene/arylidenehydrazinylidene)-1,3-thiazol-3(*2H*)-yl]benzenesulfonamide derivatives (4a-4v) proceeding through thione – thiol tautomerism between thione and N_2 357

LIST OF SYMBOLS / ABBREVIATIONS

Å: Angstrom

3D: Three-dimensional

µg: Microgram

5-FU: 5-fluorouracil

app.d: Apparent doublet

app.dd: Apparent doublet of doublets

app.t: Apparent triplet

ATP: Adenosine triphosphate

APT: Attached proton test

Ar: Aromatic

AAZ: Acetazolamide

CA: Carbonic anhydrase

CADD: Computer-aided drug design

CAI: Carbonic anhydrase inhibitor

CARP: Carbonic anhydrase-related proteins

Covid-19: Coronavirus disease

COX: Cyclooxygenase

DNA: Deoxyribonucleic acid

d: Doublet

dd: Doublet of doublets

ddd: Doublet of doublets of doublets

DMEM: Dulbecco's Modified Eagle Medium

DMSO: Dimethyl sulfoxide

dt: Doublet triplet

eq: Equivalent

ECM: Extracellular matrix

FEP: Free energy perturbation

FBS: Fetal bovine serum

fs: Femtosecond

GLUT: Glucose transporter

g: Gram

HTS: High-throughput screening

HIF: Hypoxia-inducible factor

hCA: Human carbonic anhydrase

HIV: Human immunodeficiency virus

HSQC: Heteronuclear Single Quantum Correlation

HUVEC: Umbilical Vein Endothelial control cells

IC_{50}: The half maximal inhibitory concentration

IR: Infrared

TLC: Thin layer chromatography

*K*i: Inhibition constant

K_{cat}/K_m: Catalytic efficiency of a given enzyme

LC-MS: Liquid chromatography–mass spectrometry

LBD: Ligand-based design

m: Multiplet

MD: Molecular dynamics

MM-GBSA: Molecular Mechanics with Generalised Born and Surface Area Solvation

MM-PBSA: Molecular Mechanics Poisson-Boltzmann Surface Area

MHz: Megahertz

mL: Millilitre

NAD: Nicotinamide adenine dinucleotide

NADH: Reduced nicotinamide adenine dinucleotide

nM: Nanomolar

ns: Nanoseconds

NSAID: Non-steroidal anti-inflammatory drug

NCD: Non-communicable diseases

NMR: Nuclear magnetic resonance

ppm: Parts per million

PDB: Protein Data Bank

PHD: Prolyl hydroxylase enzyme

QSAR: Quantitative structure-activity relationship

q: Quartet

RMSD: Root Mean Square Deviation

RO5: Lipinski's Rule of Five

SP: Standard precision

s: Singlet

SBD: Structure-based design

TI: Thermodynamic integration

TSC: Thiosemicarbazone

TME: Tumour microenvironment

t: Triplet

td: Triplet of doublets

VEGF: Vascular endothelial growth factor

VEGFR: Vascular endothelial growth factor receptor

VS: Virtual screening

VHL: von Hippel–Lindau

XRD: X-ray diffractometry

XP: Extra precision

ZBG: Zinc Binding Group

ABSTRACT

Trawally, M. (2023). Studies on novel 4-thiazoline-containing benzenesulfonamide derivatives targeting the tumour-associated human carbonic anhydrase IX and XII enzymes for cancer therapy. Istanbul University, Institute of Health Sciences, Department of Pharmaceutical Chemistry. Doctoral Thesis. Istanbul.

Cancer is a group of fatal diseases that can affect any part of the body. Cancer cells proliferate and multiply uncontrollably, metastasizing into other tissues and organs. They are insensitive to most available anticancer drugs and radiotherapy due to their heterogenous microenvironment characterised by hypoxia and acidosis. Carbonic anhydrases (CAs) are widespread metalloenzymes with the core function of catalysing the interconversion of CO_2 and HCO_3^-. Human CAs IX (hCAIX) and XII (hCAXII), also known as the tumour-associated carbonic anhydrase, are upregulated in various cancer types, causing hypoxia-induced acidosis, metastasis, and chemoresistance. Inhibitors of hCAIX and hCAXII have emerged as a promising area of research to develop more effective cancer treatments that can combat acidosis and reduce the insensitivity of cancer cells towards chemotherapy and radiotherapy. Based on the structure of (*Z*)-4-(4-(4-bromophenyl)-2-(pentan-3-ylidenehydrazineylidene)thiazol-3(2*H*)-yl)benzenesulfonamide which was previously synthesised by Prof. Dr. Özlen Güzel-Akdemir and selected as a lead molecule against hCAIX and hCAXII, 3/4-[4-(Non)substitutedphenyl-2-(alkylidene/arylidenehydrazinylidene)-1,3-thiazol-3(2*H*)-yl] benzenesulfonamide derivatives (**4a** – **4v**) were designed using computer-aided drug design techniques. Intermediate compounds (**E1 – E13**) and compounds **4a** – **4v** were synthesised and their structures and purities were confirmed with elemental and spectroscopic analyses. The configurations of compounds **E3**, **E8**, and **4e** were determined using single crystal X-ray diffraction studies. The inhibitory properties of compounds **E1 – E13** and **4a – 4v** against hCAIX and hCAXII, as well as the off-target hCAI and hCAII were investigated. Compounds **E1 – E13** showed promising inhibition profiles against the isoenzymes at nanomolar concentrations but lacked selectivity for hCAIX and hCAXII over hCAI and hCAII except for compound **E2**. In addition to their nanomolar inhibition of hCAIX and hCAXII, compounds **4a – 4v** generally exhibited significant selectivity towards hCAIX and hCAXII over hCAI and hCAII. Among them, compound **4u** showed the highest selectivity, with selectivity indexes of 531.4 and 646.8 for hCAIX and hCAXII, respectively. Selected compounds from **4a – 4v** derivatives were assessed for their anticancer activity against ECC-1, MCF-7, A549, HT-29, U118-MG, and Caco-2 cancer cell lines. Compound **4g** emerged as the most potent and selective compound and, in most cases, demonstrated better cytotoxicity and selectivity than the reference compound, 5-fluorouracil. Molecular modelling studies were conducted to understand the carbonic anhydrase inhibition data and the SAR of compounds **4a – 4v.**

Keywords: Carbonic anhydrase, anticancer, 4-thiazoline, benzenesulfonamide, molecular modelling.

The present work was supported by Scientific and Technological Research Council of Türkiye (TÜBİTAK). Project No. 118S580

ÖZET

Trawally, M. (2023). Tümör-ilişkili İnsan Karbonik Anhidraz IX ve XII enzimlerini hedef alan antikanser etki gösterebilecek benzensülfonamid artığı taşıyan yeni 4-tiyazolin türevleri üzerinde çalışmalar. İstanbul Üniversitesi Sağlık Bilimleri Enstitüsü, Farmasötik Kimya Anabilim Dalı. Doktora Tezi. İstanbul.

Kanser, vücudun herhangi bir bölümünü etkileyebilen ölümcül bir hastalık grubudur. Kanser hücreleri kontrolsüz bir şekilde büyüyerek ve çoğalarak diğer doku ve organlara metastaz yapar. Kanser hücreleri, hipoksi ve asidoz ile karakterize olmuş heterojen mikroçevresi nedeniyle antikanser ilaçların çoğuna ve radyoterapiye karşı duyarsızdır. Karbonik anhidrazlar (CA), CO_2 ve HCO_3^-'ün reversibl dönüşümünü katalize eden yaygın metaloenzimlerdir. Tümör-ilişkili CA olarak da bilinen insan CAIX (hCAIX) ve XII (hCAXII), çeşitli kanser türlerinde upregüle edilerek hipoksi kaynaklı asidoz, metastaz ve kemorezistansa neden olur. hCAIX ve hCAXII inhibitörleri, asidozu azaltarak ve kanser hücrelerinin kemoterapi ve radyoterapiye karşı duyarsızlığını azaltarak daha etkili kanser tedavileri geliştirmek için umut verici bir araştırma alanı olarak ortaya çıkmıştır. Daha önce Prof. Dr. Özlen Güzel-Akdemir tarafından sentezlenen ve hCAIX ve hCAXII'ye karşı öncü molekül olarak seçilen (*Z*)-4-(4-(4-bromofenil)-2-(pentan-3-ilidenhidrazineliden)tiyazol-3(2*H*)-il)benzensülfonamidin yapısına göre, bilgisayar destekli ilaç tasarım teknikleri kullanılarak 3/4-[4-(Non)substitüefenil-2-(alkiliden/arilidenhidraziniliden)-1,3-tiyazol-3(2*H*)-il] benzensülfonamid türevleri (**4a – 4v**) tasarlanmıştır. 13 ara bileşik (**E1 – E13**) ve **4a – 4v** bileşikler sentezlenmiş, yapıları ve saflıkları elementel ve spektroskopik analizlerle doğrulanmıştır. **E3**, **E8** ve **4e** bileşikleri üzerinde tek kristal X-ışınları difraktometresi çalışmaları yapılarak konfigürasyonları belirlenmiştir. **E1 – E13** ve **4a – 4v** bileşiklerinin tümör ilişkili hCAIX ve hCAXII'nin yanı sıra hedef dışı hCAI ve hCAII izoenzimlere karşı enzim inhibisyon etkileri araştırılmıştır. **E1 – E13** bileşikleri genel olarak nanomolar düzeyde izoenzimlere karşı güçlü inhibisyon profilleri göstermiştir; ancak bileşik **E2** dışında, hCAIX ve hCAII'a karşı seçicilik göstermemiştir. **4a – 4v** bileşikleri hCAIX ve hCAXII enzimlerine karşı nanomolar düzeyde güçlü inhibisyonu göstermek ile birlikte hCAIX ve hCAXII'ye karşı önemli seçicilik sergilemiştir. En seçici olan bileşik **4u** hCAIX ve hCAXII için sırasıyla 531.4 ve 646.8'lik seçicilik indeksleri göstermiştir. Hedef bileşiklerden seçilen bazılarının ECC-1, MCF-7, A549, HT-29, U118-MG ve Caco-2 kanser hücre hatlarına karşı antikanser aktiviteleri araştırılmıştır. Bileşik **4g** en güçlü ve en seçici bileşik olarak etki göstererek çoğu durumda referans bileşik olan 5-florourasil'den daha iyi sitotoksisite ve seçicilik göstermiştir. Karbonik anhidraz inhibisyon sonuçlarını ve bileşiklerin yapı-etki ilişkilerini daha iyi aydınlatmak için ileri moleküler modelleme teknikleri kullanılmıştır.

Anahtar Kelimeler: Karbonik anhidraz, antikanser, 4-tiyazolin, benzensülfonamid, moleküler modelleme.

Bu çalışma, Türkiye Bilimsel ve Teknolojik Araştırma Kurumu (TÜBİTAK) tarafından desteklenmiştir. Proje No: 118S580.

1. INTRODUCTION AND AIM

Cancer is a group of diseases, often caused by genetic or environmental factors, that affect any area of the body when cells divide and multiply in an uncontrolled manner and invade other tissues and organs (metastasis). According to a recent cancer epidemiological study, cancer is the second leading cause of death worldwide, claiming the lives of approximately 10 million people in 2020 (Sung et al. 2021; Siegel et al. 2022). Statistically, cancer accounts for 1 in every 6 deaths and it is predicted to claim the lives of 12.9 – 17 million people in 2030 (Solomon and Mulugeta 2019; Cancer Tomorrow 2022).

Tumours can either be benign or malignant cancer. Benign tumours are localized and affect the place of origin whiles malignant tumours are lethal because of their ability to metastasize and affect other tissues or organs through the vascular and lymphatic systems. Treatment choices for cancer include both surgical intervention and non-surgical approaches such as radiotherapy, chemotherapy and immune therapy. In cancer treatment, the main objective is to show anticancer effects by targeting only cancer cells with certain mechanisms of action without harming other healthy tissues and organs (selective cytotoxicity) whiles preventing recurrence and metastases that may occur after treatment (Mansoori et al. 2017). However, these therapies are often very toxic due to the lack of selectivity in targeting tumour cells and ineffective due to the insensitivity of tumour cells called cell "defiance". It is known that this behaviour of tumour cells is due to the heterogeneity of the microenvironment caused by hypoxia and its consequences (Ondriskova et al. 2015; Rani et al. 2022). The heterogeneous tumour microenvironment is required for metastasis, cancer malignancy and chemoresistance (Hass et al. 2020). As a result, it is necessary to develop novel anticancer molecules that can disrupt the microenvironment of cancer cells and target only cancer cells while sparing healthy tissues.

Carbonic anhydrases are metalloenzymes that reversibly catalyse the hydration of carbon dioxide to proton and bicarbonate, an important physiological reaction, and are involved in many pathological conditions such as cancer, glaucoma, and central nervous system diseases. There are eight evolutionarily independent types namely α, β, γ, δ, ζ, η, θ, and ι-CAs (Nocentini et al. 2021). In mammals, 16 different α-CAs have been isolated, with different important physiological roles (Chegwidden 2021). Tumour-associated hCAIX and hCAXII, which are carbonic anhydrase enzymes found in many different tissues in humans,

have an important role in hypoxia-induced acidosis, metastasis, and chemoresistance (Mboge et al. 2018; Tars and Matulis 2019). In this context, molecules that selectively inhibit tumour-associated hCAIX and hCAXII enzymes that are overexpressed in tumour cells are important in the treatment of cancer types that are insensitive to cancer treatment methods.

Sulfonamides and their isosteres are the most celebrated metal ion-binding groups that effectively inhibit carbonic anhydrases. Many sulfonamide-containing molecules have been reported to have various pharmacological activities, including anticancer activity, by inhibiting carbonic anhydrases (Carta et al. 2014).

Thiazole is an important scaffold present in numerous biological products and drugs. Together with its anticancer activity, it demonstrates many biological activities, which makes it widely studied and a privileged scaffold in drug discovery (Altıntop et al. 2014; Ayati et al. 2019). Dasatinib and Dabrafenib, which are tyrosine kinase inhibitors, are thiazole derivatives with anticancer effects (Ayati et al. 2019). Thiazoline, which is a saturated form of thiazole, is reported to have important biological activities such as anticancer in drug research (Altıntop et al. 2014). In addition, benzenesulfonamides containing either thiazole or thiazoline moieties were reported as effective hCAIX or hCAXII inhibitors (Čapkauskaitė et al. 2018; Distinto et al. 2019; Meleddu et al. 2018).

Schiff bases are important compounds with various biological activities. Recently, the anticancer effect of Schiff bases has attracted the attention of researchers. Güzel-Akdemir et al. also reported sulfonamide compounds containing Schiff base as potential inhibitors of hCAIX and hCAXII enzymes (Güzel-Akdemir et al. 2015). Azine, known as bis-Schiff base, is an important bridging system widely used in heterocyclic chemistry. Some azine-derived compounds are effective in breast cancer and leukaemia (Bondock et al. 2016).

This thesis is prepared from our research project, which was funded by the Scientific and Technological Research Institution of Turkey (TÜBİTAK) with project number 118S580. Within the scope of this project, a series of compounds were designed from a lead compound (Figure 1) previously synthesized by my supervisor, Prof. Dr. Özlen Güzel-Akdemir, using computer-aided drug design approaches. This lead compound demonstrated a low nanomolar inhibitory activity of 13.5 and 2.6 nM against hCAIX and hCAXII, respectively. However, this compound lacks selectivity by also inhibiting the off-target hCAII with a low nanomolar concentration of 3.9 nM. In addition, the lead compound showed anticancer effects against

ECC-1, MCF-7, A549, HT-29, U118-MG, and Caco-2 cancer cell lines with low micromolar concentrations.

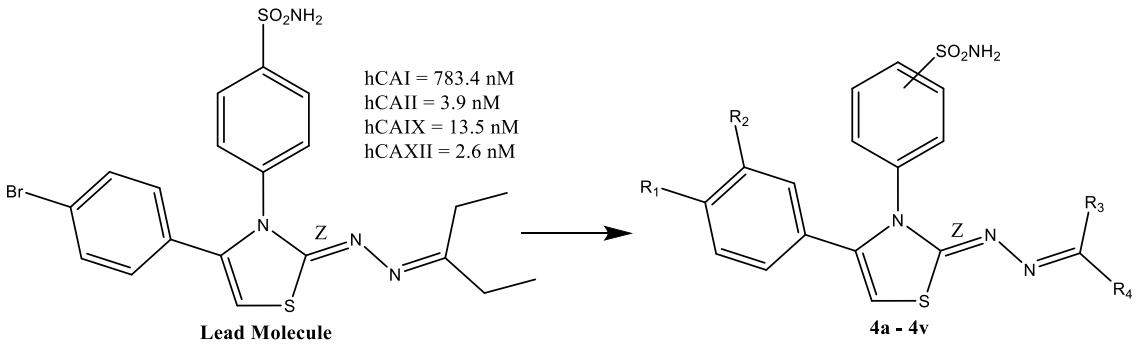

Figure 1-1: Lead Molecule

To obtain more active and selective compounds than the lead compound, a library of novel compounds that are synthetically accessible in our lab was generated based on the structure of the lead molecule. Using docking studies, 22 compounds (**4a – 4v**) expected to selectively bind to hCAIX and hCAXII were selected, successfully synthesized, characterized, and evaluated for their inhibitory activities against hCAIX and hCAXII and the off-targets hCAI and hCAII. In addition, the cytotoxic activities of these compounds against the above-mentioned cancer cells were evaluated. However, the preliminary docking results did not show a correlation with the carbonic anhydrase inhibition data. To better rationalize the carbonic anhydrase inhibition results, more advanced molecular docking techniques, such as ensemble-based reverse docking, pre-MM-GBSA calculations, molecular dynamic simulations, and post-MM-GBSA calculations, were employed on five compounds, namely compound **4f**, **4i**, **4o**, **4t** and **4u**. The obtained intermediate compounds (**E1** – **E13**) are also novel compounds and thus structurally characterized and evaluated for their inhibitory activities against the four carbonic anhydrase isoenzymes.

2. GENERAL INFORMATION/LITERATURE REVIEW

2.1. Computer-Aided Drug Design

Humans have always been on a continuous quest for new potential drugs. However, in the olden days of drug discovery, which could be dated back to the second half of the 19th century, most drugs were discovered serendipitously (Lin 2019). For a long time, drug discovery continued to be based on the extraction and testing of natural products to see if they had the desired effect. Active compounds were further identified and isolated from the active extracts. Although this method has led to the discovery of some drugs, it has limitations because the biological target is often unknown, making it challenging to optimize drugs for improved potency and pharmacokinetic properties. The concept of the rational approach to drug design and discovery started in the 1970s. It was called "one target, one drug", which means drugs should be identified based on their biological targets (Igor José dos Santos Nascimento et al. 2022).

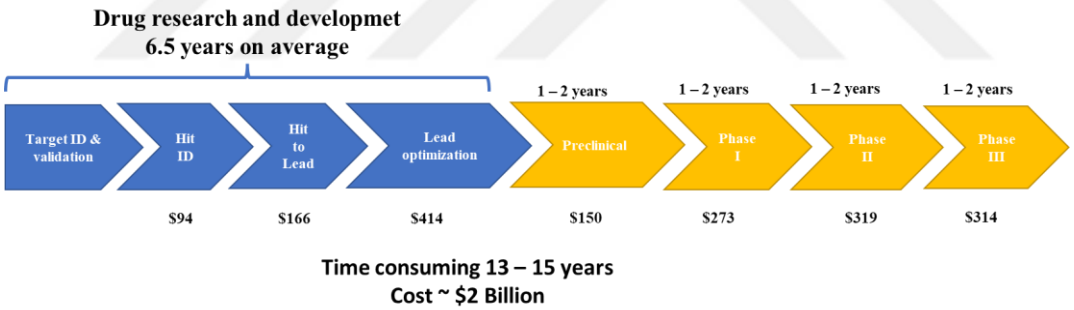

Figure 2-1: Drug discovery pipeline

The sequencing of the human genome, which began in 1990 and was concluded in 2003, led to the discovery of additional biological targets making a breakthrough in drug discovery. Nevertheless, drug discovery remains a complex, cumbersome, time-consuming and expensive process involving multiple stages. It encompasses target identification and validation, hit design/discovery, lead identification and optimization, and preclinical and clinical trials. The whole process could take up to 15 years, costing more than 2 billion USD, whiles having a little success rate (**Figure 2-1**). This lengthy and costly process thus inevitably requires an innovative intervention that would lessen the cost and shorten the

duration (Macalino et al. 2015; Igor José dos Santos Nascimento et al. 2022). And this innovation was computer-aided drug design (CADD), which was a turning point that caused great excitement in the history of drug discovery as published in the *Fortune magazine* with the title "Next Industrial Revolution: Designing Drugs by Computer at Merck" (Lin 2019).

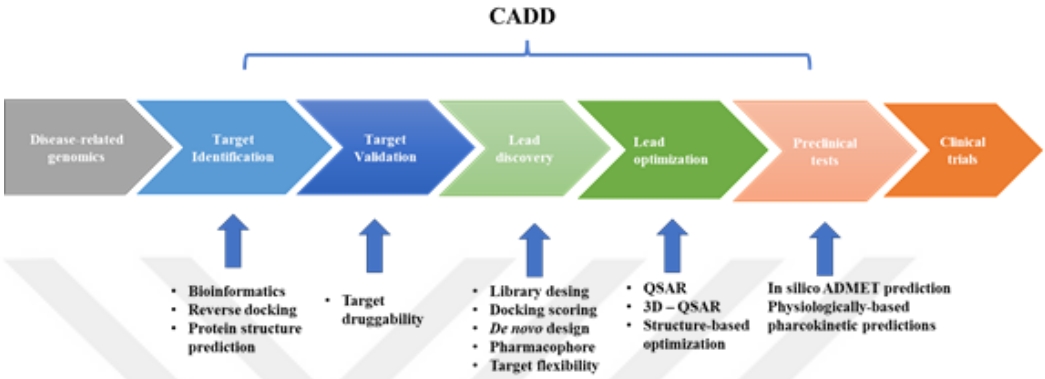

Figure 2-2: Application of CADD in drug discovery pipeline

CADD is a paramount tool in current drug discovery processes, particularly in the preliminary stages, that has undeniably decreased failures, shortened the duration and reduced cost (Macalino et al. 2015; Wang 2021). CADD is applicable in many aspects of drug discovery and development, from target identification to preclinical studies (**Figure 2-2**). Together with HIV-1 protease inhibitors, current antiviral drugs such as zanamivir and nelfinavir and anticancer drugs such as imatinib, erdafitinib and alpelisib were discovered using CADD techniques (Volarath et al. 2007; Stanzione et al. 2021; Igor José dos Santos Nascimento et al. 2022). CADD involves ligand-based design (LBD), structure-based design (SBD) and the prediction of pharmacokinetic properties and toxicity (ADMET) (**Figure 2-3**).

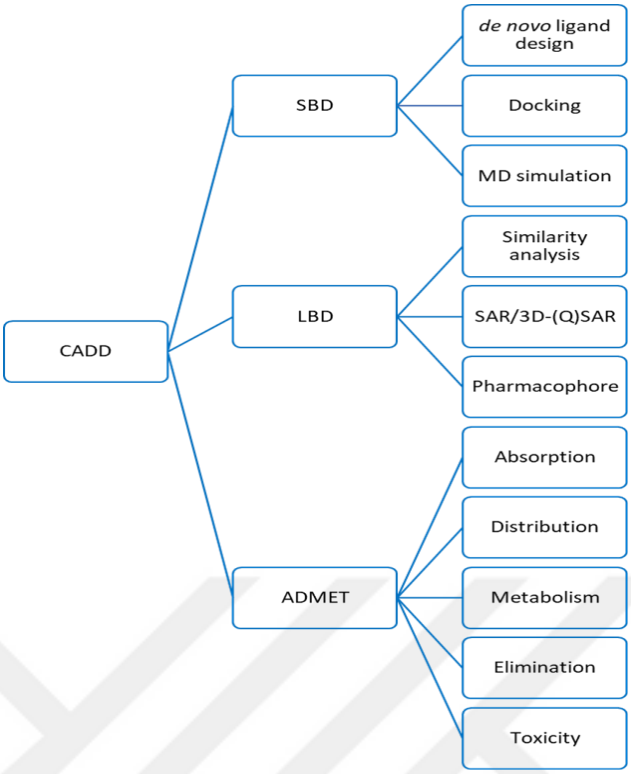

Figure 2-3: General workflow of CADD

2.1.1. Ligand-Based Design

LBD is a CADD method that is applied when there is no 3D structure of the protein structure of interest. It often relies on the structural features of the ligand that binds to the protein. LBD uses three main types of methods which are chemical similarity analysis, quantitative structure-activity relationship (QSAR) and pharmacophore modelling to predict biological activity from a chemical compound (Lin 2019; Igor José dos Santos Nascimento et al. 2022). It used to be the only rational drug design method before protein crystallography. Besides, ibuprofen was developed by Nicholson and Adams for the treatment of rheumatoid arthritis a decade prior to NSAIDs being linked to prostaglandin biosynthesis and cyclooxygenase enzymes (COX) being structurally characterized by X-ray diffraction (Stromgaard et al. 2016).

2.1.2. Structure-Based Design

SBD is the most applied CADD method that is employed to identify compounds that may bind to the biological target when the 3D protein structure is available (Stromgaard et al. 2016). The structure of a biological target can be obtained by X-ray crystallography, nuclear

magnetic resonance (NMR) or cryo-electron microscopy (cryo-EM). In a situation where these methods are not applicable, structure and computational chemists can use protein homology modelling to predict and build the target structure with high similarity (Macalino et al. 2015).

SBD includes *de novo* drug design and virtual screening. *De novo* drug design uses the information of the 3D structure of the target to generate fragments that are compatible with the binding site. These fragments are joined together to generate potential molecules that can eventually be synthesized. However, the fragments should be joined based on certain rules to ensure synthesizability (Lionta et al. 2014; Macalino et al. 2015). Virtual screening (VS), regarded as the alternative to high-throughput screening (HTS), involves the identification of potential molecules from a vast set of diverse drug-like molecules that can bind to a biological target in a manner similar to the existing ligand of that target or the discovery of new compounds for unexplored known targets using molecular docking. Contrary to the *de novo* method, VS does not necessarily provide novel molecules (Lionta et al. 2014).

2.1.2.1. Molecular Docking

Molecular docking, first used in the 1970s, is the main tool often used in VS to predict the tightness of binding between a ligand and the binding pocket, the conformation, and orientation of a ligand in a binding site of a target and the possible interactions between the ligand and the target. Molecular docking uses scoring functions to rank various poses (protein-ligand complex) obtained as the output of the docking and the top ones are considered the best candidates to be putative hits. Molecular docking was first developed for small ligands (ligand-protein docking), it has, however, later expanded to accommodate protein-protein and nucleic acid-ligand dockings (Ferreira et al. 2015; Pinzi and Rastelli 2019; Stanzione et al. 2021). Opposite to the traditional VS, docking techniques can be used in finding (new) target proteins for molecules as is the case in drug repositioning. This method is called reverse virtual screening (Park and Cho 2017; Pinzi and Rastelli 2019).

Molecular docking is either conducted rigidly, semi-flexibly or flexibly. Rigid docking is based on the “lock-and-key” hypothesis of Emil Fischer. It involves the treatment of both the ligand and the protein as rigid bodies. Semi-flexible treats the ligand as a flexible body and the protein as a rigid body, whereas flexible docking treats both the ligand and the protein as flexible bodies (OH groups) (Sefika Feyza et al. 2022). Since the majority of the docking programs use rigid or semi-flexible dockings, they often produce unreliable results because

they do not take into account protein flexibility, which is more realistic and crucial for protein-ligand interactions (Stanzione et al. 2021; Ricci-Lopez et al. 2021). A study on 980 binding sites of many proteins obtained from Protein Data Bank (PDB) revealed that at least 85% of the binding sites have up to three flexible residues and as a result, different conformations of a single protein may exist. Therefore, docking methods treating the protein as a rigid body may produce 50-70% incorrect results (Najmanovich et al. 2000; Totrov and Abagyan 2008).

In addition, Koshland has reported that enzymes change their conformations upon binding a ligand (Koshland 1995) by either adjusting their side chains or sometimes, their backbones. This phenomenon is described as induced fit binding and carbonic anhydrases are not an exception to this. Besides, two independent studies carried out by Alaei et al. and Santos and Brodbelt have revealed some conformational changes in hCAII upon binding of different ligands (Alaei et al. 2018; Santos and Brodbelt 2021). To address the above-mentioned limitations of rigid and semi-flexible dockings, induced-fit flexible docking method and ensemble docking have been employed and proven to be more efficient and accurate in generating docking poses (B-Rao et al. 2009; Stanzione et al. 2021).

2.1.2.2. Ensemble Docking

Ensemble docking, also known as multiple receptor conformations (MRC) docking, was introduced two decades ago. It helps in mimicking induced-fit effects by docking flexible ligan into multiple binding pocket conformations of a single target protein. It is hypothesized that this structural diversity leads to a more precise binding mode and exploration of a larger chemical space (Huang and Zou 2007; Tian et al. 2014; Ricci-Lopez et al. 2021). The ensemble of protein structures can be obtained by using different crystal structures of a particular target available on PDB. It can also be obtained by using molecular dynamic (MD) simulations, especially if enough diverse crystal structures of a target protein are not available on PDB. MD simulations generate different conformations at different times over the course of simulation time (Osguthorpe et al. 2012; Tian et al. 2014).

Claussen et al. have developed FLEXE, a docking program that accounts for protein flexibility. They studied the conformational changes of the binding sites of an ensemble of 10 protein targets including hCAII. The ensemble of each target structure contains at least four crystal structures. And dockings were conducted using the co-crystallized ligands. The docking results of FLEXE were compared with FLEXX, another docking program that does

semi-flexible docking. Although a significant conformational change was not observed with all the target proteins, the study demonstrated the importance of ensemble docking, particularly in the case of aldose reductase. Because with FLEXX, some ligands only bound to the proteins they were co-crystallized with and did not bind to the same protein target with different crystal structures, and have concluded if a single rigid crystal structure was used, many potent inhibitors would have been missed (Claussen et al. 2001). In addition, Osguthorpe et al have conducted an ensemble docking on HIV protease and cyclin-dependent kinase 2 and concluded that hits generated from ensemble docking are superior to those obtained from single docking (Osguthorpe et al. 2012). Rueda et al. also conducted ensemble docking on 99 protein targets containing 1068 different crystal structures. The team has demonstrated that ensemble docking provides better accuracy and improves discrimination between binders and decoys (Rueda et al. 2010). Similar results were reported by Tian et al. 2014.

On the other hand, the selection of structures and the number of structures to be selected for a target protein is challenging. Another issue that poses a significant challenge for ensemble docking is how to combine and analyse the docking results obtained from various conformations for a given target. Besides, some studies have reported that the use of too many conformations might increase the case of false positives. (Tian et al. 2014). Rescoring with more computationally intensive tools has proven to minimize the occurrence of false positives and negatives obtained from docking studies. Some of these rescoring methods are the calculation of binding free energy with Molecular Mechanics with Generalised Born and Surface Area Solvation (MM-GBSA) and MD simulations (Graves et al. 2008; Greenidge et al. 2014; Ferreira et al. 2015; Zhang et al. 2017; Maffucci et al. 2018; Ahinko et al. 2019; Wang et al. 2019a; Sahakyan 2021).

2.1.3. Molecular Mechanics with Generalised Born and Surface Area Solvation (MM-GBSA) Calculations

Various force-field-based methods such as MM-GBSA, free energy perturbation (FEP) or thermodynamic integration (TI) methods are used in the determination of free binding energy (ΔG). The MM-GBSA method, however, is the most rapid in computing ΔG. Rescoring docking poses with MM-GBSA provides a different and more accurate ranking than the classical scoring function. The more negative the MM-GBSA value, the stronger the binding is. The MM-GBSA approach uses MM energies, polar and nonpolar solvation terms,

and an entropy term that can accurately approximate the free energy of binding a ligand to a receptor. As shown in the equation below, ΔG comprises MM energy (E_{MM}), polar and nonpolar solvation terms, and an entropy term (Greenidge et al. 2013; Zhang et al. 2017). The E_{MM} on the other hand comprises E_{bat}(the sum of bond, angle, and torsion terms in the force field), a van der Waals term, E_{vdW}, and a Coulombic term, E_{coul}. $G_{solv.p}$, calculated with the Generalized-Born (GB) approximation, is the polar contribution to the solvation-free energy. $G_{solv.np}$ is the nonpolar solvation-free energy commonly calculated as a linear function of solvent-accessible surface area (Greenidge et al. 2013).

$$\Delta G = \Delta E_{MM} + \Delta G_{solv} - T.\ \Delta S$$

$$\Delta G = \Delta E_{bat} + \Delta E_{vdW} + \Delta E_{coul} + \Delta Gsolv.p + \Delta G_{solv.np} - T.\ \Delta S$$

Rastelli et al. assessed the performance of the MM-GBSA calculations in rescoring the docking poses of a variety of ligands and decoy molecules against *Plasmodium falciparum* dihydrofolate reductase that was generated by AutoDock and did not well correlate with the experimental results and found that, in most cases, it discriminated more effectively and provides a higher enrichment factor than the conventional docking approaches. (Rastelli et al. 2010). Hou et al. investigated the rescoring efficiency of MM-GBSA and MM-PBSA of 98 target-ligand complexes to predict their correct binding conformations and energies. They discovered that, in the majority of cases, MM-GBSA rescoring outperformed MM-PBSA and significantly increased the ratio of finding the correct binding poses of ligands. MM-PBSA refers to the Molecular Mechanics Poisson-Boltzmann Surface Area and similar to MM-GBSA, it has been efficient in the rescoring of docking poses. The team also mentioned that MD simulations were essential in determining the correct conformations for some complexes (Hou et al. 2011). Zhang et al. assessed the performance of the MM-GBSA rescoring of docking results obtained from Vina docking of 0.7 million actives and decoys against 38 drug targets. They found out that MM-GBSA rescoring outperforms Vina docking alone in terms of early recovery of actives. (Zhang et al. 2014). Additionally, Diao et al. conducted a docking-based virtual screening for human dihydroorotate dehydrogenase using molecules from SPECS database with Glide XP docking and MM-GBSA rescoring. They selected and tested 47 compounds for their inhibitory properties and identified 18 active compounds as hits. The group discovered that despite Glide XP generating good binding modes of the ligands, it failed to correlate the experimental values with the docking scores (r^2=13%), whereas rescoring of the Glide XP docked poses with MM-GBSA provided a much better

correlation with an r^2 of 71% (Diao et al. 2012). In 2014, Greenidge and colleagues at Novartis conducted a virtual screening on 13 targets and a total of 20 crystal structures using GOLD and Glide, followed by M-GBSA calculations to evaluate the "rescoring potential" of MM-GBSA. The team concluded that MM-GBSA can be used independently as a scoring function to identify the energetically preferred poses generated with multiple scoring functions and in multiple protein conformations. In addition, MM-GBSA could be used to effectively distinguish true binders from decoys (Greenidge et al. 2014).

On the other hand, Graves et al. and Ahinko et al. outlined that despite the efficient performance of MM-GBSA to distinguish between true binders and decoys and to show a better correlation with experimental results, it may increase false positives due to the rapid estimation of raw binding energy and the inconsideration of conformational entropy (Graves et al. 2008; Ahinko et al. 2019). Besides, Zhang et al. conducted a virtual screening on antithrombin by single docking followed by a rescoring with a single MM-GBSA binding energy calculation and eventually, an ensemble-average MM-GBSA calculation. The latter is generated from the frames of the 100 ns MD trajectories they performed. And they concluded that ensemble-average MM-GBSA calculation is twice more effective in ranking docked poses (Zhang et al. 2017).

2.1.4. Molecular Dynamic Simulations and post-MM-GBSA Evaluation

MD simulations are another widely employed method in discriminating false positives or negatives that might be generated from docking studies. It evaluates the stability of docked poses and generates ensembles upon which MM-GBSA calculations can be performed. MD simulations address the possible docking-related limitations by treating both the protein and ligand as flexible components and thus may mimic induced-fit binding (Alonso et al. 2006; Durrant and McCammon 2011; Santos et al. 2019). MD uses classical mechanics and Newton's laws of motion to calculate and simulate the motions of atoms. It allows and studies the dynamic behaviour and minor conformational changes of a protein complex at different timescales. This monitoring of the dynamic behaviour of the ligand-receptor permits the determination of the stability of the system because a stable pose of a ligand will produce stable trajectories whereas a false docked pose will produce unstable trajectories (Durrant and McCammon 2011; Santos et al. 2019). In addition, these trajectories can be used to assess the binding energy of the ligand during the simulation. In most cases, MM-GBSA calculation of the binding energy is applied and this is known as the post-MM-GBSA (Liu et al. 2018).

Numerous studies have reported the efficiency of MD simulations in predicting the right binding modes of various molecules. However, conducting MD simulations is quite expensive and time-consuming. As such, it is mostly employed to study the binding stability of selected best poses from docking studies. In addition, MD simulations may wrongly predict the dynamic behaviours of a protein complex system containing a transition metal in its binding site (Durrant and McCammon 2011).

2.1.5. *In silico* prediction of ADME properties

Approximately, 50% of drug candidates fail in clinical trials due to low efficacy caused by poor pharmacokinetic properties. Therefore, an early assessment of pharmacokinetic properties is of paramount importance in drug discovery (Li 2001). The use of *in silico* ADME (absorption, distribution, metabolism, and excretion) predictions has emerged as an essential tool in the preclinical stages of drug discovery. It saves time and money and avoids ethical concerns by identifying compounds that are likely to fail due to poor pharmacokinetic properties without the need for animal testing, which is costly and time-consuming. Computational models are used to predict the properties of molecules before they are synthesized or assayed for their biological activities. In addition, it functions as a filtering mechanism for the identification of potential lead molecules with acceptable properties, thus avoiding poor ADME properties and toxicity in clinical studies. This approach also helps medicinal chemists in the optimization of lead compounds to improve ADME properties (Cheng et al. 2013; Wang et al. 2015).

The Lipinski Rule of Five (RO5) is a fundamental set of principles commonly employed to evaluate the oral bioavailability and drug-like properties of biologically active compounds. Small molecules that comply with these principles are generally classified as drug-like compounds (Lipinski et al. 1997). RO5 states that for a molecule to possess drug-like characteristics and be orally active, it must satisfy the following criteria:

1. Its molecular weight should be less than 500 Da.
2. Its octanol/water partition coefficient (logP) should be less than 5.
3. It should have no more than 5 hydrogen bond donor groups and 10 hydrogen bond acceptor groups.
4. It should violate no more than one of the rules.

2.2. Cancer

Cancer, a global concern that has afflicted humans for centuries, is a group of more than 270 deadly non-communicable diseases that (can) affect any part of the body and are characterized by irregular, uncontrollable cell growth and metastasis (Raveesha et al. 2022; Diori Karidio and Sanlier 2021; Hassanpour and Dehghani 2017). Cancer is the world's second greatest cause of mortality, surpassed only by cardiovascular disease. The rate of cancer cases and cancer-related mortality is increasing yearly, particularly in developing countries. According to the latest worldwide cancer-related mortality estimates in 2019, more than 23 million cancer cases and 10 million deaths were registered. This shows an increase of 26.3% in incidence and 20.9% in mortality when compared to 2010 (Kocarnik et al. 2022). Although an accurate quantifying of cancer incidences and mortality rates for 2020 and 2021 is challenging due to the influence of the coronavirus disease (COVID-19) pandemic which caused a lag in the dissemination of population-based surveillance data, GLOBOCAN has estimated cancer incidence and mortality rates from 36 different types of cancer in 2020 to be approximately 19.3 million and 9.9 million, respectively (Siegel et al. 2022; Sung et al. 2021). This decrease may be a result of delays caused in cancer diagnosis and treatment in 2020 due to lockdowns, closure of health institutions, and the fear of contracting the virus during the COVID-19 pandemic. However, this short-term drop in cancer incidence may be followed by an increase in advanced-stage or metastatic cancers and, eventually, high mortality in 2022 (Siegel et al. 2022).

The United Nation’s Sustainable Development Goals (UN-SDG) Target 3.4 on non-communicable diseases, which includes cardiovascular diseases and cancer, aim at reducing premature deaths (deaths in people aged between 30 and 70) caused by non-communicable diseases (NCD) by one-third by 2030 (Bennett et al. 2020). In 2019, 20.4 million died premature death, more than 75% of which were caused by NCD. Among the 183 countries surveyed, cardiovascular diseases were the leading cause of death in 70 countries and cancer in 57 countries. These countries were mainly developed countries, however, 50 Sub-saharan countries struggled with both infectious diseases and the two NCDs (**Figure 2-4**) (Stewart et al. 2020; Bray et al. 2021). If this adopted target is not attained, cancer will affect 24.6 – 27 million and cost the lives of 12.9 – 17 million by 2030 (Solomon and Mulugeta 2019; Cancer Tomorrow 2022). Unfortunately, this projection is likely to come into reality since the fight against cancer has made less progress than other non-communicable diseases due to a lack of awareness of preventive measures, ineffective treatment of metastatic cancers,

chemoresistance, growth of an ageing population and high prevalence of risk factors (Giovannuzzi et al. 2021; Sung et al. 2021; World Health Organization 2020).

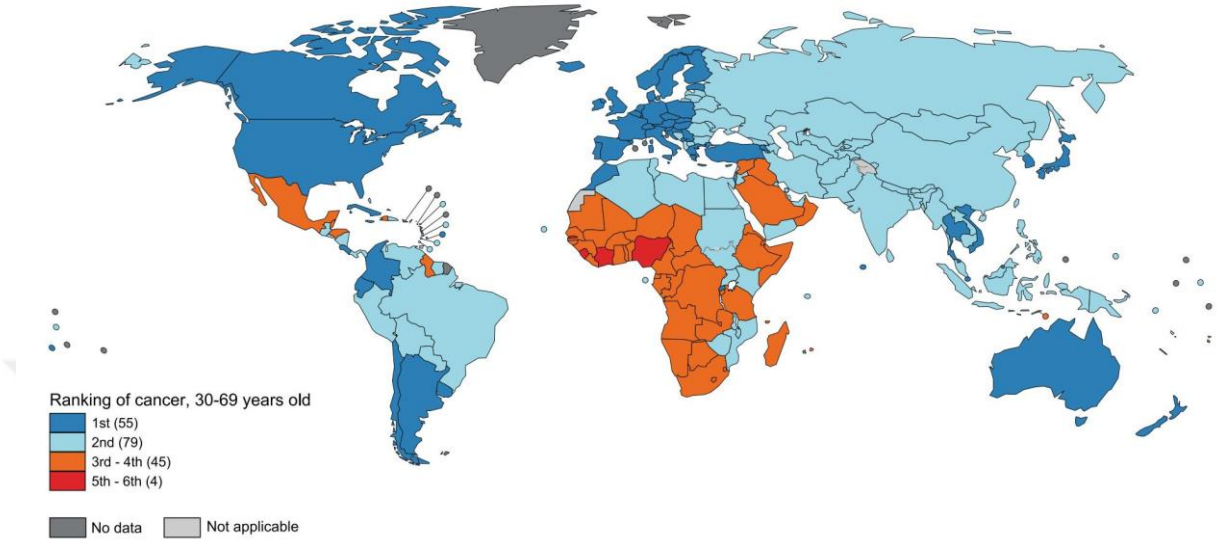

Figure 2-4: Global map of cancer as the major cause of death before age 70 (ages 30–69), with rankings and numbers of countries in parenthesis. (Stewart et al. 2020)

Although cancer is mainly caused by genetic mutations such as DNA replication errors and inherited and somatic mutations, etiological studies have revealed the heterogenicity and other numerous causal factors such as silencing of tumour-suppressing genes via hypermethylation, hypomethylation of oncogenes, viral infections, and exposure to toxins such as aflatoxin B. The alterations and modifications of normal cells lead to a dynamic and multistep process called carcinogenesis or tumourigenesis (Diori Karidio and Sanlier 2021). Cancer cells do not follow the law of maintaining homeostasis (repair/apoptosis), they rather change their proliferation control, prolong their lifespan, invade nearby cells, and consequently gain the ability to escape the immune system.

Cancer cells have characteristic features that distinguish them from normal cells and are called hallmarks of cancer. These special features are responsible for the transformation of normal human cells to invasive cancerous cells and were first described and conceptualized by Hanahan and Weinberg as six in 2000 and later expanded by Hanahan as 14 in 2022. (Hanahan 2022; Hanahan and Weinberg 2011).

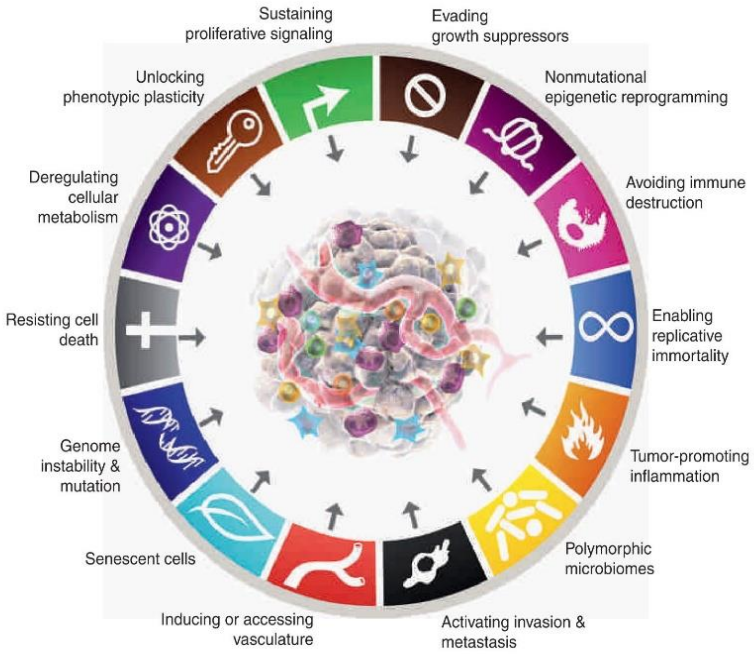

Figure 2-5: Hallmarks of Cancer (Hanahan 2022; Hanahan and Weinberg 2011)

2.2.1. The microenvironment of tumour cells

Cells do interact with react or adapt to their vicinity and this was clearly explained by Paget in 1889, where he proposed the “seed and soil hypothesis (Paget 1889), which indicated that even potential neoplastic cancer cells (seed) depend on their environment (soil) for nutrition supply to express their phenotypic properties such as high and rapid proliferation, invasiveness, the ability to adapt to harsh conditions and metastasis (Fidler 2002, 2003; Laconi 2007; Weber and Kuo 2012). Therefore an appreciation of the tumour microenvironment (TME) is essential in understanding the rapid proliferation of tumour cells and exposes potential targets in cancer therapy (Dvorak 1986).

The TME refers to the cellular niche in which tumour cells exist and communicate with surrounding cells. It is very different from the microenvironment of normal cells and a substantial amount of studies have revealed the implication of TME in tumourigenesis, metastasis, and chemoresistance by changing the metabolic pathways of cancer cells (Mboge et al. 2018; Luo 2022). TME constitutes a dense of various supportive neighbouring cells called the stroma cells. Although these constituents may vary depending on the type of the tumour, however, major constituents include immune cells, endothelial cells, and fibroblasts. It is evident from many studies that these supportive cells are being recruited by cancer cells

to help them in their growth, invasion, and metastasis. Besides, the TME includes various extracellular components including the extracellular matrix (ECM) and growth factors (Wei et al. 2020; Jiang et al. 2020; Anderson and Simon 2020; Lin et al. 2022).

Tumour cells have a distinct and altered ECM secreted by all vicinal cell types, creating an extensive fibre network composed of collagen, fibronectin, elastin, lamin, vitronectin, and tenascin. This intricate network gives the binding properties, mechanical strength, invasiveness, and metastatic properties of tumour cells. In addition, the collagen of ECM is implicated in impeding the penetration of anticancer drugs by architecting itself as a physical barrier. Some other components of the ECM can cause the sequestration of anticancer agents when bound to them (Netti et al. 2000; Kim et al. 2011; Wu and Dai 2017).

Tumour cells, like any other organ, require blood supply for nourishment, supply of oxygen, and removal of waste metabolic products. However, the rapid growth of tumour cells with limited, leaky and poor vasculature causes an uneven and insufficient supply of blood, low oxygenation, and supply of nutrients. Subsequently, hypoxia occurs (Fukumura and Jain 2007). To adapt to this new phenomenon, tumour cells express a transcription factor, hypoxia-Inducible Factor (HIF)-1, that regulates the expression of several genes necessary for the growth of cancer cells (**Figure 2-6**). Several genes are involved in the regulation of the tumour microenvironment (TME), including glucose transporters (GLUT1/3) and glycolytic enzymes, which upregulate glycolysis and produce acidic metabolites. Additionally, CAIX is responsible for regulating the acidity of the TME and intracellular pH of tumour cells. Furthermore, several growth factors stimulate the sprouting of new blood cells, resulting in angiogenesis and extravascularization (Birbrair 2020). Angiogenesis is a crucial cancer hallmark implicated in the proliferation and metastasis of tumour cells. Although various growth factors have been identified as angiogenetic activators, the vascular endothelial growth factor (VEGF) is the main effector for angiogenesis (Krock et al. 2011) and several VEGF inhibitors have demonstrated anticancer activity (Mamo et al. 2020).

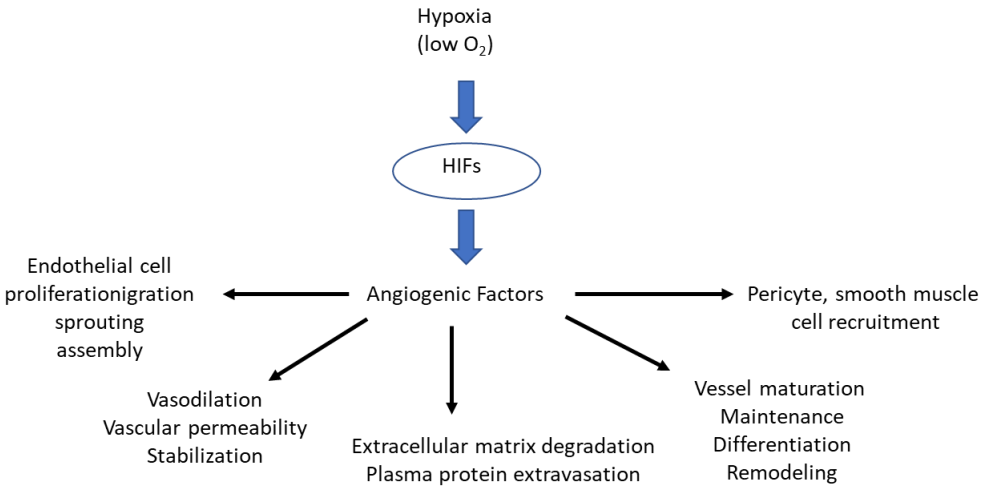

Figure 2-6: Regulation of angiogenesis by angiogenic factors induced by HIF. (Krock et al. 2011)

2.2.2. Hypoxia and Hypoxia-Inducible Factor

In 1995, Thomlinson and Gray first hypothesized the presence of hypoxic cells in human malignancies based on necrosis distribution relative to blood vessels. They observed that necrosis was caused by cells remaining at zero, or close to zero, oxygen levels for long periods (Thomlinson and Gray 1955). In 1958, Churchill-Davidson et al. observed that low levels of oxygen always protected biological systems against X-ray cytotoxicity, and this led them to believe that hypoxia in cancer cells may be one of the factors that reduce the effectiveness of radiotherapy against cancer cells (Churchill-Davidson et al. 1958). Hypoxia causes resistance to radiotherapy since it requires oxygen to develop and sustain cytotoxic-free radicals that damage DNA. Hypoxia may potentially cause resistance to various chemotherapeutic drugs, such as melphalan, etoposide, and bleomycin, which require oxygen for their activities. Extreme hypoxia slows cell division and causes cell cycle arrest, affecting drugs that target dividing cells (Green et al. 2001; Koch et al. 2003; Abaza and Luqmani 2013).

Hypoxia refers to the reduction in the normal level or deprivation of oxygen in cells. Oxygen is a terminal electron acceptor in aerobic multicellular organisms, supporting cellular respiration, energy production, and biosynthesis of signalling chemicals. Insufficient O_2 can cause liver fibrosis, diabetes, atherosclerosis, dementia, cachexia, and cancer. In cancer cells, rapid proliferation and poor vasculature lead to O_2 deprivation, which causes cells to vascularize abnormally, and subsequently require more O_2. However, this extreme increase in

demand for O_2 cannot be fulfilled by the body, causing the cells to become hypoxic (Eales et al. 2016; Graham and Unger 2018).

HIF-1 is the main cellular response to hypoxia that enables cancer cells to acclimatize to these conditions. HIF-1 is a heterodimer that belongs to the protein family of Per–Arnt–Sim (PAS). It constitutes both a hypoxic response alpha subunit (HIF-1α) and a non-hypoxic response beta subunit (HIF-1β, also known as ARNT) (Semenza 2007; Gopinath and Kathiravan 2022). HIF-1 acts as the chief transcription factor that regulates the expression of many adaptive or survival genes to regulate various essential biological functions in a different way than normal cells such as pH homeostasis, erythropoiesis, angiogenesis, cell differentiation, anaerobic metabolism, and mitophagy in hypoxic cells (Hu et al. 2003). These vital genes for cancer adaptation and survival include VEGF, CAIX, CAXII, GLUT 1/3, erythropoietin 1, and glycolytic enzymes (Lendahl et al. 2009; Rani et al. 2022). Hypoxia stabilizes HIF-1α, establishing a hostile milieu that favours solid tumour growth and survival. Prolyl hydroxylase enzyme (PHD) catalyses the hydroxylation of HIF-1α in the presence of oxygen, enabling it to interact with the von Hippel–Lindau (VHL) complex. With the help of a ubiquitin-activating enzyme, HIF-1α is ubiquitylated. Ubiquitylation targets HIF-1α to proteosome for degradation (Harris 2002). VHL is a tumour suppressor and multiple studies have established that a mutation in VHL even in the absence of hypoxia is associated with various types of cancers since the mutation prevents ubiquitylation of HIF-1α which prevents the degradation of HIF-1α, and subsequently prevents the expression of tumour associated genes (Patard et al. 2008; Lau et al. 2017). In hypoxia, PHD cannot modify HIF-1α since hydroxylation is oxygen-dependent, and thus it remains stable. Stabilized HIF-1α is moved to the nucleus, where it dimerizes with HIF-1β (Maltepe et al. 2000). The heterodimer eventually binds to the hypoxia-responsive elements (HREs) to activate a series of essential genes required for the growth of cancer cells (**Figure 2-7**). Numerous studies have shown that increased HIF-1α expression is related to poor prognosis and chemoresistance in various cancer types, and glycolytic enzymes regulated by HIF-1α- are therapeutic targets implicated in cancer proliferation. HIF-1α suppression makes drug-resistant ovarian cancer cells more cisplatin-sensitive (Selvendiran et al. 2009; Parmakhtiar et al. 2019; Wang et al. 2021).

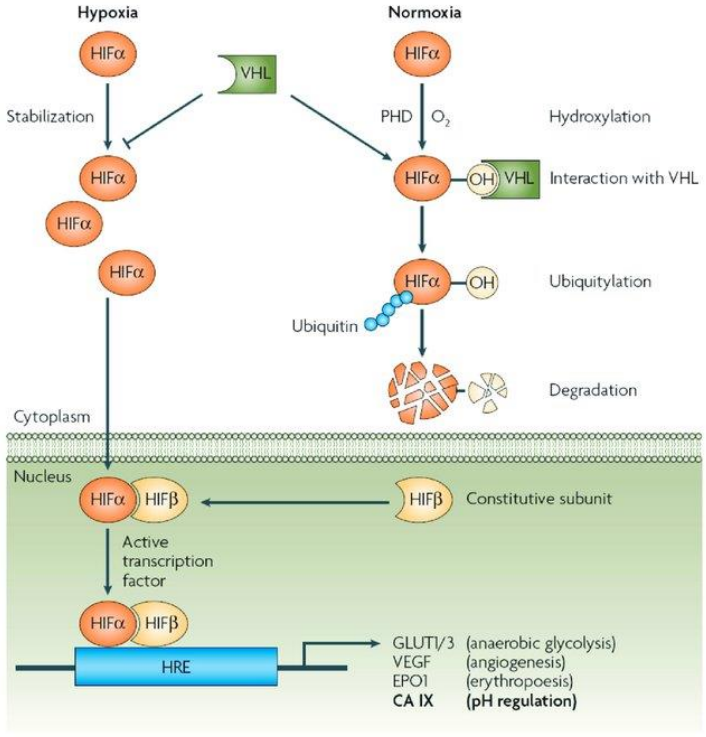

Figure 2-7: HIF orchestrates the upregulation of glycolysis, angiogenesis, erythropoiesis, and pH-regulating proteins in hypoxic (Supuran 2017b)

2.2.3. Warburg Effect and Acidosis

Cancer cells have various mechanisms to adapt to hypoxia and use it to their advantage (acquiring more aggressive tumour phenotypes) by triggering HIF-1α which initiates the activation of a series of hypoxia response genes. The overall effect of these responses is called the "metabolic shift" (Swayampakula et al. 2021). In normoxia, cells convert glucose to pyruvate via glycolysis that further oxidizes in the mitochondrial Krebs cycle to produce NADH. NADH fuels oxidative phosphorylation generating a net gain of 38 molecules of ATP, CO_2, and water. In hypoxia, oxidative phosphorylation is restricted and cells direct pyruvate to a less energy-producing metabolic pathway by producing lactic acid (H^+) and 2 molecules of ATP. The production of lactic acid leads to intracellular acidification. Although this pathway results in low ATP production, it sustains the continuity of glycolysis by cycling NADH back to NAD^+ (Rani et al. 2022). However, in 1931, Warburg observed that solid tumours preferred this inefficient energy-producing pathway even in the presence of oxygen and this phenomenon is called aerobic glycolysis of the Warburg effect (**Figure 2-8**) (Warburg 1956; Vander Heiden et al. 2009). Tumours use this pathway as a carbon source for

the biosynthesis of amino acids, nucleotides, and lipids required for cell proliferation, and thus serve as an advantage over normal cells. As a result, tumour cells overexpress GLUT 1/3, hexokinase-2, phosphofructokinase isoform, pyruvate kinase M2, lactase dehydrogenase and pyruvate dehydrogenase kinase-1&3 to increase glycolysis, the amount of pyruvate and pyruvate conversion to lactate. The activation of pyruvate dehydrogenase kinase-1&3 inhibits pyruvate dehydrogenase and prevents pyruvate from entering the Krebs cycle (Abaza and Luqmani 2013).

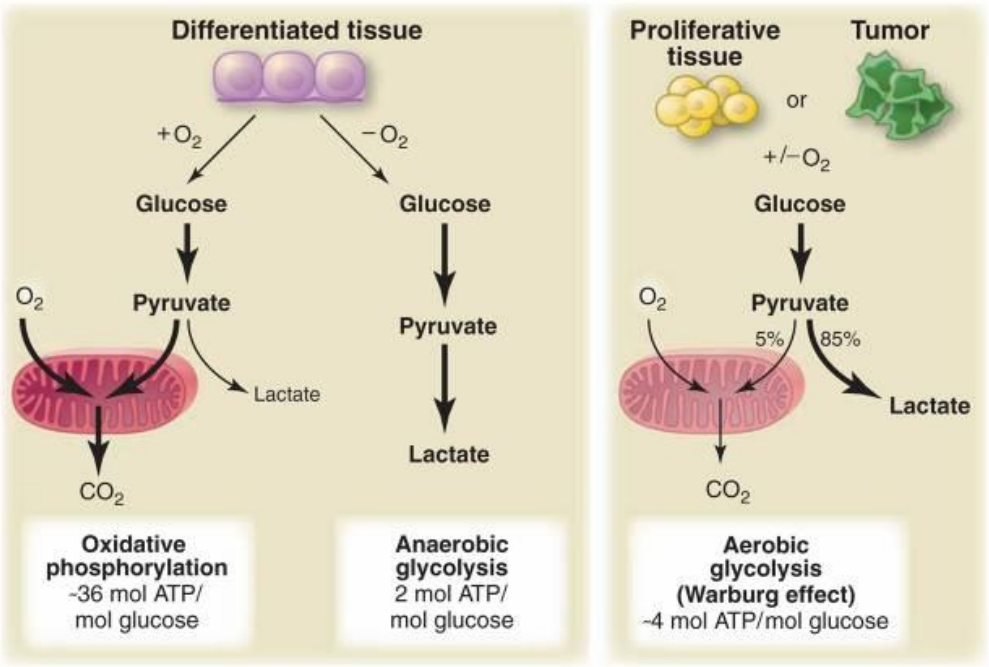

Figure 2-8: Differences between oxidative phosphorylation, anaerobic glycolysis, and aerobic glycolysis (Warburg effect) (Vander Heiden et al. 2009)

Contrary to Warburg's effect, Tannock and colleagues discovered in 1993 that tumours lacking GLUT1/3, glycolytic enzymes, and lactate dehydrogenase still cause extracellular acidification. They concluded that tumours develop metabolic heterogeneity, where extracellular acidification is caused by the production of carbonic acid from CO_2 through an oxidative energy metabolism rather than the accumulation of lactic acid (Newell et al. 1993; Yamagata et al. 1998). Tumour cells utilize the glutaminolysis pathway as well, feeding the mitochondrial TCA cycle, and thus contribute to the synthesis of fatty acids, amino acids, and nucleotides. In addition, many studies conducted over the past decades have shown that

inhibiting enzymes involved in Warburg's pathway did not prevent tumourigenesis. Consequently, it has been concluded that tumours also (mostly) utilize the mitochondrial oxidative metabolism for the biosynthesis of essential molecules required for tumour proliferation by activating oncogenes, deactivating tumour suppressor genes, and upregulating the phosphatidylinositol 3-kinase pathway, resulting in the production of CO_2. This explains one of the reasons for the high glycolytic rate of tumour cells rather than just the production of lactic acid (DeBerardinis and Chandel 2016; Lee and Griffiths 2020).

Taken all together, metabolic shift and the oncogenic metabolic reprogramming in cancer cells result in the accumulation of large amounts of lactic acid, CO_2, and protons, and consequently cause intracellular acidification (Mahon et al. 2015; Giovannuzzi et al. 2021; Tonissen and Poulsen 2021). However, a slight increase in the intracellular pH (pH_i) can cause autodigestion of cancer cells and disruption in many vital cellular functions such as ATP production, membrane permeability, metabolism, proliferation, migration, and metastasis (Chiche et al. 2009). Consequently, cancer cells try to prevent intracellular acidification by diffusing out CO_2, extruding lactic acid and proton, and intruding bicarbonate ions produced from the hydration of CO_2 (Swietach 2019; Pastorekova and Gillies 2019). This process enables cancer cells to slightly alkalify their inner compartment (increase in pHi to 7.3–7.6) whiles causing extracellular acidification (pH 6.5–7.0) (White et al. 2017; Andreucci et al. 2017; Becker and Deitmer 2020). Tumour cells, in fact, highly express a series of transporters and enzymes together with some buffering systems that help them regulate their intra/extracellular pH homeostasis. These transporters include Na^+/H^+ exchanger 1 (NHE1), Cl^-/HCO_3^- exchangers (AEs), vacuolar ATPase (VTPase), Na^+/HCO_3^- co-transporters (NBCs), H^+/lactate cotransporters (monocarboxylate transporters, MCTs), and hCAII, IX, and XII (**Figure 2-9**) (Brahimi-Horn and Pouysségur 2007; Brahimi-Horn et al. 2007; Neri and Supuran 2011; Parks et al. 2011; Abaza and Luqmani 2013; Andreucci et al. 2017).

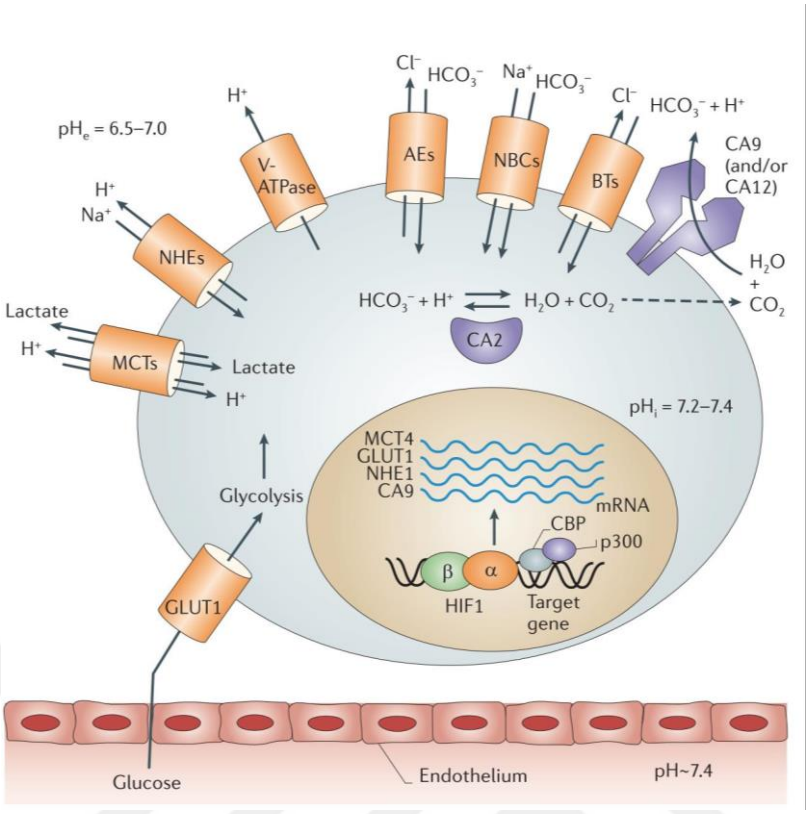

Figure 2-9: Proteins involved in pH regulation within a tumour cell (Neri and Supuran 2011)

Cancer cells can adapt and get along with extracellular acidosis, and use it to their advantage by expressing aggressive cancer phenotypes which allow them to proliferate and metastasize, whiles neighbouring normal cells cannot adapt and eventually die (Benej et al. 2014; White et al. 2017; Becker and Deitmer 2021; Queen et al. 2022). Numerous studies have recognized tumour acidosis (acidic pHe) as a hallmark of cancer since it helps cancer cells acquire aggressive cancer characteristics (Sharma et al. 2015; Pillai et al. 2019; Blaszczak and Swietach 2021). Melanoma cells that have been exposed to acidosis, for example, have a high propensity to spread, high resistance to apoptosis and chemotherapeutics, and unchanging autonomous proliferation (Andreucci et al. 2020).

Tumour acidosis is the most critical factor in metastatic progression because it increases the secretion and activation of proteolytic enzymes that promote ECM degradation and remodelling allowing cancer cells to invade and metastasize. Again, acidosis increases the expression of angiogenic factors, such as VEGF and basic fibroblast growth factor, which promote angiogenesis and thus tumour growth and metastasis. Another mechanism of

acidosis-induced metastasis is the presence of lactate, which increases the expression of hyaluronan and hyaluronidase, both of which significantly contribute to metastasis. Furthermore, acidosis leads to chemoresistance by reducing the uptake and efficacy of weakly basic anticancer agents, such as paclitaxel, mitoxantrone, vincristine, vinblastine, and doxorubicin. This is because basic drugs cross the plasma membrane in their neutral state, and because basic drugs are ionized in an acidic environment, they accumulate in the acidic milieu (Ferguson et al. 1984; Mahoney et al. 2003; Raghunand et al. 2003; Bogdanov et al. 2022). On the other hand, while the absorption and efficiency of weakly acidic drugs like cyclophosphamide generally increase in tumour acidosis, acidosis-induced metastasis may render them ineffective (Jähde et al. 1989; Gerweck et al. 2006).

As a result of the aforementioned unfavourable effects of tumour acidosis, developing novel anticancer drugs that interfere with pH regulation in tumours is of paramount importance and their combination with present anticancer drugs may increase their sensitivity and hence improve their efficacy. Besides, various studies have revealed that deacidifying TME by using sodium bicarbonate decreases cancer cell growth, invasion, and metastasis. In addition, coadministration of doxorubicin and mitoxantrone with sodium bicarbonate increases sensitivity and thus improves efficacy (Mahoney et al. 2003; Raghunand et al. 2003; Robey et al. 2009; Ibrahim-Hashim et al. 2011; Ibrahim-Hashim et al. 2012; Pillai et al. 2019).

2.3. Carbonic anhydrase enzymes

Carbonic anhydrases (CAs, EC 4.2.1.1) are zinc-containing metalloenzymes found in all living beings that catalyse the reversible hydration of carbon dioxide to bicarbonates and protons. In these living organisms, CAs play vital roles in various important physiological processes such as maintaining pH homeostasis, gluconeogenesis, electrolyte secretions, calcification, respiration, bone resorption, and tumourigenesis (Supuran 2008; Imtaiyaz Hassan et al. 2013; Chegwidden 2021).

In the early years of the 20th century, the mechanism by which CO_2 was transported in the blood and released in the lungs was still not illuminated. However, in 1928 and 1930, Henriques and Van Slyke, respectively, observed that HCO_3^- rapidly transits from the blood to the pulmonary capillary in approximately 1 second (Henriques 1928; van Slyke and Hawkins 1930). In 1932 and 1933, two different research teams led by Meldrum and Roughton in the UK, and Stadie and O'Brien in the USA, independently identified an enzyme

that catalysed the interconversion of CO_2 to HCO_3^- (Meldrum N. U. 1932; Meldrum and Roughton 1933; Stadie and O'Brien 1933). In 1939, Keilin and Mann discovered that this enzyme contains zinc metal that enables it to carry out its activity and that can be inhibited by metal-complexing anions (Mann and Keilin 1939). Shortly, this led to their discovery of primary sulfonamides as inhibitors of this enzyme (Mann and Keilin 1940). This enzyme was named carbonic anhydrase by Philip Eggleton (Davenport 1984).

2.3.1. CA Superfamily and Expression Profile

As previously mentioned, CAs are metalloenzymes found in almost all tissues that catalyse an essential physiological reaction which is the interconversion of CO_2 and HCO_3^- . CAs are classified into eight structurally independent families based on their evolutionary trend. These families are the alpha (α), beta (β), gamma (γ), delta (δ), zeta *(ζ)*, eta (η), theta (θ), and (iota) ι CAs. The α-CAs have been identified in animals, protozoa, some algae and bacteria, and plants. The β-CAs are expressed in some bacteria and algae, fungi, archaea, and chloroplasts of mon-/dicotyledons. The γ -CAs are found in some archaea, bacteria and plants. The δ-CAs were identified in marine phytoplankton including the diatoms. The ζ-CAs are encoded only in marine diatoms. The η-CA family is discovered from the protozoa *Plasmodium falciparum* (Supuran 2010; Silvia Bua 2019). Recently, the θ and ι CAs were identified in *Phaeodactylum tricornutum* and *Thalassiosira pseudonana*, respectively, which are both marine diatoms (D'Ambrosio et al. 2019; Nocentini et al. 2021). These metalloenzymes are only able to catalyse this essential physiological reaction when they have a metal ion (M^{2+}) cofactor present with the active site which is coordinated by three amino acid residues and a water molecule/hydroxide ion forming a tetrahedral geometry. Generally, Zn^{2+} is the metal cofactor found in all the eight families, however, Zn^{2+} is exchangeable with Cd^{2+} and Fe^{2+} in ζ and γ-CAs, respectively. Co^{2+} is identified in some α-CAs but no catalytic importance is associated with it (Silvia Bua 2019).

The α family is the most characterized and the only class present in mammals. To date, 16 α-CA isoenzymes have been identified, thirteen of which are catalytically active and the remaining three are catalytically non-active. However, humans contain 15 α-CA isoenzymes, lacking the thirteenth active α-CA isozyme (CAXV). Twelve of the catalytically active human CA isoenzymes are hCAI, hCAII, hCAIII, hCAIV, hCAVA, hCAVB, hCAVI, hCAVII, hCAIX, hCAXII, hCAXIII and hCAXIV. The acatalytic isoenzymes lack some histidines that are necessary for the catalytic activity of the Zn^{2+}. They are hCAVII, hCAX

and hCAXI, and are called CA-related proteins (CARPs). These isoenzymes have different molecular structures, tissue and organ distributions, physiological functions, kinetic properties, cellular localizations, and levels of expression (Imtaiyaz Hassan et al. 2013; Aspatwar et al. 2014; Supuran 2016b, 2017a; Baranauskienė and Matulis 2019).

Structurally, the isozymes are generally in a monomeric state except for hCAVI, hCAIX and hCAXII. The protein fold for hCA is characterized by a central 10-stranded antiparallel β-sheet surrounded by multiple helices and extra β-strands as depicted in **Figure 2-10A**. The catalytic active site is a wide cavity and approximately 15 Å deep. It has a conical-like shape and is divided into two different halves of different environments **Figure 2-10B**. These are the hydrophobic and the hydrophilic regions caused by the nature of the side chains of the amino acid residues present (Imtaiyaz Hassan et al. 2013; D'Ambrosio et al. 2015; Supuran 2016b, 2017a).

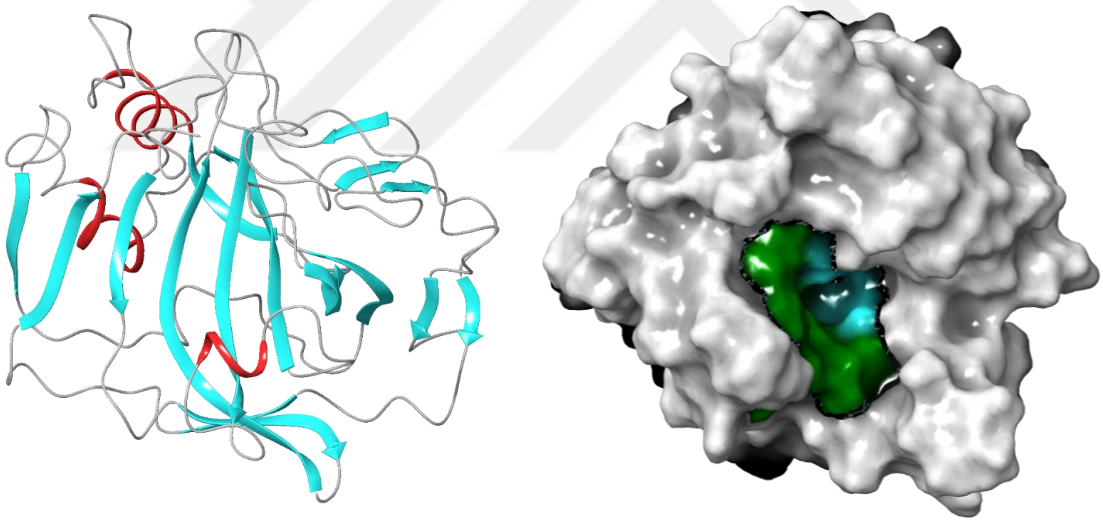

Figure 2-10 A) Turquoise represents β-sheets, red represents α-helixes B) Coloured regions represent the active site; green represents the hydrophobic region and turquoise represents the hydrophilic region.

Although the length of the amino acid sequence of hCAs varies between 260 to 459 residues, structural comparison interestingly demonstrated high similarity among the isoenzymes with the catalytic domain showing a high number of conserved amino acids. Some residual differences are observed mainly between residues 125 and 131 (based on

hCAII numbering). **Table 2-1** reveals the percentage similarity observed among hCA isozymes as calculated by Imtaiyaz Hassan et al. using ClustalW2 (http://www.ebi.ac.uk/Tools/msa/clustalw2/) (Imtaiyaz Hassan et al. 2013). Besides, the superposition of available crystal structures of hCA isoenzymes reveals the structural similarity (**Figure 2-11**).

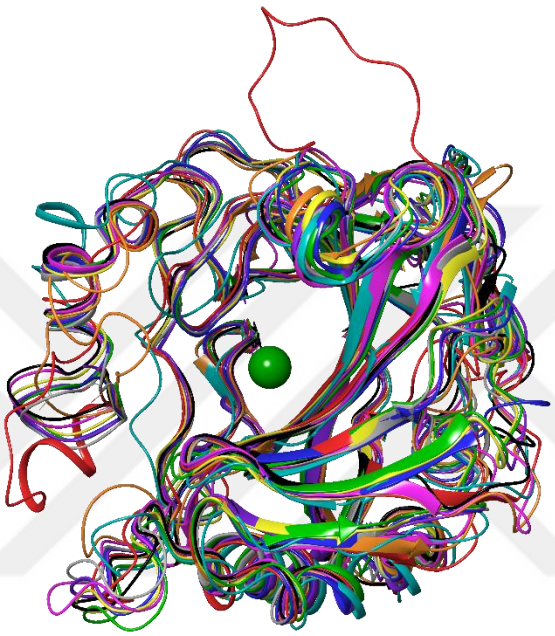

Figure 2-11 Overlay of some hCA isoenzymes. PDB IDs: 3LXE for hCAI (green), 4E3D for hCAII (blue), 1Z93 for hCAIII (yellow), 1ZNC for hCAIV (red), 3FE4 for hCAVI (teal), 6SDT for hCAVII (violet), 3IAI for hCAIX (orange), 1JD0 for hCAXII (magenta), 4KNM for hCAXIII (grey), 5CJF for hCAXIV (black).

Table 2-1: Percentage sequence similarity between hCA isoenzymes, adapted from (Imtaiyaz Hassan et al. 2013)

hCAs	hCAI	hCAII	hCAIII	hCAIV	hCAVA	hCAVB	hCAVI	hCAVII	hCAVIII	hCAIX	hCAX	hCAXI	hCAXII	hCAXIII	hCAXIV
hCAI	100														
hCAII	60	100													
hCAIII	53	58	100												
hCAIV	30	33	31	100											
hCAVA	47	50	45	23	100										
hCAVB	46	52	43	23	58	100									
hCAVI	31	33	32	26	27	24	100								
hCAVII	50	56	49	31	48	49	34	100							
hCAVIII	39	40	38	27	33	34	28	41	100						
hCAIX	31	33	20	25	27	26	35	35	31	100					
hCAX	26	28	27	23	24	24	19	27	27	20	100				
hCAXI	25	30	28	22	24	26	18	26	28	21	50	100			
hCAXII	35	34	31	26	27	25	32	37	28	36	21	19	100		
hCAXIII	59	59	57	28	46	47	33	52	39	34	27	27	34	100	
hCAXIV	34	35	34	25	29	25	32	35	27	37	19	23	40	37	100

The kinetic properties of hCAs differ due to the differences in some residues within the active site. The hCAII has the highest catalytical activity of K_{cat}/K_m = 1.5 × 10^8 $M^{-1}s^{-1}$ (**Table 2-2**) due to the cluster orientation of His3, His4, His10, His15, and His17 in a way that it helps His64 in proton transfer as posited by Briganti and colleagues (Briganti et al. 1997). On the other hand, the absence of this histidine clustering and His46 leads to a decrease in the catalytic activity of some isoenzymes. The exchange of His64 with Lys64 has led to a dramatic reduction in the catalytic efficiency in hCAIII (D'Ambrosio et al. 2015; Imtaiyaz Hassan et al. 2013).

The hCAs also show differences in subcellular localization by being cytosolic, transmembrane, mitochondrial or secreted. Cytosolic proteins include the CARPs and isoforms hCAI, hCAII, hCAIII, hCAVII, and hCAXIII. The only isoform that is secreted is the hCAVI, whereas hCAVA and hCAVB are mitochondrial. Although four of the isoenzymes, hCAIV hCAIX, hCAXII, and hCAXI, are anchored to the cell membrane, their active sites are oriented toward the extracellular space. They all have a single transmembrane helix and short intracellular fragments. Four isoforms are linked to the cell membrane with their active sites located outside of the cell. CAIV is held to the cellular membrane by the glycosylphosphatidylinositol anchor (**Figure 2-12**) (Baranauskienė and Matulis 2019).

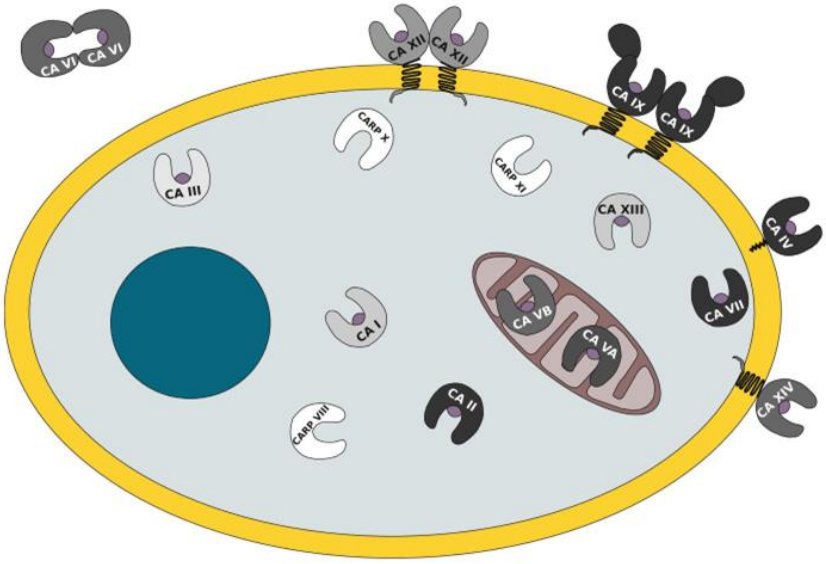

Figure 2-12 Localization of human CA isoforms in the cell. Proteins are marked as horseshoe shaped figures with their colour being proportional to the enzymatic

activity. The acatalytic isoforms are shown in white. The zinc ions in the active sites of CAs are shown as small purple spheres (Baranauskienė and Matulis 2019)

Furthermore, the distribution of hCA isoenzymes in various tissues or organs can be used to differentiate them (Table **2-2**). Some isoenzymes may be present only in one organ or tissue while some may be present in various organs or tissues. The hCAX and hCAXI are present only in the central nervous system. The hCAI is present in red blood cells and eyes, the hCAII is ubiquitous, hCAIX is expressed in cancer cells and gastric mucosa and hCAXII is found in the kidney, intestine and eye (Carta et al. 2014; Supuran and Mugelli 2019; Nocentini et al. 2019; Chegwidden 2021).

Table 2-2 Kinetic properties, subcellular localization, and tissue/organ distribution of hCA isoenzymes. Adapted from (Carta et al. 2014; Supuran and Mugelli 2019; Chegwidden 2021)

hCA	Catalytic activity	K_{cat}/K_m (M^{-1} s^{-1})	Subcellular localization	Tissue/organ distribution
hCAI	Moderate	5.0×10^7	cytosol	Erythrocytes, GI tract
hCAII	High	1.5×10^8	cytosol	Erythrocytes, eye, GI tract (ubiquitous), Bone osteoclasts, kidney, lung, testis, brain
hCAIII	Low	2.5×10^5	cytosol	Skeletal muscle, adipocytes
hCAIV	High	5.1×10^7	membrane-bound	Kidney, lung, pancreas, brain capillaries, colon, heart muscle
hCAVA	Moderate	2.9×10^7	mitochondria	liver
hCAVB	High	9.8×10^7	mitochondria	heart and skeletal muscle, pancreas,

				kidney, spinal cord, GI tract
hCAVI	Moderate	4.9×10^7	Secrete (saliva/milk)	salivary and mammary glands
hCAVII	High	8.3×10^7	cytosol	CNS
hCAVIII	–	–	cytosol	CNS
hCAIX	High	5.4×10^7	transmembrane	Tumours; GI mucosa
hCAX	–	–	cytosol	CNS
hCAXI	–	–	cytosol	CNS
hCAXII	Moderate	3.5×10^7	transmembrane	Renal, intestinal, and reproductive epithelia
hCAXIII	Moderate	1.1×10^7	cytosol	kidney, brain, lung, gut, reproductive tract
hCAXIV	Moderate	3.9×10^7	transmembrane	kidney, brain, liver

2.3.2. Catalytic Mechanism and Physiological Importance

The interconversion of CO_2 and HCO_3^- is a simple reaction and can occur without a catalyst. However, it is extremely slow at physiological pH to efficiently satisfy the metabolic needs of various organisms. CO_2 is a highly lipophilic gas and when produced in extremely high concentrations, it can harm cellular components, but when hydrated to HCO_3^- and H^+, it can disrupt the pH homeostasis of cells. Thus, organisms produce a catalyst that facilitates a rapid interconversion of CO_2 and HCO_3^- up to 10^8 $M^{-1}s^{-1}$ (**Scheme 2-1**).

Scheme 2-1: The reversible hydration of CO_2 to HCO_3^-

In addition to CO_2 and HCO_3^- interconversion, some CAs catalyse the hydration of small molecules similar to CO_2 such as carbonyl sulfide, carbon disulfide, and cyanamide. Other studies have reported the catalysation of aldehyde dehydration and hydrolysis of ester bonds in carboxylic acid esters, sulfonic acid esters, phosphate

esters, and thioesters as illustrated below (**Scheme 2-2**) (Supuran and Simone 2015; Supuran 2016b).

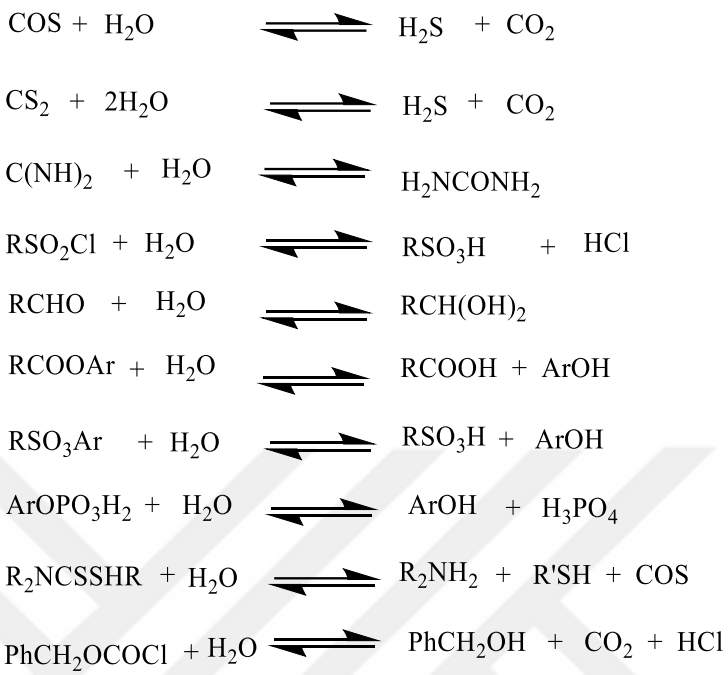

Scheme 2-2: Reactions catalyzed by CAs (Supuran 2016b)

Catalytically active CA isozymes participate in a variety of vital physiological functions, including the transport of H^+, CO_2, ions, and water, the regulation of pH homeostasis, and the provision of bicarbonate as a substrate for numerous metabolic reactions. **Table 2-3** provides a summary of some of the key physiological roles that the carbonic anhydrase isozymes play (Chegwidden 2021).

As indicated above, CA isozymes are localized in various organs and tissue with a vast variety of important physiological functions. As a result, any disruption in these processes may trigger the over/down expressions of these isoenzymes. In addition, different disorders can affect the localization of these isoenzymes causing them to appear in large amounts in unexpected areas, and this serves as the foundation for employing CA isoenzymes as biomarkers in various disorders/diseases. **Table 2-3** summarizes various diseases and disorders associated with CA isozymes. Recently, the most significant breakthrough in the history of CAs is the discovery of tumour-associated hCAIX and hCAXII which have emerged as promising diagnostics, biomarkers, and druggable targets for cancer (Chegwidden 2021).

Table 2-3: Primary physiological functions and related pathological conditions of hCA enzymes (Imtaiyaz Hassan et al. 2013; Chegwidden 2021)

hCA	**Physiological Function**	**Related pathological conditions**
hCAI	Helps with **gustation and olfaction** by maintaining CO_2 homeostasis	Retinal and cerebral oedema Bipolar disorder Glaucoma
hCAII	Helps with **gustation and olfaction** by maintaining CO_2 homeostasis. Contributes to **bile production** by facilitating HCO_3^- for bile (liver epithelial duct cells) and acidification of bile (gall bladder epithelium). Aids in the **regulation of respiration and acid-base balance** by dehydrating CO_2 to HCO_3^- in peripheral tissues, and removal of H^+ in the kidney. Helps in maintaining normal **vision** by promoting the secretion of **aqueous humour** in the ciliary body. Helps in the **secretion of cerebrospinal fluid** in the brain (choroid plexus) by providing H^+ and maintaining the pH. Contributes to **bone growth** by promoting the differentiation of osteoclasts and providing H^+ for bone resorption. Provides bicarbonate that can be used in various **metabolic processes** including the synthesis of pyrimidines.	Sleep apnea Acute mountain sickness COPD Pseudotumour cerebri Oedema Pulmonary hypertension Alzheimer's disease Epilepsy

	Help to **protect the gastro-oesophageal tract** by providing HCO_3^- which can neutralize acids in the gastro-oesophageal mucosa. Contributes to **saliva production** by providing HCO_3^- in acinar and ductal cells. Helps in the regulation of the pH and bicarbonate content of the seminal fluid in the **reproductive system**. Maintains proper **muscle function** by facilitating the diffusion of CO_2.	
hCAIII	Maintains **proper muscle function** by facilitating the diffusion of CO_2 and providing protection as an antioxidant against ROS	Myasthenia gravis Oxidative stress
hCAIV	Aids in the **regulation of respiration and acid-base balance** by dehydrating CO_2 to HCO_3^- in the lungs and reabsorption of HCO_3^- in the kidney. Maintains proper **muscle function** facilitating buffering in the sarcoplasmic reticulum. Helps with **gustation and olfaction** by maintaining CO_2 homeostasis. Contributes to **bile production** through the acidification of bile (gall bladder epithelium). Helps in the regulation of the pH and bicarbonate content of the seminal fluid in the **reproductive system**. Helps in maintaining normal **vision** by promoting the secretion of **aqueous humour** in the ciliary body.	COPD Glaucoma Retinitis pigmentosa Stroke

hCAV	Participates in **metabolic processes** like **gluconeogenesis** and **ureagenesis** through the provision of HCO_3^- and in the regulation of insulin secretion in pancreatic beta cells.	Alzheimer disease Obesity
hCAVI	Help to **protect the gastro-oesophageal tract** and **dental surfaces** by providing HCO_3^- which can neutralize acids in the gastro-oesophageal mucosa and dental surfaces.	Cariogenesis
hCAIX	Plays a role in **oncogenesis** by regulating the tumour microenvironment to facilitate tumour growth and metastasis	Cancer
hCAXII	Aids in the **regulation of respiration and acid-base balance** by facilitating the reabsorption of HCO_3^- in the kidney. Plays a role in **oncogenesis** by regulating the tumour microenvironment to facilitate tumour growth and metastasis. Helps in the **generation of cerebrospinal fluid** in the brain (choroid plexus) by providing H^+ and maintaining the pH. Helps in maintaining normal **vision** by promoting the secretion of **aqueous humour** in the ciliary body.	Cancer
hCAXIV	Facilitates absorption of HCO_3^- and modulates neuronal transmission.	Epilepsy Retinopathy

Structural similarities between hCA isoenzymes are high, and the 3D structures are quite similar. As previously mentioned, the hCAs have their catalytic active site located in a large, cone-shaped cavity that reaches the middle of the protein approximately 15 A deep. At the bottom of this cavity, three conserved histidine residues (His94, His96 and His119) (**Figure 2-13**) and a water molecule/hydroxide ion coordinate the catalytic Zn^{2+} at the bottom of this cavity. The Zn^{2+}-bound solvent molecule hydrogen bonds with deep water, the hydroxyl and the carboxylate moieties of a conserved threonine residue (Thr199 and glutamic acid residue (Glu106), respectively. These interactions make the Zn^{2+}-bound water molecule nucleophilic and orient the CO_2 substrate for nucleophilic attack (Supuran 2016b, 2017a).

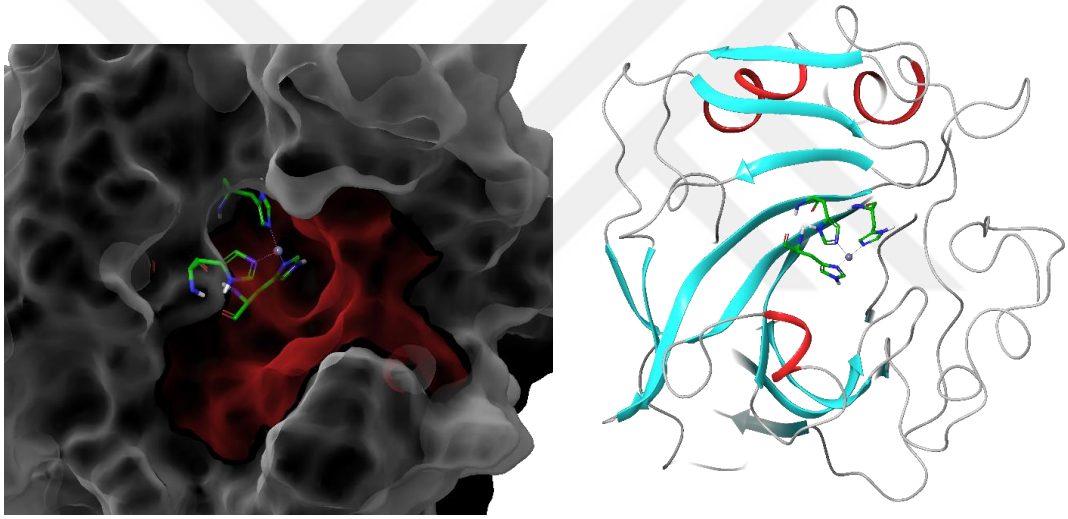

Figure 2-13: A) Active site of hACII (PDB: 4E3D) showing the cone-shaped cavity and the Zn^{2+} coordination with His94, His96, and His119. The grey sphere represents Zn^{2+}. B) Ribbon diagram; turquoise represents β-strands and grey represents α-helices.

The hCAII active site, like all hCAs, has hydrophobic residues constituting the hydrophobic half and hydrophilic amino acid residues constituting the hydrophilic half. 91, 121, 131, 135, 141, 143, 198, 201, 202 and 207 residues define the hydrophobic region, while 62, 64, 67, 69 92, 199 and 200 residues define the hydrophilic one. This very amphiphilic nature of hCAs is probably due to the hydrophobicity of CO_2 and the

hydrophilicity of its hydration reaction products (Imtaiyaz Hassan et al. 2013; Tanpure et al. 2015).

McKenna and colleagues discovered the CO_2-binding site for hCAII to be located at the bottom of the hydrophobic cavity (residues Val121, Val143, and Leu198) near the Zn^{2+} (**Figure 2-14B**). CO_2 is converted into bicarbonate by a nucleophilic attack of zinc hydroxide species. The bicarbonate is then weakly coordinated to the Zn^{2+} (**Figure 2-14C**) to form a complex that further reacts with an incoming H_2O releasing the bicarbonate from the Zn^{2+} which exits the active site via the hydrophilic region (**Figure 2-14D**). The proton transfer reaction from the zinc-coordinated water to the buffer is the rate-determining phase of the entire process where the enzyme's nucleophilically active species are produced (**Figure 2-14A**). This phase is assisted by a histidine residue called the “proton shuttle” located in the centre of the active site. This histidine is generally His64 for many hCA isoenzymes, however, other histidines such as His4, His3, His10, and His15 also play a role in this proton transfer (Supuran and Simone 2015; Supuran 2016b).

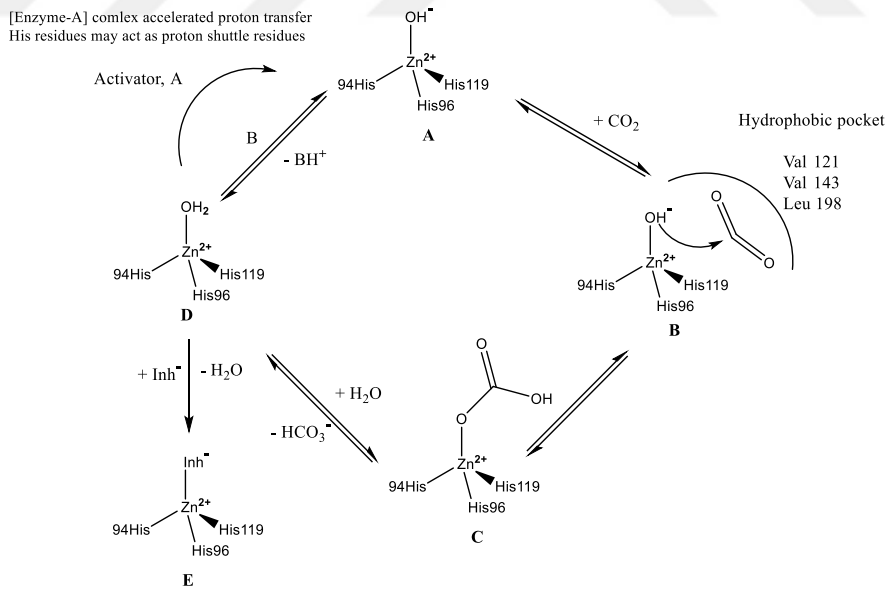

Figure 2-14: Catalytic (for the physiological reaction), inhibition (with zinc binders) and activation mechanisms of α-CAs (hCAI amino acid numbering of the zinc ligands (Supuran 2016b)

2.3.3. Structure and functions of hCAIX and XII

Originally known as membrane antigen (MN), CAIX was identified in 1992 by Pastoreková et al. as a tumour-associated antigen using the monoclonal antibody (mAb) M75. After conducting a complementary DNA sequencing on the isolated MN protein, they observed a highly conserved CA catalytic domain and the ability to bind Zn^{2+} and hydrate. As a result, MN was renamed CAIX and designated as the ninth member of the CA family. In 2000, Grabmaier et al. identified G250, a renal cancer antigen discovered by Oosterwijk et al. in 1986 as MN/CA IX (Kazokaitė et al. 2019).

In the late 1990s, using autologous antibodies from cancer patients, Tureci et al. detected a membrane protein in human renal cell carcinoma by serological expression screening. The extracellular domain of this protein showed 30 – 42% similarity with a Zn^{2+} in the active site bound to three histidines and named it the twelfth CA at that time (CAXII) (Ondriskova et al. 2015; Giovannuzzi et al. 2021).

CAIX weighs 54 – 58 kDa as a monomer. However, it exists as a homodimer transmembrane enzyme that has three main domains, the extracellular, transmembrane, and intracellular domains with a total of 459 amino acid residues (Ondriskova et al. 2015; Mahon et al. 2015; Tars and Matulis 2019; Aldera and Govender 2021). It has the highest catalytic activity among the transmembrane isoenzymes. The mature proteins lack the signal peptide with 37 residues making it 422 residues. The extracellular domain sequentially comprises an *N*-terminal proteoglycan-like domain (PG), which is exclusive to CAIX, and the catalytic domain (CD), which is followed by a short linker, a single trans-membrane helix (TM), and an intracellular tail (CT) (**Figure 2-15**) (Mahon et al. 2015; Y. Mboge et al. 2016).

The PG domain plays multiple functions by mediating in lactate transportation, helping cancer cells to easily adhere and migrate, increasing stability and affecting the catalytic activity of hCAIX in TME (Pastorekova and Gillies 2019; Aldera and Govender 2021; McDonald et al. 2022). It has been established that CAIX lacking the PG domain is 2 – 3 times less active than a whole enzyme. Although the exact process by which the PG domain affects CAIX's catalytic activity is still unknown. However, the PG domain contains negatively charged residues and is located at the edge of the active site, it is thus hypothesized that it may interact with the positively charged residues bordering the CD domain. The CD domain has CO_2 hydrase activity. It is responsible for the

deacidification and acidification of intracellular and extracellular compartments of cells, respectively. With only 23 – 26 residues, the intracellular domain is rather short. Although modelling studies indicated that the intracellular domain is in a helical configuration, experimental data describing its structure are not yet available. The intracellular domain has three phosphorylation sites, Thr443, Ser448, and Tyr449. While phosphorylation of Thr443 enhances the catalytic activity of CAIX in TME, phosphorylation of Ser448 decreases it. Some studies have revealed the functions of the intracellular tail in pH regulation (Aldera and Govender 2021; Swayampakula et al. 2021).

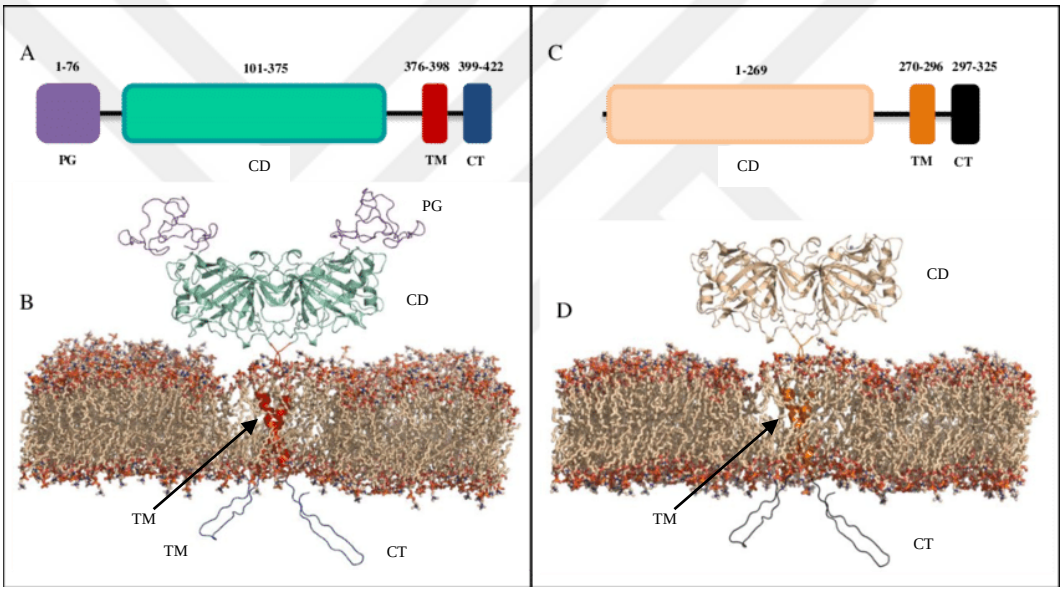

Figure 2-15 Schematic and structural models of CA IX and XII. (A) Domains of CAIX: PG (violet), CD (teal), TM (red), CT (blue). (B) Homodimeric membrane-bound CAIX (C) Domains of CAXII: CD (wheat), TM (gold), CT (black). (D) Homodimeric membrane-bound CAXII (Y. Mboge et al. 2016)

CAIX is dimeric in its physiological state. The dimerization is a result of the intermolecular covalent disulfide bond formed between Cys23 and Cys203 (**Figure 2-16**). Although this disulfide is not formed when one of these cysteines is mutated to serine, the dimeric form remains (Alterio et al. 2009; Mahon et al. 2015; Y. Mboge et al. 2016).

Similar to CAIX, CAXII is a 40 – 45 kDa dimeric membrane protein, however, the dimer-forming mechanism is different. Together with the intermolecular disulfide bond formed between Cys23 and Cys203, GXXXG and GXXXS motifs of the transmembrane domain also form a dimeric interaction. CAXII is also a glycoprotein, but in addition, it has two glycosylation sites on Asn52 and Asn136, making it different from CAIX. CAXII is expressed as 354 amino acid residues, a short linker, a TM domain, and a short CT. The mature CAXII also does not have the signal peptide (Y. Mboge et al. 2016; Waheed and Sly 2017).

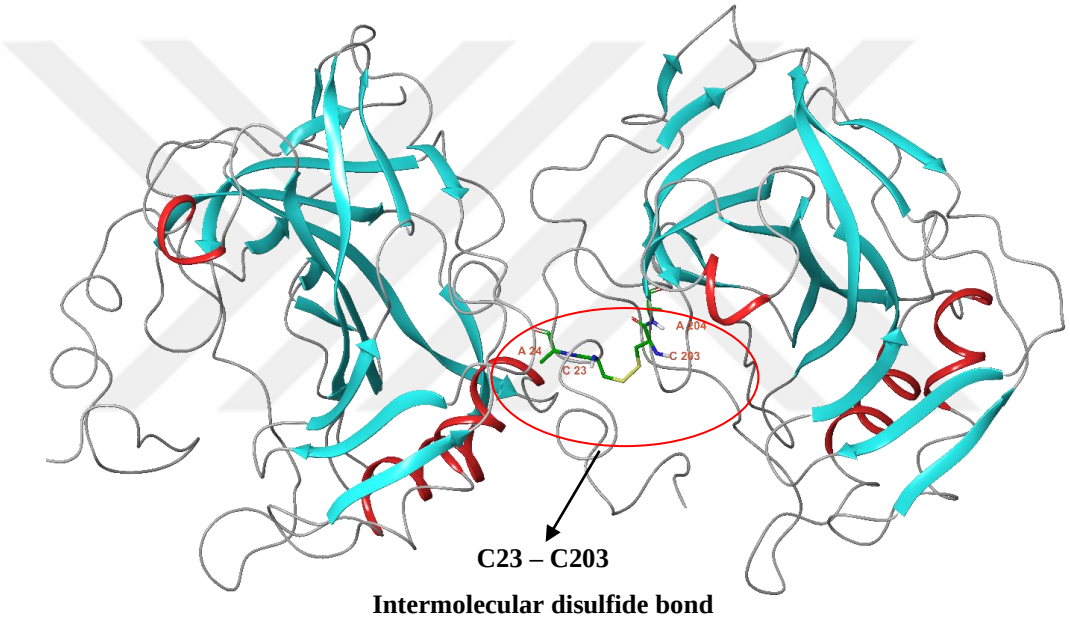

Figure 2-16: A dimeric structure of hCAIX (PDB: 3IAI) showing the intermolecular disulfide bond.

Although hCAIX is predominantly expressed in stomach and gut epithelial tissues, growing embryonic gut epithelium, skeletal muscle, and lung do contain higher hCAIX levels than adults, showing their importance at this stage. It also involves in the transportation of carbon dioxide and bicarbonate, acid-base regulation, and signal transduction. hCAXII, on the other hand, is expressed in numerous organs and developmental stages. It is highly expressed in the pancreas, appendix, colon, rectum, kidney, prostate, and intestine. It is also moderately expressed in oral mucosa, oesophagus, urinary bladder, breast, vagina, cervix, uterine, endometrium, and skin.

Similar to hCAIX, it participates in the transportation of carbon dioxide and bicarbonate. It also helps maintain a stable chloride ion concentration (Y. Mboge et al. 2016).

2.3.4. (Over)expression of hCAIX and hCAXII and their implications as diagnostic, prognostic and therapeutic targets in Cancer

As previously mentioned, whiles hCAIX is restrictively expressed in healthy gut epithelial and stomach tissues, hCAXII is widely expressed in many organs and tissues such as the pancreas, kidney, intestine prostate, and lymphocytes. However, with hCAXI being more predominant, both the transmembrane isoenzymes are shown to be expressed or overexpressed in many tumours by numerous studies. The rapid proliferation of tumours causes hypoxia, which activates HIF-1, causing the transcription of genes, including hCAIX, essential for the survival of tumours in TME (**Figure 2-17**). Studies conducted by Patard et al. 2008 and Stillebroer et al. 2010 revealed overexpression of hCAIX even in normoxia in certain cancers like clear cell renal cell carcinoma (ccRCC) due to a mutation in the VHL protein (Campos et al. 2022). On the other hand, it has been previously believed that hCAXII is also regulated by HIF-1 (Wykoff et al. 2000), however, recent studies have revealed that hCAXII is independent of HIF-1 and regulated by oestrogen receptor (Y. Mboge et al. 2016; Chen et al. 2018; Zamanova et al. 2019; Tonissen and Poulsen 2021).

hCAIX is associated with many cancer hallmarks such as acidosis, rapid proliferation, metastasis, and chemoresistance of many solid tumours including breast, brain, kidney, neck, bladder, cervical, head, and lung cancers (Potter and Harris 2003; Chen and Seimbille 2022) although few studies suggested good prognoses with hCAIX expression (Parkkila 2021). The implication of hCAIX in these hallmarks has been proven by numerous studies wherein the “knockout”, mutation, and inhibition of hCAIX with small molecules or monoclonal antibodies reduces tumour xenografts (McIntyre et al. 2012; Mahon et al. 2015; Chen et al. 2018; Kciuk et al. 2022).

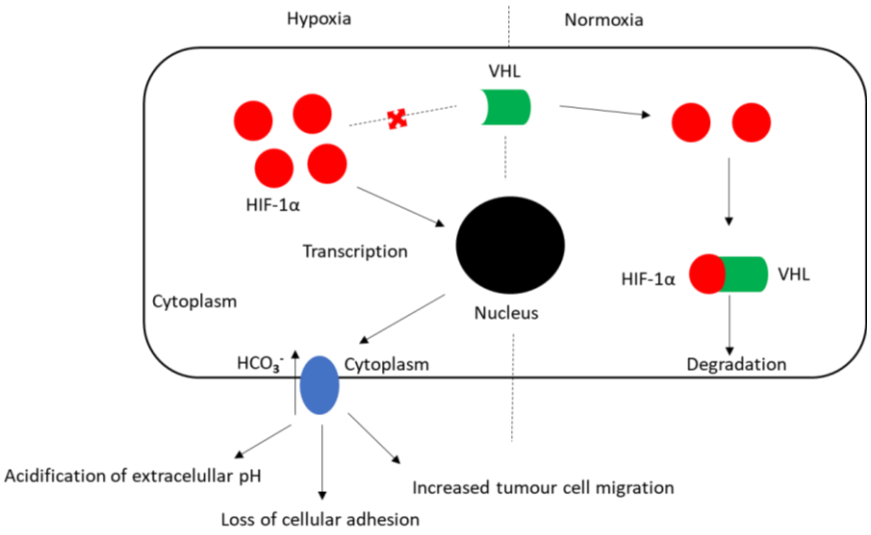

Figure 2-17: VHL protein binds to HIF-1 in normoxia, causing its degradation. Hypoxia inactivates VHL and increases cytoplasmic HIF-1 which triggers CAIX transcription (Aldera and Govender 2021)

The relationship of high CAIX with gastroesophageal reflux disease and oesophageal squamous cell carcinoma and oesophageal adenocarcinoma was investigated together with their association with the expression of biological markers in oesophageal adenocarcinoma including MCM4, MCM7, BMI1, cyclin E, and Ki67. The findings of this study revealed that high expression of CAIX may be linked to acidic gastroesophageal junction caused by gastroesophageal reflux, early tumourigenesis via BMI1, MCM4, and MCM7 and CAIX could be a potential therapeutic target in oesophageal adenocarcinoma (Huber et al. 2015).

Loncaster et al. found that CAIX expression in advanced cervical cancer is associated with poor prognosis and may act as a biomarker for hypoxia (Loncaster et al. 2001). Recently, a study conducted on cervical cancer revealed that high expression of CAIX is responsible for poor prognosis and could serve as a biomarker in heavy smoking women (Grincevičienė et al. 2022). On the contrary, a study on cervical cancer patients on radiotherapy revealed CAXII expression as a good prognostic indicator (Yoo et al. 2010). The findings of these studies are in line with a previous study on cervical cancer that linked CAIX with high metastasis and a bad prognosis, and CAXII with low metastasis and a good prognosis (Kim et al. 2006).

In a study conducted by Kang et al., CAIX expression was shown in all patients which predicted a poor prognosis after hepatocellular carcinoma surgery and an even worse prognosis in patients with high CAIX expression (Kang et al. 2015). A similar study conducted by Hyuga et al. supported these findings (Hyuga et al. 2017). Another study also revealed CAIX as a bad prognostic indicator in hepatocellular carcinoma (Finkelmeier et al. 2018). Also, a series of selective potent CAIX inhibitors conjugated with fluorescein was used to detect CAIX in hepatocellular carcinoma (Matulienė et al. 2022).

Ovarian cancers also showed strong expression of CAIX and weak expression of CAXII. Hypoxia and high CAIX expression showed a correlation with tumour malignancy, making CAIX a suitable therapeutic target (Hynninen et al. 2006). Choschzick et al. found high CAIX expression to be correlated with poor prognosis in ovarian cancer patients (Choschzick et al. 2011). Another recent study also revealed that high CAXII expression is responsible for high proliferation and poor prognosis in ovarian cancers, and can be used as a biomarker for diagnostic purposes (Hiepp et al. 2022).

Bartosová et al. and Vleugel et al. found that expression of CAIX in breast cancer is responsible for tumour malignancy, and CAIX may be a breast cancer marker (Bartosová et al. 2002; Vleugel et al. 2005). Lou et al. confirmed CAIX as a prognostic indicator in metastatic cancer. The group conducted shRNA-mediated depletion and small molecule inhibition of CAIX which both led to a remarkable inhibition of tumour proliferation and metastasis (Lou et al. 2011). Ong and colleagues investigated the correlation of CAIX expression in triple-negative breast cancer (TNBC) with survival outcomes. The findings showed that CAIX is a potential biomarker for hypoxia and high CAIX expression independently indicates poor prognosis in TNBC (Ong et al. 2022). Contrastingly, Watson et al. studied the relationship between CAXII expression in a series of 103 cases of invasive breast cancer and prognosis and found that CAXII expression was related to the absence of necrosis and a better prognosis (Watson et al. 2003). Their findings were supported by a study conducted on all types of breast cancer which revealed a correlation between poor prognosis and higher CAIX expression and between a better survival rate and CAXII expression (Chen et al. 2018).

Other studies have shown that CAIX (over)expression serves as a poor prognostic indicator in other cancer types including epidermal tumours (Syrjänen et al. 2014), thyroid tumours (Takacova et al. 2014), Hodgkin's lymphoma (Matolay et al. 2019; Méhes et al. 2019) brain cancer (Haapasalo et al. 2020), lung cancer (Nakao et al. 2009), and rectal cancer (Korkeila et al. 2009).

2.3.5. Inhibition Mechanism of CA Inhibitors

For decades, primary sulfonamide-containing compounds and inorganic anions were accepted to be the only CA inhibitors (CAIs). These two groups can form a complex with the enzyme through a coordination bond with the ion (mainly Zn^{2+}) located in the active site. As a result, they are called metal (Zinc) binders. Over the years, however, kinetic, X-ray crystallographic, and spectroscopic studies revealed extra four mechanisms that are: anchoring to the zinc-coordinated water/hydroxide, blockage of the active site entrance, binding outside the active site, an unknown mechanism as summarized below by Supuran. (Supuran 2016a, 2017a).

2.3.5.1. Binding to the active site metal

Sulfonamides and their isosteres, inorganic anions, monothiocarbamates, dithioates, carboxylates and hydroxamates, and other functional groups are famously known as the zinc binding groups (ZBG) since the zinc is present in most carbonic anhydrases (**Figure 2-18**).

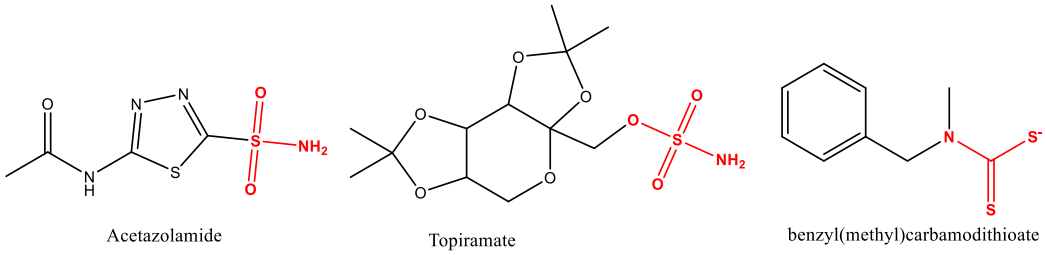

Figure 2-18: ZBG-containing CAIs

ZBG-containing molecules first get deprotonated to become negatively charged and directly bind to Zn^{2+}, forming a tetrahedral geometry. In addition, the ZBGs can also hydrogen bond to Thr199 and Glu106 known as the “gate keepers” (**Figure 2-19**). A tail attached to the ZBGs interacts with the rest of the amphiphilic part of the enzyme.

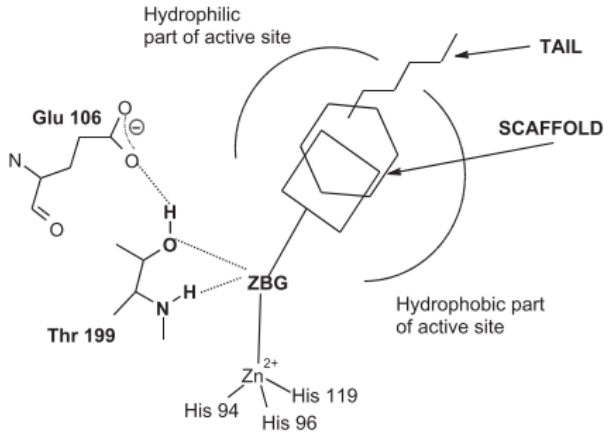

Figure 2-19: Binding mechanism of zinc-binding CAIs

2.3.5.2. Anchoring to the zinc-coordinated water/hydroxide

Phenols, carboxylic acids, ester, polyamine, and hydrolysed sulfocoumarin-containing inhibitors fall under this group (**Figure 2-20**).

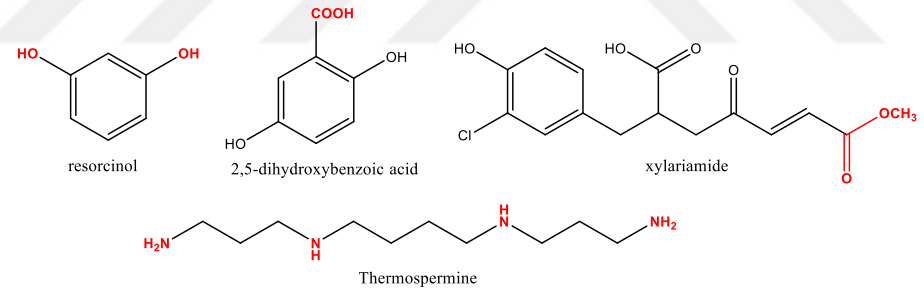

Figure 2-20: CAIs that anchor to the zinc-coordinated water/hydroxide

This mode of inhibition is similar to the Zinc binding mode. The only difference is that there is no direct attachment to the Zn^{2+}, but rather to the zinc nucleophile; the hydroxyl or H_2O molecule attached to the zinc ion (**Figure 2-21**). The group of the inhibitor binding to the zinc nucleophile is called the anchoring group (AG). Similar to the ZBGs, these groups can also form a hydrogen bond with the "gate keeper" Thr199 and have a tail attached to the AG that can interact with other residues away from the Zn^{2+} (amphiphilic region).

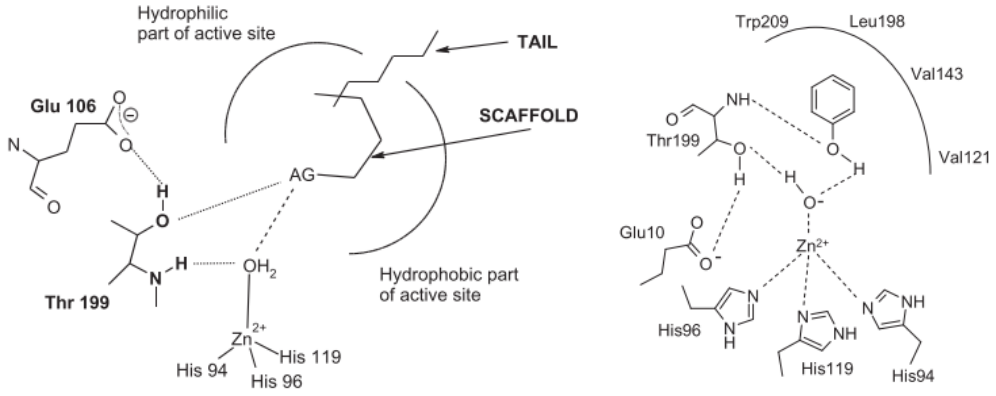

Figure 2-21: A) Binding mechanism of CAIs that anchor to the Zn(II)-coordinated water molecule/hydroxide ion B) Binding of phenol, the first CAI that anchors to zinc-coordinated water.

2.3.5.3. Blockage of the active site entrance

Coumarins were the first to demonstrate this mode of inhibition, but other compounds, such as lacosamide, substituted coumarins, 5- and 6-membered lactones, thiolactones, and quinolinones were discovered to have significant CA inhibitory properties with coumarins. Various literature reported the presence of esterase activity in α-CAs which enables them to hydrolyse the lactone moiety of coumarins producing cinnamic acid derivatives and thiolactone moiety of thiocoumarins producing thiocinnamic derivatives (**Figure 2-22**).

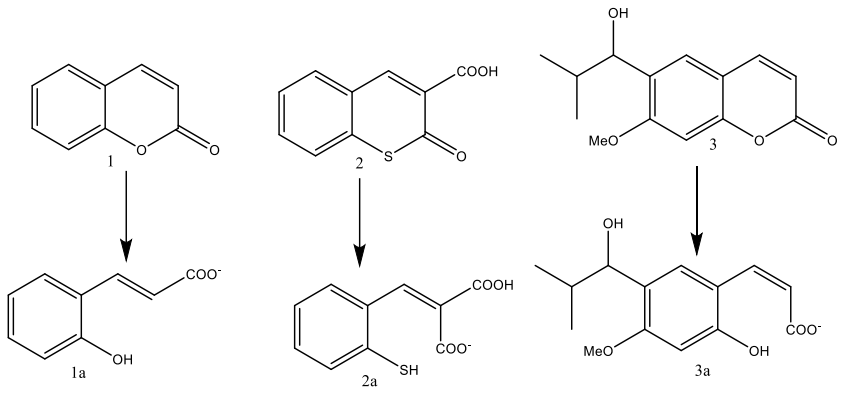

Figure 2-22: CAIs that block the active site entrance of CAs and their hydrolysed product

When compared to ZBG and AG groups, they bind much farther from Zn^{2+}. This group has a sticky group attached to a particular scaffold and the compound could also be extended with a tail to explore more interactions in the amphiphilic region (**Figure 2-23**).

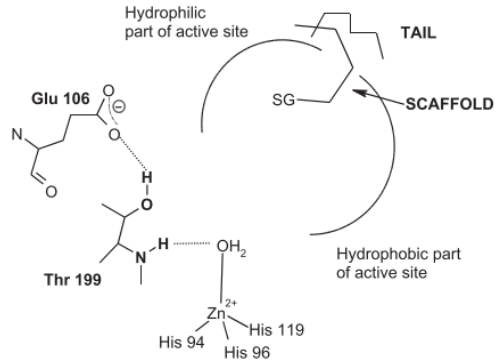

Figure 2-23: Binding mechanism of CAI that blocks the entrance to the active site. SG is a sticky group of the phenol, carboxylic acid, or amide type.

2.3.5.4. Binding outside the active site (Allosteric site)

So far only 2-(2-phenylacetyl)benzoic acid exhibited this mode of inhibition. The molecules bind to the adjacent binding site, completely out of the main binding site (**Figure 2-24**). It is hypothesized that it may inhibit the enzyme by blocking the proton shuttling phase which is the rate-determining step of the entire catalytic cycle.

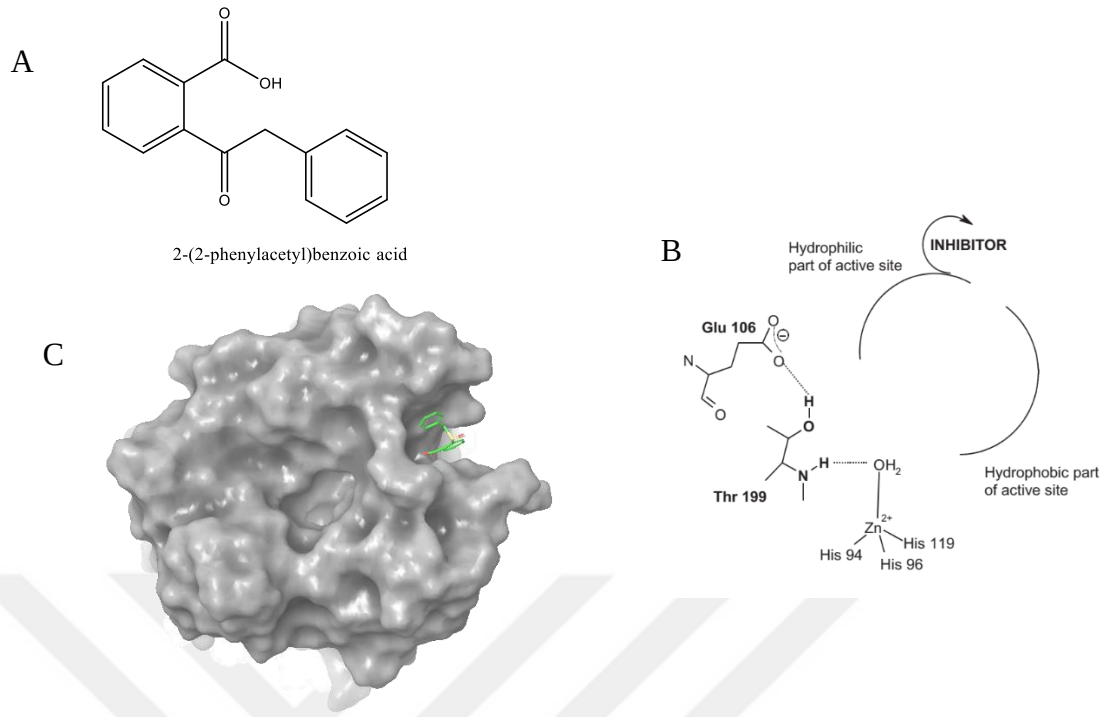

Figure 2-24: (A) 2-(2-phenylacetyl)benzoic acid (B) Binding of 2-(2-phenylacetyl)benzoic acid to the allosteric site of CA. (C) hCAII complexed with 2-(2-phenylacetyl)benzoic acid.

2.3.5.5. Unknown Mechanism

Secondary and tertiary sulfonamides and protein tyrosine kinase inhibitors such as imatinib and nilotinib (**Figure 2-25**) inhibit CAs with an unknown mechanism.

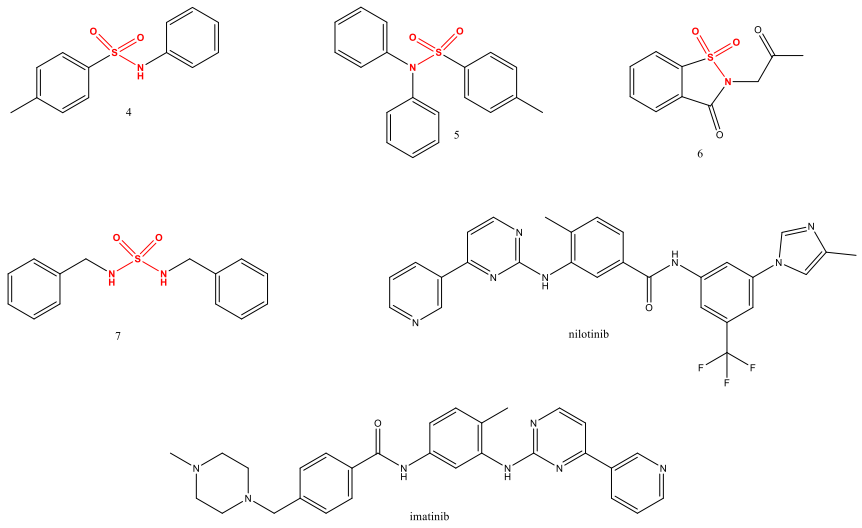

Figure 2-25: CAIs with the unknown binding mode

2.3.6. Tail-Approach in designing CAIs

CA isoenzymes display a high similarity rate which makes it challenging to obtain selective inhibitors. The binding pockets of CAs have many amino acid residues conserved throughout as illustrated in **Figure 2-26** and **Table 2-4**, and this gives the complications of developing isoenzyme-selective inhibitors. As reviewed by Bonardi et al. and Gopinath and Kathiravan, acetazolamide, methazolamide, brinzolamide, topiramate, and the other first and second-generations of zinc-binding sulfonamide derivatives are potent inhibitors of all acidosis-causing CA isoenzymes. However, this lack of selectivity causes the associated side effects, hence restricting their therapeutic application (Bonardi et al. 2022; Gopinath and Kathiravan 2022). To overcome this indiscriminative inhibition, “the tail approach” is applied. This strategy was first described in the literature by Scozzafava et al. in 1999 (Scozzafava et al. 1999), albeit it has been applied earlier before by Supuran’s group (Bonardi et al. 2020).

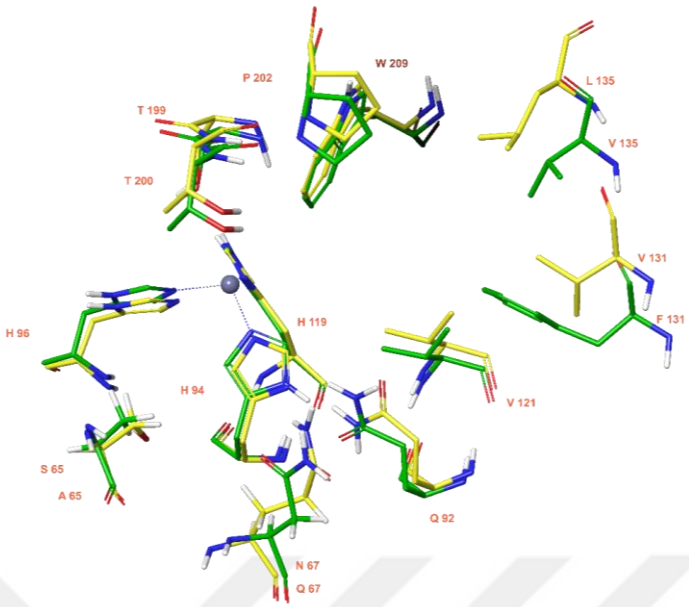

Figure 2-26: Comparison of hCAII (green) and hCAIX (yellow). Catalytic Zn^{2+} is shown as a sphere (grey)

Table 2-4: Residues forming the binding pockets of hCAI, II, IX and XII. (Akdemir et al. 2015)

hCAI	hCAII	hCAIX	hCAXII	hCAI	hCAII	hCAIX	hCAXII
Trp5	Trp5	Trp5	Trp5	Ala121	Val121	Val121	Val121
Glu58	Arg58	Arg59	Leu58	Leu131	Phe131	Val131	Ala131
Ile60	Leu60	Arg60	Thr60	Ala135	Val135	Leu135	Ser135
Val62	Asn62	Asn62	Asn62	Leu141	Leu141	Leu141	Leu141
His64	His64	His64	His64	Val143	Val143	Val143	Val143
Ser65	Ala65	Ser65	Ser65	Leu198	Leu198	Leu198	Leu198
His67	Asn67	Gln67	Lys67	Thr199	Thr199	Thr199	Thr199
Asn69	Glu69	Thr69	Asn69	His200	Thr200	Thr200	Thr200
Phe91	Ile91	Leu91	Thr91	Tyr204	Leu204	Ala204	Asn204
Gln92	Gln92	Gln92	Gln92				

The “tail approach” is the attachment of one or more "tails" to a scaffold incorporating ZBG to create an extended molecule that will enable the molecule to exploit interactions in the active site's external-middle and outer rim with diverse amino acid residues (**Figure 2-27A**). By changing the chemical moiety and size of the tail, isoenzyme-selective with low inhibitory concentrations could be obtained. Besides, in the last decade, many selective and effective hCAIX/XII inhibitors have been developed and synthesized employing the “tail approach” (Bonardi et al. 2020).

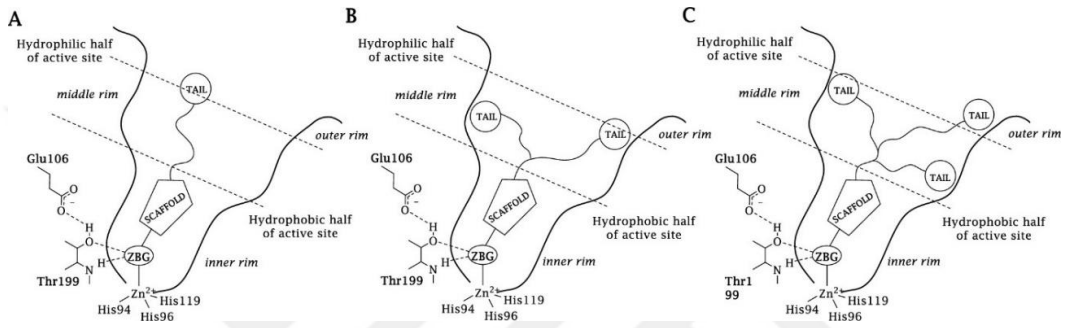

Figure 2-27: Diagrammatic representation of the tail approach for ZBG-containing CAIs. A) Single tail B) Dual-tail C) Three tails (Bonardi et al. 2020).

The dual-tail approach which showed a better approach to designing more selective inhibitors was first reported by Tanpure et al. (Tanpure et al. 2015). It has two tails attached to the ZBG-containing scaffold, aiming at forming interactions with amino acid residues located at both the hydrophilic half and the hydrophobic half (**Figure 2-27B**). The tail could be directly attached to the ZBG-containing scaffold or with a linker which could be a small open linker such as hydrazone or a ring. The three-tails approach involves attaching three different tails to the ZBG-containing scaffold to have a better interaction with the most variable residues in the middle/outer rim of the active site (**Figure 2-27C**) (Bonardi et al. 2022).

2.4. Sulfonamides

2.4.1. Chemistry of Sulfonamides

Sulfonamides, also spelt as sulphonamides, are amide forms of sulfonic acids bearing a $-SO_2NH_2$ group. The first sulfonamide compound was synthesized by Autenriet and Koburger in the early 1900s (Autenrieth and Koburger 1903).

Sulfonamides can be categorized into three groups based on the substituent attachment to the N atom. Primary sulfonamides have two hydrogen atoms in their sulfonyl groups, whereas secondary sulfonamides have just one hydrogen atom (**Figure 2-28**). The H's on primary and secondary sulfonamides are weakly acidic and this enables them to be deprotonated in physiological pH levels. Unlike other sulfonamides, tertiary sulfonamides are not acidic because they lack an ionizable proton (DeRuiter 2005).

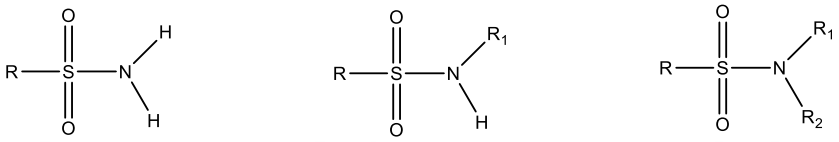

Figure 2-28: General structures of primary, secondary and tertiary sulfonamides

The sulfonamide group is generally resistant to biodegradation and this makes them a preferred bioisostere for carboxylic acids esters, and amides (Wan et al. 2021). Sulfonamides are electron-withdrawing groups and affect adjacent atoms both mesomerically and inductively (Wilden 2010). This makes it challenging, sometimes, to add substituents on aromatic rings containing sulfonamides. In chemical synthesis, the bond between the sulfonyl and the amino can be hydrolysed making sulfonamides widely used as protecting groups (Lin et al. 2000; Wilden 2010).

The introduction of sulfonamides into the realm of medicine started with the serendipitous discovery of the azo dye prontosil as an antibacterial agent in 1932 by the German chemist Gerhard Domagk. It was later discovered that prontosil acts as a prodrug and releases sulfanilamide in the bacterial cells which is responsible for the antibacterial activity (**Scheme 2-3**). This led to the usage of the famous sulfa drugs as antibacterial (Wilden 2010)

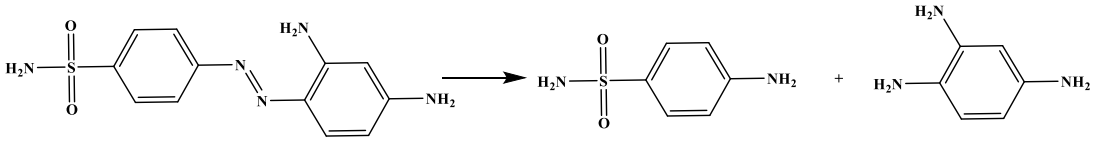

Scheme 2-3: Conversion of Prontosil to sulfanilamide

Sulfonamides can also be in a cyclic form as in saccharine and sultams which are both attractive scaffolds in drug discovery (Rosenman 1978; Debnath and Mondal 2018). Many sultam-containing drugs known as oxicams are commercially available as non-steroidal anti-inflammatory drugs (**Figure 2-29**) (Xu et al. 2014).

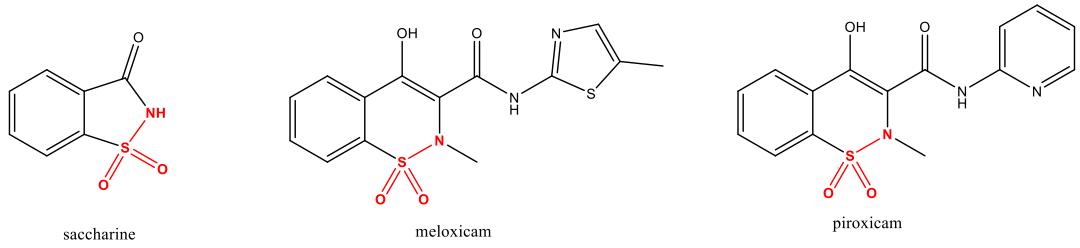

Figure 2-29: Commercially available compounds containing a cyclic sulfonamide

The fact that sulfonamides get deprotonated at physiological states to be negatively charged, enabling them to coordinate to Zn^{2+} and from stable tetrahedra complexes, they are the most-studied functional group in CA inhibition (Supuran and Mugelli 2019). Primary sulfonamides are potent inhibitors of CA enzymes, but secondary sulfonamides and cyclic sulfonamides are often poor inhibitors of CA enzymes (Moeker et al. 2014; Baronas et al. 2021)

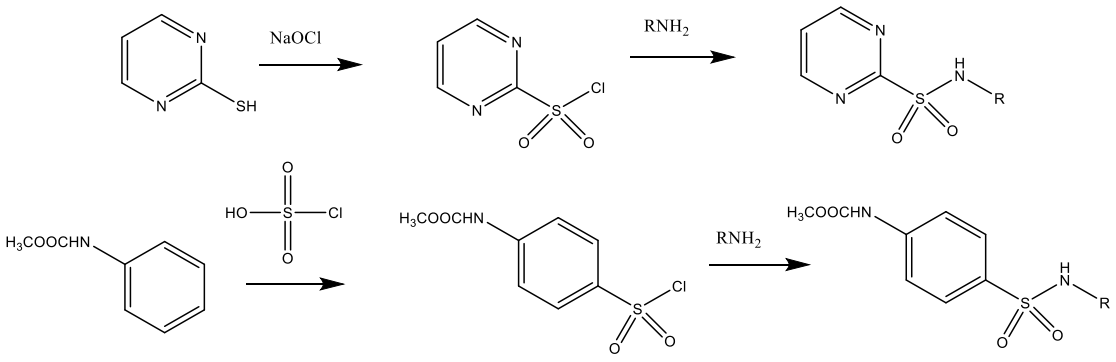

Scheme 2-4: General synthesis of sulfonamides

Sulfonamides are generally synthesized from the reaction of sulfonyl chloride and ammonia or amino groups (Autenrieth and Koburger 1903). Synthesis of sulfonyl

chlorides generally requires chlorosulfonic acid (Cremlyn 2007) or oxidation of thiol with sodium hypochlorite (**Scheme 2-4**) (Wright and Hallstrom 2006).

2.4.2. CA inhibitory properties of sulfonamide-containing compounds

After the discovery of the antibacterial effects of sulfanilamide in 1932, sulfonamides have considerably gained the attention of drug hunters. They have been widely used in the treatment of various diseases. As previously mentioned, the sulfonamide CA-inhibiting property was first discovered by (Mann and Keilin 1940). In 1948, Krebs assessed the CA inhibitory activities of 25 different sulfonamides (Krebs 1948). However, the first sulfonamides as CA (CAII and CAIV) inhibitors that were clinically approved to treat glaucoma by reducing the intraocular pressure caused by CA was acetazolamide (Becker 1955). Other systemic methazolamide, ethoxyzolamide, and dichlorphenamide were also approved within a few years. However, to minimize the side effects associated with these systemic antiglaucoma agents, topical agents dorzolamide, developed by Maren, and brinzolamide were approved in 1955 and 1999, respectively as reviewed by Masini et al and Winum et al. (Masini et al. 2013; Winum et al. 2006; Winum 2014).

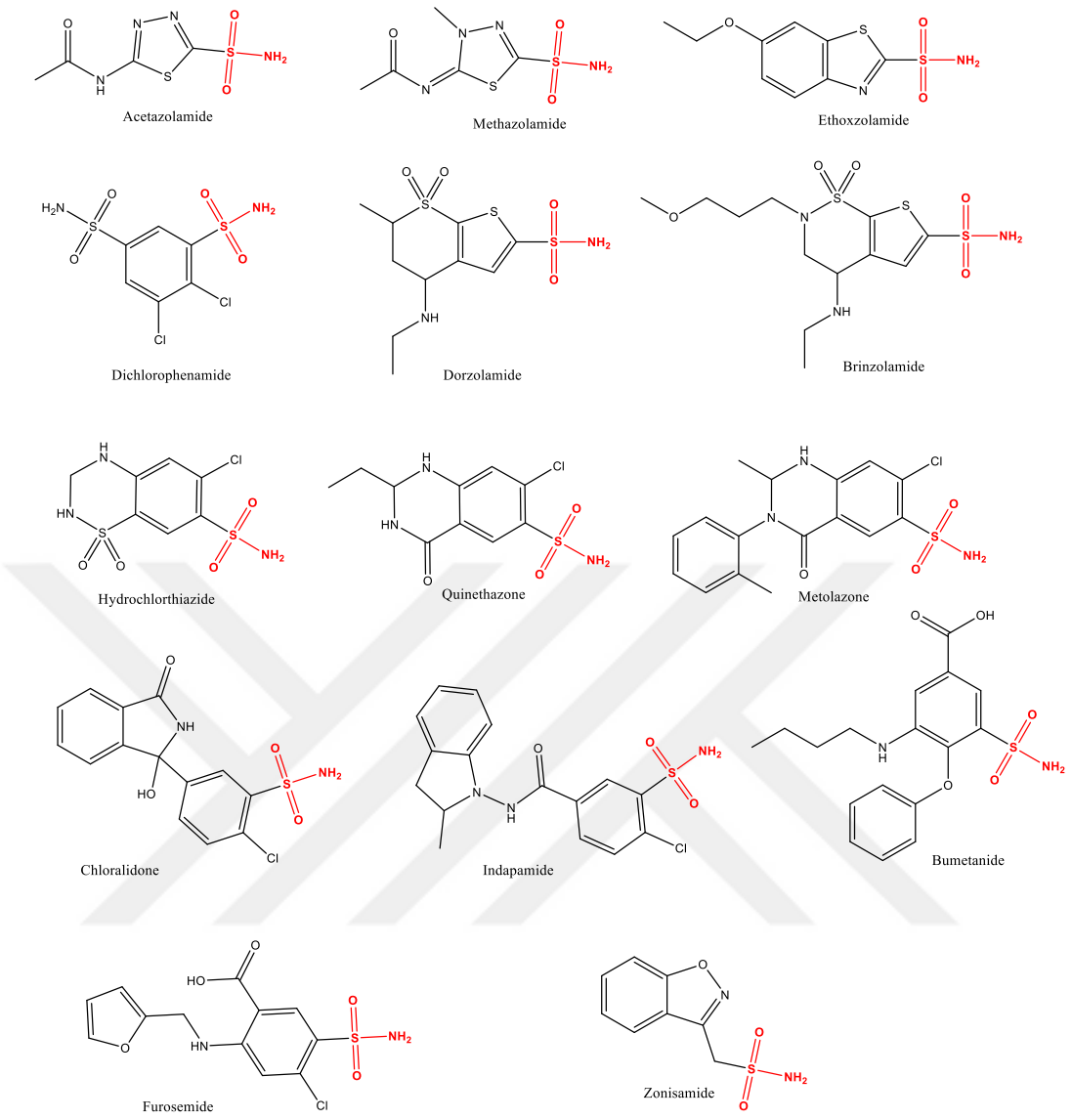

Figure 2-30: Structures of clinically approved CAIs containing a sulfonamide

In addition, CAs (CAII/IV/XVII/XIV) were implicated with oedema and hence their inhibition led to diuresis. Together with systematic antiglaucoma agents, benzothiadiazines, quinethazone, metolazone, chlorthalidone, indapamide, furosemide, and bumetanide were developed to treat oedema (**Figure 2-30** (Supuran 2008). Furthermore, an aliphatic sulfonamide, zonisamide was effectively used in the treatment of epilepsy.

Indusilam, an anticancer sulfonamide that inhibits the progression of the cell cycle by attacking the G1 phase (Owa et al. 1999) was reported to successfully inhibit

tumour-associated hCAIX at nanomolar concentrations (Abbate et al. 2004). Indisulam has been assessed in numerous clinical trials as an anticancer drug candidate independently or in combination with other anticancer drugs for the treatment of various cancers including breast, gastric, renal, skin, and rectal cancers (Search of: indisulam - List Results - ClinicalTrials.gov 2022).

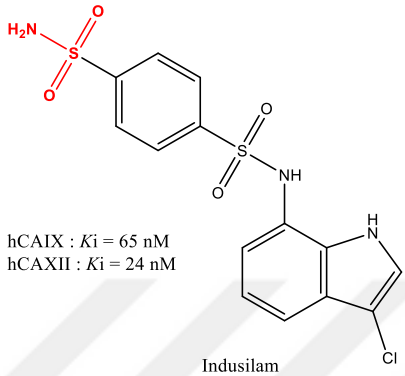

Indusilam

A ureido-substituted sulfonamide-containing drug (SLC-0111), prepared by Supuran's team, selectively inhibited hCAIX/XII at low nanomolar concentrations (Pacchiano et al. 2011) and has successfully completed Phase I clinical trial (NCT02215850) in patients with advanced solid tumours (McDonald et al. 2020). The combination of SLC-0111 and gemcitabine in metastatic pancreatic ductal adenocarcinoma has entered Phase 1b of a clinical trial (NCT03450018), however, due to a change of pharmaceutical partner, the study did not proceed (A Study of SLC-0111 and Gemcitabine for Metastatic Pancreatic Ductal Cancer in Subjects Positive for CAIX - Full Text View - ClinicalTrials.gov 2022).

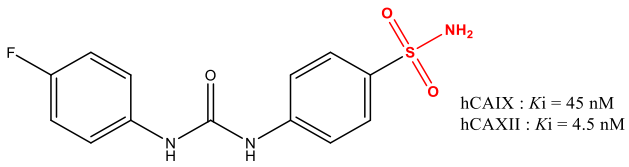

SLC-0111

Another clinical trial (NCT03467360) at phase 1 recruiting stage involves the combination of acetazolamide with platinum and etoposide-based radiochemotherapy in patients with localized small-cell lung cancer. This is the first time acetazolamide has entered clinical phases after demonstrating anticancer activities in multiple preclinical studies (British Columbia Cancer Agency et al. 2022).

Novel fluorinated benzenesulfonamide derivatives synthesized by Kazokaitė et al. selectively inhibited the recombinant hCAIX by directly binding to the Zn^{2+} in low nanomolar concentrations of between 0.05 – 1.1 nM. The mode of inhibition of these compounds was validated by mass spectrometric gas analysis in a CRISPR/Cas9-mediated CAIX knockout in HeLa cells. In addition, these compounds reduced acidosis in HeLa, H460, MDA-MB-231, and A549 cancer cells in low nanomolar concentrations (Kazokaitė et al. 2018).

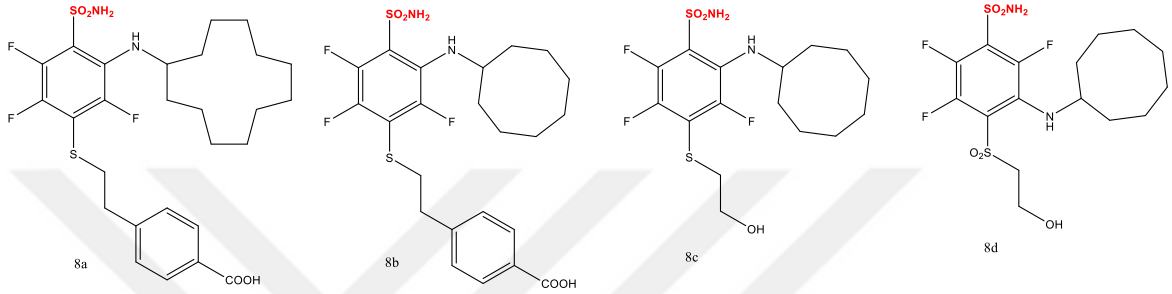

Guzel-Akdemir et al. designed and synthesized novel isatin-based sulfonamides. The compounds selectively inhibited tumour-associated hCAIX/XII at low nanomolar concentrations with a higher inhibition potential against hCAIX (Güzel-Akdemir et al. 2015).

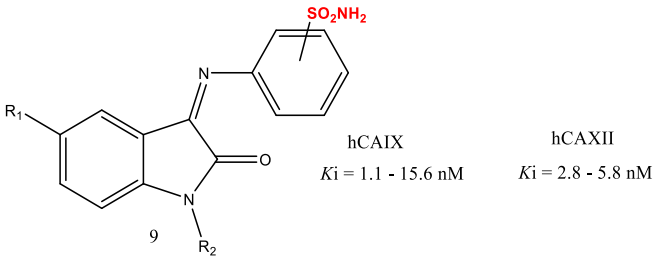

Karali et al. prepared novel benzenesulfonamide-isatin hybrids joined with a thiosemicarbazones linker. The compounds were evaluated for inhibitory potentials against cytosolic hCAI/II and tumour-associated hCAIX/XII. The inhibition profile displayed selectivity towards hCAIX/XII over hCAI/II (Karalı et al. 2017).

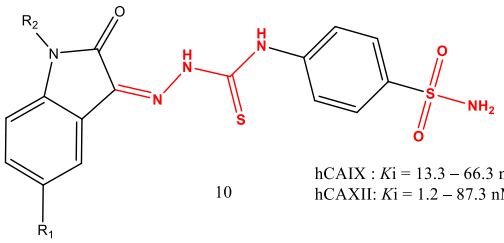

10

hCAIX : *Ki* = 13.3 – 66.3 nM
hCAXII: *Ki* = 1.2 – 87.3 nM

The synthesis, characterization, and tumour-associated hCAIX/XII selective inhibition of novel sulfonamidoindole-based hydrazones were reported by Demir-Yazıcı et al. Most of the compounds selectively and strongly inhibited hCAIX/hCAXII at low nanomolar concentrations. Six of the compounds had *K*i values lower than 10 nM with compound **11a** inhibiting hCAIX at 9.2 nM and compound **11b** inhibiting hCAXII at 1.4 nM (Demir-Yazıcı et al. 2019). Another study, conducted by Demir-Yazıcı et al., revealed these compounds are potential α-CA present in *Vibrio cholerae* (Demir-Yazıcı et al. 2020).

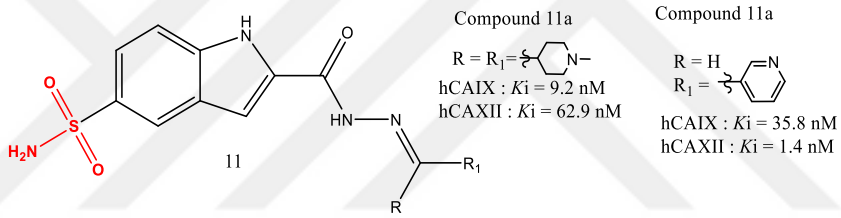

11

Compound 11a

R = R$_1$=

hCAIX : *Ki* = 9.2 nM
hCAXII : *Ki* = 62.9 nM

Compound 11a

R = H
R$_1$ =

hCAIX : *Ki* = 35.8 nM
hCAXII : *Ki* = 1.4 nM

Employing a structural extension of SLC-0111 to enhance the tail hydrophobic interactions and thus improve hCAIX and XII inhibitions, Eldehna et al designed and synthesized a series of new isatin-SLC-0111 hybrids. Indeed, the inhibitory profile of these hybrids against hCAIX generally showed a significant increase with few selectivity enhancements towards hCAIX/XII over hCAI. However, selectivity towards hCAIX/XII over the ubiquitous hCAII generally decreased. Compound **12a** displayed the highest inhibition against hCAIX and hCAXII. In addition, the compound demonstrated promising anticancer activity against breast cancer MDA-MB-231 and MCF-7 cell lines (Eldehna et al. 2019).

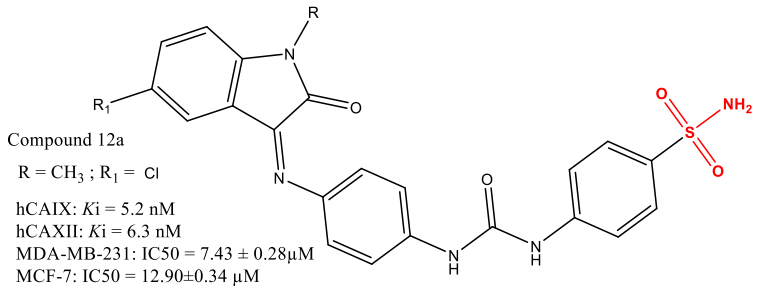

Compound 12a

R = CH_3 ; R$_1$ = Cl

hCAIX: *Ki* = 5.2 nM
hCAXII: *Ki* = 6.3 nM
MDA-MB-231: IC50 = 7.43 ± 0.28µM
MCF-7: IC50 = 12.90±0.34 µM

12

Wahaibi et al. employed the three-tail approach to synthesize a series of imidazole-benzene sulfonamide hybrids with three aromatic rings attached to the imidazole ring as selective tumour-associated hCAIX/XII inhibitors. Six of the compounds inhibited hCAIX in low micromolar concentrations (*K*i = 0.3 – 1.3 µM) and were further assayed for their antiproliferative activity against A-549, MCF-7, Panc-1, and HT-29 cancer cells. Compound **13a** demonstrated the highest antiproliferative activity (Al-Wahaibi et al. 2021).

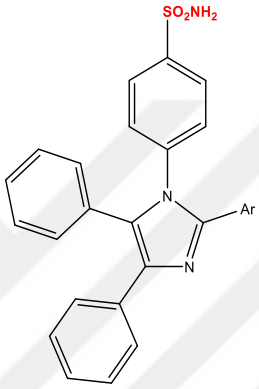

Compound 13a
Ar = 2-MeO-Phenyl
hCAIX: *K*i = 0.3 µM
hCAXII: *K*i = 3.7 µM
A-549: IC_{50} = 2.4 ± 0.5 µM
MCF-7: IC_{50} = 2.1 ± 0.2 µM
Panc-1: IC_{50} = 2.2 ± 0.4 µM
HT-29 : IC_{50} = 2.4 ± 0.4 µM

Commercial sulfonamide-containing drugs including the selective COX-2 inhibitors, celecoxib and valdecoxib, were assayed against hCAI, II, IV, IX and XII. The two COX-2 inhibitors showed the highest inhibition against the tumour-associated hCAIX/XII, functioning as dual inhibitors (Di Fiore et al. 2006).

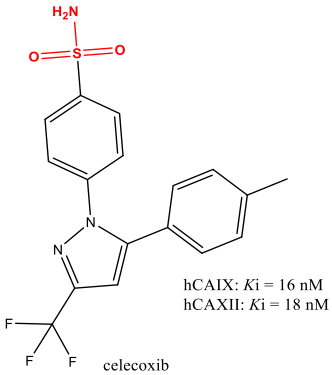

hCAIX: *K*i = 16 nM
hCAXII: *K*i = 18 nM
celecoxib

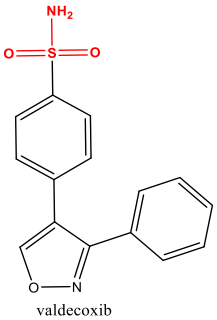

valdecoxib
hCAIX: *K*i = 27 nM
hCAXII: *K*i = 13 nM

Ozmen Ozgun and colleagues designed and synthesized a series of novel benzenesulfonamide-pyrazoline hybrids (**14**) and were tested for their inhibition potency against hCAI/II. The compounds inhibited these cytosolic enzymes below 55nM concentrations. In addition, the compounds were tested for their anticancer activity against oral squamous cancer cell carcinoma cell lines and non-cancer cells,

however, the compound generally inhibited both cancer and non-cancer cells at micromolar concentrations (Ozmen Ozgun et al. 2019).

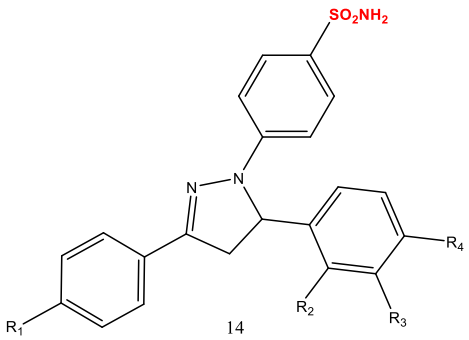

14

Again, novel benzenesulfonamide-pyrazoline hybrids synthesized by Abdel-Aziz et al were assessed for their inhibitory activity against both the cytosolic hCAI/II and tumour-associated hCAIX/XII. The compounds generally showed better inhibition of hCAIX/hCAXII compared to the cytosolic ones. Compound **15a** inhibited hCAIX and hCAXII at 5.5 and 7.1nM concentrations respectively (Abdel-Aziz et al. 2019).

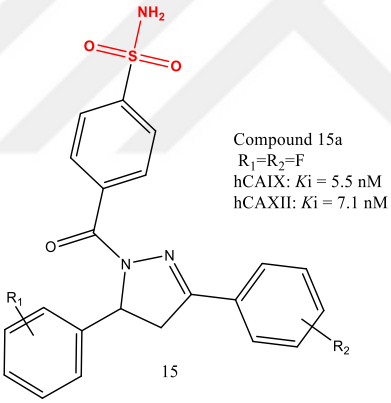

15

To obtain selective hCAIX inhibitors using the “tail approach”, Abdel-Aziz et al also designed and synthesized a series of novel benzenesulfonamide containing isoindoline-1,3-dione (**16**). The compounds were tested against hCAI, II, IV and IX and showed selectivity towards hCAIX with low nanomolar inhibitory concentrations of 17.3 - 83.9 nM (Abdel-Aziz et al. 2018).

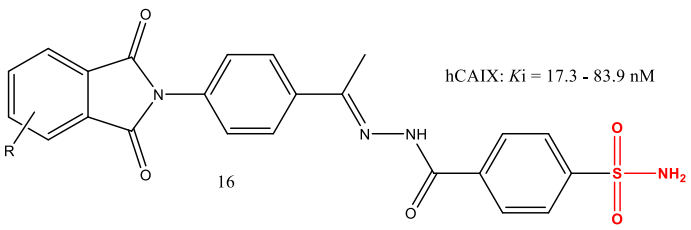

16

Said et al. designed and synthesized new triazolopyrimidine and triazole-based benzenesulfonamides that were tested for their inhibitory activity against hCAI, II, IX, and XII the newly synthesized sulfonamides. The compounds inhibited hCAIX and XII at low nanomolar concentrations. Although the compounds generally displayed selectivity towards hCAIX/XII over hCAI. However, compounds also inhibited hCAII at low nanomolar concentrations except for compounds **17a** and **17b** which displayed improved selectivity (Said et al. 2020).

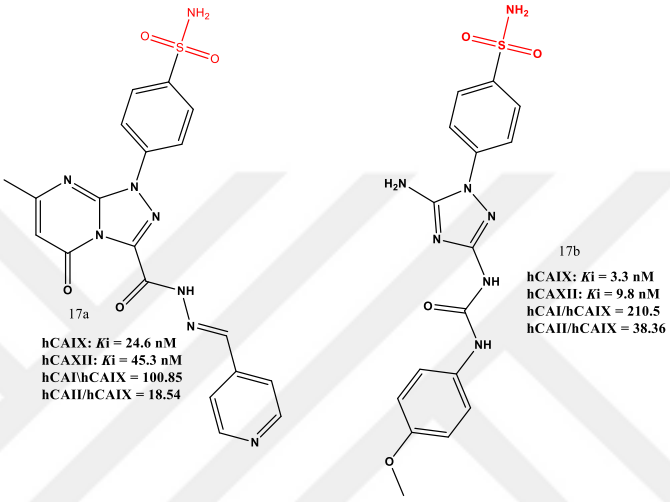

2.5. Synthesis of Isothiocyanates

Various synthetic methods have been applied to obtain isothiocyanates, however, the traditional method is the use of thiophosgene as described by Mckee and Bost in 1946 (**Scheme 2-5A**). This method involves the dissolution of primary amines in water containing concentrated HCl. One equivalent of thiophosgene is subsequently added to the mixture and further stirred until the red colour of the thiophosgene disappears. The resulting crystalline product is filtered and washed with water. This reaction is facile with a yield of >70%. Using this method, McKee and Bost synthesized 4-isothiocyanatobenzenesulfonamide and isothiocyanate derivatives of various sulfa drugs (McKee and Bost 1946). Ghorab et al. and Karali et al. also used the same method to synthesize 4-isothiocyanatobenzenesulfonamide (Ghorab et al. 2016; Karalı et al. 2017). Posner et al. and Mays et al. also synthesized alkylisothiocyanates derivates by reacting primary aliphatic amines with thiophosgene in H_2O, $CH_2Cl_2/CHCl_3$ and 2% NaOH (**Scheme 2-5B**). However, the yields vary between 6 – 38% (Posner et al. 1994; Mays et al. 2008). In addition, Ghorab and the team successfully converted several sulfa drugs to their corresponding isothiocyanate derivatives by reacting them with

thiophosgene in an aqueous medium in the presence of dilute HCl (Ismail et al. 2008; El-Gaby et al. 2018). However, thiophosgene is no longer a preferred choice due to its toxicity and bad odour. Besides, thiophosgene can react with other functional groups to form side products. As a result, more convenient methods were developed that involved the use of other agents rather than thiophosgene.

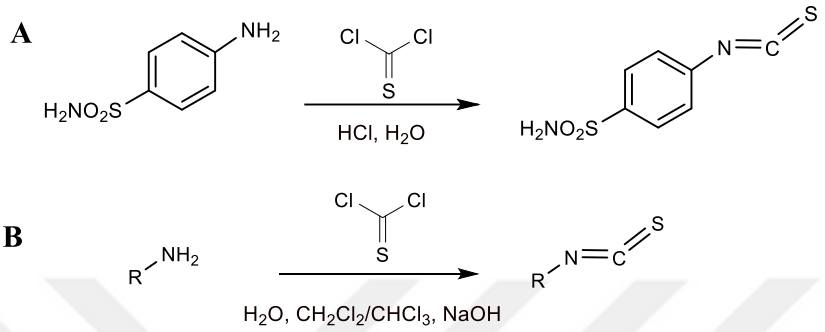

Scheme 2-5: Synthesis of isothiocyanate derivatives from amines and thiophosgene

As an alternative to thiosphosgene, Kim and Yi used di-2-pyridyl thionocarbonate (DPT) as a thiocarbonyl source (**Scheme 2-6**). This reaction is instantaneous and produces high yields of 80 – 90% (Kim and Yi 1985).

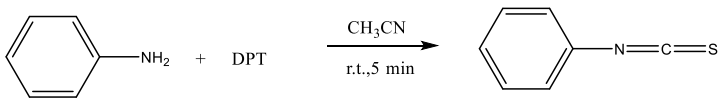

Scheme 2-6: Synthesis of isothiocyanatobenzene from aniline and DPT

However, DPT is also synthesized from the reaction of thiophosgene with 2 eq. of 2-hydroxyprydine in the presence of 2 eq TEA (**Scheme 2-7**) (Kim and Yi 1985).

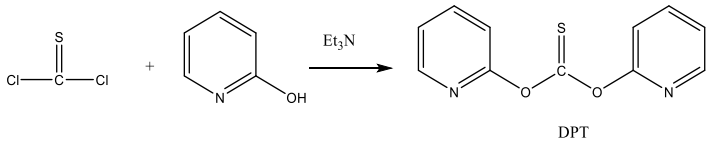

Scheme 2-7: Synthesis of DPT

In addition, one of the most common methods of synthesizing isothiocyanates is the Staudinger/aza Wittig tandem reaction. This reaction works in two steps. First, triphenylphosphine reacts with azides to produce the intermediate, iminophosphorane. In the presence of CS_2, the intermediate is converted to the corresponding isothiocyanate (Psurski et al. 2017; Santhosh et al. 2018).

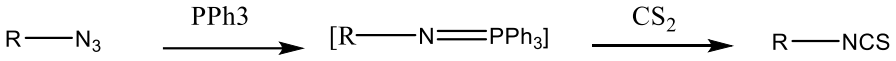

Scheme 2-8: Synthesis of isothiocyanates from azides

SitaRam et al. described the synthesis of isothiocyanates using CS_2 and TEA. TEA is added to methanol at 0 ºC. While stirring, CS_2 is added dropwise. After a further stirring of the reaction for 10 mins, the amine is added to give the triethyl ammonium dithiocarbamate salt. The salt is extracted with ethyl acetate:H_2O, followed by a treatment of $NaHCO_3$ and I_2 to give the corresponding isothiocyanates (SitaRam et al. 2014).

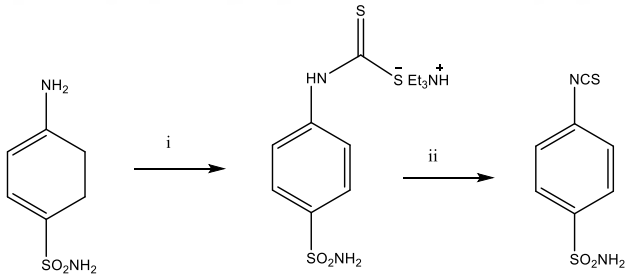

Scheme 2-9: Synthesis of 4-isothiocyanatobenzenesulfonamide from CS_2 and TEA

Recently, Janczewski et al. described a microwave-assisted synthesis of isothiocyanates derivatives of aliphatic, aromatic, natural and unnatural amino acids using 4-(4,6-dimethoxy-1,3,5-triazin-2-yl)-4-methylmorpholinium toluene-4-sulfonate (DMT/NMM/TsO^-) as a new, efficient desulfurating agent for the formation of isothiocyantes from primary amines or hydrochlorides (**Scheme 10**). The yields varied from 50 – 92% for aliphatic isothiocyanates. Janczewski et al. described DMT/NMM/TsO^- as an efficient and environmentally friendly coupling reagent,

however, low yields were obtained in the synthesis of aromatic isothiocyanates. (Janczewski et al. 2021)

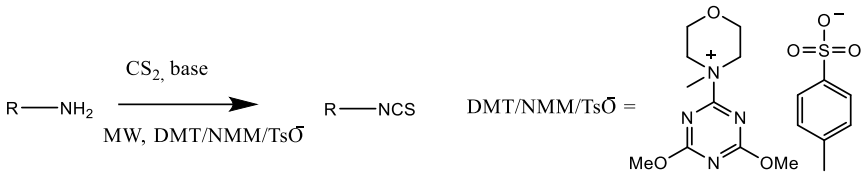

Scheme 2-10: Synthesis of isothiocyanates from amines and CS_2 using DMT/NMM/TsO^- catalyst.

2.6. Thiosemicarbazides

2.6.1. Synthesis of thiosemicarbazides

Thiosemicarbazides are a group of compounds with the general formula $H_2NC(S)NHNH_2$. They are often used in organic chemistry as a precursor in the synthesis of thiosemicarbazones and many pharmacologically relevant heterocycles (Metwally et al. 2011). Thiosemicarbazides can also be used as linkers between two scaffolds in drug design and in addition, they display various biological activities (Gazieva and Kravchenko 2012). The traditional method of preparing thiosemicarbazides involves the addition of an appropriate isothiocyanate (1 eq) suspended/dissolved in ethanol or 2-propanol dropwise to an ethanolic solution of 1 eq hydrazine hydrate whiles vigorously stirring in an ice bath. The precipitate obtained is filtered off and recrystallized from ethanol. The reaction is spontaneous and with high yields of >70% (Tišler 1956; Karalı et al. 2017; Hałdys et al. 2018; Soylu Eter et al. 2021).

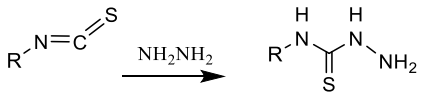

Scheme 2-11: General synthesis of thiosemicarbazides from isothiocyanates and hydrazine

Bhartin et al. described a two-step synthesis of alkylthiosemicarbazides by reacting KOH, CS_2 and alkyl amine derivatives in H_2O: ethanol (1:3) mixture below 20º C. Sodium chloroacetate is added to the reaction mixture and left overnight, followed by

the addition of conc. HCl to precipitate thioglycolic acid derivatives. Thiosemicarbazide derivatives were obtained via hydrazinolysis with hydrazine hydrate (Bharti et al. 2002).

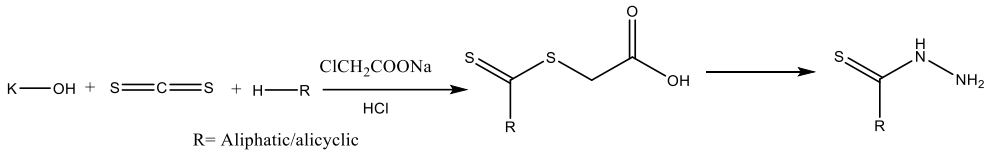

Scheme 2-12: General synthesis of thiosemicarbazides starting from alkylamines using KOH and CS_2

Metwally et al. reviewed a three-step synthesis of arylthiosemicarbazides by reacting arylamines with CS_2 in the presence of KOH as a catalyst to potassium arylcarbamodithioate salts. This salt is reacted with methyl iodide to obtain *N*-arylmethyldithiocarbamates which on hydrazinolysis give 4-arylthiosemicarbazides (Metwally et al. 2011).

Scheme 2-13: General synthesis of thiosemicarbazides starting from arylamines using KOH and CS_2

2.7. Thiosemicarbazones

Thiosemicarbazones (TSC) are Schiff bases that are generated through the condensation of a carbonyl-containing group (aldehyde or ketone) with an appropriate thiosemicarbazide. The availability of hydrogen bonding donors and acceptors and potential donor sites for coordination are indicated by the general formula for thiosemicarbazones (**Figure 2-31**).

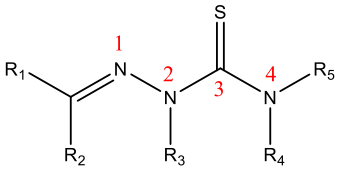

Figure 2-31: General structures of TSC

TSCs are generally in their thione forms in a solid state but may display thione-thiol tautomerism in solutions. They are also utilized in coordination chemistry as strong ligands with varying densities that bind well to transition and non-transition metal ions to produce co-ordination complexes. TSCs have a wide range of biological applications. The versatility of biological activity is the driving force behind the high interest of medicinal chemists in TSC and their metal complexes. TSCs are often explored as potential antifungal, antibacterial, antiviral, antiprotozoal, antituberculosis, and anticancer agents (George et al. 2022).

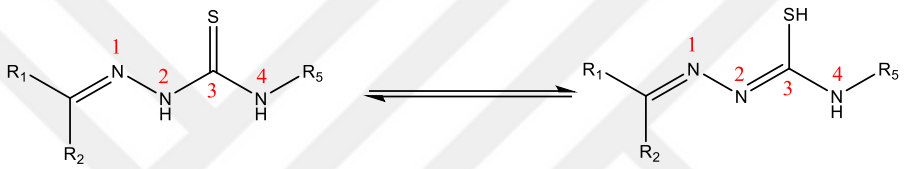

Scheme 2-14: Thione-thiol tautomerism of TSCs

2.7.1. Synthesis and biological activities of thiosemicarbazones

Bauer who has been working on the antiviral activities of TSCs, especially isatin 3-thiosemicarbazones since 1955, communicated the antiviral activity of methisazone (also known as marboran) against smallpox virus in an *in vivo* study in 1960. Based on these results, Bauer conducted a clinical trial on methisazone and the findings revealed that methisazone could be used as a prophylaxis for smallpox and a therapeutic agent for *eczema vaccinatum* and *vaccinia gangrenosa* (Bauer 1965). Patskovsky also revealed that methisazone reduces adenovirus1 type 1 resistance against interferon. (Patskovsky et al. 1996)

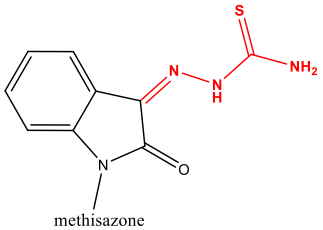

Another TSC-containing drug is thioacetazone used as an antitubercular agent. Thioacetazone was used in combination with isoniazid to reduce mycobacterial

resistance against isoniazid. However, due to its toxicity, particularly in HIV-positive patients, it has been pulled out from the market (Halloum et al. 2017).

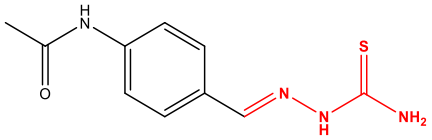

Thioacetazone

Critical Outcome Technologies Inc. developed COTI-2, a TSC derivative that has entered clinical phase 1 trial (NCT02433626) for the treatment of recurrent gynaecological, pancreatic, head and neck, colorectal, and lung cancers as a monotherapy or in combination with cisplatin (Study of COTI-2 as Monotherapy or Combination Therapy for the Treatment of Malignancies - Full Text View - ClinicalTrials.gov 2023).

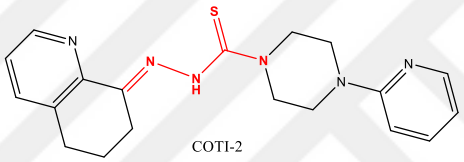

COTI-2

Oncochel Therapeutics has developed DpC which has completed clinical phase I (NCT02688101) for the treatment of patients with advanced solid tumours (Collaborative Medicinal Development Pty Limited 2019).

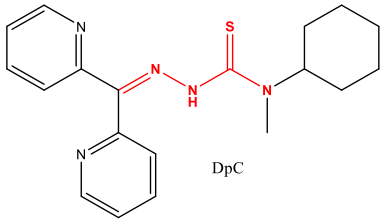

DpC

In general, the synthesis of TSC derivatives involves the condensation of thiosemicarbazide with either aldehyde or ketone in ethanol or methanol. The reaction could proceed with or without a catalyst. However, the use of various acid catalysts such as HCl, sulfuric acid, glacial acetic acid, and p-toluenesulfonic acid has considerably reduced the reaction time (Güzel et al. 2008; Parker et al. 2015; Song et al. 2020; Lima et al. 2002).

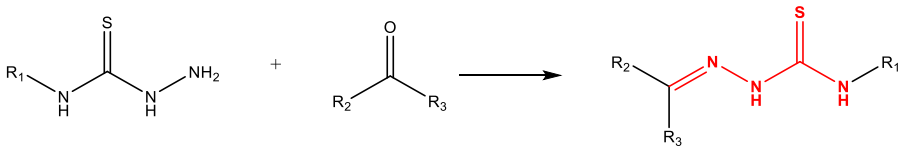

Scheme 2-15: General synthesis of TSC

Lima et al. communicated the synthesis, characterization and single crystal X-ray studies of 2-(1-(thiophen-2-yl)ethylidene)hydrazine-1-carbothioamide (**18a**) and *N*-phenyl-2-(1-(thiophen-2-yl)ethylidene)hydrazine-1-carbothioamide (**18b**). The compounds were prepared by refluxing 1-(thiophen-2-yl)ethan-1-one with the relevant thiosemicarbazide in ethanol in the presence of H_2SO_4 (Lima et al. 2002).

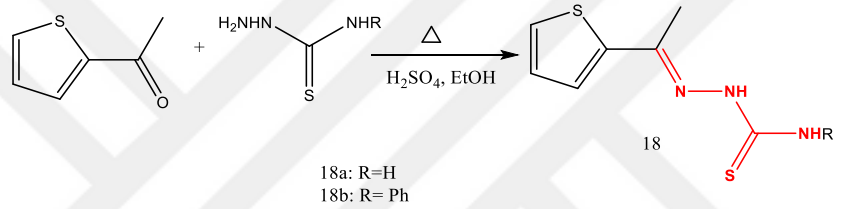

18a: R=H
18b: R= Ph

18

Güzel et al. reported the preparation, characterization and antimycobacterial activity of isatin-containing TSC derivatives (**19**). Appropriate isatins were refluxed in ethanol with suitable thiosemicarbazides for 5hr with a catalytic amount of sulfuric acid. The yields of the products were between 60 - 90%. Some of the compounds demonstrated good antimycobacterial activities at low micromolar concentrations (Güzel et al. 2008).

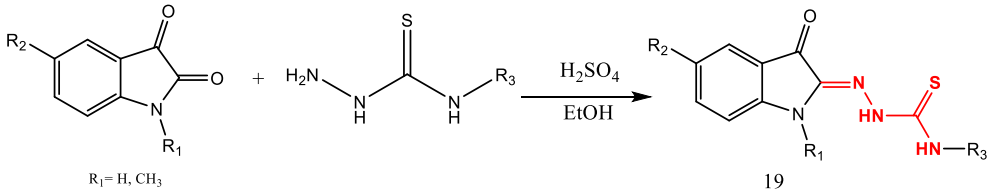

R_1= H, CH_3

19

Sevinçli et al. reported the synthesis, characterization, single crystal X-ray diffractometry studies and anticancer/antituberculosis activities of 5-fluoro-1-methyl/ethyl-1*H*-indole-2,3-dione 3-thiosemicarbazones. *N*-susbstituted-5-fluoroisatins were refluxed with suitable thiosemicarbazides in the presence of a catalytic amount of H_2SO_4 to give the corresponding TSC derivatives. The compounds were assayed for their antiviral activities against HS1, HSV-2, HSV-1 thymidine kinase-negative and Coxsackie B4 virus. Some of the compounds showed good inhibition against the viruses

(Sevinçli et al. 2020b). Sevinçli et al., in another study, reported the antitubercular and anticancer activities of the compounds (Sevinçli et al. 2020a).

Parker et al reported the preparation and characterization of benzoylbenzophenone-TSC derivatives and their anticancer activity and inhibition potential against cathepsin L and B. The compounds were inactive against cathepsin B, but generally inhibited cathepsin L with compound 2-((3-bromo-5-(2-fluorobenzoyl)phenyl)(2-fluorophenyl)methylene)hydrazine-1-carbothioamide (**20a**) displaying the highest inhibition with IC_{50} values of 8.1 nM. The syntheses were carried out under different conditions as summarized below (Parker et al. 2015).

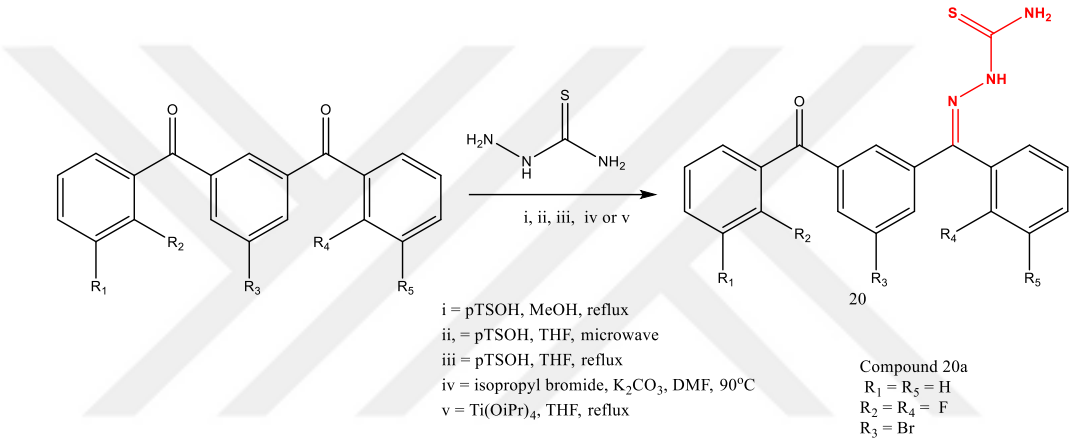

Shehzad et al. synthesized various TSC derivatives by refluxing appropriate N4-substituted thiosemicarbazides with aldehydes or ketones in methanol with a few drops of glacial acetic acid as a catalyst (Shehzad et al. 2021).

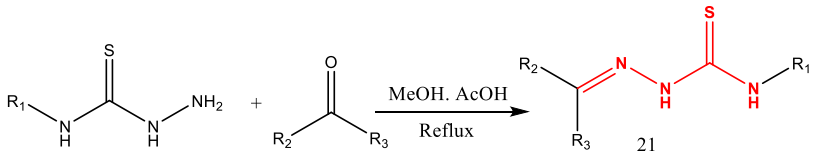

Othman et al. synthesized novel semicarbazones/thiosemicarbazone-containing 1,2,3-triazoles that inhibited VEGFR-2 signalling. The compounds were designed according to the SAR of sorafenib with VEGFR-2. The TSCs were synthesized by reacting 1-(4-substitutedphenyl)-4-(1-hydrazineylideneethyl)-5methyl-1*H*-1,2,3-triazole derivatives (1 eq) with suitable isocyanates/isothiocyanates (1.2 eq) in THF. The reactions were carried out at room temperature. The addition of hexane gave precipitates of the TSC derivatives. All the compounds were tested for their antiproliferative activity against sixty cancer cells. The TSCs demonstrated a better

inhibition profile than the semicarbazones. In addition, the TSC **22** inhibited VEGFR-2 with IC_{50} value of 0.067 µM which is comparable to the reference drug, Sorafenib (IC_{50} = 0.048 µM) (Othman et al. 2022).

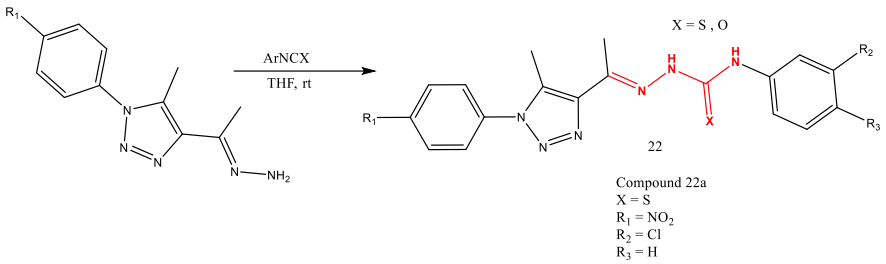

The outbreak of the Covid-19 pandemic caused a lot of havoc to human health, which led to the screening of millions of compounds against the main protease (Mpro) of SARS-CoV-2. One of the screenings was performed by Xu et al. The findings of this screening revealed several TSC-containing compounds as strong Mpro inhibitors with more than 94% inhibition with IC_{50} values of 2.43 – 34.22 µM. Compound **23** showed the lowest IC_{50} value of 2.43 µM and was determined as a competitive inhibitor of Mpro from enzyme kinetic studies (Xu et al. 2022).

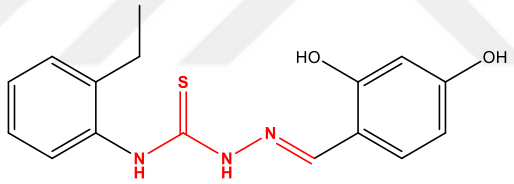

23

2.8. Biological activities azine-containing molecules

Azines are a class of chemicals that go through a wide range of chemical processes and have been considered prospective substrates for crosswise cycloaddition events and a flexible intermediate in heterocyclic synthesis. Azines are 2,3-diazabuta-1,3-dienes, also known as bis-Schiff bases. Because an N-N link connects the two imine bonds that make up the azine moiety, they can be viewed as polar acceptor groups

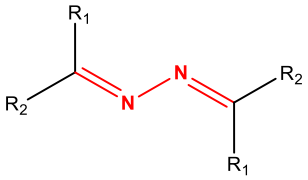

Figure 2-32: Structure of azine

oriented in opposition to one another (Bondock et al. 2016). Azines are considered to be bioisosteres for 1,3-butadienes for serving as conjugation bridges (switchers) between conjugated scaffolds by facilitating the delocalization of π electrons. However, unlike 1,3-butadienes, azines may function as conjugation stoppers by preventing electron delocalization between the two systems. Many studies have concluded that azines generally function as conjugation switchers, however, they may preclude conjugation if the fractions attached do not provide a sufficient driving force to continue conjugation. Azines in their planar conformation (trans) continue conjugation whiles preventing it in their twisted form (cis). (Lewis and Glaser 2002; McLoughlin et al. 2007; Belyaev et al. 2021). The trans conformation provides the optimal overlap allowing conjugation between C=N bond p-orbitals without involving the lone pairs on N. On the other hand, whiles overlapping with the lone pairs on N occurs, overlapping of p-orbitals does not occur as shown in **Figure 2-33** (McLoughlin et al. 2007).

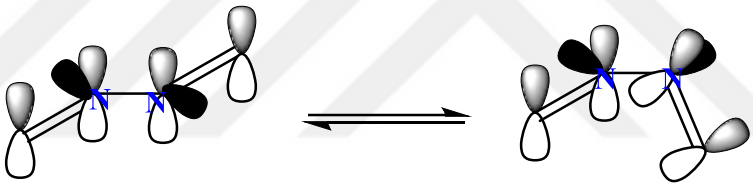

Figure 2-33: Azines as conjugation switches: a planar conformation (left) and twisted conformation (right). p-orbitals of C=N bonds (grey), lone pairs on N (black) (McLoughlin et al. 2007).

Azines exist in both linear and heterocyclic forms. Azine-containing compounds exhibit versatile biological activities as reported in the literature (Amariucai-Mantu et al. 2022). In addition, azine may demonstrate hydrazone-azine tautomerism depending on the pH of the solution (**Scheme 2-16**). Phiromphu et al. reported from a study conducted on (*Z*)-3-(2-(thiazol-2-yl)hydrazineylidene)pyridine-2,6(1*H*,3*H*)-dione that azine can exit in hydrazone in an acidic medium (Phiromphu et al. 2021).

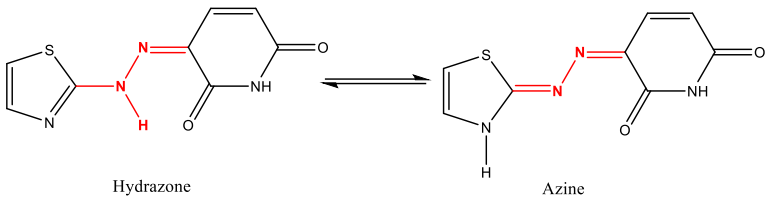

Scheme 2-16: Hydrazone-azine tautomerism

A stereospecific synthesis and antimicrobial screening of thiazolidinone-containing azines and thiazole-containing hydrazones were reported by Aridoss and colleagues. This study revealed that thiazolidinone-containing azines are better than thiazole-containing hydrazone in their biological properties (Aridoss et al. 2009).

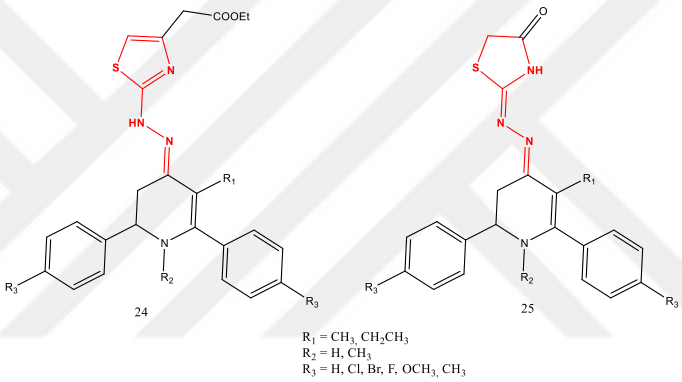

Qayed et al. reported the *in silico*, preparation, characterization, anticancer activity and molecular modelling studies of 26 novel 2-indolinone-thiazolidinone hybrids linked by azines. All the compounds were assessed for their anticancer activity against the human liver (HepG2), MCF7, HCT-29 cell lines. All the compounds inhibited all the cancer cell lines in low nanomolar concentrations with compound **26** showing the best profile (Qayed et al. 2022).

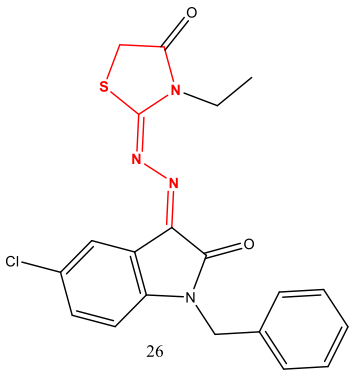

A series of novel asymmetric azines (**27**) was prepared from the condensation reaction of 6-(1-hydrazineylideneethyl)-1,3,7-trimethylpteridine-2,4(1*H*,3*H*)-dione and aldehydes. The azines were tested for their antiproliferative activity against neuroblastoma NB69, glioma U373, MCF-7 and EVSA-T cancer cell lines. These compounds showed significant antiproliferative activities between 4–10 µM (Picón-Ferrer et al. 2009).

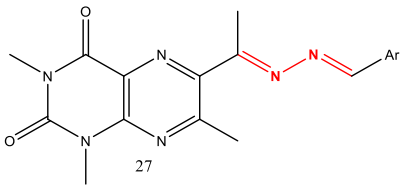

27

Bondock et al. prepared several novel unsymmetrical 1-hetaryl-4-(2-chloroquinolin-3-yl) azines (**28**) and tested their anticancer properties against the cancer cells MCF-7, NCI-H460, and SF-268. Azine **28a** has an unexpected anticancer effect against the human tumour cell lines MCF-7, NCI-H460, and SF-268 with IC_{50} values of 0.02, 0.01, and 0.06 µg/mL, respectively. These values indicate that Azine **28a** is more potent than the standard drug, doxorubicin (Bondock et al. 2016).

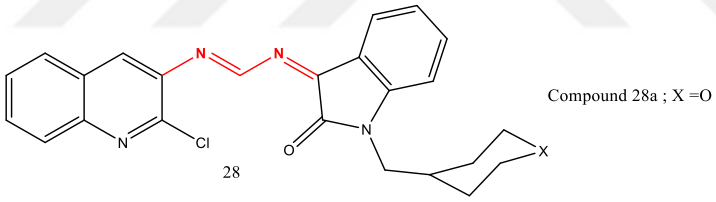

28

Compound 28a ; X =O

Ganga and Sankaran reported the synthesis, anticancer activities and in silico studies of two new asymmetrical azines of 3,5-dimethoxy-4-hydroxy benzaldehyde. The two compounds, **29a** and **29b** were evaluated for their anticancer activities against MCF-7 cell. Compounds **29a** inhibited MCF at 73.7 µM (Ganga and Sankaran 2020).

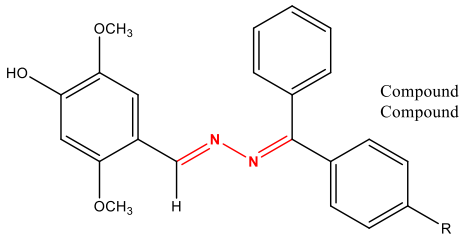

Compound 29a, R = Cl
Compound 29b, R = Br

2.9. Thiazole and Thiazolines

2.9.1. Chemistry of Thiazole and Thiazolines

Thiazole, a 1,3-azole, is a five-membered heterocyclic ring containing sulfur and nitrogen at positions one and three, respectively (**Figure 2-34**). Thiazole is a pale yellow liquid with a boiling point of 118.24 °C and a pyridine-like odour. It has a molecular formula of C_3H_3NS with a molecular weight of 85,13 g/mol and a density of 1,2 g/ mL. Thiazole is a weaker base with a pKa value of 2.5. It is sparingly soluble in water but readily dissolves in alcohol and ether (Gupta et al. 1999; Uslu 2016; Borcea et al. 2021; Singh et al. 2022). Four different numbering systems of thiazole have been reported but the widely accepted system is the one proposed by Chemical Abstracts (Sezer 1996).

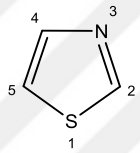

Figure 2-34: Structure of thiazole

In 1887, Hantzsch and his friend, Weber, registered the birth certificate of thiazole and called them “pyridines of the thiophene series”. After two years, the structure was confirmed by Popp. Thiazole is identified as a bioisostere of thiophene when a trivalent bioisosteric substitution of the -CH= group in thiophene with -N= takes place (**Figure 2-35**). Although Hantszsch structurally related them to thiophene and pyridine, which could not be completely wrong when we consider the fact that both thiophene and pyridine are bioisosteres of benzene, they are geometrically closer to thiophene and 1,3,4-thiadiazole (Sezer 1996; Singh et al. 2022).

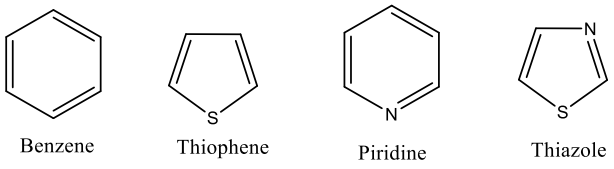

Figure 2-35: Isosteres of thiazole

Thiazole is stable and planar with strong aromaticity. Molecular orbital calculations of π-bond orders have confirmed the aromaticity of thiazole with some dienic properties. The bond length between C_2 and N_3 is shorter than the bond length between N_3 and C_4 (**Table 2-5**) indicating the presence of a double bond (more *p*-character) between C_2 and C_3. The nonbonded electron pair on the N_3 does not participate in resonance. However, one of the nonbonded electron pairs on the S_1 participates in resonance resulting in resonating structures (**Figure 2-36**) (Gupta et al. 1999; Borcea et al. 2021).

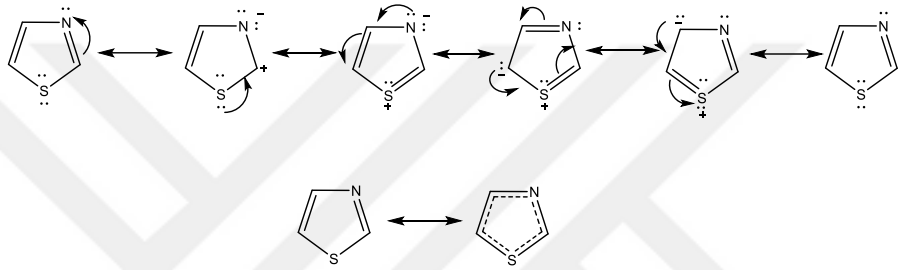

Figure 2-36: Resonance structures of thiazole

Table 2-5 Bond lengths and bond angles of thiazole ring (Gupta et al. 1999)

Bond Lengths (Å)		Bond Angles (°)	
S_1-C_2	1.724	C_2-S_1-C_5	89.3
C_2- N_3	1.304	S_1-C_2-N_3	115.2
N_3-C_4	1.372	C_2-N_3-C_4	110.1
C_4-C_5	1.367	N_3- C_4 C_5	115.8
C_5- S_1	1.713	C_4-C_5- S_1	109.6

Due to the heteroatoms, it contains, thiazole is characterized by extreme π density. The calculated π-electron densities predicted C_2 to be the carbon with the lowest electron density due to the electron-withdrawing effect of the nitrogen. This makes C_2 the most suitable site for nucleophilic attacks. C_5 with the highest electron density favours electrophilic substitution. If C_5 is blocked, electrophilic substitution takes place at C_4 (**Figure 2-37**) (Gupta et al. 1999; Uslu 2016; Borcea et al. 2021).

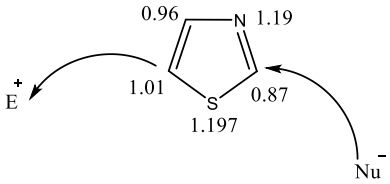

Figure 2-37: Calculated π-electron density of thiazole ring

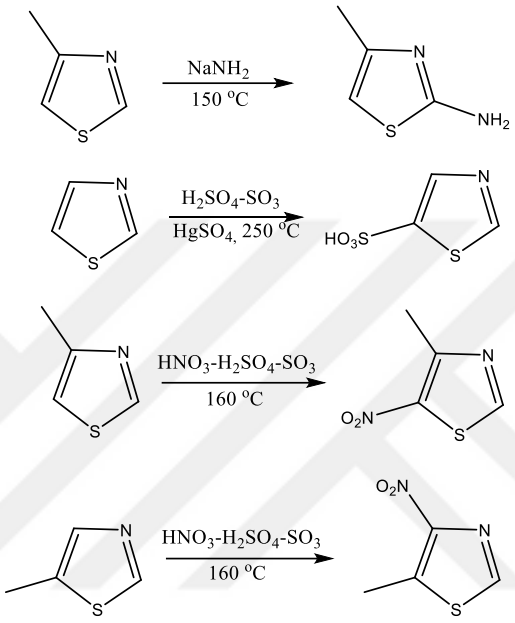

Scheme 2-17: Some aromatic nucleophilic and electrophilic substitutions of thiazole

Thiazoline and thiazolidine are analogues of thiazole. Thiazolines have a single double bond, whereas thiazolidne have no double bond.

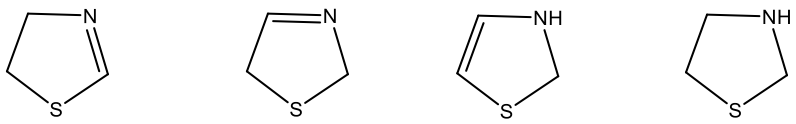

Figure 2-38: Structures of partially and fully saturated thiazoles

2.9.2. General synthesis of thiazole and 4-thiazoline derivatives

Over decades, numerous synthetic methods of thiazoles have been reported which reflects its enormous importance in drug discovery. These methods have different

reagents and therefore, different ways of bond formation as explained in **Figure 2-39**. Scheme A, which is Hantzsch's Synthesis, is the most known and applied method in thiazole synthesis (Katritzky 2008).

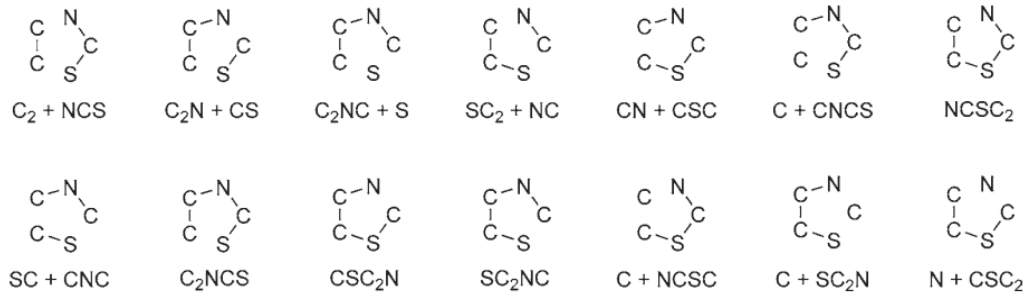

Figure 2-39 Fragments generated by retrosynthetic (Katritzky 2008)

2.9.2.1. Hantzsch's Synthesis

The Hantzsch synthesis involves the cyclocondensation of α-haloaldehyde or α-haloketone with thioamides. It is the most general method for the synthesis of thiazoles and proceeds in three steps. The reaction begins with the nucleophilic attack of the sulfur atom of thioamide on the α-carbon atom of α-haloaldehyde or α-haloketone producing α-thioketone which is subsequently transprotonated and dehydrated to produce the corresponding thiazole (**Scheme 2-18**) (Gupta et al. 1999; Eicher et al. 2003; Mustafa et al. 2004; Joule and Mills 2010).

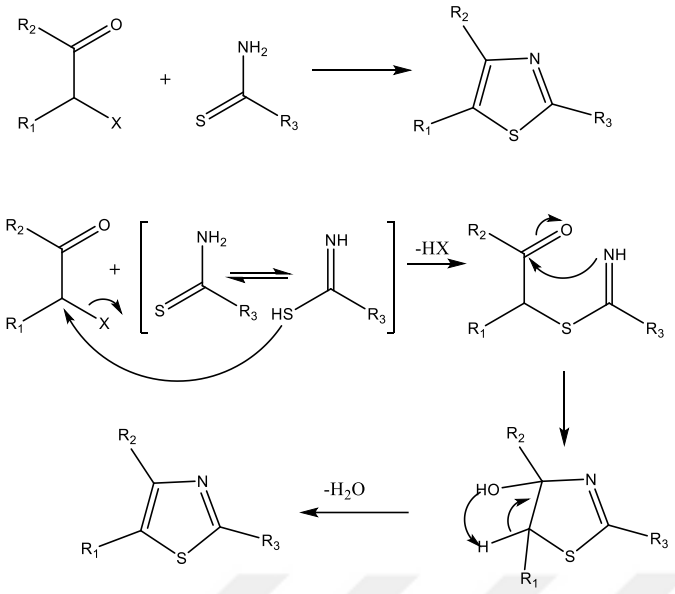

Scheme 2-18: The general synthesis scheme of Hantzsch's synthesis

Thiazole itself was synthesized from the cyclocondensation of chloroacetaldehyde with thioformamide. This method can be used to synthesize variety of thiazoles with some structural modifications in the α-haloketones and thioamides.

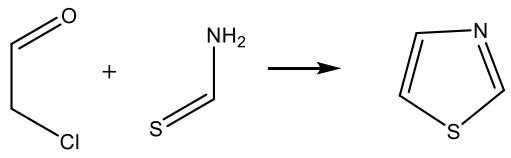

Scheme 2-19: Thiazole synthesis from the condensation of chloroacetaldehyde with thioformamide

Besides thioamide, other thiokeketone derivates such as thiourea, thiosemicarbazides, thiosemicarbazones, and dithiocarbamates are used in the synthesis of various thiazole and thiazoline derivatives. 2-Aminothiazoles which are widely explored as thiazole derivatives are synthesized by treating α-haloketones with thiourea (Gupta et al. 1999; Narasimhamurthy et al. 2020).

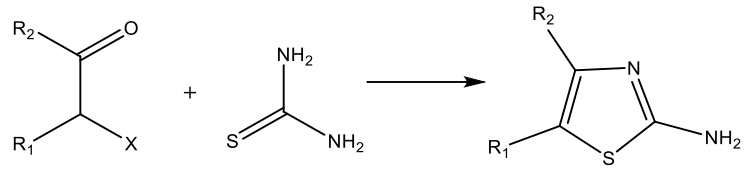

Scheme 2-20: The general synthesis of 2-aminothiazole derivatives

Also, the reaction of unsymmetrical thioureas with α-haloketones leads to the formation of 2-imino-4-thiazoline derivatives (Bramley et al. 1987; Katritzky 2008).

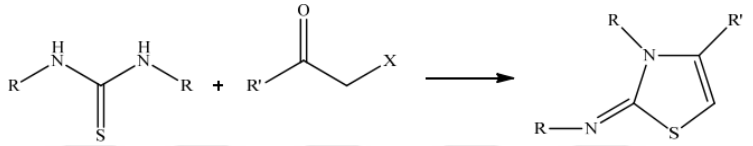

Scheme 2-21: General synthesis of 2-imino-4-thiazoline derivatives from thioureas and α-haloketones

One pot synthesis reaction of α-haloketone derivatives with sodium/potassium thiocyanate and aromatic amines in ethanol at 80 ºC leads to the formation of 2-aminothiazole derivatives (Suh et al. 2012).

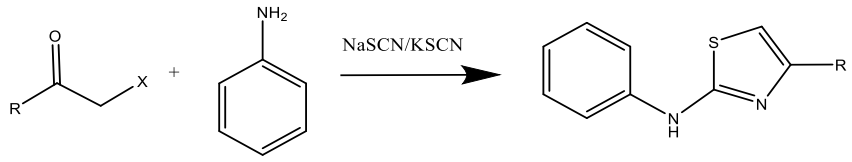

Scheme 2-22: General synthesis of 2-phenylamino-4-thiazole derivatives from aniline and α-haloketones using sodium/potassium thiocyanate

The cyclocondensation of thiosemicarbazide with α-haloketones leads to the formation of 2-imino-4-thiazoline and 2-hydrazino-4-thiazoline derivatives (Mustafa et al. 2004).

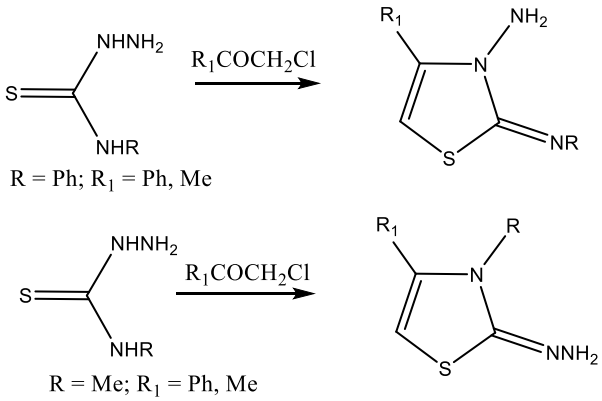

Scheme 2-23: General synthesis of 2-imino-4-thiazoline and 2-hydrazino-4-thiazoline derivatives

Similar to the thiosemicarbazides, thiosemicarbazones also cyclocondense with α-haloketones leads to the formation of 2-azino/hydrazino-4-thiazoline derivatives (Özbey et al. 2003; Hassan 2007; Pfeiffer et al. 2014; Pervez et al. 2015; Nechak et al. 2019; Shehzad et al. 2020).

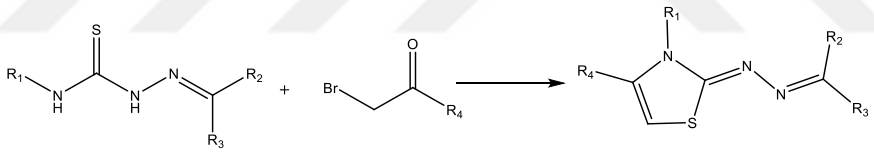

Scheme 2-24: General synthesis of 2-azino/hydrazino-4-thiazoline derivatives

2.9.2.2. Cook- Heilborn's Synthesis

5-aminothiazoles can be synthesized from the reaction of α-aminonitriles with carbon disulfide, isothiocyanates, carbon oxysulfide and dithioacids or esters under mild conditions results. This method represents Scheme B in **Figure 2-39** (Gupta et al. 1999; Eicher et al. 2003; Mustafa et al. 2004).

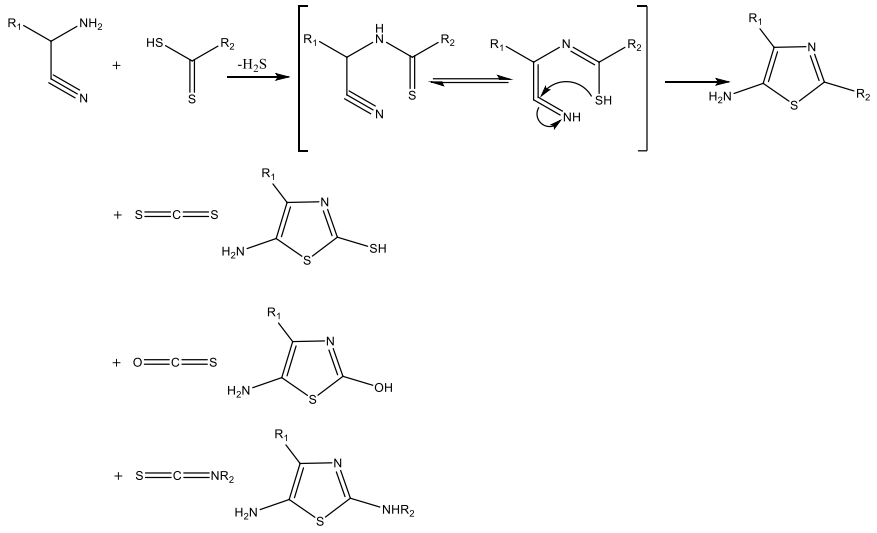

Scheme 2-25: The general synthesis scheme of the Cook-Heilbron synthesis

2.9.2.3. Gabriel Synthesis

Siegmund Gabriel described thiazole synthesis in 1910 by reacting α-acylaminoketones with a stoichiometric amount of phosphorus pentasulfide (P_2S_5) (Gupta et al. 1999; Eicher et al. 2003). This method represents schemes C, I and K in **Figure 2-39** (Mustafa et al. 2004). Lawessons's reagent has been successfully used as an alternative to P_2S_5 (Kaur 2022).

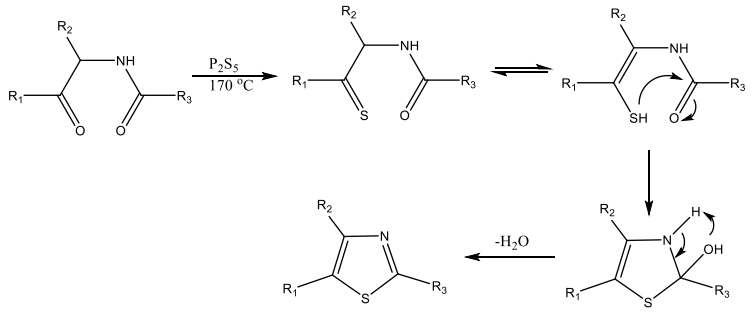

Scheme 2-26: The general synthesis scheme of the Gabriel synthesis

2.9.2.4. Erlenmeyer Synthesis

This method represents scheme D in **Figure 2-39** and involves the cyclocondensation of α-mercaptoketones or α-mercaptoaceticacids with nitriles to yield 2-aminothiazoles (Gupta et al. 1999; Mustafa et al. 2004; Belskaya et al. 2020).

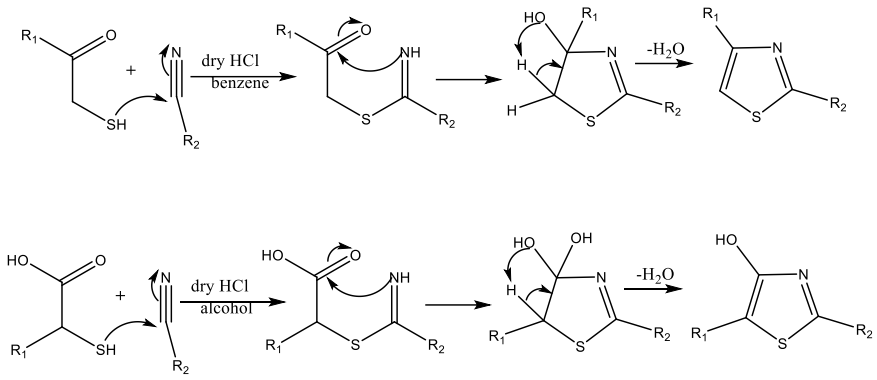

Scheme 2-27: The general synthesis scheme of the Erlenmeyer synthesis

2.9.2.5. Tcherniac's Synthesis

Tcherniac's synthesis is mainly used in the synthesis of 2-substituted thiazoles. It involves the acidic hydrolysis of α-thiocyanoketones or their reactions with amino or sulfur-containing compounds. This method represents scheme G in **Figure 2-39** (Gupta et al. 1999; Mustafa et al. 2004).

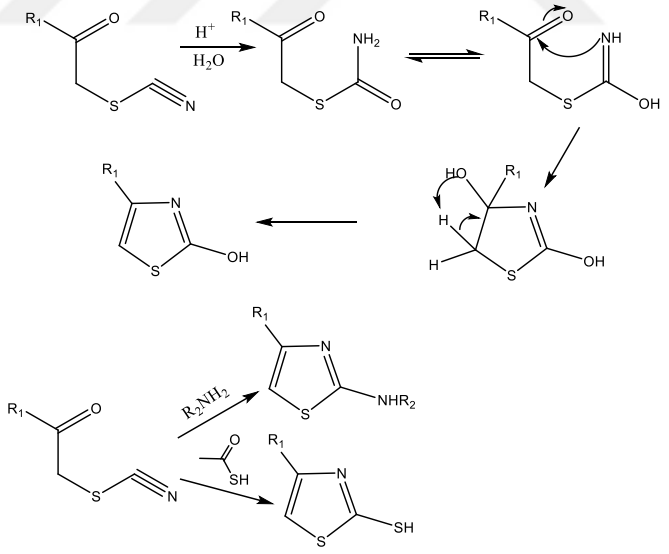

Scheme 2-28: The general synthesis scheme of the 2.9.2.5. Tcherniac's Synthesis

2.9.3. Biological Activities of thiazole derivatives

Thiazole and its saturated derivatives continue to be a magnetism point in the quest for potential novel agents against various diseases. The thiazole nucleus is present

in many natural products such as thiamine (Vitamin B1), penicillin, luciferin, micacocidin, curacin A and thiangazole (**Figure 2-40**).

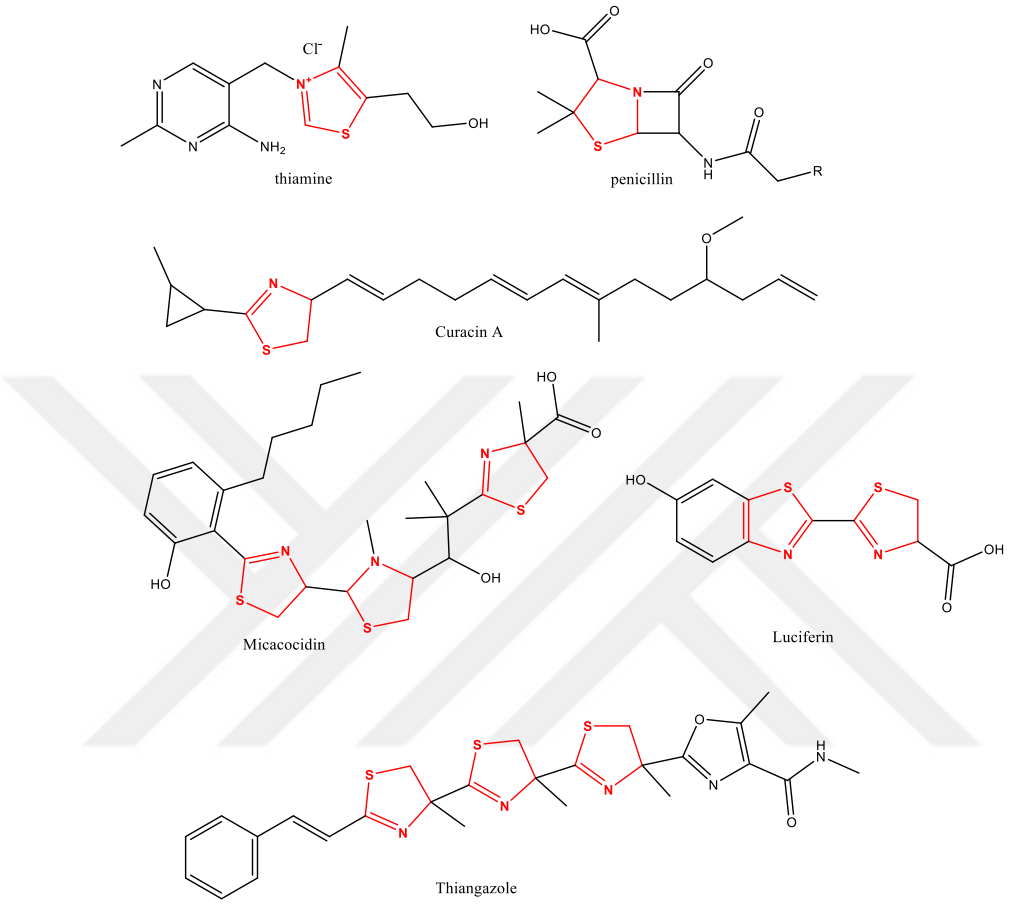

Figure 2-40: Thiazole-containing natural compounds

In addition, thiazoles make important pharmacophores for many commercially available drugs (**Figure 2-41**). Multiple studies have shown thiazole to be an essential scaffold in combating drug resistance in various diseases with enhanced pharmacokinetic properties and fewer side effects. Thiazole and saturated derivatives have demonstrated a wide versatile pharmacological spectrum including, antibacterial, antitubercular, antiviral, anthelmintic, anti-inflammatory, antidiabetic, anti-Parkinson, anti-Alzheimer, anticancer and many others (Sharma et al. 2020; Borcea et al. 2021; Singh et al. 2022).

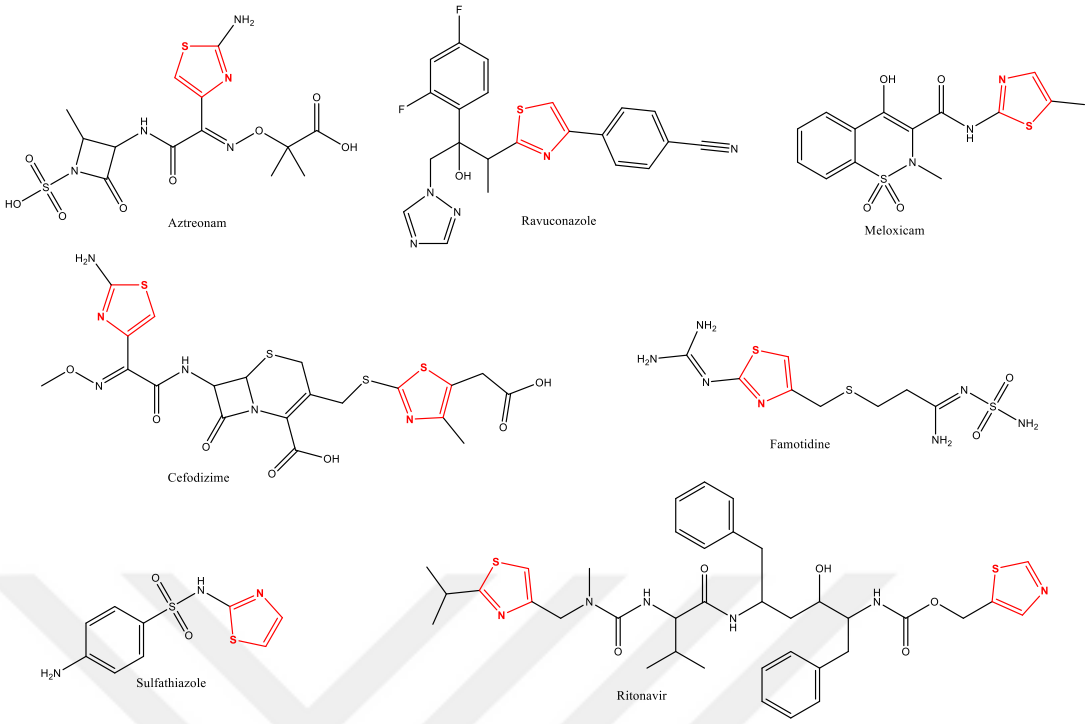

Figure 2-41: Thiazole-containing commercially available drugs

Hybrids of thiazole and aminobenzothiazole derivatives (**30)** were synthesized by Amnerkar and Bhusari and tested for their antifungal, antibacterial and anthelmintic properties. The majority of the compounds displayed moderate to good inhibitory activity against the microorganisms. Compounds **30a** and **30b** exhibited good antibacterial and antifungal activities, while compound **30c** displayed the most significant anthelmintic activity. Compounds **30a** and **30b** demonstrated considerable antibacterial and antifungal actions, whereas compound **30c** exhibited the strongest anthelmintic activity (Amnerkar and Bhusari 2011).

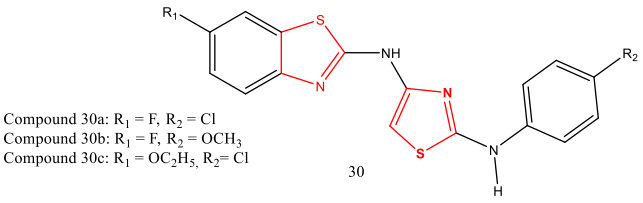

Compound 30a: R_1 = F, R_2 = Cl
Compound 30b: R_1 = F, R_2 = OCH_3
Compound 30c: R_1 = OC_2H_5, R_2= Cl

30

Kouatly et al. described the three-step synthesis of a series of adamantan-thiazol derivatives (**31),** as well as their anti-inflammatory and lipoxygenase/cyclooxygenase inhibitory activities. Most of the compounds effectively reduced inflammation (29.6–81.5%). However, low inhibitory activity was observed against lipoxygenase. The

COX-1 and COX-2 inhibitory activities of the compounds were evaluated. Some of the compounds have a COX-1 inhibitory potential comparable to naproxen and a low to moderate COX-2 inhibitory potential (Kouatly et al. 2009).

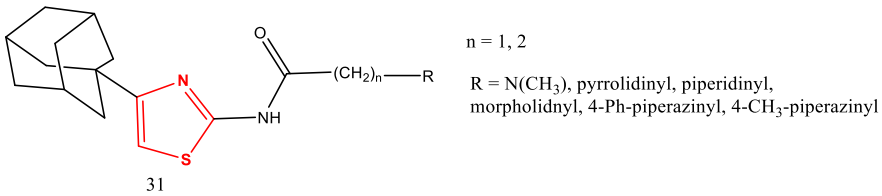

31

Again, Kouatly et al. synthesized a set of 2-((4-(adamantan-1-yl)thiazol-2-yl)imino)-5-(arylidene)thiazolidin-4-ones (**32**) and tested them for their antibacterial and antifungal activities. Most of the compounds showed a better low micromolar inhibition than the reference compounds (Omar et al. 2010).

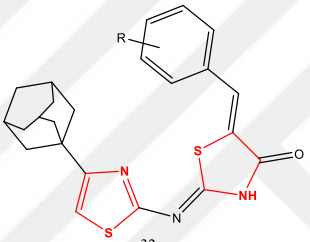

32

Bikobo et al. described the synthesis and antimicrobial activity of 2-phenylamino-thiazole derivatives (**33**). The derivatives were categorized as two sets: those with a single thiazole nucleus and those with two. The result of the antimicrobial assay showed that compounds with two thiazole nuclei have better activities with compound **33a** manifesting better inhibitory activities against gram-positive bacteria strains (31.25 µg/mL) and candida strains (7.81 µg/mL) compared to the standard drugs spectinomycin and fluconazole, respectively (Bikobo et al. 2017).

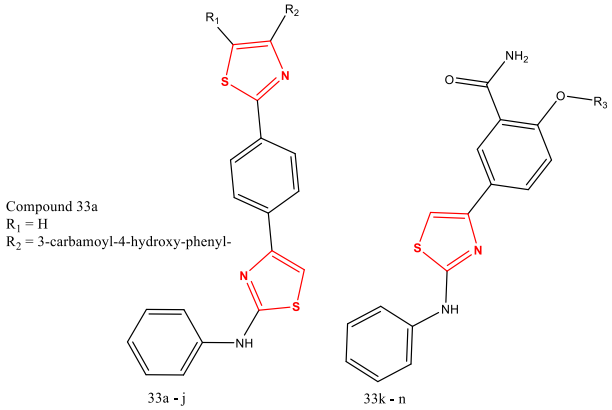

33a - j 33k - n

Dos Santos Silva et al. reported the synthesis of 24 pyridine-containing thiazole derivatives and their anticancer activities against HL-60 (leukaemia), MCF-7, NCI-H292 (lung carcinoma) human tumour cell lines and non-tumour cells (PBMC). The compounds were prepared under ultrasonic radiation by reacting 2-(pyridin-2-ylmethylene)hydrazine-1-carbothioamide or 2-(1-(pyridin-2-yl)ethylidene)hydrazine-1-carbothioamide with appropriate α-bromoketone derivatives in 2-propanol in the presence $CaCO_3$ at room temperature for an hour. Most of the compounds showed satisfactory inhibitions in micromolar concentrations against the cancer cells. Compounds **34a** and **34b** inhibited all the cancer cells including HepG2, the most resistant cell line (IC_{50} 2.2 and 5.6 μM, respectively) without showing cytotoxic effects on PBMC (IC_{50} > 30 μM). These two compounds were discovered to induce apoptosis in HepG2 cells and to have an anticancer effect in severe combined immunodeficient mice in a hepatocellular xenograft cancer model. Treatment with compounds **34a** and 3**4b** resulted in no substantial indicators of toxicity as determined by biochemical and histological tests (Dos Santos Silva et al. 2017).

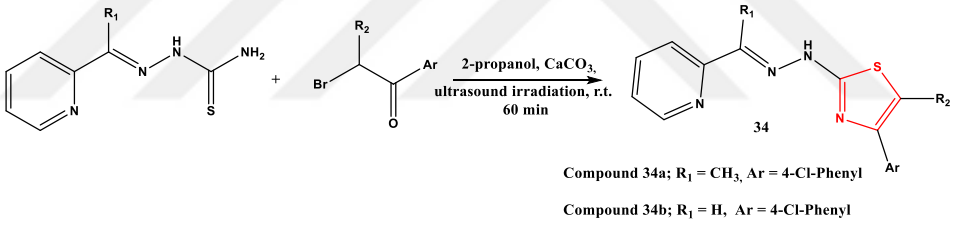

Compound 34a; R_1 = CH_3, Ar = 4-Cl-Phenyl

Compound 34b; R_1 = H, Ar = 4-Cl-Phenyl

Joshi et al. described the synthesis and antimycobacterial activity of a series of pyrrole-thiazole hybrids. The compounds were synthesized in a two-step reaction. First, the condensation of thiourea and 4-bromoacetophenone yielded a 2-aminothiazole derivative. The obtained 2-aminothiazole derivative was treated with pyrrolylbenzoic acid to yield the pyrrole-thiazole hybrids. In contrast to other multistep Hansztch syntheses, this synthesis was conducted as a one-pot reaction involving 24-hour reflux of bromine or iodine, thiourea and an acetophenone derivative as described by Pattan et al. The compounds were assayed against *Mycobacterium tuberculosis H37Rv*, and compound **35** was found to be the most potent inhibitor with a MIC value of 1.6 μg/mL. Compound **35** also inhibited *S. aureus* and *E. coli* with low micromolar MIC values (SR Pattan et al. 2009; Joshi et al. 2019).

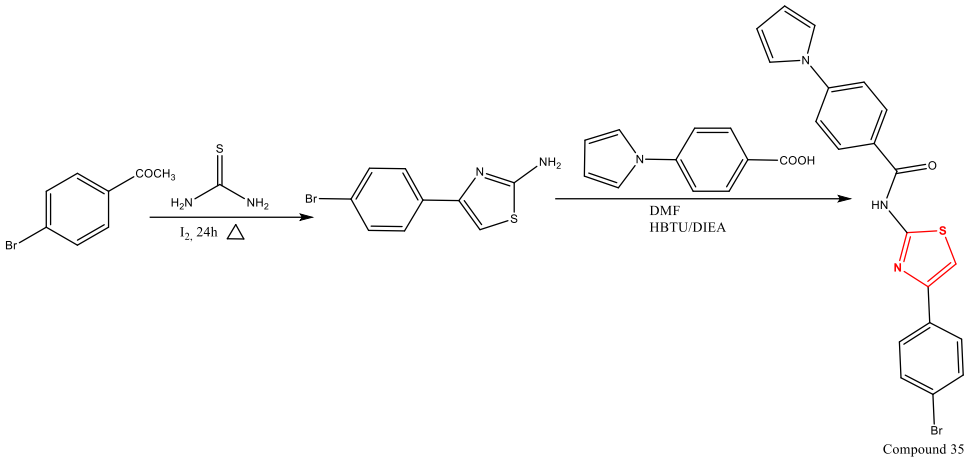

Compound 35

Kim et al. investigated the anti-pigmentation properties of 2-imino-1,3-thiazoline derivatives and identified compound **36** as the lead compound. The result showed that compound **36** strongly reduces melanin production in a dose-dependent manner through the downregulation of microphthalmia-associated transcription factor (Mitf), and thus tyrosinase. They concluded that 2-imino-1,3-thiazoline derivatives are potential skin-whitening agents (Kim et al. 2007).

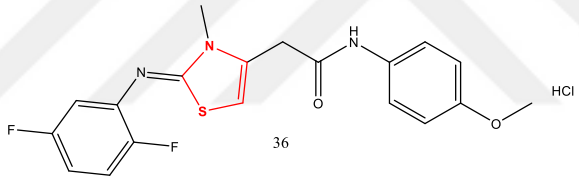

36

Shehzad et al. described the synthesis, characterization, urease inhibitory activity and in silico studies of a series of 4-thiazoline derivatives (**37**). The compounds were synthesized by cyclocondesing a suitable thiosemicarbazone with α-bromoacetophenone in ethanol in the presence of sodium acetate. The compounds were tested for their inhibitory properties against urease where they generally exhibited satisfactory inhibition with compound **37a** as the most potent compound (IC_{50} =1.73 µM). The 4-thiazoline derivatives displayed better inhibitory properties against urease than their corresponding thiosemicarbazones (Shehzad et al. 2020).

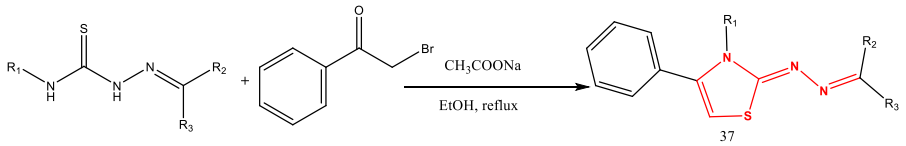

37

Compound 37a ; R_1 = 3-MeO-Ph
$R_2 = CH_3$
R_3 =

In another study, Shehzad et al. reported the preparation, characterisation, and aldose reductase inhibitory properties of 4-thiazoline derivatives as potential antidiabetic agents. The 4-thiazoline compounds were synthesized from the reaction of equimolar amounts of appropriate thiosemicarbazone derivative with 4-substituted phenacylbromide in the presence of anhydrous sodium acetate in absolute ethanol. The reaction mixture was refluxed for 12 – 24 h. Compounds **38a** and **38b** demonstrated a better inhibition than the reference sorbinil with IC_{50} values of 1.39 +/- 2.21 mM and 1.52 +/- 0.78 mM, respectively. (Shehzad et al. 2021)

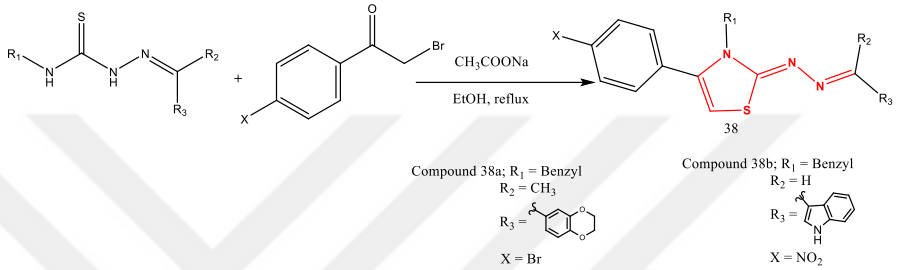

Pereira et al. described the design and preparation of a series of 4-thiazoline derivatives (**39**) and investigated their inhibitory potential for NorA efflux pump of S. aureus 1199B. The compounds were prepared by condensing thiosemicarbazide with 2–methoxy-5–bromobenzaldehyde to form a thiosemicarbazone which was subsequently cyclocondensed with (un)substituted 2-chloro/bromoacetophenones in the presence of sodium acetate as a base for 24 hours to yield 4-thiazoline derivatives. Among the thiazoline derivatives, compound **39a** exhibited the highest inhibitory activity with a MIC of 40.3 µg/mL (Pereira et al. 2019).

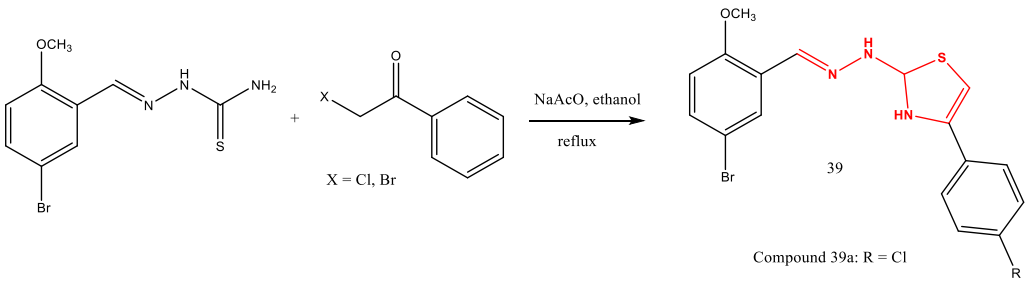

Cardoso et al. accomplished the synthesis of thirteen 2-(phenylthio)ethylidenethiazole derivatives and screened them for their trypanocidal activity against *Trypanosoma cruzi*. In the presence of acetic acid as a catalyst and ultrasound irradiation, the compounds were prepared by condensing thiosemicarbazide with 2-(phenylthio)acetaldehyde in ethanol to yield thiosemicarbazones, which were

then cyclocondensed with α-bromoacetophenone derivatives using propanol and ultrasound irradiation at room temperature to produce the thiazole derivatives. Among them, compound **40** demonstrated the highest inhibition with IC_{50} value of 2.6 μM. The compound was further assayed in vitro and revealed a good inhibition with an IC_{50} value of 10.15 μM. Besides, compound **40** did not show any significant toxicity for rat splenocytes (Cardoso et al. 2019).

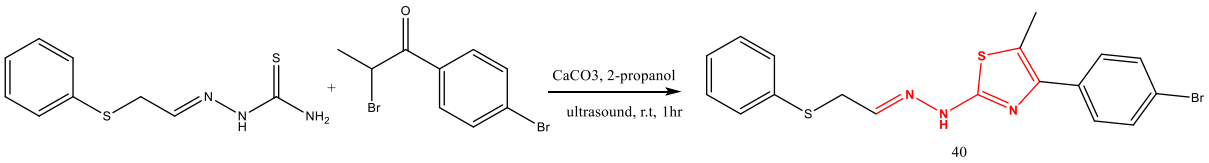

Nechak et al. prepared a novel series of 4-thiazoline-containing dehydroacetic acid derivatives by refluxing various α-chloroacetones with a methanolic solution of thiosemicarbazones in the presence of anhydrous sodium acetate. All the compounds were assayed for their inhibitory properties against six clinically important pathogenic bacteria and fungi. Most of the compounds exhibited significant inhibition compared to the standard drug, gentamycin (Nechak et al. 2019).

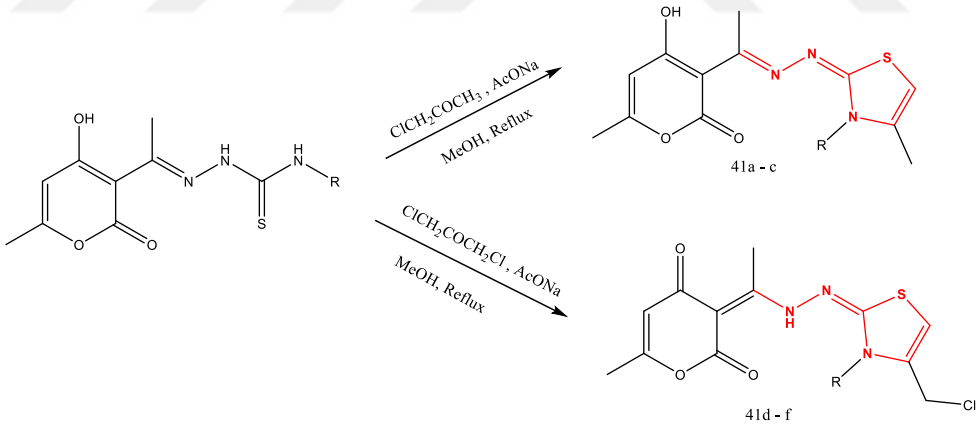

Kryshchyshyn et al. also communicated the synthesis and antitrypanosomal activity of a series of imidazothiadiazoles or indoles hybridized with 4-thiazoline or thiazolidinone via an azine link. Suitable imidazothiadiazole/indole-containing thiosemicarbazone derivatives were cyclocondensed under reflux in acetic acid with equimolar amount of substituted α-bromoacetophenones or ethyl 2-chloroacetoacetates in the presence of anhydrous sodium acetate to give the 4-thiazoline derivatives. Although uncommon, the 4-thiazoline derivative may undergo azino-hydrazino tautomerism to produce corresponding thiazoles The synthesized hybrids were

evaluated for their antitrypanosomal activity against *Trypanosoma brucei* and *Trypanosoma brucei gambiense* and generally displayed effective inhibition at low micromolar concentrations. The thiazolines generally showed a better inhibition profile than the other derivatives (Kryshchyshyn et al. 2019).

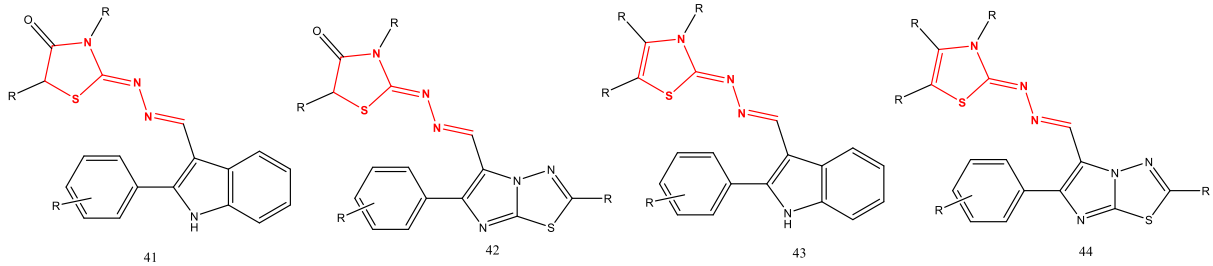

41 42 43 44

Maghraby et al. designed and synthesized a series of benzimidazole derivatives containing both thiazole and 4-thiazoline nuclei. The compounds were prepared by cyclocondensing the thiosemicarbazone **47** with 4-(un)substituted α-bromoacetophenones under reflux for 24 hours in the presence of sodium acetate producing the desired compound **48**. The compounds were further evaluated for their cyclooxygenase (COX) and 15-lipoxygenase (15-LOX) inhibitory activities as anti-inflammatory agents. The compounds displayed decent inhibitions against both the enzymes at low micromolar concentrations with compound **48a** (4-chlorophenyl) emerging as the most potent dual inhibitor (COX-1: IC_{50} = 13.22 μM, COX-2: IC_{50} = 0.045 μM and 15-LOX: IC_{50} = 1.67 μM). In vivo studies of anti-inflammatory activity on rats showed that compound **48a** reduced oedema by 75.67% in 3 hours. The desired compounds with both thiazole and 4-thiazoline nuclei showed a better inhibitory pattern against COX-2 and 15-LOX than their corresponding precursors with a single thiazole nucleus (Maghraby et al. 2020).

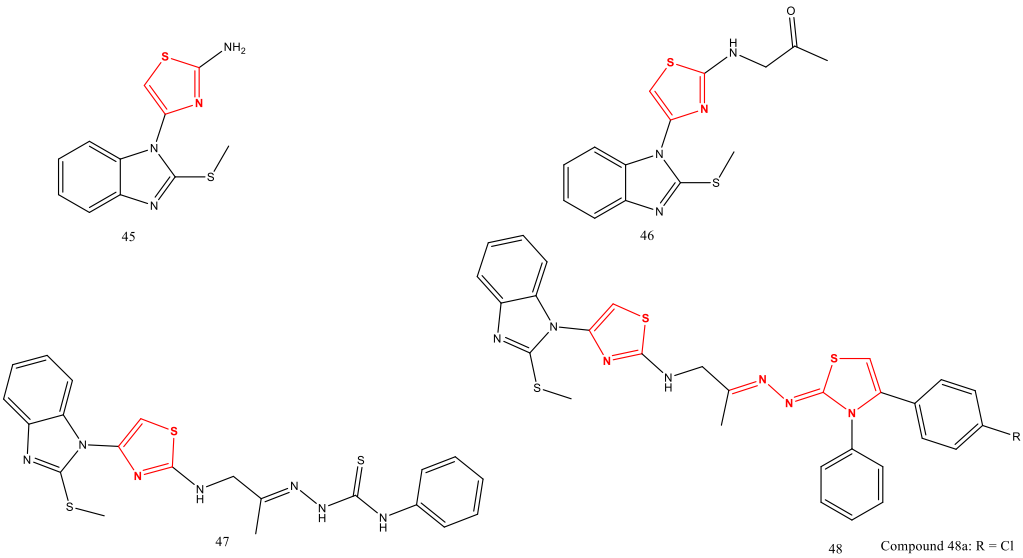

2.9.4. Anticancer activities of thiazole derivatives

Gomha et al. communicated the synthesis, anticancer activities and *in silico* studies of a series of thiazole and 4-thiazoline derivatives. In an ethanolic medium, cyclocondensation of thiosemicarbazone **49** with a suitable α-halocarbonyl compound yielded the corresponding thiazoles (**50 – 53**) whereas the cyclocondensation of thiocarbohydrazone **54** with a suitable α-halocarbonyl compound yielded the corresponding 4-thiazoline derivatives (**55 – 58**). The anticancer activities of the compounds were evaluated against MCF-7 cancer cell lines. Compound **51** demonstrated the best inhibition with an IC_{50} value of 14.6 ± 0.8 (Gomha et al. 2021).

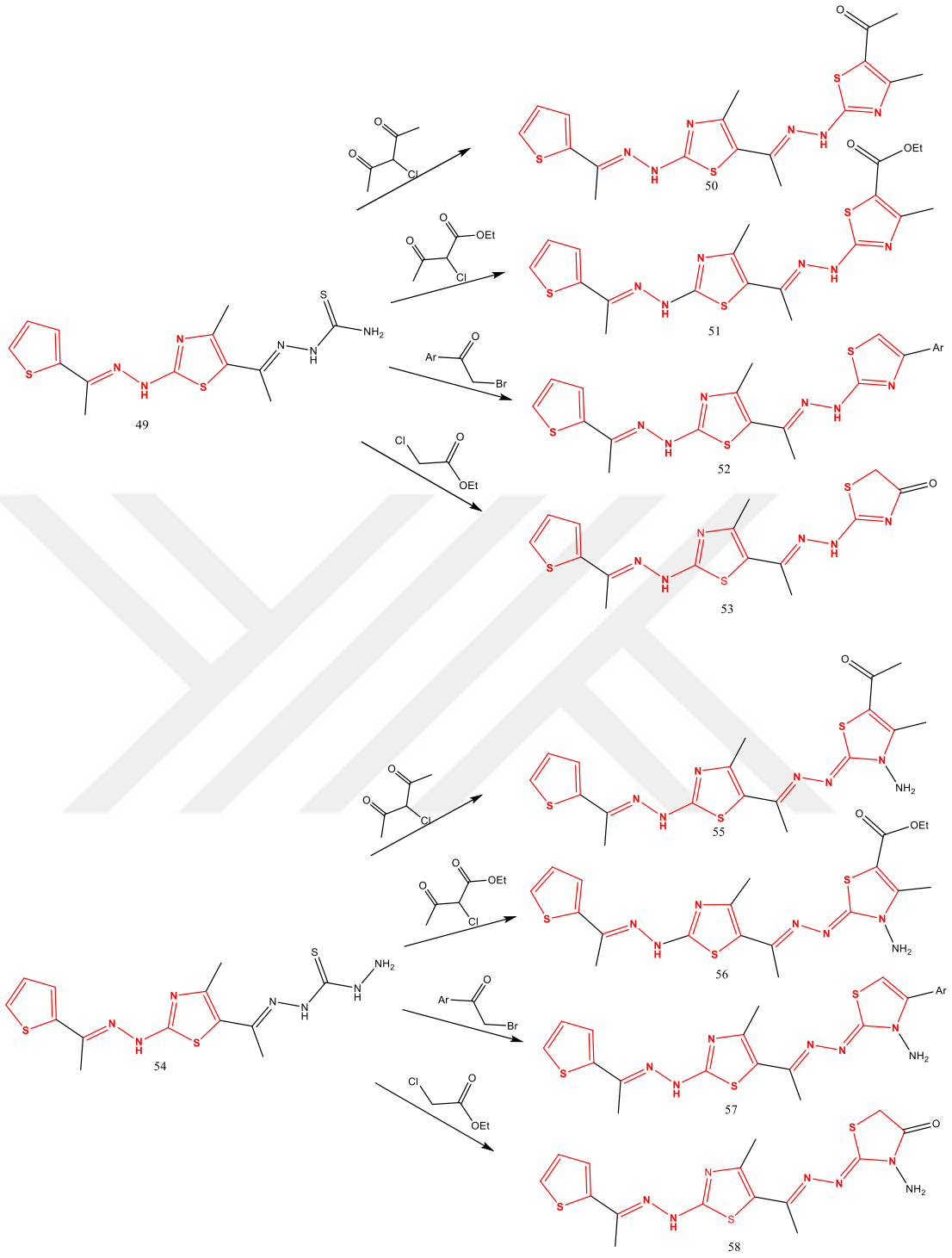

Wang et al. described the design, preparation, characterisation, and anticancer activities of a series of hydrazonothiazole derivatives against a spectrum of human cancer cell lines. Treatment of a suitable thiosemicarbazone derivative with a substituted 2- bromoacetophenone in presence of ethanol and sodium acetate yielded the desired thiazole derivatives. Among these, compound **59a** demonstrated the strongest anticancer activity against A549 (IC_{50} = 2.61 μM), HepG2 (IC_{50} = 14.5 μM), CaCo-2

(IC_{50} = 14.6 μM), U87 MG (IC_{50} = 29.9 μM). The compound showed low toxicity against HUVEC with an IC_{50} of 79.5 μM. Additional *in vivo* testing demonstrated that compound **59a** inhibited the growth of A549 xenograft tumours by 70% at 50 mg/kg per day while showing no significant cytotoxicity studies (Wang et al. 2019b).

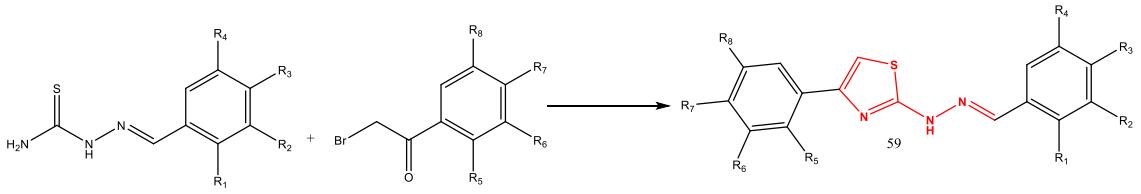

Compound 59a
R_1 = H, R_2 = F, R_3 = F, R_4 = H, R_5 = H, R_6 = H, R_7 = CF_3, R_8 = H

Aly et al. accomplished the synthesis of a series of quinolin-2-one hybridized with 4-thiazoline via a hydrazone link. The hybrids were assayed for their anticancer activity against a spectrum of cancer cell lines. The compounds were prepared from the cyclization of a suitable 2-quinlonylthiosemicarbazones with substituted 2-bromoacetophenone in the presence of triethylamine. Compound **60a** demonstrated the highest antitumour activity by inhibiting the lung cancer NCI-H322M, colon cancer HCT-15, and ovarian cancer OVCAR-3 by 81.78%, 79.49% and 75.84%, respectively (Aly et al. 2020).

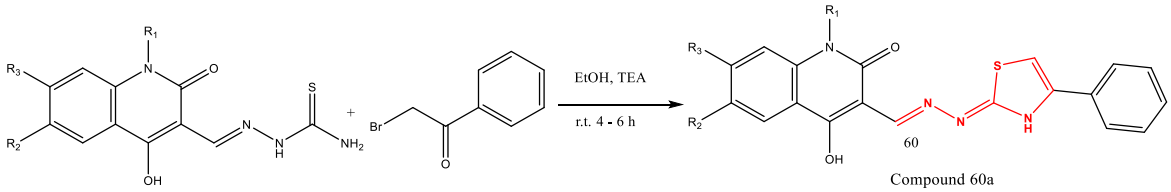

Compound 60a
R_1 = H, R_2 = OCH_3, R_3 = H

Using a scaffold hybridization approach, Ibrar et al. designed, synthesized, and tested a set of new bis-coumarin–iminothiazole hybrids for their biological action against alkaline phosphatase, leishmaniasis, and cancerous cells. The hybrids were synthesized by refluxing an equimolar amount of 3-(2-bromoacetyl)-2*H*-chromen-2-one with substituted thiosemicarbazide in methanol in the presence of anhydrous AcONa. Compound **61a** emerged as the strongest inhibitor with an IC_{50} value of 1.38 ± 0.42 μM, twice more potent than the standard inhibitor. The analogues were further tested for their anti-leishmanial activity against Leishmania major, with Compound **61a** emerging as the lead candidate with 70.4% inhibition. The compounds also showed cytotoxic

behaviour against kidney fibroblast (BHK-21) and lung carcinoma (H-157) cancer cell lines (Ibrar et al. 2015).

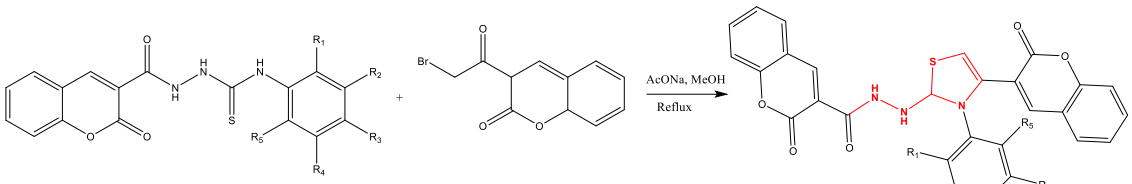

61

Comound 61a : $R_1 = R_3 = CH_3$; $R_2 = R_4 = R_5 = H$

A new set of 4-thiazoline–coumarin hybrid compounds with D-glucose and D-galactose moieties were synthesized by Ngoc Toan and Dinh Thanh and screened against breast adenocarcinoma (MCF-7), human liver cancer (HepG2), human cervical cancer (HeLa), human melanoma cancer (SK-Mel-2) and human lung cancer (LU-1) cells. In various solvents, 4-thiazoline derivatives were produced by heating suitable thiosemicarbazone derivatives α-bromoacetophenone at 50 ºC for 2 hours in the presence of anhydrous sodium acetate. The compounds showed promising inhibitions against the cancer cells with IC_{50} values of low micromolar concentration. Compounds **62a - c** showed comparable antiproliferative activity to that of sorafenib. In addition, the three compounds inhibited EGFR and HER2 kinases at low micromolar concentrations similar to sorafenib (Ngoc Toan and Dinh Thanh 2021).

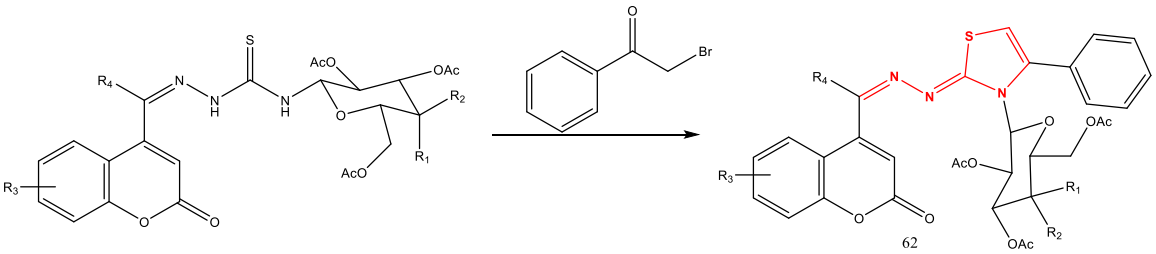

62

Compound 62a: R_1 = H, R_2 = OAc, R_3 = 6-OC_5H_{11}
Compound 62b: R_1 = H, R_2 = OAc, R_3 = 7-OC_4H_9
Compound 62c: R_1 = H, R_2 = OAc, R_3 = 7-OC_5H_{11}

El-Haggar et al investigated the bioisosteric substitution of the aminoquinazoline pharmacophore of erlotinib, an EGFR inhibitor, with 2-azino-4-thiazoline moiety. The designed 4-thiazoline derivatives were synthesized and evaluated for their anticancer properties against a panel of 60 cancer cell lines. Syntheses of the compounds were achieved by refluxing various aryl-thiosemicarbazones with 2-bromo-1-(4-methoxyphenyl)ethan-1-one in propan-2-ol for 2 hours. Compound **63a** was active against 12 different cell lines, with an IC_{50} of 6.9 0.013 μM against HCT-116 cells and

no discernible toxicity toward normal human fibroblasts (WI-38) showing a better inhibition profile than the reference compound doxorubicin. The compounds were further studied as potential EGFR inhibitors and compound **63a** showed a good micromolar inhibition. In addition, compound **63a** was able to induce tumour cell cycle arrest and cell apoptosis in HCT-116 cells (El-Haggar et al. 2022).

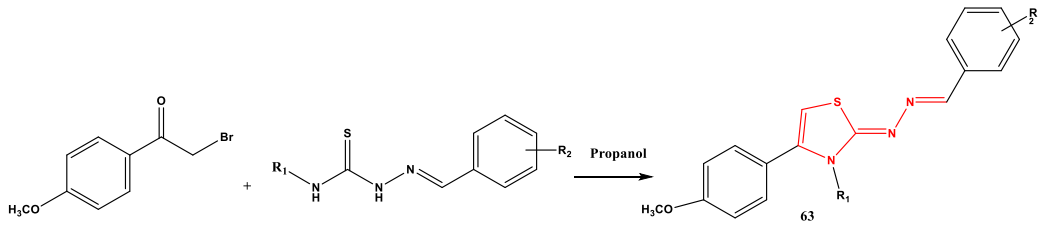

2.9.5. CA inhibitory properties of 4-thiazoline derivatives

Meleddu et al. described the dual-tail design, synthesis, characterisation, and inhibitory activities of novel benzenesulfonamide-containing 2-imino-3-cyclohexyl-4-thiazoline derivatives against the tumour-associated hCAIX and hCAXII. The compounds were also tested against the cytosolic hCAI and hCAII to assess their selectivity. The compounds were obtained from the cyclocondensation of substituted α-haloacetophenones with 1-cyclohexyl-3-(4-sulfamoylphenyl)thiourea in propanol under reflux. The compounds showed nanomolar inhibition of hCAIX and hCAXII with a higher affinity towards hCAXII. However, the compounds were not selective towards hCAIX and hCAXII over hCAII, however, significant selectivity was observed over hCAI. Besides a low selectivity, the substitution of the aromatic ring in the 4th position made a dramatic increase in activity (Meleddu et al. 2015).

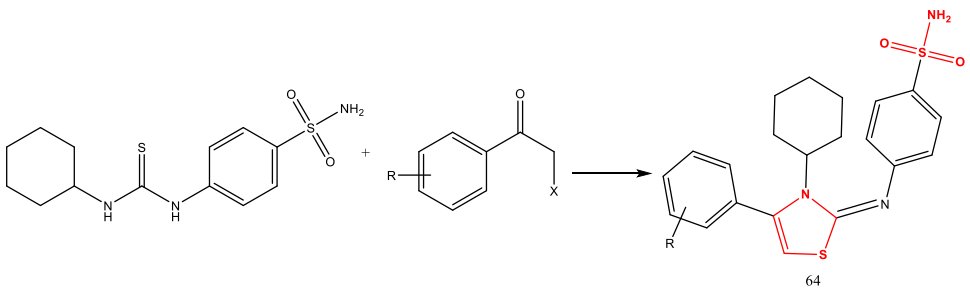

Meleddu et al. also communicated the replacement of the cyclohexyl ring on analogues **64** with phenyl and examined their biological activities as dual inhibitors of CA and COX enzymes. The introduction of the phenyl group significantly reduced the

activity of all the synthesized compounds without showing selectivity. On the other hand, the compounds preferentially inhibited COX-2 to COX-1 (Meleddu et al. 2018).

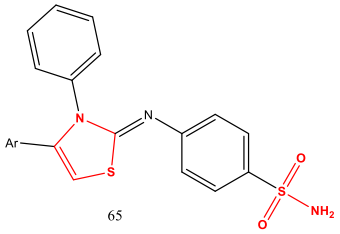

65

In another work, Meleddu and colleagues synthesized a series of novel benzenesulfonamide-containing 2-imino-3-methyl-4-thiazoline derivatives (**66**) and tested their inhibitory activities against both the cytosolic hCA/hCAII and tumour-associated hCAIX/hCAXII. Similar to the previous study, the compounds were not active against hCAI. The substitution of the cyclohexyl group with a methyl group generally decreased the affinity towards the tumour-associated hCAIX and hCAXII, whereas the affinity towards the cytosolic hCAII was enhanced (Distinto et al. 2019).

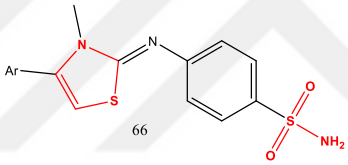

66

In their continuous quest for selective CA inhibitors, the length of the methyl group was increased to ethyl which has dramatically reduced affinity towards hCAIX and hCAXII and increased the affinity toward hCAII. Compared to previous derivatives, these analogues demonstrated the highest hCAII inhibition (Meleddu et al. 2020).

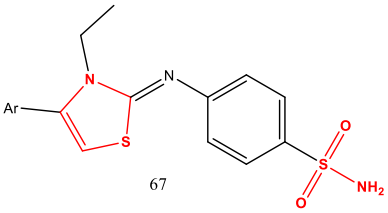

67

3. EXPERIMENTAL

3.1. Materials and Instruments

3.1.1. Chemicals

3-aminobenzenesulfonamide, 4-aminobenzenesulfonamide, thiophosgene, hydrazine monohydrate, thiophene-2-carbaldehyde, 5-bromothiophene-2-carbaldehyde, 1*H*-pyrrole-2-carbaldehyde, 1-methyl-1*H*-pyrrole-2-carbaldehyde, furan-2-carbaldehyde, acetone, 3-pentanone, 2-pentanone, cyclopentanone, 2-bromo-1-phenylethan-1-one, 2-bromo-1-(4-bromophenyl)ethane-1-one, 2-bromo-1-(4-hydroxyphenyl)ethane-1-one, 2-bromo-1-(4-(trifluoromethoxy)phenyl)ethan-1-one, 2-bromo-1-(4-fluorophenyl)ethan-1-one, 2-bromo-1-(3-(trifluoromethyl)phenyl)ethan-1-one, 2-bromo-1-(4-methylphenyl)ethan-1-one, 1-(4-hydroxyphenyl)ethan-1-one, copper(II) bromide.

3.1.2. Analytical instruments

1. Melting Point: Büchi B-540 and M-560 (BÜCHI Labortechnik AG, Flawil, Switzerland)
2. Elemental analysis: Thermo Finnigan Flash EA 1112 (Thermo Electron GmbH, Bremen, Germany).
3. IR Spectroscopy: Shimadzu IRAffinity-1 FTIR Spectrophotometer.
4. NMR (^{1}H NMR, ^{13}C-NMR (decoupled), and HSQC-2D) analyses: Bruker Advance Neo 500 MHz, Varian Mercury (Agilent, Palo Alto, CA, USA) 400 MHz NMR spectrophotometers.
5. Mass Spectroscopy: Agilent 1260 II LC-MS System

3.1.3. Chromatography

The progress of the reactions was monitored, and the purity of the synthesized compounds was determined using the thin-layer chromatography (TLC) method. 0.2 mm thick ready-made silica gel F-254 (Merck) plates (20 x 20 cm) were used as the stationary phase. Chloroform: Methanol (9:1, v/v, room temperature) was used as the mobile phase.

3.1.4. *In silico* studies

Computers	DELL Work Station, Intel Xeon Silver 4214R, 24 x CPU 2.40 GHz, NVIDIA TU104GL Quadro RTX 5000
	DELL Work Station, Intel CoreI7-7700K,8 x 4.20 GHz, NVIDIA GeForce GTX 1060
Servers	Headnode (1 unit): 2U Rack Server, 64 GB DDR4, 240 GB enterprise SATA SSD, Intel 2.2 Ghz 12 cores
	General Purpose Compute node (2 units): 2U Rack Server, 1.8 TB DDR4, 480 GB enterprise SATA SSD, Intel 2.2 Ghz 28 cores (x86_64)
	GPU Intensivenode (2 units): 2U Rack Server, 1.5 TB DDR4, 480 GB Enterprise SATA SSD, Intel 2.2 Ghz 28 cores (x86_64), NVIDIA TESLA, VOLTA 100 PCIE 32 GB
	NFS Server: 2U Rack Server, Dual Port 40Gb QSFP, 480GB Enterprise SATA SSD, 8 TB Enterprise SATA 7.2K RPM, 32GB DDR4, Intel 2.2 GHz 12 Cores

3.2. Synthetic Procedures

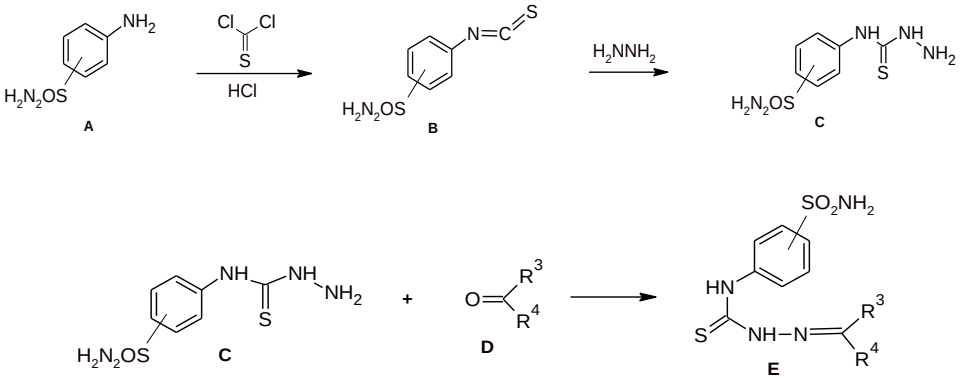

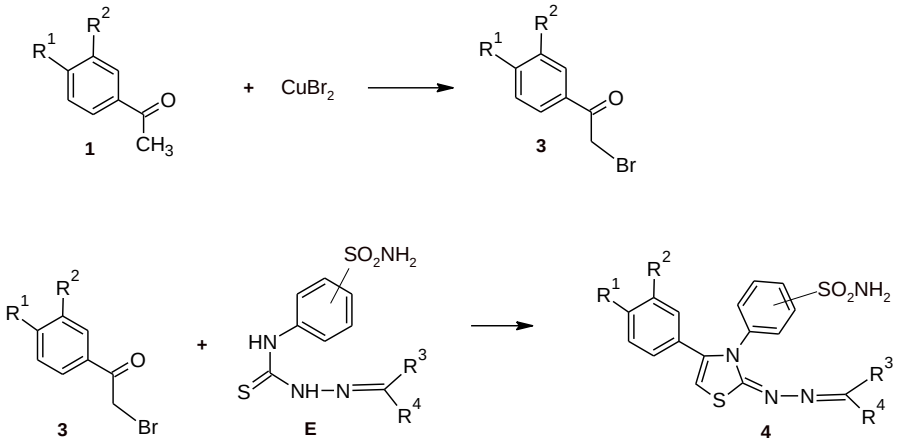

Scheme 3-1: General Synthesis Scheme of 3/4-[4-(Non)substitutedphenyl-2-(alkylidene/arylidenehydrazinylidene)-1,3-thiazol-3(*2H*)-yl]benzenesulfonamide derivatives (4a – 4v)

3.2.1. General Synthesis of 3/4-isothiocyanatobenzenesulfonamide (B)

In a 100 mL of water containing 25 mL of concentrated HCl, 60 mmol of 3/4-aminobenzenesulfonamide (**A**) is dissolved. Then 60 mmol (6.79 g) of thiophosgene is added to the mixture and further stirred until the red colour of the thiophosgene disappears. The resulting white crystalline product is filtered and washed with water (McKee and Bost 1946).

3.2.2. General Synthesis of *N*-(3/4-sulfamoylphenyl)hydrazinecarbothioamide (C)

With continuous stirring, a solution of 50 mmol of 3/4-isothiocyanatobenzenesulfonamide (**B**) in 20 mL of ethanol is added dropwise to a solution of 2.4 mL (50 mmol) of hydrazine monohydrate cooled in ice water in 20 mL of ethanol. The immediately precipitated product is filtered and purified by crystallization from ethanol (Karalı et al. 2017).

3.2.3. General Synthesis of 2-(Alkylidene/arylidene)-*N*-(3/4-sulfamoylphenyl)hydrazine-1-carbothioamide derivatives (E)

An ethanolic solution of 0.0061 mol of an appropriate ketone or aromatic aldehydes (**D**) is added to an ethanolic solution of 0.0061 mol of *N*-(3/4-sulfamoylphenyl)hydrazinecarbothioamide (**C**). The reaction mixture is heated under reflux for an additional 1–8 hours. The course of the reaction is followed by TLC. The resulting precipitate is filtered, dried, and purified by recrystallization from ethanol. In

cases of aliphatic ketones where no precipitate forms, the reaction mixture is left overnight to precipitate. The resulting crude product is filtered and recrystallized from ethanol and purified (Gürsoy and Karalı 2003; Güzel et al. 2008).

3.2.4. General Synthesis of ω-Bromoacetophenone derivatives (3)

0.1 mol of (non)substituted acetophenone (**1**) is dissolved in $CHCl_3$. The prepared mixture is added to the mixture containing 0.2 mol of $CuBr_2$ suspended in ethyl acetate. The reaction mixture is refluxed for 5 – 6 hours. TLC was used to determine the completion of the reaction, as well as the colour change of the reaction mixture from green to amber and the conversion of black $CuBr_2$ to white CuBr. The formed CuBr is filtered out. The ethyl acetate phase is washed with H_2O twice (2 x 100 ml) and dried with anhydrous Na_2SO_4. Ethyl acetate is removed under reduced pressure to obtain the desired **3** derivatives (L. C. King and G. K. Ostrum 1964; Ertas et al. 2018).

3.2.5. General synthesis of 3/4-[4-(Non)substitutedphenyl-2-(alkylidene/arylidenehydrazinylidene)-1,3-thiazol-3(*2H*)-yl]benzenesulfonamide derivatives (4a-4v)

A mixture of 0.0025 mol ω-bromoacetophenone (3) and 0.0025 mol of 2-(alkylidene/arylidene)-*N*-(3/4-sulfamoylphenyl)hydrazine-1-carbothioamide in 15 ml of chloroform-ethanol (2:1) is heated under reflux for 2–8 hours. The completion of the reaction is determined by TLC. The solid product formed is filtered and purified by recrystallization from ethanol or ethanol-chloroform (2:1) mixture or by using preparative TLC plates (Gürsoy and Karalı 2003).

3.3. Single X-ray Diffraction Analyses

The compounds were crystallized using slow evaporation and vapour diffusion methods. For the single crystal X-ray analysis, the crystal was mounted on a micro-mount and was attached to a goniometer head on a Bruker D8 VENTURE diffractometer equipped with PHOTON100 detector. The measurement was performed using graphite monochromated Mo-Kα radiation (λ = 0.71073 Å) with 1.0° of Ω and F rotation frames at room temperature. The structure was solved and refined using SHELXS-1997 (Sheldrick and Schneider 1997).

3.4. *In Silico* ADME Predictions and Molecular Modelling Studies

The *in silico* studies were conducted using the software modules available in the Schrödinger package (v2022-1, Schrödinger, Inc., New York).

3.4.1. *In Silico* ADME Predictions

The ADME properties of the compounds were predicted with the QikProp module. The three-dimensional (3D) structures of all the ligands were generated using the Builder module.

3.4.2. Preparation of Ligands

The 3D structures of all the ligands were generated using the Builder module. The sulfonamide group of all the ligands is given a negative charge ($R\text{-}SO_2NH^-$) since sulfonamide-containing compounds are anionically bound to the Zn^{2+} ion present in hCA enzyme active sites (Carta et al. 2014). The geometric isomerism of the compounds was taken into consideration when constructing the compounds. The preliminary studies suggested that the hydrazino part attached to the thiazoline ring is Z configuration while the other part is *E* configuration to allow the lowest energy conformation of the compounds and avoid steric hindrance. The elucidation of the structures of compound **4e** with single X-ray diffractometry (XRD) technique supports this geometrical configuration of these compounds. The LigPrep module was used to prepare the ligands. No tautomers and charges were generated during the process. All the ligands were energy minimized using the OPLS4 force field to obtain the lowest 3D structures.

3.4.3. Preparation of Protein Structures

All the protein crystal structures given in **Table 3-1** for hCAIX and hCAXII were obtained from the RCSB Protein Data Bank. Chain A of each crystal structure was retained whiles the rest of the chains together with the water molecules were deleted. The Protein Preparation Wizard was used to prepare the retained chains by completing the missing side chains, adding hydrogens, and energy minimizing with the OPLS4 force field. The N- and C-terminal ends of the protein were capped with *N*-acetyl and *N*-methylamide groups, respectively.

Table 3-1: Crystal Structures of hCAIX and hCAXII used in molecular modelling studies

hCA	PDB ID	Resolution (Å)	Mutation	Molecules or inhibitors in the active site
hCAIX	3IAI	2.20	Yes	Acetazolamide
	5FL6	1.90	Yes	5-(1-(4-Methylphenyl)-1*H*-1,2,3-triazol-4-yl)thiophene-2- sulfonamide
	6FE0	1.91	Yes	2-(Cyclooctylamino)-3,5,6-trifluoro-4-[(2-hydroxyethyl)sulfanyl]benzenesulfonamide
	6G9U	1.75	Yes	4-[2-[3-(cyclooctylamino)-2,5,6-tris(fluoranyl)-4-sulfamoyl-phenyl]sulfanylethyl]benzoic acid
	6QN2	1.95	Yes	Methyl 4-[(4-chloroanyl-2-cyclohexylsulfanyl-5-sulfamoylphenyl)carbonylamino]butanoate
	6TL5	2.21	Yes	3,5-diphenylbenzenesulfonamide
	6TL6	2.15	Yes	naphthalene-2-sulfonamide
hCAXII	1JD0	1.50	No	Acetazolamide
	4KP5	1.45	No	2-Chloro-4-[(pyrimidin-2-ylsulfanyl)acetyl]benzenesulfonamide
	4QJ0	1.55	No	2,3,6-trifluoro-5-{[(1*R*,2S)-2-hydroxy-1,2-diphenylethyl]amino}-4-[(2-hydroxyethyl)sulfonyl]benzenesulfonamide
	4QJO	1.80	No	3-(benzylamino)-2,5,6-trifluoro-4-[(2-phenylethyl)sulfonyl]benzenesulfonamide
	4QJW	1.55	No	3-(benzylamino)-2,5,6-trifluoro-4-[(2-phenylethyl)sulfonyl]benzenesulfonamide
	5LL5	1.42	No	4-(*1H* -benzimidazole-1-ylacetyl)benzenesulfonamide
	5LLO	1.60	No	3-[(1S)-2,3-Dihydro- *1H* -inden-1-ylamino]-2,5,6-trifluoro-4-[(2-hydroxyethyl)sulfonyl]benzenesulfonamide
	5MSA	1.20	No	2,3,5,6-Tetrafluoro-4-(propylthio)benzenesulfonamide
	6R6Y	1.38	No	4-Chloro-2-cyclohexylsulfanyl- *N*- (2-hydroxyethyl)-5-sulfamoyl benzamide

3.4.4. Receptor Grid Generation

The receptor Grid Generation module was utilized to produce all the grids. A grid box was generated around the centre of each cocrystallized ligand within the protein crystal structures to define the binding pocket. All ligands' sulfonamide groups were required to occupy the same region as observed for the cocrystallized ligands. To this end, the N, S and O atoms were used to define positional constraints. In addition, ligands with length <= 22 Å were allowed to dock. Free rotation was allowed for hydroxyl groups within 5 Å of cocrystallized ligands that are not involved in the protien hydrogen bonding network.

3.4.5. Reverse Ensemble Docking and Rescoring with MM-GBSA

The Glide Docking module was utilized to conduct retrospective docking of the cocrystallized ligands with Standard Precision (SP) settings using the generated grids. The default scaling factor of 0.8 and partial charge cut-off of 0.15 were preserved for Van der Waals radii. The planarity of conjugated π groups was improved, and docking penalties based on the Epik state were implemented. The positional constraints created within the grid files were applied and each ligand was docked 25 times producing the best three poses. The retrospective docking tests the ability of the docking protocol to produce similar poses with the cocrystallized ligands, and most importantly, to have the sulfonamide groups finely superimposed. The same settings were used for the preliminary docking studies of the ligand. For the ensemble docking, the Virtual Screening Workflow Module was used to dock the ligands with the Extra Precision (XP) settings, keeping three poses per compound state. The obtained poses from XP docking were subjected MM-GBSA binding free energy calculations using the Prime MM-GBSA module where the amino acid residues within 3 Å of the binding side were included in the flexible region except for Zn^{2+} and the three Zn^{2+}-binding histidines. The VSGB implicit solvation model and OPLS4 Force Field parameters were used and minimized sampling method to calculate the binding energies. The obtained poses were visually examined. Poses with higher binding affinities were selected for molecular dynamics simulation based on the superposition of the sulfonamide moiety of the ligand with the reference cocrystallised ligand, protein-ligand interactions and protein-ligand complementarity.

3.4.6. Molecular Dynamics Simulations

The molecular dynamics simulations were conducted utilising the Desmond module. The selected docked poses were initially positioned at the centre of an orthorhombic box with periodic boundary conditions (minimum distance of 10 Å between protein and boundary). Afterwards, by combining water molecules (Tip5p) and counter ions, a solvated and neutral system was created (NaCl; 0.15 M). All protein and ligand atoms were positionally constrained during the 100 ps energy minimization of the system (OPLS4). The system was finally simulated for 250 ns at constant temperature (300 K, Nose-Hoover Chain, default values) and pressure (1 bar, Martyna-Tobias-Klein, default values) utilising the RESPA integrator and without position

restraints. The time step was set to 0.002 fs. With the Simulation Interaction Diagram (SID), ligand-protein interactions, the RMSD of the ligand and protein Cα-atoms were studied from the generated trajectories. The MM-GBSA binding free energies of the frames generated from the ligand-protein complexes during the 250 ns simulation period were calculated using the *thermal_MMGBSA.py* script.

3.5. Biological activity

3.5.1. CA Inhibition assay

3/4-[4-(Non)substituted phenyl-2-(alkylidene/arylidenehydrazinylidene)-1,3-thiazol-3(2*H*)-yl]benzenesulfonamide derivatives and the reference CAI, Acetazolamide (AAZ), were tested in enzyme inhibition assays against the widespread cytosolic off-target hCAI and hCAII and the tumour-associated human hCAIX and hCAXII. The assays were carried out by Prof. Dr. Claudiu T Supuran and his team from the Department of Pharmaceutical Sciences, University of Florence, Neurofarba Department.

Stopped-flow device (SX.18MV-R Applied Photophysics model) is used for inhibition measurements of hCA isoenzymes. In these measurements, phenol red (0.2 mM) is used as an indicator, 10 mM Hepes (pH 7.4) as a buffer solution, and 0.1 Na_2SO_4 or $NaClO_4$ (used to provide constant ionic strength; these anions have no inhibitory effect at the concentration used). Measurements are made at the wavelength where the maximum absorption is at 557nm. The hCA-catalyzed CO_2 hydration reaction rate is measured in 5 – 10 second periods. A water solution saturated with CO_2 at 25 °C is used as the substrate. Stock solutions of the inhibitor molecules to be tested are prepared at a concentration of 10 mM and diluted with the above-mentioned buffer solution up to a concentration of 0.01 nM. Inhibitor and enzyme solutions are incubated at room temperature for 15 minutes before the measurement, allowing the formation of the enzyme-inhibitor complex. The results of measurements repeated three times for each inhibitor concentration are evaluated. The IC_{50} value is calculated from the dose-response curve of the test molecule studied at seven different concentrations, using the PRISM program and the nonlinear little squares method. The inhibition constant (K_i) is calculated from the IC_{50} value using the Cheng-Prusoff equation. Cheng-Prusoff equation: $K_i = IC_{50}/(1+[S]/K_m)$. where [S] is the CO_2 concentration at which the measurement is made; K_m represents the substrate concentration with half-maximum

enzyme activity. All enzymes used are obtained by recombinant technology in Prof. Dr. Supuran's laboratory (Akdemir et al. 2013).

3.5.2. Anticancer Assay (In vitro cytotoxicity Assay against some cancer cells)

3.5.2.1. Cell Culture

The endometrium (ECC 1, ATCC CRL-2923), lung (A549, ATCC CCL-185), colon (Caco-2, ATCC HTB-37; HT-29 ATCC HTB-38), breast (MCF 7, ATCC HTB-22), and glioblastoma (U118 MG, ATCC HTB-15) cancer cell lines in which hCA IX/XII enzymes are overexpressed were used to examine the cytotoxic effects of new synthesized molecules, and the human umbilical vein endothelial (HUVEC, ATCC PCS 100-010) cell line was used as a control.

Cells were cultured in a humidified oven at 37 °C with 5% CO_2. Cells were subcultured every 2 or 3 days. Cells that would not be used were frozen and kept in a nitrogen tank. Cell lines were grown using standard laboratory techniques and treated with the newly synthesized molecules. The molecules were dissolved using dimethyl sulfoxide (DMSO) and 0.01% DMSO was used as a control. The dilutions of the molecules were made as 100µg/mL-0.7813 µg/mL.

The cell lines described above were grown as follows: ECC-1 cells were cultured in RPMI media supplemented with 10% fetal bovine serum (FBS) and 100 U/mL penicillin-100 g/mL streptomycin. The cell lines A549, U118MG, and HUVEC were cultured in Dulbecco's Modified Eagle Medium (DMEM) containing 10% FBS (Fetal Bovine Serum), 100 U/ml penicillin, and 100 g/mL streptomycin. Caco-2 and HT-29 cell lines were cultured in a DMEM-F12 mixture supplemented with 10% FBS (Fetal Bovine Serum), 100 U/ml penicillin, and 100 g/mL streptomycin. MCF-7 cells were cultured in EMEM media supplemented with 10% FBS (Fetal Bovine Serum), 100 U/ml penicillin, 100 g/mL streptomycin, and 0.1 g/mL insulin.

3.5.2.2. Cell Viability Assay

ECC-1 ($1x10^4$), A549 ($1x10^4$), Caco-2 ($1.5x10^4$), HT-29 ($1.5x10^4$), MCF-7 ($5x10^4$), U118 MG ($1.5x10^4$), and HUVEC ($1x10^4$) cell lines were seeded in 96-well plates and allowed to adhere to the surface overnight. The seeded cells were incubated with different concentrations of pure substances (100 µg/mL-0.78125 µg/mL) for 72 hours. After incubation, 20 µL of a mixture of 3-(4,5-dimethylthiazol-2-yl)-5-(3-

carboxymethoxyphenyl)-2-(4-sulphophenyl)-2*H*-tetrazolium (MTS) and phenazine methosulfate (PMS) was added, and the mixture was incubated for another 2 hours. At the end of this period, absorbance values were read at 490 nm in a microplate reader. Experiments were repeated three times. The % inhibition and IC_{50} values were determined over the determined absorbance values (Buttke et al. 1993).

4. RESULTS

4.1. Preliminary Molecular Modelling studies

4.1.1. Retrospective Docking Studies

Retrospective docking studies were conducted to validate the pose generation procedures with the Glide SP scoring function. For this purpose, the cocrystallised ligands were docked into their respective crystal structures and both the docked and the cocrystallised ligand were compared. The close resemblance between the docked pose and the cocrystallized ligands (**Figure 4-1**) supports the efficacy of the docking protocol in accurately predicting ligand binding interactions.

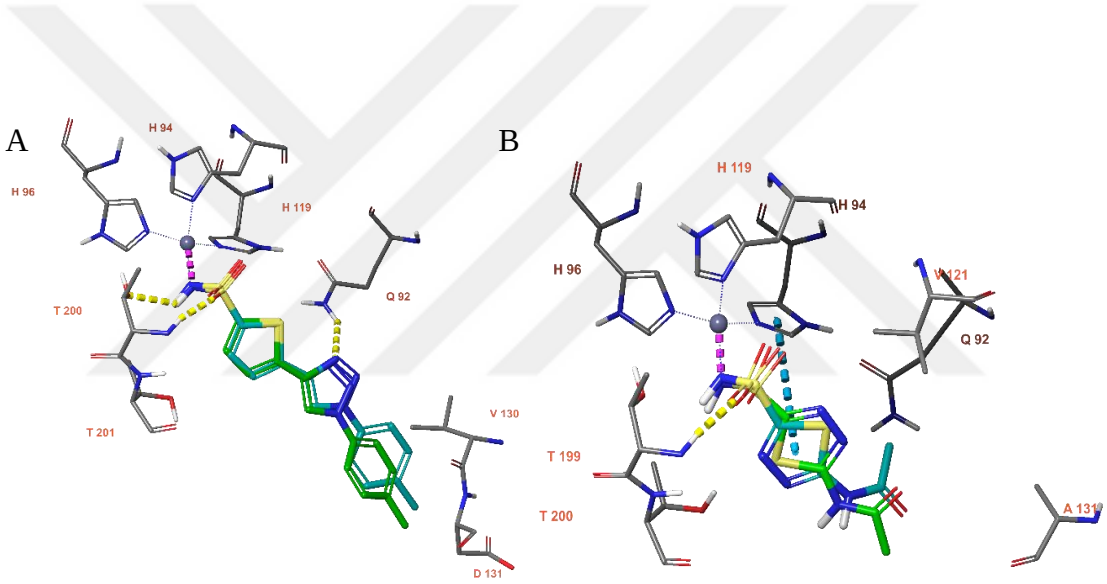

Figure 4-1 A) Retrospective docked pose of 5-(1-(4-Methylphenyl)-1*H*-1,2,3-triazol-4-yl)thiophene-2- sulfonamide in hCAIX (PDB:5FL6) B) Retrospective docked pose of AAZ in hCAXII (PDB:1JD0). The grey sphere represents the Zn^{2+}. Pink dashed lines represent metal coordination. Yellow dashed lines represent hydrogen bonding. Turquoise dashed lines represent π-π stackings.

4.1.2. Library Screening with SP Docking and Suggestion of compounds for Synthesis

Using the validated protocol, the library of molecules was docked against hCAIX and hCAXII using the Glide SP function, generating three poses for each compound. The poses of the compounds were analysed based on the location and the

interaction of the sulfonamide group of the ligands and the similarity with the cocrystallised ligands, ligand protein interactions and complementarity. The SP docking scores for the selected compounds were given in **Table 4-1**.

Table 4-1: Preliminary SP docking scores of the designed ligands.

Ligands	Structures	Preliminary SP Docking score	
		hCAIX (PDB: 3IAI)	hCAXII (PDB: 1JD0)
4a	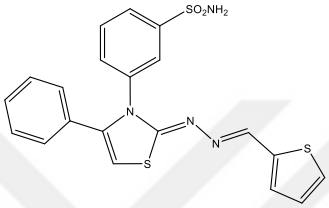	-5.82	-5.34
4b	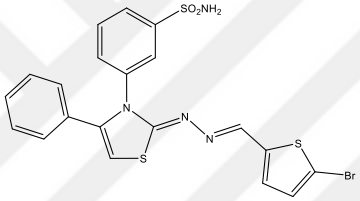	-6.07	-4.77
4c	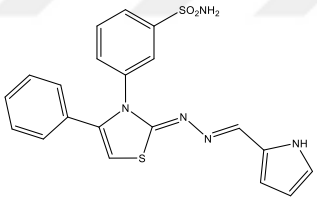	-5.59	-4.94
4d	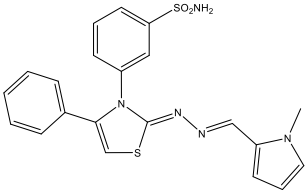	-7.76	-
4e	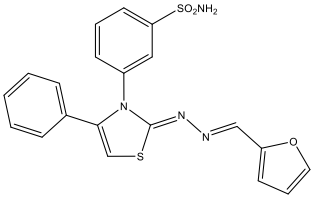	-6.16	-5.26
4f	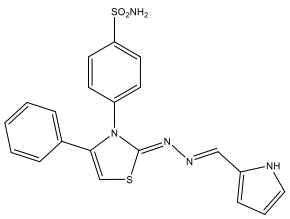	-7.49	-6.48

4g	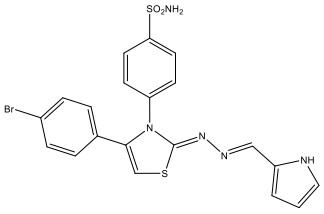	-4.24	-7.23
4h	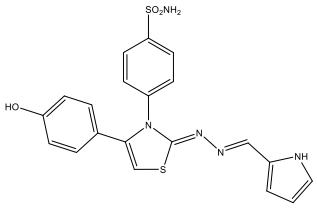	-7.25	-6.47
4i	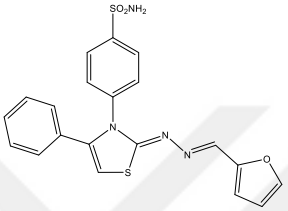	-7.24	-6.86
4j	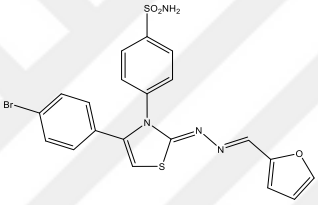	-5.79	-6.96
4k	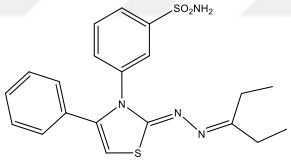	-6.11	-7.76
4l	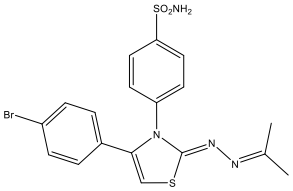	-6.13	-7.58
4m	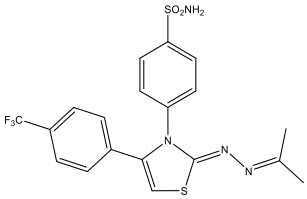	-4.91	-7.31
4n	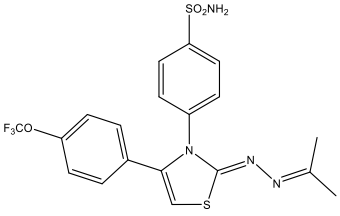	-5.29	-6.89

4o	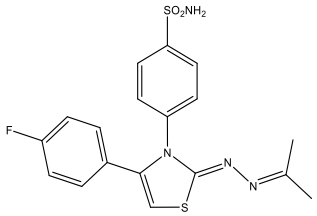	-7.28	-6.22
4p	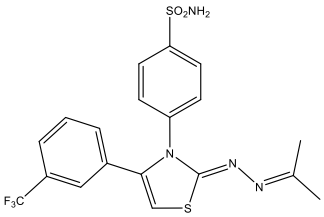	-6.85	-6.75
4q	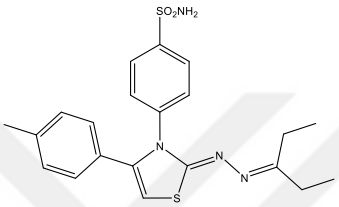	-6.69	-4.75
4r	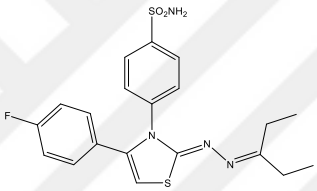	-7.13	-7.85
4s	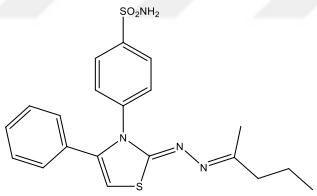	-7.80 (Z) -7.32 (E)	-8.01 (Z) -6.00 (E)
4t	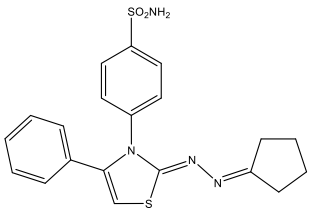	-7.38	-6.52
4u	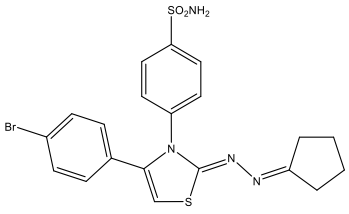	-5.48	-6.02

4v	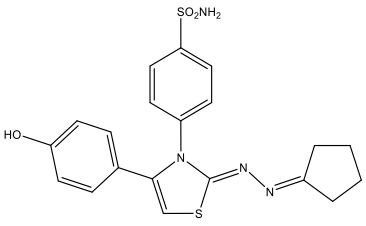	-7.00	-8.01
AAZ	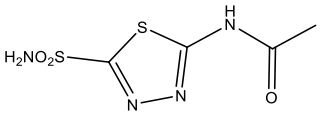	-6.16	-7.72

Higher negative docking scores indicate strong binding of the ligands, and therefore, compounds **4d, 4f, 4h, 4i, 4o**, and **4t** were expected to strongly bind to hCAIX and compounds **4g, 4j, 4k, 4l**, and **4m** were expected to strongly bind to hCAXII. Compounds **4r, 4s**, and **4v** were expected to strongly bind to both hCAIX and hCAXII.

The docking pose of compound **4s** (*Z*) expected to bind to both hCAIX and hCAXII is given in **Figures 4-2A** and **B**, respectively. In hCAIX, the sulfonamide group of compound **4s** forms a coordinate interaction with Zn^{2+} and a hydrogen bonding with the backbone of Thr199, whereas the benzenesulfonamide ring formed a π – π interaction with His94. The 4-pheneyl moiety faced the hydrophobic region while the 2-pentylideneazine moiety faced the hydrophilic region. In hCAXII, while the sulfonamide made similar interactions, the 4-phenyl ring faced the hydrophilic region forming π – π interaction with His94.

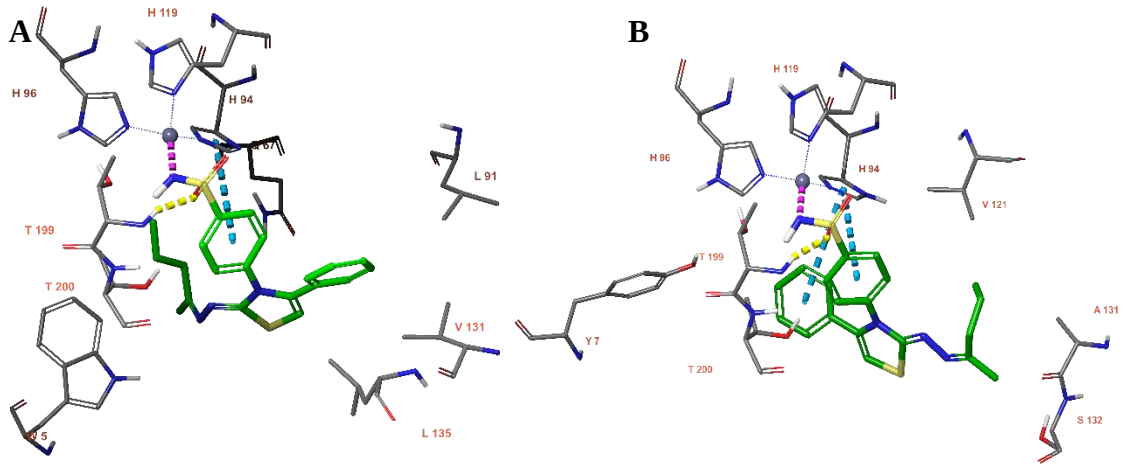

Figure 4-2: A) The SP docked pose of 4s in the active site of hCAIX (3IAI). B) The SP docked pose of 4s in the active site of hCAXII (1JD0). The grey sphere represents the Zn^{2+}. Pink dashed lines represent metal coordination. Yellow dashed lines represent hydrogen bonding. Turquoise dashed lines represent π-π stackings

The docking pose of compounds **4d** in hCAIX and **4v** in hCAXII are given in **Figures 4-3A** and **B**, respectively. In the docking pose of compound **4d** in hCAIX, while the 4-phenyl and the 2-(((1*H*-pyrrol-2-yl)methylene)hydrazineylidene) moieties faced the hydrophilic the hydrophobic regions, respectively, the sulfonamide group of formed a coordinate interaction with Zn^{2+} and a hydrogen bonding with the backbone of Thr199, and the benzenesulfonamide ring formed a π – π interaction with His94. In hCAXII, while the sulfonamide made a coordinate interaction with Zn^{2+} and two hydrogen bonds with the backbone and side chain of Thr199, the 4-(4-hydroxy)phenyl ring faced the hydrophilic region forming π – π interaction with His94.

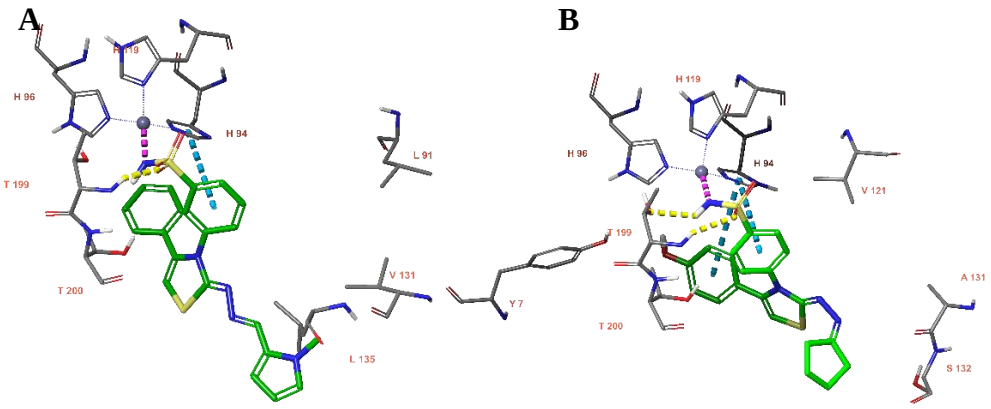

Figure 4-3: A) The SP docked pose of 4d in the active site of hCAIX (3IAI). B) The SP docked pose of 4v in the active site of hCAXII (1JD0). The grey sphere represents the Zn^{2+}. Pink dashed lines represent metal coordination. Yellow dashed lines represent hydrogen bonding. Turquoise dashed lines represent π-π stackings.

It is observed from these poses that since both the alkylidene/arylideneazine moiety has both hydrophilic and hydrophobic parts and 4-phenyl moiety may also contain hydrophilic groups, they can either face the hydrophobic or the hydrophilic parts. These binding patterns were observed for the rest of the compounds.

4.2. *In Silico* ADME Prediction

The ADME properties of compounds **4a – 4v** were predicted with the Qikprop module. Important ADME parameters obtained from QikProp are given in **Table 4-2** with the recommended values given in parentheses. These parameters are the number of hydrogen bond donors (donorHB) and acceptors (accptHB), octanol/water partition coefficient (QPlogPo/w), solubility (QPlogS), Caco cell permeability (QPPCaco), brain/blood partition coefficient (QPlogBB), (percentage of) human oral absorption, binding of human serum albumin, Van der Waals surface area (PSA), the possible number of metabolic reactions (#metab) and the number of violations of RO5.

Table 4-2: ADME properties of compounds 4a – 4v

Compounds	MW (130.0 – 725.0)	donorHB (0.0 – 6.0)	accptHB (2.0 – 20.0)	QPlogPo/w (–2.0 – 6.5)	QPlogS (–6.5 – 0.5)	QPPCaco (<25 poor, >500 great)	QPlogBB (–3.0 – 1.2)	QPlogKhsa (–1.5 – 1.5)	Human Oral Absorption (1=low, 2=medium, 3=high)	Percent Human Oral Absorption (>80% is high <25% is poor)	PSA (7.0 – 200.0)	#metab (1 – 8)	RO5
4a	440.55	2.00	7.00	3.98	-5.89	501.63	-0.90	0.40	3.00	100.00	87.77	3	0.00
4b	519.45	2.00	7.00	4.55	-6.75	501.76	-0.76	0.53	1.00	88.94	87.77	3	1.00
4c	423.51	3.00	7.00	3.35	-5.45	283.58	-1.28	0.31	3.00	90.45	101.42	2	0.00
4d	437.53	2.00	7.00	4.02	-6.02	478.77	-1.06	0.50	3.00	100.00	90.64	2	0.00
4e	424.49	2.00	7.50	3.37	-5.07	497.07	-0.98	0.22	3.00	94.96	96.71	3	0.00
4f	423.51	3.00	7.00	3.29	-5.72	198.53	-1.51	0.32	3.00	87.34	101.73	2	0.00
4g	502.40	3.00	7.00	3.84	-6.53	198.58	-1.37	0.45	1.00	77.61	101.77	2	1.00
4h	439.51	4.00	7.75	2.55	-5.45	60.48	-2.17	0.15	3.00	73.75	124.29	3	0.00
4i	424.49	2.00	7.50	3.32	-5.39	341.26	-1.21	0.24	3.00	91.75	96.97	3	0.00
4j	503.39	2.00	7.50	3.88	-6.20	344.61	-1.06	0.37	1.00	82.13	97.02	3	1.00
4k	414.54	2.00	6.50	3.91	-5.43	625.42	-0.92	0.46	3.00	100.00	92.67	4	0.00
4l	465.38	2.00	6.50	3.60	-6.10	260.97	-1.08	0.43	3.00	91.29	96.63	2	0.00
4m	454.48	2.00	6.50	4.11	-6.84	297.12	-0.97	0.56	1.00	95.27	96.39	2	0.00
4n	470.48	2.00	6.50	4.16	-6.67	263.91	-1.06	0.56	1.00	94.62	104.67	3	0.00
4o	404.48	2.00	6.50	3.35	-5.65	294.23	-1.05	0.36	3.00	90.75	96.40	2	0.00
4p	454.48	2.00	6.50	4.11	-6.83	294.90	-0.97	0.56	1.00	95.20	96.40	2	0.00
4q	428.57	2.00	6.50	4.03	-6.20	319.00	-1.33	0.64	3.00	95.36	93.47	5	0.00
4r	432.53	2.00	6.50	3.89	-5.99	292.97	-1.24	0.52	3.00	93.89	93.39	4	0.00
4s	414.54	2.00	6.50	3.75	-5.75	314.53	-1.28	0.49	3.00	93.64	94.38	3	0.00
4t	412.52	2.00	6.50	3.58	-5.91	308.48	-1.17	0.50	3.00	92.46	97.00	4	0.00
4u	491.42	2.00	6.50	4.14	-6.74	310.93	-1.02	0.63	1.00	95.82	96.99	4	0.00
4v	428.52	3.00	7.25	2.85	-5.65	93.29	-1.82	0.34	3.00	78.86	119.52	5	0.00

4.3. Chemistry

4.3.1. Synthesis of 2-(Alkylidene/arylidene)-*N*-(3/4-sulfamoylphenyl)hydrazine-1-carbothioamide derivatives (E)

4.3.1.1. (*E*)-N-(3-sulfamoylphenyl)-2-(thiophen-2-ylmethylene)hydrazine-1-carbothioamide (E1)

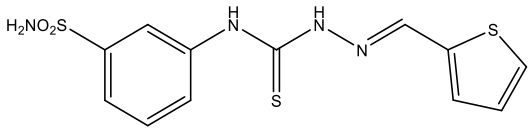

An ethanolic solution of 0.0061 mol (0.55 ml) of thiophene-2-carbaldehyde (**D1**) is added to an ethanolic solution of 0.0061 mol (1.5 g) of *N*-(3-sulfamoylphenyl)hydrazinecarbothioamide (**C1**). The reaction mixture is heated under reflux for 6 hours. The resulting precipitate is filtered, dried, and purified by recrystallization from ethanol.

Physical appearance	: Yellow powder
Yield	: 82
Retention factor (R_f)	: 0.62; Chloroform : Methanol (9:1)
Melting point (°C)	: 209.8-212.0

Elemental Analysis

Molecular formula	: $C_{12}H_{12}N_4O_2S_3$
Molecular weight (g/mol)	: 340.444

Element	C	H	N	S
Calculated (%)	42.34	3.55	16.46	28.26
Found (%)	42.45	3.28	16.24	28.57

Spectral Analysis

Fourier Transform Infrared (FT-IR) Spectrum

IR(KBr): υ_{max} (cm^{-1}) 3360, 3334, 3250 (NH s.b); 1593, 1585, 1550, 1519, 1498 (Ar. C=C s.b, C=N s.b and N-H b.b), 1330, 1151 (S=O s.b); 1330 (C-N s.b.); 1271 (C=S, s.b) 879, 740, 702 (1,3-disubs. Ar-C-H b.b).

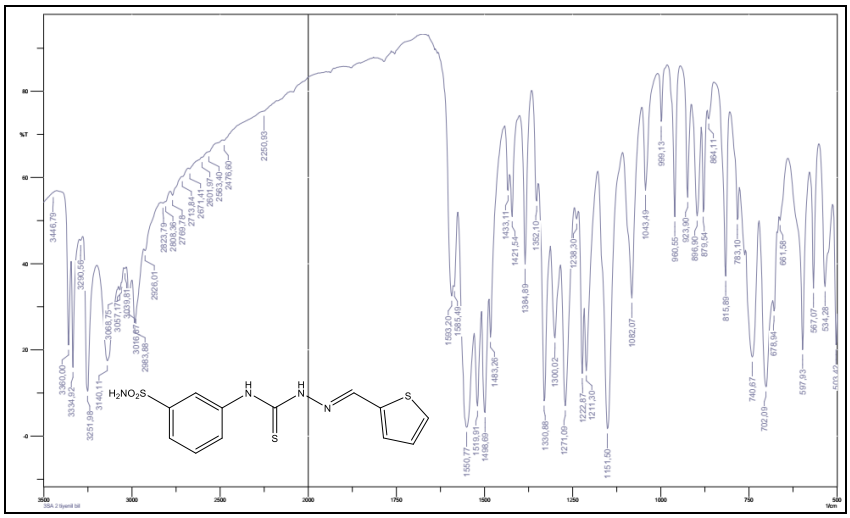

Figure 4-4: IR spectrum of compound E1

^{1}H-NMR Spectrum

^{1}H NMR (DMSO-d_6 / 500 MHz δ (ppm): 7.15 (1H, dd, J=3.7, 3.6 Hz, thiophene C_4-H), 7.40 (2H, s, -SO_2NH_2), 7.50-7.58 (2H, m, 3-sulfamoylphenyl C_5-H and thiophene C_3-H), 7.64 (1H, dt, J=7.8, 1.7 Hz, 3-sulfamoylphenyl C_4-H), 7.71 (1H, d, J=5.0 Hz, thiophene C_5-H), 7.82 (1H, ddd, J=8.1, 2.2, 1.0 Hz, 3-sulfamoylphenyl C_6-H), 8.05 (1H, t, J=2.0 Hz, 3-sulfamoylphenyl C_2-H), 8.37 (1H, s, N=CH), 10.07 (1H, s, tsc N_4-H), 11.94 (1H, s, tsc N_2-H).

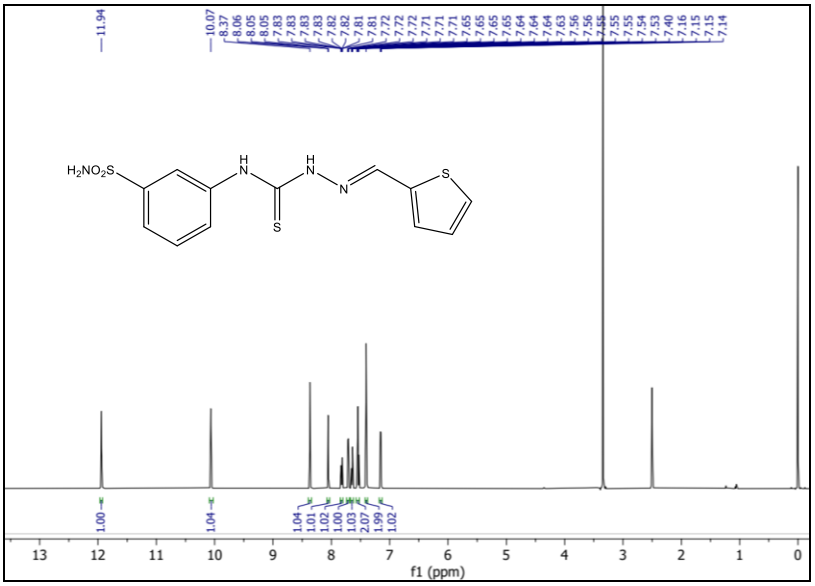

Figure 4-5: ^{1}H-NMR Spectrum of compound E1

^{13}C-NMR Spectrum

^{13}C NMR (decoupled, DMSO-d_6, 125 MHz) δ (ppm): 122.3 (3-sulfamoylphenyl C_4), 122.6 (3-sulfamoylphenyl C_2), 128.0 (thiophene C_4), 128.6 (3-sulfamoylphenyl C_5), 129.0 (3-sulfamoylphenyl C_6), 129.5 (thiophene C_5), 131.2 (thiophene C_3), 138.3 (thiophene C_2), 138.6 (N=CH), 139.6 (3-sulfamoylphenyl C_1), 144.0 (3-sulfamoylphenyl C_3), 175.7 (C=S).

Figure 4-6: ^{13}C-NMR Spectrum of compound E1

^{13}C NMR (HSQC-2D, DMSO-d_6, 125 MHz) δ (ppm): **122.3** [3-sulfamoylphenyl C_4 - **7.64** (1H, dt, *J*=7.8, 1.7 Hz, 3-sulfamoylphenyl C_4-H)], **122.6** [3-sulfamoylphenyl C_2 - **8.05** (1H, t, *J*=2.0 Hz, 3-sulfamoylphenyl C_2-H)], **128.0** [thiophene C_4 - **7.15, 7.16** (1H, 2d, *J*=3.7, 3.6 Hz, thiophene C_4-H)], **128.6** [3-sulfamoylphenyl C_5 - **7.50-7.58** (2H, m, 3-sulfamoylphenyl C_5-H and thiophene C_3-H)], **129.0** [3-sulfamoylphenyl C_6 - **7.82** (1H, ddd, *J*=8.1, 2.2, 1.0 Hz, 3-sulfamoylphenyl C_6-H)], **129.5** [thiophene C_5 - 7.71 (1H, d, *J*=5.0 Hz, thiophene C_5-H)], **131.2** [thiophene C_3 - **7.50-7.58** (2H, m, 3-sulfamoylphenyl C_5-H and thiophene C_3-H)], **138.6** [N=CH - **8.37** (1H, s, N=CH)].

Figure 4-7: HSQC Spectrum of compound E1

LC-MS Spectrum

m/z ESI (negative): 339.0 $(M-H)^-$; $C_{12}H_{12}N_4O_2S_3$ (MA= 340.444; Exact Mass= 340.01)

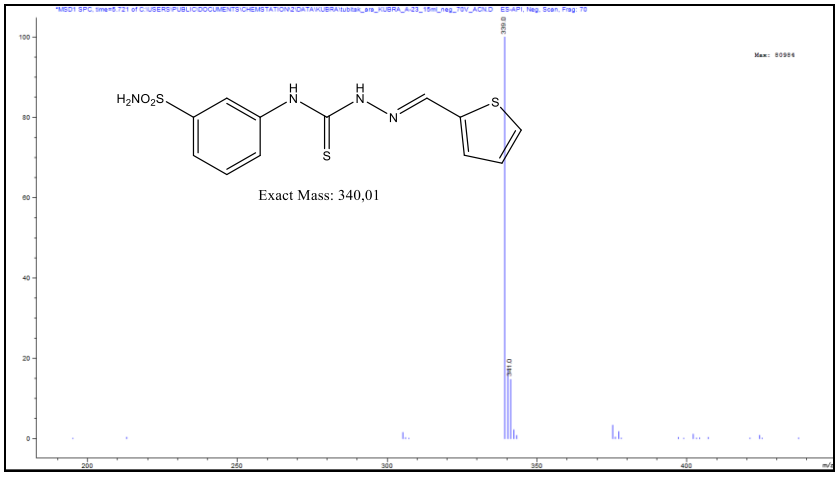

Figure 4-8: Mass Spectrum of compound E1

4.3.1.2. (*E*)-2-((5-bromothiophen-2-yl)methylene)-*N*-(3-sulfamoylphenyl)hydrazine-1-carbothioamide (E2)

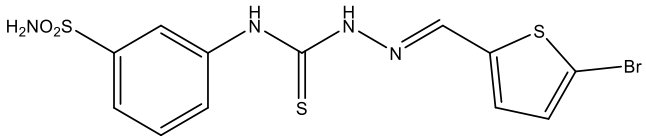

An ethanolic solution of 0.0061 mol (0.65 ml) of 5-bromothiophene-2-carbaldehyde (**D2**) is added to an ethanolic solution of 0.0061 mol (1.5 g) of *N*-(3-sulfamoylphenyl)hydrazinecarbothioamide (**C1**). The reaction mixture is heated under reflux for 6 hours. The resulting precipitate is filtered, dried, and purified by recrystallization from ethanol.

Physical appearance	: Greenish yellow powder
Yield (%)	: 78
Retention factor	: 0.56; Chloroform : Methanol (9:1)
Melting point (ºC)	: 207.1-208.8

Elemental Analysis

Molecular formula	: $C_{12}H_{11}BrN_4O_2S_3$
Molecular weight (g/mol)	: 419.340

Element	C	H	N	S
Calculated (%)	34.37	2.64	13.36	22.94
Found (%)	34.25	2.60	13.14	22.63

Spectral Analysis

Fourier Transform Infrared (FT-IR) Spectrum

IR(KBr): υ 3334, 3307, 3273, 3255, 3155 (NH s.b); 3076, 3022 (Ar.C-H s.b., =CH s.b) ; 1587, 1548 1518, 1504, 1485 (Ar. C=C s.b, C=N s.b, N-H b.b); 1336, 1155 (S=O s.b); 1307 (C-N s.b); 1265 (C=S s.b); 1080 (Ar-Br b.b); 883, 754, 704 (1,3-disubs. Ar-C-H b.b)

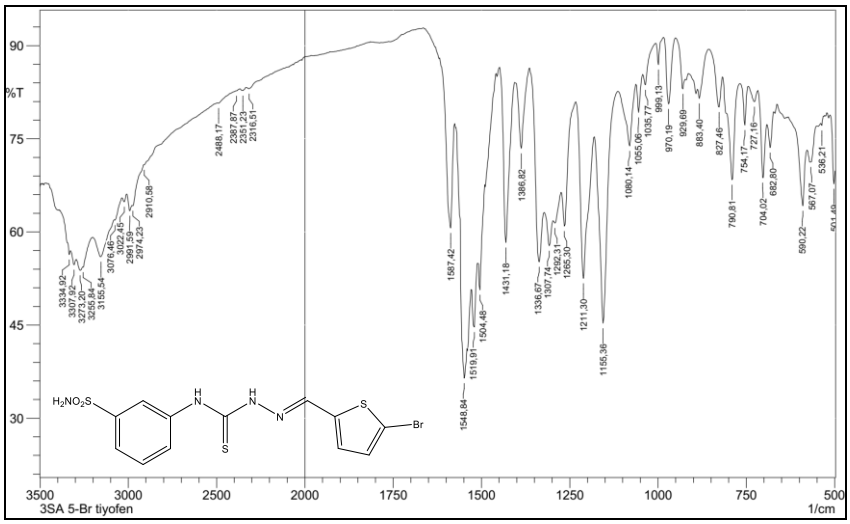

Figure 4-9: IR spectrum of compound E2

^{1}H-NMR Spectrum

^{1}H NMR (DMSO-d_6 / 500 MHz δ (ppm): 7.27 (1H, d, J=3.9 Hz, thiophene C_4-H), 7.37 (1H, d, J=3.9 Hz, thiophene C_3-H), 7.40 (2H, s, -SO_2NH_2), 7.55 (1H, t, J=7.9 Hz, 3-sulfamoylphenyl C_5-H), 7.65 (1H, dt, J=7.8, 1.8 Hz, 3-sulfamoylphenyl C_4-H), 7.80 (1H, ddd, J=8.0, 2.2, 1.0 Hz, 3-sulfamoylphenyl C_6-H), 8.03 (1H, t, J=2.0 Hz, 3-sulfamoylphenyl C_2-H), 8.26 (1H, s, N=CH), 10.09 (1H, s, tsc N_4-H), 12.01 (1H, s, tsc N_2-H).

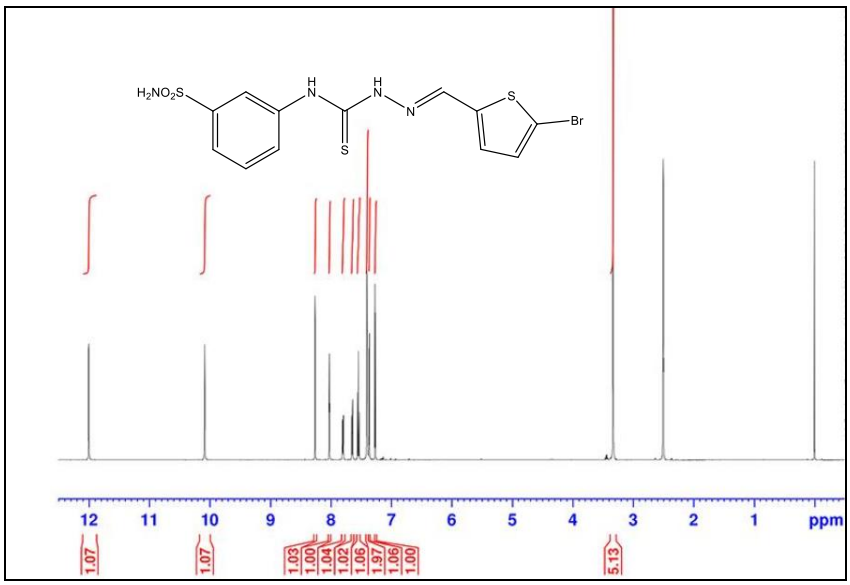

Figure 4-10: ^{1}H-NMR Spectrum of compound E2 (0 – 12 ppm)

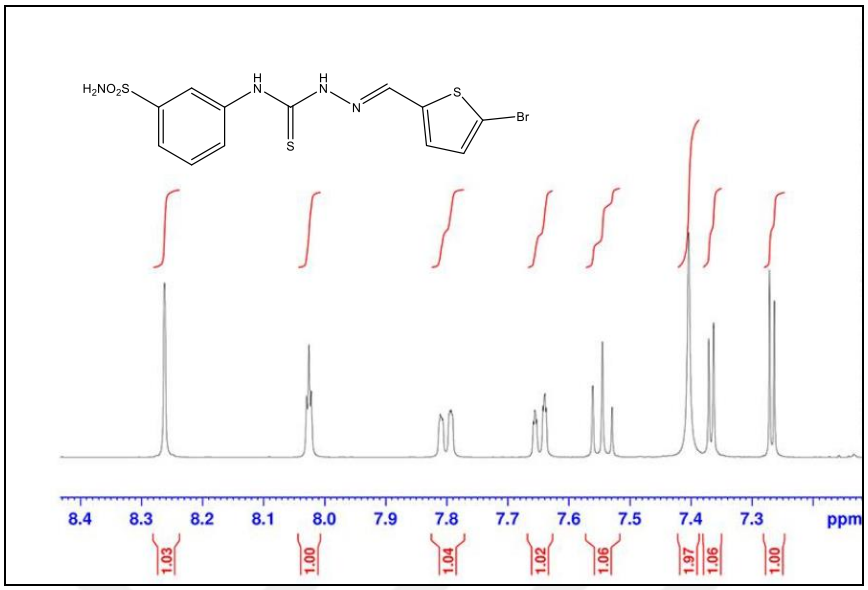

Figure 4-11: ^{1}H-NMR Spectrum of compound E2 (7.2 – 8.4 ppm)

LC-MS Spectrum

m/z ESI (negative): 418.9 $(M+2-H)^-$; $C_{12}H_{11}BrN_4O_2S_3$ (MA= 419.340; Exact Mass= 417.92)

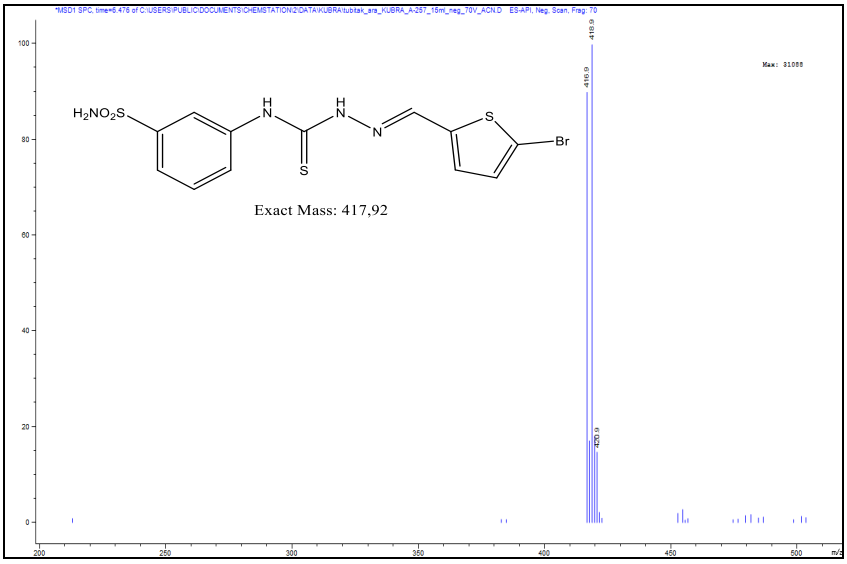

Figure 4-12: Mass Spectrum of compound E2

4.3.1.3. (*E*)-2-((1*H*-pyrrol-2-yl)methylene)-*N*-(3-sulfamoylphenyl)hydrazine-1-carbothioamide (E3)

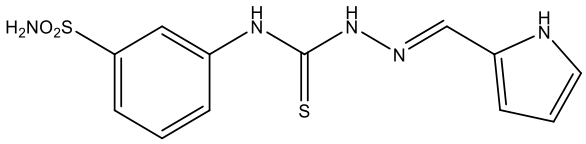

An ethanolic solution of 0.0061 mol (0.57 g) of 1*H*-pyrrole-2-carbaldehyde (**D3**) is added to an ethanolic solution of 0.0061 mol (1.5 g) of *N*-(3-sulfamoylphenyl)hydrazinecarbothioamide (**C1**). The reaction mixture is heated under reflux for 6 hours. The resulting precipitate is filtered, dried, and purified by recrystallization from ethanol.

Physical appearance	: Greenish yellow crystals
Yield (%)	: 80
Retention factor	: 0.5; Chloroform : Methanol (9:1)
Melting point (ºC)	: 215.9 -216.5

Elemental Analysis

Molecular formula	: $C_{12}H_{13}N_5O_2S_2$
Molecular weight (g/mol)	: 323.393

Element	C	H	N	S
Calculated (%)	44.57	4.05	21.66	19.83
Found (%)	44.32	3.85	21.43	19.58

Spectral Analysis

Fourier Transform Infrared (FT-IR) Spectrum

IR(KBr): υ 3375, 3294, 3255 (NH s.b); 3124, 3088, 3055, 3005 (Ar.C-H s.b., =CH s.b) ; 1614, 1585, 1556, 1533, 1489 (Ar. C=C s.b, C=N s.b, N-H b.b); 1311, 1149 (S=O s.b); 1300 (C-N s.b); 1263 (C=S s.b); 883, 748, 690 (1,3-disubs. Ar-C-H b.b)

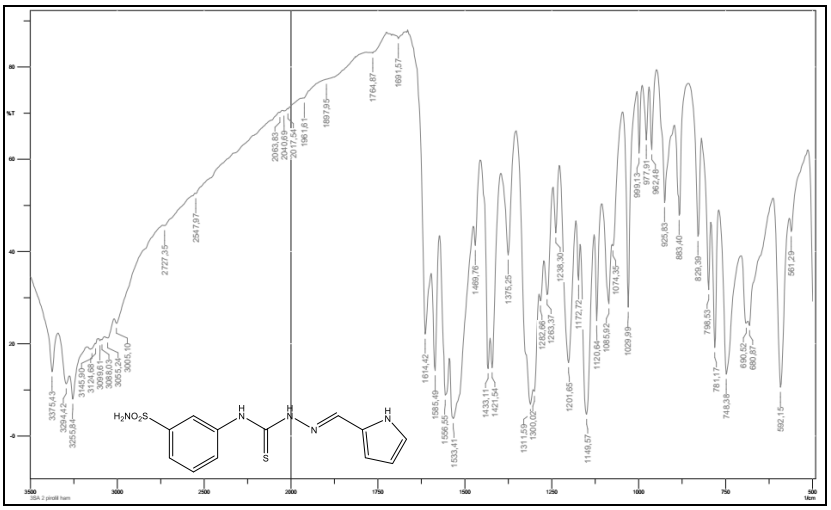

Figure 4-13: IR spectrum of compound E3

^{1}H-NMR Spectrum

^{1}H NMR (DMSO-d_6 / 500 MHz δ (ppm): 6.16 (1H, dd, J=4.3, 1.8 Hz, pyrrole C_4-H), 6.50-6.51 (1H, m, pyrrole C_3-H), 7.08-7.10 (1H, m, pyrrole C_5-H), 7.42 (2H, s, -SO_2NH_2), 7.58 (1H, t, J=7.9 Hz, 3-sulfamoylphenyl C_5-H), 7.65 (1H, dt, J=7.8, 1.8 Hz, 3-sulfamoylphenyl C_4-H), 7.92 (1H, ddd, J=7.9, 2.2, 1.1 Hz, 3-sulfamoylphenyl C_6-H), 7.97 (1H, s, N=CH), 8.07 (1H, t, J=1.9 Hz, 3-sulfamoylphenyl C_2-H), 10.21 (1H, s, tsc N_4-H), 11.50 (1H, s, pyrrole), 11.85 (1H, s, tsc N_2-H).

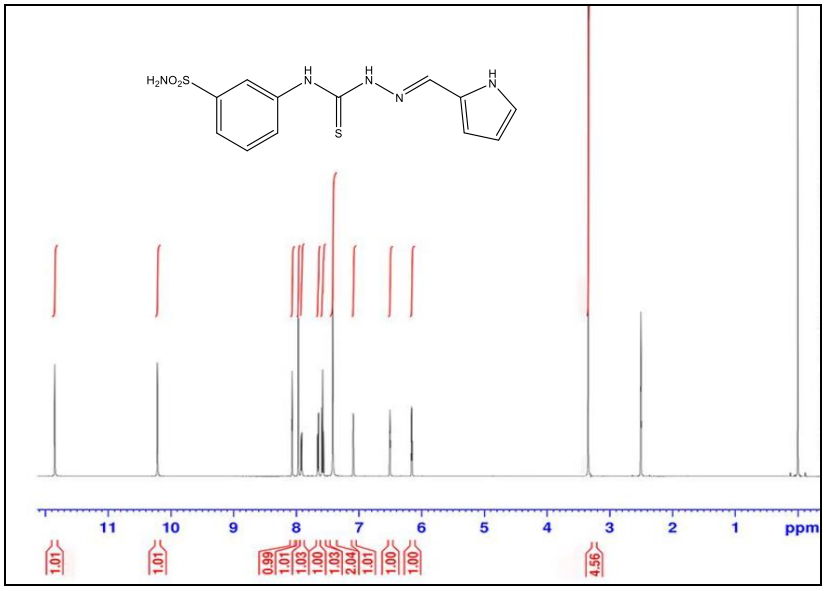

Figure 4-14: ^{1}H-NMR spectrum of compound E3 (0 – 12 ppm)

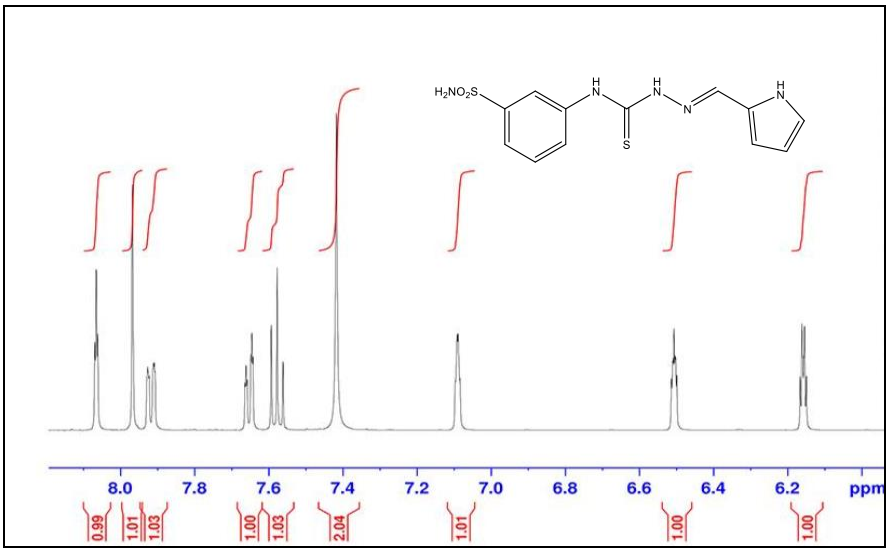

Figure 4-15: ^{1}H-NMR spectrum of compound E3 (6.0 – 8.1 ppm)

^{13}C-NMR Spectrum

^{13}C NMR (decoupled, DMSO-d_6, 125 MHz) δ (ppm): 108.9 (pyrrole C_4), 113.3 (pyrrole C_3), 121.3 (3-sulfamoylphenyl C_2), 121.5 (3-sulfamoylphenyl C_4), 121.7 (pyrrole C_5), 126.7 (pyrrole C_2), 128.1 (3-sulfamoylphenyl C_5), 127.7 (3-sulfamoylphenyl C_6), 134.1 (N=CH), 138.8 (3-sulfamoylphenyl C_1), 143.5 (3-sulfamoylphenyl C_3), 174.1 (C=S).

Figure 4-16: ^{13}C-NMR spectrum of compound E3 (0 – 200 ppm)

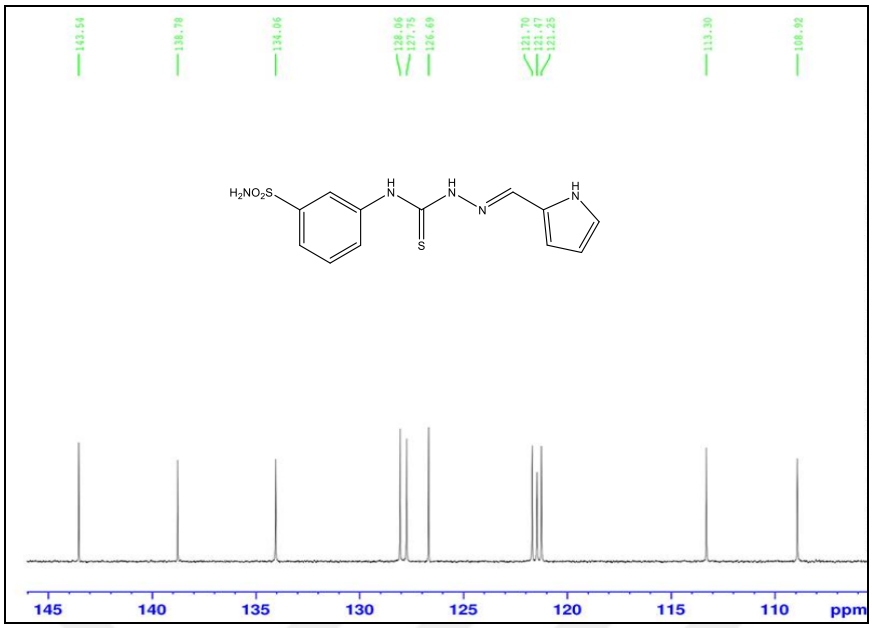

Figure 4-17: ^{13}C-NMR spectrum of compound E3 (110 – 145 ppm)

^{13}C NMR (HSQC-2D, DMSO-*d*$_6$, 125 MHz) δ (ppm): **108.9** [pyrrole C$_4$ - **6.16** (1H, dd, *J*=4.3, 1.8 Hz, pyrrole C$_4$-H)], **113.3** [pyrrole C$_3$ - **6.50-6.51** (1H, m, pyrrole C$_3$-H)], **121.3** [3-sulfamoylphenyl C$_2$ - **8.07** (1H, t, *J*=1.9 Hz, 3-sulfamoylphenyl C$_2$-H)], **121.5** [3-sulfamoylphenyl C$_4$ - **7.65** (1H, dt, *J*=7.8, 1.8 Hz, 3-sulfamoylphenyl C$_4$-H)], **121.7** [pyrrole C$_5$ - **7.08-7.10** (1H, m, pyrrole C$_5$-H)], **128.1** [3-sulfamoylphenyl C$_5$ - **7.58** (1H, t, *J*=7.9 Hz, 3-sulfamoylphenyl C$_5$-H)], **127.7** [3-sulfamoylphenyl C$_6$ - **7.92** (1H, ddd, *J*=7.9, 2.2, 1.1 Hz, 3-sulfamoylphenyl C$_6$-H)], **134.1** [N=CH - **7.97** (1H, s, N=CH)].

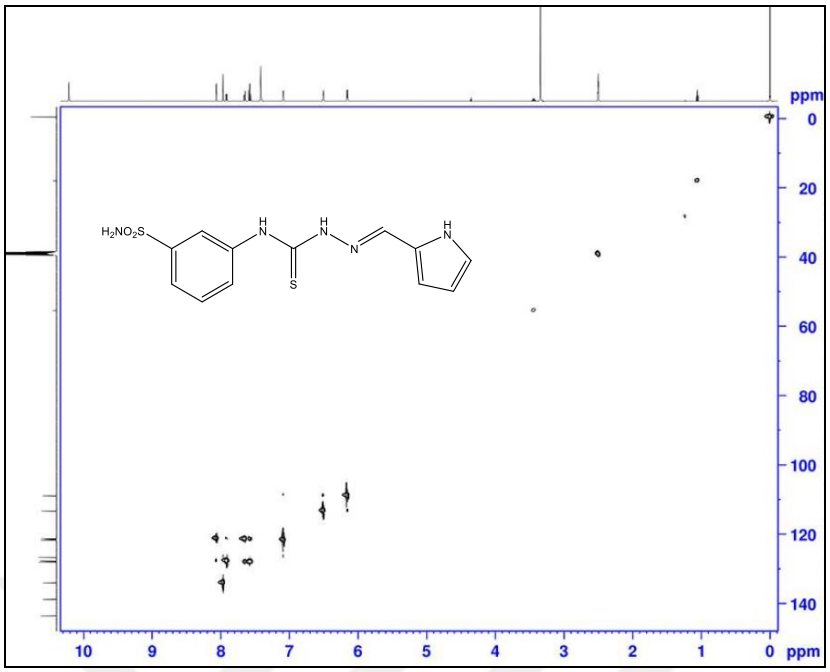

Figure 4-18: HSQC spectrum of compound E3

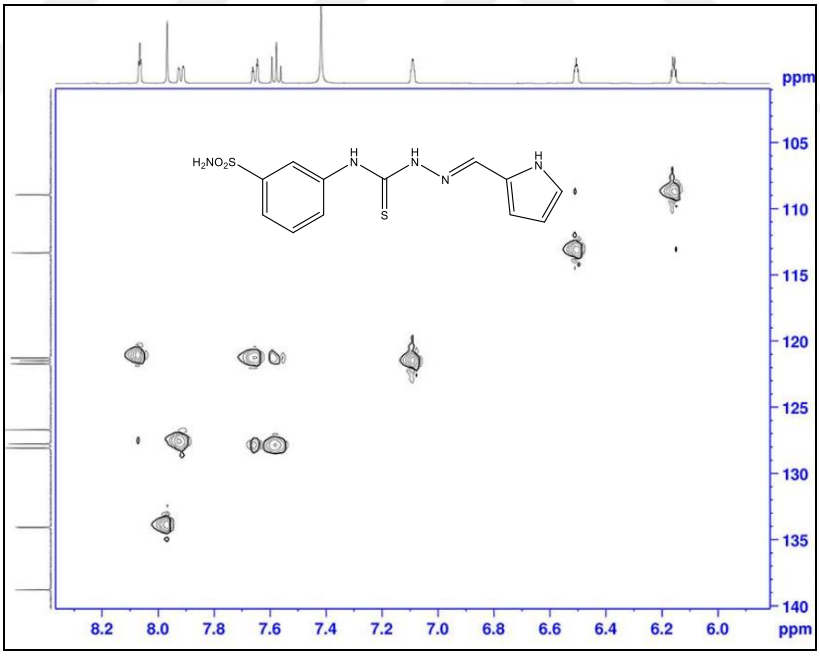

Figure 4-19: HSQC spectrum of compound E3 (6 – 8.2 ppm; 105 – 140 ppm)

LC-MS Spectrum

m/z ESI (negative): 322.0 $(M-H)^-$; $C_{12}H_{13}N_5O_2S_2$ (MA= 323.393; Exact Mass= 323.05)

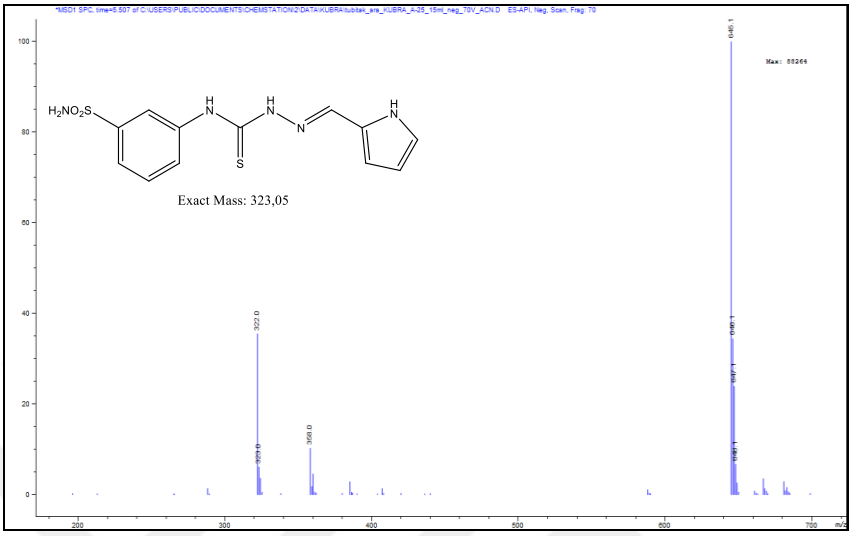

Figure 4-20: Mass spectrum of compound E3

4.3.1.4. (*E*)-2-((1-methyl-1*H*-pyrrol-2-yl)methylene)-*N*-(3-sulfamoylphenyl)hydrazine-1-carbothioamide (E4)

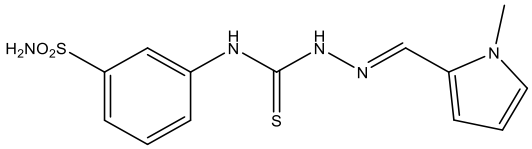

An ethanolic solution of 0.0061 mol (0.61 ml) of 1-methyl-1*H*-pyrrole-2-carbaldehyde (**D4**) is added to an ethanolic solution of 0.0061 mol (1.5 g) of *N*-(3-sulfamoylphenyl)hydrazinecarbothioamide (**C1**). The reaction mixture is heated under reflux for 7 hours. The resulting precipitate is filtered, dried, and purified by recrystallization from ethanol.

Physical appearance	: Yellow powder
Yield (%)	: 91
Retention factor	: 0.63; Chloroform : Methanol (9:1)
Melting point (ºC)	: 201.3 – 202.4

Elemental Analysis

Molecular formula	: $C_{13}H_{15}N_5O_2S_2$
Molecular weight (g/mol)	: 337.420

Element	C	H	N	S
Calculated (%)	46.27	4.48	20.76	19.01
Found (%)	46.07	4.28	20.52	18.78

Spectral Analysis

Fourier Transform Infrared (FT-IR) Spectrum

IR(KBr): υ 3313, 3211 (NH s.b); 3155, 3037, 3001 (Ar.C-H s.b., =CH s.b); 2933 (Al. C-H s.b.); 1616, 1585, 1552, 1527, 1510, 1485 (Ar. C=C s.b, C=N s.b, N-H b.b); 1425, 1364 (Al.C-H b.b.); 1336, 1166 (S=O s.b); 1303 (C-N s.b); 1273 (C=S s.b); 889, 773, 723 (1,3-disubs. Ar-C-H b.b)

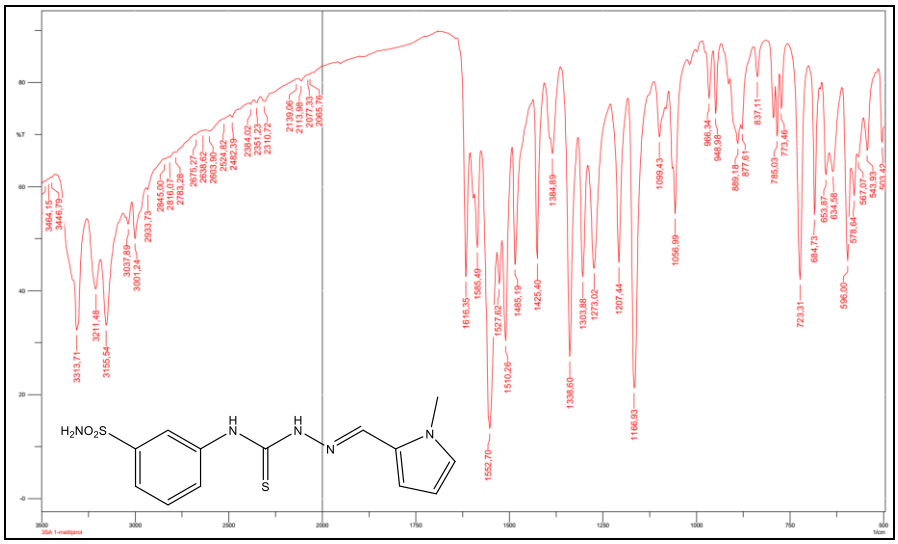

Figure 4-21: IR spectrum of compound E4

^{1}H-NMR Spectrum

^{1}H NMR (DMSO-d_6 / 500 MHz δ (ppm): 3.85 (3H, s, N-CH_3), 6.11 (1H, dd, J=3.9, 2.5 Hz, pyrrole C_4-H), 6.65 (1H, dd, J=3.9, 1.7 Hz, pyrrole C_3-H), 7.00 (1H, t, J=2.2 Hz, pyrrole C_5-H), 7.39 (2H, s, -SO_2NH_2), 7.53 (1H, t, J=7.9 Hz, 3-sulfamoylphenyl C_5-H), 7.62 (1H, dt, J=7.8, 1.8 Hz, 3-sulfamoylphenyl C_4-H), 7.81 (1H, d, J=8.0 Hz, 3-sulfamoylphenyl C_6-H), 8.12 (1H, t, J=2.0 Hz, 3-sulfamoylphenyl C_2-H), 8.15 (1H, s, N=CH), 9.77 (1H, s, tsc N_4-H), 11.68 (tsc N_2-H).

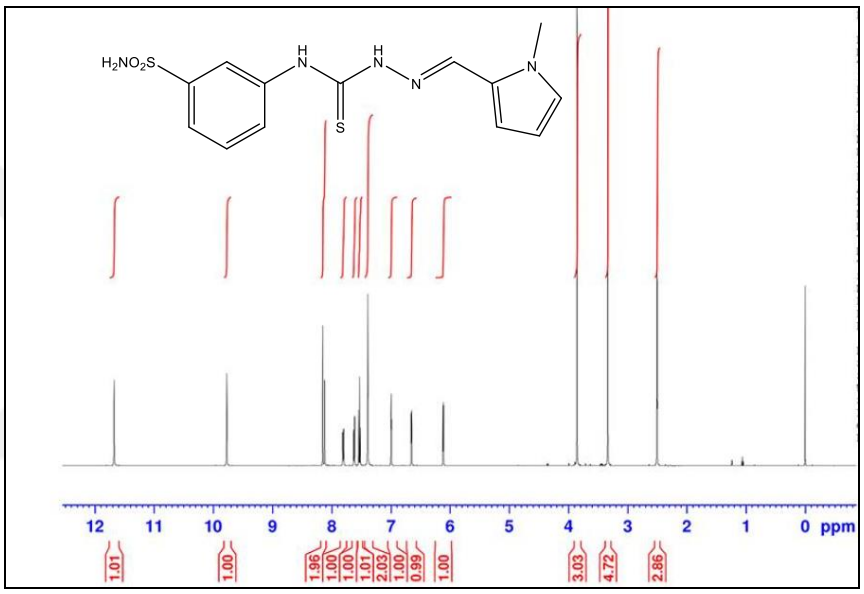

Figure 4-22: ^{1}H-NMR spectrum of compound E4 (0 – 12 ppm)

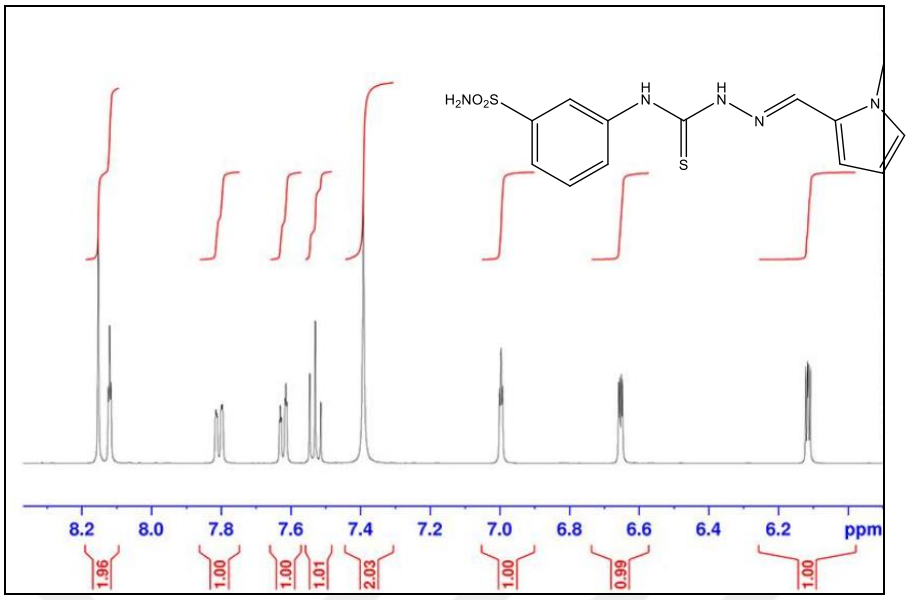

Figure 4-23: ^{1}H-NMR spectrum of compound E4 (6.0 – 8.2 ppm)

LC-MS Spectrum

m/z ESI (negative): 336.0 $(M-H)^-$; $C_{13}H_{15}N_5O_2S_2$ (MA= 337.420; Exact Mass= 337.07)

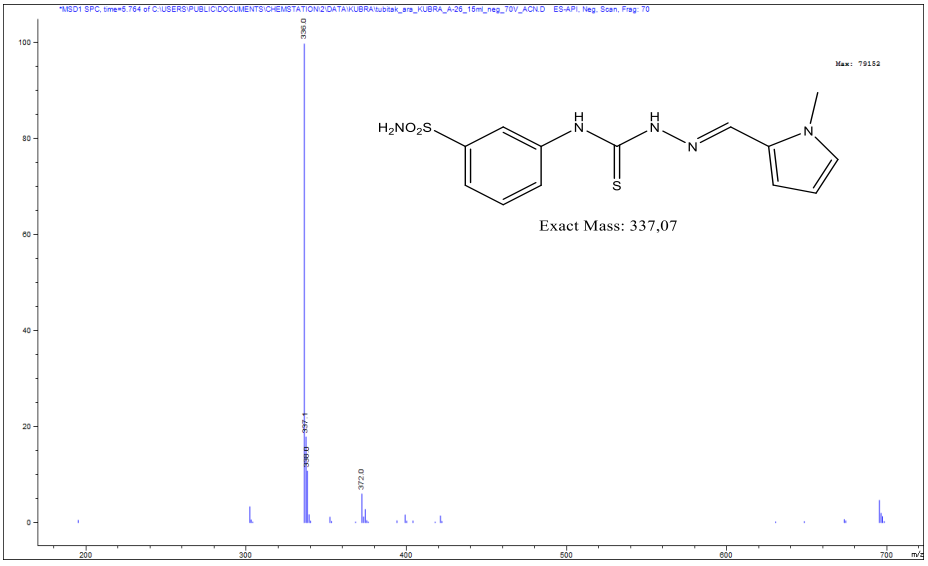

Figure 4-24: Mass spectrum of compound E4

4.3.1.5. (*E*)-2-(furan-2-ylmethylene)-*N*-(3-sulfamoylphenyl)hydrazine-1-carbothioamide (E5)

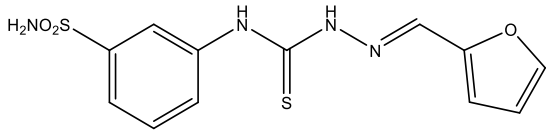

An ethanolic solution of 0.0061 mol (0.5 ml) of furan-2-carbaldehyde (**D5**) is added to an ethanolic solution of 0.0061 mol (1.5 g) of *N*-(3-sulfamoylphenyl)hydrazinecarbothioamide (**C1**). The reaction mixture is heated under reflux for 5 hours. The resulting precipitate is filtered, dried, and purified by recrystallization from ethanol.

Physical appearance	: Yellow powder
Yield (%)	: 63
Retention factor	: 0.46; Chloroform : Methanol (9:1)
Melting point (ºC)	: 201.6-202.5

Elemental Analysis

Molecular formula	: $C_{12}H_{12}N_4O_3S_2$
Molecular weight (g/mol)	: 324.378

Element	C	H	N	S
Calculated (%)	44.43	3.73	17.27	19.77
Found (%)	44.28	3.65	16.92	19.47

Spectral Analysis

Fourier Transform Infrared (FT-IR) Spectrum

IR(KBr): υ 3367, 3292, 3271 (NH s.b); 3147, 3045, 2976 (Ar.C-H s.b., =CH s.b); 1625, 1564, 1541, 1508 (Ar. C=C s.b, C=N s.b, N-H b.b); 1340, 1149 (S=O s.b); 1288 (C-N s.b); 1269 (C=S s.b); 871, 758, 725 (1,3-disubs. Ar-C-H b.b)

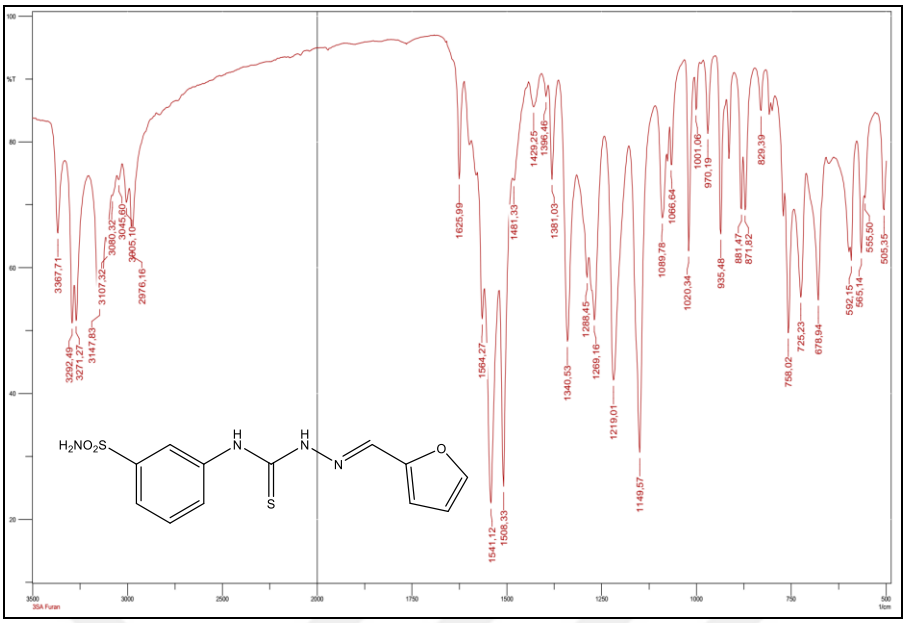

Figure 4-25: IR spectrum of compound E5

^{1}H-NMR Spectrum

^{1}H NMR (DMSO-d_6 / 500 MHz δ (ppm): 6.67 (1H, dd, J=3.5, 1.8 Hz, furan C_4-H), 7.10 (1H, dd, J=3.4, 0.7 Hz, furan C_3-H), 7.40 (2H, s, -SO_2NH_2), 7.54 (1H, t, J=7.9 Hz, 3-sulfamoylphenyl C_5-H), 7.63 (1H, dt, J=7.8, 1.8 Hz, 3-sulfamoylphenyl C_4-H), 7.84 (1H, ddd, J=8.1, 2.3, 1.1 Hz, 3-sulfamoylphenyl C_6-H), 7.87 (1H, dd, J=1.8, 0.7 Hz, furan C_5-H), 8.05-8.12 (2H, m, 3-sulfamoylphenyl C_2-H and N=CH), 10.13 (1H, s, tsc N_4-H), 11.95 (tsc N_2-H).

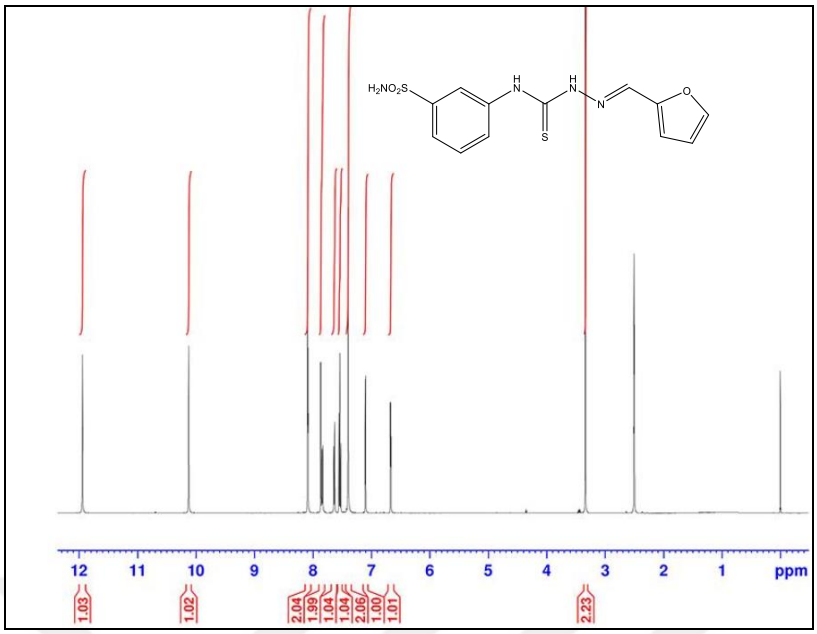

Figure 4-26: ^{1}H-NMR spectrum of compound E5 (0 – 12 ppm)

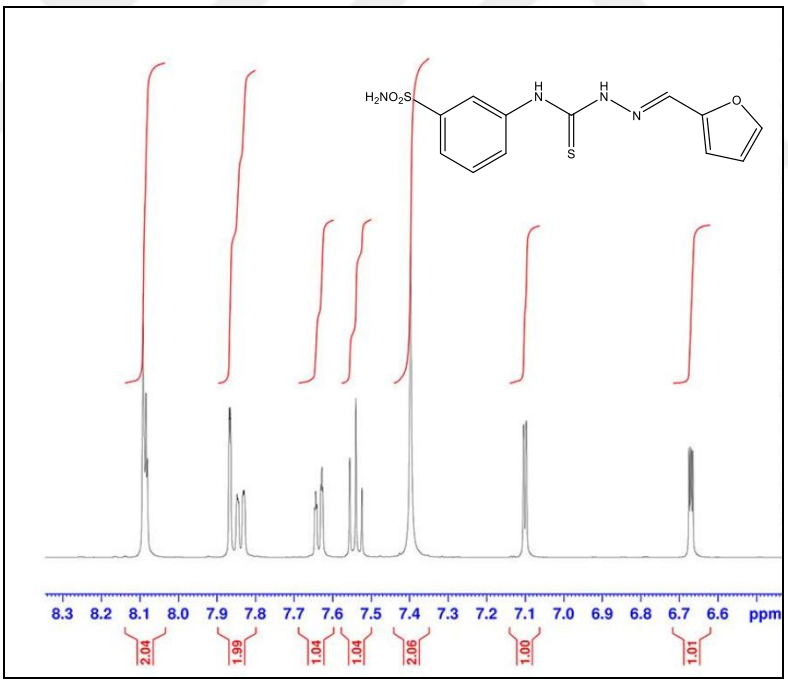

Figure 4-27: ^{1}H-NMR spectrum of compound E5 (6.6 – 8.3 ppm)

^{13}C-NMR Spectrum

^{13}C NMR (decoupled, DMSO-d_6, 125 MHz) δ (ppm): 111.9 (furan C_4), 112.9 (furan C_3), 121.6 (3-sulfamoylphenyl C_4), 121.7 (3-sulfamoylphenyl C_2), 128.0 (3-

sulfamoylphenyl C_5), 128.0 (3-sulfamoylphenyl C_6), 132.7 (N=CH), 138.8 (3-sulfamoylphenyl C_1), 143.4 (3-sulfamoylphenyl C_3), 144.70 (furan C_5), 148.7 (furan C_2), 175.1 (C=S).

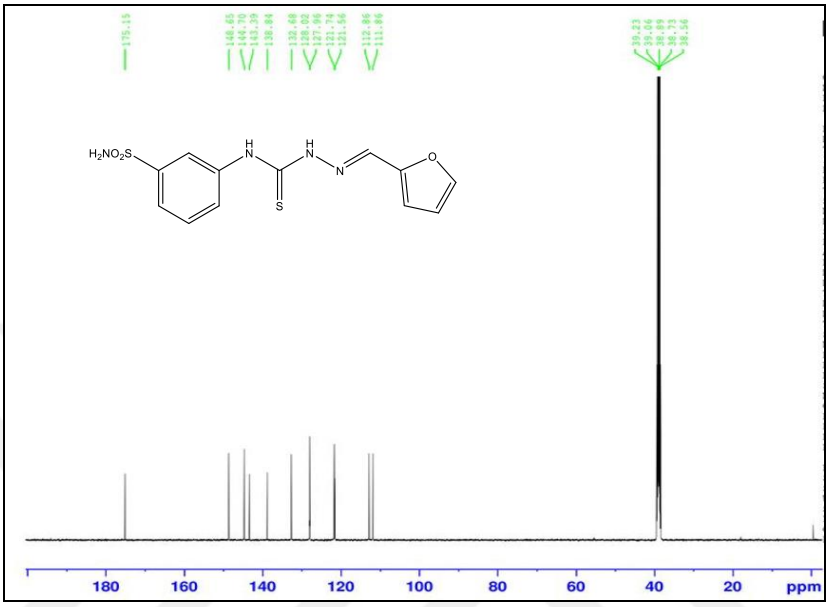

Figure 4-28: ^{13}C-NMR spectrum of compound E5 (0 – 180 ppm)

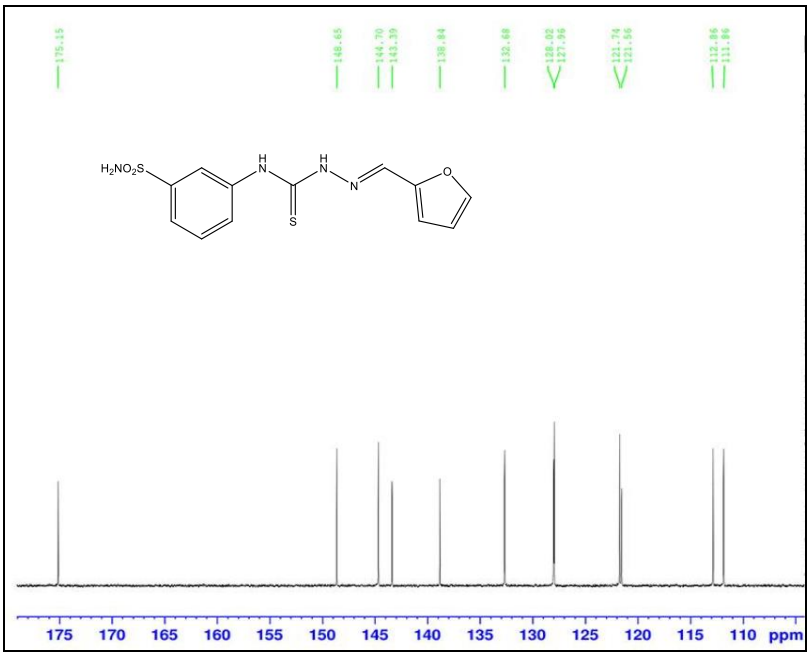

Figure 4-29: ^{13}C-NMR spectrum of compound E5 (110 – 1175 ppm)

^{13}C NMR (HSQC-2D, DMSO-d_6, 125 MHz) δ (ppm): **111.9** [furan C_4 - **6.67** (1H, dd, *J*=3.5, 1.8 Hz, furan C_4-H)], **112.9** [furan C_3 - **7.10** (1H, dd, *J*=3.4, 0.7 Hz, furan C_3-H)], **121.6** [3-sulfamoylphenyl C_4 - **7.63** (1H, dt, *J*=7.8, 1.8 Hz, 3-sulfamoylphenyl C_4-H)], **121.7** [3-sulfamoylphenyl C_2 - **8.05-8.12** (2H, m, 3-sulfamoylphenyl C_2-H and N=CH)], **128.0** [3-sulfamoylphenyl C_5 - **7.54** (1H, t, *J*=7.9 Hz, 3-sulfamoylphenyl C_5-H)], **128.0** [3-sulfamoylphenyl C_6 - **7.84** (1H, ddd, *J*=8.1, 2.3, 1.1 Hz, 3-sulfamoylphenyl C_6-H)], **132.7** [N=CH - **8.05-8.12** (2H, m, 3-sulfamoylphenyl C_2-H and N=CH)], **144.7** [furan C_5 - **7.87** (1H, dd, *J*=1.8, 0.7 Hz, furan C_5-H)].

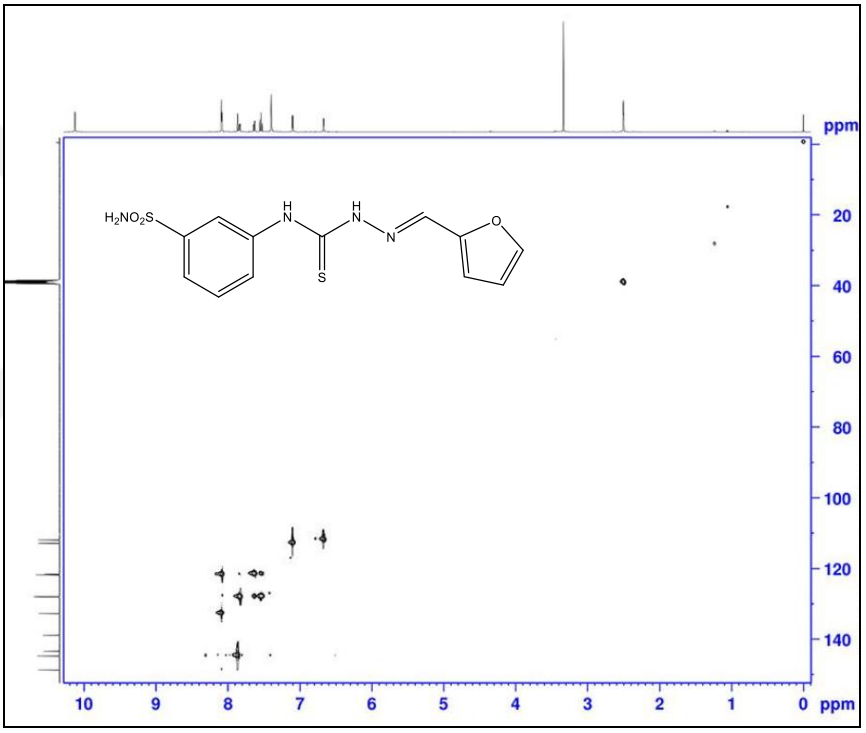

Figure 4-30: HSQC spectrum of compound E5 (0 – 10 ppm; 0 – 140 ppm)

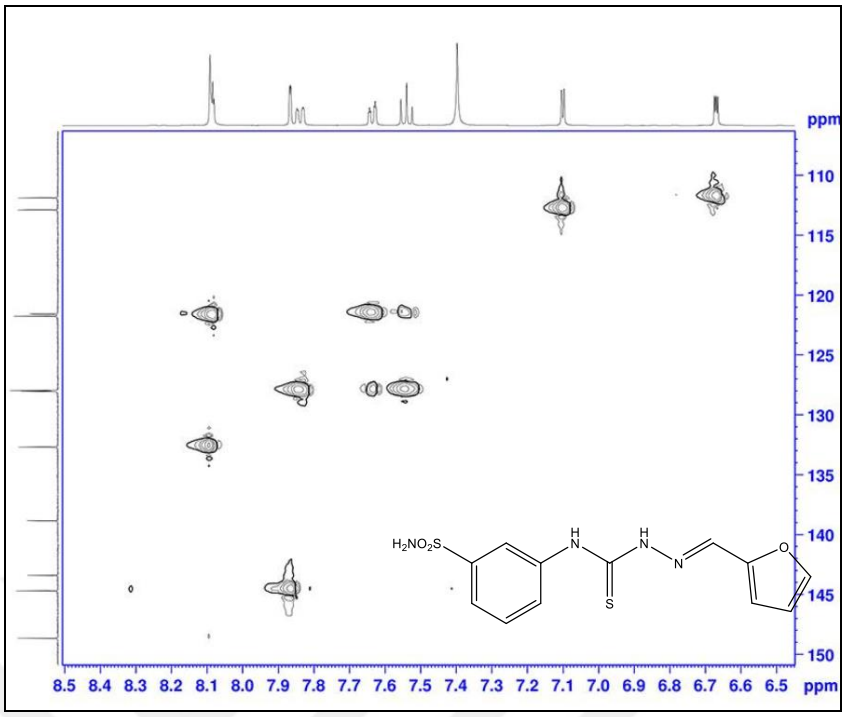

Figure 4-31: HSQC spectrum of compound E5 (6.5 – 8.5 ppm; 110 – 150 ppm)

LC-MS Spectrum

m/z ESI (negative): 323.0 $(M-H)^-$; $C_{12}H_{12}N_4O_3S_2$ (MA= 324.378; Exact Mass= 324.04)

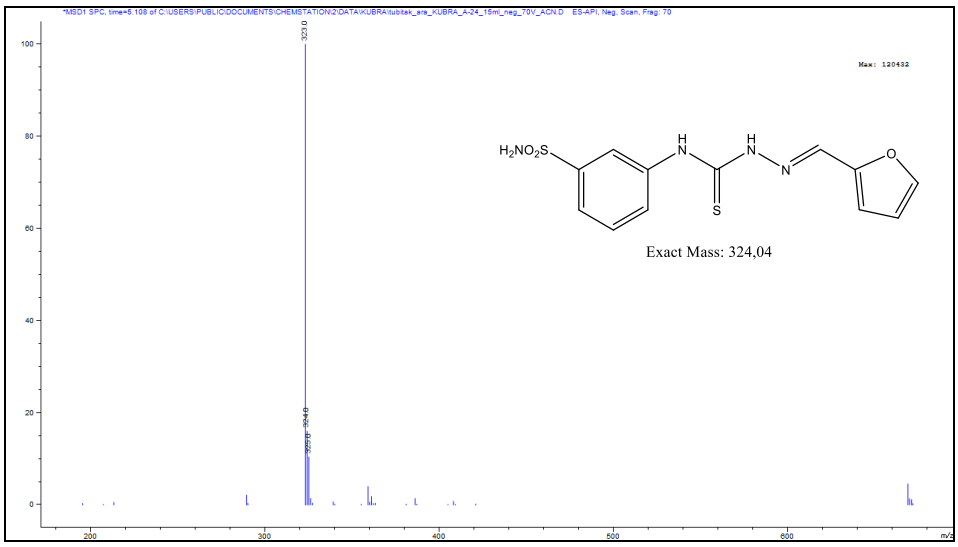

Figure 4-32: Mass spectrum of compound E5

4.3.1.6. (*E*)-2-((1*H*-pyrrol-2-yl)methylene)-*N*-(4-sulfamoylphenyl)hydrazine-1-carbothioamide (E6)

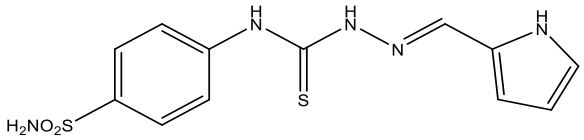

An ethanolic solution of 0.0061 mol (0.57 g) of 1*H*-pyrrole-2-carbaldehyde (**D3**) is added to an ethanolic solution of 0.0061 mol (1.5 g) of *N*-(4-sulfamoylphenyl)hydrazinecarbothioamide (**C2**). The reaction mixture is heated under reflux for 6 hours. The resulting precipitate is filtered, dried, and purified by recrystallization from ethanol.

Physical appearance	: Green powder
Yield (%)	: 82
Retention factor	: 0.54; Chloroform : Methanol (9:1)
Melting point (ºC)	: 228.5-229.0

Elemental Analysis

Molecular formula	: $C_{12}H_{13}N_5O_2S_2$
Molecular weight (g/mol)	: 323.39

Element	C	H	N	S
Calculated (%)	44.57	4.05	21.66	19.83
Found (%)	44.23	3.82	21.36	19.55

Spectral Analysis

Fourier Transform Infrared (FT-IR) Spectrum

IR(KBr): υ 3377, 3284, 3149, 3134 (NH s.b); 3037, 2991 (Ar.C-H s.b., =CH s.b); 1610, 1585, 1537, 1506 (Ar. C=C s.b, C=N s.b, N-H b.b); 1328, 1151 (S=O s.b); 1303 (C-N s.b); 1273 (C=S s.b); 839 (1,4-disubs. Ar-C-H b.b)

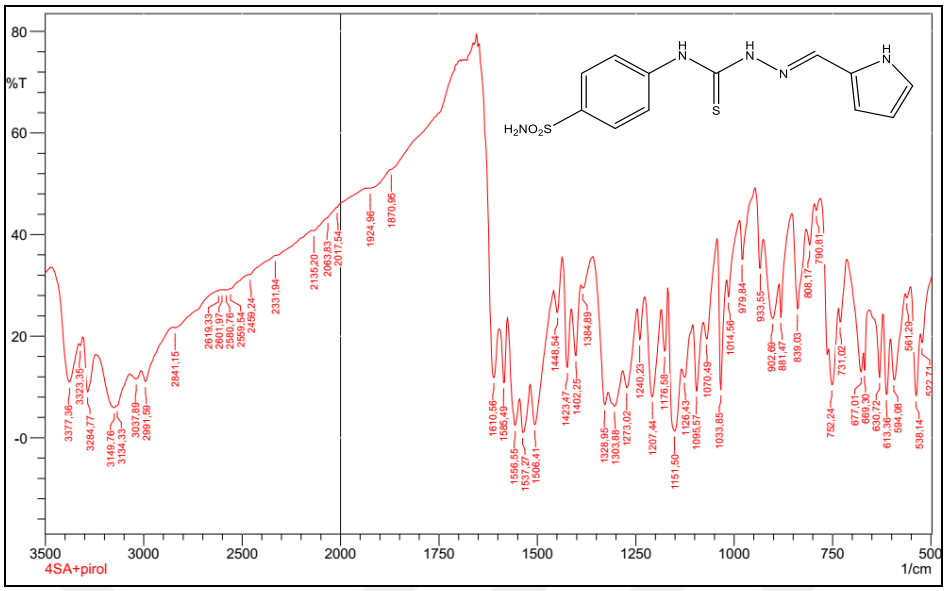

Figure 4-33: IR spectrum of compound E6

^{1}H-NMR Spectrum

^{1}H NMR (DMSO-d_6 / 500 MHz δ (ppm): 6.14-6.17 (1H, m, pyrrole C_4-H), 6.50-6.51 (1H, m, pyrrole C_3-H), 7.09-7.11 (1H, m, pyrrole C_5-H), 7.35 (2H, s, -SO_2NH_2), 7.82 (2H, app.d (AA'BB'), *J*=8.6 Hz, 4-sulfamoylphenyl $C_{2,6}$-H), 7.87 (2H, app.d (AA'BB'), *J*=8.6 Hz, 4-sulfamoylphenyl $C_{3,5}$-H), 7.97 (1H, s, N=CH), 10.21 (1H, s, tsc N_4-H), 11.59 (1H, s, pyrrole NH), 11.91 (tsc N_4-H N_2-H).

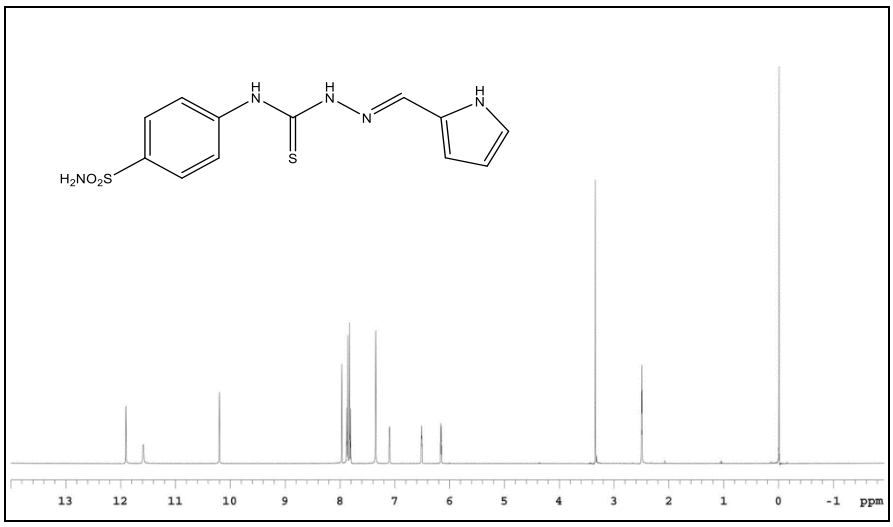

Figure 4-34: ^{1}H-NMR spectrum of compound E6 (0 – 14 ppm)

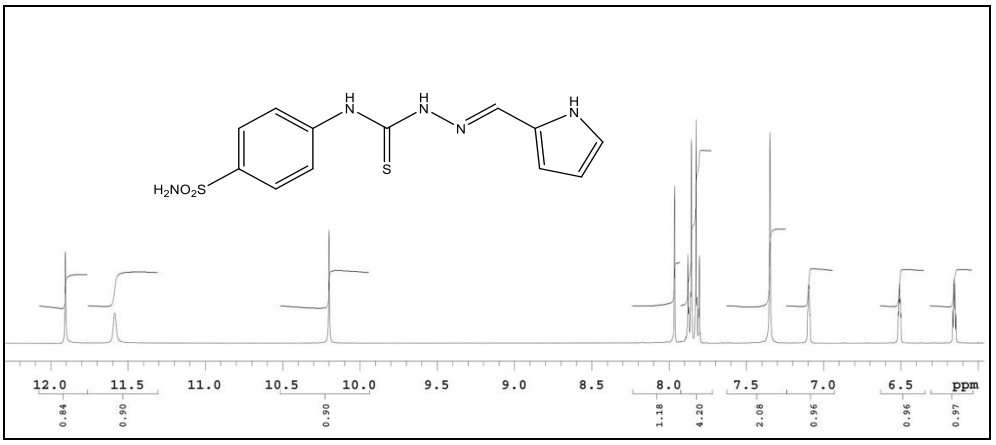

Figure 4-35: ^{1}H-NMR spectrum of E6 compound (6.5 – 12 ppm)

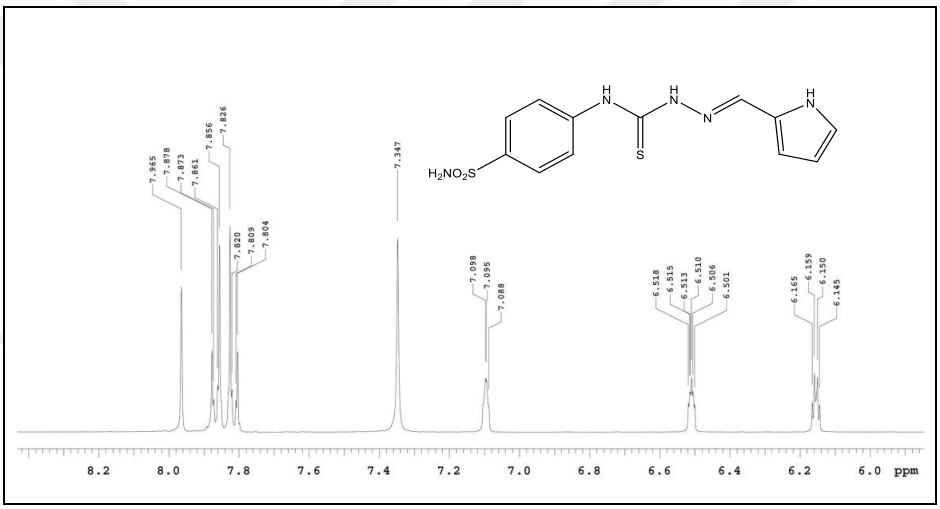

Figure 4-36: ^{1}H-NMR spectrum of compound E6 (6.0 – 8.2 ppm)

LC-MS Spectrum

m/z ESI (negative): 322.0 $(M-H)^-$; $C_{12}H_{13}N_5O_2S_2$ (MA= 323.393; Exact Mass= 323.05)

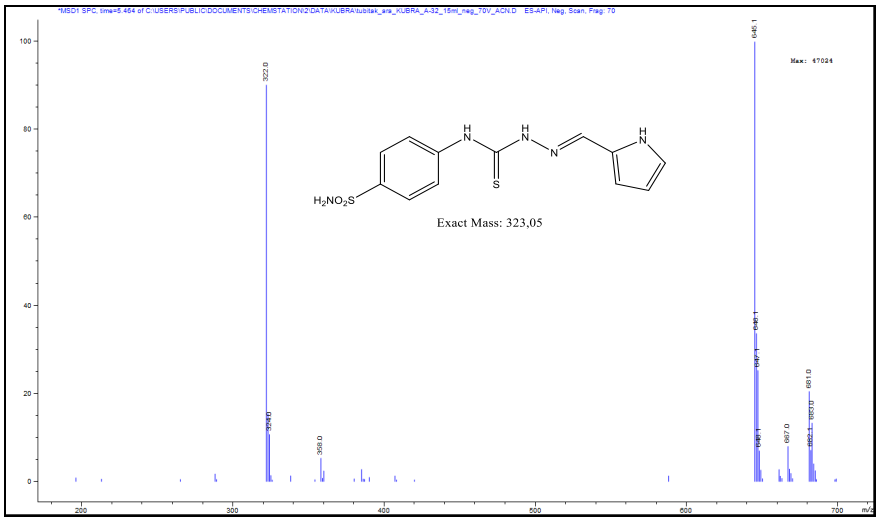

Figure 4-37: Mass spectrum of compound E6

4.3.1.7. (*E*)-2-(furan-2-ylmethylene)-*N*-(4-sulfamoylphenyl)hydrazine-1-carbothioamide (E7)

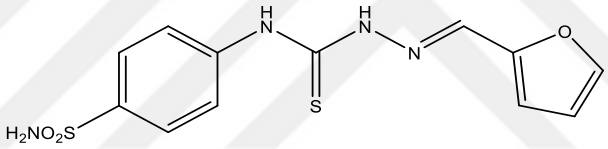

An ethanolic solution of 0.0061 mol (0.5 ml) of furan-2-carbaldehyde (**D5**) is added to an ethanolic solution of 0.0061 mol (1.5 g) of *N*-(4-sulfamoylphenyl)hydrazinecarbothioamide (**C2**). The reaction mixture is heated under reflux for 6 hours. The resulting precipitate is filtered, dried, and purified by recrystallization from ethanol.

Physical appearance	: Yellow powder
Yield (%)	: 83
Retention factor	: 0.46; Chloroform : Methanol (9:1)
Melting point (ºC)	: 214.3-214.9

Elemental Analysis

Molecular formula	: $C_{12}H_{12}N_4O_3S_2$
Molecular weight (g/mol)	: 324.38

Element	C	H	N	S
Calculated (%)	44.43	3.73	17.27	19.77
Found (%)	44.14	3.38	16.96	19.43

Spectral Analysis

Fourier Transform Infrared (FT-IR) Spectrum

IR(KBr): υ 3410, 3251, 3205 (NH s.b); 3140, 3047, 2997 (Ar.C-H s.b., =CH s.b); 1618, 1583, 1556, 1537, 1510 (Ar. C=C s.b, C=N s.b, N-H b.b); 1334, 1153 (S=O s.b); 1307 (C-N s.b); 1271 (C=S s.b); 842 (1,4-disubs. Ar-C-H b.b)

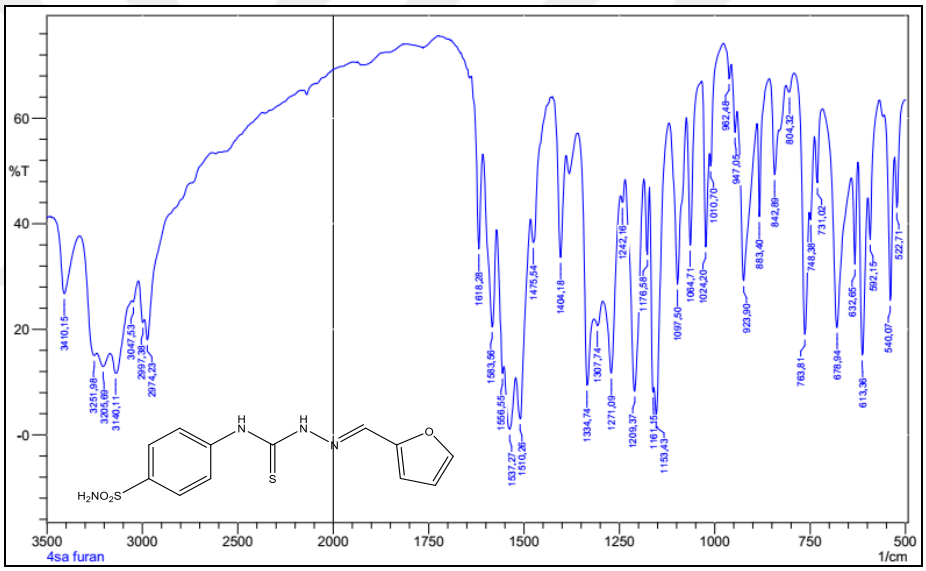

Figure 4-38: IR spectrum of compound E7

^{1}H-NMR Spectrum

^{1}H NMR (DMSO-d_6 / 500 MHz δ (ppm): 6.67 (1H, dd, J=3.5, 1.6 Hz, furan C_4-H), 7.09 (1H, d, J=3.5 Hz, furan C_3-H), 7.34 (2H, s, -SO_2NH_2), 7.77 (2H, app.d (AA'BB'), J=8.6 Hz, 4-sulfamoylphenyl $C_{2,6}$-H), 7.83 (2H, app.d (AA'BB'), J=8.6 Hz, 4-sulfamoylphenyl $C_{3,5}$-H), 7.87 (1H, d, J=1.2 Hz, furan C_5-H), 8.09 (1H, s, N=CH), 10.09 (1H, s, tsc N_4-H), 12.00 (1H, s, tsc N_2-H).

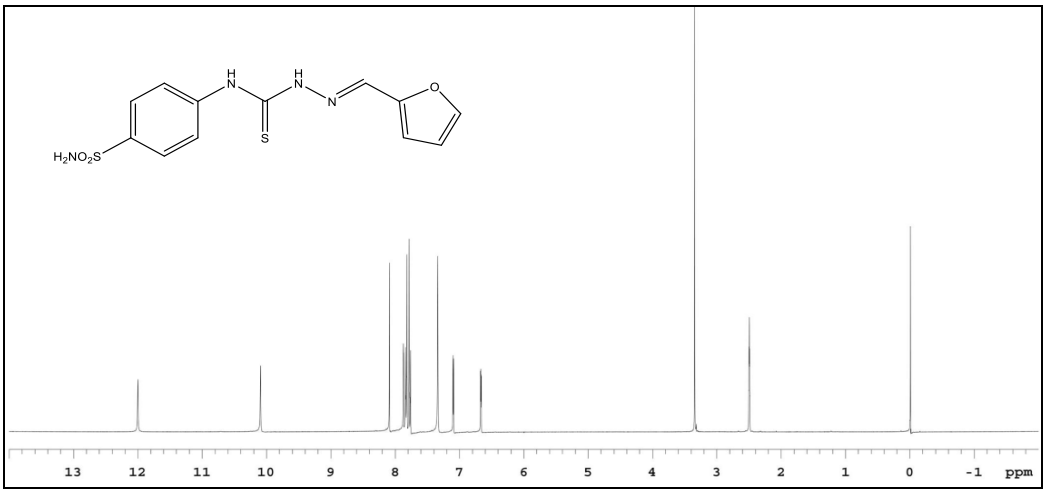

Figure 4-39: ^{1}H-NMR spectrum of compound E7 (0 – 14 ppm)

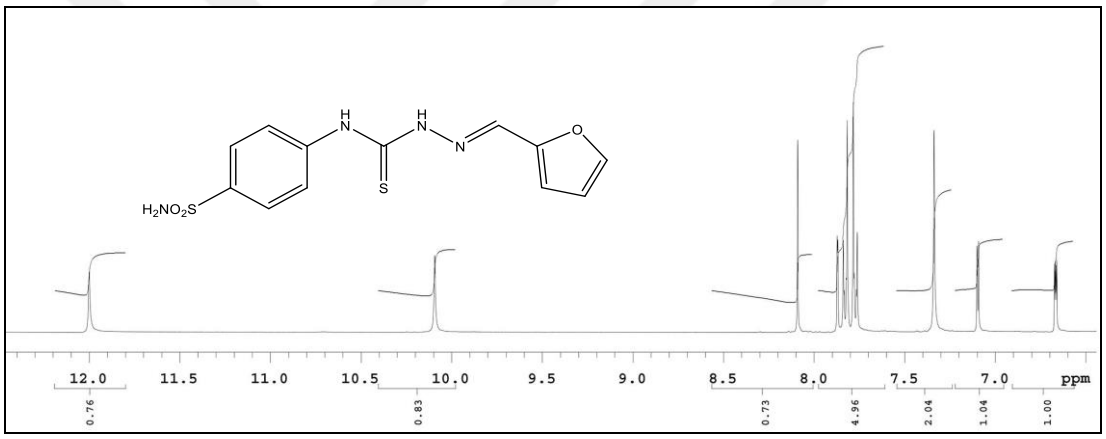

Figure 4-40: ^{1}H-NMR spectrum of compound E7 (6.5 – 12.5 ppm)

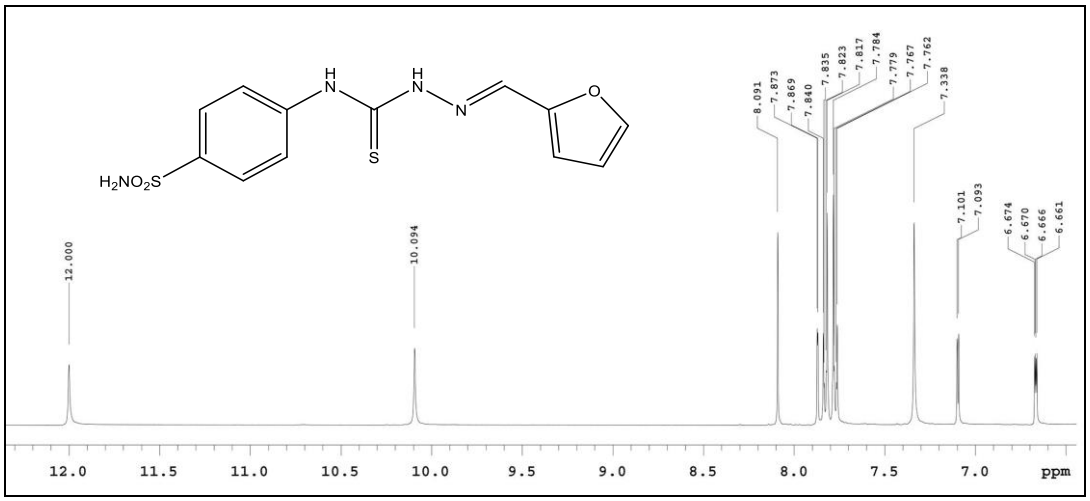

Figure 4-41: ^{1}H-NMR spectrum of compound E7 (6.5 – 12 ppm)

LC-MS Spectrum

m/z ESI (negative): 323.0 $(M-H)^-$; $C_{12}H_{12}N_4O_3S_2$ (MA= 324.378; Exact Mass= 324.04)

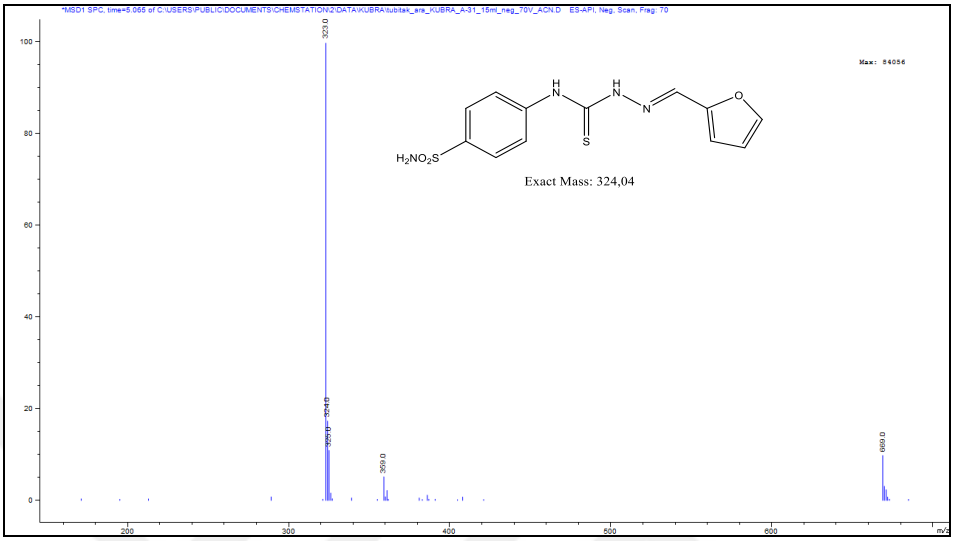

Figure 4-42: Mass spectrum of compound E7

4.3.1.8. 2-(propan-2-ylidene)-*N*-(3-sulfamoylphenyl)hydrazine-1-carbothioamide (E8)

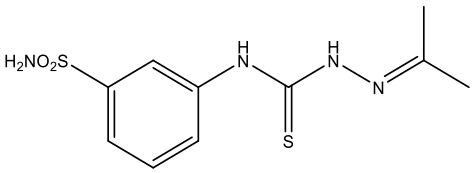

An ethanolic solution of 0.01 mol (0.75 ml) of acetone (**D6**) is added to an ethanolic solution of 0.01 mol (2.5 g) of *N*-(3-sulfamoylphenyl)hydrazinecarbothioamide (**C1**). The reaction mixture is heated under reflux for 4 hours. The reaction mixture was left to precipitate. The resulting precipitate is filtered, dried, and purified by recrystallization from ethanol.

Physical appearance	: White crystals
Yield (%)	: 82
Retention factor	: 0.51; Chloroform : Methanol (9:1)
Melting point (ºC)	: 184.9-187.1

Elemental Analysis

Molecular formula	: $C_{10}H_{14}N_4O_2S_2$
Molecular weight (g/mol)	: 286.373

Element	C	H	N	S
Calculated (%)	41.94	4.93	19.56	22.39
Found (%)	41.70	4.86	19.74	22.06

Spectral Analysis

Fourier Transform Infrared (FT-IR) Spectrum

IR(KBr): υ 3327, 3292 (NH s.b); 3136, 3035 (Ar.C-H s.b., =CH s.b); 2916 (Al.C-H s.b.); 1651, 1600, 1585, 1519, 1483 (Ar. C=C s.b, C=N s.b, N-H b.b); 1435, 1359 (Al.C-H b.b.); 1321, 1151 (S=O s.b); 1305 (C-N s.b); 1259 (C=S s.b); 908, 786, 702 (1,3-disubs. Ar-C-H b.b)

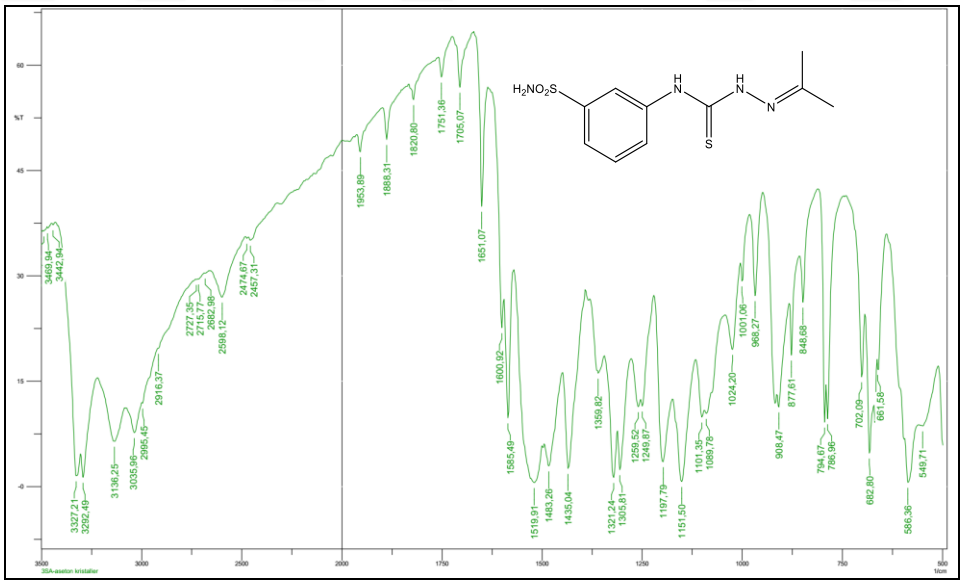

Figure 4-43: IR spectrum of compound E8

^{1}H-NMR Spectrum

^{1}H NMR (DMSO-d_6 / 400 MHz δ (ppm): 1.97 (3H, s, -CH_3), 1.99 (3H, s, -CH_3), 7.35 (2H, s, -SO_2NH_2), 7.49 (1H, t, J=8.2 Hz, 3-sulfamoylphenyl C_5-H), 7.58 (1H, dt, J=8.2, 1.6 Hz, 3-sulfamoylphenyl C_4-H), 7.80 (1H, d, J=7.8 Hz, 3-sulfamoylphenyl C_6-H), 8.08 (1H, t, J=1.6 Hz, 3-sulfamoylphenyl C_2-H), 10.04 (1H, s, tsc N_4-H), 10.46 (tsc N_2-H).

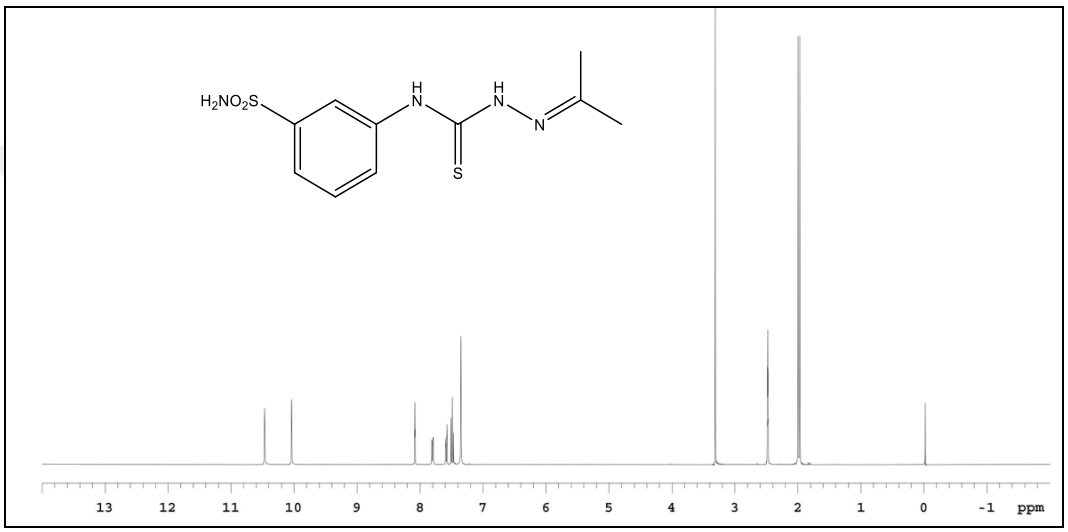

Figure 4-44: ^{1}H-NMR spectrum of E8 (0 – 14 ppm)

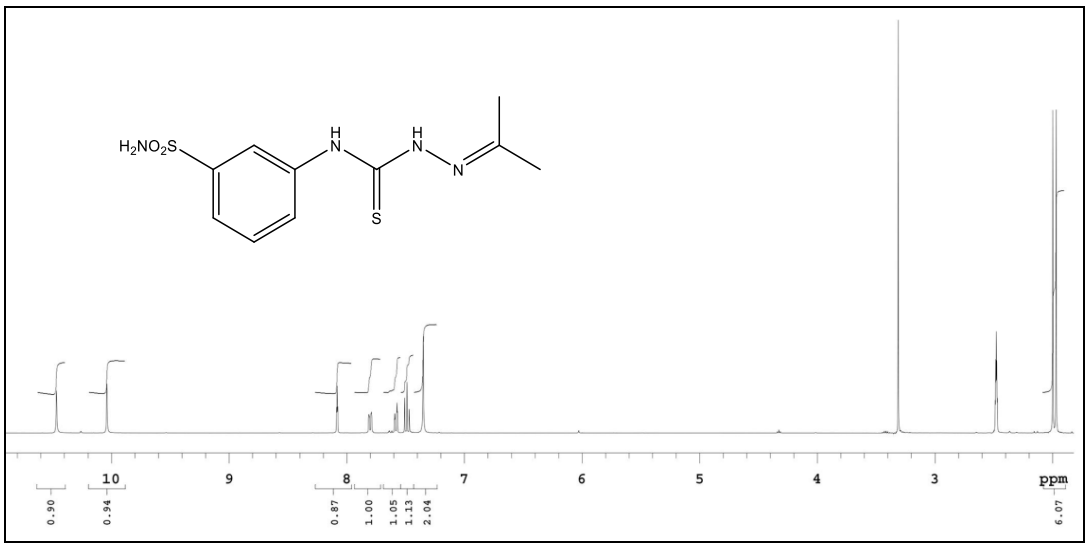

Figure 4-45: ^{1}H-NMR spectrum of compound E8 (1 – 11 ppm)

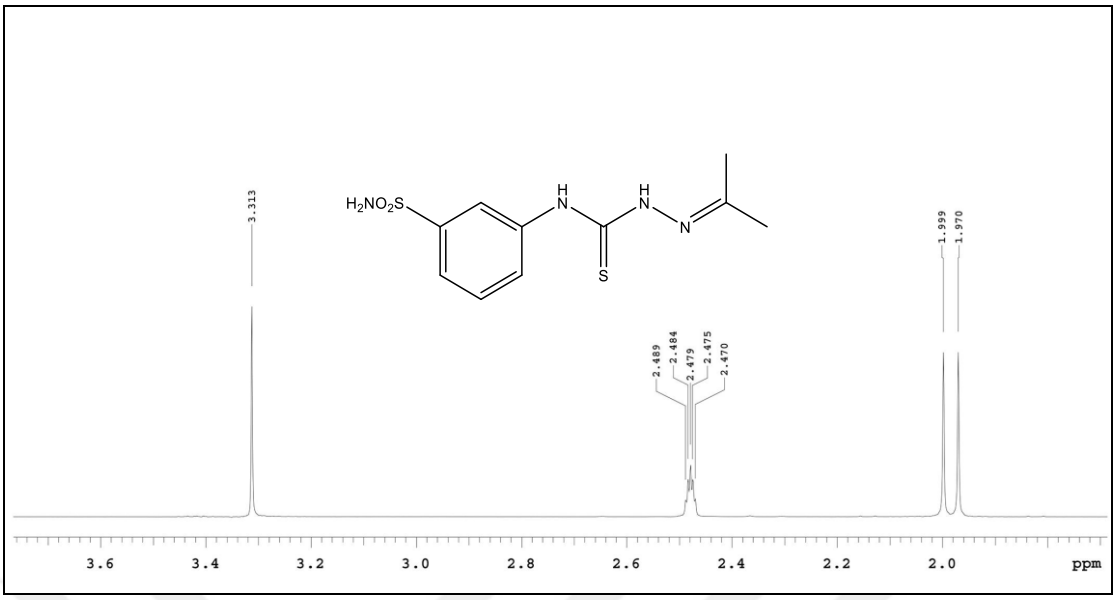

Figure 4-46: ^{1}H-NMR spectrum of compound E8 (2 – 3.6 ppm)

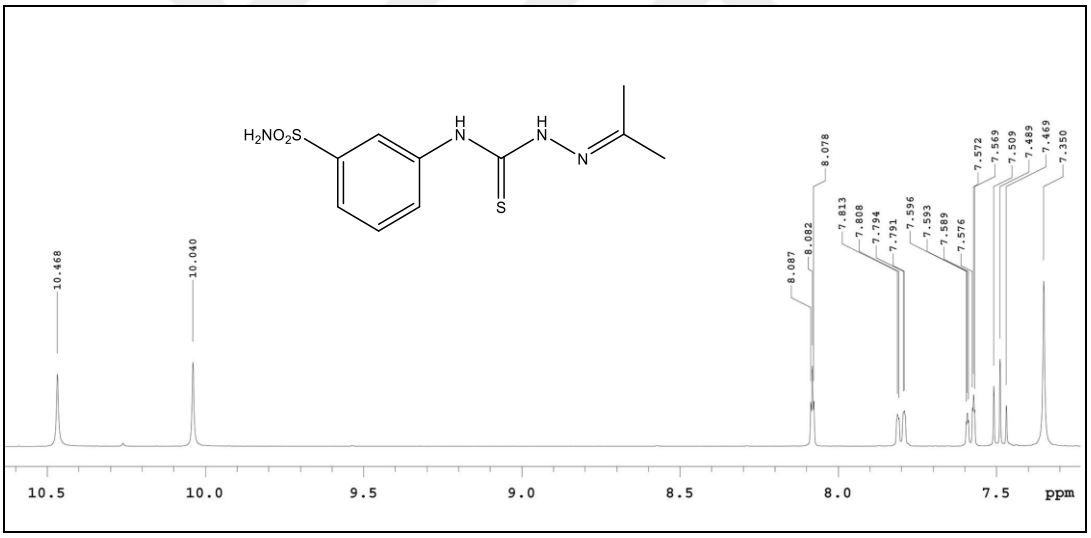

Figure 4-47: ^{1}H-NMR spectrum of compound E8 (7.3 – 10.5 ppm)

^{13}C-NMR Spectrum

^{13}C NMR (decoupled, DMSO-*d*$_6$, 100 MHz) δ (ppm): 17.9 (-CH_3), 24.9 (-CH_3), 121.8 (3-sulfamoylphenyl C_4), 121.9 (3-sulfamoylphenyl C_2), 128.1 (3-sulfamoylphenyl C_6), 128.3 (3-sulfamoylphenyl C_5), 139.5 (3-sulfamoylphenyl C_1), 143.8 (3-sulfamoylphenyl C_3), 153.2 (N=C), 176.4 (C=S).

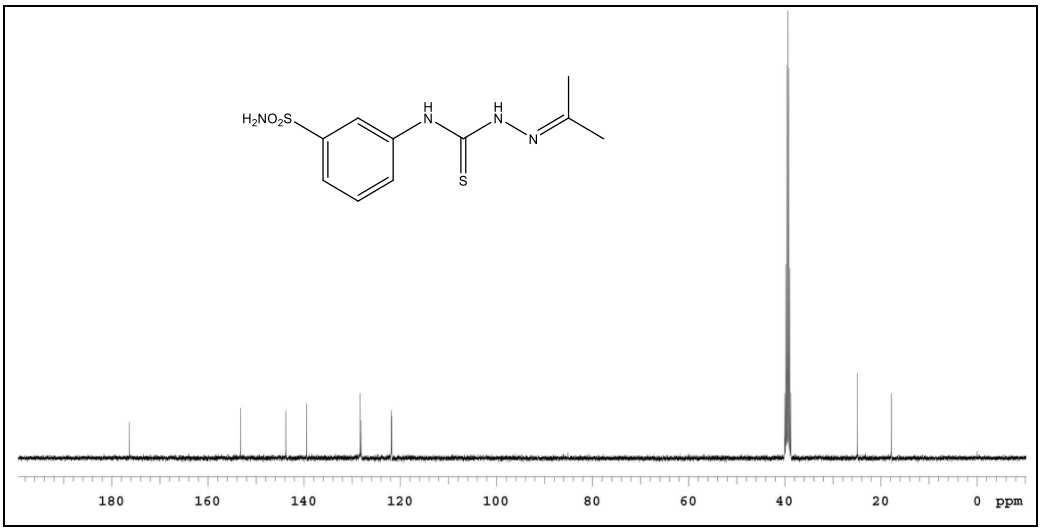

Figure 4-48: ^{13}C-NMR spectrum of compound E8 (0 – 190 ppm)

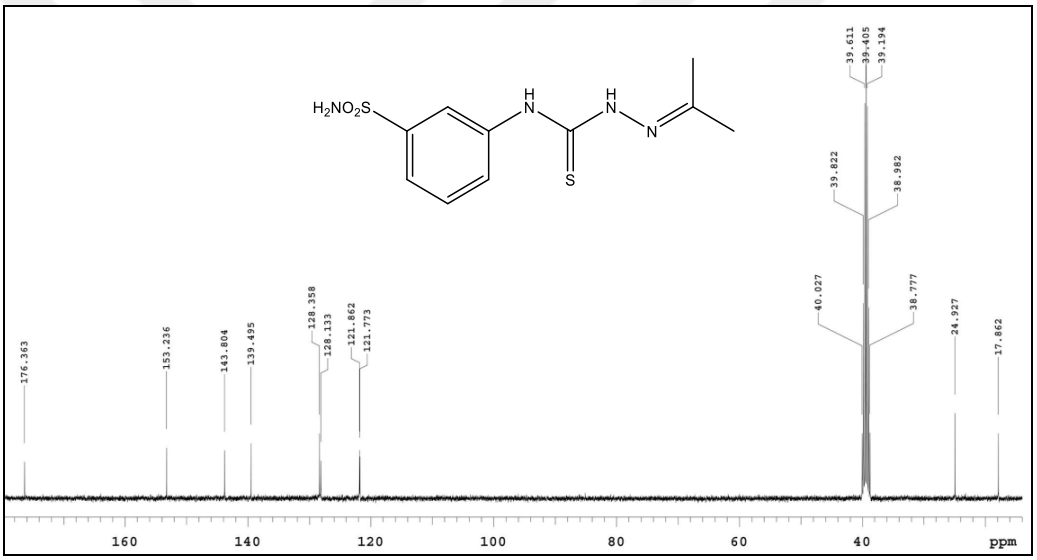

Figure 4-49: ^{13}C-NMR spectrum of compound E8 (17 – 175 ppm)

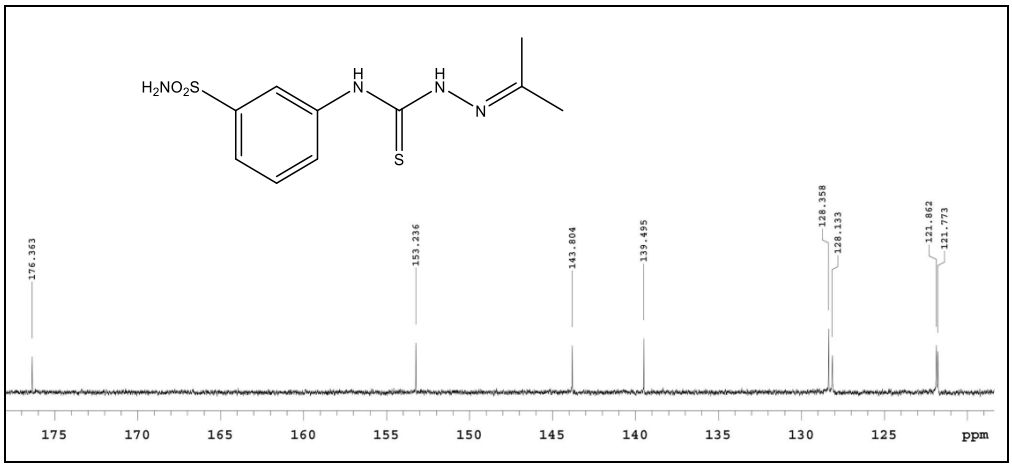

Figure 4-50: ^{13}C-NMR spectrum of compound E8 (120 – 177 ppm)

^{13}C NMR (HSQC-2D, DMSO-*d*$_6$, 100 MHz) δ (ppm): **17.9** [-CH_3 - **1.97** (3H, s, -CH_3)], **24.9** [-CH_3 - 1.99 (3H, s, -CH_3)], **121.8** [3-sulfamoylphenyl C_4 - **7.58** (1H, dt, *J*=8.2, 1.6 Hz, 3-sulfamoylphenyl C_4-H)], **121.9** [3-sulfamoylphenyl C_2 - **8.08** (1H, t, *J*=1.6 Hz, 3-sulfamoylphenyl C_2-H)], **128.1** [3-sulfamoylphenyl C_6 - **7.80** (1H, d, *J*=7.8 Hz, 3-sulfamoylphenyl C_6-H)], **128.3** [3-sulfamoylphenyl C_5 - **7.49** (1H, t, *J*=8.2 Hz, 3-sulfamoylphenyl C_5-H)].

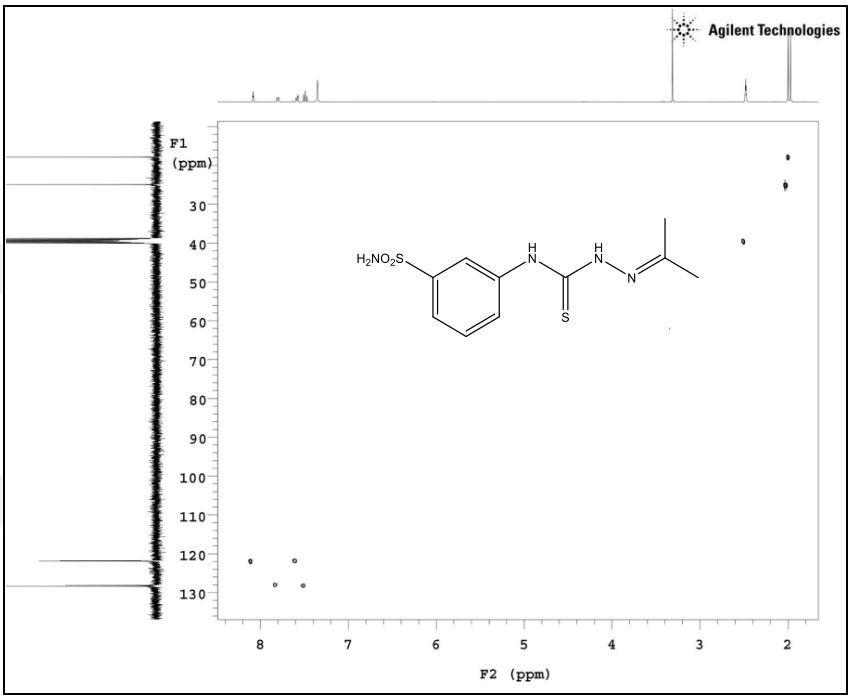

Figure 4-51: HSQC spectrum of compound E8 (1.9 – 8.5 ppm; 0 – 130 ppm)

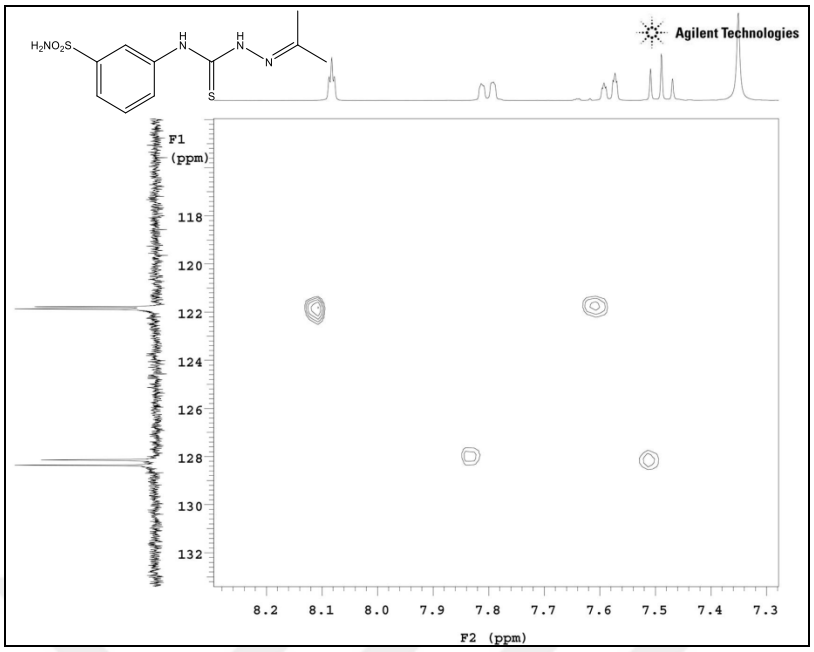

Figure 4-52: HSQC spectrum of compound E8 (7.3 – 8.2 ppm; 114 – 133 ppm)

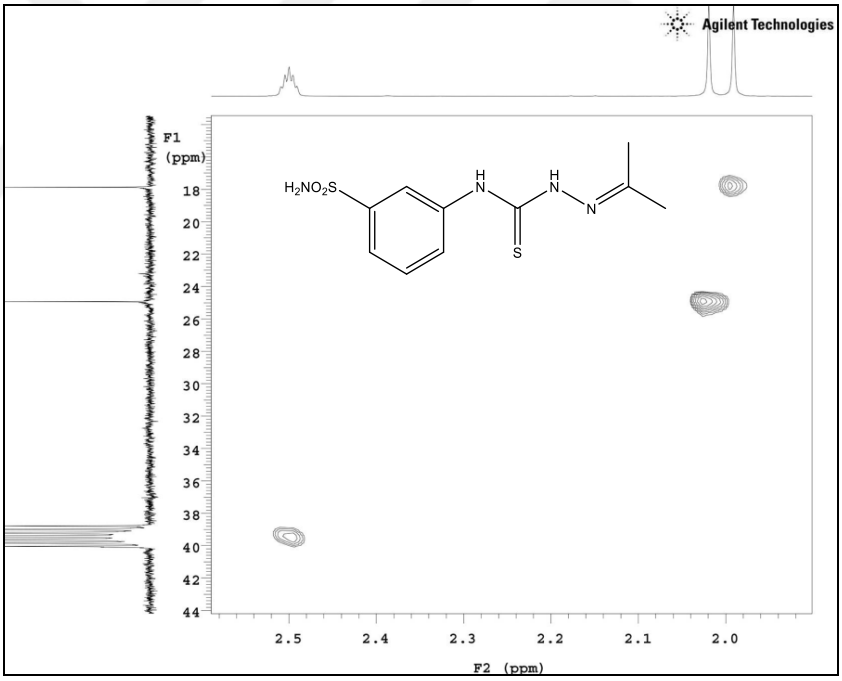

Figure 4-53: HSQC spectrum of compound E8 (1.9 – 2.6 ppm; 0 – 44 ppm)

LC-MS Spectrum

m/z ESI (negative): 285.0 $(M-H)^-$; $C_{10}H_{14}N_4O_2S_2$ (MA= 286.373; Exact Mass= 286.06)

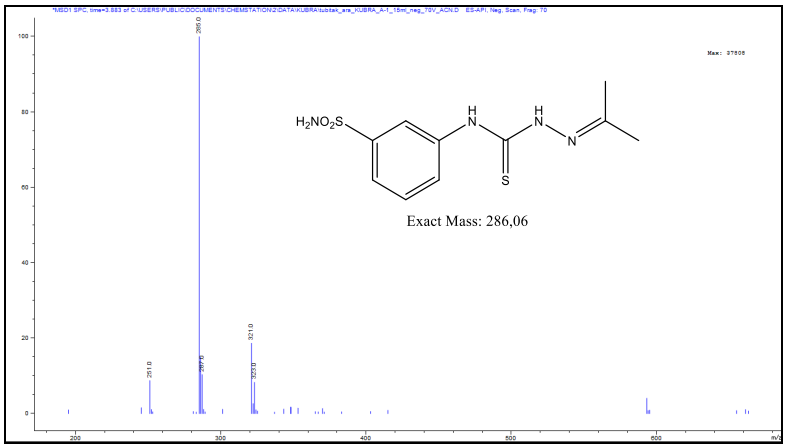

Figure 4-54: Mass spectrum of compound E8

4.3.1.9. 2-(pentan-3-ylidene)-*N*-(3-sulfamoylphenyl)hydrazine-1-carbothioamide (E9)

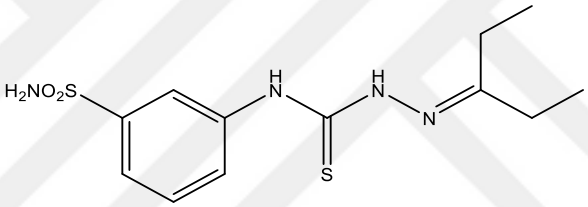

An ethanolic solution of 0.0061 mol (1.1 ml) of 3-pentanone (**D7**) is added to an ethanolic solution of 0.01 mol (2.5 g) of *N*-(3-sulfamoylphenyl)hydrazinecarbothioamide (**C1**). The reaction mixture is heated under reflux for 4 hours. The reaction mixture was left to precipitate. The resulting precipitate is filtered, dried, and purified by recrystallization from ethanol.

Physical appearance	: White powder
Yield (%)	: 50
Retention factor	: 0.52; Chloroform : Methanol (9:1)
Melting point (ºC)	: 171.8 – 172.9

Elemental Analysis

Molecular formula	: $C_{12}H_{18}N_4O_2S_2$
Molecular weight (g/mol)	: 314.426

Element	C	H	N	S
Calculated (%)	45.84	5.77	17.82	20.40
Found (%)	45.58	5.75	17.74	20.12

Spectral Analysis

Fourier Transform Infrared (FT-IR) Spectrum

IR(KBr): υ 3344, 3275, 3248 (NH s.b); 3089, 3062, 3045 (Ar.C-H s.b., =CH s.b); 2974, 2935, 2887, 2831 (Al. C-H s.b.); 1598, 1587, 1487 (Ar. C=C s.b, C=N s.b, N-H b.b); 1463, 1379 (Al. C-H b.b.); 1321, 1163 (S=O s.b); 1307 (C-N s.b); 1263 (C=S s.b); 900, 761, 702 (1,3-disubs. Ar-C-H b.b)

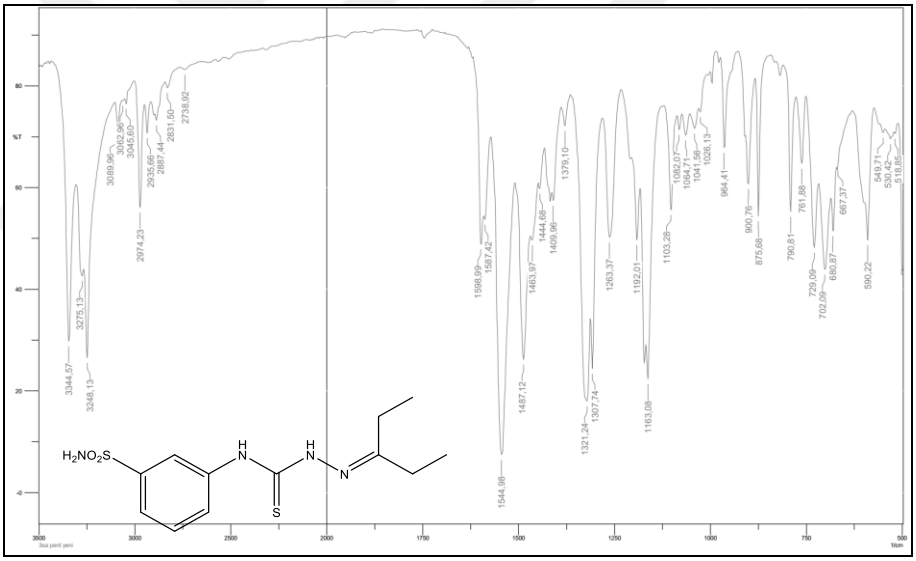

Figure 4-55: IR spectrum of compound E9

^{1}H-NMR Spectrum

^{1}H NMR (Aseton-d_6 / 500 MHz δ (ppm): 1.12-1.19 (6H, m, 2 x CH_3), 2.41 (2H, q, J=7.4 Hz, -**CH**$_2$$CH_3$), 2.56 (2H, q, J=7.6 Hz, -**CH**$_2$$CH_3$), 7.34 (2H, s, -$SO_2NH_2$), 7.52 (1H, t, J=8.0 Hz, 3-sulfamoylphenyl C_5-H), 7.69 (1H, dt, J=7.9, 1.8 Hz, 3-sulfamoylphenyl C_4-H), 7.99 (1H, ddd, J=8.0, 2.3, 1.1 Hz, 3-sulfamoylphenyl C_6-H), 8.27 (1H, t, J=2.0 Hz, 3-sulfamoylphenyl C_2-H), 9.48 (1H, s, tsc N_4-H), 9.95 (tsc N_2-H).

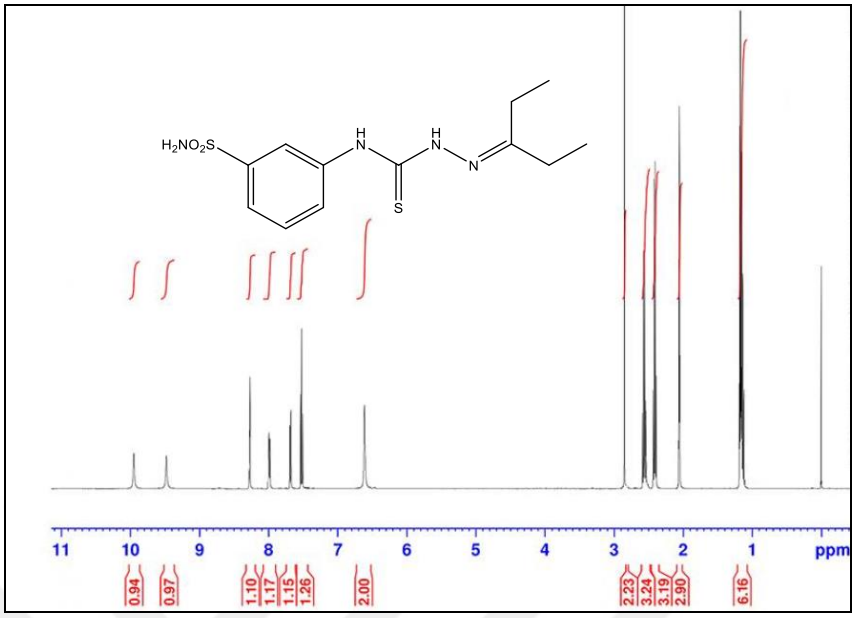

Figure 4-56: ^{1}H-NMR spectrum of compound E9 (0 – 11 ppm)

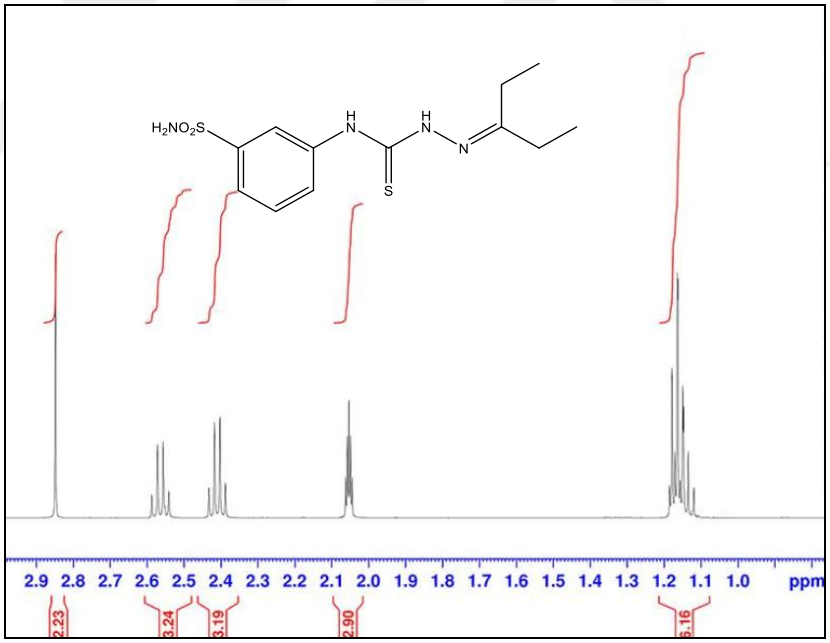

Figure 4-57: ^{1}H-NMR spectrum of compound E9 (0 – 2.9 ppm)

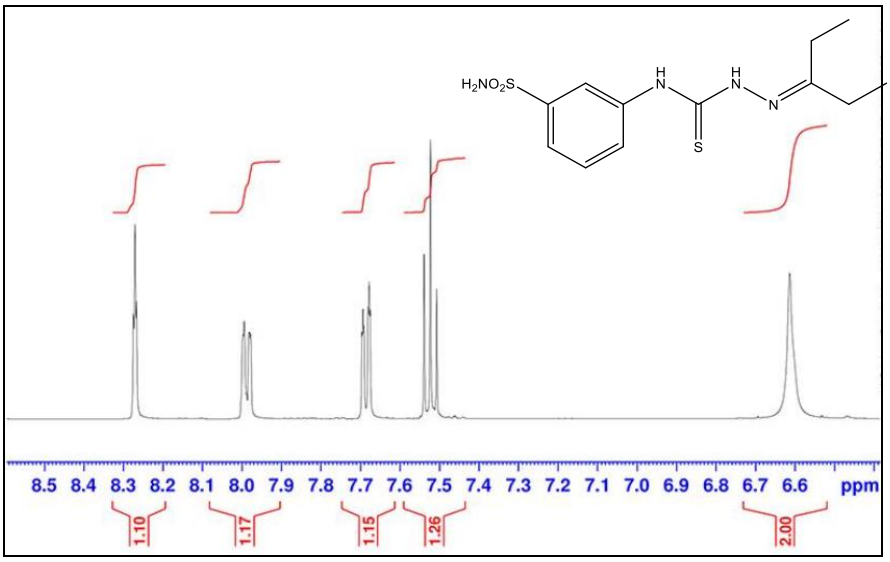

Figure 4-58: ^{1}H-NMR spectrum of compound E9 (6.6 – 8.5 ppm)

LC-MS Spectrum

m/z ESI (negative): 313.1 $(M-H)^-$; $C_{12}H_{18}N_4O_2S_2$ (MA= 314.426; Exact Mass= 314.09)

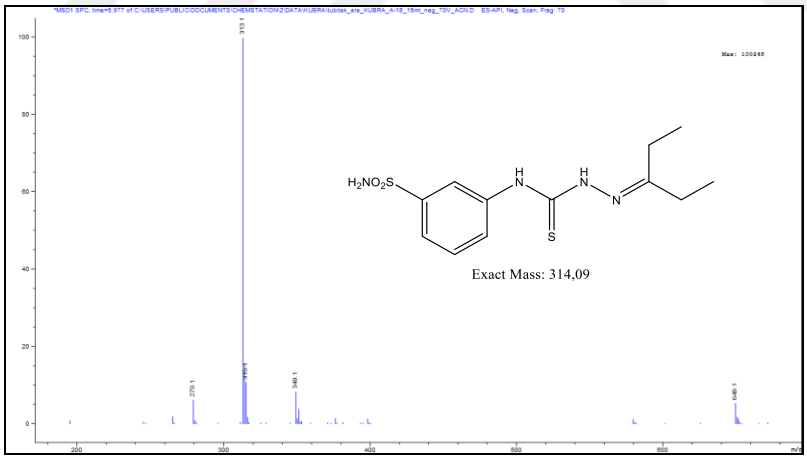

Figure 4-59: Mass spectrum of compound E9

4.3.1.10. 2-(propan-2-ylidene)-*N*-(4-sulfamoylphenyl)hydrazine-1-carbothioamide (E10)

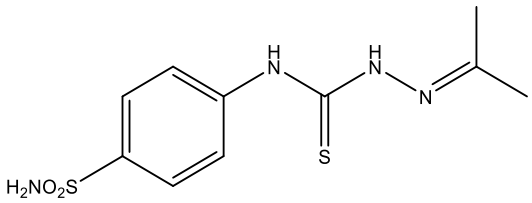

An ethanolic solution of 0.01 mol (0.75 ml) of acetone (**D6**) is added to an ethanolic solution of 0.01 mol (2.5 g) of *N*-(4-sulfamoylphenyl)hydrazinecarbothioamide (**C2**). The reaction mixture is heated under reflux for 4 hours. The reaction mixture was left to precipitate. The resulting precipitate is filtered, dried, and purified by recrystallization from ethanol.

Physical appearance	: White crystals
Yield (%)	: 78
Retention factor	: 0.48; Chloroform : Methanol (9:1)
Melting point (ºC)	: 178.0 – 178.8

Elemental Analysis

Molecular formula	: $C_{10}H_{14}N_4O_2S_2$
Molecular weight (g/mol)	: 286.373

Element	C	H	N	S
Calculated (%)	41.94	4.93	19.56	22.39
Found (%)	41.84	4.97	19.41	22.25

Spectral Analysis

Fourier Transform Infrared (FT-IR) Spectrum

IR(KBr): υ 3344, 3238, 3209 (NH s.b); 3084 (Ar.C-H s.b., =CH s.b); 2960, 2931 (Al. C-H s.b.); 1587, 1541, 1487 (Ar. C=C s.b, C=N s.b, N-H b.b); 1444, 1384 (Al. C-H b.b.); 1334, 1153 (S=O s.b); 1307 (C-N s.b); 1273 (C=S s.b); 844 (1,4-disubs. Ar-C-H b.b)

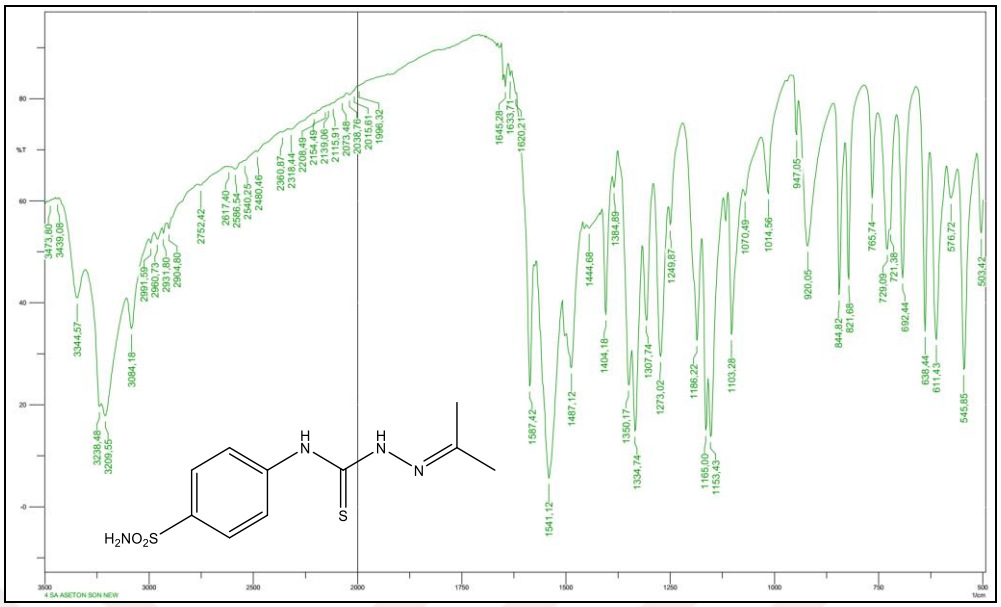

Figure 4-60: IR spectrum of compound E10

^{1}H-NMR Spectrum

^{1}H NMR (DMSO-*d*$_6$ / 400 MHz δ (ppm): 1.97, 2.00 (6H, 2s, -CH_3), 7.28 (2H, s, -SO_2NH_2), 7.73 (2H, app.d (AA'BB'), *J*=8.7 Hz, 4-sulfamoylphenyl $C_{3,5}$-H), 7.83 (2H, app.d (AA'BB'), *J*=8.7 Hz, 4-sulfamoylphenyl $C_{2,6}$-H), 10.02 (1H, s, tsc N_4-H), 10.52 (tsc N_2-H).

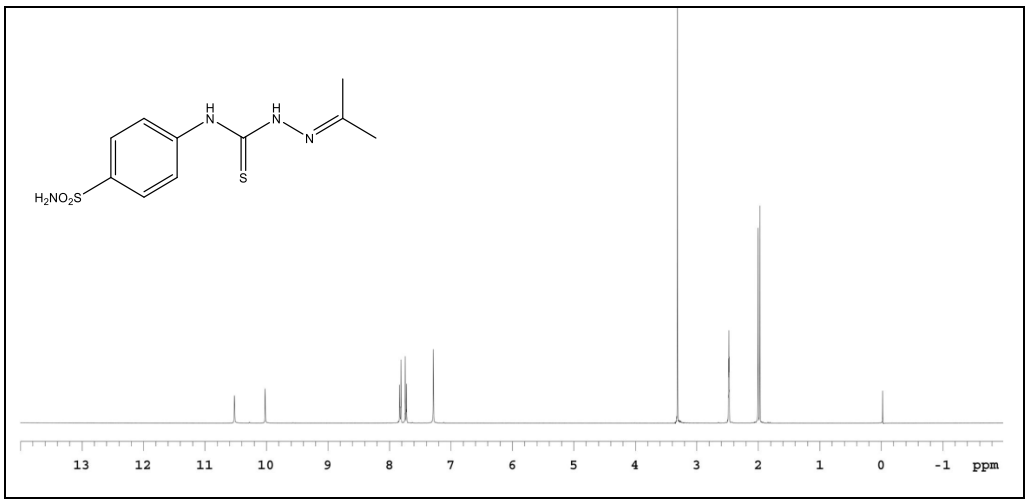

Figure 4-61: ^{1}H-NMR spectrum of compound E10 (0 – 14 ppm)

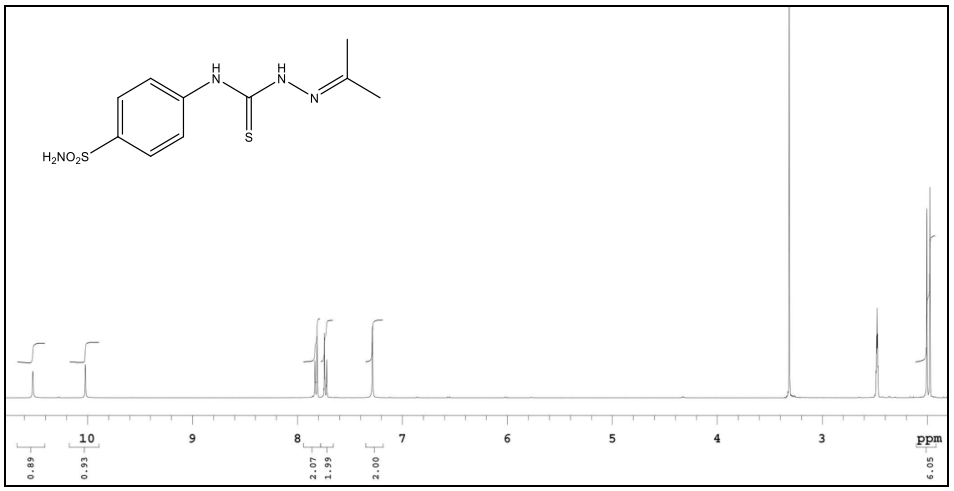

Figure 4-62: ^{1}H-NMR spectrum of compound E10 (0 – 10.6 ppm)

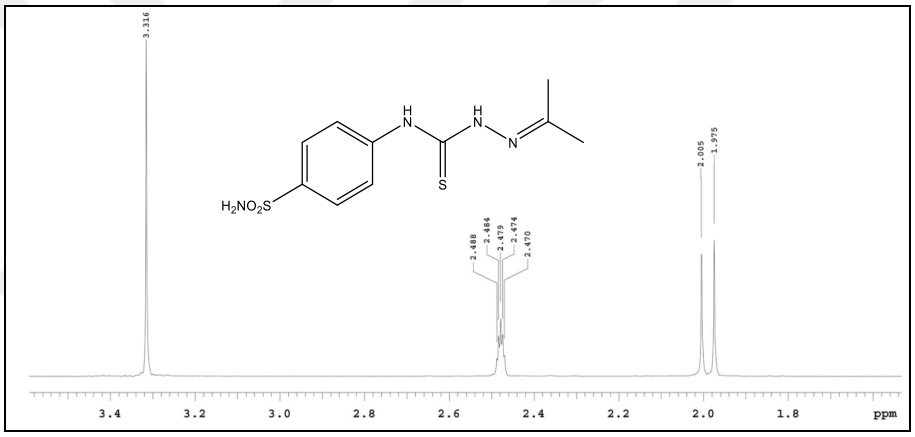

Figure 4-63: ^{1}H-NMR spectrum of compound E10 (0 – 3.4 ppm)

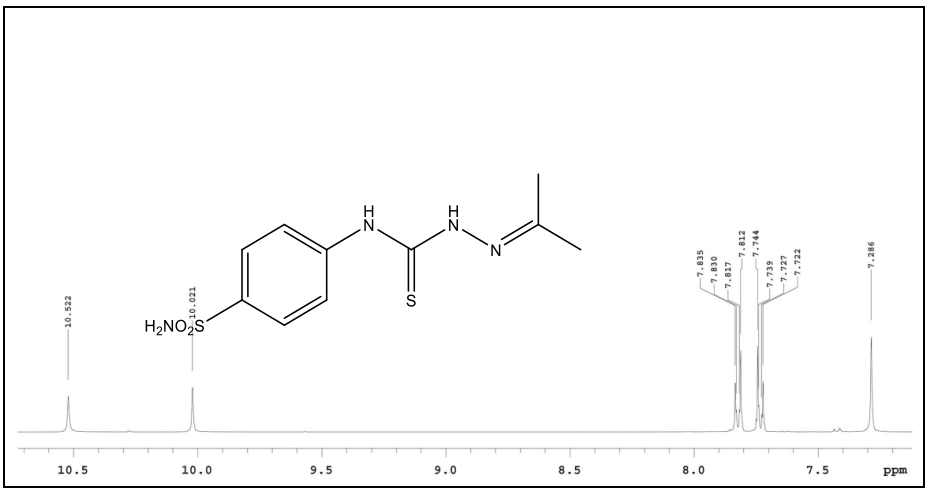

Figure 4-64: ^{1}H-NMR spectrum of E9 (7.4 – 10.6 ppm)

^{13}C-NMR Spectrum

^{13}C NMR (decoupled, DMSO-*d*$_6$, 100 MHz) δ (ppm): 18.0, 25.0 (2 x CH_3), 124.3 (4-sulfamoylphenyl $C_{2,6}$), 125.6 (4-sulfamoylphenyl $C_{3,5}$), 139.7 (4-sulfamoylphenyl C_4), 142.1 (4-sulfamoylphenyl C_1), 153.7 (N=C), 176.1 (C=S).

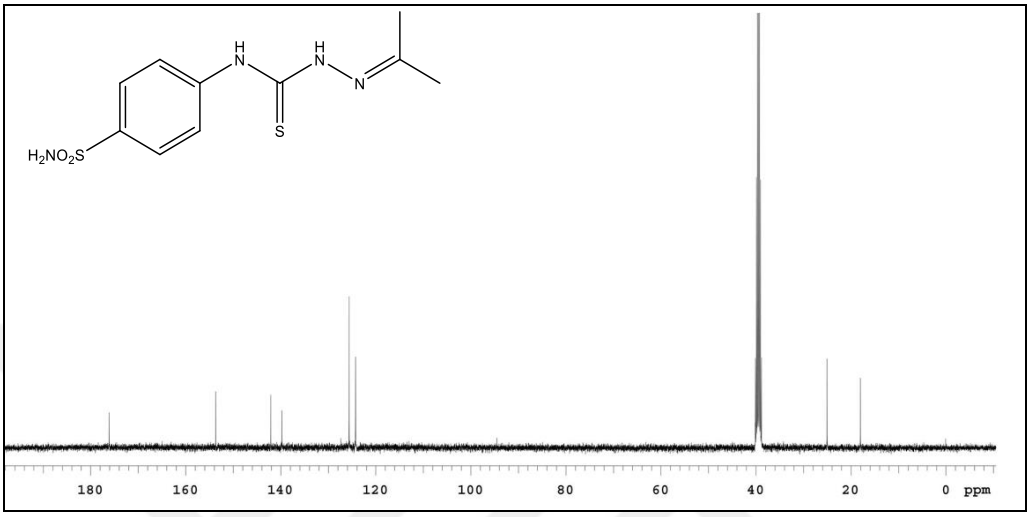

Figure 4-65: ^{13}C-NMR spectrum of compound E10 (0 – 200 ppm)

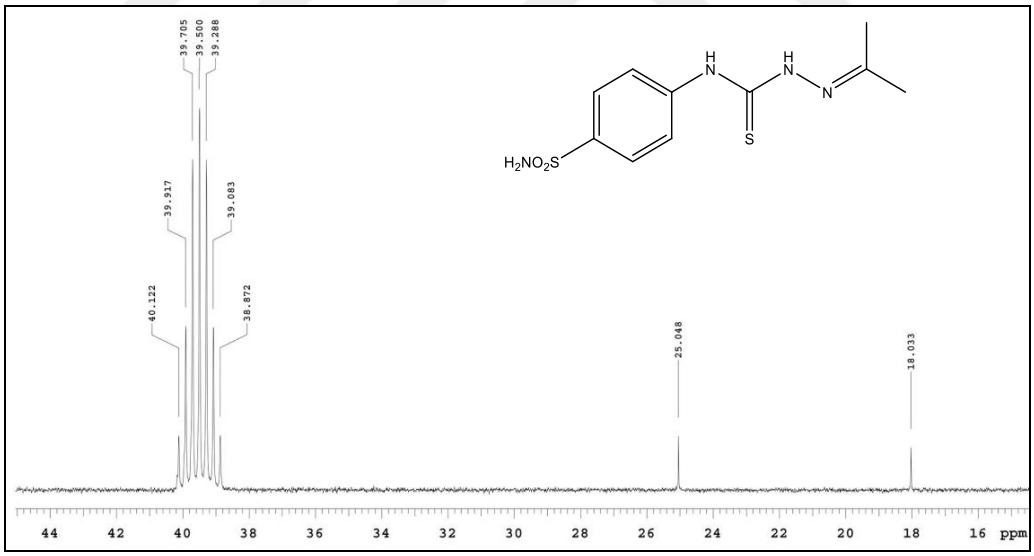

Figure 4-66: ^{13}C-NMR spectrum of compound E10 (16 – 44 ppm)

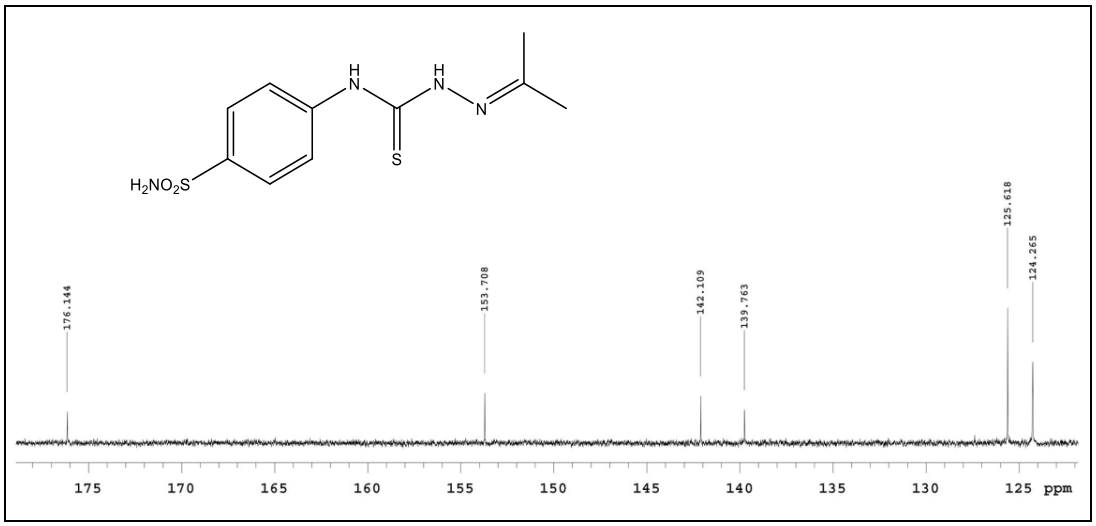

Figure 4-67: ^{13}C-NMR spectrum of compound E10 (123 – 177 ppm)

^{13}C NMR (HSQC-2D, DMSO-*d*$_6$, 100 MHz) δ (ppm): **18.0**, **25.0** [-CH_3 - **1.97**, **2.00** (6H, 2s, -CH_3)], **124.3** [4-sulfamoylphenyl $C_{2,6}$ - **7.83** (2H, AA'BB', *J*=8.7, 2.3, 1.9 Hz, 4-sulfamoylphenyl $C_{2,6}$-H)], **125.6** [4-sulfamoylphenyl $C_{3,5}$ - **7.73** (2H, AA'BB', *J*=8.7, 2.3, 1.9 Hz, 4-sulfamoylphenyl $C_{3,5}$-H)].

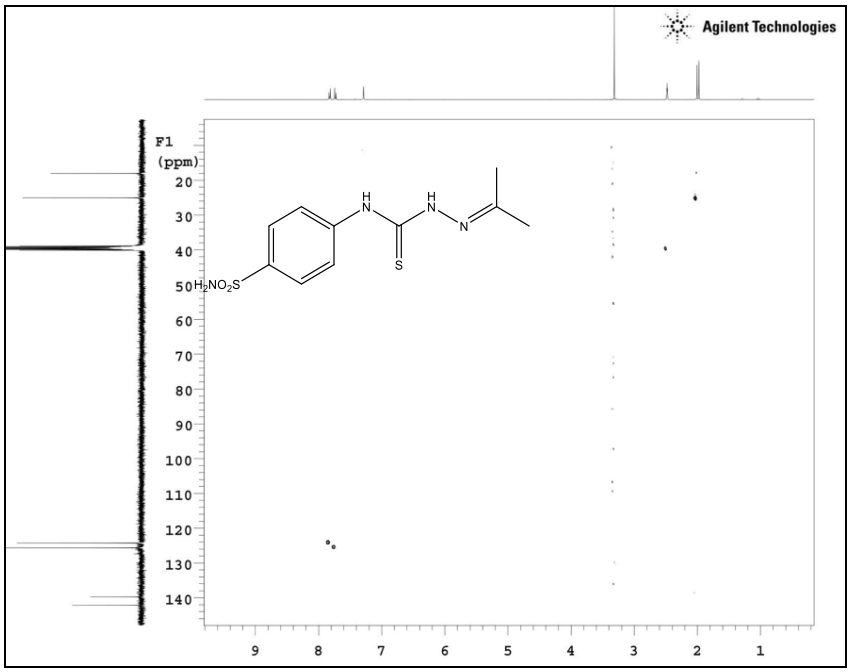

Figure 4-68: HSQC spectrum of compound E10 (0 – 10 ppm; 0 – 140 ppm)

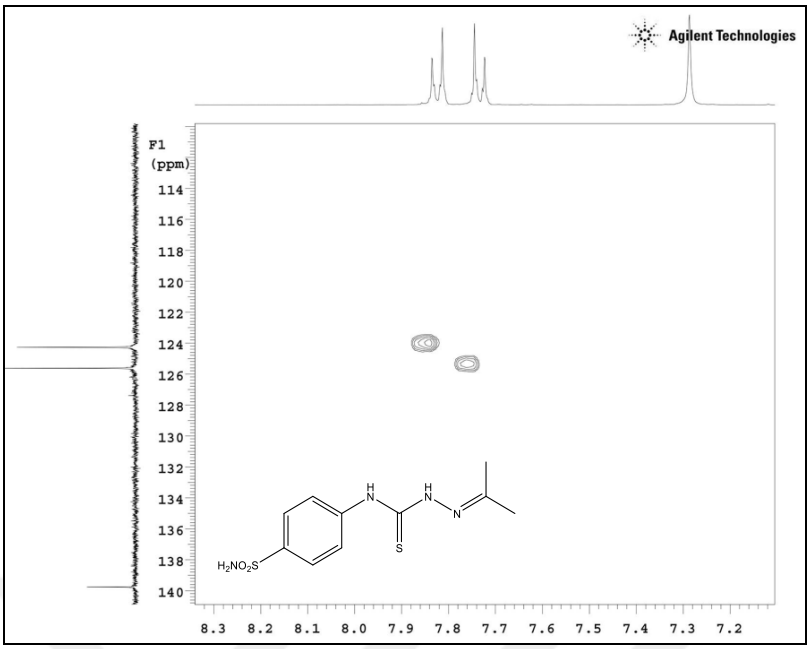

Figure 4-69: HSQC spectrum of compound E10 (7.2 – 8.3 ppm; 114 – 140 ppm)

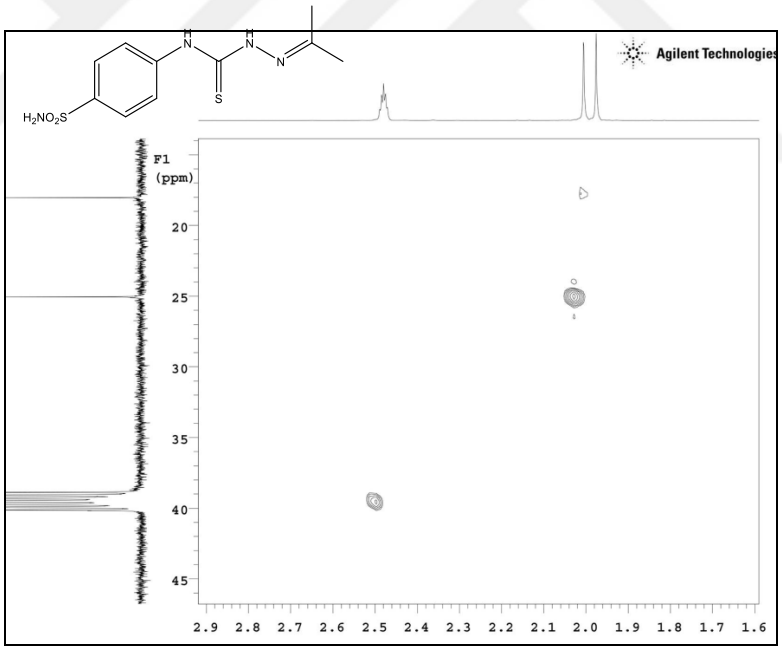

Figure 4-70: HSQC spectrum of compound E10 (1.6 – 2.9 ppm; 15 – 45 ppm)

LC-MS Spectrum

m/z ESI (negative): 285.0 $(M-H)^-$; $C_{10}H_{14}N_4O_2S_2$ (MA= 286.373; Exact Mass= 286.06)

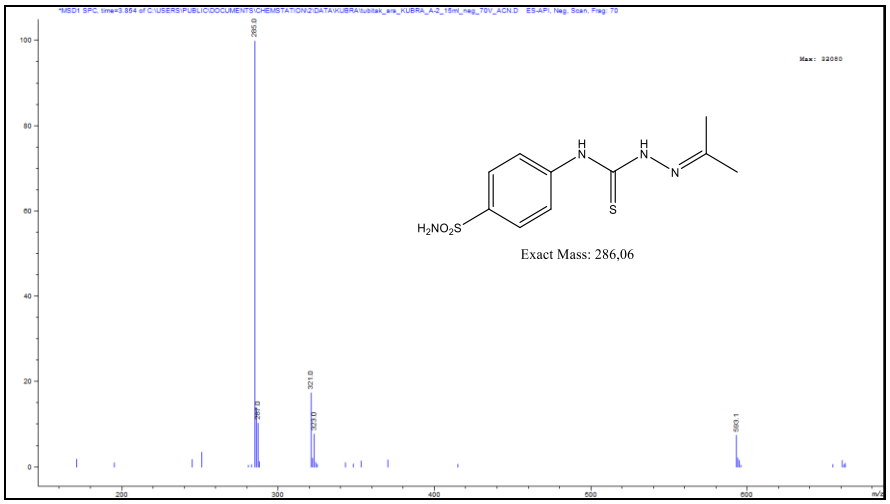

Figure 4-71: Mass spectrum of compound E10

4.3.1.11. 2-(pentan-3-ylidene)-*N*-(4-sulfamoylphenyl)hydrazine-1-carbothioamide (E11)

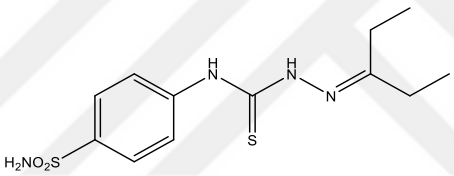

An ethanolic solution of 0.01 mol (1.1 ml) of 3-pentanone (**D7**) is added to an ethanolic solution of 0.01 mol (2.5 g) of *N*-(4-sulfamoylphenyl)hydrazinecarbothioamide (**C2**). The reaction mixture is heated under reflux for 4 hours. The reaction mixture was left to precipitate. The resulting precipitate is filtered, dried, and purified by recrystallization from ethanol.

Physical appearance	: White powder
Yield (%)	: 48
Retention factor	: 0.59; Chloroform : Methanol (9:1)
Melting point (ºC)	: 199.5-199.8

Elemental Analysis

Molecular formula	: $C_{12}H_{18}N_4O_2S_2$
Molecular weight (g/mol)	: 314.426

Element	C	H	N	S
Calculated (%)	45.84	5.77	17.82	20.40
Found (%)	45.65	5.82	17.56	20.04

Spectral Analysis

Fourier Transform Infrared (FT-IR) Spectrum

IR(KBr): υ 3290, 3246 (NH s.b); 3097 (Ar.C-H s.b., =CH s.b); 2966, 2929, 2889 (Al. C-H s.b.); 1589, 1548, 1531, 1494 (Ar. C=C s.b, C=N s.b, N-H b.b); 1443 (Al. C-H s.b.); 1321, 1161 (S=O s.b); 1274 (C=S s.b); 833 (1,4-disubs. Ar-C-H b.b)

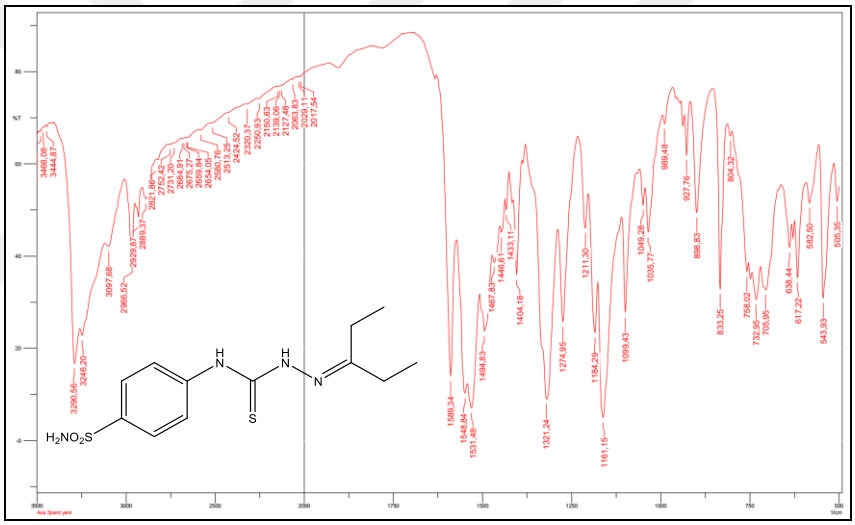

Figure 4-72: IR spectrum of compound E11

^{1}H-NMR Spectrum

^{1}H NMR (DMSO-d_6 / 400 MHz δ (ppm): 1.0, 1.10 (6H, 2t, J=7.4 Hz, 2 x CH_3), 2.34, 2.45 (4H, 2q, J=7.4 Hz, 2 x -CH_2-), 7.31 (2H, s, -SO_2NH_2), 7.76 (2H, app.d (AA'BB'), J=8.5 Hz, 4-sulfamoylphenyl $C_{3,5}$-H), 7.85 (2H, app.d (AA'BB'), J=8.5, Hz, 4-sulfamoylphenyl $C_{2,6}$-H), 9.97 (1H, s, tsc N_4-H), 10.65 (tsc N_2-H).

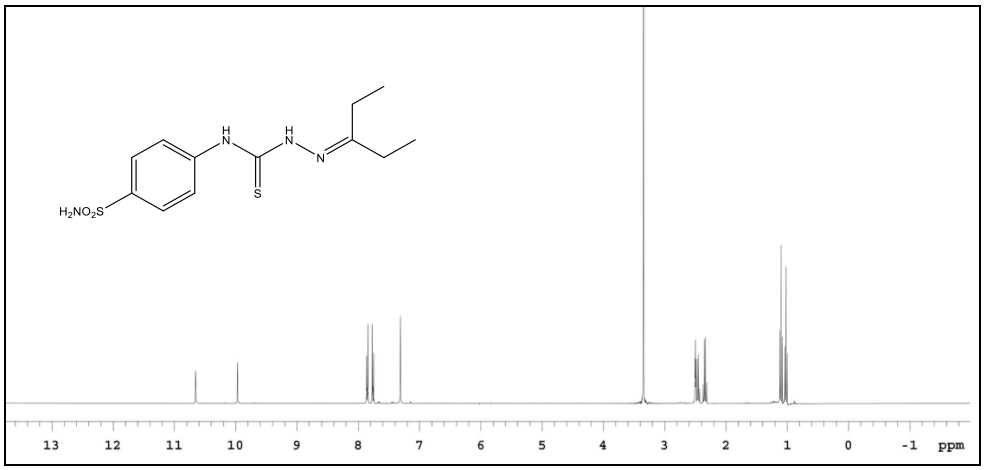

Figure 4-73: ^{1}H NMR spectrum of compound E11 (0 – 14 ppm)

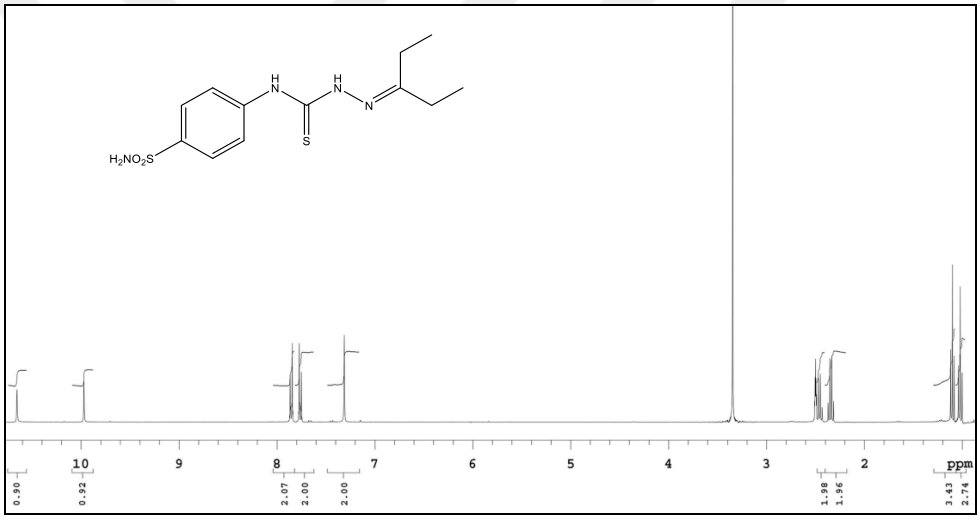

Figure 4-74: ^{1}H NMR spectrum of compound E11 (1 – 10.5 ppm)

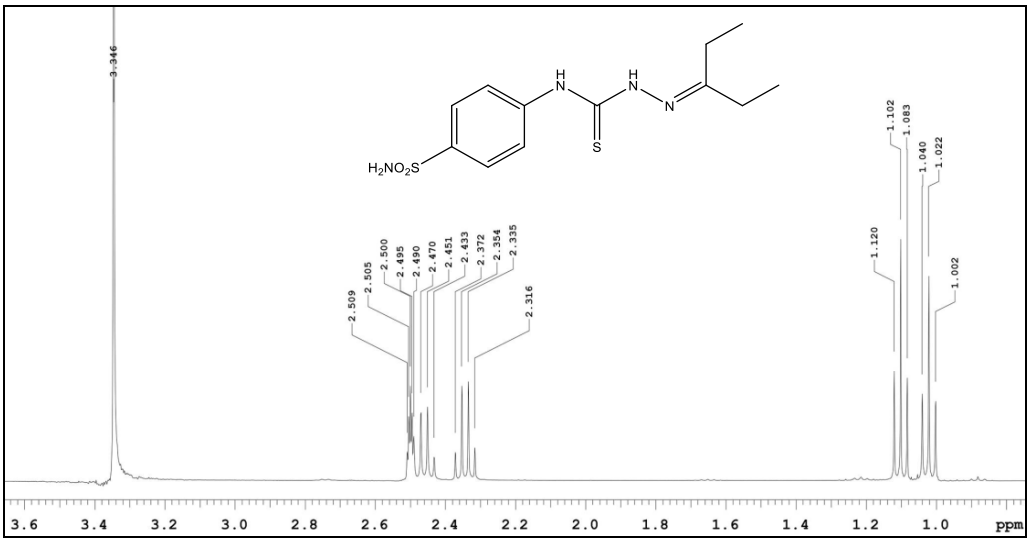

Figure 4-75[1]H NMR spectrum of compound E11 (0.9 – 3.6 ppm)

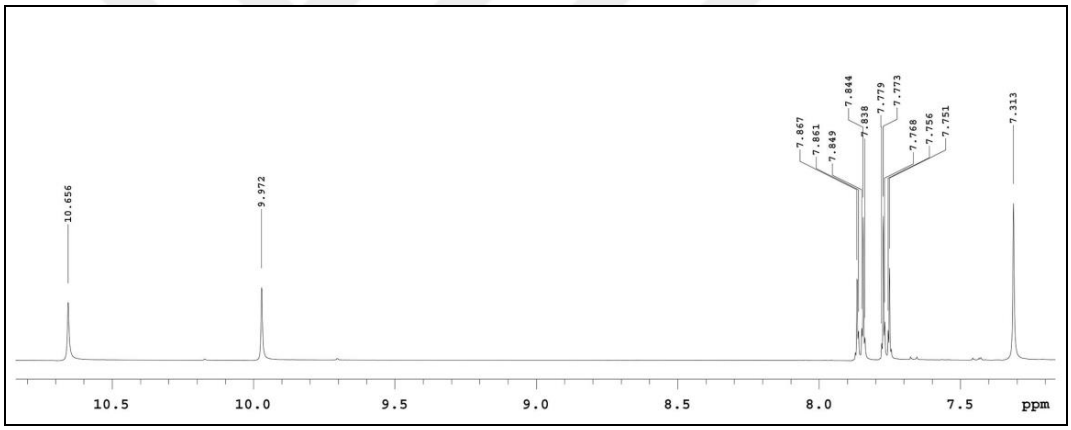

Figure 4-76: [1]H NMR spectrum of compound E11 (7.2 – 10.8 ppm)

LC-MS Spectrum

m/z ESI (negative): 313.1 $(M-H)^-$; $C_{12}H_{18}N_4O_2S_2$ (MA= 314.426; Exact Mass= 314.09)

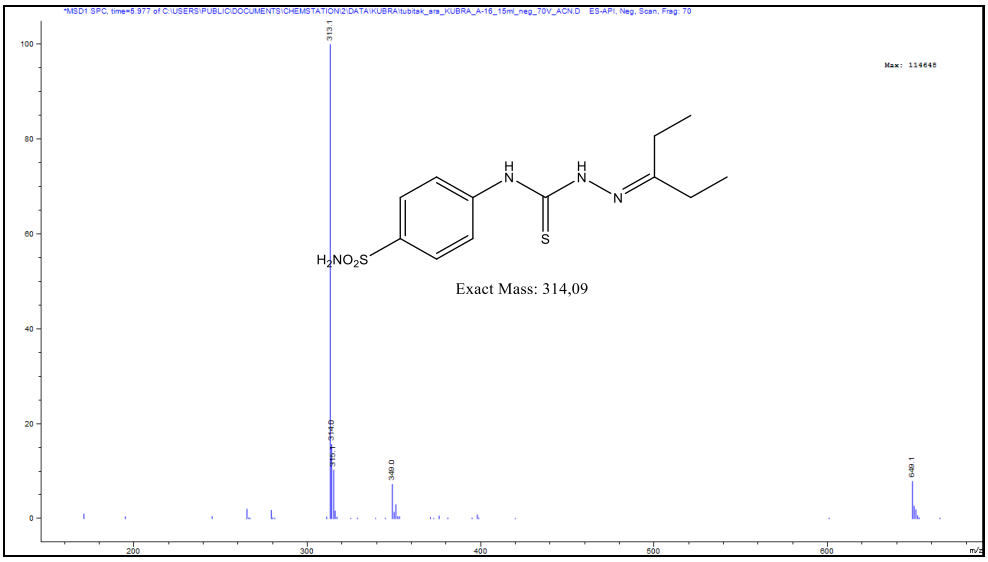

Figure 4-77: Mass spectrum of compound E11

4.3.1.12. (E)-2-(pentan-2-ylidene)-*N*-(4-sulfamoylphenyl)hydrazine-1-carbothioamide (E12)

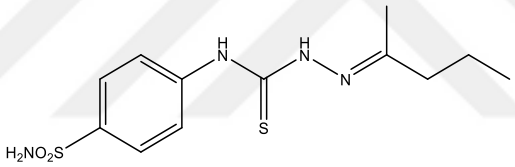

An ethanolic solution of 0.01 mol (1.1 ml) of 2-pentanone (**D8**) is added to an ethanolic solution of 0.01 mol (2.5 g) of *N*-(4-sulfamoylphenyl)hydrazinecarbothioamide (**C2**). The reaction mixture is heated under reflux for 7 hours. The resulting precipitate is filtered, dried, and purified by recrystallization from ethanol.

Physical appearance	: Amber white powder
Yield (%)	: 49
Retention factor	: 0.59; Chloroform : Methanol (9:1)
Melting point (ºC)	: 186.6-187.1

Elemental Analysis

Molecular formula	: $C_{12}H_{18}N_4O_2S_2$
Molecular weight (g/mol)	: 314.426

Element	C	H	N	S
Calculated (%)	45.84	5.77	17.82	20.40
Found (%)	45.74	5.48	18.16	20.08

Spectral Analysis

Fourier Transform Infrared (FT-IR) Spectrum

IR(KBr): υ 3360, 3240 (NH s.b); 3196, 3078 (Ar.C-H s.b., =CH s.b); 2958, 2931, 2872, 2812 (Al. C-H s.b.); 1585, 1525, 1487 (Ar. C=C s.b, C=N s.b, N-H b.b); 1406, 1369 (Al. C-H b.b.); 1323, 1157 (S=O s.b); 1301 (C-N s.b); 1261 (C=S s.b); 833 (1,4-disubs. Ar-C-H b.b)

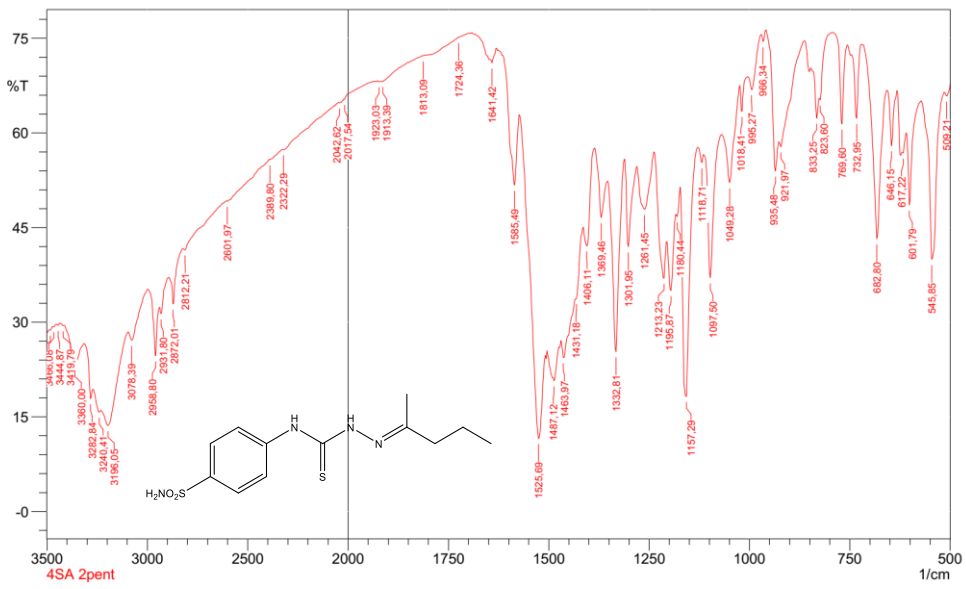

Figure 4-78: IR spectrum of compound E12

^{1}H-NMR Spectrum

^{1}H NMR (DMSO-d_6 / 400 MHz δ (ppm): 0.88-0.92 (3H, m, -CH_2CH_2**CH_3**), 1.57 (2H, sextet, *J*=7.4 Hz, -CH_2**CH_2**CH_3), 1.94 (3H, d, *J*=5.1 Hz, -CH_3), 2.24 (2H, t, *J*=7.8 Hz, -**CH_2**CH_2CH_3), 7.3 (2H, s, -SO_2NH_2), 7.76 (2H, d, *J*=8.6 Hz, 4-sulfamoylphenyl $C_{3,5}$-H), 7.85 (2H, d, *J*=8.6 Hz, 4-sulfamoylphenyl $C_{2,6}$-H), 10.45 (1H, s, tsc N_4-H), 10.71 (tsc N_2-H).

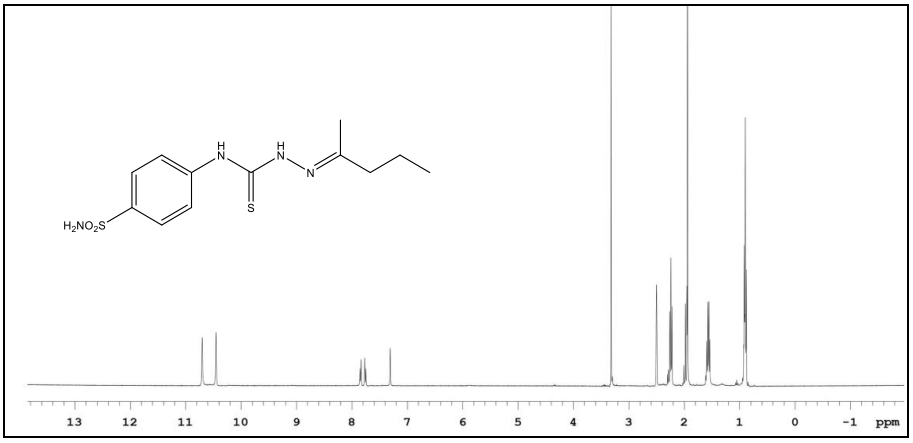

Figure 4-79: ^{1}H-NMR spectrum of compound E12 (0 – 14 ppm)

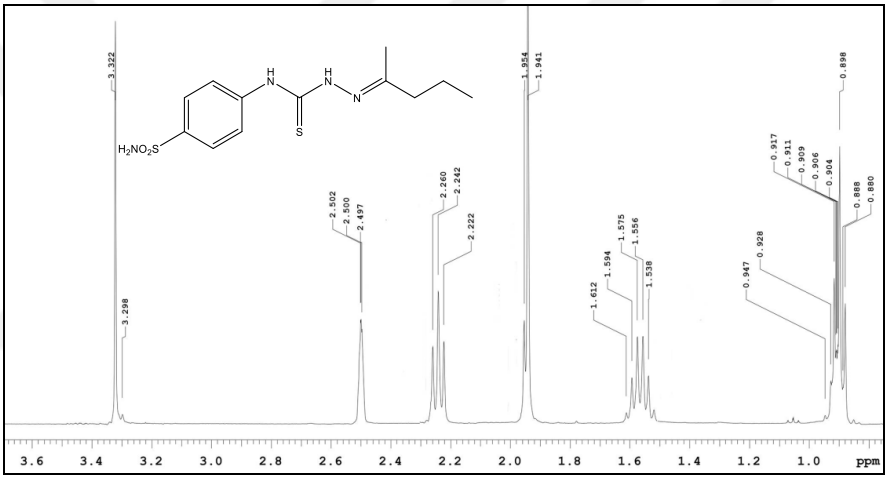

Figure 4-80: ^{1}H-NMR spectrum of compound E12 (0.8 – 3.6 ppm)

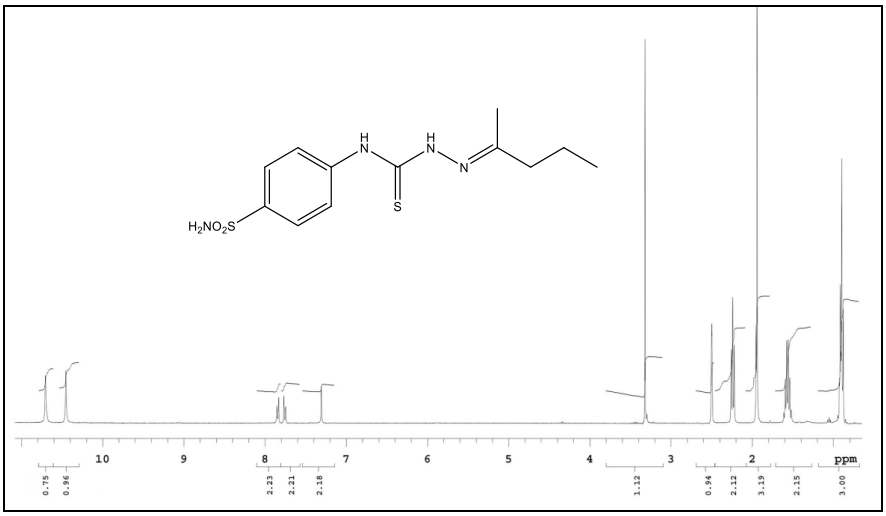

Figure 4-81: ^{1}H-NMR spectrum of compound E12 (1 – 11 ppm)

LC-MS Spectrum

m/z ESI (negative): 313.1 $(M-H)^-$; $C_{12}H_{18}N_4O_2S_2$ (MA= 314.426; Exact Mass= 314.09)

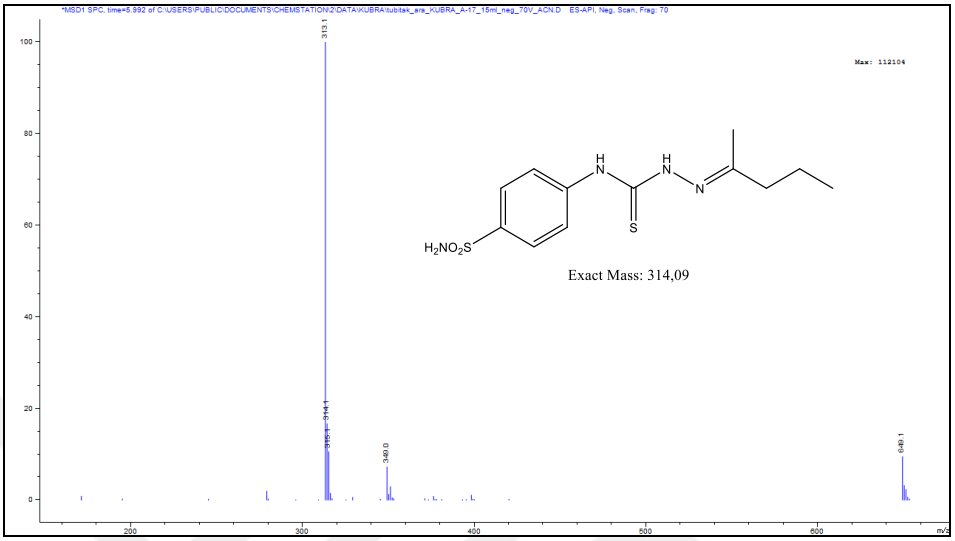

Figure 4-82: Mass spectrum of compound E12

4.3.1.13. 2-cyclopentylidene-N-(4-sulfamoylphenyl)hydrazine-1-carbothioamide (E13)

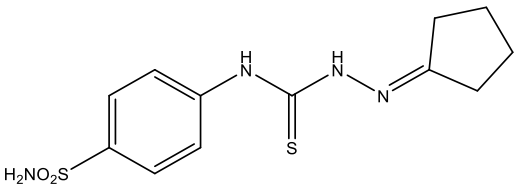

An ethanolic solution of 0.01 mol (0.9 ml) of cyclopentanone (**D9**) is added to an ethanolic solution of 0.01 mol (2.5 g) of *N*-(4-sulfamoylphenyl)hydrazinecarbothioamide (**C2**). The reaction mixture is heated under reflux for 7 hours. The resulting precipitate is filtered, dried, and purified by recrystallization from ethanol.

Physical appearance	: White crystals
Yield (%)	: 92
Retention factor	: 0.59; Chloroform : Methanol (9:1)
Melting point (ºC)	: 208.8-209.8

Elemental Analysis

Molecular formula	: $C_{12}H_{16}N_4O_2S_2$
Molecular weight (g/mol)	: 312.411

Element	C	H	N	S
Calculated (%)	46.13	5.16	17.93	20.53
Found (%)	46.38	5.45	17.62	20.31

Spectral Analysis

Fourier Transform Infrared (FT-IR) Spectrum

IR(KBr): υ 3331, 3296, 3253 (NH s.b); 3183, 3097 (Ar.C-H s.b., =CH s.b); 2965, 2945, 2877 (Al. C-H s.b.); 1585,1533, 1477 (Ar. C=C s.b, C=N s.b, N-H b.b); 1404, 1365 (Al. C-H b.b.); 1332, 1151 (S=O s.b); 1303 (C-N s.b); 1267 (C=S s.b); 835 (1,4-disubs. Ar-C-H b.b)

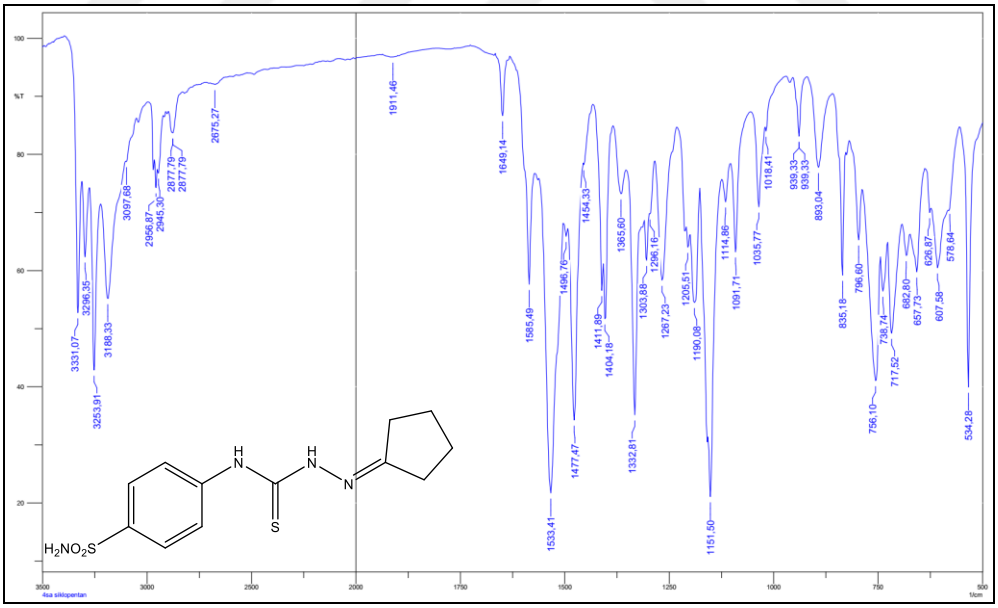

Figure 4-83: IR spectrum of compound E13

^{1}H-NMR Spectrum

^{1}H NMR (DMSO-d_6 / 400 MHz δ (ppm): 1.71, 1.78 (4H, 2p, J=7.0 Hz, cyclopentane $C_{3,4}$-H), 2.39-2.49 (4H, m, cyclopentane $C_{2,5}$-H), 7.30 (2H, s, -SO_2NH_2), 7.74 (2H,

app.d (AA'BB'), *J*=8.6 Hz, 4-sulfamoylphenyl $C_{2,6}$-H), 7.82 (2H, app.d (AA'BB'), *J*=8.6 Hz, 4-sulfamoylphenyl $C_{3,5}$-H), 10.03 (1H, s, tsc N_4-H), 10.47 (tsc N_2-H).

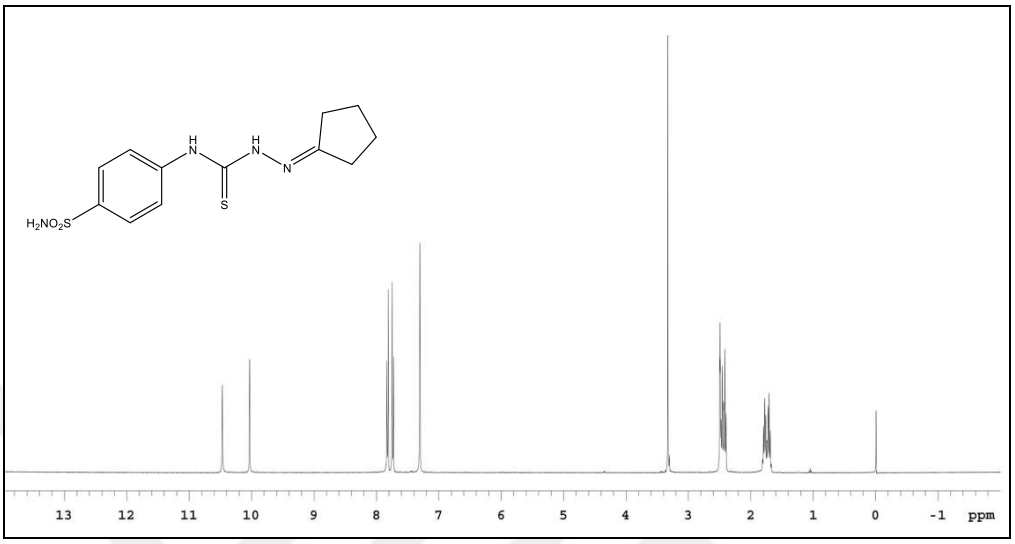

Figure 4-84: ^{1}H NMR spectrum of compound E13 (0 – 14 ppm)

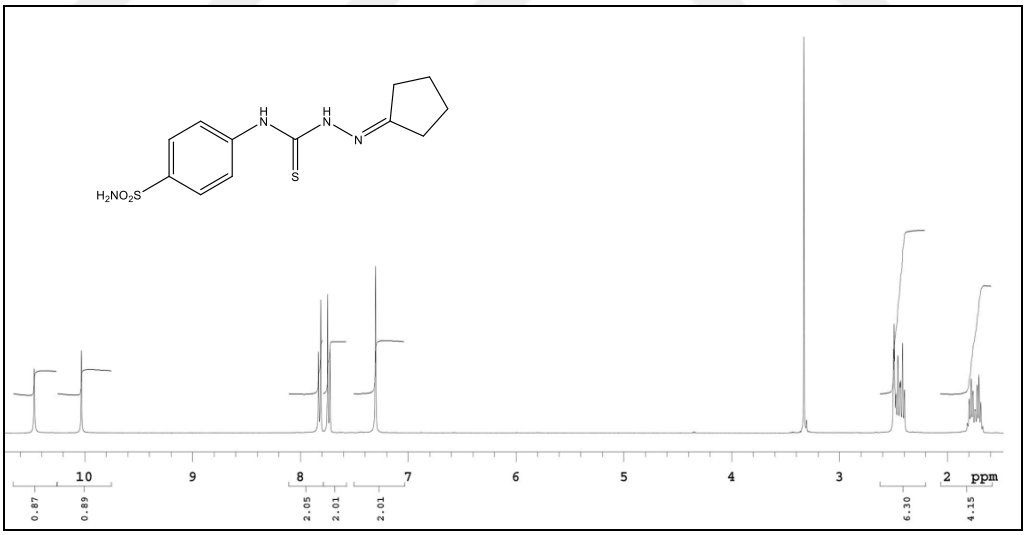

Figure 4-85: ^{1}H NMR spectrum of compound E13 (2.6 – 10.6 ppm)

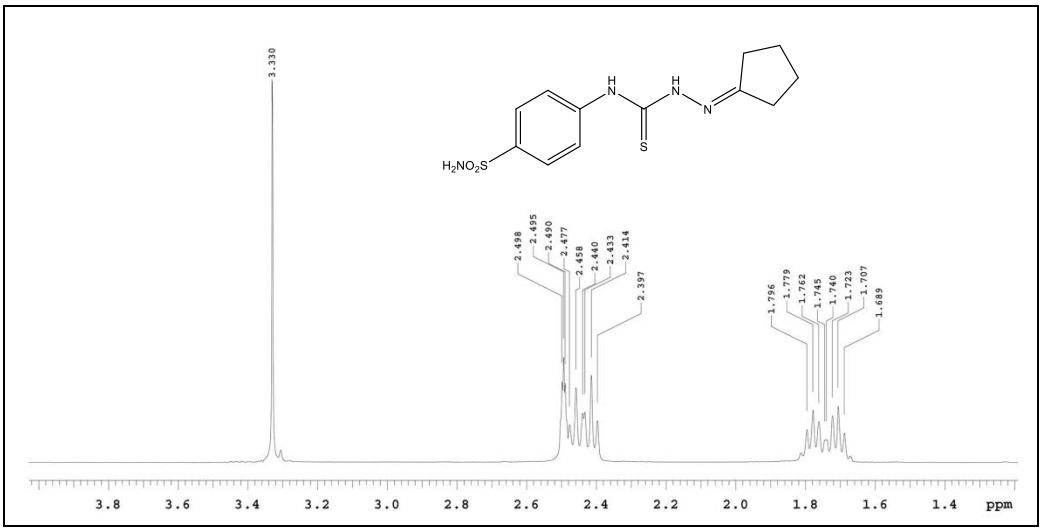

Figure 4-86: ^{1}H NMR spectrum of compound E13 (1.2 – 4 ppm)

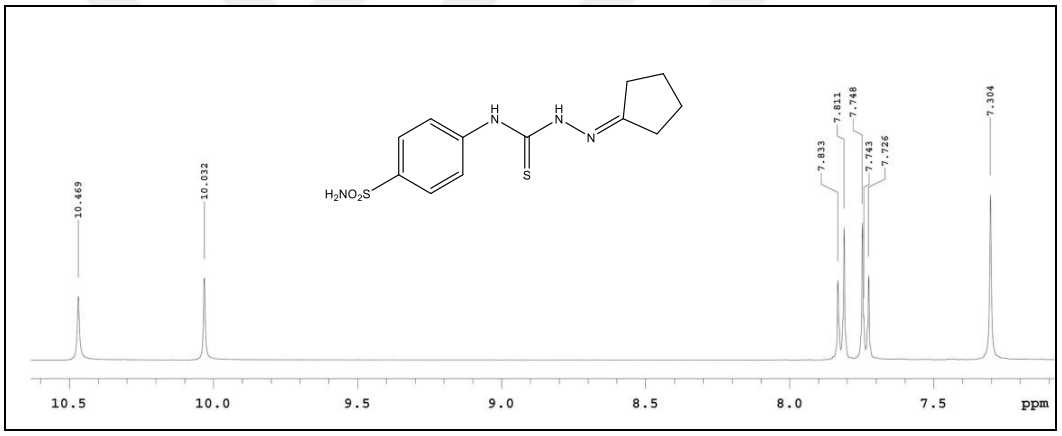

Figure 4-87: ^{1}H NMR spectrum of compound E13 (7 – 10.5 ppm)

LC-MS Spectrum

m/z ESI (negative): 311.0 $(M-H)^-$; $C_{12}H_{16}N_4O_2S_2$ (MA= 312.411; Exact Mass= 312.07)

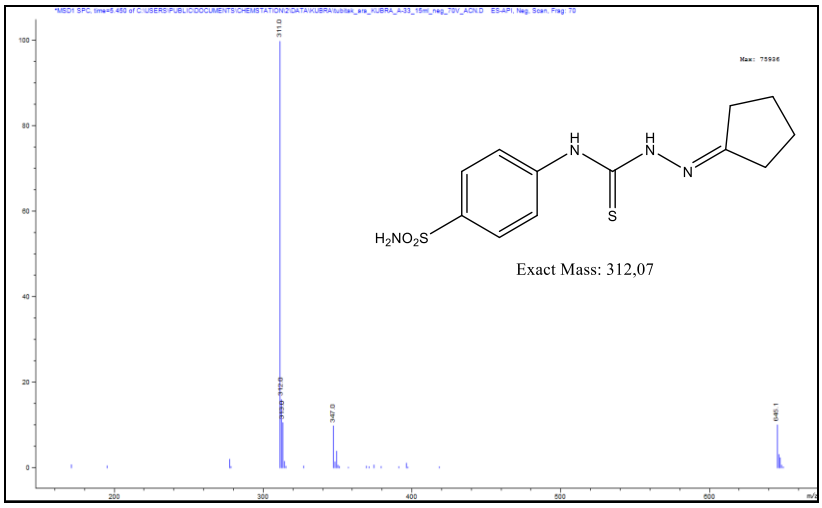

Figure 4-88: Mass spectrum of compound E13

4.3.2. Synthesis of Targeted Compounds 3/4-[4-(Non)substitutedphenyl-2-(alkylidene/arylidenehydrazinylidene)-1,3-thiazol-3(*2H*)-yl]benzenesulfonamide Derivatives (4a-4v)

4.3.2.1. 3-((*Z*)-4-phenyl-2-(((*E*)-thiophen-2-ylmethylene)hydrazineylidene)thiazol-3(2*H*)-yl)benzenesulfonamide (4a)

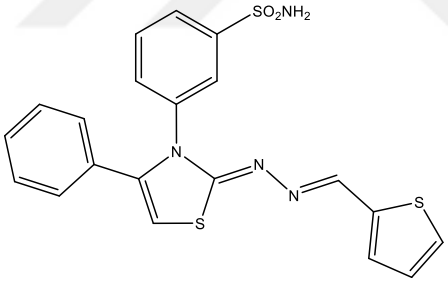

0.0021 mol (0.42g) of 2-bromo-1-phenylethan-1-one (**3a**) and 0.0021 mol (0.7g) of *N*-(3-sulfamoylphenyl)-2-(thiophen-2-ylmethylene)hydrazine-1-carbothioamide (**E1**) are suspended in chloroform-ethanol (2:1). The reaction mixture is heated under reflux for 5.5 hours. The solid product formed is filtered and purified by recrystallization from ethanol.

Physical appearance	: Yellow powder
Yield (%)	: 94
Retention factor	: 0.75; Chloroform : Methanol (9:1)
Melting point (ºC)	: 271.7-273.0

Elemental Analysis

Molecular formula	: $C_{20}H_{16}N_4O_2S_3$
Molecular weight (g/mol)	: 440.56

Element	C	H	N	S
Calculated (%)	54.52	3.66	12.72	21.83
Found (%)	54.81	3.35	13.12	21.57

Spectral Analysis

Fourier Transform Infrared (FT-IR) Spectrum

IR(KBr): υ 3170, 3122 (NH s.b); 3064, 3047 (Ar.C-H s.b., =CH s.b); 1598, 1589, 1579, 1573, 1566 (Ar. C=C s.b, C=N s.b, N-H b.b); 1342, 1163 (S=O s.b); 1315 (C-N s.b); 732, 684 (monosubs. Ar-C-H b.b); 891, 756, 700 (1,3-disubs. Ar-C-H b.b)

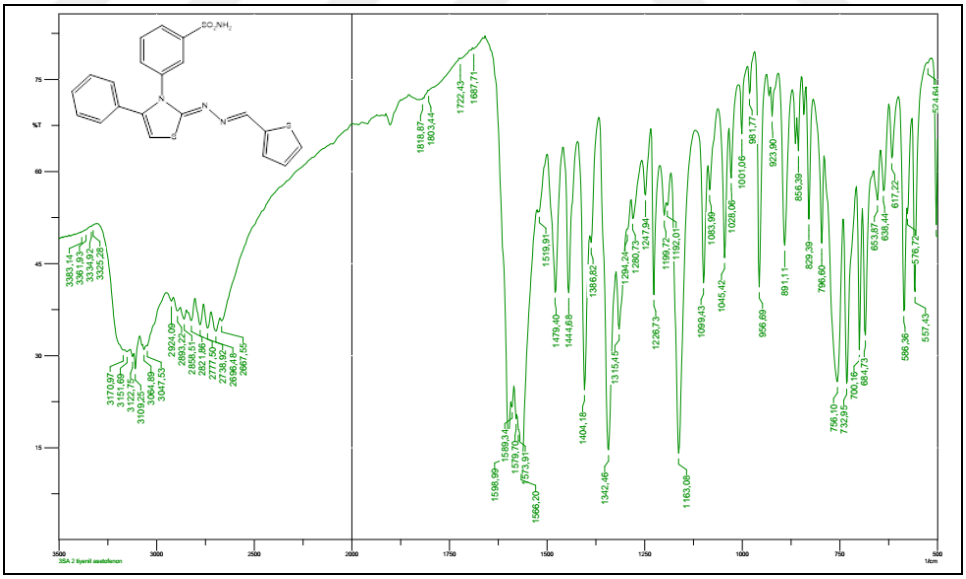

Figure 4-89: IR spectrum of compound 4a

^{1}H-NMR Spectrum

^{1}H NMR (DMSO-d_6 / 500 MHz δ (ppm): 6.73 (1H, s, thiazole C_5-H), 7.10 (1H, dd, J=5.1, 3.5 Hz, thiophene C_4-H), 7.19 (2H, dd, J=7.8, 1.9 Hz, phenyl $C_{2,6}$-H), 7.24-7.30

(3H, m, phenyl $C_{3,4,5}$-H), 7.34 (1H, dd, *J*=3.6, 1.2 Hz, thiophene C_3-H), 7.46 (2H, broad s, -SO_2NH_2), 7.49 (1H, ddd, *J*=7.9, 2.0, 1.1 Hz, benzenesulfonamide C_4-H), 7.56 (1H, t, *J*=7.8 Hz, benzenesulfonamide C_5-H), 7.60 (1H, dt, *J*=5.0, 1.0 Hz, thiophene C_5-H), 7.71-7.81 (2H, m, benzenesulfonamide $C_{2,6}$-H), 8.35 (1H, s, N=CH).

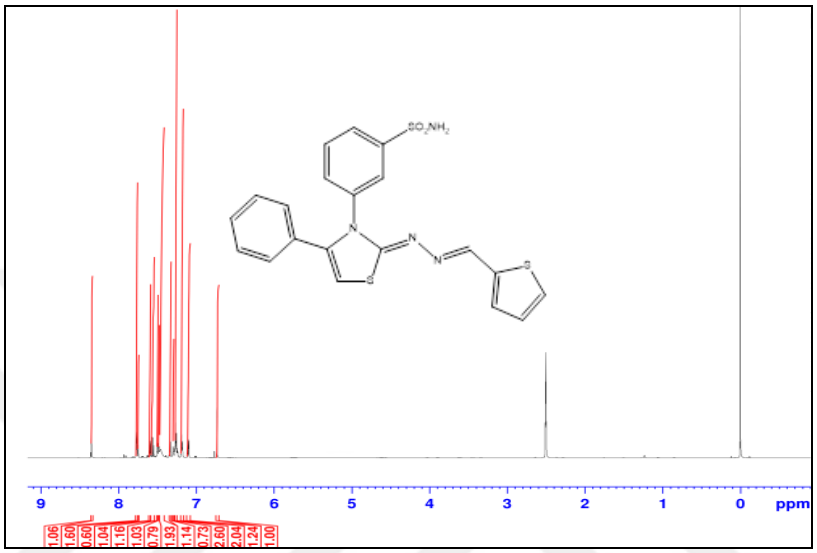

Figure 4-90: ^{1}H-NMR spectrum of compound 4a (0 – 9 ppm)

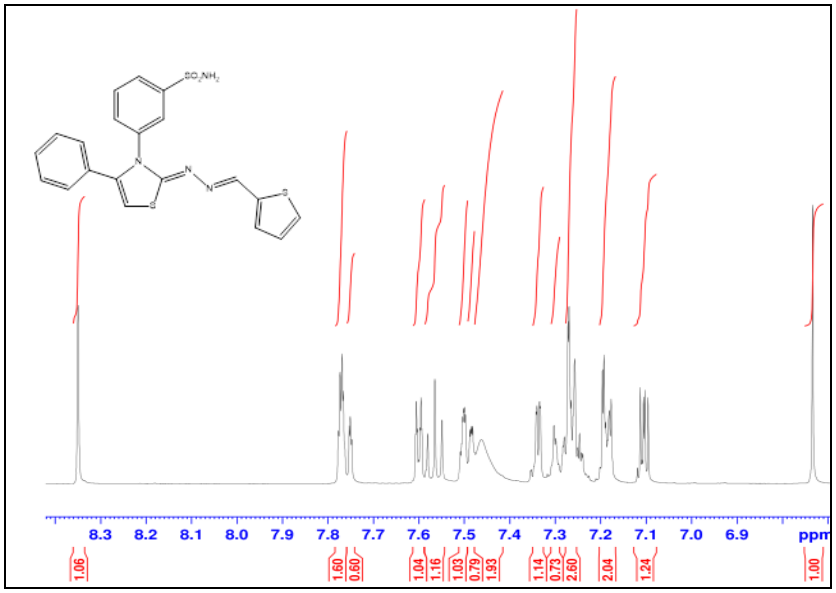

Figure 4-91: ^{1}H-NMR spectrum of compound 4a (6.8 – 8.4 ppm)

^{13}C-NMR Spectrum

^{13}C NMR (decoupled, DMSO-*d*$_6$, 100 MHz) δ (ppm): 103.1 (thiazole C_5), 125.5, 125.9 (3-benzenesulfonamide $C_{2,6}$), 127.9 (thiophene C_4), 128.4, 128.5, 128.7, 128.8 (phenyl $C_{2,3,4,5,6}$ / thiophene C_5), 129.8, 129.9 (phenyl C_1/ 3-benzenesulfonamide C_5), 130.6 (thiophene C_3), 132.1 (3-benzenesulfonamide C_4), 137.1 (3-benzenesulfonamide C_3), 139.3 (3-benzenesulfonamide C_1), 139.5 (thiophene C_2), 145.0 (thiazole C_4), 146.8 (N=CH), 169.0 (thiazole C_2).

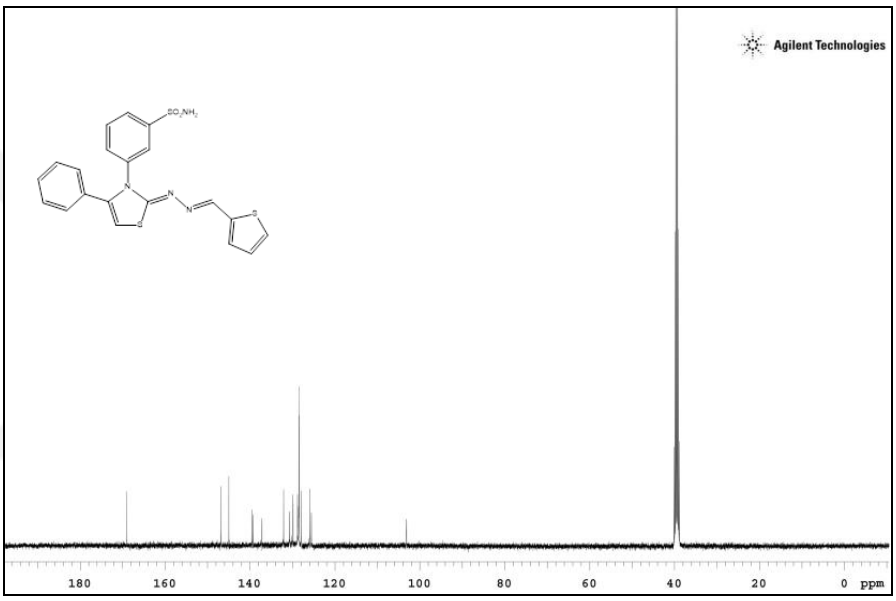

Figure 4-92: ^{13}C-NMR spectrum of compound 4a (0 – 200 ppm)

^{13}C NMR (HSQC-2D, DMSO-*d*$_6$, 100 MHz) δ (ppm): **103.1** [thiazole C_5 - **6.73** (1H, s, thiazole C_5-H)], **125.5, 125.9** [3-benzenesulfonamide $C_{2,6}$ - **7.71-7.81** (2H, m, benzenesulfonamide $C_{2,6}$-H)], **127.9** [thiophene C4 - **7.10** (1H, dd, *J*=5.1, 3.5 Hz, thiophene C_4-H)], **128.4, 128.5, 128.8, 128.8** (phenyl $C_{2,3,4,5,6}$ / thiophene C_5 -), **7.19** (2H, dd, *J*=7.8, 1.9 Hz, phenyl $C_{2,6}$-H) / **7.24-7.30** (3H, m, phenyl $C_{3,4,5}$-H) / **7.60** (1H, dt, *J*=5., 1.0 Hz, thiophene C_5-H)], **129.8, 129.9** [phenyl C_1/ 3-benzenesulfonamide C_5 - **7.56** (1H, t, *J*=7.8 Hz, benzenesulfonamide C_5-H)], **130.6** [thiophene C_3 - **7.34** (1H, dd, *J*=3.6, 1.2 Hz, thiophene C_3-H)], **132.1** [3-benzenesulfonamide C_4 - **7.49** (1H, ddd, *J*=7.9, 2.0, 1.1 Hz, benzenesulfonamide C_4-H)], **146.8** [N=CH - **8.35** (1H, s, N=CH)].

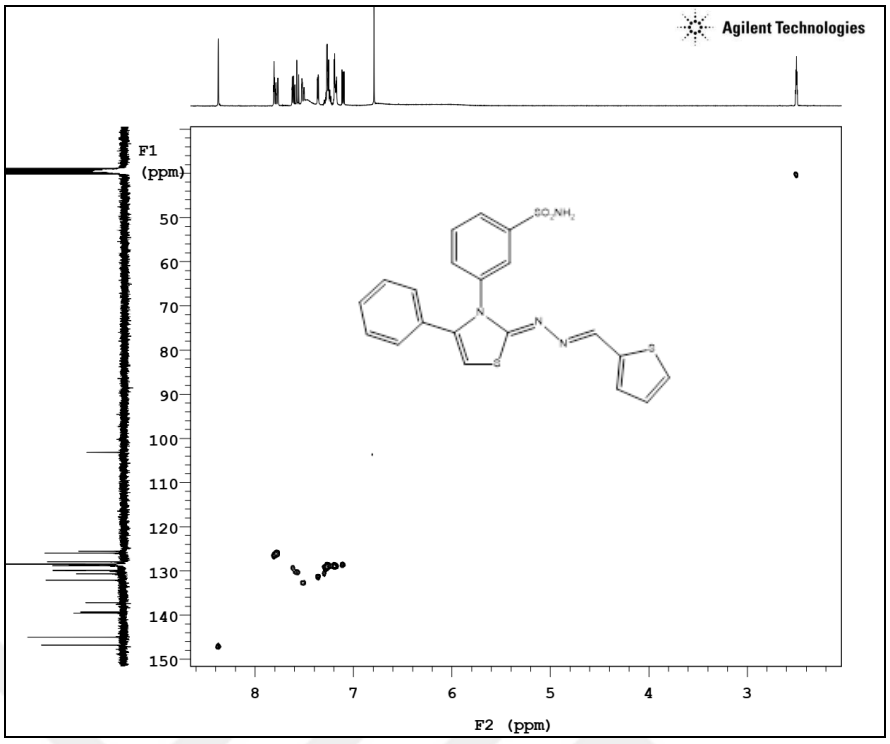

Figure 4-93: HSQC spectrum of compound 4a (2.2 – 8.6 ppm; 0 – 150 ppm)

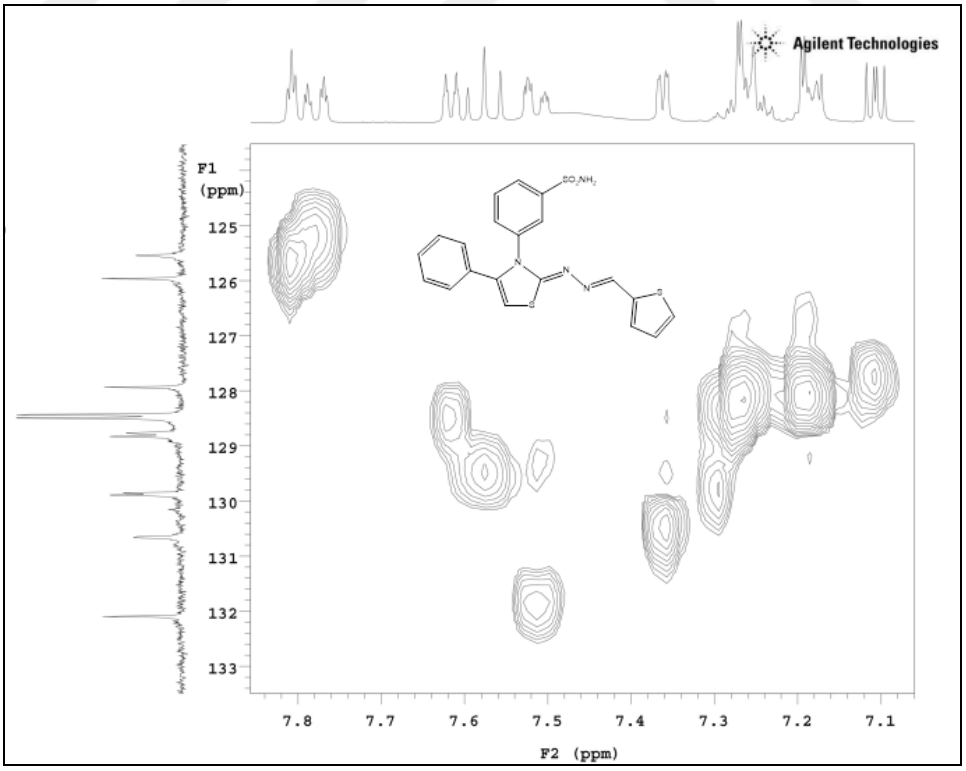

Figure 4-94: HSQC spectrum of compound 4a (7.1 – 7.8 ppm; 124 – 133 ppm)

LC-MS Spectrum

m/z ESI (positive): 441.0 $(M+H)^+$; $C_{20}H_{16}N_4O_2S_3$ (MA= 440.561; Exact Mass= 440.04)

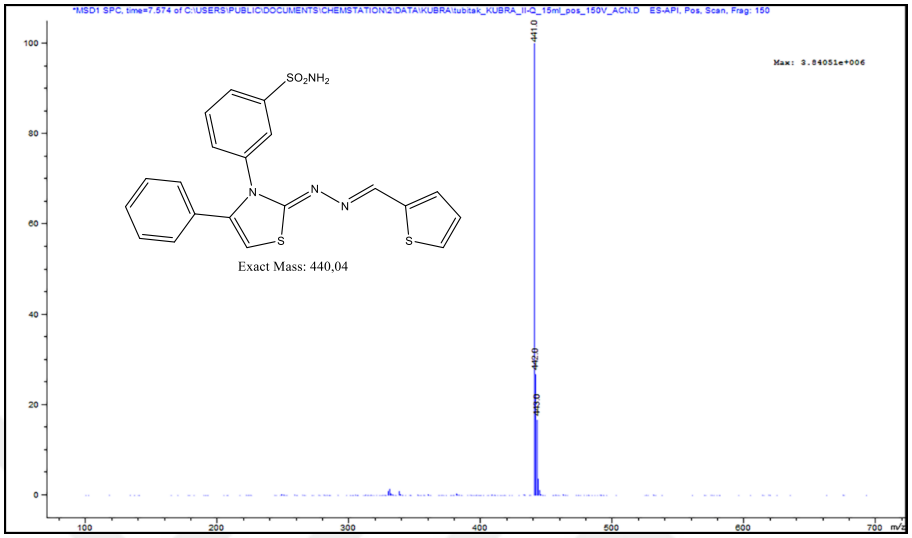

Figure 4-95: Mass spectrum of compound 4a

4.3.2.2. 3-((Z)-2-(((E)-(5-bromothiophen-2-yl)methylene)hydrazineylidene)-4-phenylthiazol-3(2H)-yl)benzenesulfonamide (4b)

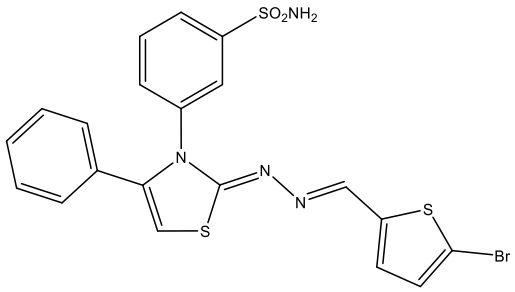

0.0017 mol (0.34g) of 2-bromo-1-phenylethan-1-one (**3a**) and 0.0017 mol (0.7g) of 2-((5-bromothiophen-2-yl)methylene)-*N*-(3-sulfamoylphenyl)hydrazine-1-carbothioamide (**E2**) are suspended in chloroform-ethanol (2:1). The reaction mixture is heated under reflux for 5.5 hours. The solid product formed is filtered and purified by recrystallization from ethanol.

Physical appearance	: Dark orange powder
Yield (%)	: 63
Retention factor	: 0.68; Chloroform : Methanol (9:1)

Melting point (ºC)	: 251.0 – 251.8

Elemental Analysis

Molecular formula	: $C_{20}H_{15}BrN_4O_2S_3$
Molecular weight (g/mol)	: 519.457

Element	C	H	N	S
Calculated (%)	46.24	2.91	10.79	18.52
Found (%)	45.96	2.77	10.77	18.21

Spectral Analysis

Fourier Transform Infrared (FT-IR) Spectrum

IR(KBr): υ 3402, 3387 (NH s.b); 3174, 3109, 3064 (Ar.C-H s.b., =CH s.b); 1598, 1591, 1579, 1566 (Ar. C=C s.b, C=N s.b, N-H b.b); 1344, 1163 (S=O s.b); 1315 (C-N s.b); 1080 (Ar-Br); 732, 686 (monosubs. Ar-C-H b.b); 893, 752, 700 (1,3-disubs. Ar-C-H b.b)

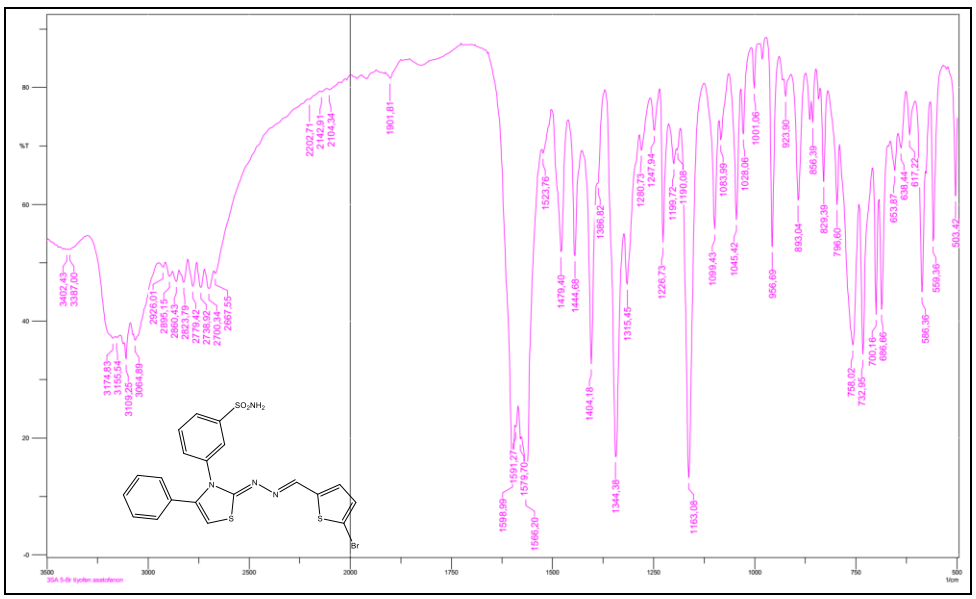

Figure 4-96: IR spectrum of compound 4b

^{1}H-NMR Spectrum

^{1}H NMR (DMSO-d_6 / 500 MHz δ (ppm): 6.73 (1H, s, thiazole C_5-H), 7.14 (1H, d, J=4.2 Hz, 5-bromothiophene C_4-H), 7.18 (2H, dd, J=7.9, 1.8 Hz, phenyl $C_{2,6}$-H), 7.22 (1H, d, J=3.9 Hz, 5-bromothiophene C_3-H), 7.25-7.28 (3H, m, phenyl $C_{3,4,5}$-H), 7.46 (2H, broad s, -SO_2NH_2), 7.48 (1H, ddd, J=7.9, 2.1, 1.2 Hz, 3-benzenesulfonamide C_4-H), 7.56 (1H, t, J=8.1 Hz, 3-benzenesulfonamide C_5-H), 7.68-7.83 (2H, m, 3-benzenesulfonamide $C_{2,6}$-H), 8.25 (1H, s, N=CH).

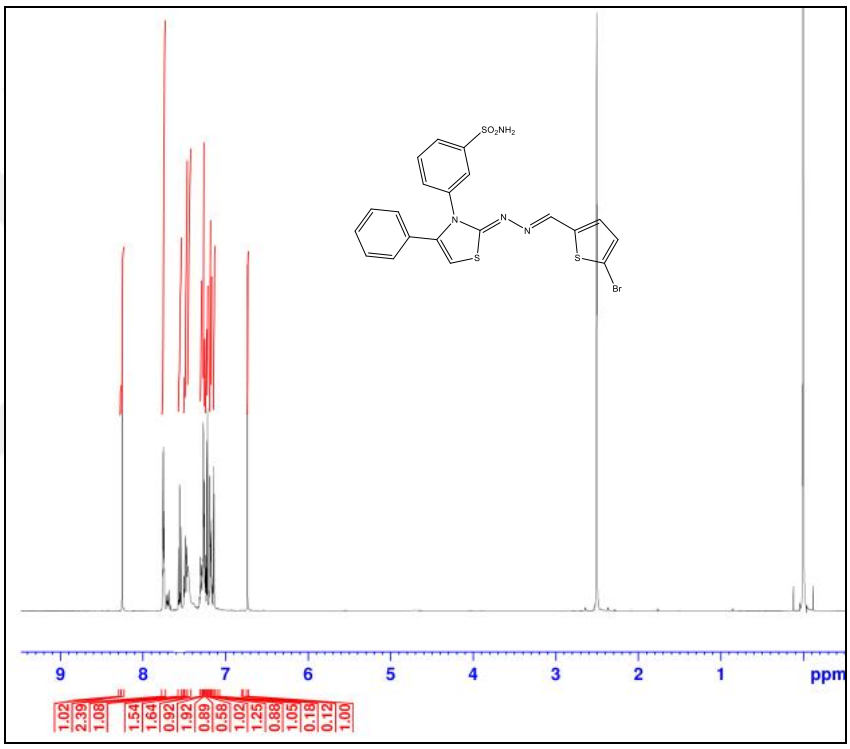

Figure 4-97: ^{1}H-NMR spectrum of compound 4b (0 – 9 ppm)

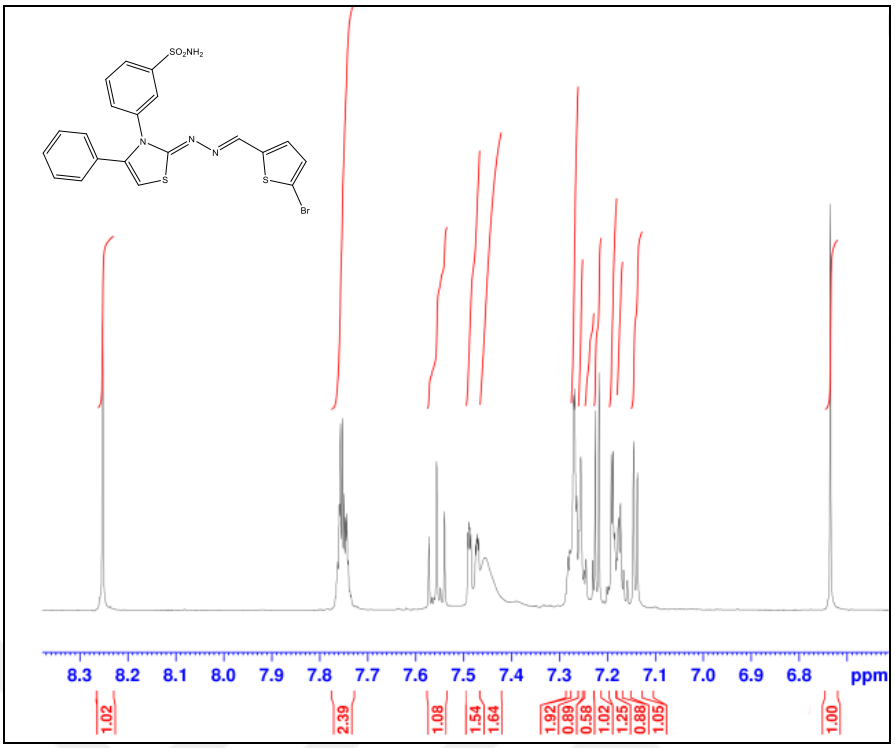

Figure 4-98: ^{1}H-NMR spectrum of compound 4b (6.7 – 8.3 ppm)

^{13}C-NMR Spectrum

^{13}C NMR (APT, DMSO-d_6, 125 MHz) δ (ppm): 103.2 (thiazole C_5), 114.5 (5-bromothiophene C_5), 125.8, 126.4 (3-benzenesulfonamide $C_{2,6)}$, 128.9, 129.2 (phenyl $C_{2,3,4,5,6}$), 130.2 (3-benzenesulfonamide C_5), 130.4 (phenyl C_1), 131.0 (5-bromothiophene C_4), 131.8 (5-bromothiophene C_3), 132.5 (3-benzenesulfonamide C_4), 138.0 (3-benzenesulfonamide C_3), 139.8 (3-benzenesulfonamide C_1), 142.0 (5-bromothiophene C_2), 145.4 (thiazole C4), 146.2 (N=CH), 170.1 (thiazole C_2).

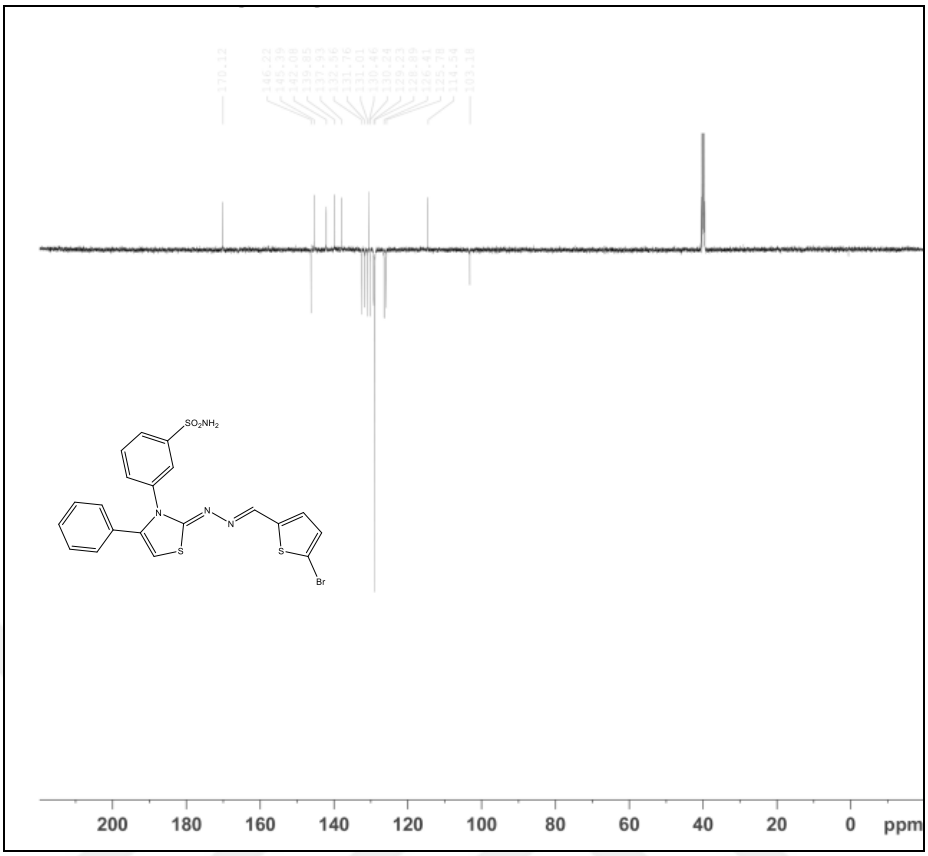

Figure 4-99: APT spectrum of compound 4b (0 – 200 ppm)

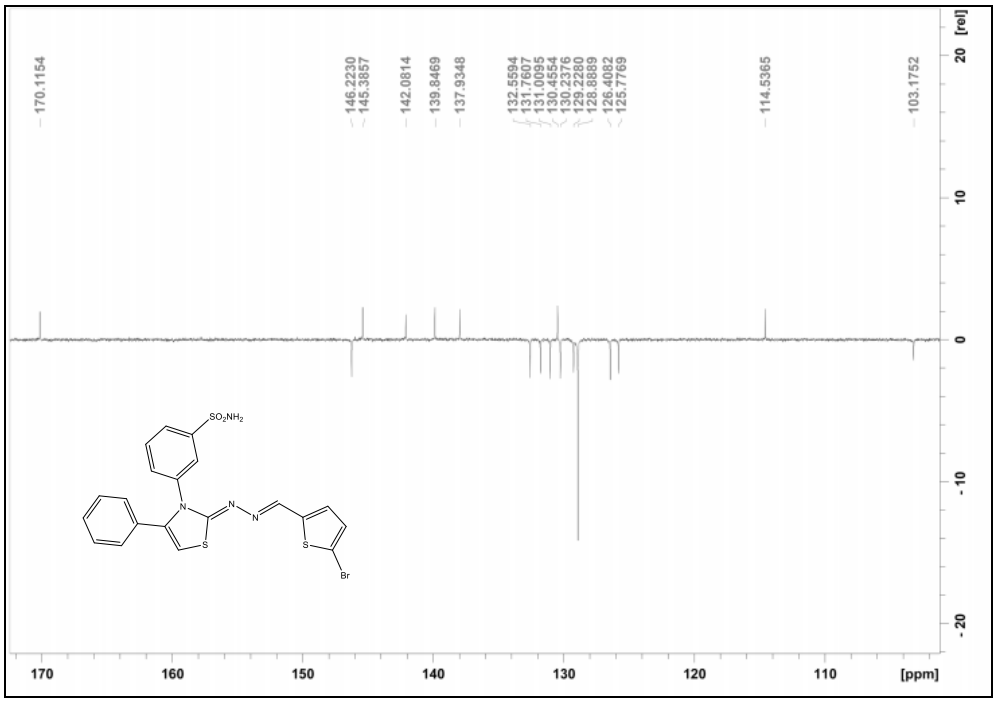

Figure 4-100: APT spectrum of compound 4b (100 – 170 ppm)

^{13}C NMR (HSQC-2D, DMSO-*d*$_6$, 125 MHz) δ (ppm): **103.2** [thiazole C_5 - **6.73** (1H, s, thiazole C_5-H)], **125.8**, **126.4** [3-benzenesulfonamide $C_{2,6}$ - **7.68-7.83** (2H, m, 3-benzenesulfonamide $C_{2,6}$-H)], **128.9**, **129.2** [phenyl $C_{2,3,4,5,6}$ - **7.18** (2H, dd, *J*=7.9, 1.8 Hz, phenyl $C_{2,6}$-H) and **7.25-7.28** (3H, m, phenyl $C_{3,4,5}$-H)], **130.2** [3-benzenesulfonamide C_5 - **7.56** (1H, t, *J*=8.1 Hz, 3-benzenesulfonamide C_5-H)], **131.0** [5-bromothiophene C_4 - **7.14** (1H, d, *J*=4.2 Hz, 5-bromothiophene C_4-H)], **131.8** [5-bromothiophene C_3 - **7.22** (1H, d, *J*=3.9 Hz, 5-bromothiophene C_3-H)], **132.5** [3-benzenesulfonamide C_4 - **7.48** (1H, ddd, *J*=7.9, 2.1, 1.2 Hz, 3-benzenesulfonamide C_4-H)], **146.2** [N=CH - **8.25** (1H, s, N=CH)].

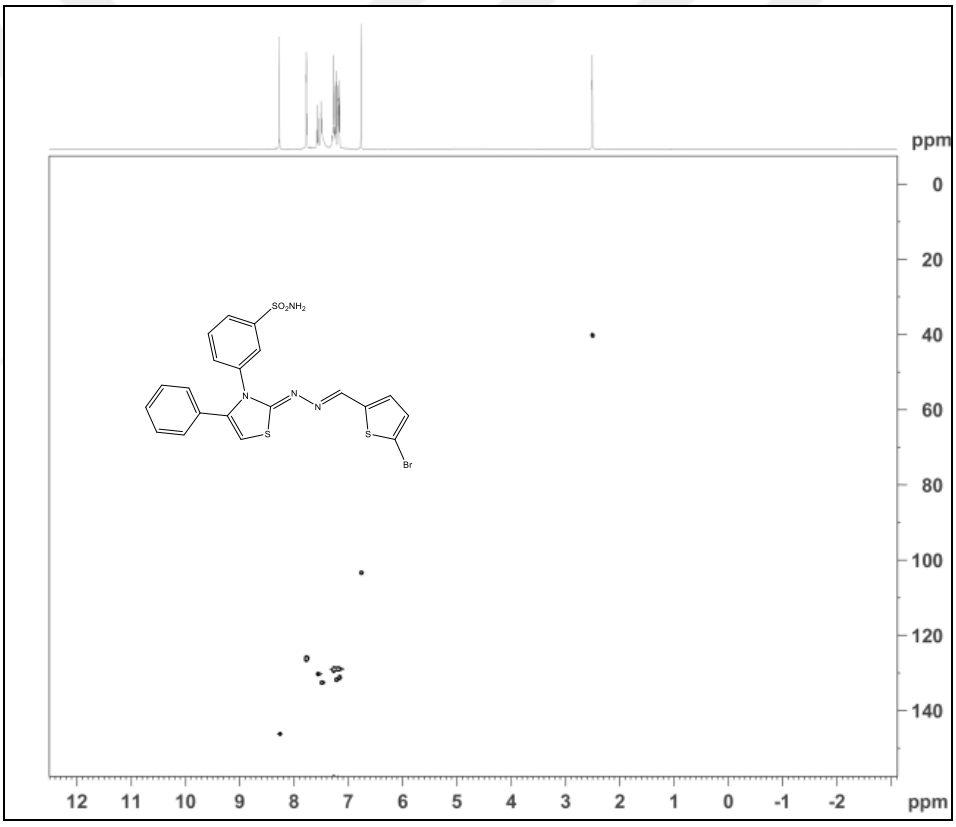

Figure 4-101: HSQC spectrum of compound 4b

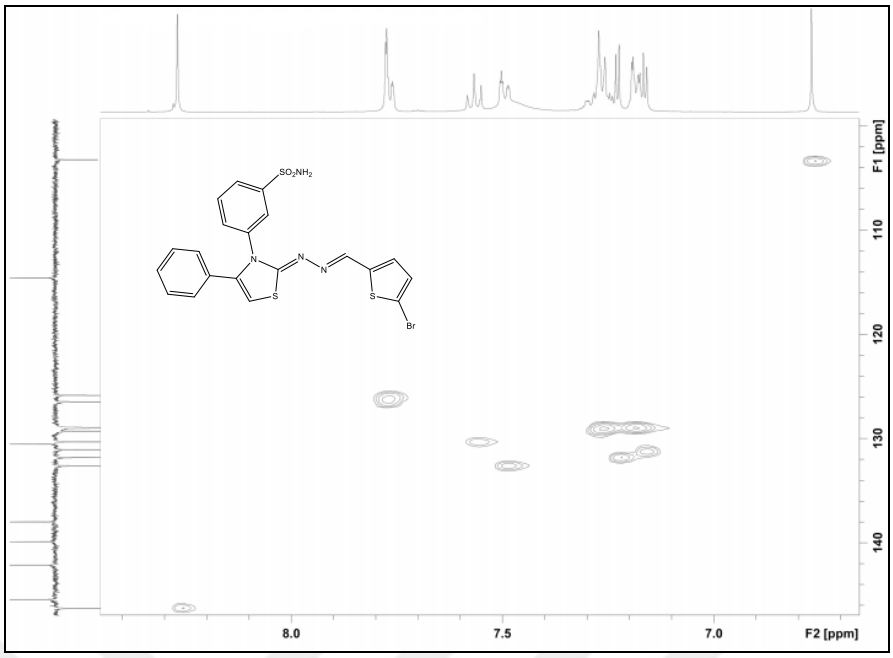

Figure 4-102: HSQC spectrum of compound 4b (6.7 – 8.5 ppm; 100 – 150 ppm)

LC-MS Spectrum

m/z ESI (positive): 520.9 $(M+2+H)^+$; $C_{20}H_{15}BrN_4O_2S_3$ (MA= 519.457; Exact Mass= 517.95)

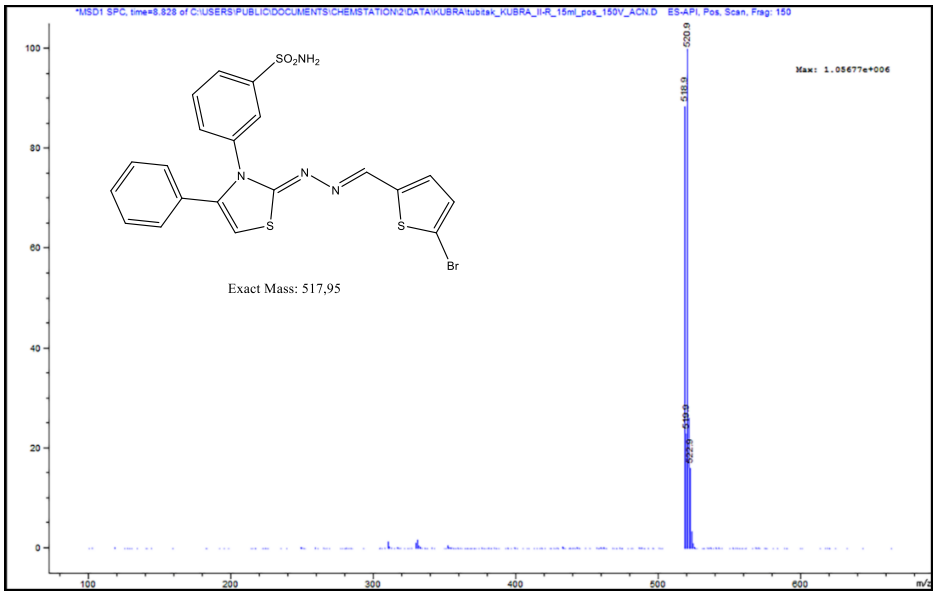

Figure 4-103: Mass spectrum of compound 4b

4.3.2.3. 3-((*Z*)-2-(((*E*)-(1*H*-pyrrol-2-yl)methylene)hydrazineylidene)-4-phenylthiazol-3(2*H*)-yl)benzenesulfonamide (4c)

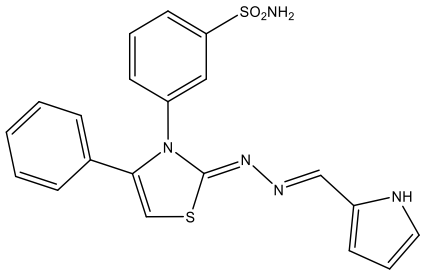

0.0022 mol (0.44g) of 2-bromo-1-phenylethan-1-one (**3a**) and 0.0022 mol (0.7g) of 2-((1*H*-pyrrol-2-yl)methylene)-*N*-(3-sulfamoylphenyl)hydrazine-1-carbothioamide (**E3**) are suspended in chloroform-ethanol (2:1). The reaction mixture is heated under reflux for 6 hours. The solid product formed is filtered and purified by recrystallization from ethanol.

Physical appearance	: Dark green powder
Yield (%)	: 56
Retention factor	: 0.62; Chloroform : Methanol (9:1)
Melting point (ºC)	: 245.2 - 246.4

Elemental Analysis

Molecular formula	: $C_{20}H_{17}N_5O_2S_2$
Molecular weight (g/mol)	: 423.511

Element	C	H	N	S
Calculated (%)	56.72	4.05	16.54	15.14
Found (%)	56.50	3.72	16.10	15.61

Spectral Analysis

Fourier Transform Infrared (FT-IR) Spectrum

IR(KBr): υ 3464, 3421, 3365 (NH s.b); 3132, 3089, 3059 (Ar.C-H s.b., =CH s.b); 1612, 1602, 1593, 1583 (Ar. C=C s.b, C=N s.b, N-H b.b); 1323, 1149 (S=O s.b); 1305 (C-N s.b); 744, 688 (monosubs. Ar-C-H b.b); 881, 752, 700 (1,3-disubs. Ar-C-H b.b)

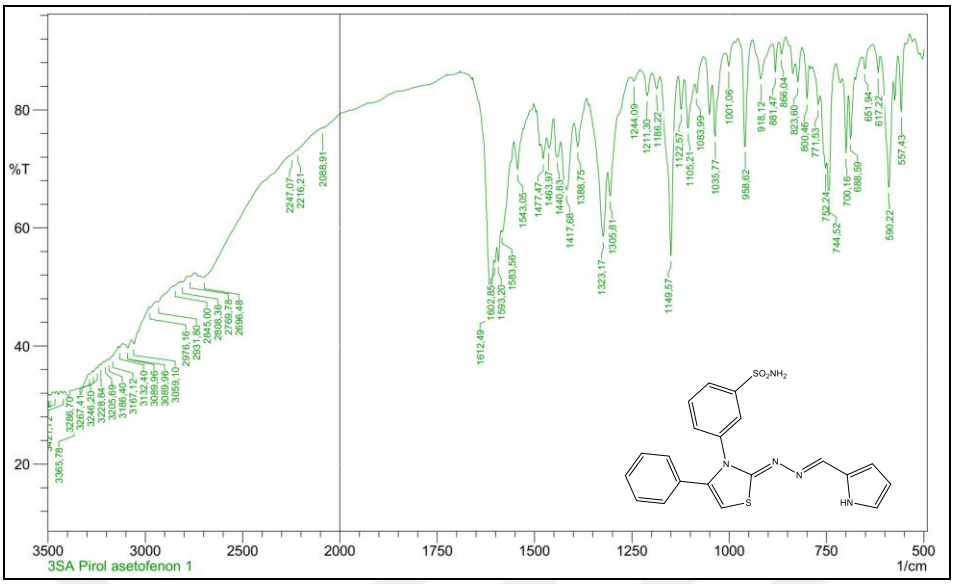

Figure 4-104: IR spectrum of compound 4c

^{1}H-NMR Spectrum

^{1}H NMR (DMSO-d_6 / 500 MHz δ (ppm): 6.15 (1H, dt, J=3.6, 2.4 Hz, pyrrole C_4-H), 6.45-6.53 (1H, m, pyrrole C_3-H), 6.91 (1H, s, thiazole C_5-H), 6.98 (1H, d, J=1.5 Hz, pyrrole C_5-H), 7.19 (2H, dd, J=8., 1.7 Hz, phenyl $C_{2,6}$-H), 7.25-7.31 (3H, m, phenyl $C_{3,4,5}$-H), 7.49 (2H, broad s, -SO_2NH_2), 7.56 (1H, d, J=8.3 Hz, benzenesulfonamide C_4-H), 7.61 (1H, t, J=7.8 Hz, benzenesulfonamide C_5-H), 7.81 (1H, dt, J=7.7, 1.5 Hz, benzenesulfonamide C_6-H), 7.89 (1H, s, benzenesulfonamide C_2-H), 8.07 (1H, s, N=CH), 11.39 (1H, s, pyrrole NH).

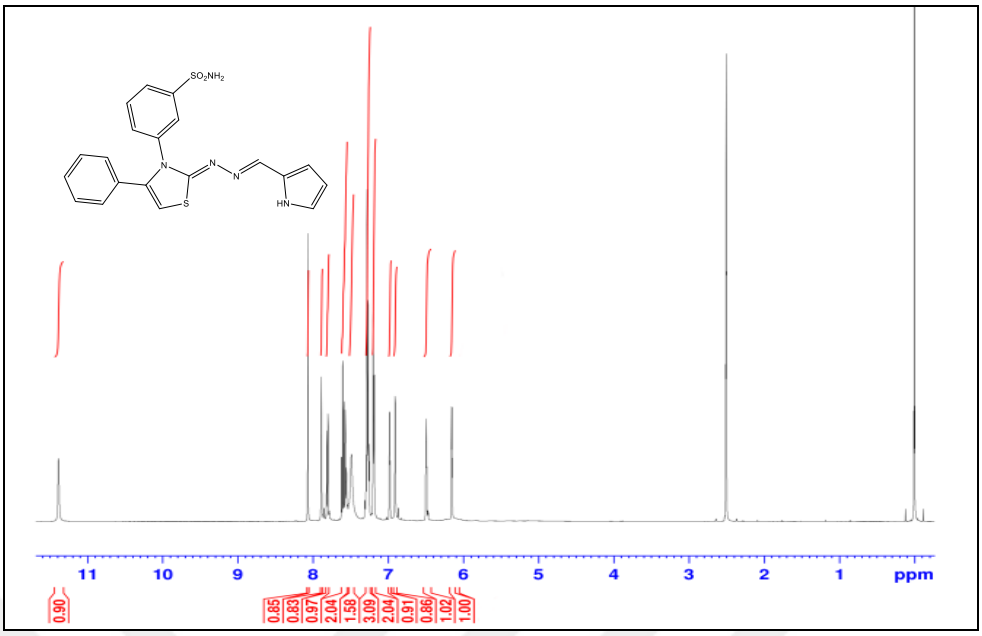

Figure 4-105: ^{1}H-NMR spectrum of compound 4c (0 – 11.5 ppm)

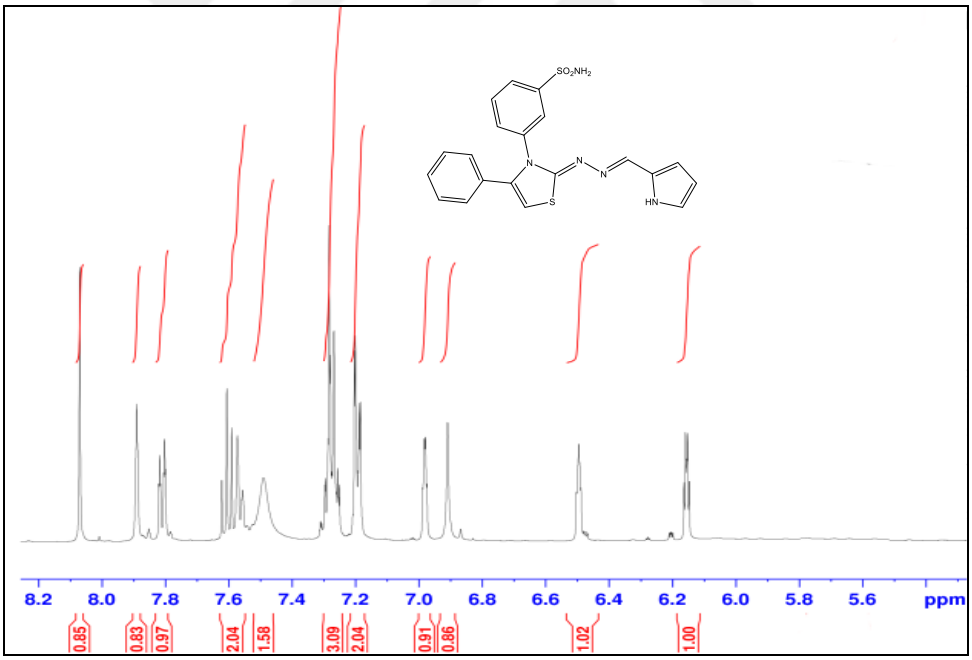

Figure 4-106: ^{1}H-NMR spectrum of compound 4c (5.4 – 8.2 ppm)

^{13}C-NMR Spectrum

^{13}C NMR (decoupled, DMSO-d_6, 100 MHz) δ (ppm): 103.3 (thiazole C_5), 109.0 (pyrrole C_4), 113.2 (pyrrole C_3), 122.4 (pyrrole C_5), 131.5 (pyrrole C_2), 125.4, 126.3 (3-

benzenesulfonamide $C_{2,6}$), 127.8, 127.9, 128.0 (phenyl $C_{2,3,4,5,6}$), 128.3 (3-benzenesulfonamide C_5), 129.0 (3-benzenesulfonamide C_4), 129.5 (phenyl C_1), 136.0 (3-benzenesulfonamide C_3), 144.0 (thiazole C_4), 144.5 (N=CH), 166.6 (thiazole C_2).

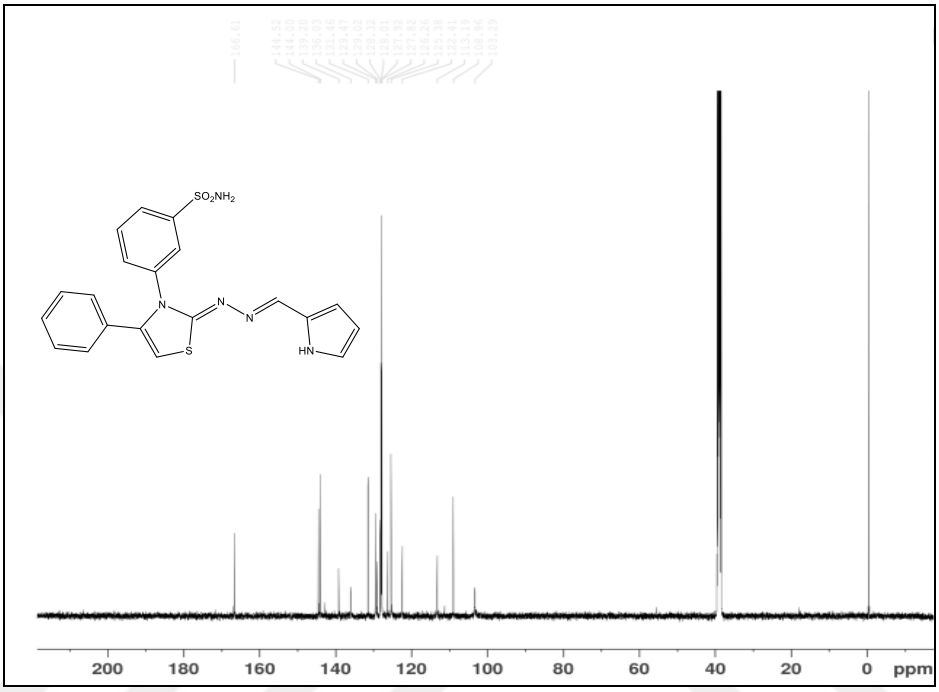

Figure 4-107: ^{13}C-NMR spectrum of compound 4c (0 – 200 ppm)

^{13}C NMR (HSQC-2D, DMSO-*d*$_6$, 100 MHz) δ (ppm): **103.3** [thiazole C_5 - **6.91** (1H, s, thiazole C_5-H)], **109.0** [pyrrole C_4 - **6.15** (1H, dt, *J*=3.60, 2.40 Hz, pyrrole C_4-H)], **113.2** [pyrrole C_3 - **6.45-6.53** (1H, m, pyrrole C_3-H)], **125.4, 126.3** [3-benzenesulfonamide $C_{2,6}$ - **7.81** (1H, dt, *J*=7.7, 1.5 Hz, benzenesulfonamide C_6-H) and **7.89** (1H, s, benzenesulfonamide C_2-H)], **127.8, 127.9, 128.0** [phenyl $C_{2,3,4,5,6}$ - **7.19** (2H, dd, *J*=8.0, 1.7 Hz, phenyl $C_{2,6}$-H) and **7.25-7.31** (3H, m, phenyl $C_{3,4,5}$-H)], **128.3** [3-benzenesulfonamide C_5 - **7.61** (1H, t, *J*=7.8 Hz, benzenesulfonamide C_5-H)], **129.0** [3-benzenesulfonamide C_4 - **7.56** (1H, d, *J*=8.3 Hz, benzenesulfonamide C_4-H)], **144.5** [N=CH - **8.07** (1H, s, N=CH)].

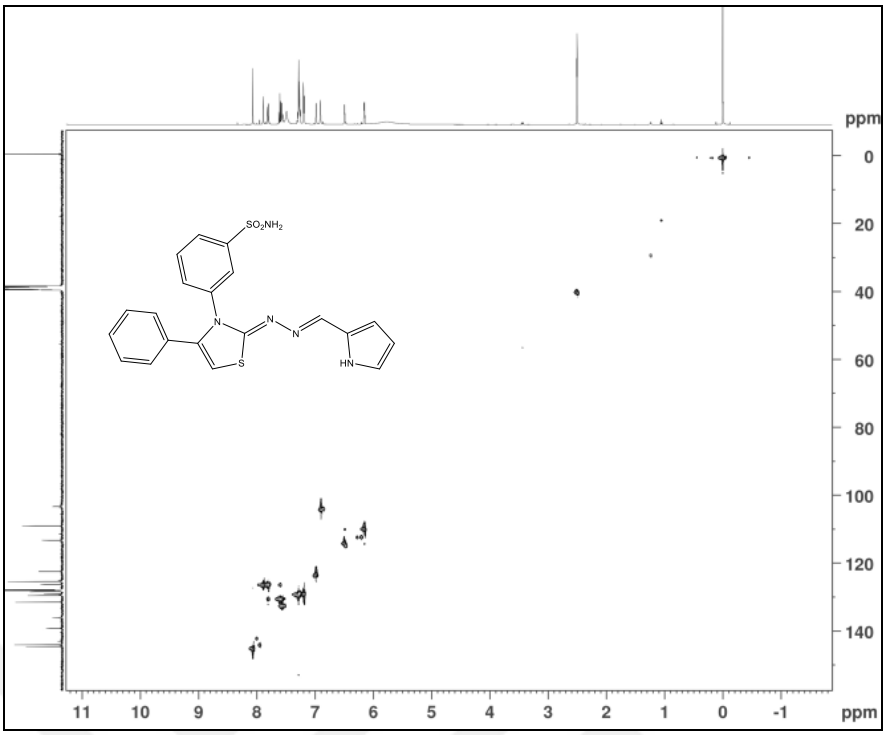

Figure 4-108: HSQC spectrum of compound 4c (-1 – 11 ppm; 0 – 140 ppm)

LC-MS Spectrum

m/z ESI (positive): 424.0 $(M+H)^+$; $C_{20}H_{17}N_5O_2S_2$ (MA= 423.511; Exact Mass= 423.08)

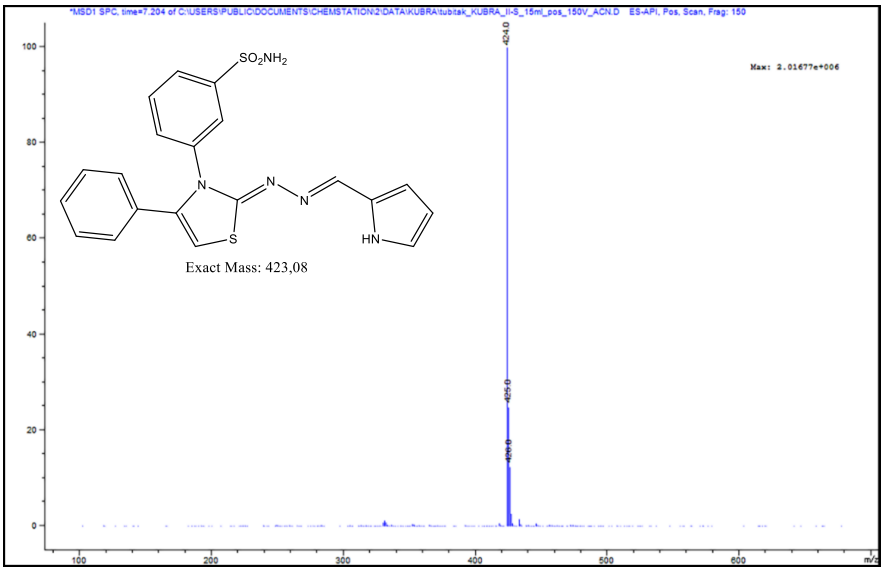

Figure 4-109: Mass spectrum of compound 4c

4.3.2.4. 3-((*Z*)-2-(((*E*)-(1-methyl-1*H*-pyrrol-2-yl)methylene)hydrazineylidene)-4-phenylthiazol-3(2*H*)-yl)benzenesulfonamide (4d)

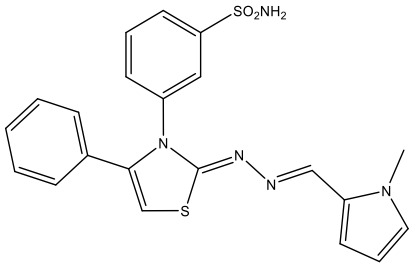

0.0021 mol (0.42g) of 2-bromo-1-phenylethan-1-one (**3a**) and 0.0021 mol (0.7g) of 2-((1-methyl-1*H*-pyrrol-2-yl)methylene)-*N*-(3-sulfamoylphenyl)hydrazine-1-carbothioamide (**E4**) are suspended in chloroform-ethanol (2:1). The reaction mixture is heated under reflux for 6 hours. The solid product formed is filtered and purified by recrystallization from ethanol.

Physical appearance	: Dark green powder
Yield (%)	: 61
Retention factor	: 0.70; Chloroform: Methanol (9:1)
Melting point (ºC)	: 247.0 - 249.9

Elemental Analysis

Molecular formula	: $C_{21}H_{19}N_5O_2S_2$
Molecular weight (g/mol)	: 437.537

Element	C	H	N	S
Calculated (%)	57.65	4.38	16.01	14.66
Found (%)	57.53	4.04	15.86	14.46

Spectral Analysis

Fourier Transform Infrared (FT-IR) Spectrum

IR(KBr): υ 3255 (NH s.b); 3130, 3099, 3064 (Ar.C-H s.b., =CH s.b); 2949, 2856 (Al.

C-H s.b.); 1602, 1589, 1560 (Ar. C=C s.b, C=N s.b, N-H b.b); 1425, 1364 (Al.C-H b.b.); 1346, 1161 (S=O s.b); 1307 (C-N s.b); 756, 696 (monosubs. Ar-C-H b.b); 864, 773, 696 (1,3-disubs. Ar-C-H b.b)

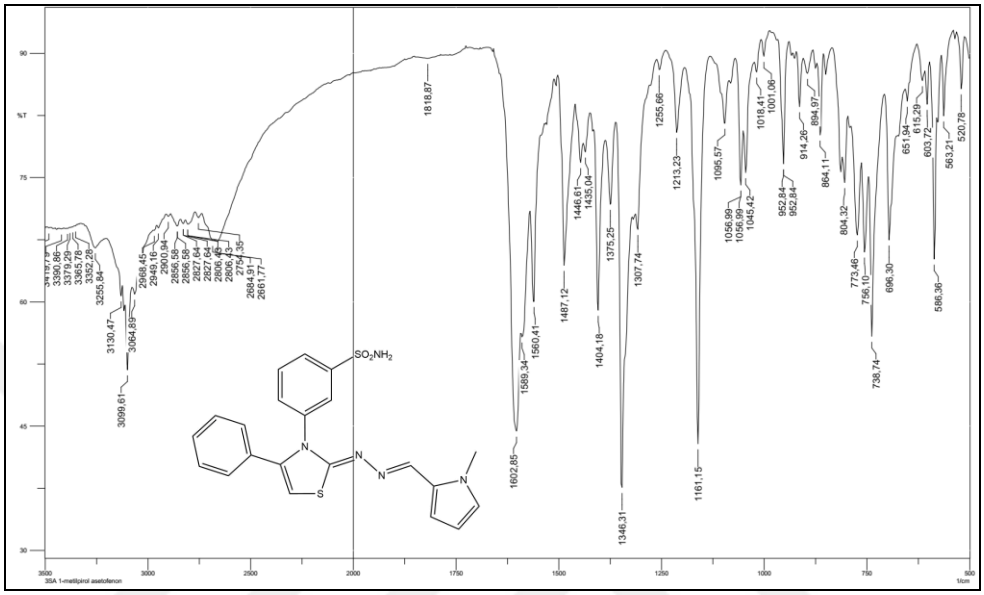

Figure 4-110: IR spectrum of compound 4d

^{1}H-NMR Spectrum

^{1}H NMR (DMSO-d_6 / 500 MHz δ (ppm): 3.88 (3H, s, N-CH_3), 6.09 (1H, dd, *J*=3.8, 2.6 Hz, pyrrole C_4-H), 6.48 (1H, dd, *J*=3.8, 1.7 Hz, pyrrole C_3-H), 6.78 (1H, s, thiazole C_5-H), 6.99 (1H, t, *J*=2.1 Hz, pyrrole C_5-H), 7.19 (2H, dd, *J*=7.9, 1.8 Hz, phenyl $C_{2,6}$-H), 7.24-7.29 (3H, m, phenyl $C_{3,4,5}$-H), 7.48 (2H, broad s, -SO_2NH_2), 7.53 (1H, dt, *J*=7.9, 2.1 Hz, benzenesulfonamide C_4-H), 7.59 (1H, t, *J*=7.9 Hz, benzenesulfonamide C_5-H), 7.78 (1H, dt, *J*=7.8, 1.8 Hz, benzenesulfonamide C_6-H), 7.83 (1H, t, *J*=1.9 Hz, benzenesulfonamide C_2-H), 8.13 (1H, s, N=CH).

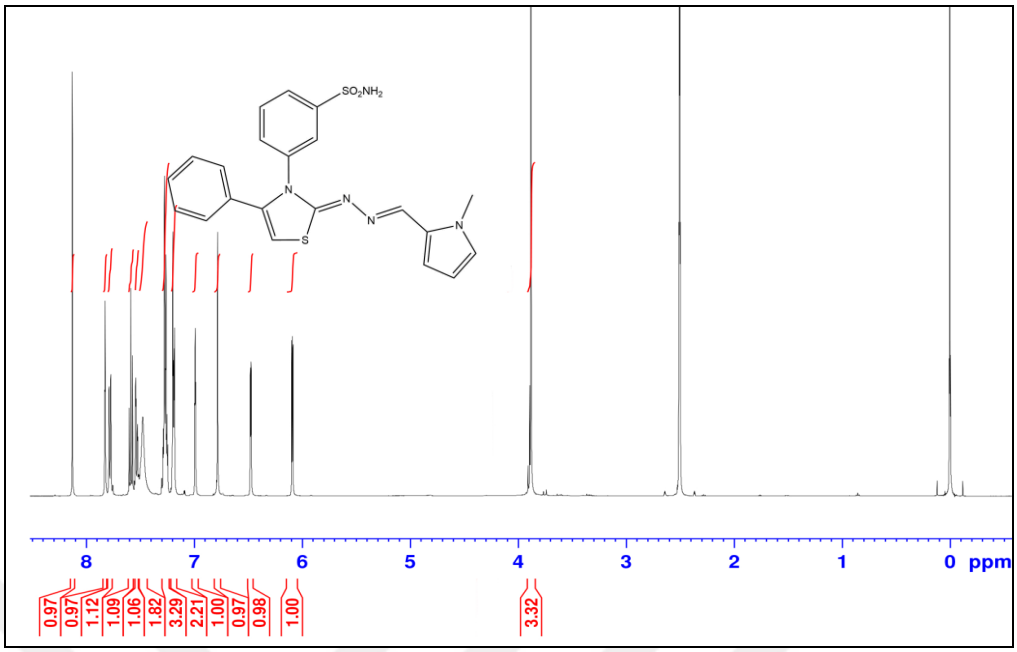

Figure 4-111: ^{1}H-NMR spectrum of compound 4d (0 – 8.5 ppm)

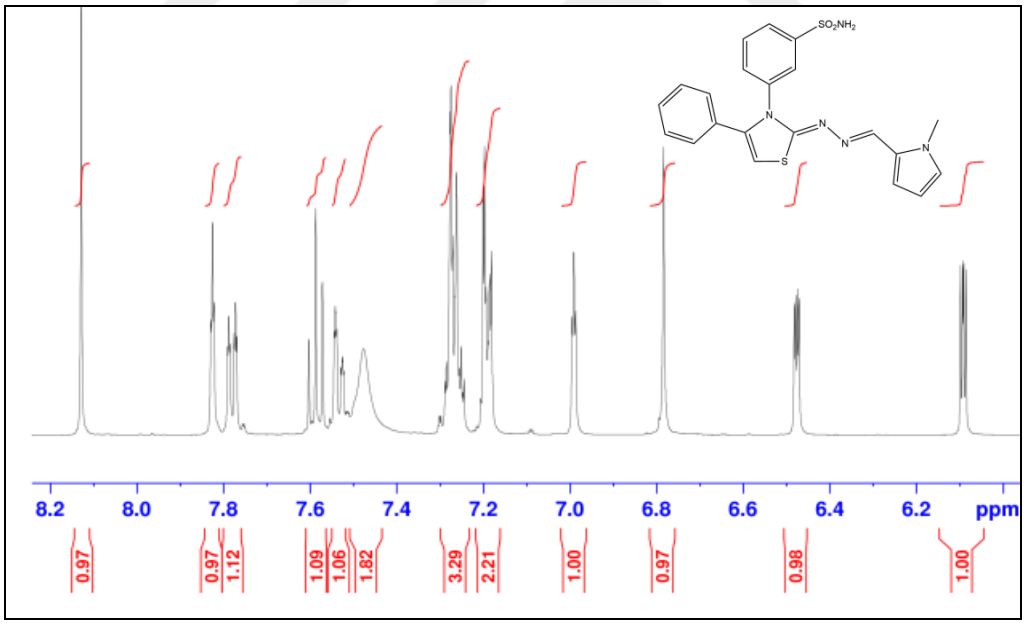

Figure 4-112: ^{1}H-NMR spectrum of compound 4d (6.2 – 8.2 ppm)

^{13}C-NMR Spectrum

^{13}C NMR (decoupled, DMSO-d_6, 100 MHz) δ (ppm): 35.9 (CH_3), 101.9 (thiazole C_5), 107.6 (pyrrole C_4), 114.8 (pyrrole C_3), 124.6 (pyrrole C_5), 127.7, 127.8, 128.1 (phenyl $C_{2,3,4,5,6}$), 125.3, 126.9 (3-benzenesulfonamide $C_{2,6}$), 129.2 (3-benzenesulfonamide C_5),

129.5 (3-benzenesulfonamide C_4 / phenyl C_1), 137.0 (3-benzenesulfonamide C_3), 144.3 (thiazole C_4), 144.5 (N=CH), 167.0 (thiazole C_2).

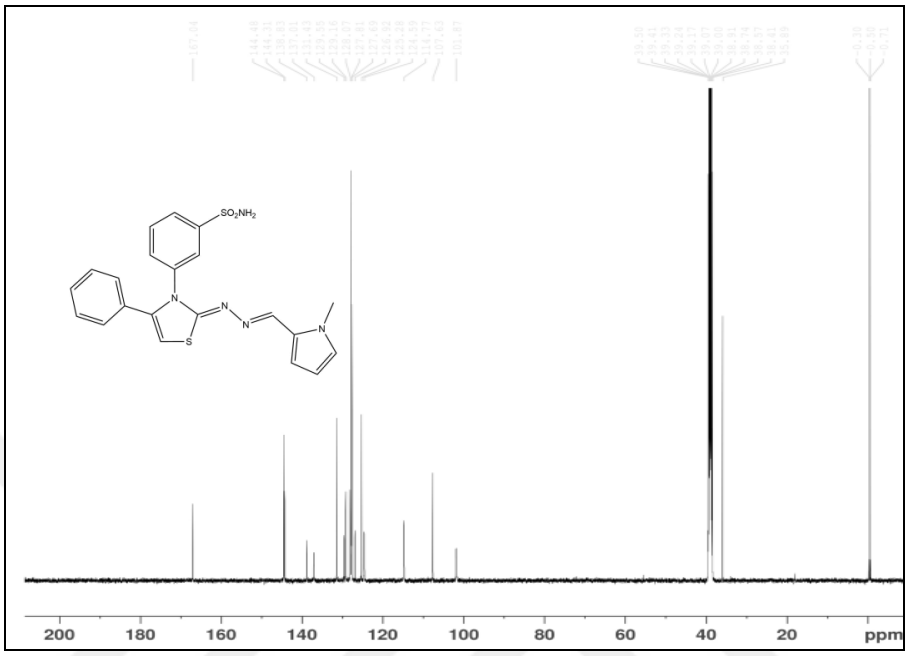

Figure 4-113: ^{13}C-NMR spectrum of compound 4d (0 – 200 ppm)

LC-MS Spectrum

m/z ESI (positive): 438.0 $(M+H)^+$; $C_{21}H_{19}N_5O_2S_2$ (MA= 437.537; Exact Mass= 437.10)

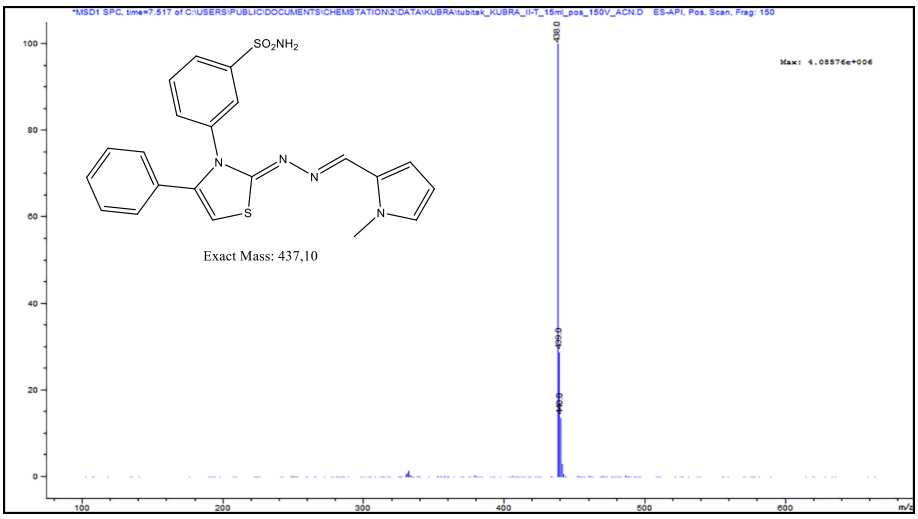

Figure 4-114: Mass spectrum of compound 4d

4.3.2.5. 3-((*Z*)-2-(((*E*)-furan-2-ylmethylene)hydrazineylidene)-4-phenylthiazol-3(2*H*)-yl)benzenesulfonamide (4e)

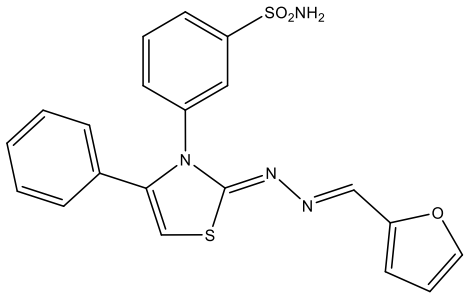

0.0018 mol (0.36g) of 2-bromo-1-phenylethan-1-one (**3a**) and 0.0018 mol (0.6g) of 2-(furan-2-ylmethylene)-*N*-(3-sulfamoylphenyl)hydrazine-1-carbothioamide (**E5**) are suspended in chloroform-ethanol (2:1). The reaction mixture is heated under reflux for 6 hours. The solid product formed is filtered and purified by recrystallization from ethanol.

Physical appearance	: Yellow powder
Yield (%)	: 98
Retention factor	: 0.67; Chloroform : Methanol (9:1)
Melting point (ºC)	: 237.4 (decompositon)

Elemental Analysis

Molecular formula	: $C_{20}H_{16}N_4O_3S_2$
Molecular weight (g/mol)	: 424.50

Element	C	H	N	S
Calculated (%)	56.59	3.80	13.20	15.11
Found (%)	56.60	3.49	13.37	14.78

Spectral Analysis

Fourier Transform Infrared (FT-IR) Spectrum

IR(KBr): υ 3263, 3226 (NH s.b); 3151, 3136, 3099, 3064 (Ar.C-H s.b., =CH s.b); 1595, 1579, 1558, 1525 (Ar. C=C s.b, C=N s.b, N-H b.b); 1350, 1168 (S=O s.b); 1330 (C-N s.b); 748, 688 (monosubs. Ar-C-H b.b); 885, 759, 700 (1,3-disubs. Ar-C-H b.b)

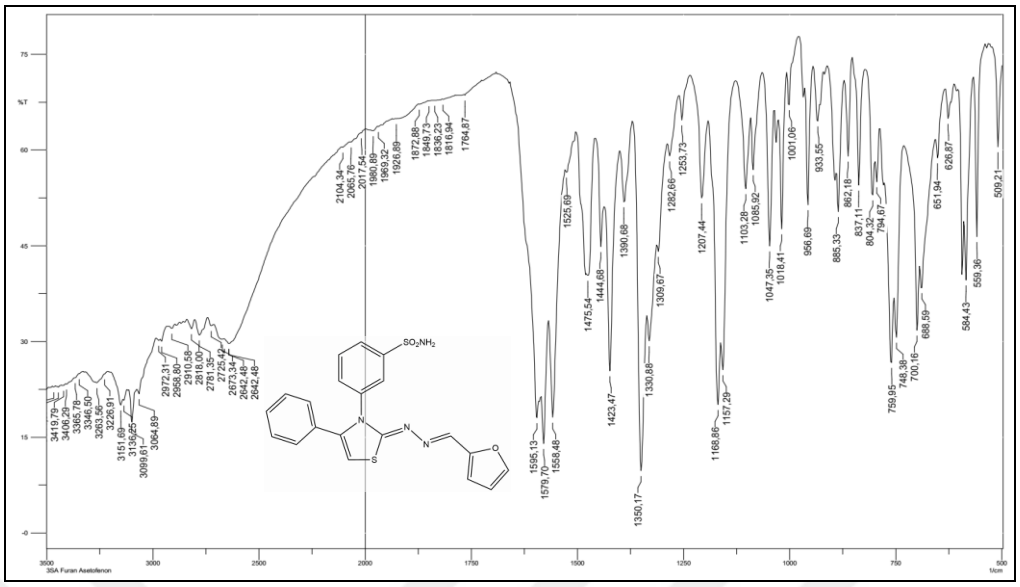

Figure 4-115: IR spectrum of compound 4e

^{1}H-NMR Spectrum

^{1}H NMR (DMSO-d_6 / 500 MHz δ (ppm): 6.61 (1H, dd, J=3.4, 1.8 Hz, furan C_4-H), 6.75 (1H, s, thiazole C_5-H), 6.81 (1H, d, J=2.7 Hz, furan C_3-H), 7.19 (2H, dd, J=7.8, 1.8 Hz, phenyl $C_{2,6}$-H), 7.25-7.30 (3H, m, phenyl $C_{3,4,5}$-H), 7.46 (2H, broad s, -SO_2NH_2), 7.49 (1H, ddd, J=7.9, 2.2, 1.2 Hz, benzenesulfonamide C_4-H), 7.56 (1H, t, J=7.8 Hz, benzenesulfonamide C_5-H), 7.76 (1H, dt, J=7.8, 1.5 Hz, benzenesulfonamide C_6-H), 7.78 (1H, t, J=1.9 Hz, benzenesulfonamide C_2-H), 7.82 (1H, d, J=1.3 Hz, furan C_5-H), 8.04 (1H, s, N=CH).

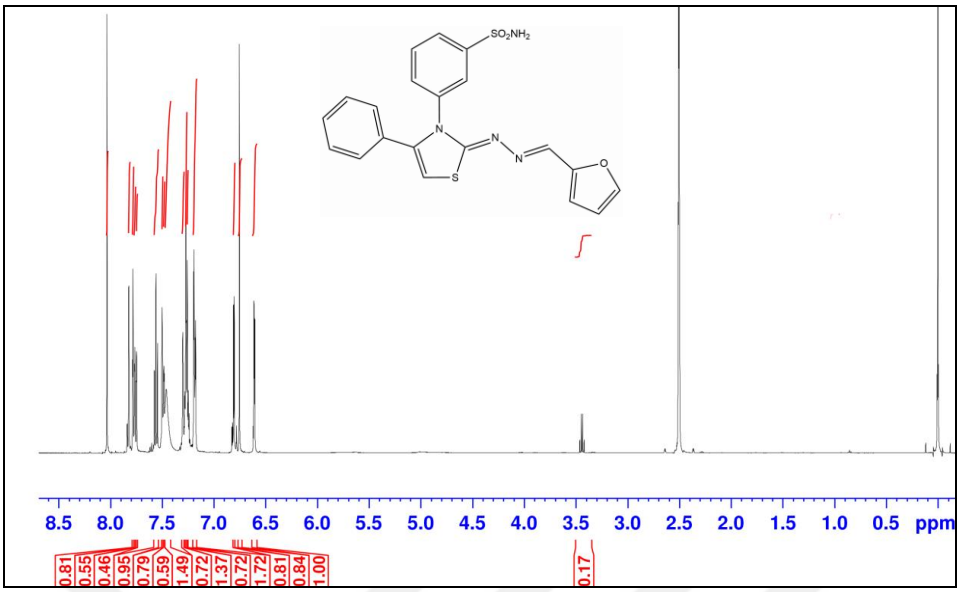

Figure 4-116: ^{1}H-NMR spectrum of compound 4e (0 – 8.5 ppm)

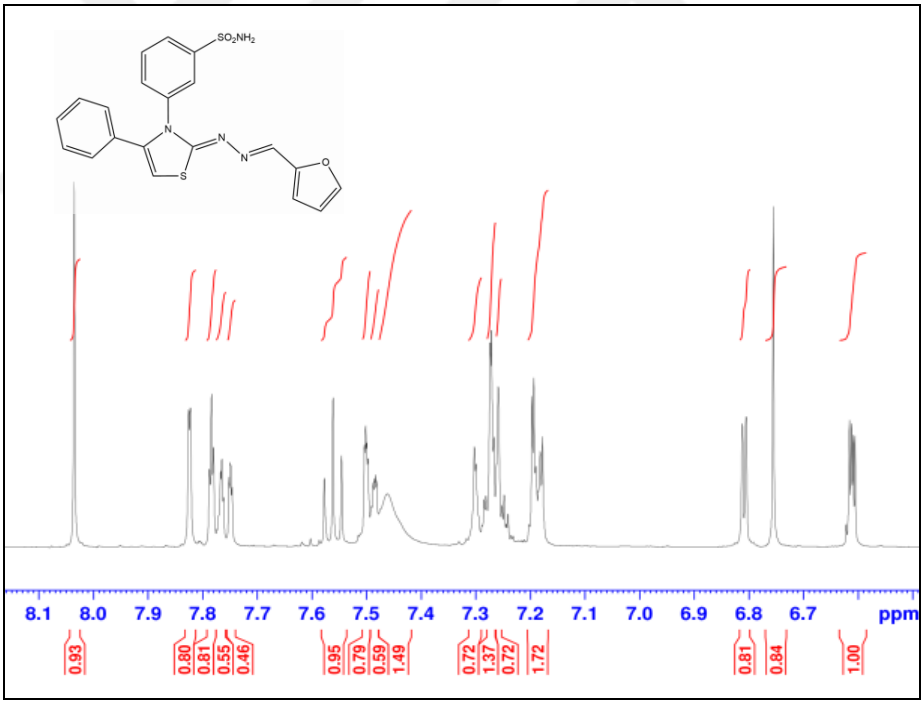

Figure 4-117: ^{1}H-NMR spectrum of compound 4e (6.5 – 8.1 ppm)

^{13}C-NMR Spectrum

^{13}C NMR (decoupled, DMSO-d_6, 100 MHz) δ (ppm): 103.1 (thiazole C_5), 112.2 (furan C_4), 114.1 (furan C_3), 149.6 (furan C_2), 125.5 (3-benzenesulfonamide C_6), 126.0 (furan

C_5, 3-benzenesulfonamide C_2), 128.4, 128.5, 128.8 (phenyl $C_{2,3,4,5,6}$), 129.8 (3-benzenesulfonamide C_5), 132.1 (3-benzenesulfonamide C_4), 137.1 (phenyl C_1), 139.5 (3-benzenesulfonamide C_3), 141.7 (N=CH), 145.0 (3-benzenesulfonamide C_1), 145.2 (thiazole C_4), 169.3 (thiazole C_2).

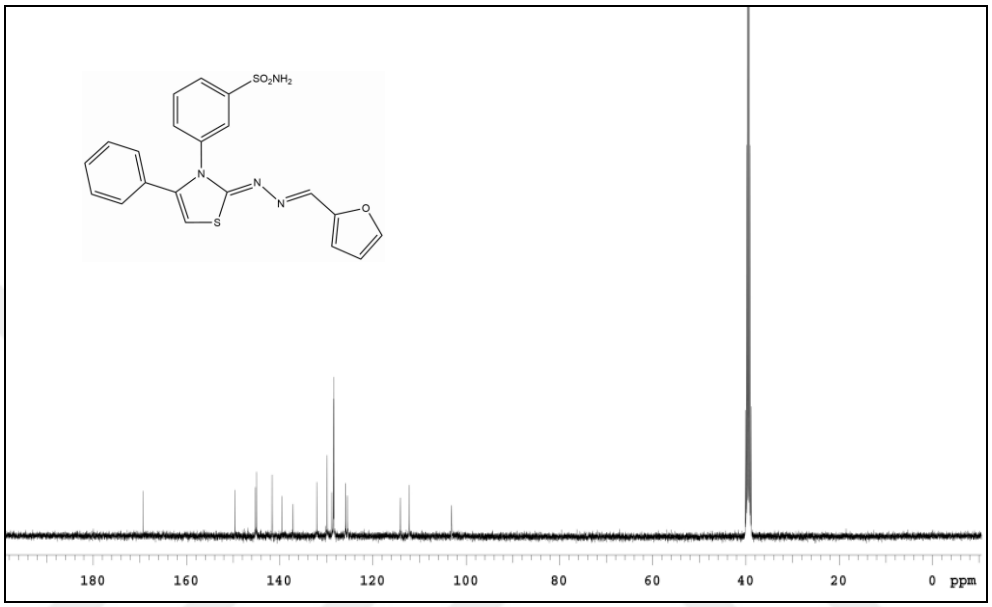

Figure 4-118: ^{13}C-NMR spectrum of compound 4e (0 – 200 ppm)

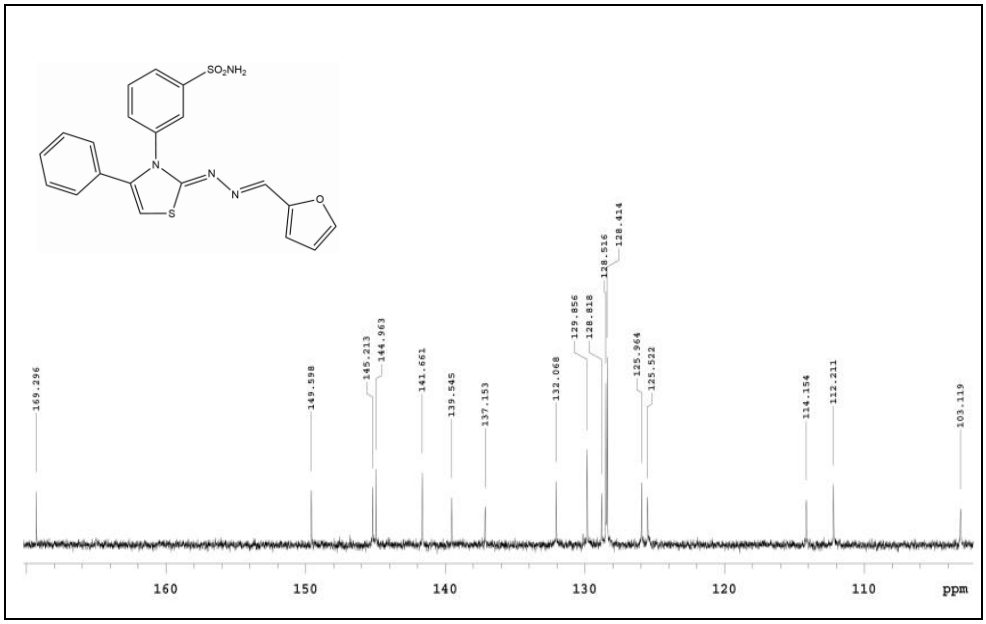

Figure 4-119: ^{13}C-NMR spectrum of compound 4e (103 – 170 ppm)

^{13}C NMR (HSQC-2D, DMSO-d_6, 100 MHz) δ (ppm): **103.1** [thiazole C_5 - **6.75** (1H, s, thiazole C_5-H)], **112.2** [furan C_4 - **6.61** (1H, dd, *J*=3.4, 1.8 Hz, furan C_4-H)], **114.1** [furan C_3 - **6.81** (1H, d, *J*=2.7 Hz, furan C_3-H)], **125.5** [3-benzenesulfonamide C_6 - **7.76** (1H, dt, *J*=7.8, 1.5 Hz, benzenesulfonamide C_6-H)], **126.0** [furan C_5, 3-benzenesulfonamide C_2 - **7.82** (1H, d, *J*=1.3 Hz, furan C_5-H), **7.78** (1H, t, *J*=1.9 Hz, benzenesulfonamide C_2-H)], **128.4, 128.5, 128.8** [phenyl $C_{2,3,4,5,6}$ - **7.25-7.30** (3H, m, phenyl $C_{3,4,5}$-H), **7.19** (2H, dd, *J*=7.8, 1.8 Hz, phenyl $C_{2,6}$-H)], **129.8** [3-benzenesulfonamide C_5 - **7.56** (1H, t, *J*=7.8 Hz, benzenesulfonamide C_5-H)], **132.1** [3-benzenesulfonamide C_4 - **7.49** (1H, ddd, *J*=7.9, 2.2, 1.2 Hz, benzenesulfonamide C_4-H)], **141.7** [N=CH - **8.04** (1H, s, N=CH)].

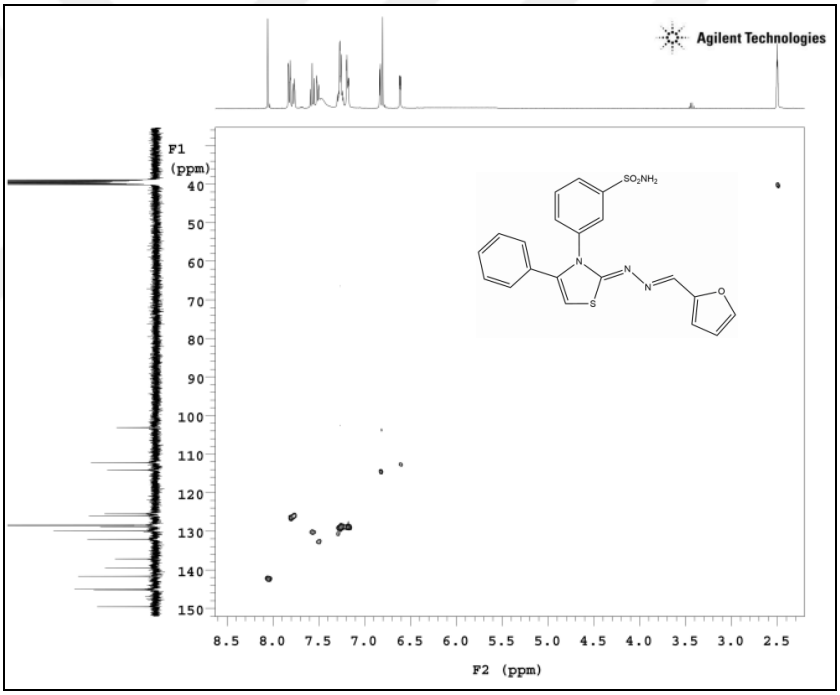

Figure 4-120: HSQC spectrum of compound 4e (2.5 – 8.5; 30 – 150 ppm)

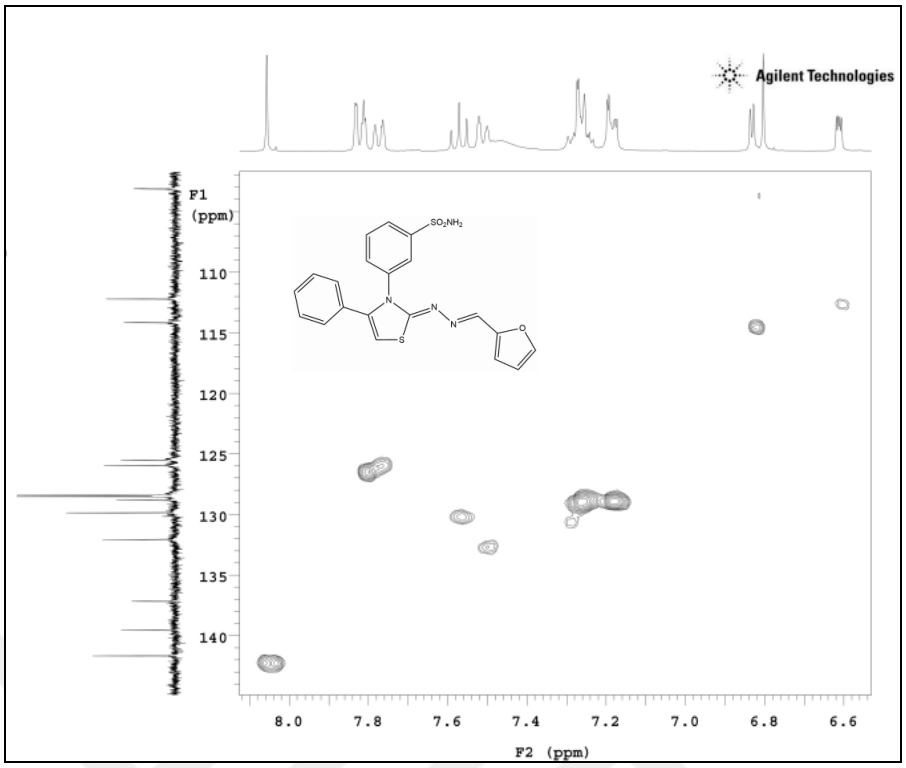

Figure 4-121: HSQC spectrum of compound 4e (6.6 – 8.2; 100 – 145 ppm)

LC-MS Spectrum

m/z ESI (positive): 425.0 $(M+H)^+$; $C_{20}H_{16}N_4O_3S_2$ (MA= 424.496; Exact Mass= 424.07)

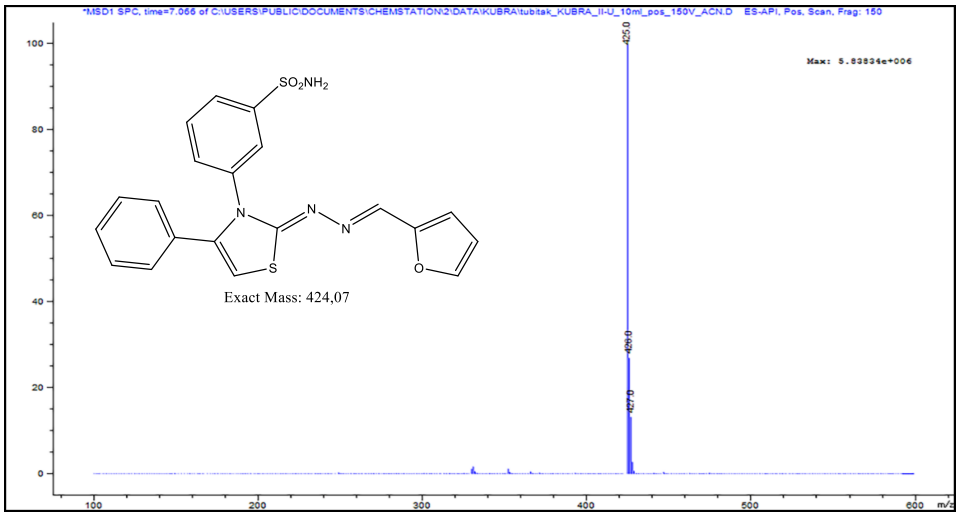

Figure 4-122: Mass spectrum of compound 4e

4.3.2.6. 4-((*Z*)-2-(((*E*)-(1*H*-pyrrol-2-yl)methylene)hydrazineylidene)-4-phenylthiazol-3(2*H*)-yl)benzenesulfonamide (4f)

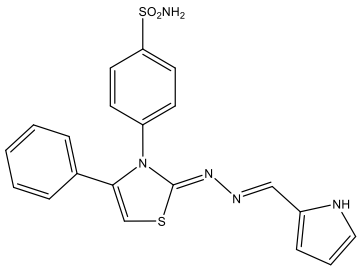

0.0015 mol (0.3g) of 2-bromo-1-phenylethan-1-one (**3a**) and 0.0015 mol (0.5g) of 2-((1*H*-pyrrol-2-yl)methylene)-*N*-(4-sulfamoylphenyl)hydrazine-1-carbothioamide (**E6**) are suspended in chloroform-ethanol (2:1). The reaction mixture is heated under reflux for 6 hours. The solid product formed is filtered and purified by recrystallization from ethanol.

Physical appearance	: Dark green powder
Yield (%)	: 94
Retention factor	: 0.63; Chloroform: Methanol (9:1)
Melting point (ºC)	: 249.9 - 251.5

Elemental Analysis

Molecular formula	: $C_{20}H_{17}N_5O_2S_2$
Molecular weight (g/mol)	: 423.51

Element	C	H	N	S
Calculated (%)	56.72	4.05	16.54	15.14
Found (%)	56.35	3.88	16.21	14.87

Spectral Analysis

Fourier Transform Infrared (FT-IR) Spectrum

IR(KBr): υ 3444, 3321, 3265 (NH s.b); 3124, 3084, 3032 (Ar.C-H s.b., =CH s.b); 1610, 1585, 1566, 1550, 1535 (Ar. C=C s.b, C=N s.b, N-H b.b); 1325, 1155 (S=O s.b); 1317 (C-N s.b); 750, 702 (monosubs. Ar-C-H b.b); 829 (1,4-disubs. Ar-C-H b.b)

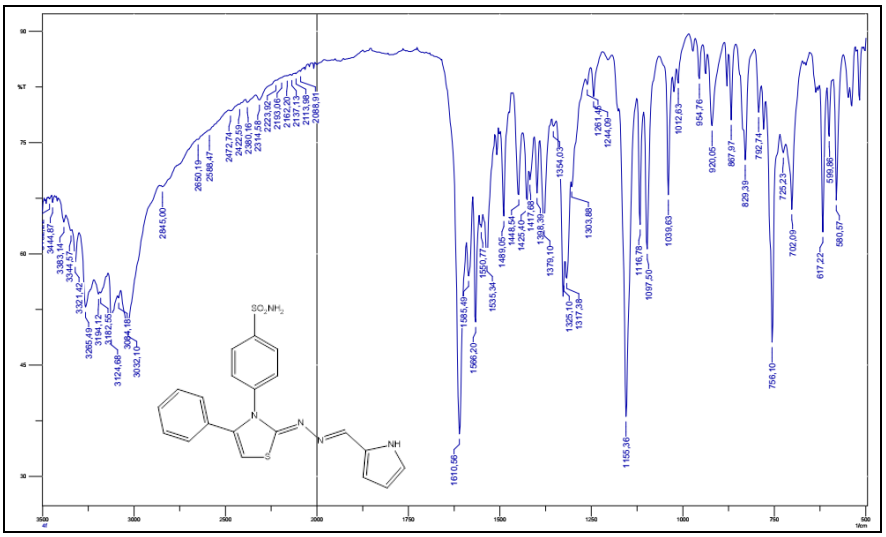

Figure 4-123: IR spectrum of compound 4f

^{1}H-NMR Spectrum

^{1}H NMR (DMSO-d_6 / 400 MHz δ (ppm): 6.14 (1H, d, J=3.1 Hz, pyrrole C_4-H), 6.48 (1H, s, pyrrole C_3-H), 6.89 (1H, s, thiazole C_5-H), 6.97 (1H, s, pyrrole C_5-H), 7.19-7.21 (2H, m, phenyl $C_{2,6}$-H), 7.27-7.29 (3H, m, phenyl $C_{3,5}$-H), 7.50 (2H, broad s, -SO_2NH_2), 7.57 (2H, d, J=8.2 Hz, 4-benzenesulfonamide $C_{3,5}$-H), 7.82 (2H, d, J=8.6 Hz, 4-benzenesulfonamide $C_{2,6}$-H), 8.06 (1H, s, N=CH), 11.38 (1H, s, pyrrole NH).

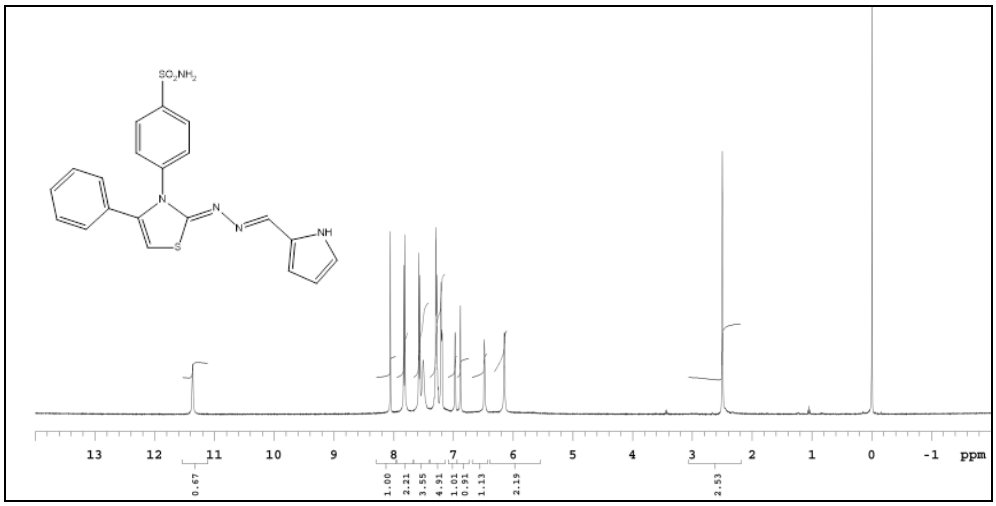

Figure 4-124: ^{1}H-NMR spectrum of compound 4f (0 – 14 ppm)

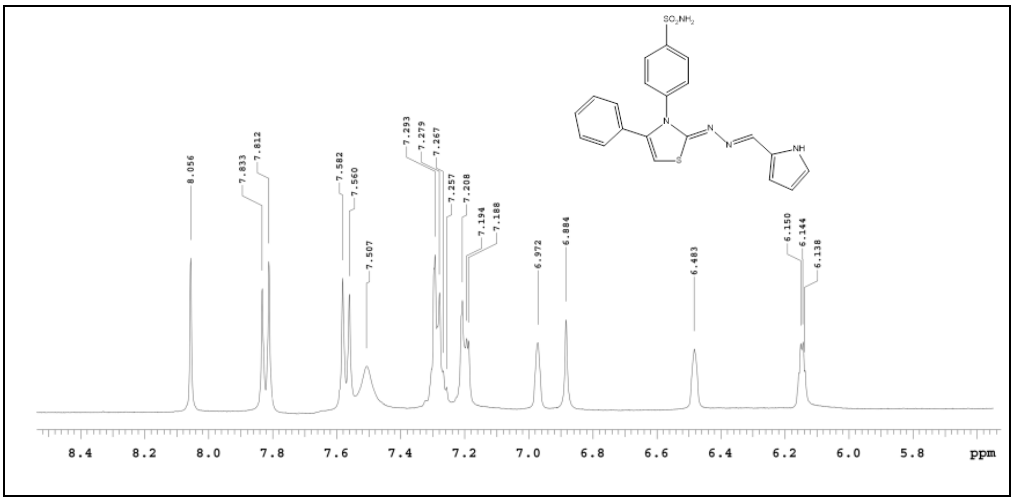

Figure 4-125: ^{1}H-NMR spectrum of compound 4f (5.8 – 8.4 ppm)

^{13}C-NMR Spectrum

^{13}C NMR (decoupled, DMSO-d_6, 125 MHz) δ (ppm): 104.7 (thiazole C_5), 110.1 (pyrrole C_4), 114.4 (pyrrole C_3), 123.6 (pyrrole C_5), 127.1, 127.6 (4-benzenesulfonamide $C_{2,6}$), 128.9, 129.0, 129.1, 129.5 (phenyl $C_{2,3,4,5,6}$), 129.8 (4-benzenesulfonamide $C_{3/5}$), 130.2 (pyrrole C_2), 136.5 (phenyl C_1), 139.4 (4-benzenesulfonamide C_4), 140.2 (4-benzenesulfonamide C_1), 144.1 (thiazole C_4), 145.1 (N=CH), 167.6 (thiazole C_2).

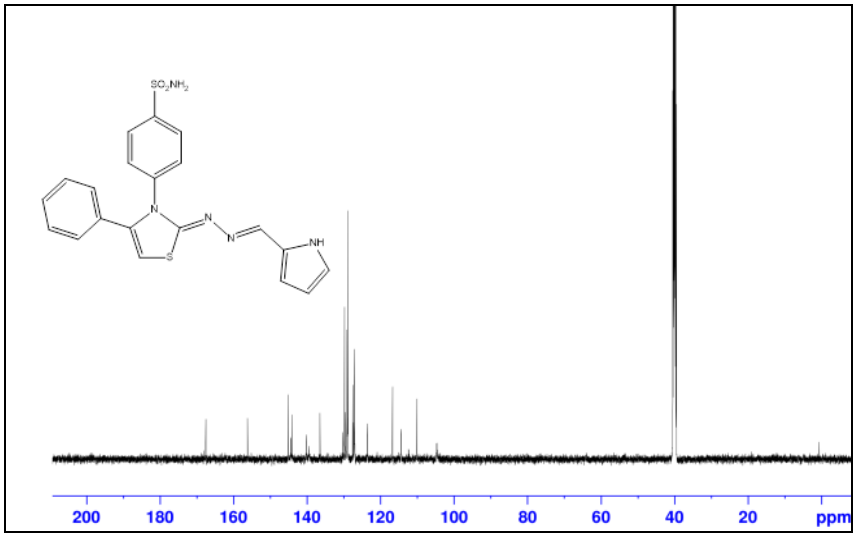

Figure 4-126: ^{13}C-NMR spectrum of compound 4f (0 – 200 ppm)

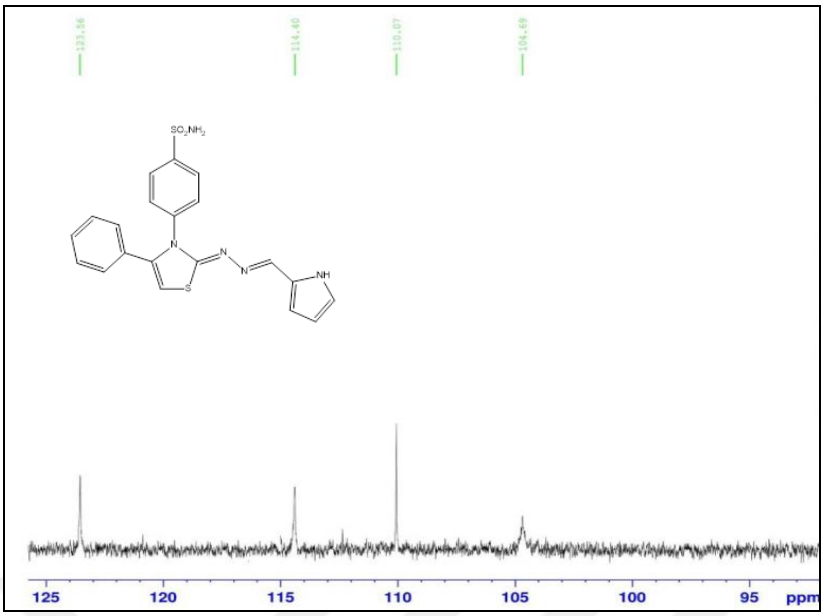

Figure 4-127: ^{13}C-NMR spectrum of compound 4f (95 – 125 ppm)

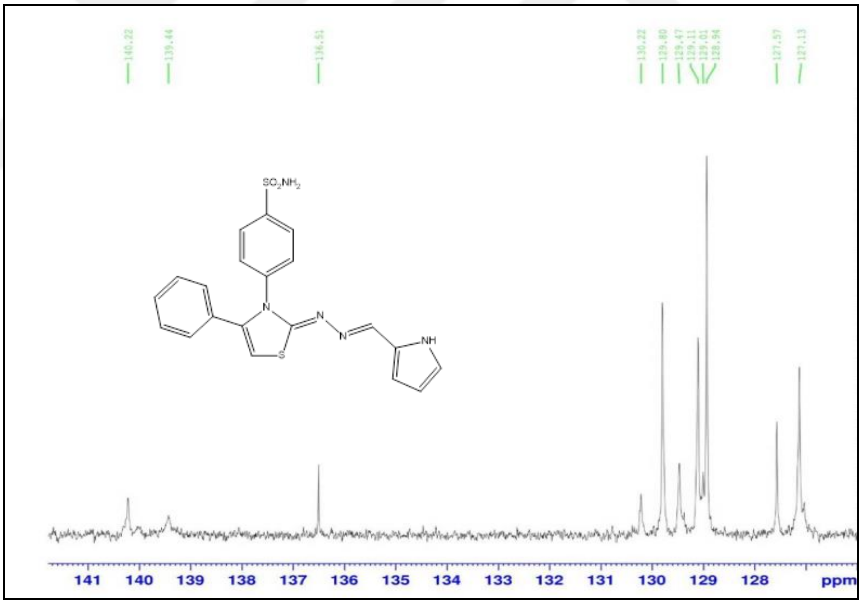

Figure 4-128: ^{13}C-NMR spectrum of compound 4f (127 – 141 ppm)

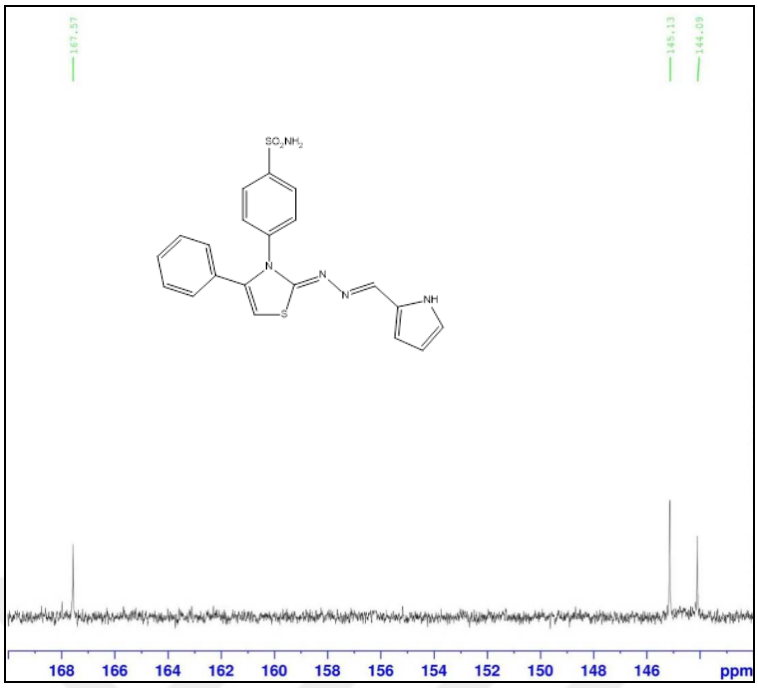

Figure 4-129: ^{13}C-NMR spectrum of compound 4f (144 – 168 ppm)

^{13}C NMR (HSQC-2D, DMSO-*d*$_6$, 125 MHz) δ (ppm): **104.7** [thiazole C_5 - **6.89** (1H, s, thiazole C_5-H)], **110.1** [pyrrole C_4 - **6.14** (1H, d, *J*=3.1 Hz, pyrrole C_4-H)], **114.4** [pyrrole C_3 - **6.48** (1H, s, pyrrole C_3-H)], **123.6** [pyrrole C_5 - **6.97** (1H, s, pyrrole C_5-H)], **127.1, 127.6** [4-benzenesulfonamide $C_{2,6}$ - **7.82** (2H, d, *J*=8.6 Hz, 4-benzenesulfonamide $C_{2,6}$-H)], **128.9**, **129.0, 129.1, 129.5** [phenyl $C_{2,3,4,5,6}$ - **7.19-7.21** (2H, m, phenyl $C_{2,6}$-H), **7.27-7.29** (3H, m, phenyl $C_{3,5}$-H)], **129.8** [4-benzenesulfonamide $C_{3/5}$ - **7.57** (2H, d, *J*=8.21 Hz, 4-benzenesulfonamide $C_{3,5}$-H)], **145.1** [N=CH - **8.06** (1H, s, N=CH)].

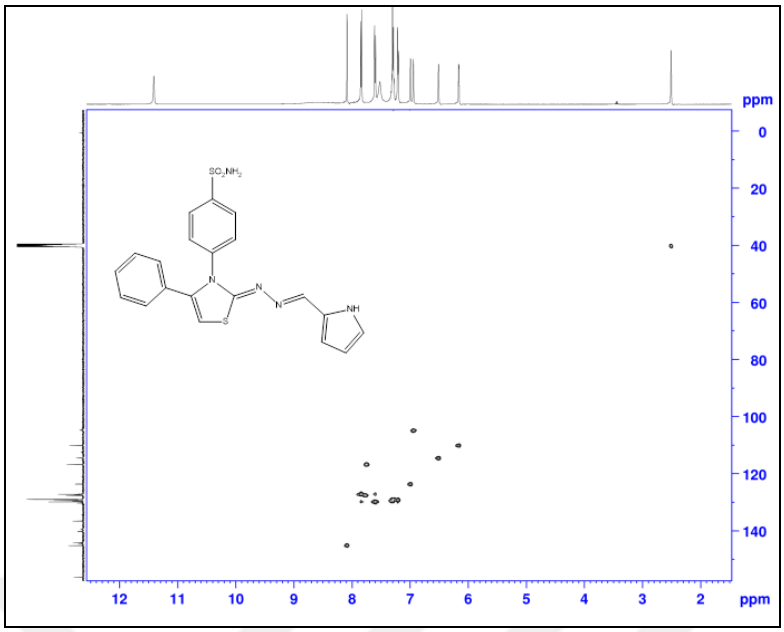

Figure 4-130: HSQC spectrum of compound 4f (2 – 12; 0 – 140 ppm)

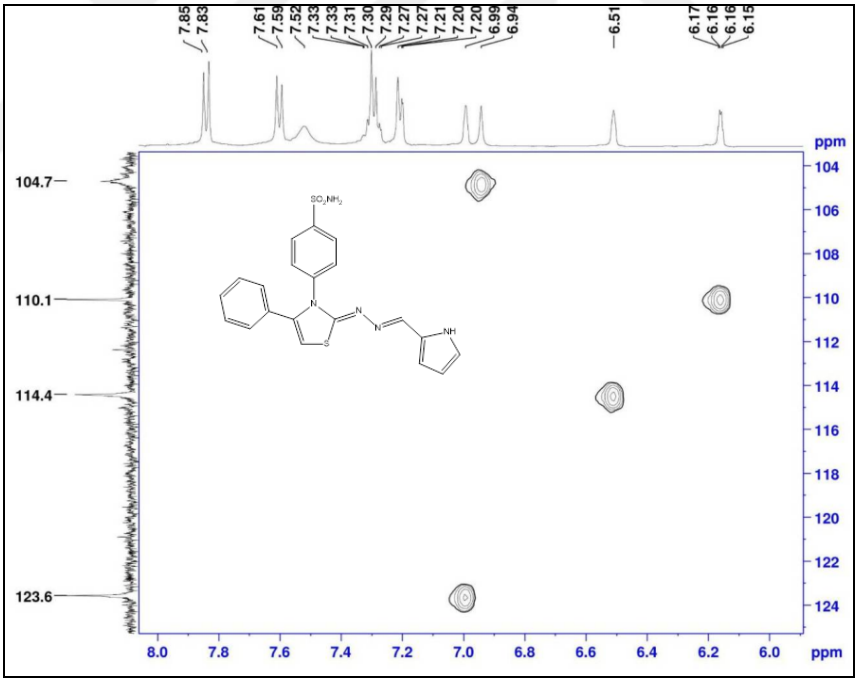

Figure 4-131: HSQC spectrum of compound 4f (6 – 8; 104 – 124 ppm)

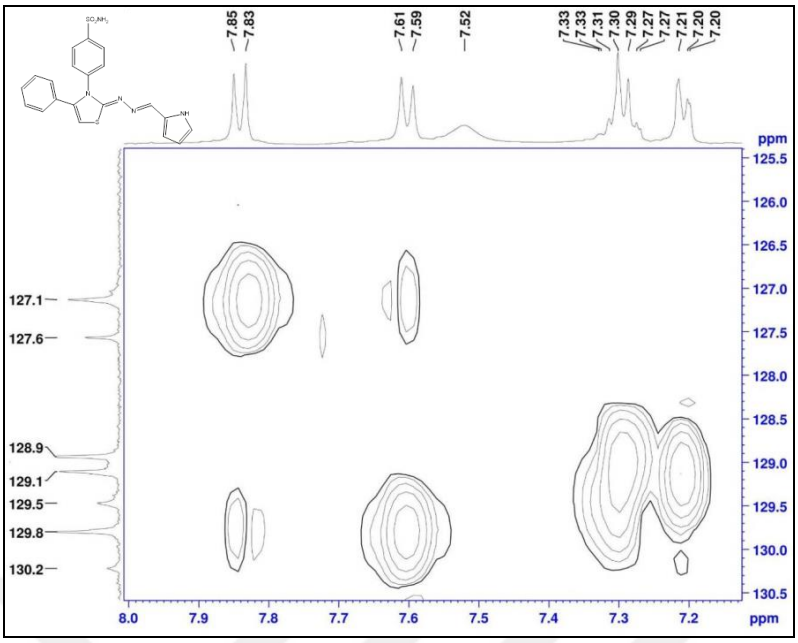

Figure 4-132: HSQC spectrum of compound 4f (6 – 8; 104 – 124 ppm)

LC-MS Spectrum

m/z ESI (positive): 424.0 $(M+H)^+$; $C_{20}H_{17}N_5O_2S_2$ (MA= 423.51; Exact Mass= 423.07)

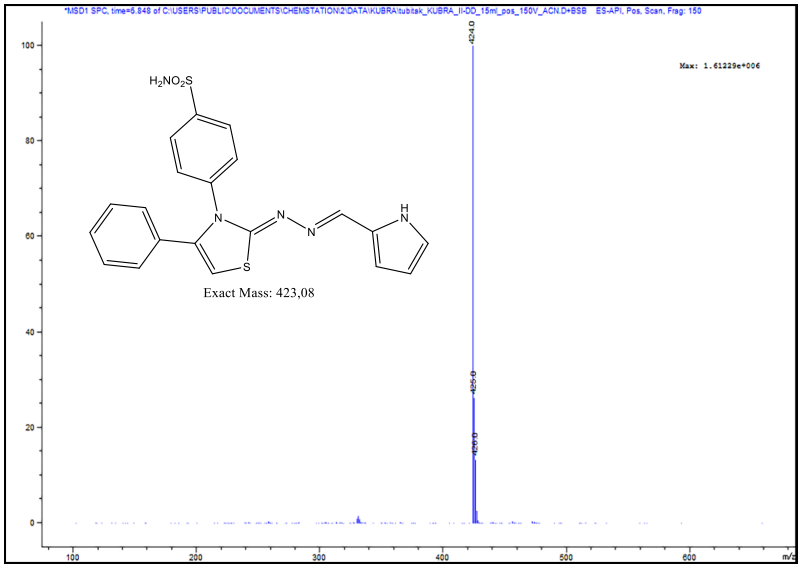

Figure 4-133: Mass spectrum of compound 4f

4.3.2.7. 4-((*Z*)-2-(((*E*)-(1*H*-pyrrol-2-yl)methylene)hydrazineylidene)-4-(4-bromophenyl)thiazol-3(2*H*)-yl)benzenesulfonamide (4g)

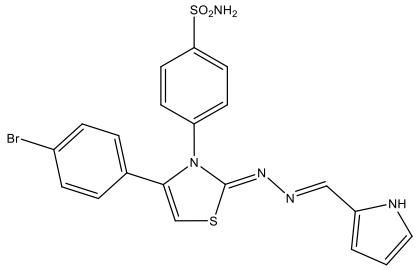

0.0015 mol (0.42g) of 2-bromo-1-(4-bromophenyl)ethane-1-one (**3b)** and 0.0015 mol (0.5g) of 2-((1*H*-pyrrol-2-yl)methylene)-*N*-(4-sulfamoylphenyl)hydrazine-1-carbothioamide (**E6**) are suspended in chloroform-ethanol (2:1). The reaction mixture is heated under reflux for 6 hours. The solid product formed is filtered and purified by recrystallization from ethanol.

Physical appearance	: Dark green powder
Yield (%)	: 58
Retention factor	: 0.61; Chloroform: Methanol (9:1)
Melting point (ºC)	: 238.4 - 239.5

Elemental Analysis

Molecular formula	: $C_{20}H_{16}BrN_5O_2S_2$
Molecular weight (g/mol)	: 502.41

Element	C	H	N	S
Calculated (%)	47.81	3.21	13.94	12.76
Found (%)	47.57	2.95	13.62	12.48

Spectral Analysis

Fourier Transform Infrared (FT-IR) Spectrum

IR(KBr): υ 3444, 3352, 3234 (NH s.b); 3120, 3169, 3030 (Ar.C-H s.b., =CH s.b); 1633, 1597, 1581, 1552, 1517 (Ar. C=C s.b, C=N s.b, N-H b.b); 1334, 1163 (S=O s.b); 1312 (C-N s.b); 1080 (Ar-Br s.b); 856 (1,4-disubs. Ar-C-H b.b)

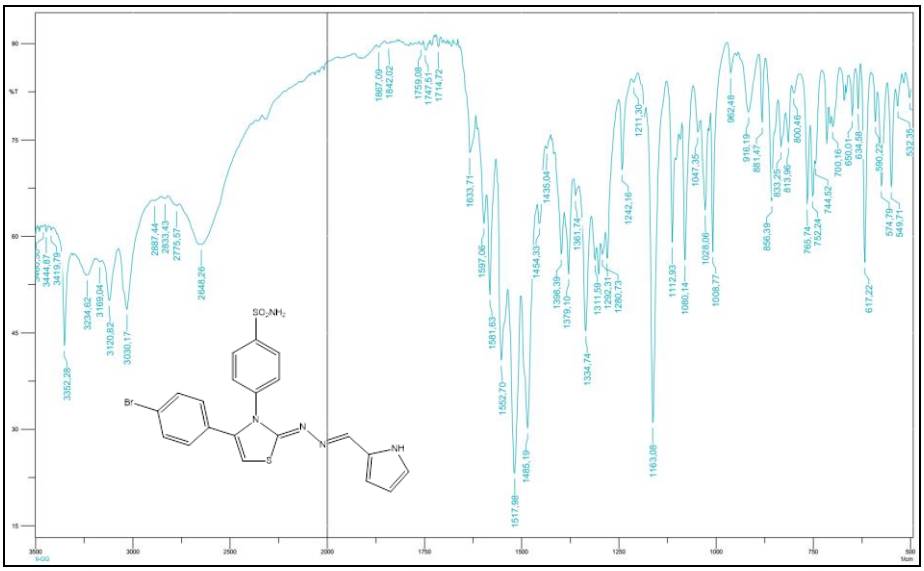

Figure 4-134: IR spectrum of compound 4g

^{1}H-NMR Spectrum

^{1}H NMR (DMSO-d_6 / 400 MHz δ (ppm): 6.11 (1H, q, J=3.1 Hz, pyrrole C_4-H), 6.52 (1H, t, J=1.6 Hz, pyrrole C_3-H), 6.85 (1H, s, thiazole C_5-H), 6.89 (1H, broad s, pyrrole C_5-H), 7.21 (2H, app.d (AA'BB'), J=8.2 Hz, 4-bromophenyl $C_{2,6}$-H), 7.49 (1H, s, N=CH), 7.52 (2H, app.d (AA'BB'), J=8.2 Hz, 4-bromophenyl $C_{3,5}$-H), 7.55 (2H, broad s, -SO_2NH_2), 7.63 (2H, app.d (AA'BB'), J=8.6 Hz, 4-benzenesulfonamide $C_{3,5}$-H), 7.93 (2H, app.d (AA'BB'), J=8.6 Hz, 4-benzenesulfonamide $C_{2,6}$-H), 10.79 (1H, s, pyrrole NH).

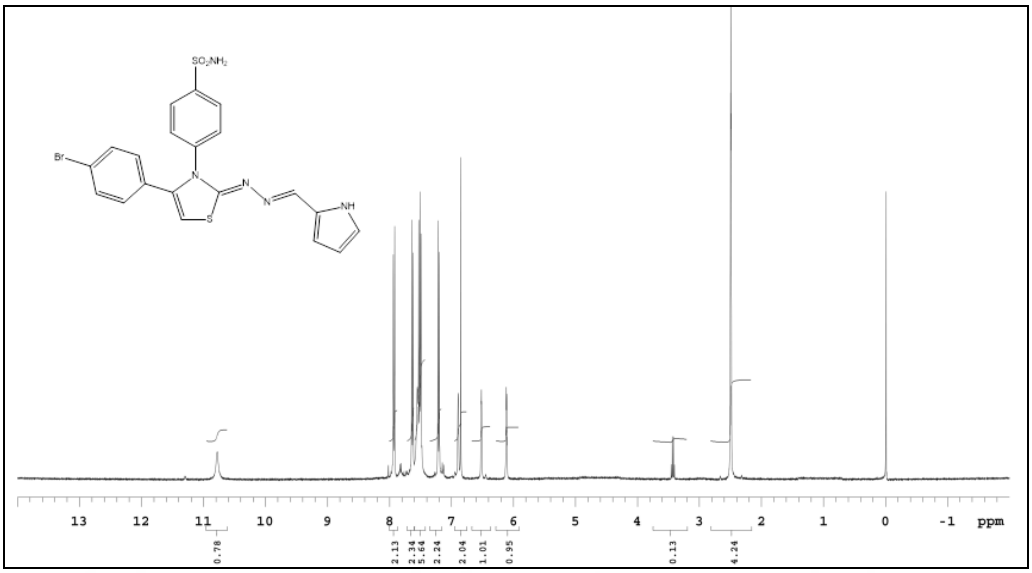

Figure 4-135: ^{1}H-NMR spectrum of compound 4g (0 – 14 ppm)

^{13}C-NMR Spectrum

^{13}C NMR (decoupled, DMSO-*d*$_6$, 100 MHz) δ (ppm): 103.3 (thiazole C_5), 109.5 (pyrrole C_4), 113.7 (pyrrole C_3), 122.1 (4-bromophenyl C_4 / pyrrole C_5), 126.7 (4-benzenesulfonamide $C_{2,6}$), 129.2 (4-benzenesulfonamide $C_{3/5}$), 129.3 (4-bromophenyl C_1), 130.2 (4-bromophenyl $C_{2,6}$), 131.4 (4-bromophenyl $C_{3,5}$), 137.6 (4-benzenesulfonamide C_4), 139.8 (4-benzenesulfonamide C_1), 140.4 (thiazole C_4), 143.8 (N=CH), 168.3 (thiazole C_2).

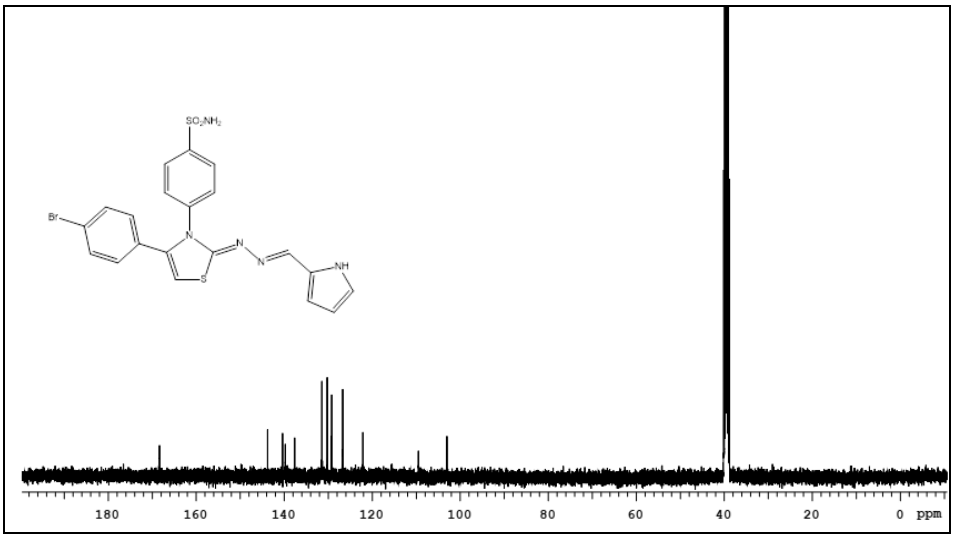

Figure 4-136: ^{13}C-NMR spectrum of compound 4g (0 – 200 ppm)

LC-MS Spectrum

m/z ESI (positive): 503.9 $(M+2+H)^+$; $C_{20}H_{16}BrN_5O_2S_2$ (MA= 502.41; Exact Mass= 500.99)

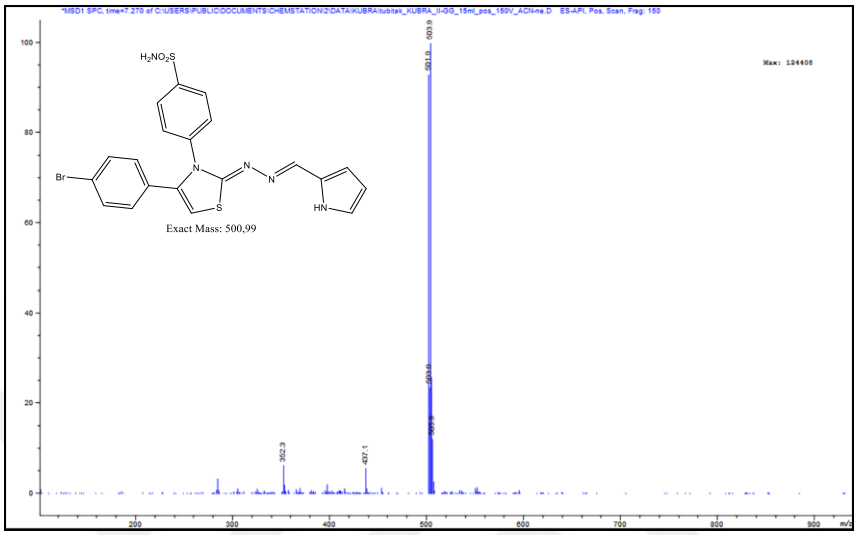

Figure 4-137: Mass spectrum of compound 4g

4.3.2.8. 4-((*Z*)-2-(((*E*)-(1*H*-pyrrol-2-yl)methylene)hydrazineylidene)-4-(4-hydroxyphenyl)thiazol-3(2*H*)-yl)benzenesulfonamide (4h)

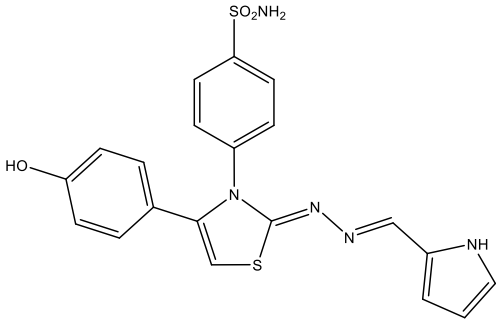

0.0019 mol (0.41g) of 2-bromo-1-(4-hydroxyphenyl)ethane-1-one (**3c**) and 0.0019 mol (0.61 g) of 2-((1*H*-pyrrol-2-yl)methylene)-*N*-(4-sulfamoylphenyl)hydrazine-1-carbothioamide (**E6**) are suspended in chloroform-ethanol (2:1). The reaction mixture is heated under reflux for 6 hours. The solid product formed is filtered and purified by recrystallization from ethanol.

Physical appearance	: Dark green powder

Yield (%)	: 85
Retention factor	: 0.34; Chloroform : Methanol (9:1)
Melting point (ºC)	: 207.3 - 290.6

Elemental Analysis

Molecular formula	: $C_{20}H_{17}N_5O_3S_2$
Molecular weight (g/mol)	: 439.51

Element	C	H	N	S
Calculated (%)	54.65	3.90	15.93	14.59
Found (%)	54.48	4.23	15.72	14.33

Spectral Analysis

Fourier Transform Infrared (FT-IR) Spectrum

IR(KBr): υ 3479 (OH s.b); 3371, 3286 (NH s.b); 3176, 3118, 3093, 3059 (Ar.C-H s.b., =CH s.b); 1606, 1585, 1568, 1541, 1508 (Ar. C=C s.b, C=N s.b, N-H b.b); 1354, 1166 (S=O s.b); 1300 (C-N s.b); 873, 833 (1,4-disubs. Ar-C-H b.b)

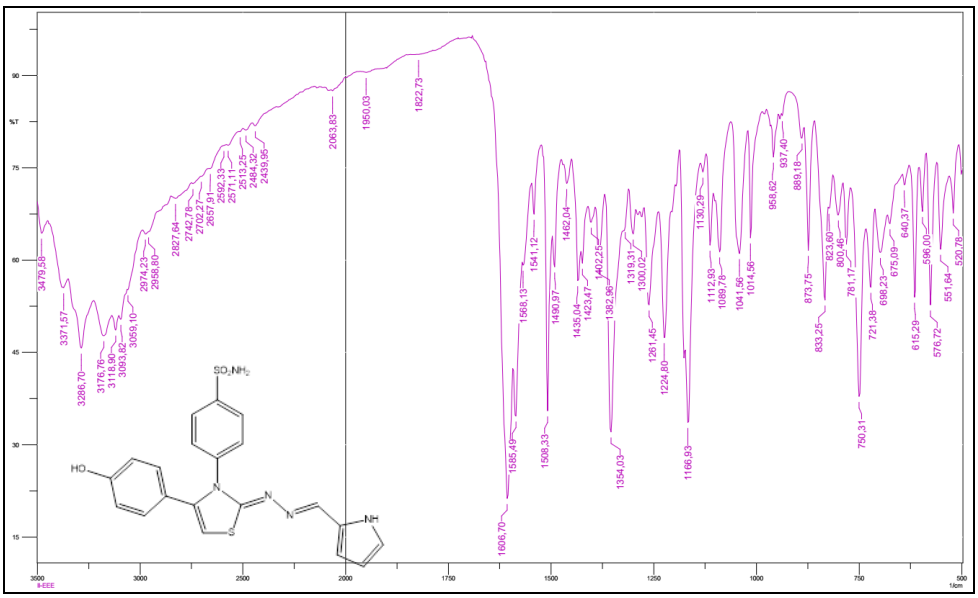

Figure 4-138: IR spectrum of compound 4h

^{1}H-NMR Spectrum

^{1}H NMR (DMSO-d_6 / 500 MHz δ (ppm): 3.42 (broad singlet, OH, etanol ile), 6.15-6.17 (1H, m, pyrrole C_4-H), 6.51 (1H, broad singlet, pyrrole C_3-H), 6.81 (1H, broad s, thiazole C_5-H), 6.99-7.01 (3H, M, pyrrole C_5-H and 4- hydroxyphenyl $C_{2,6}$-H), 6.64 (2H, d, *J*=8.7 Hz, 4- hydroxyphenyl $C_{3,5}$-H), 7.59 (2H, d, *J*=8.5 Hz, 4-benzenesulfonamide $C_{3,5}$-H), 7.53 (2H, broad s, -SO_2NH_2), 7.86 (2H, d, *J*=8.5 Hz, 4-benzenesulfonamide $C_{2,6}$-H), 8.08 (1H, s, N=CH), 11.41 (1H, s, pyrrole NH).

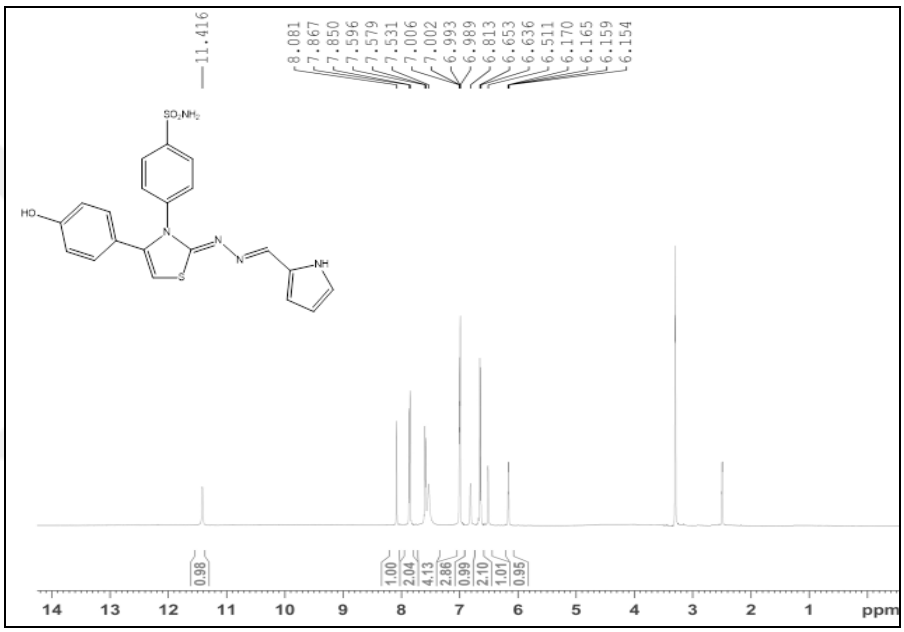

Figure 4-139: ^{1}H-NMR spectrum of compound 4h (0 – 14 ppm)

^{13}C-NMR Spectrum

^{13}C NMR (APT, DMSO-d_6, 125 MHz) δ (ppm): 103.3 (thiazole C_5), 110.1 (pyrrole C_4), 114.5 (pyrrole C_3), 123.7 (pyrrole C_5), 115.7 (4-hydroxyphenyl $C_{3,5}$), 120.6 (4-hydroxyphenyl C_1), 127.2 (4-benzenesulfonamide $C_{2,6}$), 129.9 (4-benzenesulfonamide $C_{3,5}$), 130.4, 130.8 (4- hydroxyphenyl $C_{2,6}$), 139.2 (4-benzenesulfonamide C_4), 140.8 (4-benzenesulfonamide C_1), 144.6 (thiazole C_4), 158.5 (4-hydroxyphenyl C_4),144.9 (N=CH), 167.7 (thiazole C_2).

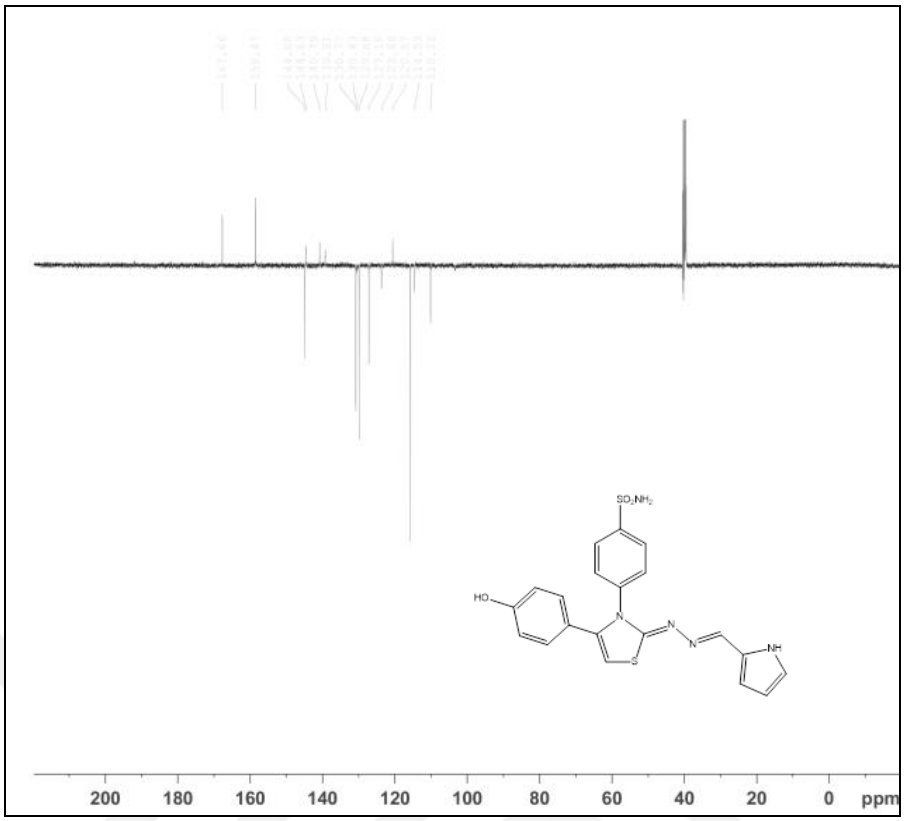

Figure 4-140: APT spectrum of compound 4h (0 – 200 ppm)

LC-MS Spectrum

m/z ESI (positive): 440.0 $(M+H)^+$; $C_{20}H_{17}N_5O_3S_2$ (MA= 439.51; Exact Mass= 439.08)

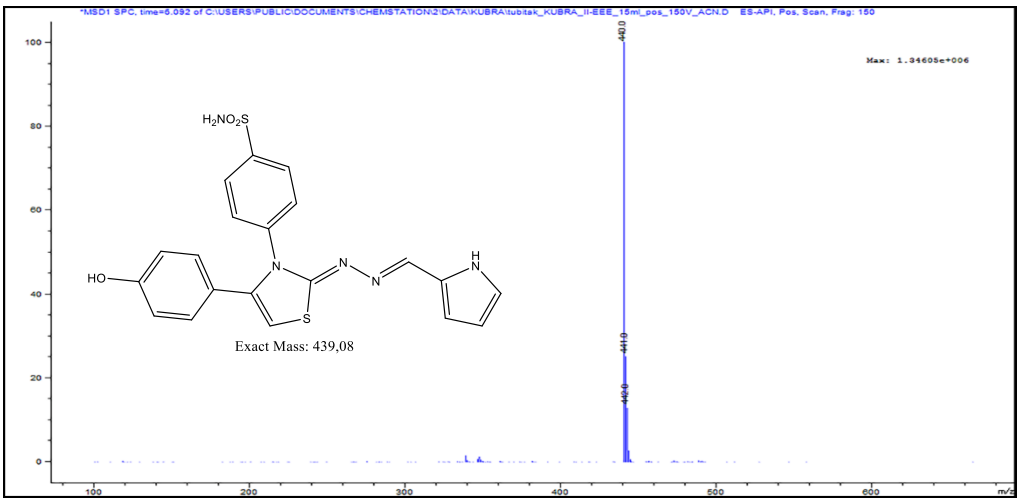

Figure 4-141: APT spectrum of compound 4h

4.3.2.9. 4-((*Z*)-2-(((*E*)-furan-2-ylmethylene)hydrazineylidene)-4-phenylthiazol-3(2*H*)-yl)benzenesulfonamide (4i)

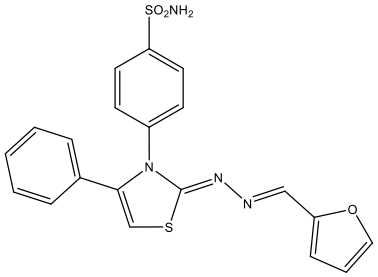

0.0018 mol (0.36g) of 2-bromo-1-phenylethan-1-one (**3a**) and 0.0018 mol (0.6 g) of 2-(furan-2-ylmethylene)-*N*-(4-sulfamoylphenyl)hydrazine-1-carbothioamide (**E7**) are suspended in chloroform-ethanol (2:1). The reaction mixture is heated under reflux for 6 hours. The solid product formed is filtered and purified by recrystallization from ethanol.

Physical appearance	: Fine yellow crystals
Yield (%)	: 65
Retention factor	:0.64; Chloroform : Methanol (9:1)
Melting point (ºC)	: 263.2 - 264.4

Elemental Analysis

Molecular formula	: $C_{20}H_{16}N_4O_3S_2$
Molecular weight (g/mol)	: 424.50

Element	C	H	N	S
Calculated (%)	56.59	3.80	13.30	15.11
Found (%)	56.44	3.63	12.95	15.36

Spectral Analysis

Fourier Transform Infrared (FT-IR) Spectrum

IR(KBr): υ 3340, 3257 (NH s.b); 3097,3057, 3039 (Ar.C-H s.b., =CH s.b); 1616, 1598, 1566, 1548, 1516 (Ar. C=C s.b, C=N s.b, N-H b.b); 1346, 1166 (S=O s.b); 1321 (C-N s.b); 769, 698 (monosubs. Ar-C-H b.b); 862 (1,4-disubs. Ar-C-H b.b)

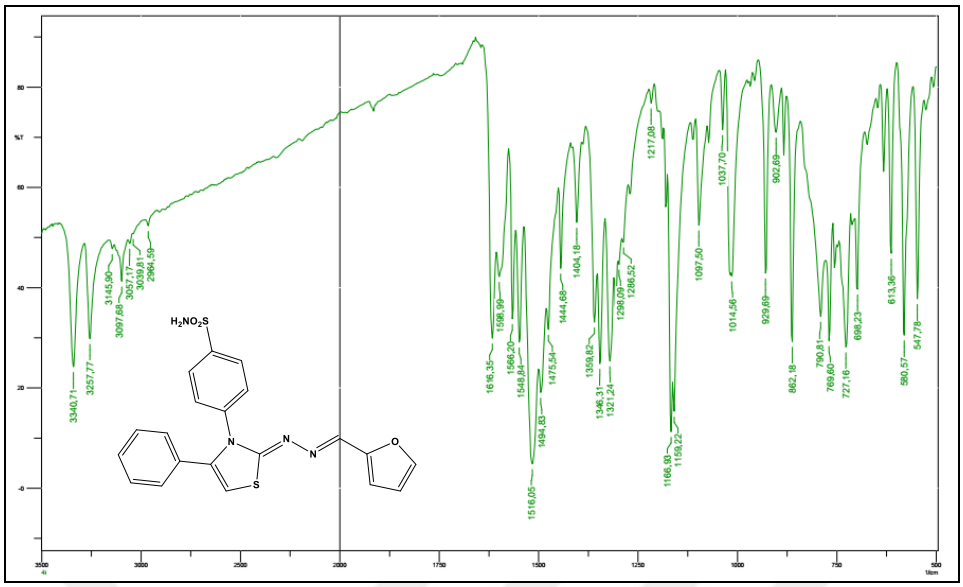

Figure 4-142: IR spectrum of compound 4i

^{1}H-NMR Spectrum

^{1}H NMR (DMSO-d_6 / 400 MHz δ (ppm): 6.60 (1H, dd, J=3.1, 1.6 Hz, furan C_4-H), 6.68 (1H, s, thiazole C_5-H), 6.77 (1H, d, J=3.1 Hz, furan C_3-H), 7.18-7.20 (2H, m, phenyl $C_{2,6}$-H), 7.25-7.28 (3H, m, phenyl $C_{3,4,5}$-H), 7.48 (4H, app.d (AA'BB'), J=8.6 Hz, 4-benzenesulfonamide $C_{3,5}$-H and -SO_2NH_2), 7.77 (2H, app.d (AA'BB'), J=8.6 Hz, 4-benzenesulfonamide $C_{2,6}$-H), 7.81 (1H, d, J=1.6 Hz, furan C_5-H), 8.02 (1H, s, N=CH).

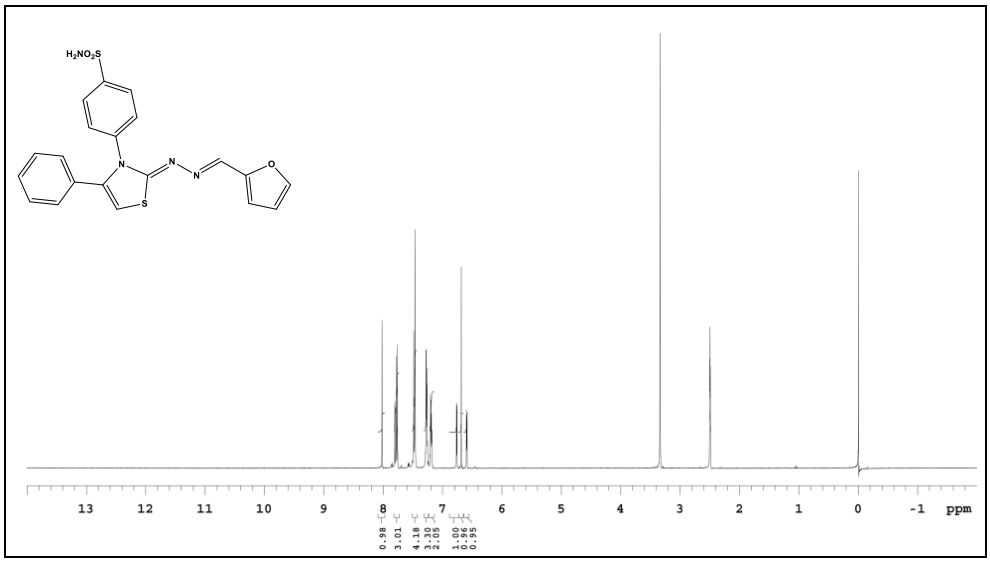

Figure 4-143: ^{1}H-NMR spectrum of compound 4i (0 – 14 ppm)

^{13}C-NMR Spectrum

^{13}C NMR (decoupled, DMSO-*d*$_6$, 125 MHz) δ (ppm): 102.1 (thiazole C_5), 111.8 (furan C_4), 112.9 (furan C_3), 125.7, 125.8 (4-benzenesulfonamide $C_{2,6}$), 127.7 (phenyl $C_{2,6}$), 128.6, 128.7 (4-benzenesulfonamide $C_{3/5}$), 127.8, 127.9, 128.0 (phenyl $C_{3,4,5}$), 129.8 (phenyl C_1), 138.5 (4-benzenesulfonamide C_4), 139.6 (4-benzenesulfonamide C_1), 141.2 (N=CH), 142.5 (thiazole C4), 144.3 (furan C_5), 149.4 (furan C_2), 168.6 (thiazole C_2).

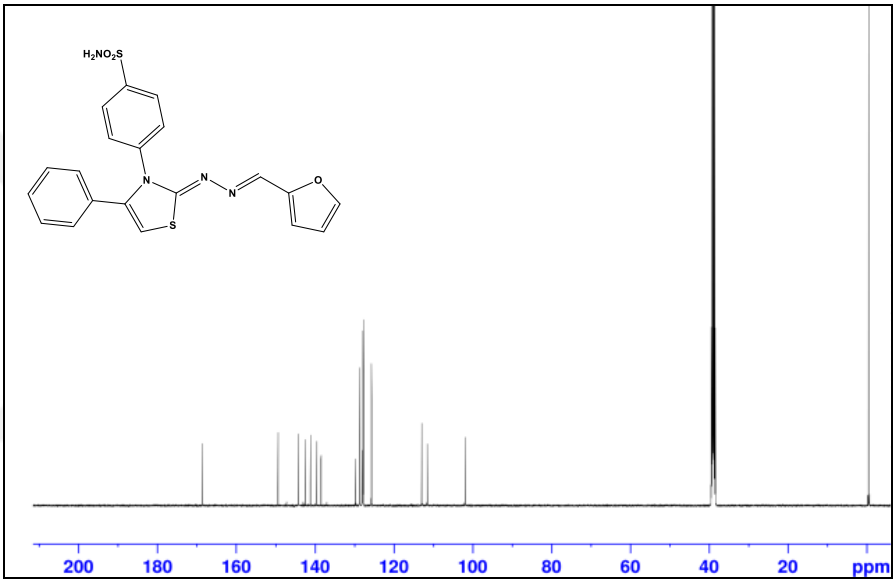

Figure 4-144: ^{1}H-NMR spectrum of compound 4i (0 – 200 ppm)

^{13}C NMR (HSQC-2D, DMSO-*d*$_6$, 125 MHz) δ (ppm): **102.1** [thiazole C_5 - **6.60** (1H, s, thiazole C_5-H)], **111.8** [furan C_4 - **6.60** (1H, dd, *J*=3.1, 1.6 Hz, furan C_4-H)], **112.9** [furan C_3 - **6.77** (1H, d, *J*=3.13 Hz, furan C_3-H)], **125.7, 125.8** [4-benzenesulfonamide $C_{2,6}$ - **7.77** (2H, app.d (AA'BB'), *J*=8.6 Hz, 4-benzenesulfonamide $C_{2,6}$-H)], **127.7** [phenyl $C_{2,6}$ - **7.18-7.20** (2H, m, phenyl $C_{2,6}$-H)], **128.6, 128.7** [4-benzenesulfonamide $C_{3/5}$ - **7.48** (4H, app.d (AA'BB'), *J*=8.6 Hz, 4-benzenesulfonamide $C_{3,5}$-H and -SO_2NH_2)], **127.8, 127.9, 128.0** [phenyl $C_{3,4,5}$ - **7.25-7.28** (3H, m, phenyl $C_{3,4,5}$-H)], **141.2** [N=CH - **8.02** (1H, s, N=CH)], **144.3** [furan C_5 - **7.81** (1H, d, *J*=1.56 Hz, furan C_5-H)].

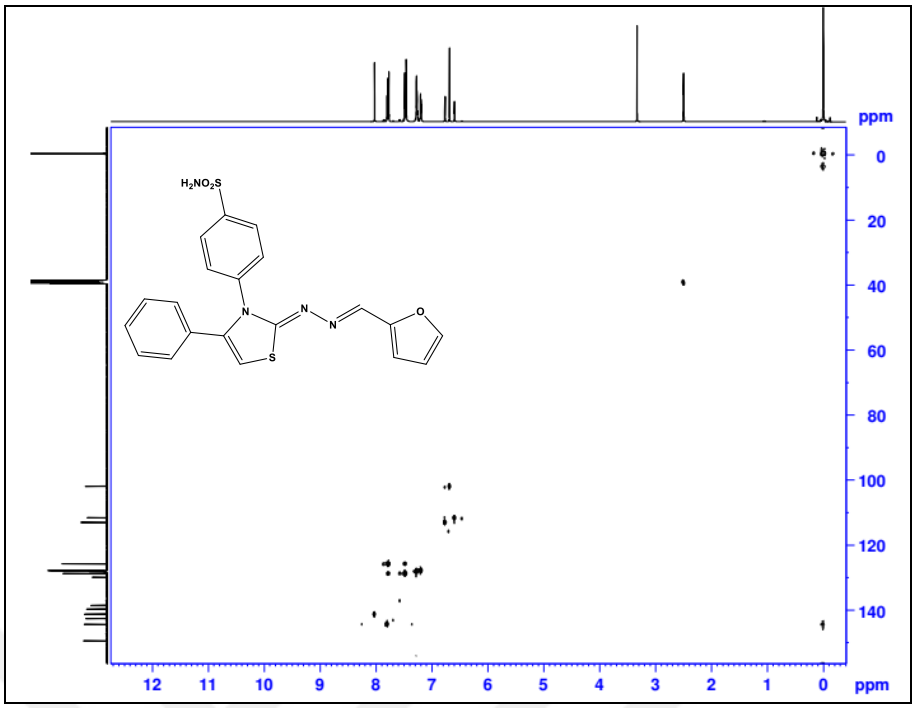

Figure 4-145: HSQC spectrum of compound 4i (0 – 12; 0 – 140 ppm)

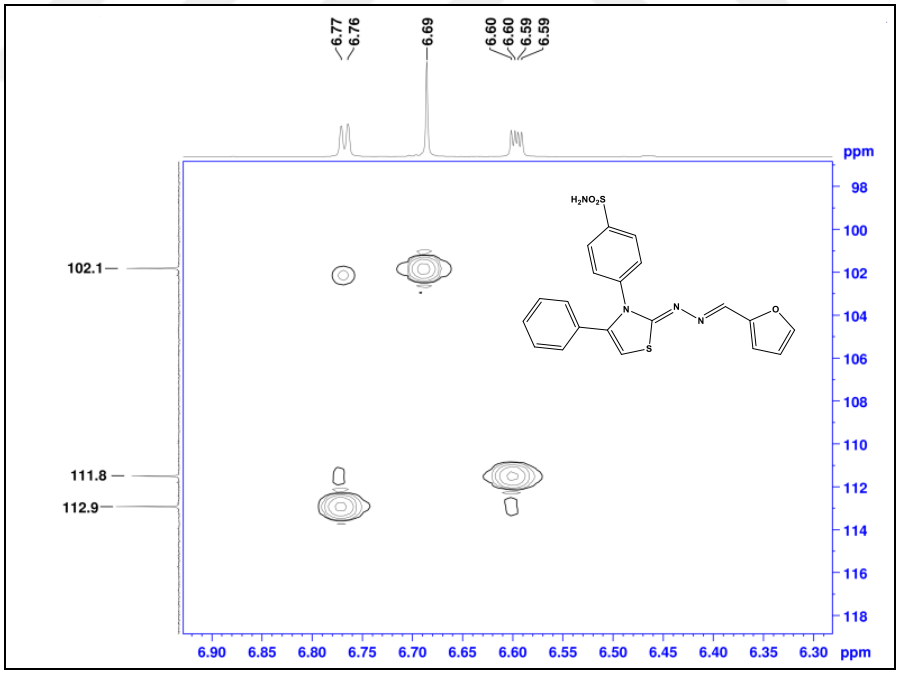

Figure 4-146: HSQC spectrum of compound 4i (6.3 – 6.9; 98 – 118 ppm)

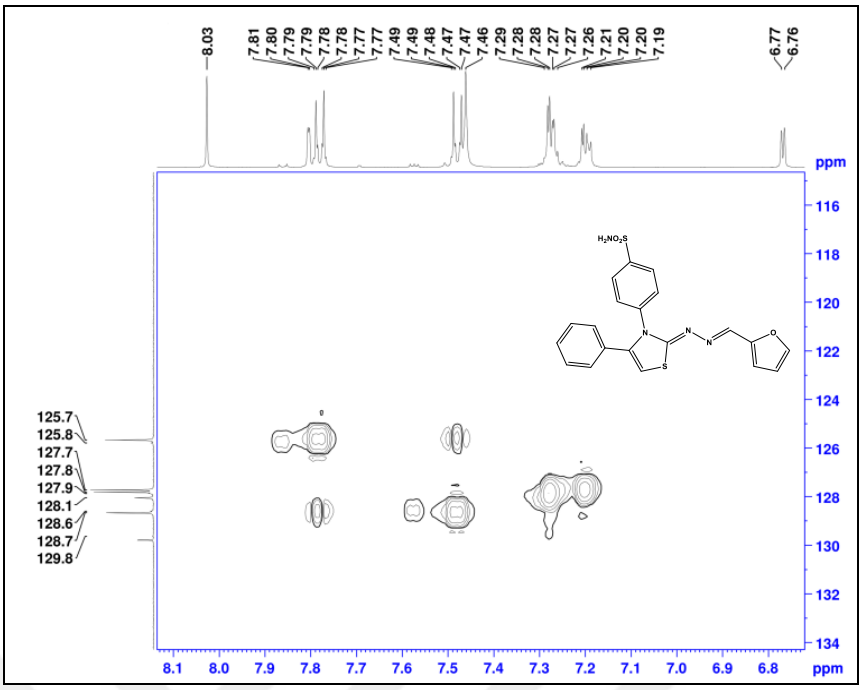

Figure 4-147: HSQC spectrum of compound 4i (6.7 – 8.1; 116 – 134 ppm)

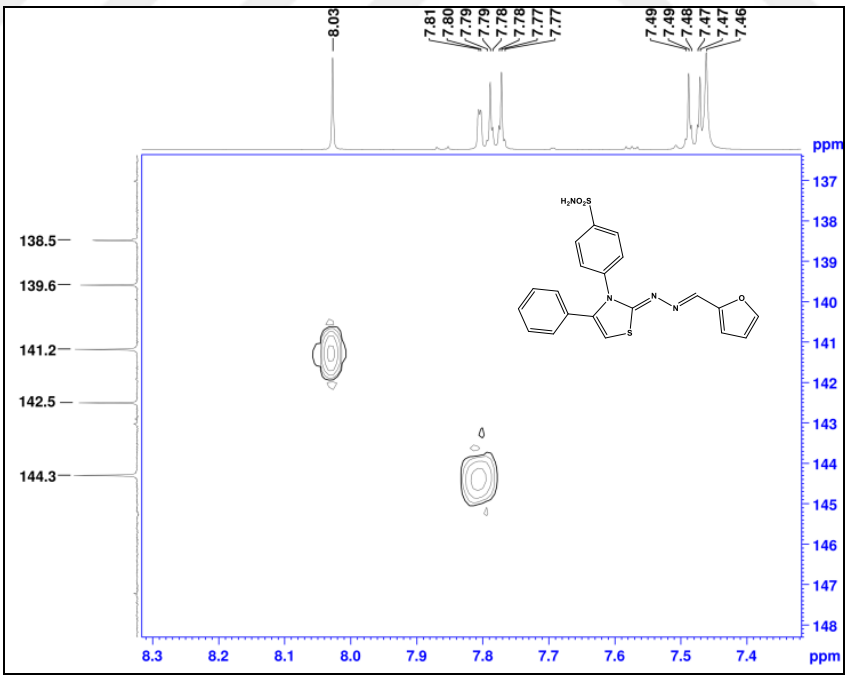

Figure 4-148: HSQC spectrum of compound 4i (7.4 – 8.3; 137 – 148 ppm)

LC-MS Spectrum

m/z ESI (positive): 425.0 $(M+H)^+$; $C_{20}H_{16}N_4O_3S_2$ (MA= 424.50; Exact Mass= 424.07)

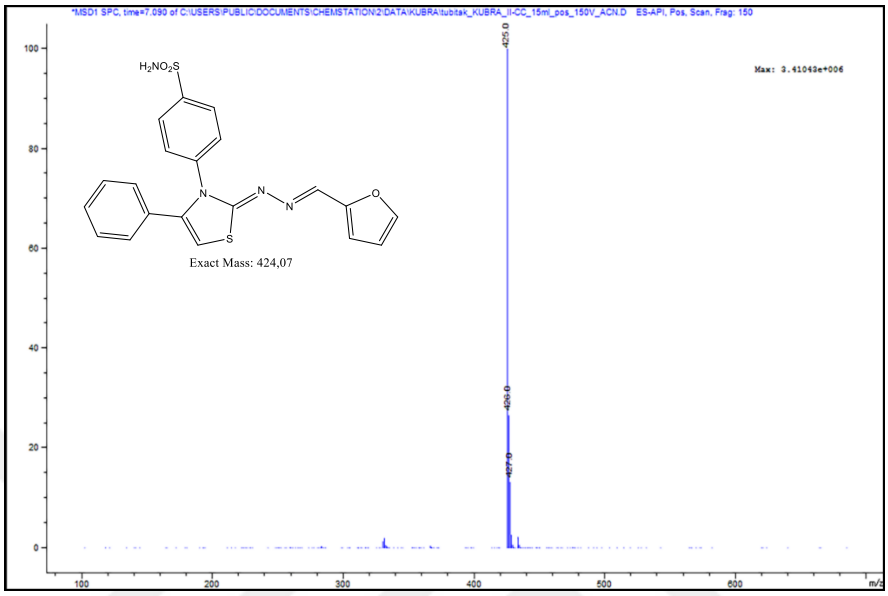

Figure 4-149: Mass spectrum of compound 4i

4.3.2.10. 4-((*Z*)-4-(4-bromophenyl)-2-(((*E*)-furan-2-ylmethylene)hydrazineylidene)thiazol-3(2*H*)-yl)benzenesulfonamide (4j)

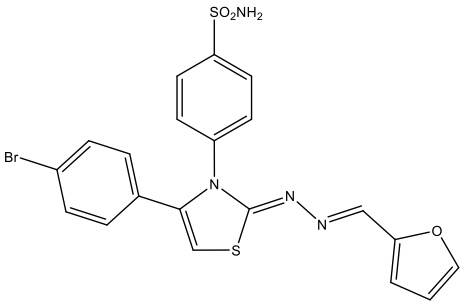

0.0018 mol (0.5g) of 2-bromo-1-(4-bromophenyl)ethane-1-one (**3b)** and 0.0018 mol (0.6 g) of 2-(furan-2-ylmethylene)-*N*-(4-sulfamoylphenyl)hydrazine-1-carbothioamide (**E7**) are suspended in chloroform-ethanol (2:1). The reaction mixture is heated under reflux for 6 hours. The solid product formed is filtered and purified by recrystallization from ethanol.

Physical appearance	: Yellow powder
Yield (%)	: 74

Retention factor	:0.63; Chloroform : Methanol (9:1)
Melting point (ºC)	: 233.5-235.8

Elemental Analysis

Molecular formula	: $C_{20}H_{15}BrN_4O_3S_2$
Molecular weight (g/mol)	: 503.39

Element	C	H	N	S
Calculated (%)	47.72	3.00	11.13	12.74
Found (%)	47.54	2.65	11.51	12.47

Spectral Analysis

Fourier Transform Infrared (FT-IR) Spectrum

IR(KBr): υ 3458, 3336 (NH s.b); 3143, 3109, 3095, 3068 (Ar.C-H s.b., =CH s.b); 1624, 1591, 1573, 1546 (Ar. C=C s.b, C=N s.b, N-H b.b); 1354, 1168 (S=O s.b); 1325 (C-N s.b); 1072 (Ar-Br s.b); 839, 819 (1,4-disubs. Ar-C-H b.b)

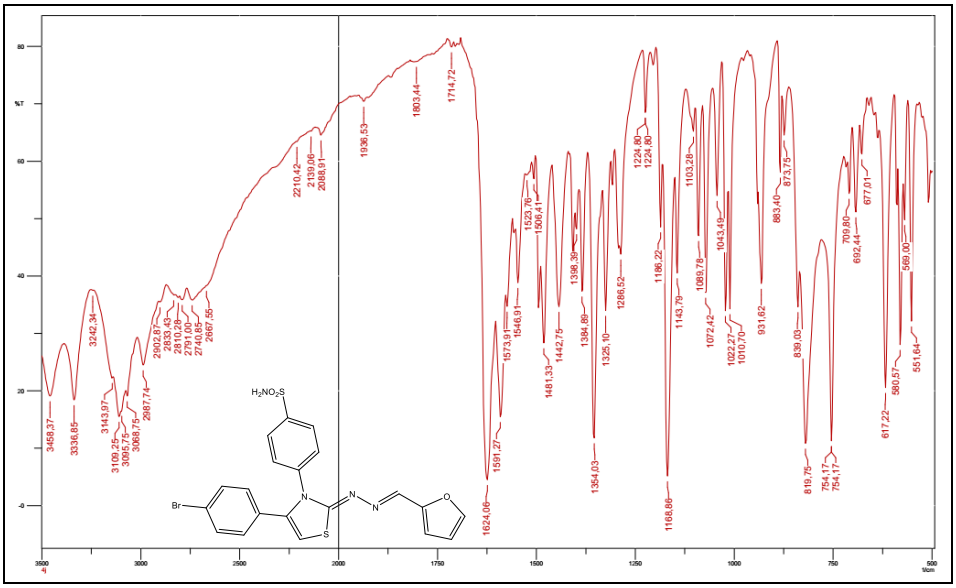

Figure 4-150: IR spectrum of compound 4j

^{1}H-NMR Spectrum

^{1}H NMR (DMSO-*d*$_6$ / 400 MHz δ (ppm): 6.60 (1H, dd, *J*=3.1, 1.6 Hz, furan C_4-H), 6.80 (1H, d, *J*=3.1 Hz, furan C_3-H), 6.81 (1H, s, thiazole C_5-H), 7.14 (2H, app.d (AA'BB'), *J*=8.6 Hz, 4-bromophenyl $C_{2,6}$-H), 7.47-7.52 (6H, m, 4-bromophenyl $C_{3,5}$-H, 4-benzenesulfonamide $C_{3,5}$-H and -SO_2NH_2), 7.81 (3H, d, *J*=8.6 Hz, 4-benzenesulfonamide $C_{2,6}$-H and furan C_5-H), 8.04 (1H, s, N=CH).

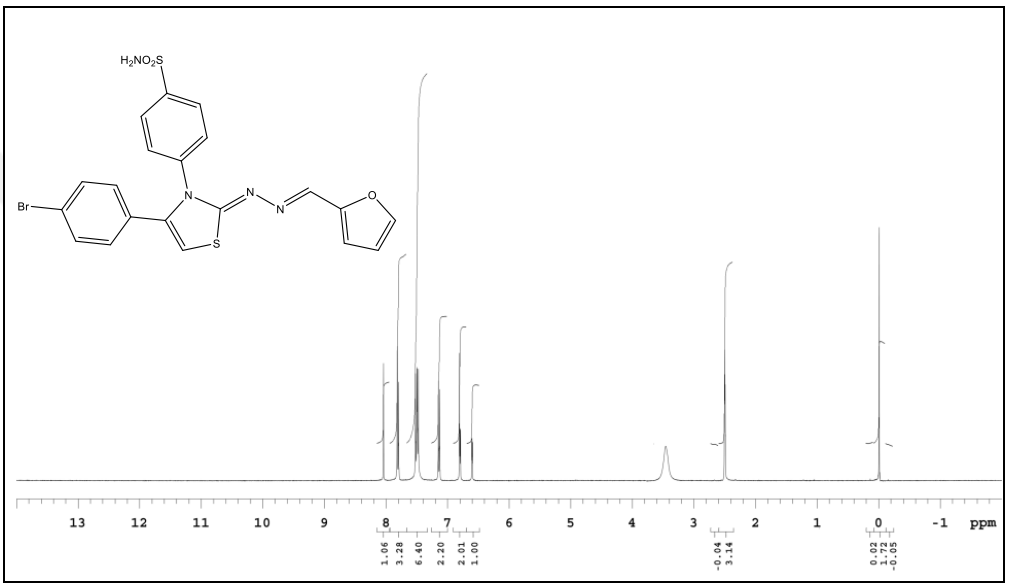

Figure 4-151: ^{1}H-NMR spectrum of compound 4j (0 – 14 ppm)

^{13}C-NMR Spectrum

^{13}C NMR (decoupled, DMSO-*d*$_6$, 125 MHz) δ (ppm): 104.3 (thiazole C_5), 112.7 (furan C_4), 114.6 (furan C_3), 122.7 (4-bromophenyl C_4), 126.8, 127.0 (4-benzenesulfonamide $C_{2,6}$), 129.8, 129.9 (4-benzenesulfonamide $C_{3/5}$), 128.4 (4-bromophenyl C_1), 130.9 (4-bromophenyl $C_{2,6}$), 131.9, 132.0 (4-bromophenyl $C_{3,5}$), 138.6 (4-benzenesulfonamide C_4), 140.0 (4-benzenesulfonamide C_1), 142.4 (N=CH), 143.9 (thiazole C_4), 147.62 (furan C_5), 150.1 (furan C_2), 169.5 (thiazole C_2).

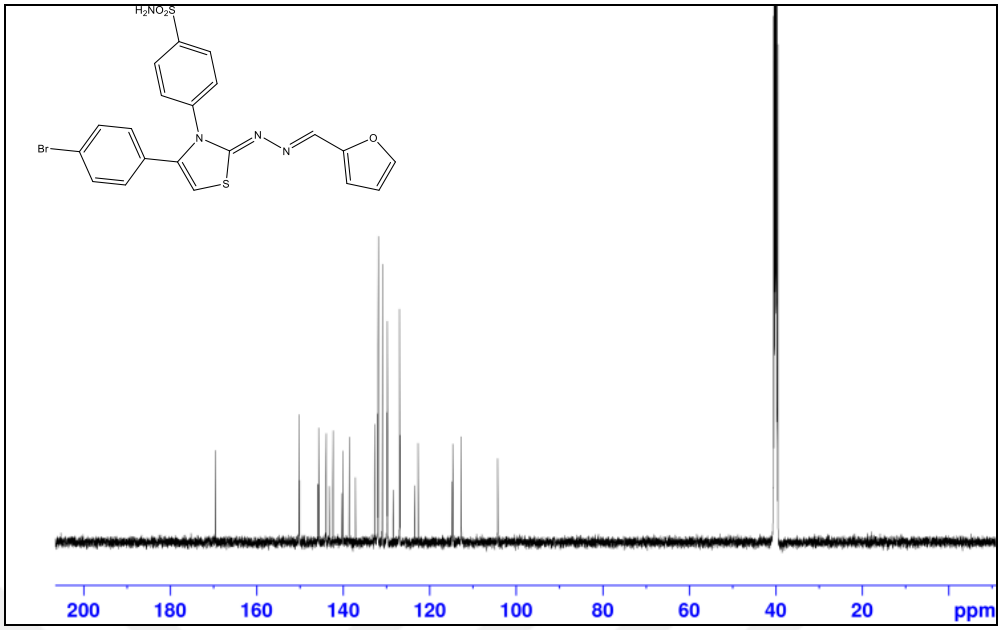

Figure 4-152: ^{13}C-NMR spectrum of compound 4j (0 – 200 ppm)

^{13}C NMR (HSQC-2D, DMSO-*d*$_6$, 125 MHz) δ (ppm): **104.3** [thiazole C_5 - **6.60** (1H, s, thiazole C_5-H)], **112.7** [furan C_4 - **6.60** (1H, dd, *J*=3.1, 1.6 Hz, furan C_4-H)], **114.6** [furan C_3 - **6.80** (1H, d, *J*=3.1 Hz, furan C_3-H)], **126.8, 127.0** [4-benzenesulfonamide $C_{2,6}$ - **7.81** (3H, d, *J*=8.6 Hz, 4-benzenesulfonamide $C_{2,6}$-H and furan C_5-H)], **129.8, 129.9** (4-benzenesulfonamide $C_{3/5}$ - **7.47-7.52** (6H, m, 4-bromophenyl $C_{3,5}$-H, 4-benzenesulfonamide $C_{3,5}$-H and -SO_2NH_2)], **130.9** [4-bromophenyl $C_{2,6}$ - **7.14** (2H, app.d (AA'BB'), *J*=8.6 Hz, 4-bromophenyl $C_{2,6}$-H)], **131.9, 132.0** [4-bromophenyl $C_{3,5}$ - **7.47-7.52** (6H, m, 4-bromophenyl $C_{3,5}$-H, 4-benzenesulfonamide $C_{3,5}$-H and -SO_2NH_2)], **147.6** [furan C_5 - 7.81 (3H, d, *J*=8.6 Hz, 4-benzenesulfonamide $C_{2,6}$-H and furan C_5-H)], **142.4** [N=CH - **8.04** (1H, s, N=CH)].

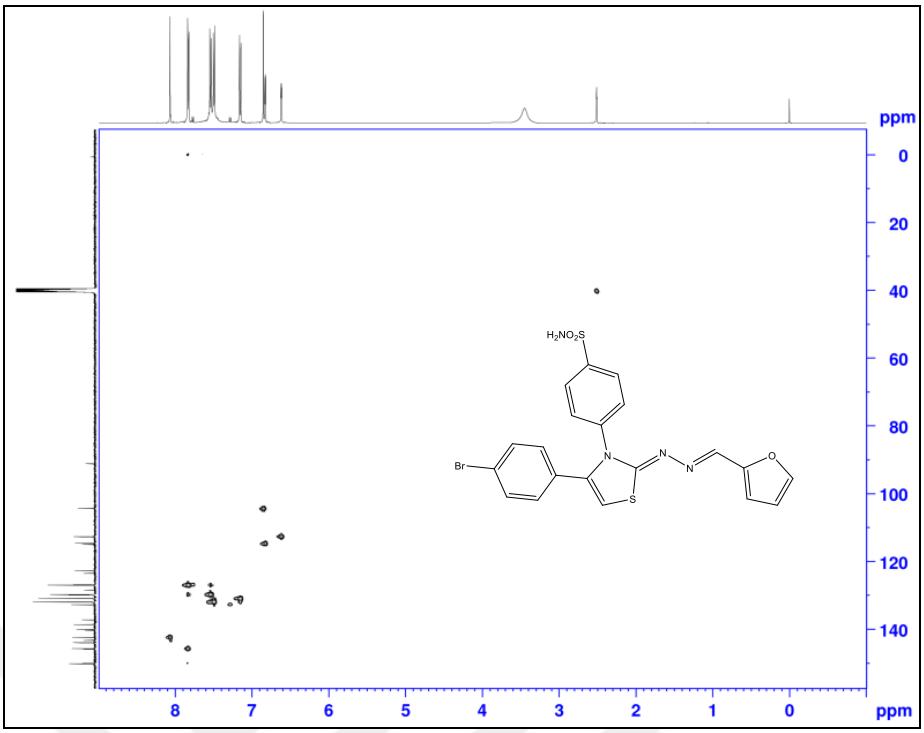

Figure 4-153: HSQC spectrum of compound 4j (0 – 9; 0 – 140 ppm)

LC-MS Spectrum

m/z ESI (positive): 504.9 $(M+2+H)^+$; $C_{20}H_{15}BrN_4O_3S_2$ (MA= 503.39; Exact Mass= 501.98)

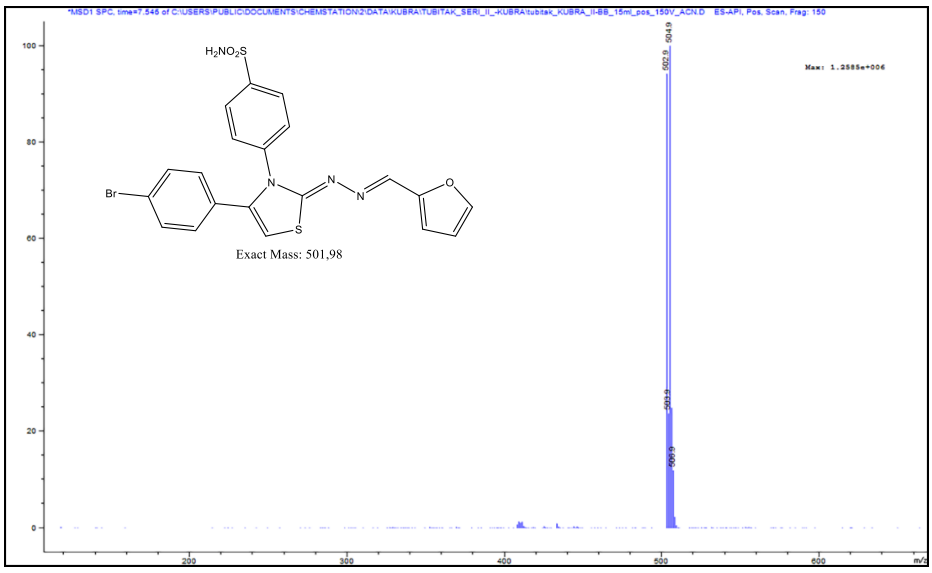

Figure 4-154: Mass spectrum of compound 4j

4.3.2.11. (*Z*)-3-(2-(pentan-3-ylidenehydrazineylidene)-4-phenylthiazol-3(2*H*)-yl)benzenesulfonamide (4k)

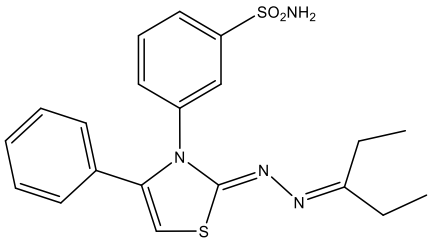

0.0019 mol (0.38 g) of 2-bromo-1-phenylethan-1-one (**3a)** and 0.0019 mol (0.6g) of 2-(pentan-3-ylidene)-*N*-(3-sulfamoylphenyl)hydrazine-1-carbothioamide (**E9**) are suspended in chloroform-ethanol (2:1). The reaction mixture is heated under reflux for 3 hours. The solid product formed is filtered and purified by recrystallization from ethanol.

Physical appearance	: Brown Powder
Yield (%)	: 45
Retention factor	: 0.7; Chloroform : Methanol (9:1)
Melting point (ºC)	: 217.0 – 218.1

Elemental Analysis

Molecular formula	: $C_{20}H_{22}N_4O_2S_2$
Molecular weight (g/mol)	: 414.54

Element	C	H	N	S
Calculated (%)	57.95	5.35	13.52	15.47
Found (%)	57.64	5.04	13.14	15.32

Spectral Analysis

Fourier Transform Infrared (FT-IR) Spectrum

IR(KBr): υ 3313, 3261 (NH s.b); 3072 (Ar.C-H s.b., =CH s.b); 2991, 2978, 2937, 2873, 2806 (Al.C-H s.b); 1639, 1589, 1588, 1527, 1479 (Ar. C=C s.b, C=N s.b, N-H b.b); 1442, 1427 (Al.C-H b.b); 1352, 1163 (S=O s.b); 1309 (C-N s.b); 746, 686 (monosubs. Ar-C-H b.b); 877, 758, 698 (1,3-disubs. Ar-C-H b.b)

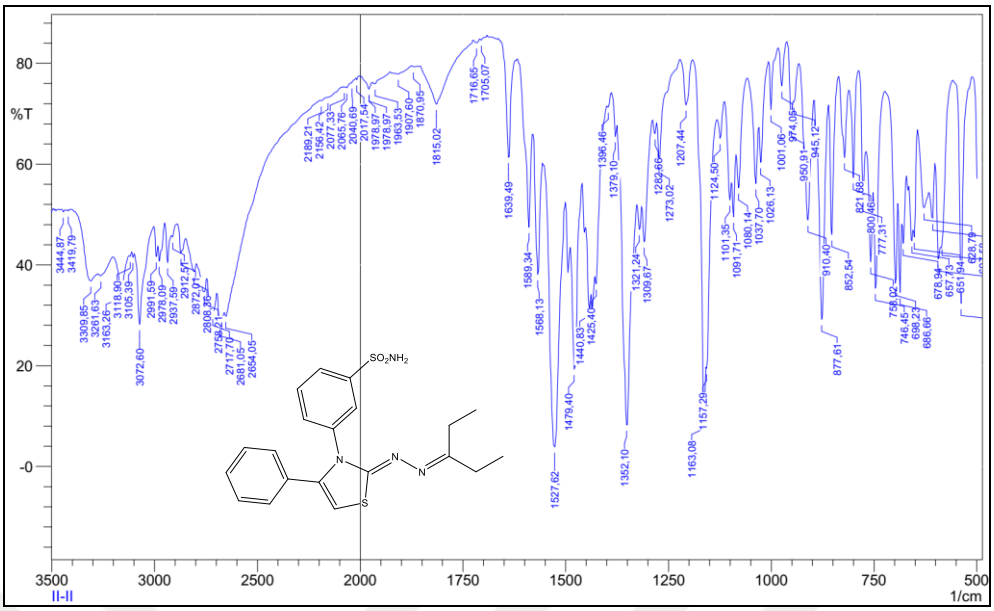

Figure 4-155: IR spectrum of compound 4k

^{1}H-NMR Spectrum

^{1}H NMR (DMSO-d_6 / 400 MHz δ (ppm): 0.90 (3H, t, J=7.6 Hz, -CH_3), 1.06 (3H, t, J=7.5 Hz, -CH_3), 2.23-2.31 (4H, m, 2 x CH_2), 6.64 (1H, d, J=2.0 Hz, thiazole C_5-H), 7.12-7.21 (2H, m, phenyl $C_{2,6}$-H), 7.25 – 7.30 (3H, m, phenyl $C_{3,4,5}$-H), 7.37-7.44 (3H, m, -SO_2NH_2 and 3-benzenesulfonamide C_6-H), 7.51 (1H, t, J=7.9 Hz, 3-benzenesulfonamide C_5-H), 7.71 (1H, d, J=7.9 Hz, 3-benzenesulfonamide C_4-H), 7.80 (1H, s, 3-benzenesulfonamide C_2-H).

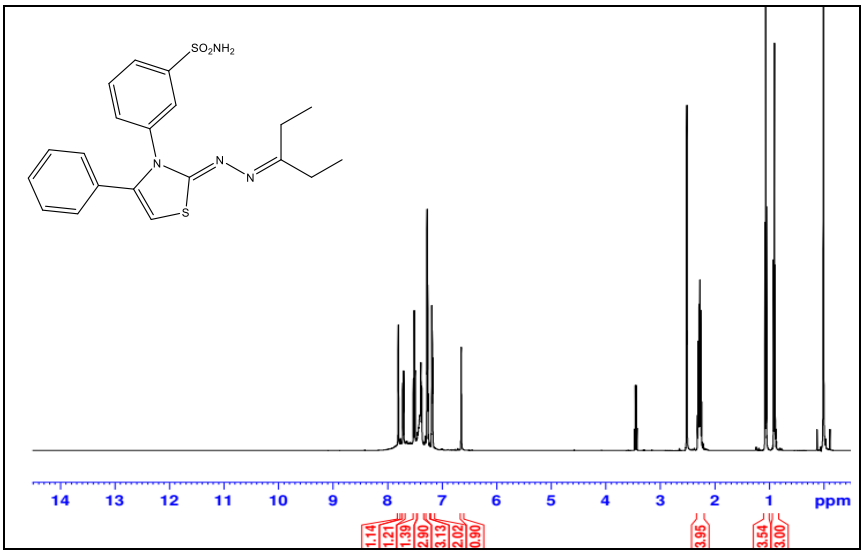

Figure 4-156: ^{1}H-NMR spectrum of compound 4k (0 – 14 ppm)

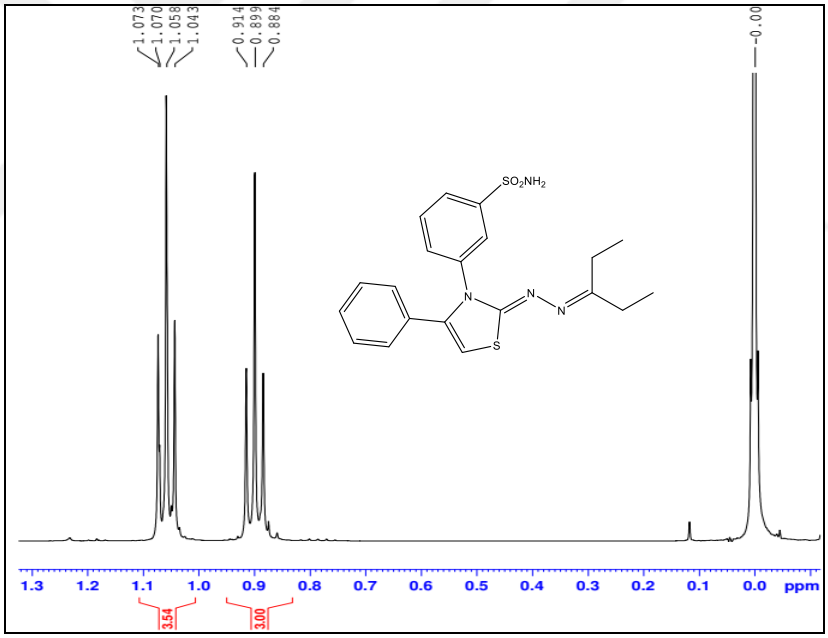

Figure 4-157: ^{1}H-NMR spectrum of compound 4k (0 – 1.3 ppm)

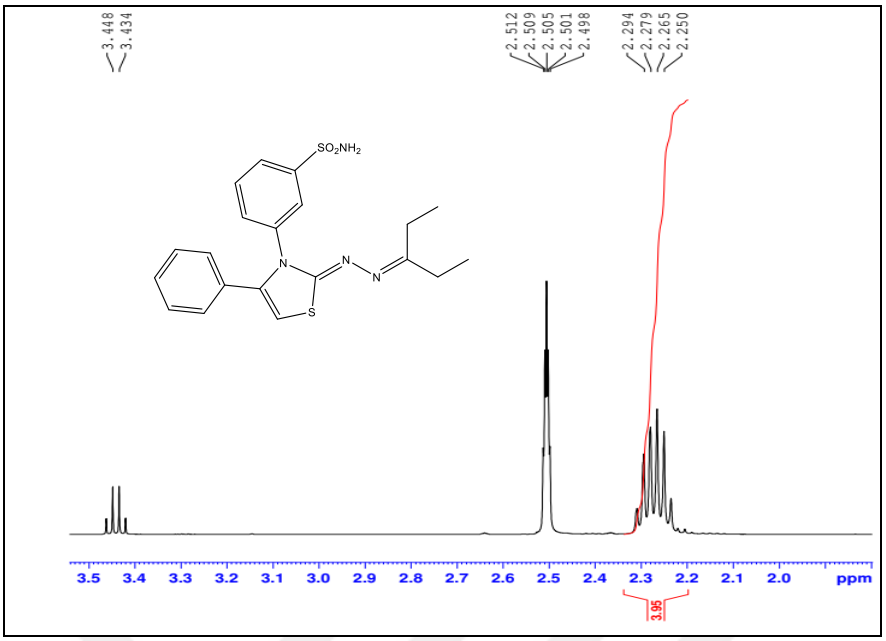

Figure 4-158: ^{1}H-NMR spectrum of compound 4k (2.0 – 3.5 ppm)

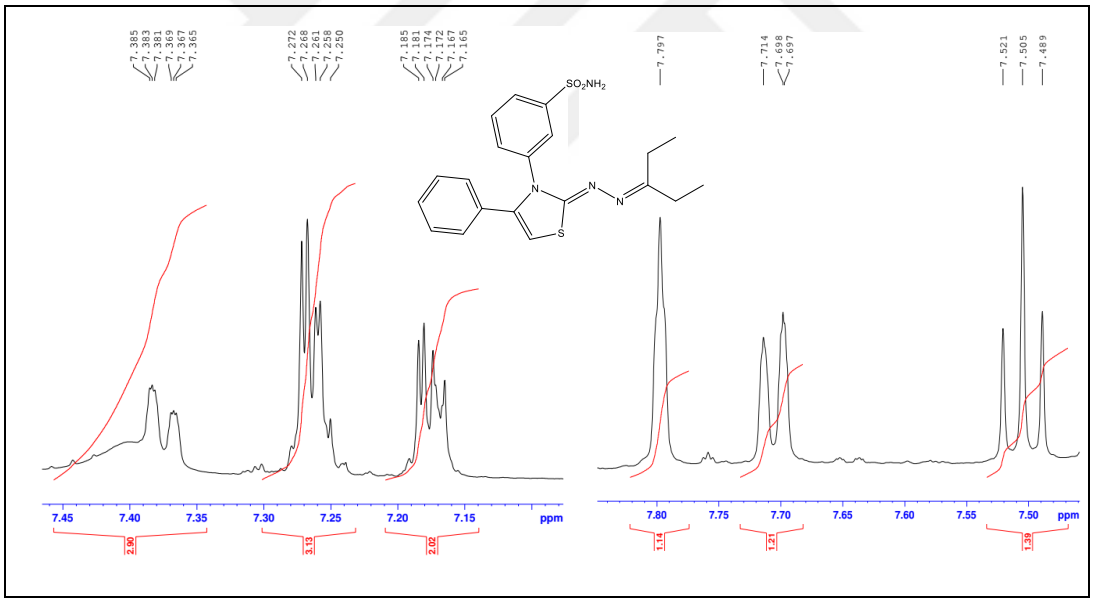

Figure 4-159: ^{1}H-NMR spectrum of compound 4k (7.15 – 7.80 ppm)

^{13}C-NMR Spectrum

^{13}C NMR (decoupled, DMSO-d_6, 100 MHz) δ (ppm): 10.4 (CH_3), 10.8 (CH_3), 23.9 (-CH_2-), 28.4 (-CH_2-), 102.3 (thiazole C_5), 124.5, 125.6 (3-benzenesulfonamide $C_{2,6}$), 128.0, 128.4, 128.5 (phenyl $C_{2,3,4,5,6}$), 129.2 (phenyl C_1), 130.4 (3-benzenesulfonamide

C_5), 131.3 (3-benzenesulfonamide C_4), 138.0 (3-benzenesulfonamide C_3), 138.8 (3-benzenesulfonamide C_1), 144,6 (thiazole C_4), 166.3 (N=C), 169.4 (thiazole C_2).

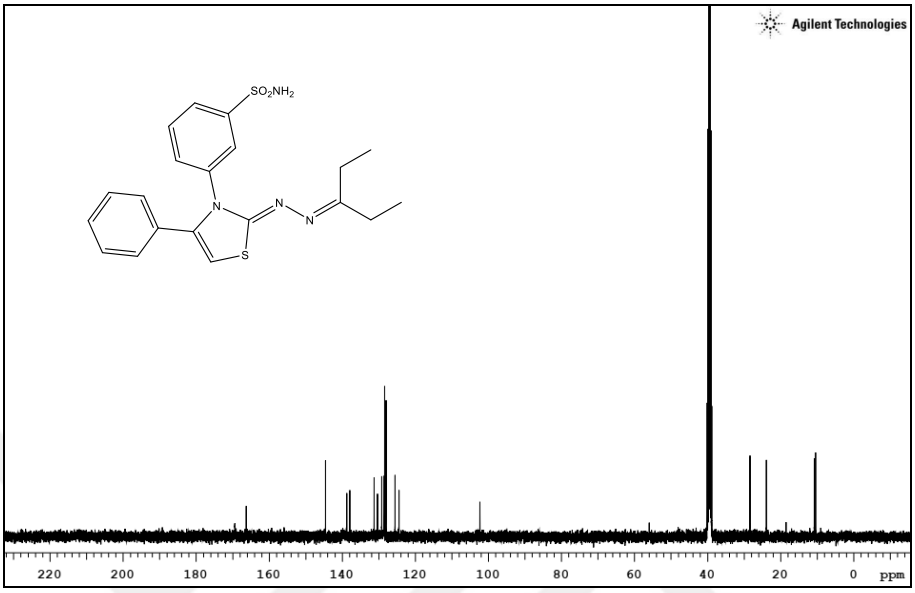

Figure 4-160: ^{13}C-NMR spectrum of compound 4k (0 – 220 ppm)

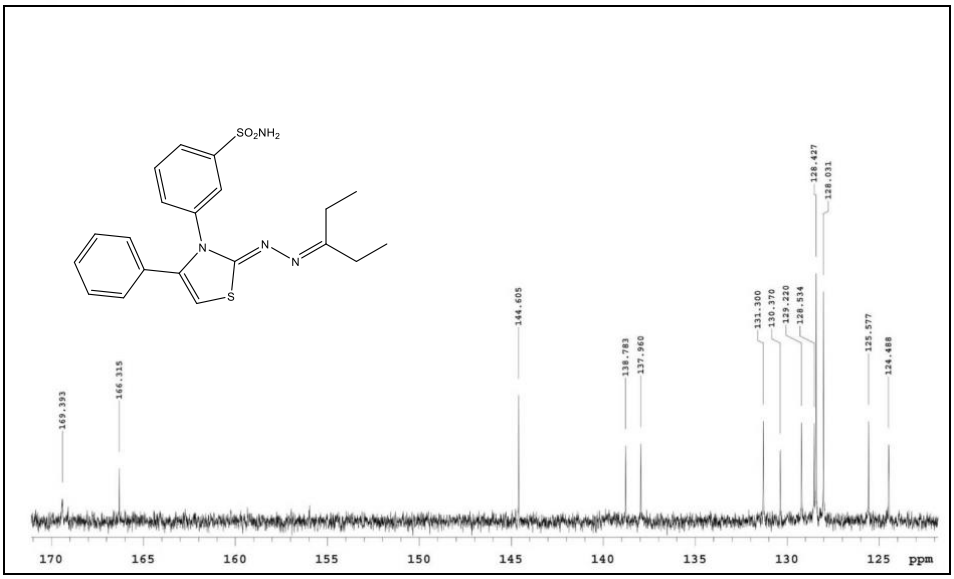

Figure 4-161: ^{13}C-NMR spectrum of compound 4k (123 – 170 ppm)

4.3.2.12. (*Z*)-4-(4-(4-bromophenyl)-2-(propan-2-ylidenehydrazineylidene)thiazol-3(2*H*)-yl)benzenesulfonamide (4l)

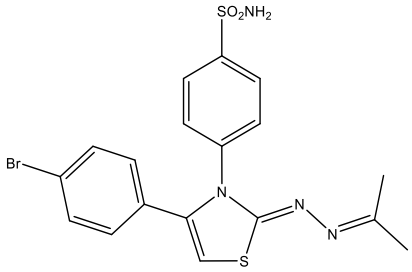

0.0018 mol (0.5g) of 2-bromo-1-(4-bromophenyl)ethane-1-one (**3b)** and 0.0018 mol (0.52g) of 2-(propan-2-ylidene)-*N*-(4-sulfamoylphenyl)hydrazine-1-carbothioamide (**E10**) are suspended in chloroform-ethanol (2:1). The reaction mixture is heated under reflux for 2.5 hours. The solid product formed is filtered and purified by recrystallization from ethanol.

Physical appearance	: Orange Crystals
Yield (%)	: 71
Retention factor	: 0.61; Chloroform : Methanol (9:1)
Melting point (ºC)	: 176.1-177.1

Elemental Analysis

Molecular formula	: $C_{18}H_{17}BrN_4O_2S_2$
Molecular weight (g/mol)	: 465.39

Element	C	H	N	S
Calculated (%)	46.45	3.68	12.04	13.78
Found (%)	46.17	3.37	11.76	13.42

Spectral Analysis

Fourier Transform Infrared (FT-IR) Spectrum

IR(KBr): υ 3425, 3385 (NH s.b); 3196, 3116, 3057 (Ar.C-H s.b., =CH s.b); 2926, 2889 (Al.C-H s.b); 1595, 1585,1575, 1550, 1489 (Ar. C=C s.b, C=N s.b, N-H b.b); 1435 (Al.C-H b.b); 1355, 1170 (S=O s.b); 1290 (C-N s.b); 1074 (Ar-Br s.b); 813, 800 (1,4-disubs. Ar-C-H b.b)

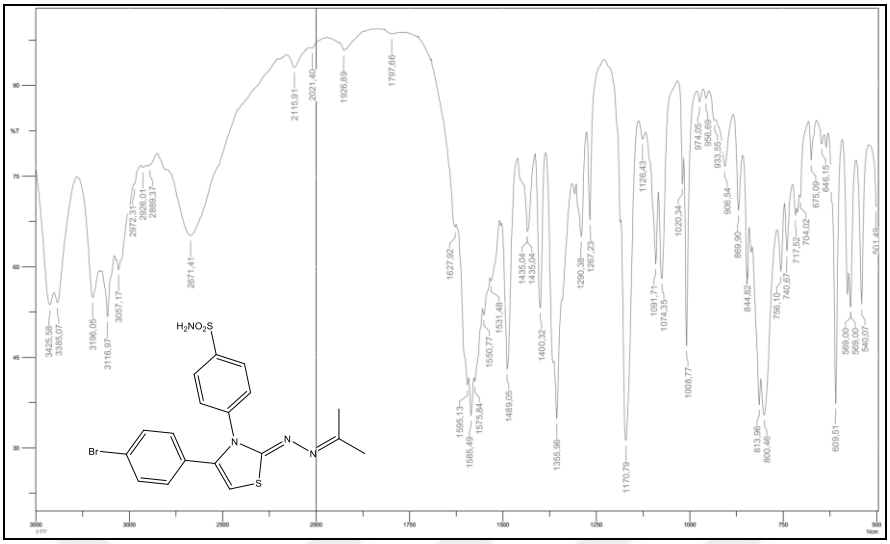

Figure 4-162: IR spectrum of compound 4l

^{1}H-NMR Spectrum

^{1}H NMR (DMSO-d_6 / 400 MHz δ (ppm): 1.84 (3H, s, -CH_3), 1.94 (3H, s, -CH_3), 7.03 (1H, s, thiazole C_5-H), 7.11 (2H, app.d (AA'BB'), J=8.6 Hz, 4-bromophenyl $C_{2,6}$-H), 7.38-7.50 (6H, m, 4-bromophenyl $C_{3,5}$-H and 4-benzenesulfonamide $C_{3,5}$-H and -SO_2NH_2), 7.76 (2H, app.d (AA'BB'), J=8.6 Hz, 4-benzenesulfonamide $C_{2,6}$-H).

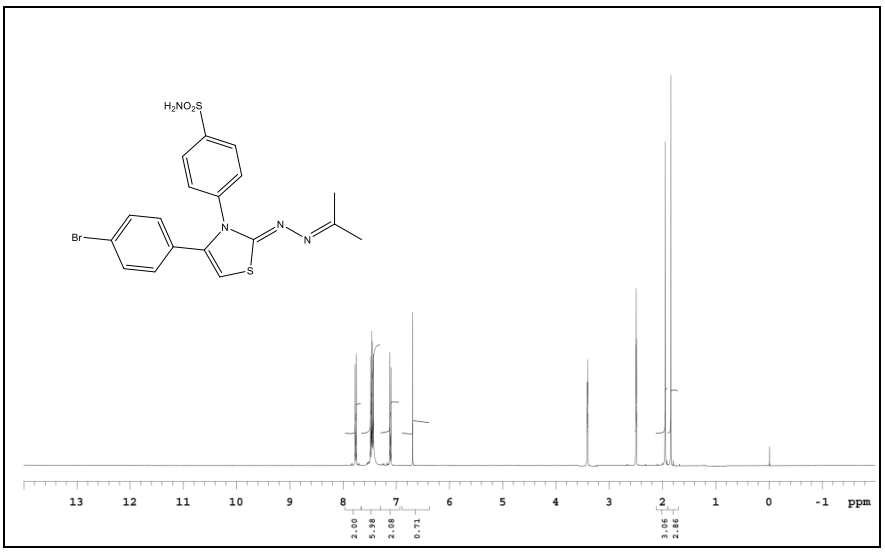

Figure 4-163: ^{1}H-NMR spectrum of compound 4l (0 – 14 ppm)

^{13}C-NMR Spectrum

^{13}C NMR (decoupled, DMSO-*d*$_6$, 100 MHz) δ (ppm): 18.7 (CH_3), 24.1 (CH_3), 103.3 (thiazole C_5), 121.9 (4-bromophenyl C_4), 126.2 (4-benzenesulfonamide $C_{2,6}$), 128.7 (4-benzenesulfonamide $C_{3/5}$), 129.7 (4-bromophenyl C_1), 130.1 (4-bromophenyl $C_{2,6}$), 131.4 (4-bromophenyl $C_{3,5}$), 137.7 (4-benzenesulfonamide C_4), 140.1 (4-benzenesulfonamide C_1), 142.8 (thiazole C_4), 162.4 (N=C), 165.8 (thiazole C_2).

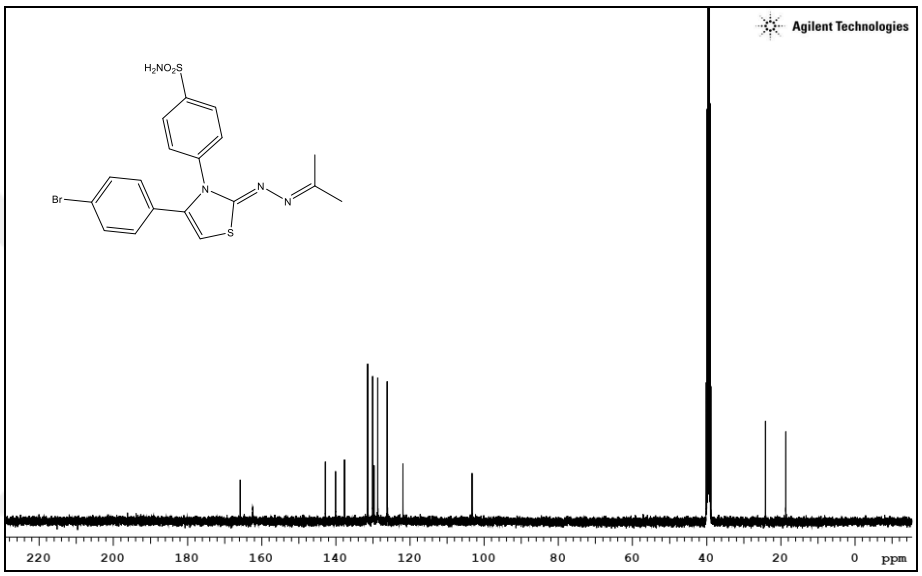

Figure 4-164: ^{13}C-NMR spectrum of compound 4l (0 – 220 ppm)

^{13}C NMR (HSQC-2D, DMSO-*d*$_6$, 100 MHz) δ (ppm): **18.7** [CH_3 - **1.84** (3H, s, -CH_3)], **24.1** (CH_3 - **1.94** (3H, s, -CH_3)], **103.3** [thiazole C_5 – **6.73** (1H, s, thiazole C_5-H)], **126.2** (4-benzenesulfonamide $C_{2,6}$ - **7.76** (2H, app.d (AA'BB'), *J*=8.6 Hz, 4-benzenesulfonamide $C_{2,6}$-H)], **128.7** (4-benzenesulfonamide $C_{3/5}$ - **7.38-7.50** (6H, m, 4-bromophenyl $C_{3,5}$-H and 4-benzenesulfonamide $C_{3,5}$-H and -SO_2NH_2)], **130.1** (4-bromophenyl $C_{2,6}$ - **7.11** (2H, app.d (AA'BB'), *J*=8.6 Hz, 4-bromophenyl $C_{2,6}$-H)], **131.4** [4-bromophenyl $C_{3,5}$ - **7.38-7.50** (6H, m, 4-bromophenyl $C_{3,5}$-H and 4-benzenesulfonamide $C_{3,5}$-H and -SO_2NH_2)].

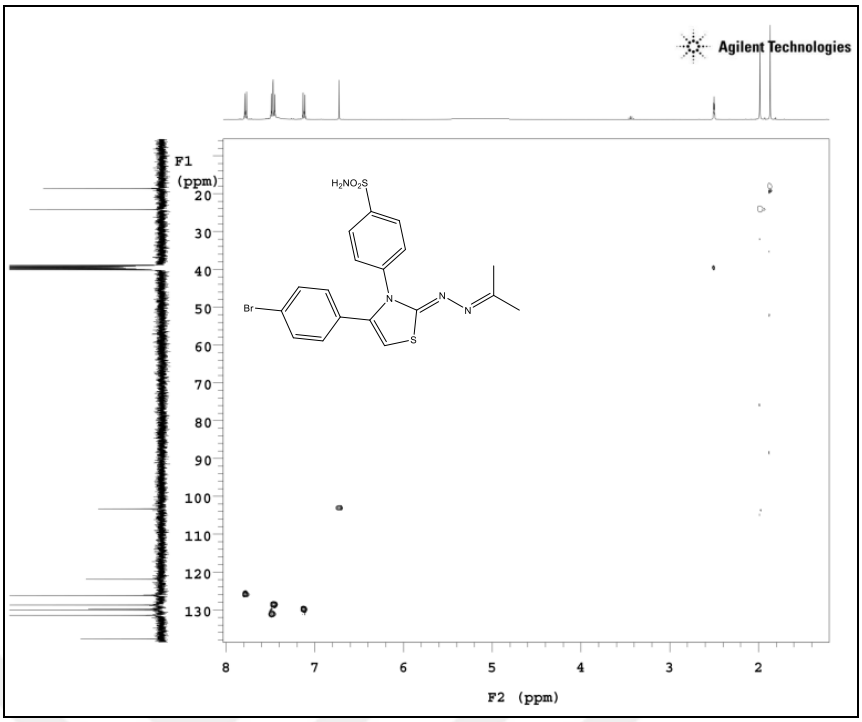

Figure 4-165: HSQC spectrum of compound 4l (0 – 14; 0 – 140 ppm)

LC-MS Spectrum

m/z ESI (positive): 467.0 $(M+2+H)^+$; $C_{18}H_{17}BrN_4O_2S_2$ (MA= 465.39; Exact Mass= 464.00)

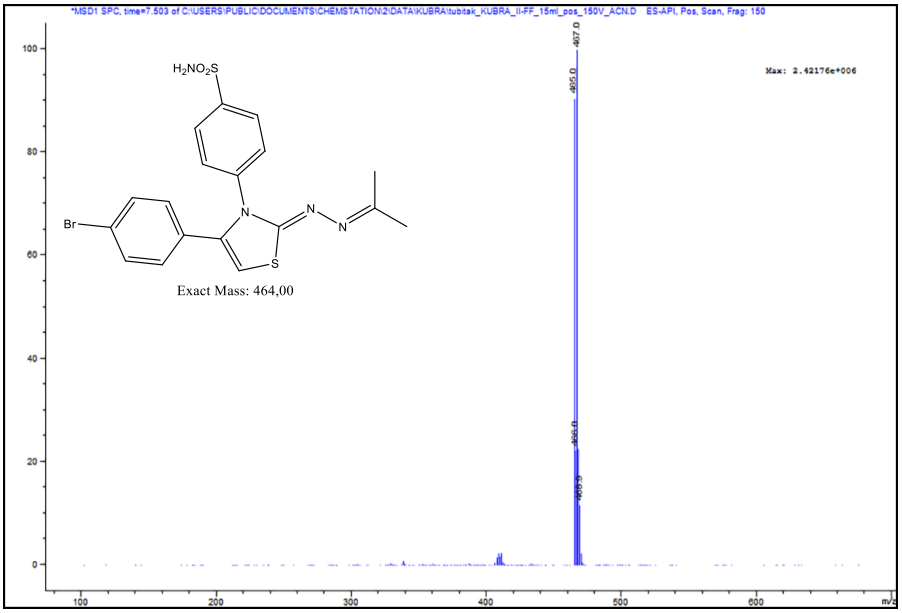

Figure 4-166: Mass spectrum of compound 4l

4.3.2.13. (*Z*)-4-(2-(propan-2-ylidenehydrazineylidene)-4-(4-(trifluoromethyl)phenyl)thiazol-3(2*H*)-yl)benzenesulfonamide (4m)

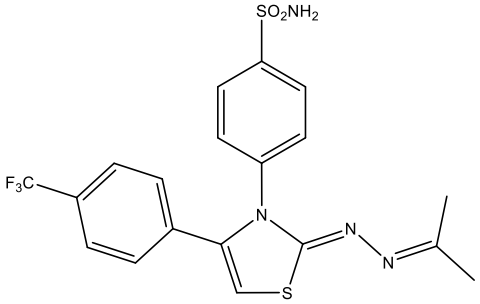

0.0018 mol (0.48g) of 2-bromo-1-(4-(trifluoromethyl)phenyl)ethan-1-one (**3d**) and 0.0018 mol (0.52g) of 2-(propan-2-ylidene)-*N*-(4-sulfamoylphenyl)hydrazine-1-carbothioamide (**E10**) are suspended in chloroform-ethanol (2:1). The reaction mixture is heated under reflux for 2.5 hours. The solid product formed is filtered and purified by recrystallization from ethanol.

Physical appearance	: Yellow powder
Yield (%)	: 41
Retention factor	: 0.61; Chloroform : Methanol (9:1)
Melting point (ºC)	: 163.3-165.1

Elemental Analysis

Molecular formula	: $C_{19}H_{17}F_3N_4O_2S_2$
Molecular weight (g/mol)	: 454.49

Element	C	H	N	S
Calculated (%)	50.21	3.77	12.33	14.11
Found (%)	50.48	4.15	12.62	14.44

Spectral Analysis

Fourier Transform Infrared (FT-IR) Spectrum

IR(KBr): υ 3402, 3371 (NH s.b); 3188, 3120, 3062 (Ar.C-H s.b., =CH s.b); 2933 (Al.C-H s.b); 1620, 1600, 1583, 1558, 1492 (Ar. C=C s.b, C=N s.b, N-H b.b); 1436, 1409

(Al.C-H b.b); 1325, 1174 (S=O s.b); 1290 (C-N s.b); 1357, 1138, 1116 (C-F s.b); 856, 827 (1,4-disubs. Ar-C-H b.b)

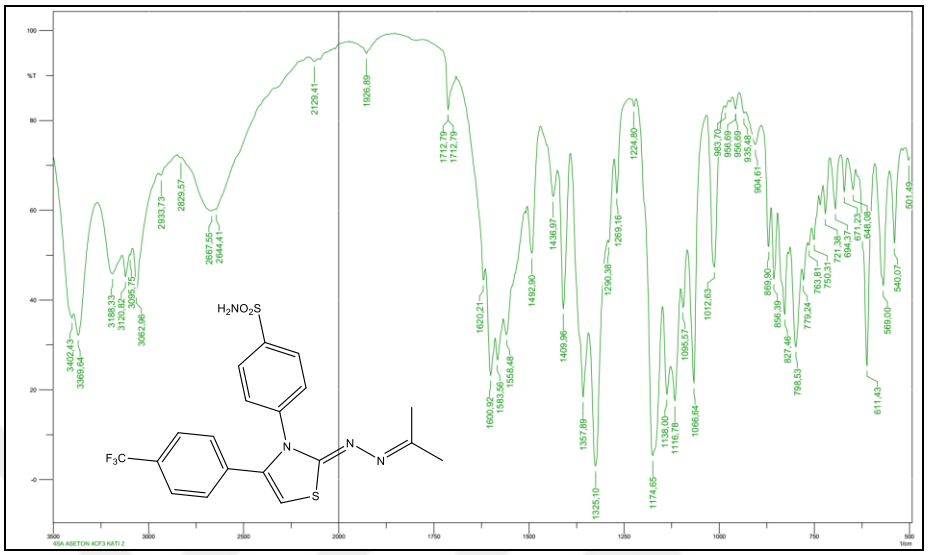

Figure 4-167: IR spectrum of compound 4m

^{1}H-NMR Spectrum

^{1}H NMR (DMSO-d_6 / 400 MHz δ (ppm): 1.84 (3H, s, -CH_3), 1.94 (3H, s, -CH_3), 6.81 (1H, s, thiazole C_5-H), 7.39 (2H, d, J=8.2 Hz, 4-trifluoromethylphenyl $C_{2,6}$-H), 7.65 (2H, d, J=8.2 Hz, 4-trifluoromethylphenyl $C_{3,5}$-H), 7.43 (2H, broad s, -SO_2NH_2), 7.46 (2H, d, J=8.6 Hz, 4-benzenesulfonamide $C_{3,5}$-H), 7.77 (2H, d, J=8.6 Hz, 4-benzenesulfonamide $C_{2,6}$-H).

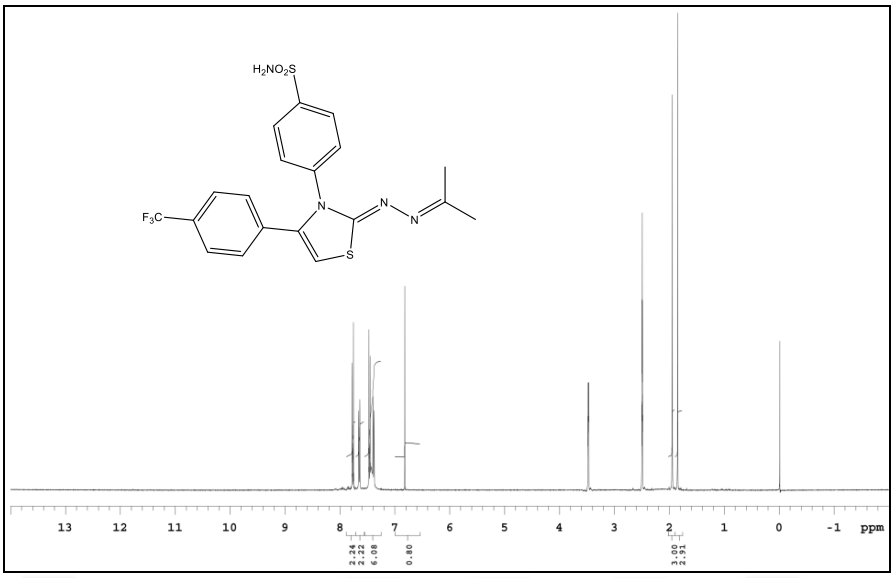

Figure 4-168: ^{1}H-NMR spectrum of compound 4m (0 – 14 ppm)

^{13}C-NMR Spectrum

^{13}C NMR (decoupled, DMSO-d_6, 125 MHz) δ (ppm): 19.1 (CH_3), 24.7 (CH_3), 105.3 (thiazole C_5), 125.4 (t, distinguishable), J=270.0 Hz, CF_3), 125.9, 125.9 (4-trifluoromethylphenyl $C_{3,5}$), 126.5, 126.6 (4-benzenesulfonamide $C_{2,6}$), 128.9, 129.1, 129.2, 129.6 (4-trifluoromethylphenyl $C_{2,4,6}$ / 4-benzenesulfonamide $C_{3,5}$), 131.4 (4-trifluoromethylphenyl C_4), 135.0 (4-trifluoromethylphenyl C_1), 137.7 (4-benzenesulfonamide C_4), 140.6 (4-benzenesulfonamide C_1), 143.4 (thiazole C_4), 163.7 (N=C), 166.0 (thiazole C_2).

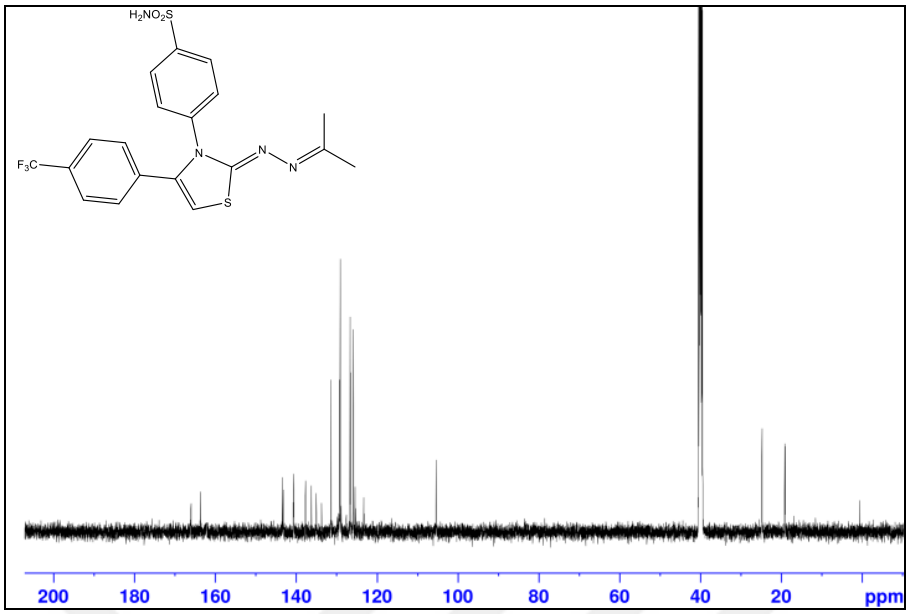

Figure 4-169: ^{13}C-NMR spectrum of compound 4m (0 – 220 ppm)

^{13}C NMR (HSQC-2D, DMSO-*d*$_6$, 125 MHz) δ (ppm): **19.1** [CH_3 - **1.84** (3H, s, -CH_3)], **24.7** [CH_3 - **1.94** (3H, s, -CH_3)], **125.9, 125.9** [4-trifluoromethylphenyl $C_{3,5}$ - **7.65** (2H, d, *J*=8.2 Hz, 4-trifluoromethylphenyl $C_{3,5}$-H)], **126.5, 126.6** [3-benzenesulfonamide $C_{2,6}$ - **7.77** (2H, d, *J*=8.6 Hz, 4-benzenesulfonamide $C_{2,6}$-H)], **128.9, 129.1, 129.2, 129.6** (4-trifluoromethylphenyl $C_{2,6}$ / 4-benzenesulfonamide $C_{3,5}$ - **7.39** (2H, d, *J*=8.2 Hz, 4-trifluoromethylphenyl $C_{2,6}$-H) and **7.46** (2H, d, *J*=8.6 Hz, 4-benzenesulfonamide $C_{3,5}$-H)].

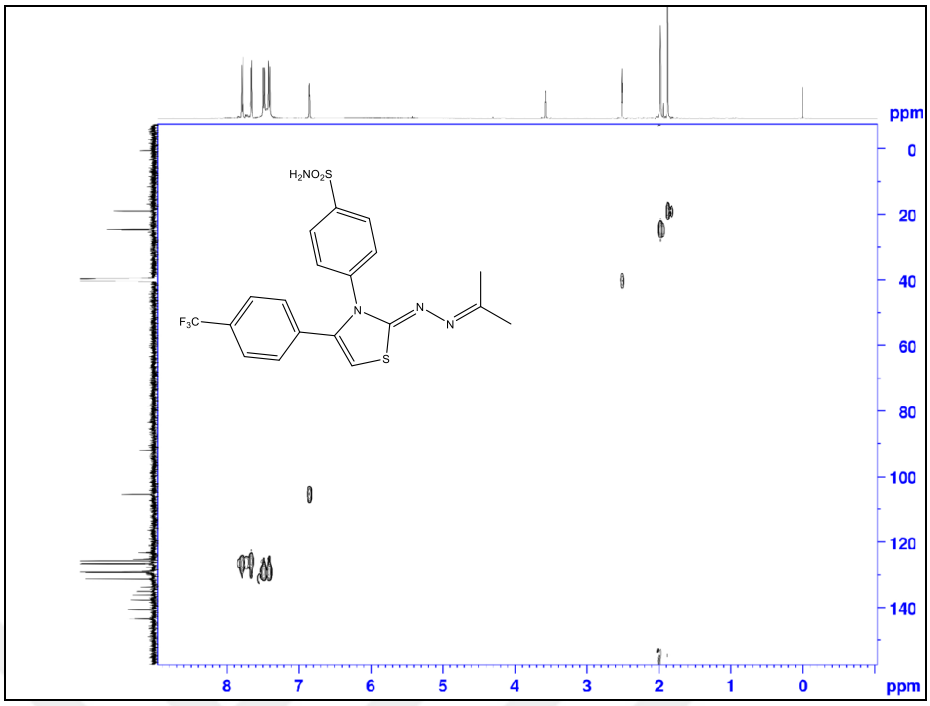

Figure 4-170: HSQC spectrum of compound 4m (0 – 8; 0 – 140 ppm)

LC-MS Spectrum

m/z ESI (positive): 455.0 $(M+H)^+$; $C_{19}H_{17}F_3N_4O_2S_2$ (MA= 454.49; Exact Mass= 454.07)

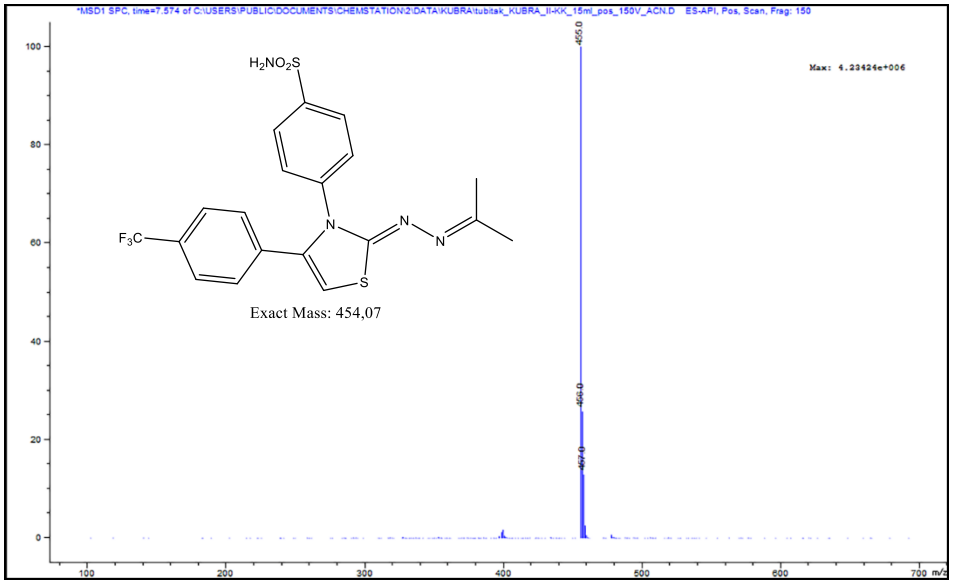

Figure 4-171: Mass spectrum of compound 4m

4.3.2.14. (*Z*)-4-(2-(propan-2-ylidenehydrazineylidene)-4-(4-(trifluoromethoxy)phenyl)thiazol-3(2*H*)-yl)benzenesulfonamide (4n)

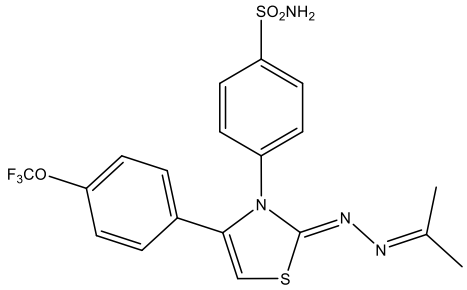

0.0019 mol (0.53g) of 2-bromo-1-(4-(trifluoromethoxy)phenyl)ethan-1-one (**3e**) and 0.0019 mol (0.54g) of 2-(propan-2-ylidene)-*N*-(4-sulfamoylphenyl)hydrazine-1-carbothioamide (**E10**) are suspended in chloroform-ethanol (2:1). The reaction mixture is heated under reflux for 2.5 hours. The solid product formed is filtered and purified by recrystallization from ethanol.

Physical appearance	: Yellow powder
Yield (%)	: 43
Retention factor	: 0.5; Chloroform : Methanol (9:1)
Melting point (ºC)	: 150.8-151.3

Elemental Analysis

Molecular formula	: $C_{19}H_{17}F_3N_4O_3S_2.CH_3CH_2OH$
Molecular weight (g/mol)	: 516.55

Element	C	H	N	S
Calculated (%)	48.83	4.49	10.85	12.41
Found (%)	48.47	4.26	10.51	12.05

Spectral Analysis

Fourier Transform Infrared (FT-IR) Spectrum

IR(KBr): υ 3292, 3234 (NH s.b); 3107, 3022, 2976 (Ar.C-H s.b., =CH s.b); 2877, 2773, 2721 (Al.C-H s.b); 1598, 1585, 2568, 1504, 1492 (Ar. C=C s.b, C=N s.b, N-H b.b);

1435, 1404 (Al.C-H b.b); 1342, 1168 (S=O s.b); 1313 (C-N s.b); 827 (1,4-disubs. Ar-C-H b.b)

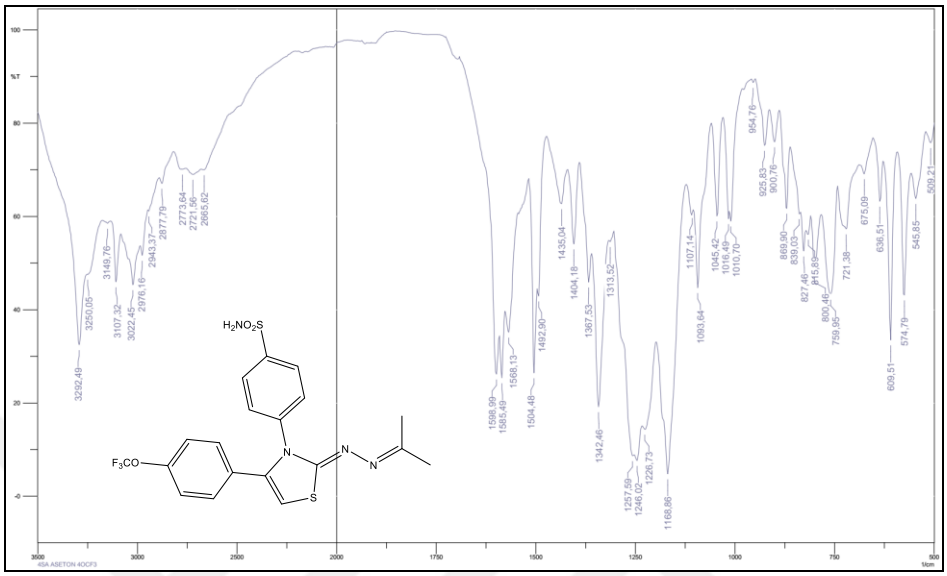

Figure 4-172: IR spectrum of compound 4n

^{1}H-NMR Spectrum

^{1}H NMR (DMSO-d_6 / 400 MHz δ (ppm): 1.04 (t, *J*= 7,00 Hz, CH_3CH_2OH), 1.84 (3H, s, -CH_3), 1.95 (3H, s, -CH_3), 3.44(q, *J*= 7,00 Hz, CH_3CH_2OH), 4.85 (s, CH_3CH_2OH), 6.71 (1H, s, thiazole C_5-H), 7.27-7.31 (4H, m, 4-trifluoromethoxyphenyl $C_{2,3,5,6}$-H), 7.45 (2H, app.d (AA'BB'), *J*=8.2 Hz, 4-benzenesulfonamide $C_{3,5}$-H and -SO_2NH_2), 7.76 (2H, app.d (AA'BB'), *J*=8.2 Hz, 4-benzenesulfonamide $C_{2,6}$-H).

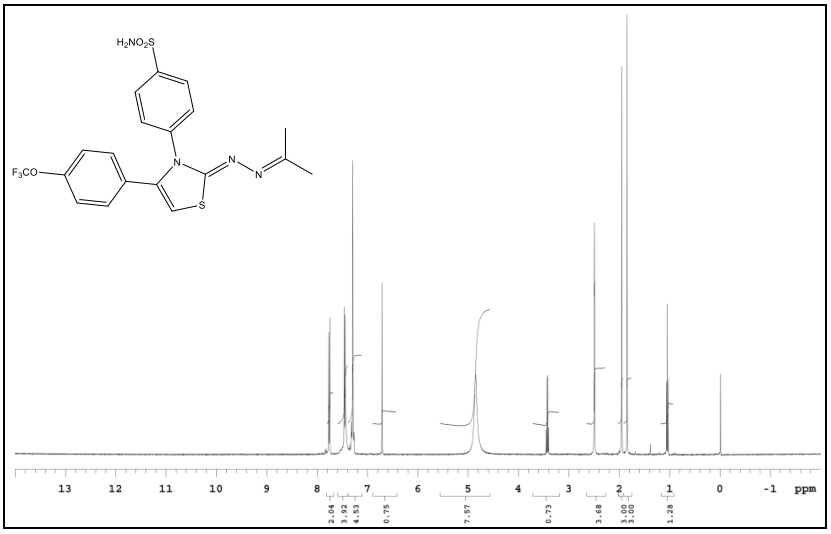

Figure 4-173: ^{1}H-NMR spectrum of compound 4n (0 – 14 ppm)

^{13}C-NMR Spectrum

^{13}C NMR (decoupled, DMSO-*d*$_6$, 125 MHz) δ (ppm): 19.14 (CH_3), 24.6 (CH_3), 104.0 (thiazole C_5), 119.4 (OCF_3, non-distinguishable), 121.4 (4-trifluoromethoxyphenyl $C_{3,5}$), 126.6 (4-benzenesulfonamide $C_{2,6}$), 129.2 (4-benzenesulfonamide $C_{3,5}$), 130.6 (4-trifluoromethoxyphenyl $C_{2,6}$), 132.7 (4-trifluoromethoxyphenyl C_1), 137.9 (4-benzenesulfonamide C_4), 140.5 (4-benzenesulfonamide C_1), 143.3 (thiazole C_4), 148.6 (4-trifluoromethoxyphenyl C_4), 163.0 (N=C), 166.3 (thiazole C_2).

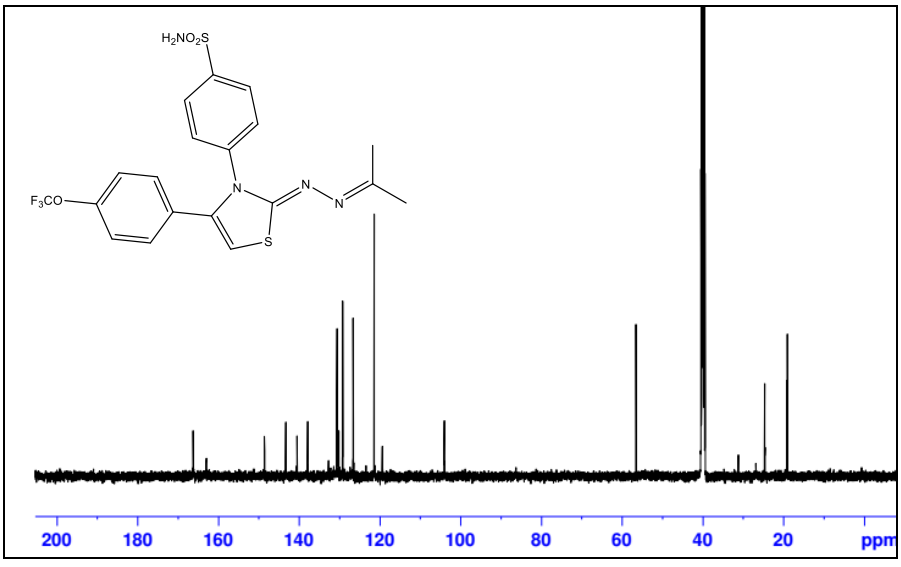

Figure 4-174: ^{13}C-NMR spectrum of compound 4n (0 – 200 ppm)

^{13}C NMR (HSQC-2D, DMSO-*d*$_6$, 125 MHz) δ (ppm): **19.1** [CH_3 - **1.84** (3H, s, -CH_3)], **24.6** [CH_3 - **1.95** (3H, s, -CH_3)], **104.0** [thiazole C5 - **6.71** (1H, s, thiazole C_5-H)], **121.4** [4-trifluoromethoxyphenyl $C_{3,5}$ - **7.27-7.31** (4H, m, 4-trifluoromethoxyphenyl $C_{2,3,5,6}$-H)], **126.6** [4-benzenesulfonamide $C_{2,6}$ - **7.76** (2H, app.d (AA'BB'), *J*=8.2 Hz, 4-benzenesulfonamide $C_{2,6}$-H)], **129.2** [4-benzenesulfonamide $C_{3,5}$ - **7.45** (2H, app.d (AA'BB'), *J*=8.2 Hz, 4-benzenesulfonamide $C_{3,5}$-H and -SO_2NH_2)], **130.6** [4-trifluoromethoxyphenyl C2,6 - **7.27-7.31** (4H, m, 4-trifluoromethoxyphenyl $C_{2,3,5,6}$-H)].

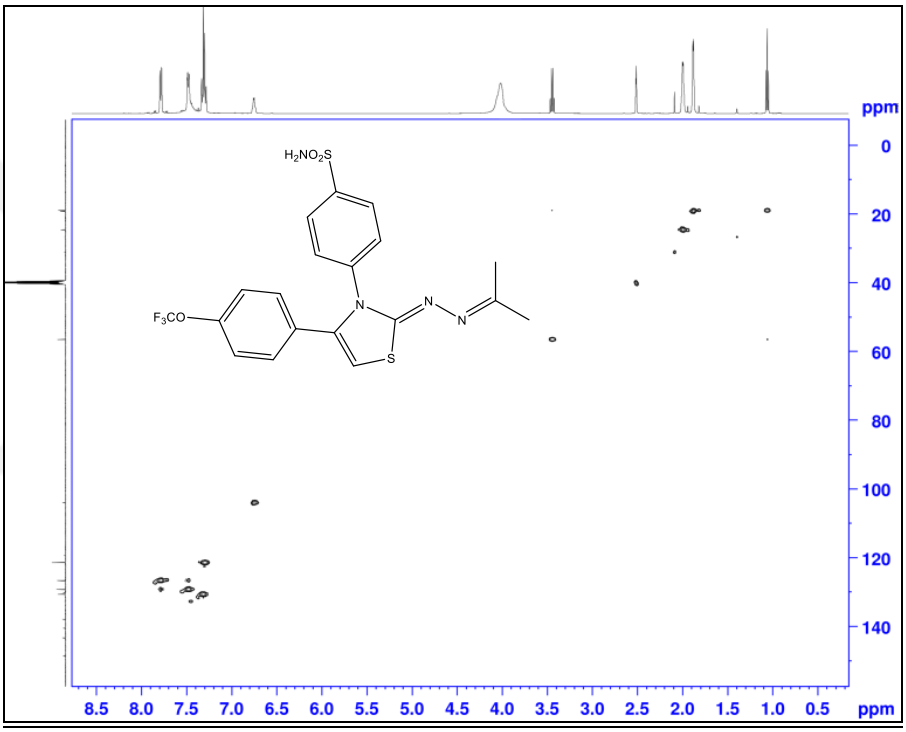

Figure 4-175: HSQC spectrum of compound 4n (0 – 8.5; 0 – 140 ppm)

LC-MS Spectrum

m/z ESI (positive): 471.0 $(M+H)^+$; $C_{19}H_{17}F_3N_4O_2S_2$ (MA= 470.49; Exact Mass= 470.07)

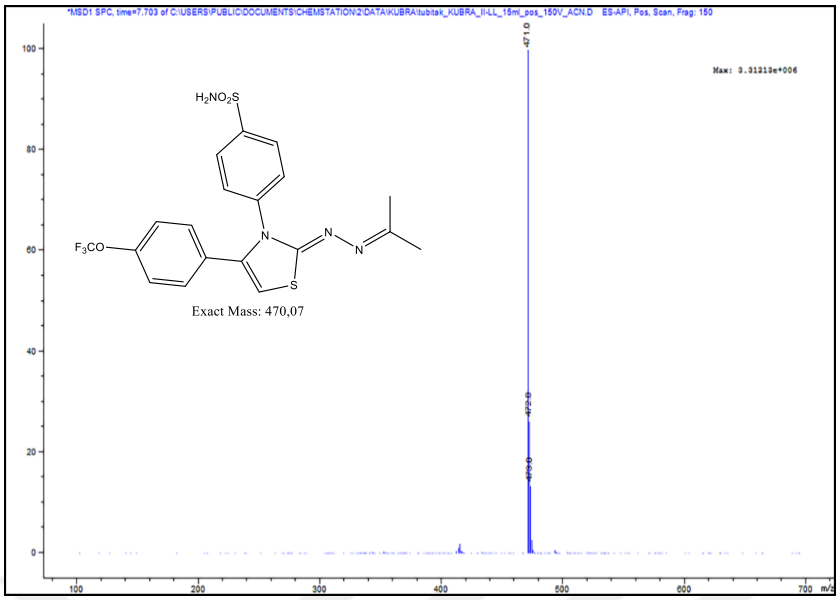

Figure 4-176: Mass spectrum of compound 4n

4.3.2.15. (*Z*)-4-(4-(4-fluorophenyl)-2-(propan-2-ylidenehydrazineylidene)thiazol-3(2*H*)-yl)benzenesulfonamide (4o)

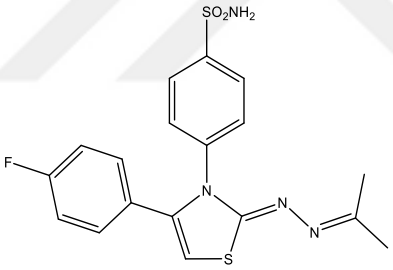

0.0019 mol (0.41g) of 2-bromo-1-(4-fluorophenyl)ethan-1-one (**3f**) and 0.0019 mol (0.54g) of 2-(propan-2-ylidene)-*N*-(4-sulfamoylphenyl)hydrazine-1-carbothioamide (**E10**) are suspended in chloroform-ethanol (2:1). The reaction mixture is heated under reflux for 2.5 hours. The solid product formed is filtered and purified by recrystallization from ethanol.

Physical appearance	: Brown crystals
Yield (%)	: 66
Retention factor	: 0.6; Chloroform : Methanol (9:1)
Melting point (ºC)	: 226.9 – 228.0

Elemental Analysis

Molecular formula	: $C_{18}H_{17}FN_4O_2S_2$
Molecular weight (g/mol)	: 404.48

Element	C	H	N	S
Calculated (%)	53.45	4.24	13.85	15.85
Found (%)	53.22	4.01	13.48	15.54

Spectral Analysis

Fourier Transform Infrared (FT-IR) Spectrum

IR(KBr): υ 3477, 3417 (NH s.b); 3148, 3113, 3047 (Ar.C-H s.b., =CH s.b); 2789, 2727 (Al.C-H s.b); 1633, 1598, 1583, 1560, 1504, 1490 (Ar. C=C s.b, C=N s.b, N-H b.b); 1435, 1404 (Al.C-H b.b); 1340, 1165 (S=O s.b); 1228 (Ar-F s.b); 839, 829 (1,4-disubs. Ar-C-H b.b)

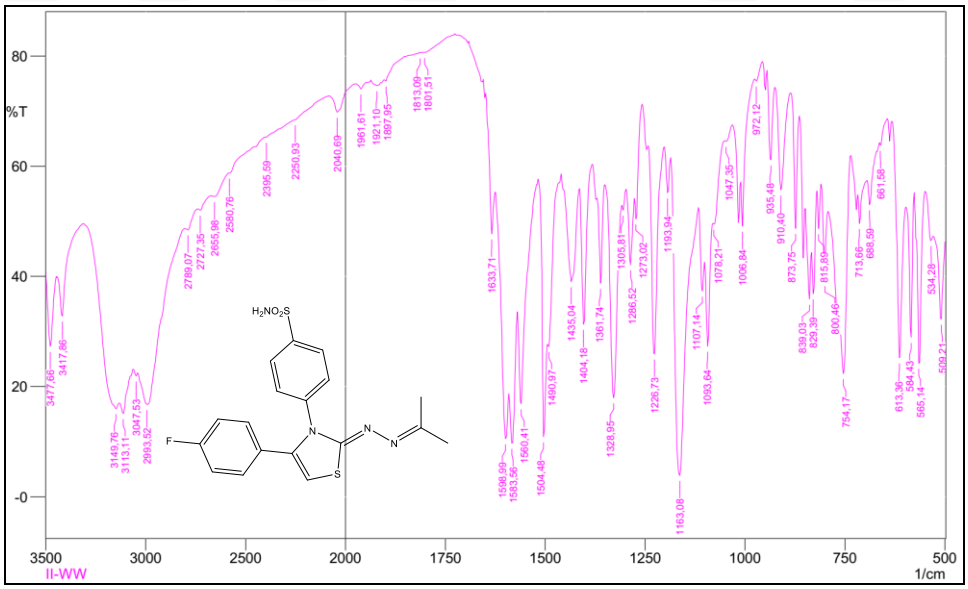

Figure 4-177: IR spectrum of compound 4o

^{1}H-NMR Spectrum

^{1}H NMR (DMSO-d_6 / 400 MHz δ (ppm): 1.88 (3H, s, CH_3), 2.01 (3H, s, CH_3), 6.69 (1H, s, thiazole C_5-H), 7.11 (2H, app.t (AA'BB'X), J=8.6 Hz, 4-fluorophenyl $C_{3,5}$-H), 7.23 (2H, app.dd (AA'BB'X), J= 8.6, 5.5 Hz, 4-fluorophenyl $C_{2,6}$-H), 7.37 (2H, broad s, SO_2NH_2, A broad singlet hidden below the other peaks between 7.22 and 7.46), 7.46 (2H, app.d (AA'BB'), J=8.6 Hz, 4-benzenesulfonamide $C_{3,5}$-H), 7.77 (2H, app.d (AA'BB'), J=8.6 Hz, 4-benzenesulfonamide $C_{2,6}$-H).

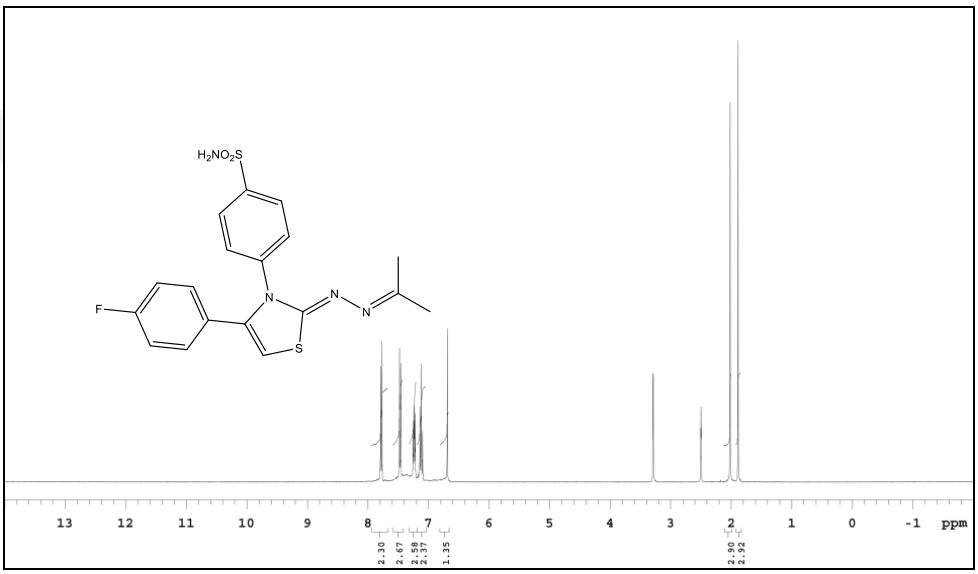

Figure 4-178: ^{1}H-NMR spectrum of compound 4o (0 – 14 ppm)

^{13}C-NMR Spectrum

^{13}C NMR (decoupled, DMSO-d_6, 100 MHz) δ (ppm): 18.6 (CH_3), 24.0 (CH_3), 102.6 (thiazole C_5), 115.4 (d, J=21.9 Hz, 4-fluorophenyl $C_{3,5}$), 126.1 (4-benzenesulfonamide $C_{2,6}$), 126.8 (4-fluorophenyl C_1), 128.8, (4-benzenesulfonamide $C_{3,5}$), 130.5 (d, J=11.6 Hz, 4-fluorophenyl $C_{2,6}$), 137.9 (4-benzenesulfonamide C_4), 139.9 (4-benzenesulfonamide C_1), 143.0 (thiazole C_4), 161.9 (d, J=245.1 Hz, 4-fluorophenyl C_4), 163.7 (N=C), 165.9 (thiazole C_2).

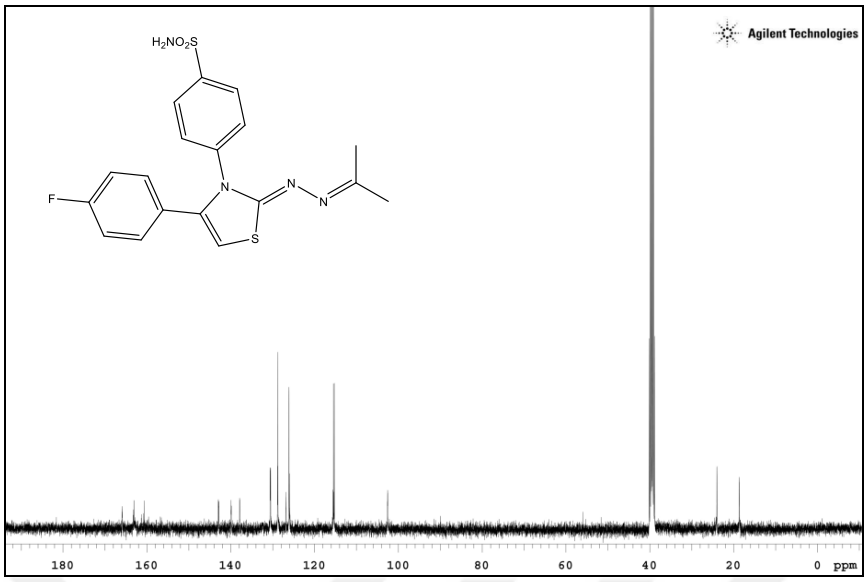

Figure 4-179: ^{13}C-NMR spectrum of compound 4o (0 – 200 ppm)

LC-MS Spectrum

m/z ESI (positive): 405.1 $(M+H)^+$; $C_{18}H_{17}FN_4O_2S_2$ (404.48); Exact Mass= 404.08)

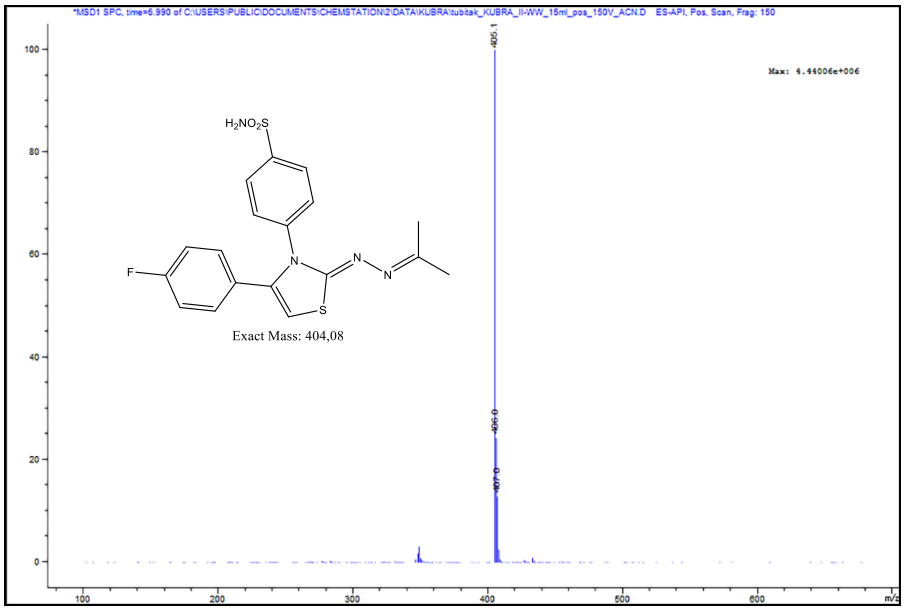

Figure 4-180: Mass spectrum of compound 4o

4.3.2.16. (*Z*)-4-(2-(propan-2-ylidenehydrazineylidene)-4-(3-(trifluoromethyl)phenyl)thiazol-3(2*H*)-yl)benzenesulfonamide (4p)

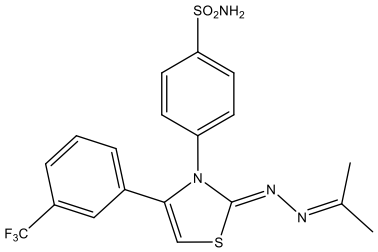

0.0019mol (0.51g) of 2-bromo-1-(3-(trifluoromethyl)phenyl)ethan-1-one (**3g**) and 0.0019 mol (0.54g) of 2-(propan-2-ylidene)-*N*-(4-sulfamoylphenyl)hydrazine-1-carbothioamide (**E10**) are suspended in chloroform-ethanol (2:1). The reaction mixture is heated under reflux for 2.5 hours. The solid product formed is filtered and purified with preparative TLC.

Physical appearance	: Yellow Powder
Yield (%)	: 30
Retention factor	: 0.61; Chloroform : Methanol (9:1)
Melting point (ºC)	: 178.0 – 178.8

Elemental Analysis

Molecular formula	: $C_{19}H_{17}F_3N_4O_2S_2$
Molecular weight (g/mol)	: 454.489

Element	C	H	N	S
Calculated (%)	50.21	3.77	12.33	14.11
Found (%)	49.85	3.50	12.60	13.80

Spectral Analysis

Fourier Transform Infrared (FT-IR) Spectrum

IR(KBr): υ 3323, 3251 (NH s.b); 3105, 3076 (Ar.C-H s.b., =CH s.b); 1629, 1600, 1585, 1562, 1494 (Ar. C=C s.b, C=N s.b, N-H b.b); 1433 (Al.C-H b.b); 1346, 1168 (S=O s.b); 1327, 1161, 1138 (C-F s.b); 1311 (C-N s.b); 867, 756, 698 (monosubs. Ar-C-H b.b); 800 (1,4-disubs. Ar-C-H b.b)

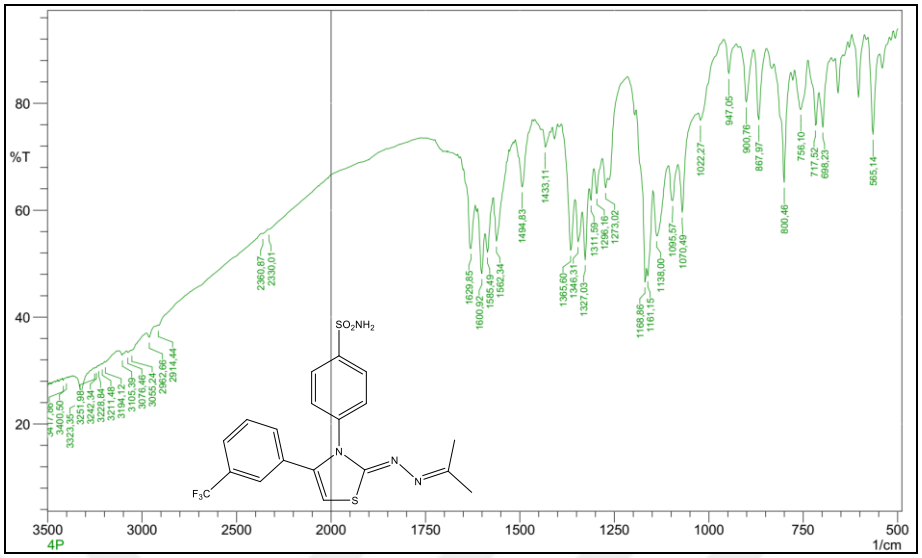

Figure 4-181: IR spectrum of compound 4p

^{1}H-NMR Spectrum

^{1}H NMR (DMSO-d_6 / 400 MHz δ (ppm): 1.80 (3H, s, -CH_3), 1.90 (3H, s, -CH_3), 6.77 (1H, s, thiazole C_5-H), 7.39-7.48 (6H, m, -SO_2NH_2 and 4-benzenesulfonamide $C_{3,5}$-H and 3-trifluorophenyl $C_{5,6}$-H), 7.52 (1H, s, 3-trifluorophenyl C_2-H), 7.61 (1H, d, J=7.8 Hz, 3-trifluorophenyl C_4-H), 7.73 (2H, d, J=8.6 Hz, 4-benzenesulfonamide $C_{2,6}$-H).

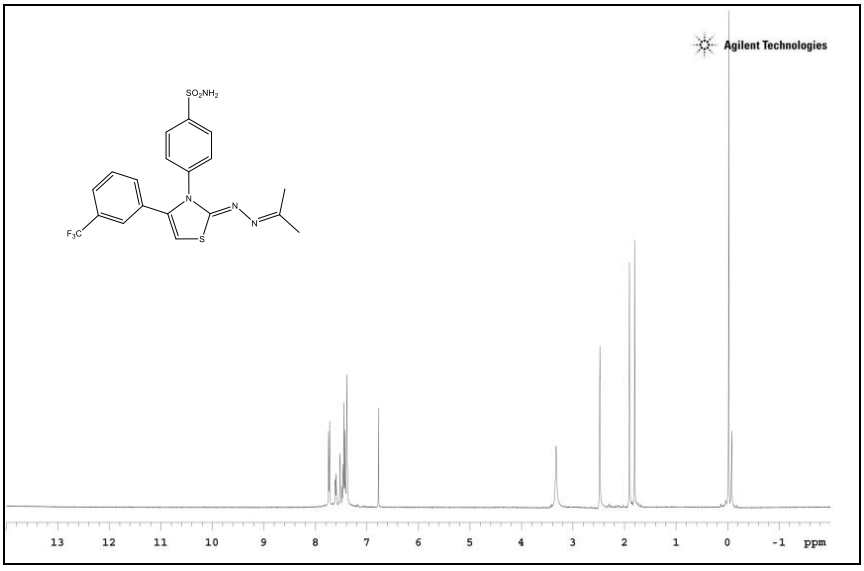

Figure 4-182: ^{1}H-NMR spectrum of compound 4p (0 – 14 ppm)

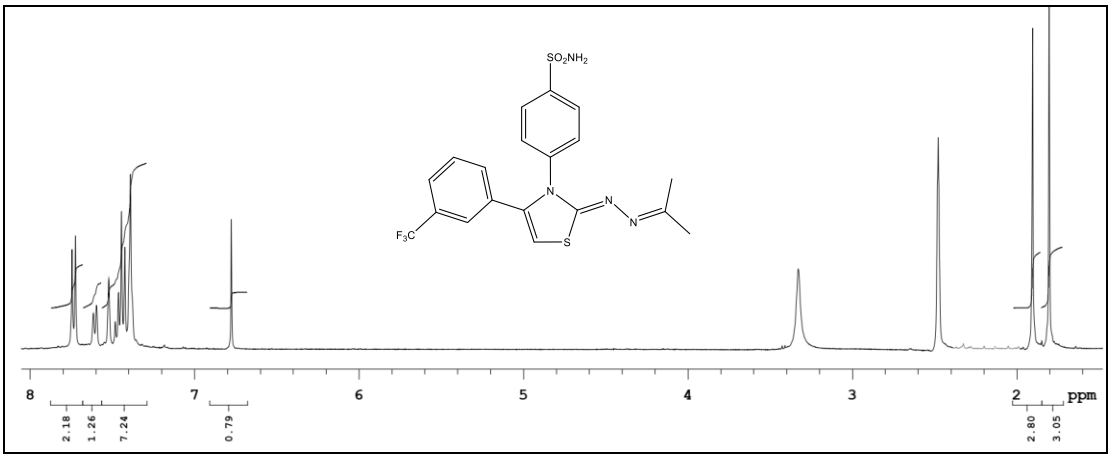

Figure 4-183: ^{1}H-NMR spectrum of compound 4p (1 – 8 ppm)

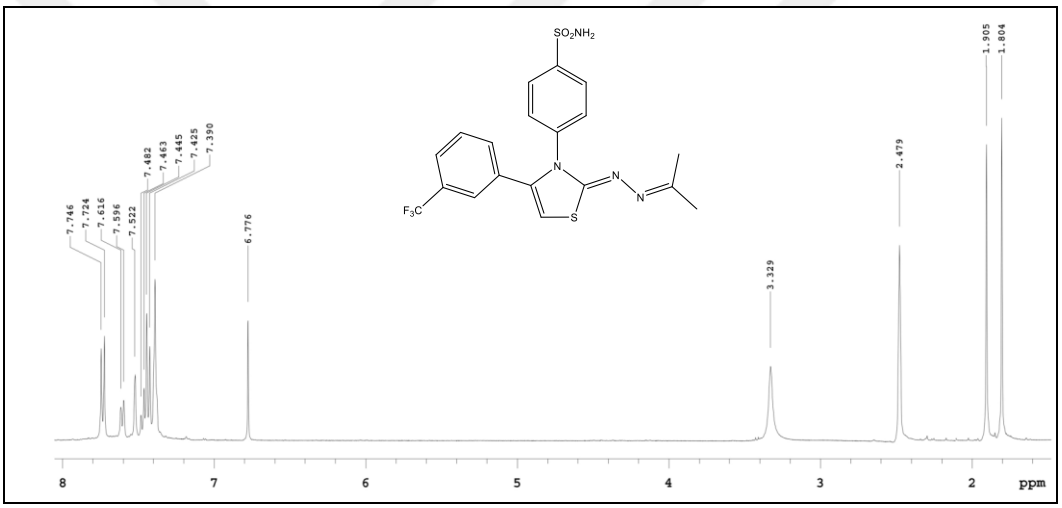

Figure 4-184: ^{1}H-NMR spectrum of compound 4p (1.5 – 8 ppm)

4.3.2.17. (*Z*)-4-(2-(pentan-3-ylidenehydrazineylidene)-4-(4-methylphenyl)thiazol-3(2*H*)-yl)benzenesulfonamide (4q)

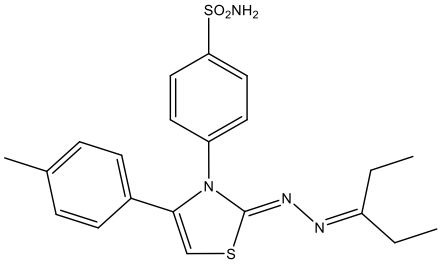

0.0021 mol (0.45g) of 2-bromo-1-(4-methylphenyl)ethan-1-one (**3h**) and 0.0021 mol (0.66g) of 2-(pentan-3-ylidene)-*N*-(4-sulfamoylphenyl)hydrazine-1-carbothioamide

(**E11**) are suspended in chloroform-ethanol (2:1). The reaction mixture is heated under reflux for 3 hours. The solid product formed is filtered and purified by recrystallization from ethanol.

Physical appearance	: Brown Powder
Yield (%)	: 50
Retention factor	:0.73; Chloroform : Methanol (9:1)
Melting point (ºC)	: 209.9-210.6

Elemental Analysis

Molecular formula	: $C_{19}H_{17}F_3N_4O_3S_2$
Molecular weight (g/mol)	: 428.57

Element	C	H	N	S
Calculated (%)	58.85	5.64	13.07	14.96
Found (%)	58.58	5.77	12.86	14.67

Spectral Analysis

Fourier Transform Infrared (FT-IR) Spectrum

IR(KBr): υ 3429, 3419 (NH s.b); 3165, 3116, 3039 (Ar.C-H s.b., =CH s.b); 2983, 2968, 2937, 2875 (Al.C-H s.b); 1620, 1602, 1573, 1508, 1489 (Ar. C=C s.b, C=N s.b, N-H b.b); 1411, 1404 (Al.C-H b.b); 1354, 1170 (S=O s.b); 1317 (C-N s.b); 815, 814 (1,4-disubs. Ar-C-H b.b)

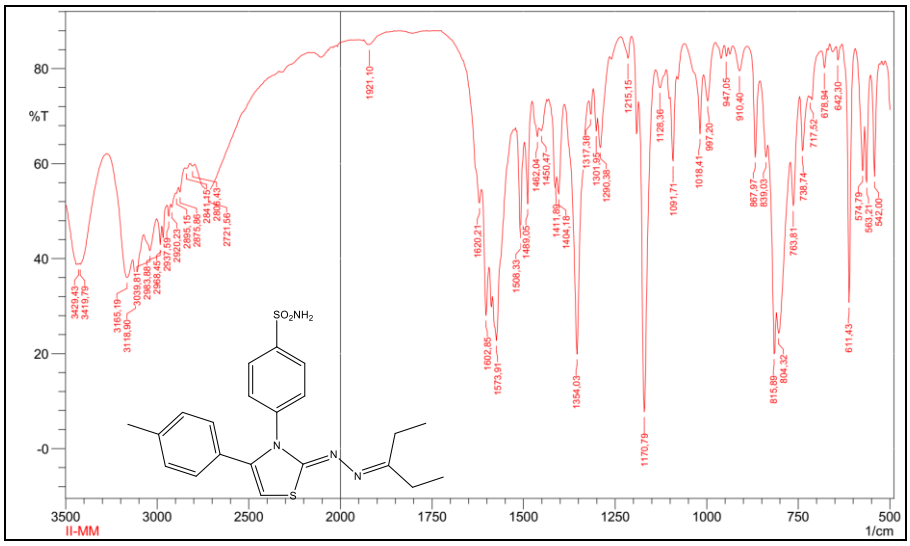

Figure 4-185: IR spectrum of compound 4q

^{1}H-NMR Spectrum

^{1}H NMR (DMSO-d_6 / 400 MHz δ (ppm): 0.91 (3H, t, J=7.4 Hz, -CH_3), 1.04 (3H, t, J=7.4 Hz, -CH_3), 2.23 (3H, s, 4-methylphenyl -CH_3), 2.26 (4H, m, 2 x CH_2), 6.54 (1H, s, thiazole C_5-H), 7.03-7.08 (4H, m, 4-methylphenyl $C_{2,3,5,6}$-H), 7.40-7.43 (4H, m, 4-benzenesulfonamide $C_{3,5}$-H, app.d (AA'BB') J=8.6 Hz and -SO_2NH_2), 7.75 (2H, app.d (AA'BB'), J=8.6 Hz, 4-benzenesulfonamide $C_{2,6}$-H).

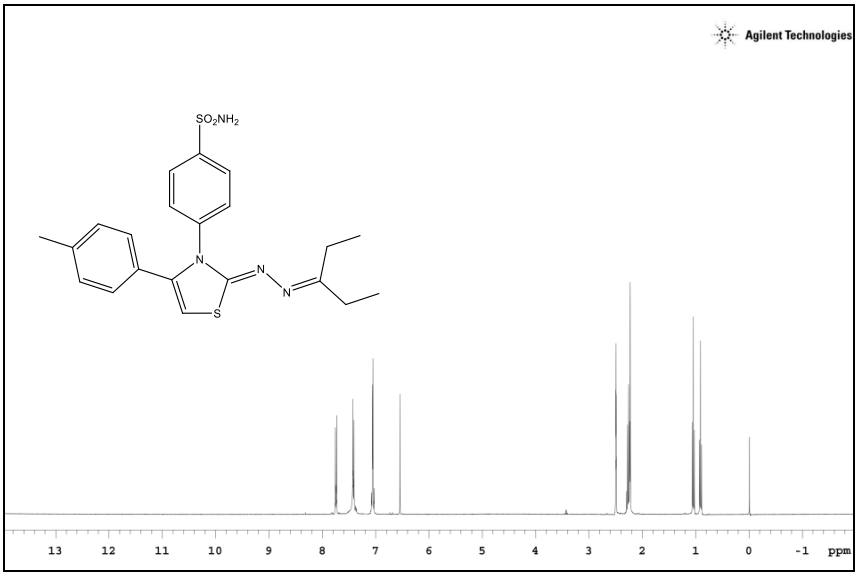

Figure 4-186: ^{1}H-NMR spectrum of compound 4q (0 – 14 ppm)

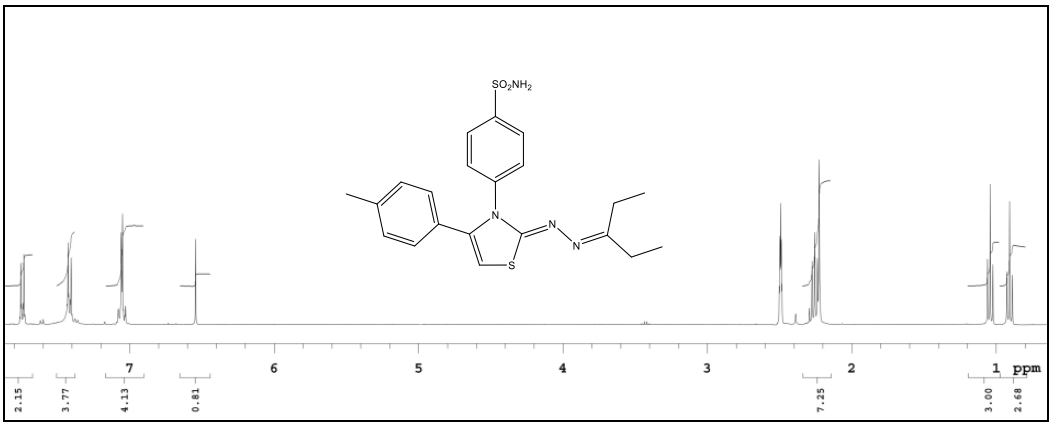

Figure 4-187: ^{1}H-NMR spectrum of compound 4q (0 – 14 ppm)

^{13}C-NMR Spectrum

^{13}C NMR (decoupled, DMSO-d_6, 125 MHz) δ (ppm): 10.9 (CH_3), 11.2 (CH_3), 21.2 (4-methylphenyl CH_3), 24.4 (-CH_2-), 28.8 (-CH_2-), 102.6 (thiazole C_5), 126.4, 126.6 (4-benzenesulfonamide $C_{2,6}$), 128.4, 129.5 (4-methylphenyl $C_{2,3,5,6}$), 129.1, 129.4 (4-benzenesulfonamide $C_{3,5}$), 130.3 (4-methylphenyl C_1), 138.6 (4-methylphenyl C_4), 139.4 (4-benzenesulfonamide C_4), 141.0 (4-benzenesulfonamide C_1), 143.2 (thiazole C_4), 164.6 (N=C), 169.9 (thiazole C_2).

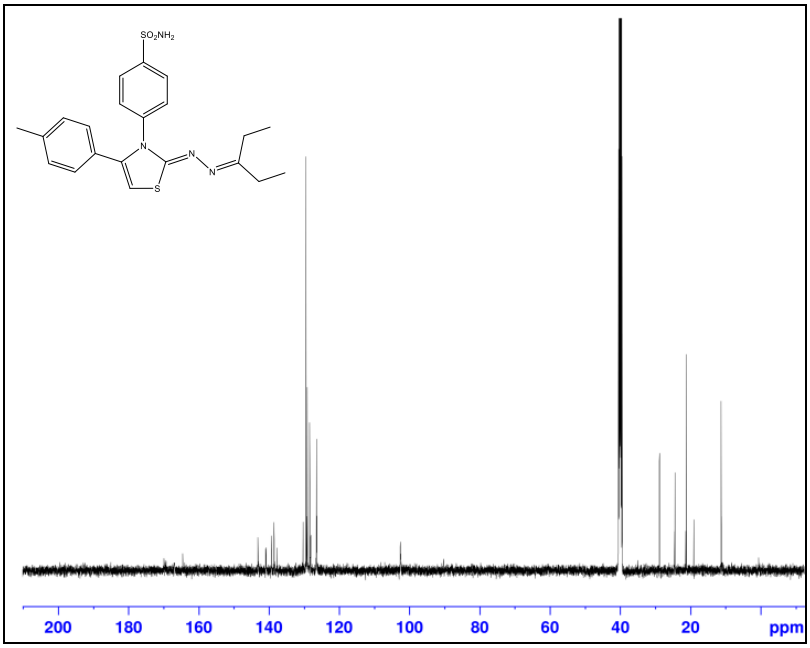

Figure 4-188: ^{13}C-NMR spectrum of compound 4q (0 – 200 ppm)

LC-MS Spectrum

m/z ESI (positive): 429.1 $(M+H)^+$; $C_{21}H_{24}N_4O_2S_2$ (MA= 428.57; Exact Mass= 428.13)

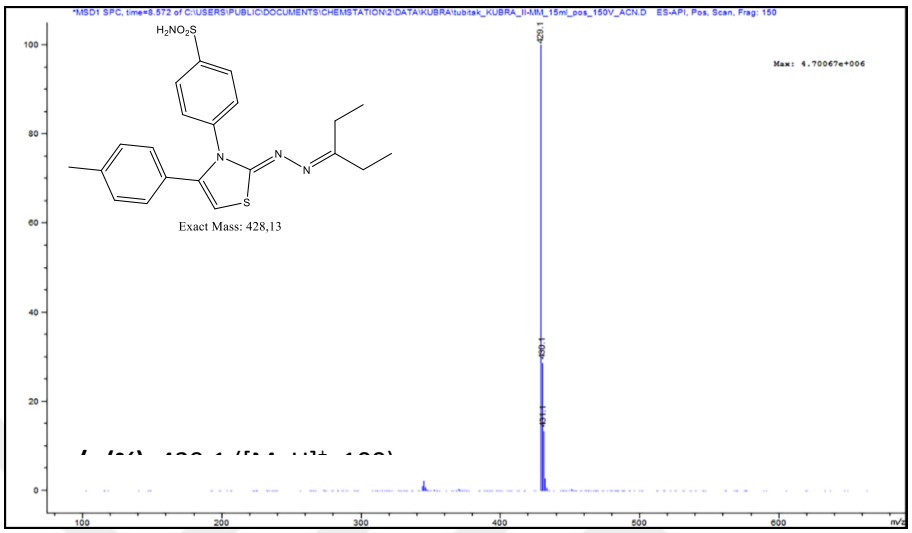

Figure 4-189: Mass spectrum of compound 4q

4.3.2.18. (*Z*)-4-(4-(4-fluorophenyl)-2-(pentan-3-ylidenehydrazineylidene)thiazol-3(2*H*)-yl)benzenesulfonamide (4r)

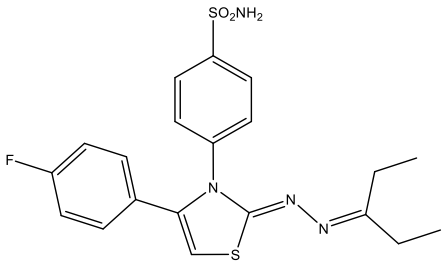

0.0021 mol (0.46g) of 2-bromo-1-(4-fluorophenyl)ethan-1-one (**3f**) and 0.0021 mol (0.66g) of 2-(pentan-3-ylidene)-*N*-(4-sulfamoylphenyl)hydrazine-1-carbothioamide (**E11**) are suspended in chloroform-ethanol (2:1). The reaction mixture is heated under reflux for 3 hours. The solid product formed is filtered and purified by recrystallization from ethanol.

Physical appearance	: Yellow powder
Yield (%)	: 30
Retention factor	: 0.68; Chloroform : Methanol (9:1)

Melting point (ºC)	:231.2 – 231.8

Elemental Analysis

Molecular formula	: $C_{20}H_{21}FN_4O_2S_2$
Molecular weight (g/mol)	: 432.53

Element	C	H	N	S
Calculated (%)	55.54	4.89	12.95	14.83
Found (%)	55.31	4.60	12.63	14.54

Spectral Analysis

Fourier Transform Infrared (FT-IR) Spectrum

IR(KBr): υ 3429, 3305 (NH s.b); 3140, 3101, 3062 (Ar.C-H s.b., =CH s.b); 2978, 2945, 2883, (Al.C-H s.b); 1589, 1575, 1556, 1516, 1500, 1489 (Ar. C=C s.b, C=N s.b, N-H b.b); 1398 (Al.C-H b.b); 1342, 1172 (S=O s.b); 1313(C-N s.b); 1222 (Ar-F s.b); 864, 825 (1,4-disubs. Ar-C-H b.b)

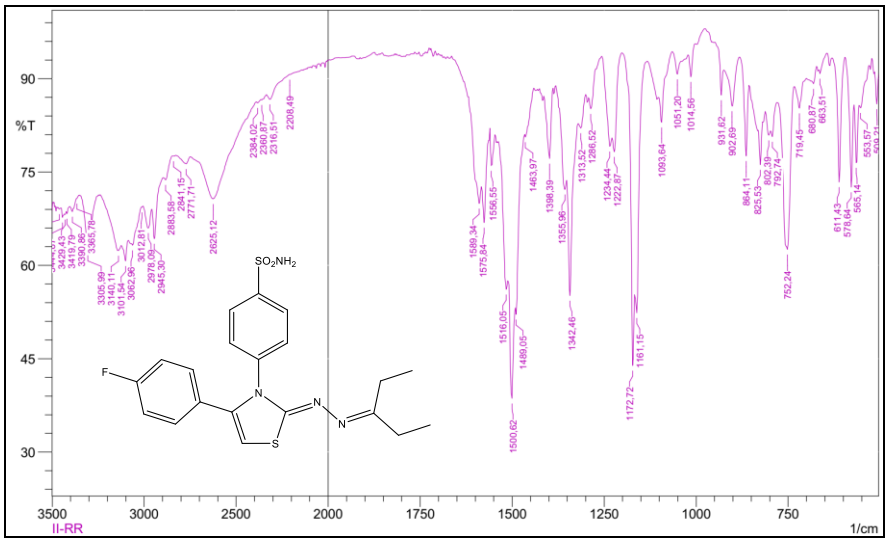

Figure 4-190: IR spectrum of compound 4r

^{1}H-NMR Spectrum

^{1}H NMR (DMSO-*d*$_6$ / 400 MHz δ (ppm): 0.91 (3H, t, *J*=7.4 Hz, -CH_3), 1.04 (3H, td, *J*=7.4, 1.6 Hz, -CH_3), 2.25 (4H, qd, *J*=7.4, 1.9 Hz, 2 x CH_2), 6.59 (1H, s, thiazole C_5-H), 7.12 (2H, app.t (AA'BB'X), *J*=9.0 Hz, 4-fluorophenyl $C_{3,5}$-H), 7.19-7.24 (2H, app.dd (AA'BB'X), *J*=8.3, 5.2 Hz, 4-fluorophenyl $C_{2,6}$-H), 7.40-7.43 (4H, m, 4-benzenesulfonamide $C_{3,5}$-H, app.d (AA'BB'), *J*=8.6 Hz and -SO_2NH_2), 7.74 (2H, app.d (AA'BB') *J*=8.6 Hz, 4-benzenesulfonamide $C_{2,6}$-H).

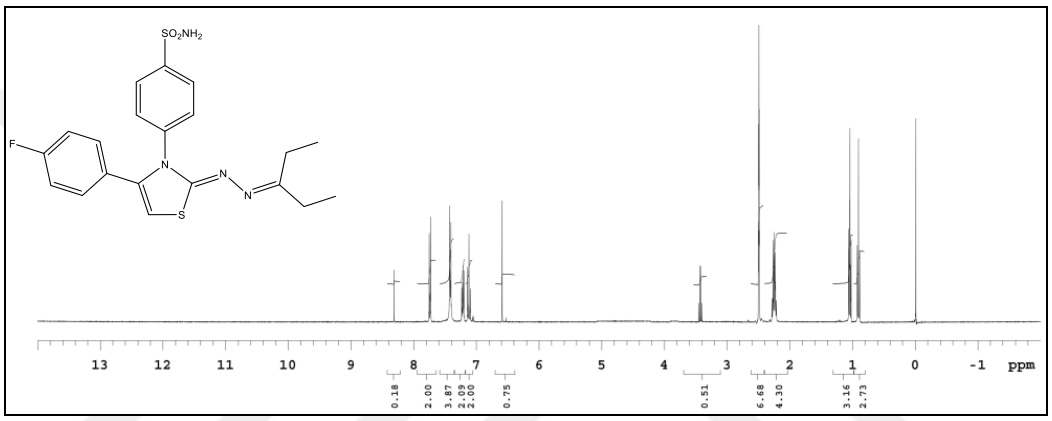

Figure 4-191: ^{1}H-NMR spectrum of compound 4r (0 – 14 ppm)

^{13}C-NMR Spectrum

^{13}C NMR (decoupled, DMSO-*d*$_6$, 100 MHz) δ (ppm): 10.8 (CH_3), 10.6 (CH_3), 23.8 (-CH_2-), 28.4 (-CH_2-), 102.5 (thiazole C_5), 115.5 (d, *J*=22.7 Hz, 4-fluorophenyl $C_{3/5}$), 125.9 (4-benzenesulfonamide $C_{2,6}$), 127.2 (4-fluorophenyl C_1), 128.7 (4-benzenesulfonamide $C_{3,5}$), 130.3 (d, *J*=8.3 Hz, 4-fluorophenyl $C_{2/6}$), 137.6 (4-benzenesulfonamide C_4), 140.4 (4-benzenesulfonamide C_1), 142.5 (thiazole C_4), 161.7 (d, *J*=259.1 Hz, 4-fluorophenyl C_4), 166.1 (N=C), 168.3 (thiazole C_2).

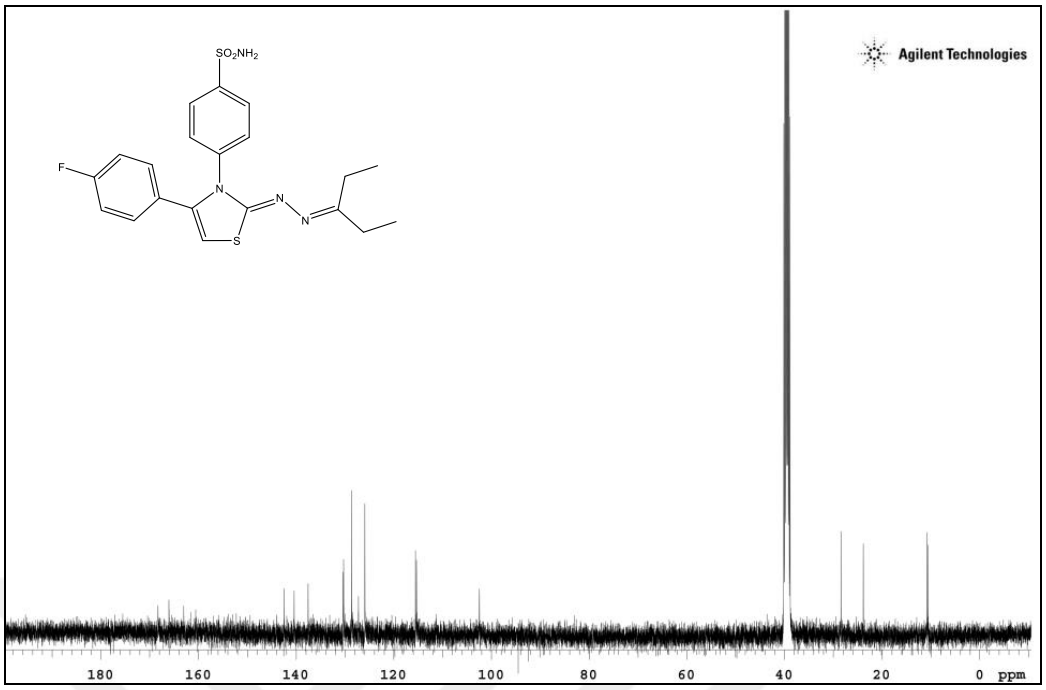

Figure 4-192: ^{13}C-NMR spectrum of compound 4r (0 – 180 ppm)

4.3.2.19. 4-((*Z*)-2-(((*E*)-pentan-2-ylidene)hydrazineylidene)-4-phenylthiazol-3(2*H*)-yl)benzenesulfonamide (4s)

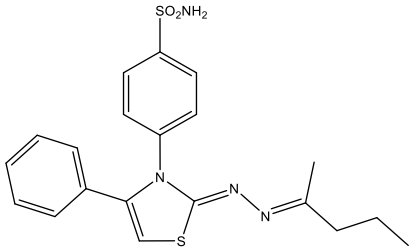

0.0017 mol (0.34g) of 2-bromo-1-phenylethan-1-one (**3a**) and 0.0017 mol (0.53g) of 2-(pentan-2-ylidene)-*N*-(4-sulfamoylphenyl)hydrazine-1-carbothioamide (**E12**) are suspended in chloroform-ethanol (2:1). The reaction mixture is heated under reflux for 3 hours. The solid product formed is filtered and purified by recrystallization from ethanol.

Physical appearance	: Orange Powder
Yield (%)	: 75
Retention factor	: 0.70; Chloroform : Methanol (9:1)
Melting point (ºC)	: 150.0 – 152.1

Elemental Analysis

Molecular formula	: $C_{20}H_{22}N_4O_2S_2.CH_3CH_2OH$
Molecular weight (g/mol)	: 460.61

Element	C	H	N	S
Calculated (%)	57.37	6.13	12.16	13.92
Found (%)	57.22	5.87	11.85	13.56

Spectral Analysis

Fourier Transform Infrared (FT-IR) Spectrum

IR(KBr): υ 3302, 3257 (NH s.b); 3105, 3024 (Ar.C-H s.b., =CH s.b); 2960, 2927, 2870, 2709 (Al.C-H s.b); 1579, 1564, 1529, 1492 (Ar. C=C s.b, C=N s.b, N-H b.b); 1444, 1406 (Al.C-H b.b); 1342, 1170 (S=O s.b); 1309 (C-N s.b); 765, 694 (monosubs. Ar-C-H b.b); 829 (1,4-disubs. Ar-C-H b.b)

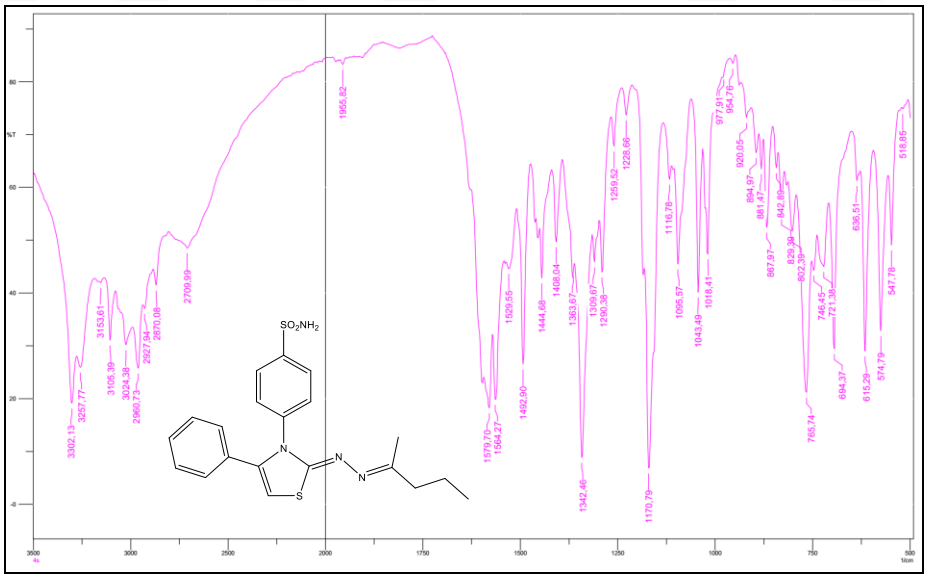

Figure 4-193: IR spectrum of compound 4s

^{1}H-NMR Spectrum

^{1}H NMR (DMSO-*d_6* / 400 MHz δ (ppm): 0.89 (3H, t, *J*=7.4 Hz, pentan-2-ylidene C_5-H), 1.52 (2H, sextet, *J*=7.4 Hz, pentan-2-ylidene C_4-H), 1.82 (3H, s, pentan-2-ylidene C_1-H), 1.84 (3H, s, -CH_3), 2.21 (2H, t, *J*=7.8 Hz, pentan-2-ylidene C_3-H), 3.43 (q, *J*= 7,00 Hz, CH_3*CH_2*OH), 4.85 (s, CH_3CH_2*OH*), 6.63 (1H, s, thiazole C_5-H), 7.15-7.17 (2H, m, phenyl $C_{2,6}$-H), 7.25 – 7.28 (3H, m, phenyl $C_{3,4,5}$-H), 7.40-7.53 (4H, m, 4-benzenesulfonamide $C_{3,5}$-H, app.d (AA'BB') *J*=8.6 Hz and -SO_2NH_2), 7.74 (2H, app.d (AA'BB'), *J*=8.6 Hz, 4-benzenesulfonamide $C_{2,6}$-H).

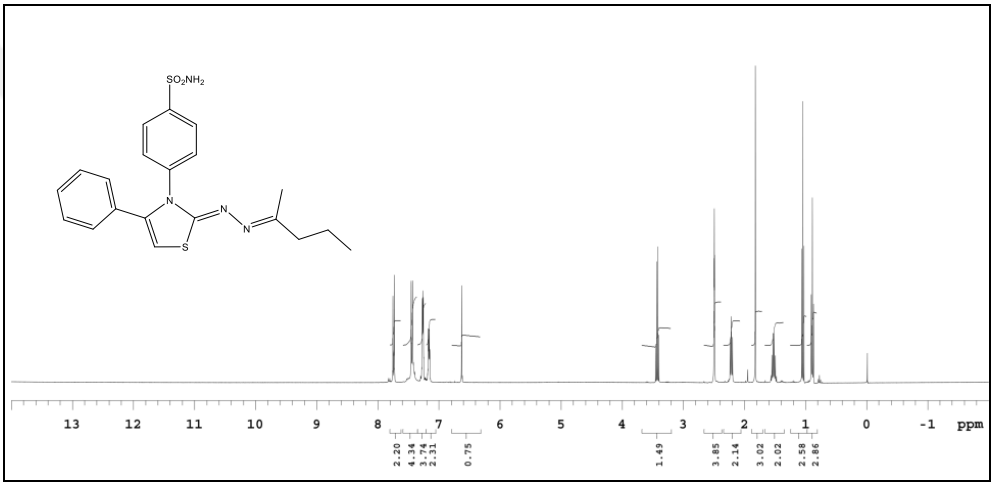

Figure 4-194: ^{1}H-NMR spectrum of compound 4s (0 – 14 ppm)

^{13}C-NMR Spectrum

^{13}C NMR (decoupled, DMSO-*d_6*, 100 MHz) δ (ppm): 13.6 (pentan-2-ylidene C_5), 17.4 (pentan-2-ylidene C_1), 19.9 (pentan-2-ylidene C_4), 33.9 (pentan-2-ylidene C_3), 103.0 (thiazole C_5), 126.0, 126.2 (4-benzenesulfonamide C2/6), 128.1, 128.2 (phenyl C2/6), 128.5 (phenyl $C_{3,4,5}$), 128.7, 128.8 (4-benzenesulfonamide $C_{3/5}$), 130.3 (phenyl C_1), 139.1 (4-benzenesulfonamide C_4), 140.0 (4-benzenesulfonamide C_1), 143.0 (thiazole C_4), 165.3 (N=C), 166.6 (thiazole C_2).

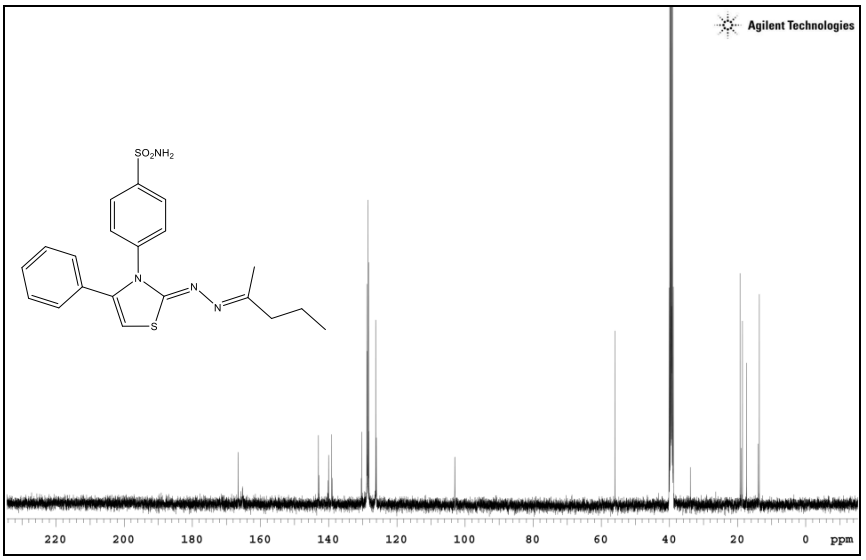

Figure 4-195: ^{13}C-NMR spectrum of compound 4s (0 – 220 ppm)

^{13}C NMR (HSQC-2D, DMSO-*d*$_6$, 100 MHz) δ (ppm): **13.6** [pentan-2-ylidene C_5 - **0.89** (3H, t, *J*=7.4 Hz, pentan-2-ylidene C_5-H)], C_5), **17.4** [pentan-2-ylidene C_1 - **1.82** (3H, s, pentan-2-ylidene C_1-H)], **18.9** (pentan-2-ylidene C_4 - **1.52** (2H, sextet, *J*=7.4 Hz, pentan-2-ylidene C_4-H)], **33.9** [pentan-2-ylidene C_3 - **2.21** (2H, t, *J*=7.8 Hz, pentan-2-ylidene C_3-H)], **103.0** [thiazole C_5 - **6.63** (1H, s, thiazole C_5-H)], C_5), **126.0, 126.2** [4-benzenesulfonamide $C_{2/6}$ - **7.74** (2H, app.d (AA'BB'), *J*=8.6 Hz, 4-benzenesulfonamide $C_{2,6}$-H)], **128.1, 128.2** [phenyl $C_{2/6}$ - **7.15-7.17** (2H, m, phenyl $C_{2,6}$-H)], **128.5** [phenyl $C_{3,4,5}$ - **7.27** (3H, dd, *J*=5.5, 2.3 Hz, phenyl $C_{3,4,5}$-H)], **128.7, 128.8** [4-benzenesulfonamide $C_{3/5}$ - **7.40-7.53** (4H, m, 4-benzenesulfonamide $C_{3,5}$-H, app.d (AA'BB'), *J*=8.6 Hz and - SO_2NH_2)].

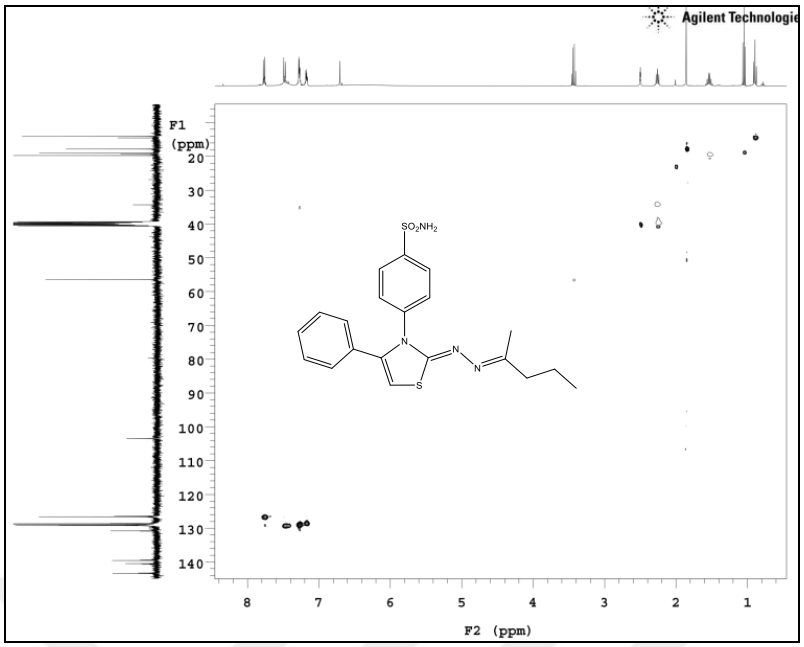

Figure 4-196: HSQC spectrum of compound 4s (1 – 8; 0 – 140 ppm)

LC-MS Spectrum

m/z ESI (positive): 415.1 $(M+H)^+$; $C_{23}H_{20}N_4O_2S_3$ (MA= 414.54; Exact Mass= 414.12)

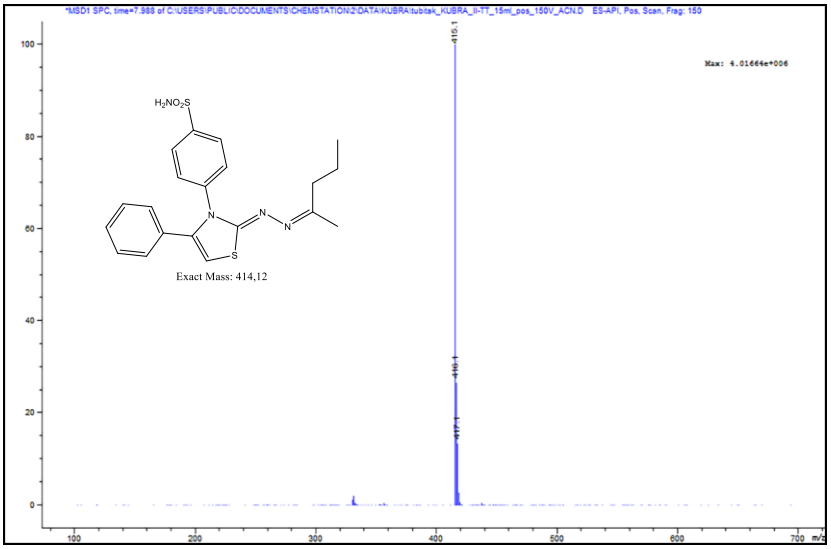

Figure 4-197: Mass spectrum of compound 4s

4.3.2.20. (*Z*)-4-(2-(cyclopentylidenehydrazineylidene)-4-phenylthiazol-3(2*H*)-yl)benzenesulfonamide (4t)

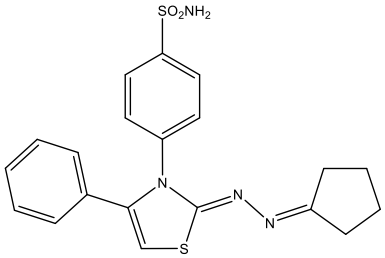

0.0021 mol (0.41g) of 2-bromo-1-phenylethan-1-one (**3a**) and 0.0021 mol (0.65g) of 2-cyclopentylidene-*N*-(4-sulfamoylphenyl)hydrazine-1-carbothioamide (**E13**) are suspended in chloroform-ethanol (2:1). The reaction mixture is heated under reflux for 6 hours. The solid product formed is filtered and purified by recrystallization from ethanol.

Physical appearance	: Ivory crystals
Yield (%)	: 99
Retention factor	: 0.75; Chloroform : Methanol (9:1)
Melting point (ºC)	: 260.9 – 262.4

Elemental Analysis

Molecular formula	: $C_{20}H_{20}N_4O_2S_2$
Molecular weight (g/mol)	: 412.53

Element	C	H	N	S
Calculated (%)	58.23	4.89	13.58	15.55
Found (%)	58.49	5.25	13.14	15.26

Spectral Analysis

Fourier Transform Infrared (FT-IR) Spectrum

IR(KBr): υ 3369, 3296 (NH s.b); 3064, 3039 (Ar.C-H s.b., =CH s.b); 2966, 2926, 2887, 2677 (Al.C-H s.b); 1660, 1633, 1577, 1562, 1492 (Ar. C=C s.b, C=N s.b, N-H b.b); 1444, 1408 (Al.C-H b.b); 1346, 1172 (S=O s.b); 1307 (C-N s.b); 763, 696 (monosubs. Ar-C-H b.b); 840 (1,4-disubs. Ar-C-H b.b)

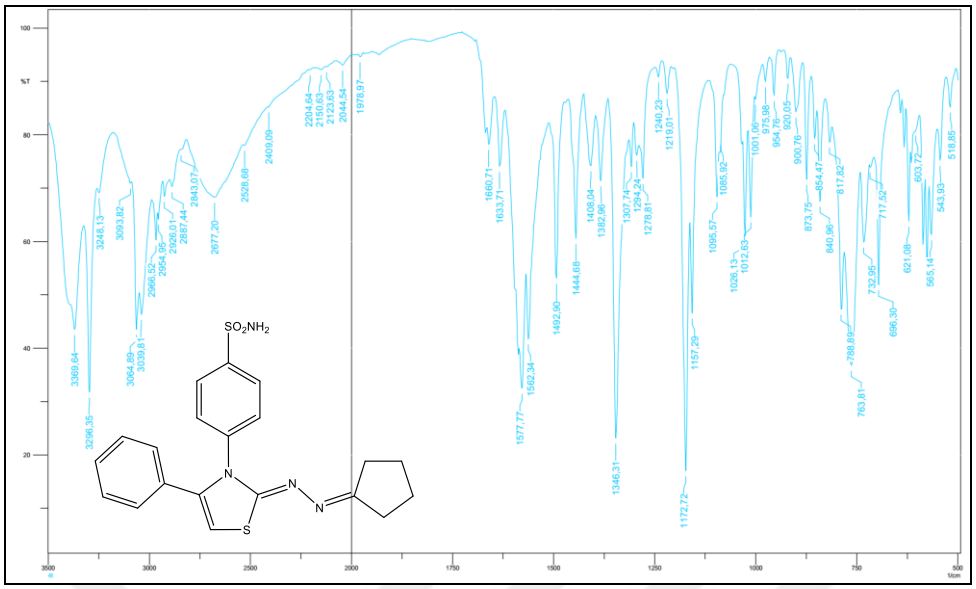

Figure 4-198: IR spectrum of compound 4t

^{1}H-NMR Spectrum

^{1}H NMR (DMSO-d_6 / 400 MHz δ (ppm): 1.63-1.69 (4H, m, cyclopentylidene $C_{3,4}$-H), 2.27 (2H, t, J=6.6 Hz, cyclopentylidene $C_{2/5}$-H), 2.37 (2H, t, J=7.0 Hz, cyclopentylidene $C_{2/5}$-H), 6.66 (1H, s, thiazole C_5-H), 7.15-7.17 (2H,m, phenyl $C_{2,6}$-H), 7.25 (3H, m, phenyl $C_{3,4,5}$-H), 7.44 (4H, d, J=8.6 Hz, 4-benzenesulfonamide $C_{3,5}$-H and -SO_2NH_2), 7.74 (2H, AA'BB', J=8.6, 2.6, 1.7 Hz, 4-benzenesulfonamide $C_{2,6}$-H).

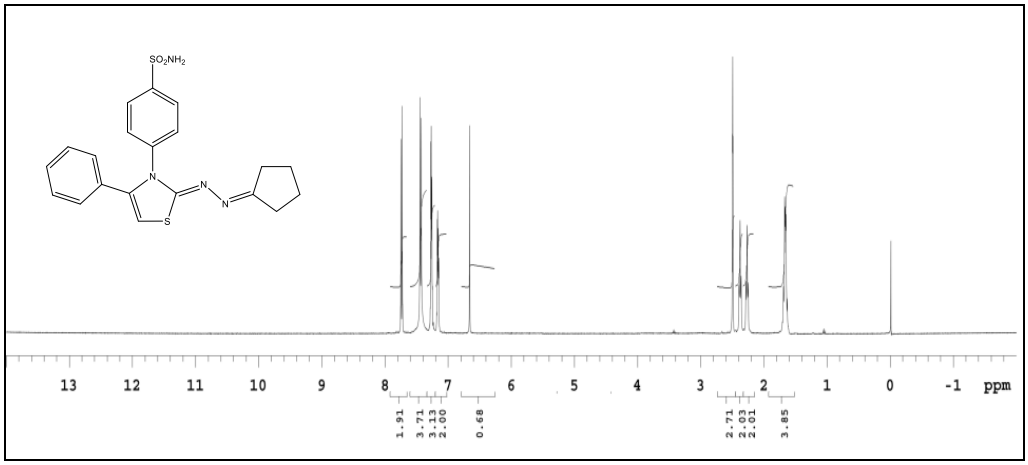

Figure 4-199: ^{1}H-NMR spectrum of compound 4t (0 – 14 ppm)

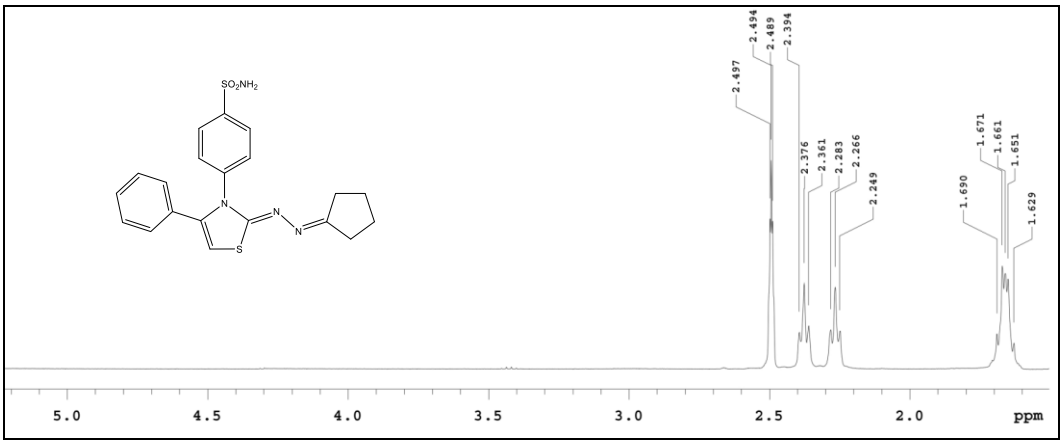

Figure 4-200: ^{1}H-NMR spectrum of compound 4t (1.5 – 5 ppm)

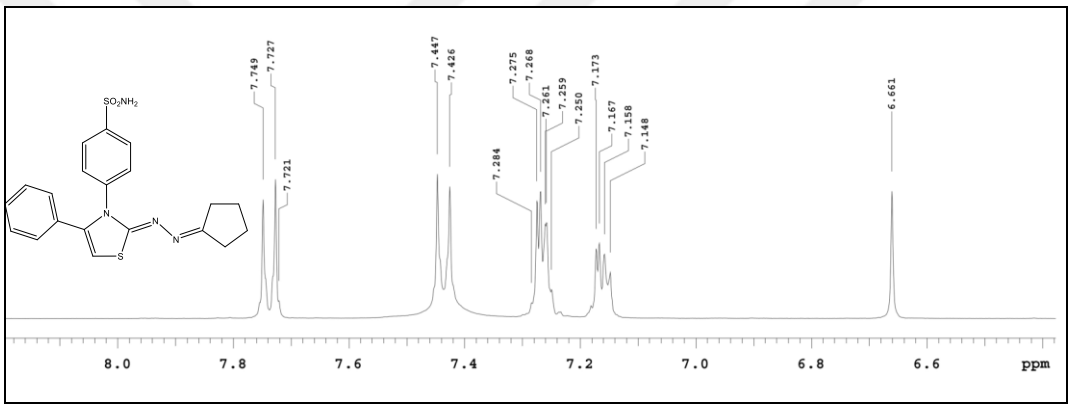

Figure 4-201: ^{1}H-NMR spectrum of compound 4t (6.5 – 8 ppm)

^{13}C-NMR Spectrum

^{13}C NMR (decoupled, DMSO-d_6, 100 MHz) δ (ppm): 24.0, 24.4 (cyclopentylidene $C_{3,4}$), 30.3, 32.4 (cyclopentylidene $C_{2,5}$), 102.8 (thiazole C_5), 126.1 (4-benzenesulfonamide $C_{2,6}$), 128.2, 128.4, 128.7 (phenyl $C_{2,3,4,5,6}$ and 4-benzenesulfonamide $C_{3,5}$), 130.1 (phenyl C_1), 139.1 (4-benzenesulfonamide C_4), 140.0 (4-benzenesulfonamide C_1), 142.9 (thiazole C_4), 165.9 (N=C), 174.9 (thiazole C_2).

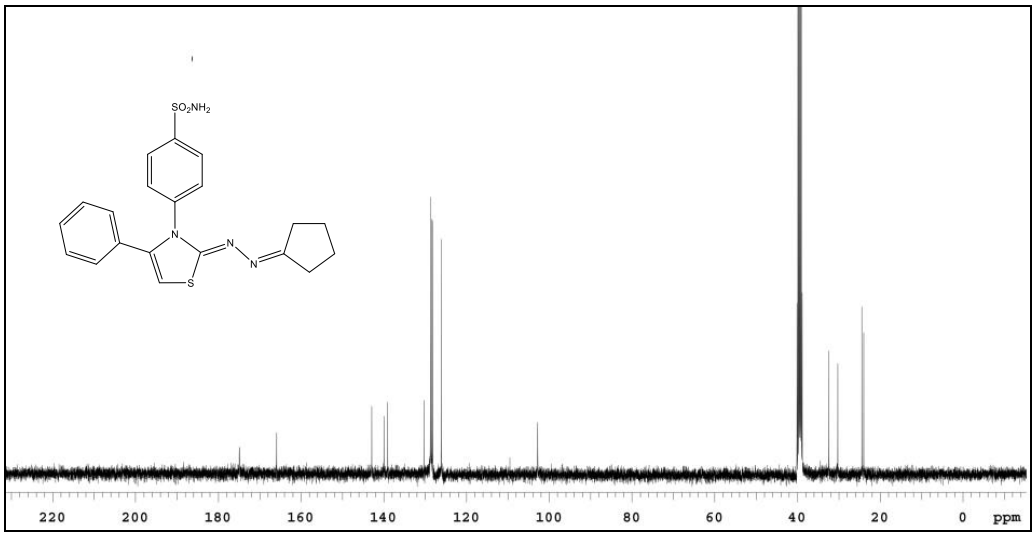

Figure 4-202: ^{13}C-NMR spectrum of compound 4t (0 – 220 ppm)

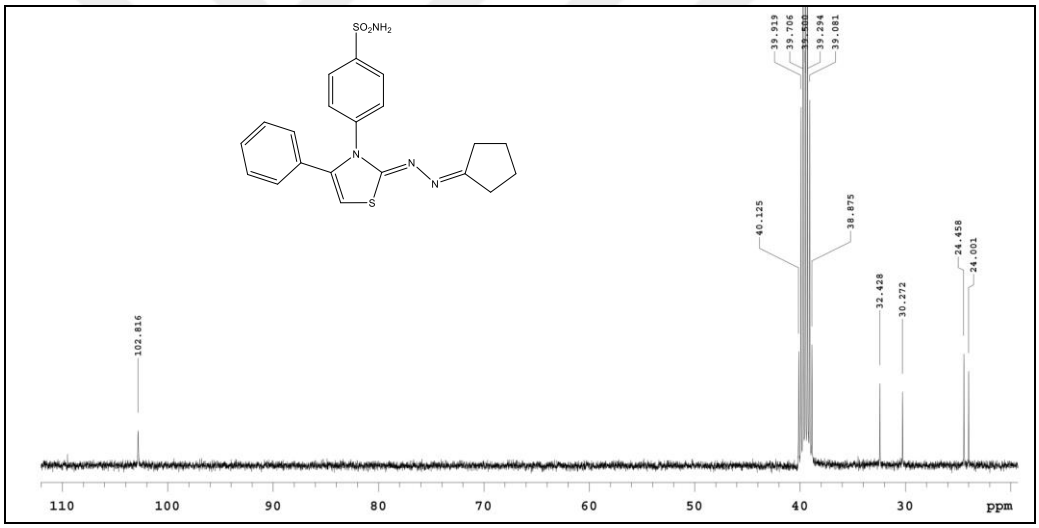

Figure 4-203: ^{13}C-NMR spectrum of compound 4t (20 – 110 ppm)

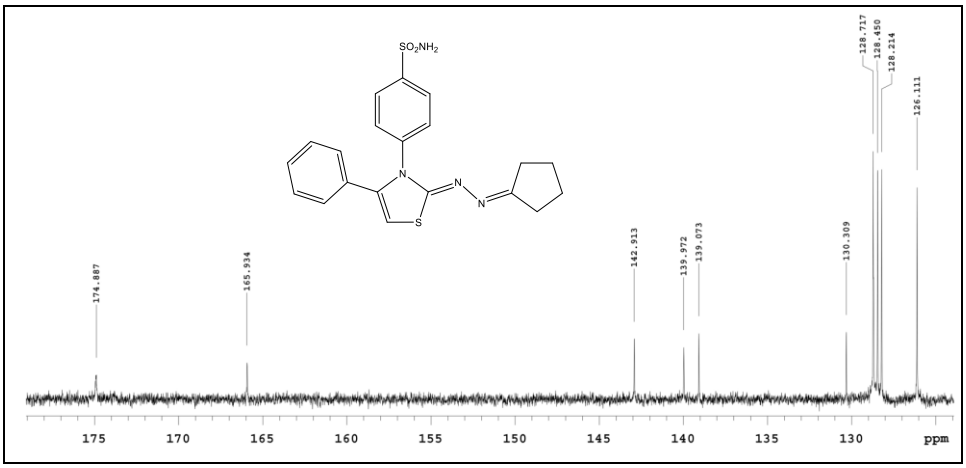

Figure 4-204: ^{13}C-NMR spectrum of compound 4t (125 – 175 ppm)

LC-MS Spectrum

m/z ESI (positive): 413.1 $(M+H)^+$; $C_{20}H_{20}N_4O_2S_2$ (MA= 412.53; Exact Mass= 412.10)

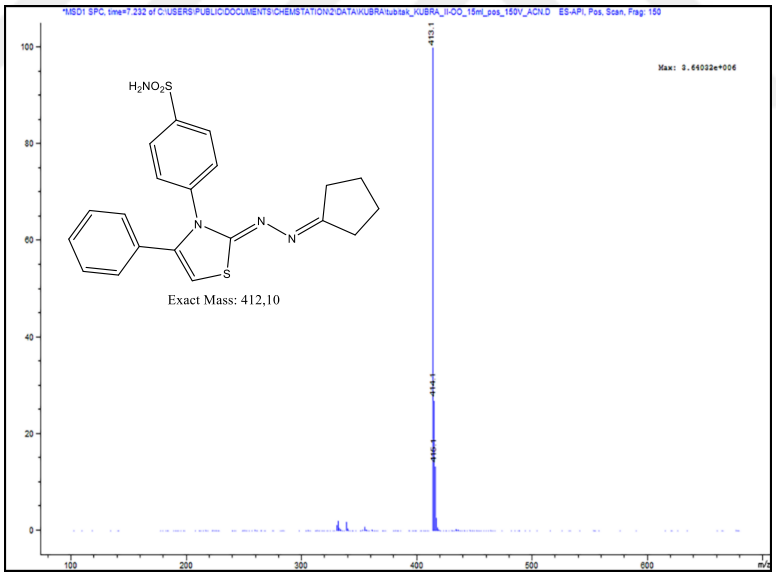

Figure 4-205: Mass spectrum of compound 4t

4.3.2.21. (*Z*)-4-(4-(4-bromophenyl)-2-(cyclopentylidenehydrazineylidene)thiazol-3(2*H*)-yl)benzenesulfonamide (4u)

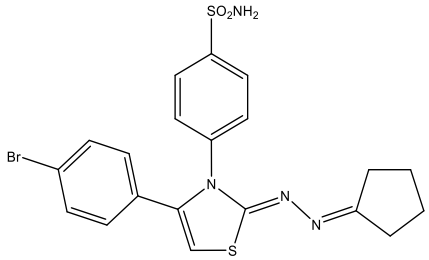

0.0021mol (0.58g) of 2-bromo-1-(4-bromophenyl)ethane-1-one (**3b)** and 0.0021 mol (0.65g) of 2-cyclopentylidene-*N*-(4-sulfamoylphenyl)hydrazine-1-carbothioamide (**E13**) are suspended in chloroform-ethanol (2:1). The reaction mixture is heated under reflux for 6 hours. The solid product formed is filtered and purified by recrystallization from ethanol.

Physical appearance	: Amber white powder
Yield (%)	: 99
Retention factor	: 0.65; Chloroform : Methanol (9:1)
Melting point (ºC)	: 234.7-238

Elemental Analysis

Molecular formula	: $C_{20}H_{19}BrN_4O_2S_2 .CH_3CH_2OH$
Molecular weight (g/mol)	: 537.49

Element	C	H	N	S
Calculated (%)	49.16	4.69	10.42	11.93
Found (%)	48.87	4.36	10.03	11.57

Spectral Analysis

Fourier Transform Infrared (FT-IR) Spectrum

IR(KBr): υ 3417, 3379 (NH s.b); 3182, 3103, 3055 (Ar.C-H s.b., =CH s.b); 2972, 2945, 2885 (Al.C-H s.b); 1645, 1606, 1683, 1548, 1487 (Ar. C=C s.b, C=N s.b, N-H b.b); 1413, 1398 (Al.C-H b.b); 1355, 1172 (S=O s.b); 1296 (C-N s.b); 1070 (Ar-Br s.b); 819, 802 (1,4-disubs. Ar-C-H b.b)

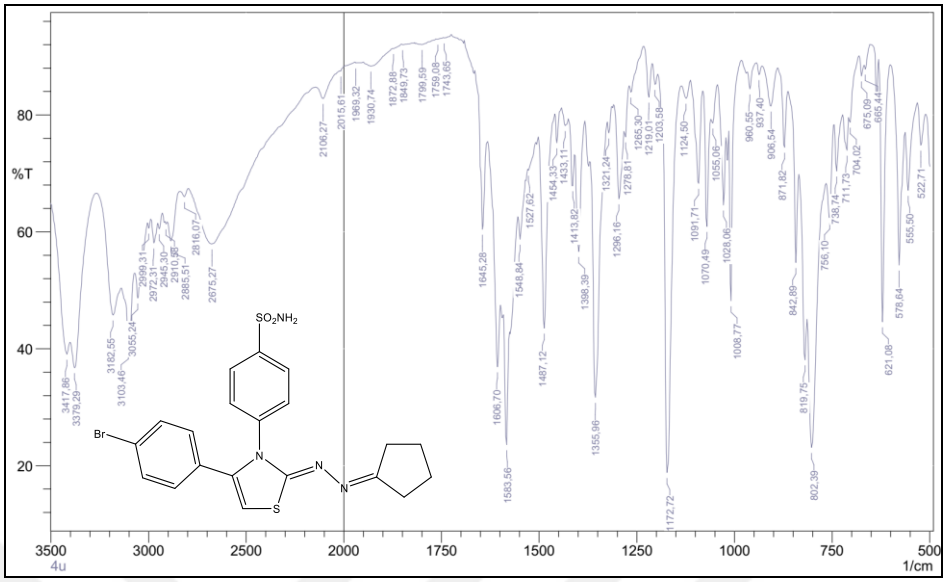

Figure 4-206: IR spectrum of compound 4u

^{1}H-NMR Spectrum

^{1}H NMR (DMSO-d_6 / 400 MHz δ (ppm): 1.04 (t, *J*= 7,00 Hz, CH_3CH_2OH), 1.62-1.68 (4H, m, cyclopentylidene $C_{3,4}$-H), 2.25 (2H, t, *J*=7.0 Hz, cyclopentylidene $C_{2/5}$-H), 2.36 (2H, t, *J*=6.6 Hz, cyclopentylidene $C_{2/5}$-H), 3.43 (q, *J*= 7,00 Hz, CH_3CH_2OH), 4.74 (s, CH_3CH_2OH), 6.69 (1H, s, thiazole C_5-H), 7.11 (2H, app.d (AA'BB'), *J*=8.5 Hz, 4-bromophenyl $C_{2,6}$-H), 7.43 (4H, app.d (AA'BB'), *J*=8.5 Hz, 4-bromophenyl $C_{3,5}$-H and $-SO_2NH_2$), 7.48 (2H, app.d (AA'BB'), *J*=8.6 Hz, 4-benzenesulfonamide $C_{3,5}$-H), 7.75 (2H, app.d (AA'BB'), *J*=8.6 Hz, 4-benzenesulfonamide $C_{2,6}$-H).

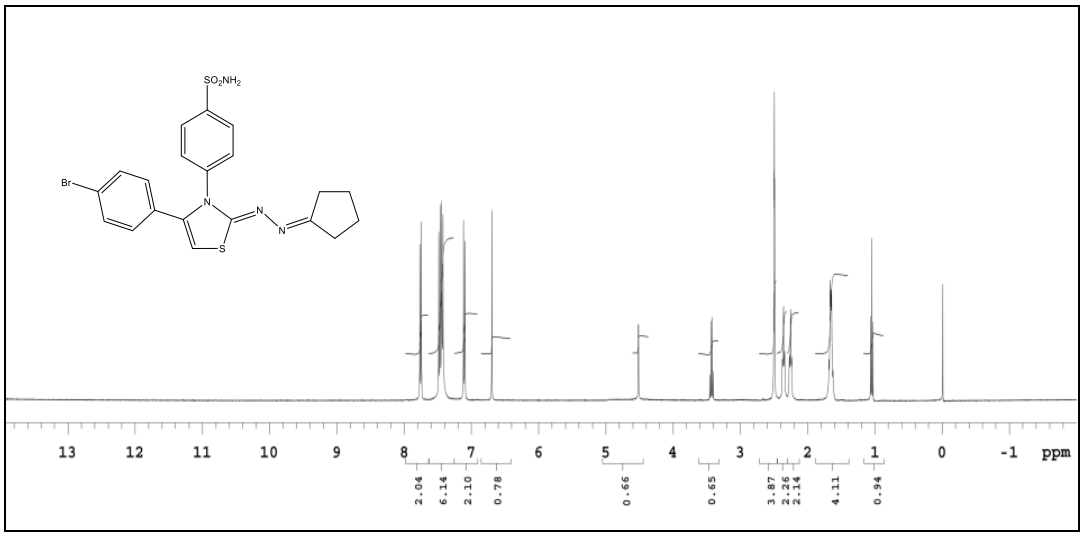

Figure 4-207: ^{1}H-NMR spectrum of compound 4u (0 – 13 ppm)

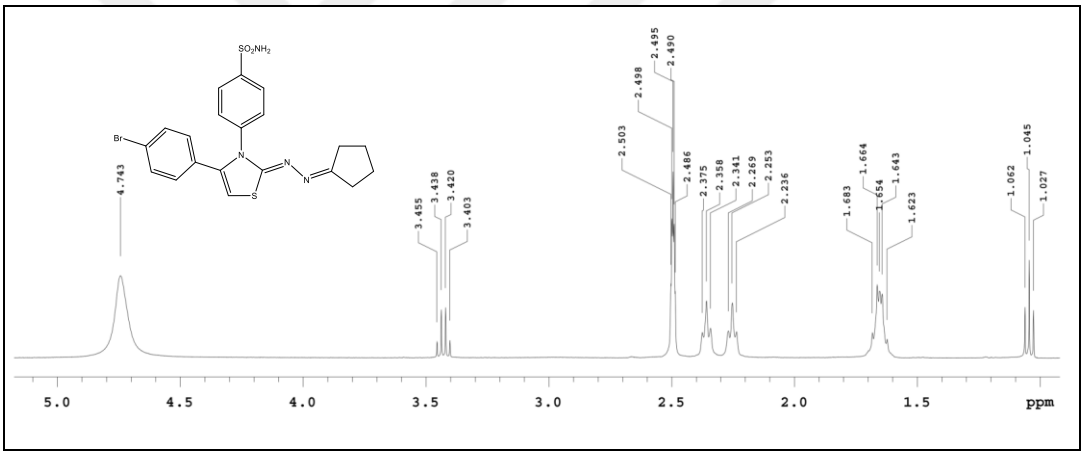

Figure 4-208: ^{1}H-NMR spectrum of compound 4u (1 – 5 ppm)

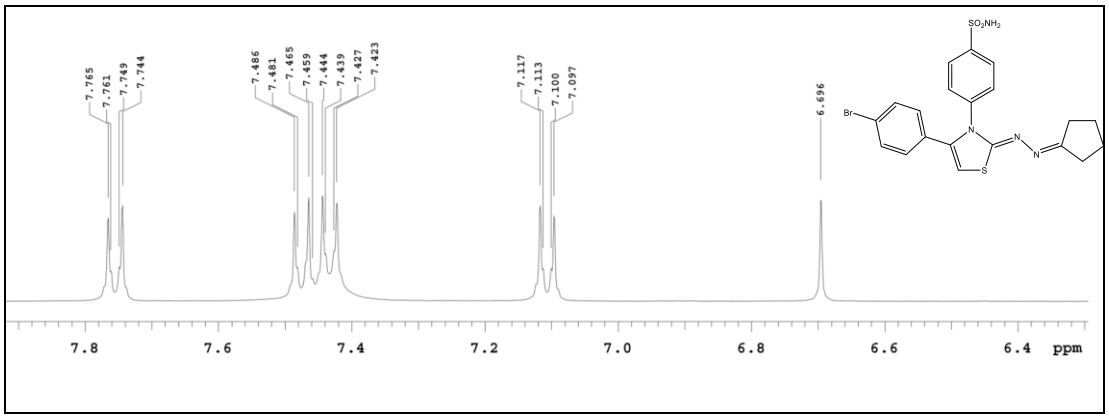

Figure 4-209: ^{1}H-NMR spectrum of compound 4u (6.4 – 7.8 ppm)

^{13}C-NMR Spectrum

^{13}C NMR (decoupled, DMSO-*d*$_6$, 100 MHz) δ (ppm): 24.0, 24.4 (cyclopentylidene $C_{3,4}$), 30.2 (cyclopentylidene $C_{2,5}$), 103.4 (thiazole C_5), 121.9 (4-bromophenyl C_4), 126.1 (4-benzenesulfonamide $C_{2,6}$), 128.6 (4-benzenesulfonamide $C_{3,5}$), 129.6 (4-bromophenyl C_1), 130.1 (4-bromophenyl $C_{2,6}$), 131.4 (4-bromophenyl $C_{3,5}$), 137.7 (4-benzenesulfonamide C_4), 139.9 (4-benzenesulfonamide C_1), 142.8 (thiazole C_4), 165.5 (N=C), 174.6 (thiazole C_2).

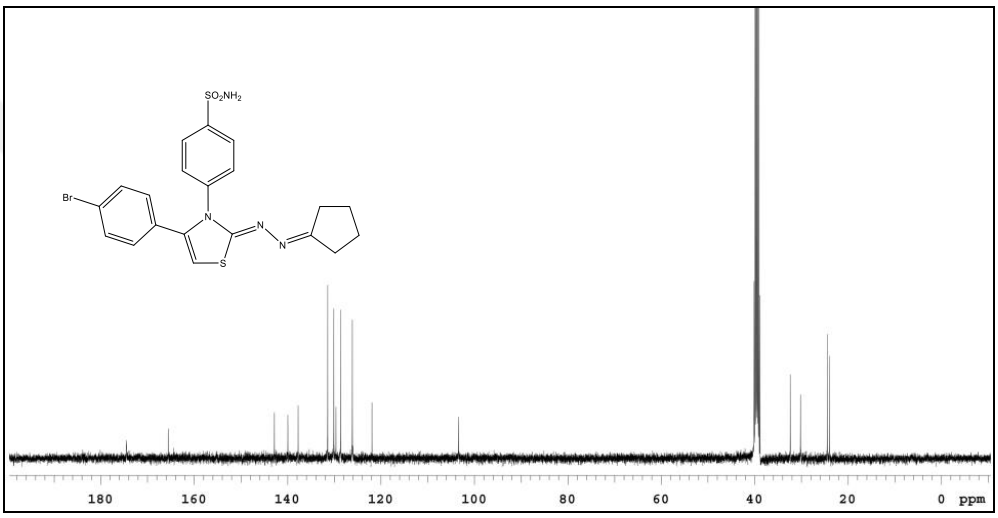

Figure 4-210: ^{13}C-NMR spectrum of compound 4u (0 – 200 ppm)

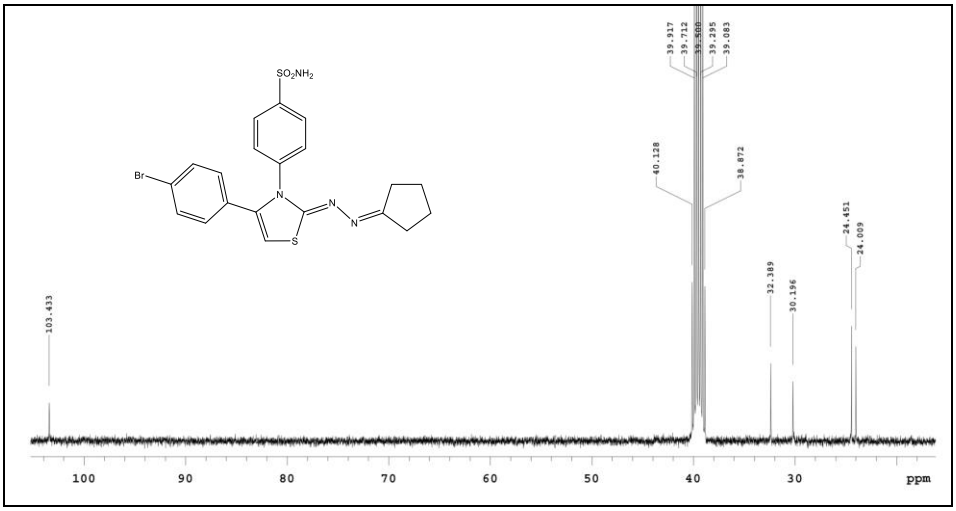

Figure 4-211: ^{13}C-NMR spectrum of compound 4u (20 – 104 ppm)

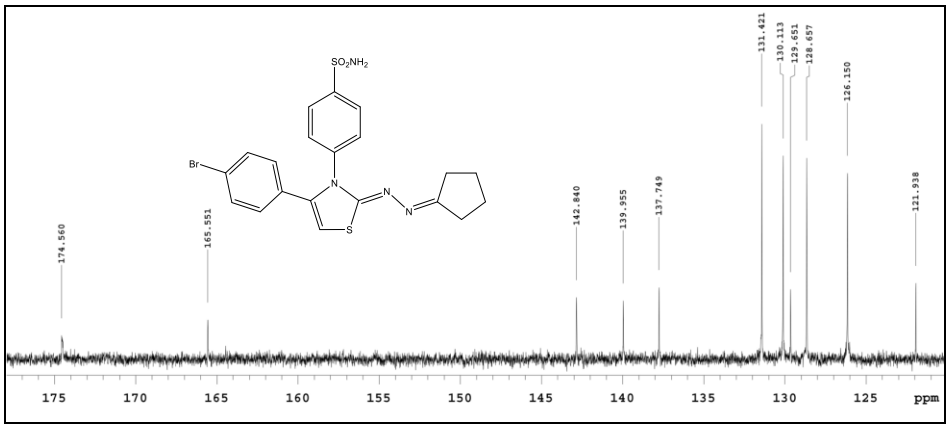

Figure 4-212: ^{13}C-NMR spectrum of compound 4u (120 – 175 ppm)

^{13}C NMR (HSQC-2D, DMSO-d_6, 100 MHz) δ (ppm): **24.0, 24.4** [cyclopentylidene $C_{3,4}$ - **1.62-1.68** (4H, m, cyclopentylidene $C_{3,4}$-H)], **30.2** [cyclopentylidene $C_{2,5}$ - **2.25** (2H, t, *J*=7.0 Hz, cyclopentylidene $C_{2/5}$-H)], **103.4** [thiazole C_5 - **6.69** (1H, s, thiazole C_5-H)], **126.1** (4-benzenesulfonamide $C_{2,6}$ - **7.75** (2H, , app.d (AA'BB'), *J*=8.6 Hz, 4-benzenesulfonamide $C_{2,6}$-H)], **128.6** [4-benzenesulfonamide $C_{3,5}$ – **7.36-7.51** [4-benzenesulfonamide $C_{3,5}$-H, 4-bromophenyl $C_{3,5}$-H and -SO_2NH_2)], **130.1** [4-bromophenyl $C_{2,6}$ - **7.11** (2H, app.d (AA'BB'), *J*=8.5 Hz, 4-bromophenyl $C_{2,6}$-H)], **131.4** [4-bromophenyl $C_{3,5}$ - **7.36-7.51** [4-benzenesulfonamide $C_{3,5}$-H, 4-bromophenyl $C_{3,5}$-H and -SO_2NH_2)].

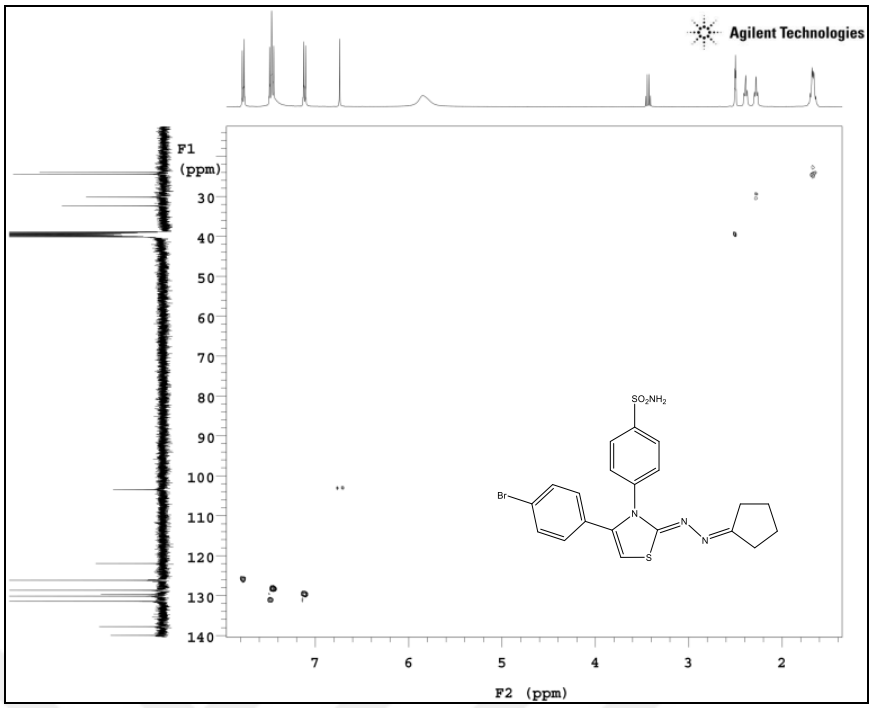

Figure 4-213: HSQC spectrum of compound 4u (2 – 8; 0 – 140 ppm)

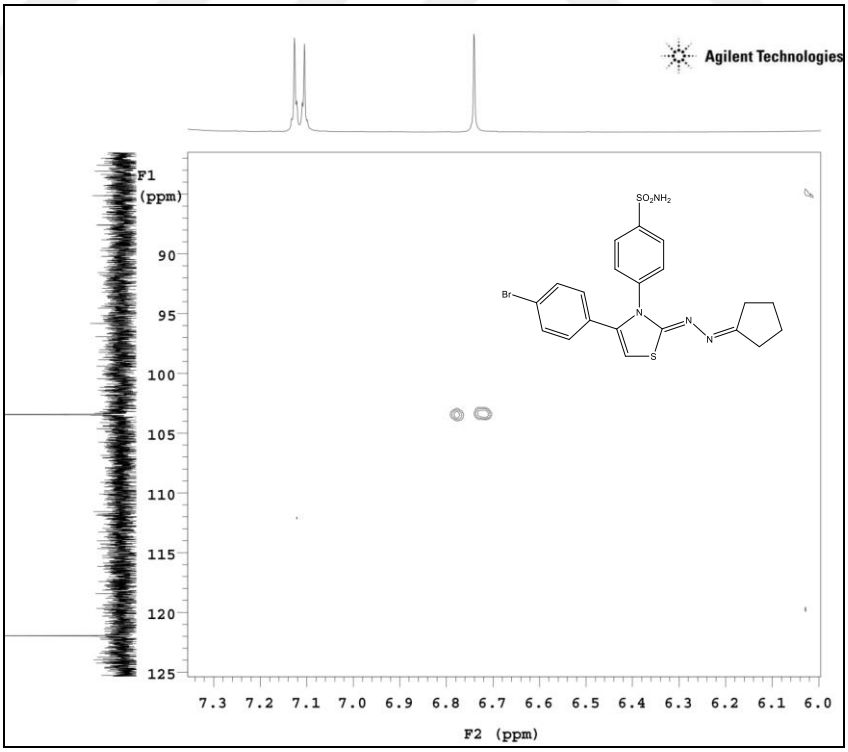

Figure 4-214: HSQC spectrum of compound 4u (6 – 7.3; 85 – 125 ppm)

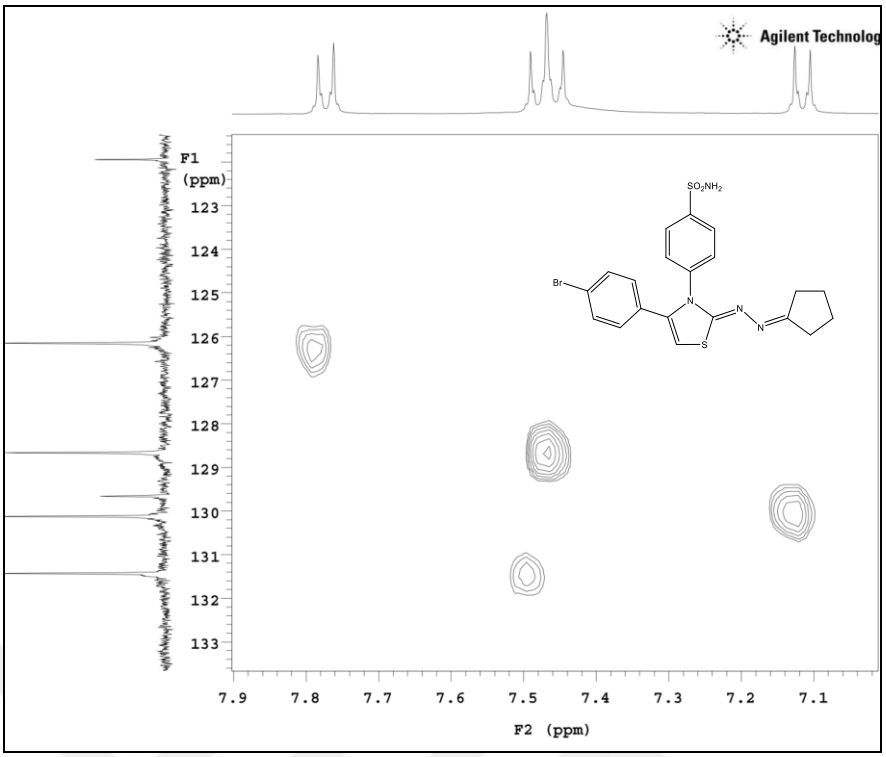

Figure 4-215: HSQC spectrum of compound 4u (7.1 – 7.9; 123 – 133 ppm)

LC-MS Spectrum

m/z ESI (positive): 493.0 $(M+2+H)^+$; $C_{21}H_{24}N_4O_2S_2$ (MA= 491.42; Exact Mass= 490.01)

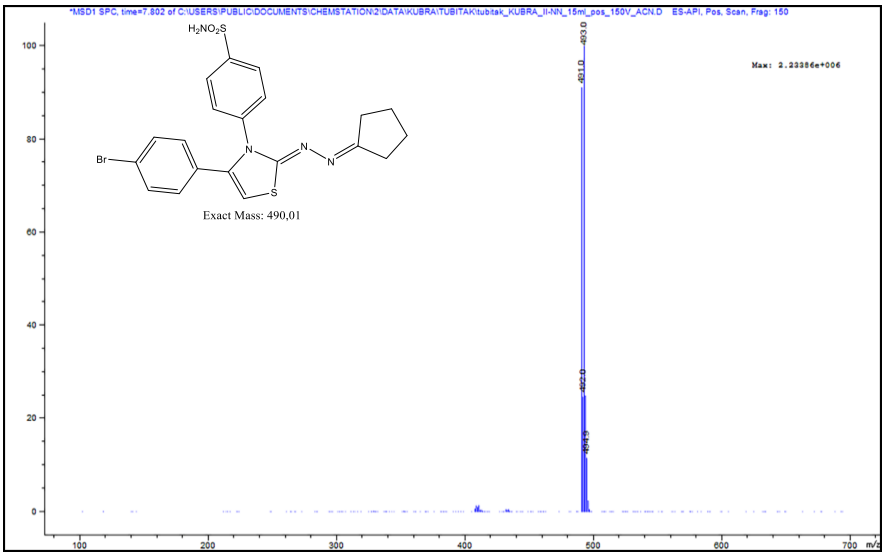

Figure 4-216: Mass spectrum of compound 4u

4.3.2.22. (*Z*)-4-(2-(cyclopentylidenehydrazineylidene)-4-(4-hydroxyphenyl)thiazol-3(2*H*)-yl)benzenesulfonamide (4v)

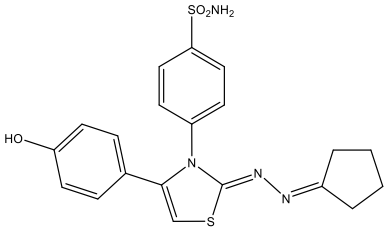

0.0021 mol (0.45g) of 2-bromo-1-(4-hydroxyphenyl)ethane-1-one (**3c)** and 0.0021 mol (0.65g) of 2-cyclopentylidene-*N*-(4-sulfamoylphenyl)hydrazine-1-carbothioamide (**E13**) are suspended in chloroform-ethanol (2:1). The reaction mixture is heated under reflux for 6 hours. The solid product formed is filtered and purified by recrystallization from ethanol.

Physical appearance	: Yellow crystals
Yield (%)	: 82
Retention factor	: 0.48; Chloroform : Methanol (9:1)
Melting point (ºC)	: 206-207.9

Elemental Analysis

Molecular formula	: $C_{20}H_{20}N_4O_3S_2$
Molecular weight (g/mol)	: 428.53

Element	C	H	N	S
Calculated (%)	56.06	4.70	13.07	14.97
Found (%)	56.26	4.66	12.88	14.64

Spectral Analysis

Fourier Transform Infrared (FT-IR) Spectrum

IR(KBr): υ 3464 (OH s.b); 3373, 3269 (NH s.b); 3190, 3116, 3068 (Ar.C-H s.b., =CH s.b); 2970, 2872, 2725 (Al.C-H s.b); 1651, 1604, 1585, 1575, 1508 (Ar. C=C s.b, C=N

s.b, N-H b.b); 1438, 1404 (Al.C-H b.b); 1340, 1166 (S=O s.b); 1307 (C-N s.b); 837, 829 (1,4-disubs. Ar-C-H b.b)

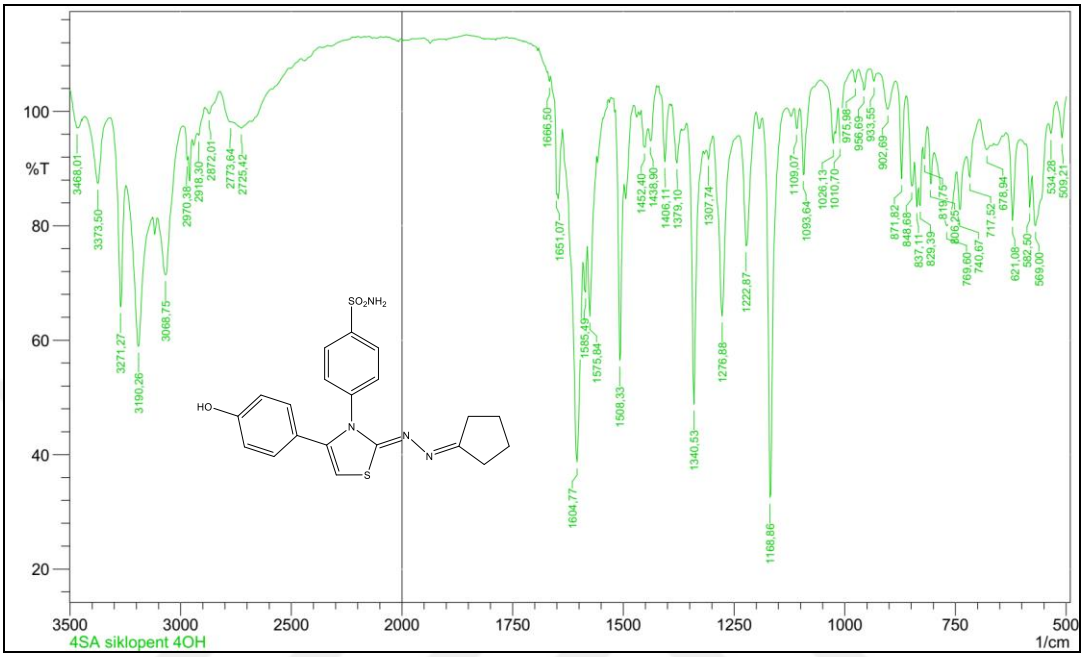

Figure 4-217: IR spectrum of compound 4v

^{1}H-NMR Spectrum

^{1}H NMR (DMSO-d_6 / 500 MHz δ (ppm): 1.66-1.71 (4H, m, cyclopentylidene $C_{3,4}$-H), 2.30 (2H, t, J=6.7 Hz, cyclopentylidene $C_{2/5}$-H), 2.42 (2H, t, J=6.7 Hz, cyclopentylidene $C_{2/5}$-H), 6.57 (1H, s, thiazole C_5-H), 6.64 (2H, app.d (AA'BB'), J=8.7 Hz, 4-hydroxyphenyl $C_{3,5}$-H), 6.96 (2H, app.d (AA'BB'), J=8.7 Hz, 4-hydroxyphenyl $C_{2,6}$-H), 7.45 (4H, d, J=8.5 Hz, 4-benzenesulfonamide $C_{3,5}$-H and -SO_2NH_2), 7.78 (2H, app.d (AA'BB'), J=8.7 Hz, 4-benzenesulfonamide $C_{2,6}$-H).

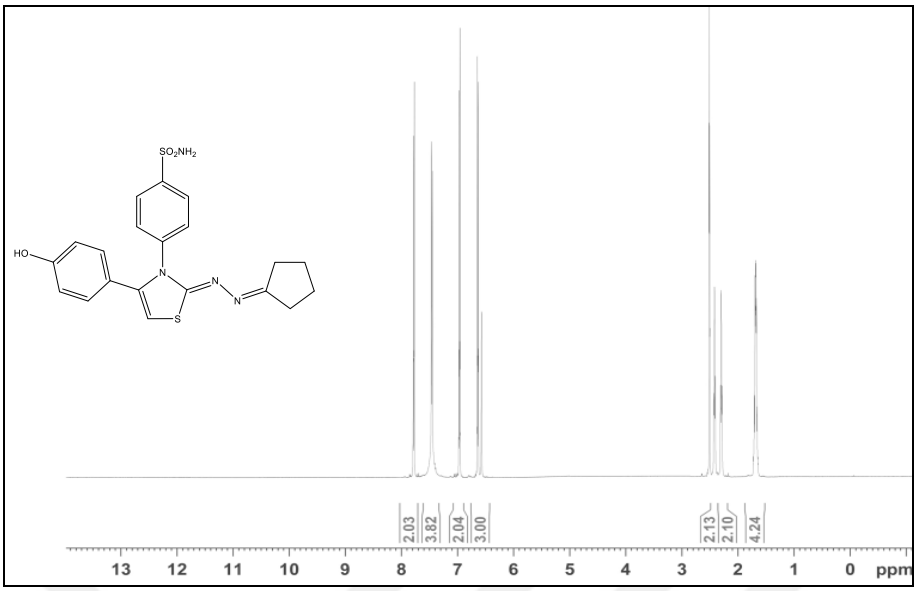

Figure 4-218: ^{1}H-NMR spectrum of compound 4v (0 – 14 ppm)

^{13}C-NMR Spectrum

^{13}C NMR (APT, DMSO-d_6, 125 MHz) δ (ppm): 24.5, 24.9 (cyclopentylidene $C_{3,4}$), 30.8, 32.9 (cyclopentylidene $C_{2,5}$), 101.5 (thiazole C_5), 115.7 (4-hydroxyphenyl $C_{3,5}$), 121.3 (4-hydroxyphenyl C_1), 126.6 (4-benzenesulfonamide $C_{2,6}$), 129.3 (4-benzenesulfonamide $C_{3,5}$), 130.3 (4-hydroxyphenyl $C_{2,6}$), 140.0 (4-benzenesulfonamide C_4), 140.4 (4-benzenesulfonamide C_1), 143.5 (thiazole C_4), 158.2 (4-hydroxyphenyl C_4), 166.7 (N=C), 175.4 (thiazole C_2).

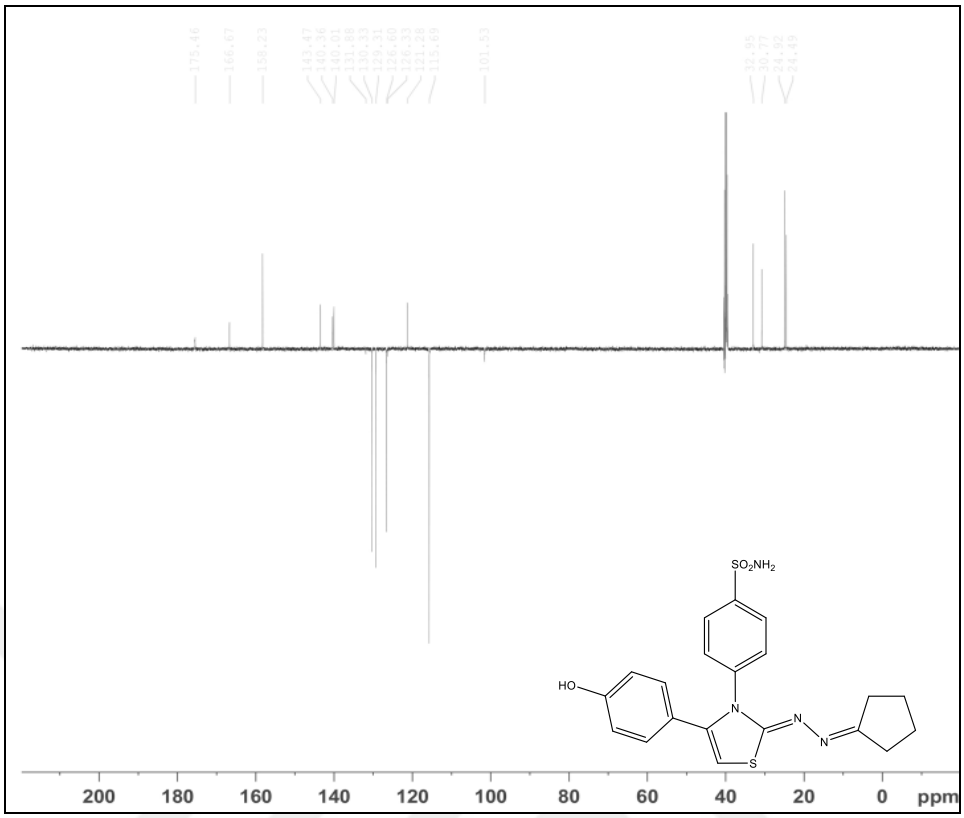

Figure 4-219: APT spectrum of compound 4v (0 – 200 ppm)

LC-MS Spectrum

m/z ESI (positive): 429.1 $(M+H)^+$; $C_{20}H_{20}N_4O_3S_2$ (MA= 428.53; Exact Mass= 428.10)

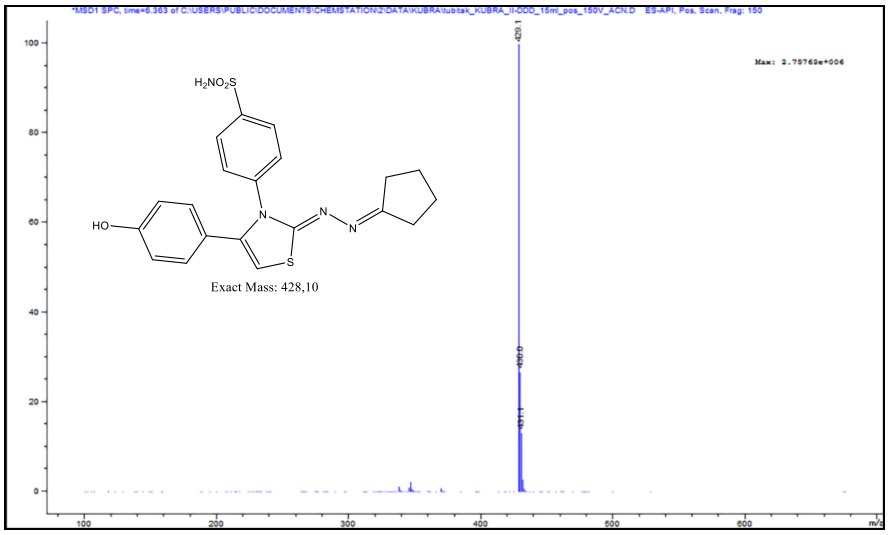

Figure 4-220: Mass spectrum of compound 4v

4.4. Single X-ray Diffraction Analyses

Due to the presence of double bonds, hydrazones and azines exhibit geometric isomerism. Geometric isomerism influences the biological activities of compounds by interfering with their pharmacokinetic properties and, ultimately, their interaction and compatibility with their target proteins. Therefore, it is important to elucidate the structure of the compounds and know their configuration. For this purpose, compounds **E3**, **E8** and **4e** were crystallised and their structures were subsequently elucidated with XRD studies. The results of this study are summarized in **Table 4-3 – 19** and **Figure 4-221 – 225**. Note that the numbering was not done in accordance with IUPAC rules.

4.4.1. Crystal data of compound E3

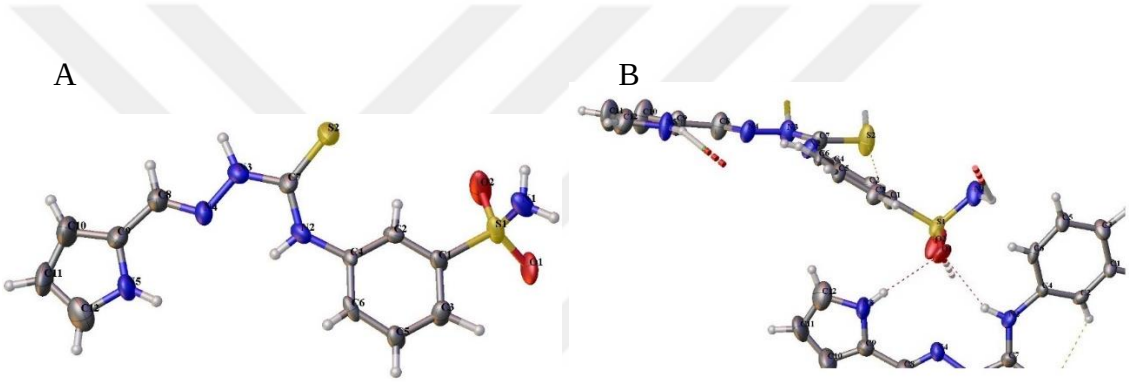

Figure 4-221: A) Crystal structure of compound E3 illustrated with thermal ellipsoids drawn at 50% probability to show the spatial arrangement of atoms. B) Molecular packing showing intermolecular hydrogen bondings.

Table 4-3: Crystal data and structure refinement for E3

Identification code	**E3**
Empirical formula	$C_{12}H_{13}N_5O_2S_2$
Formula weight	323.39 g/mol
Temperature/K	298(2)
Crystal system	monoclinic
Space group	$P2_1/n$
a/Å	4.9751(7)
b/Å	21.858(3)
c/Å	14.698(2)
α/°	90

β/°	96.563(4)
γ/°	90
Volume/Å^3	1587.9(4)
Z	1
ρ_{calc}g/cm^3	1.349
μ/mm^{-1}	0.346
F(000)	668.0
Radiation	MoKα (λ = 0.71073)
2Θ range for data collection/°	4.656 to 52.772
Index ranges	-6 ≤ h ≤ 5, -27 ≤ k ≤ 20, -18 ≤ l ≤ 18
Reflections collected	12420
Independent reflections	3236 [R_{int} = 0.0477, R_{sigma} = 0.0511]
Data/restraints/parameters	3236/0/223
Goodness-of-fit on F^2	7.238
Final R indexes [I>=2σ (I)]	R_1 = 0.1349, wR_2 = 0.2909
Final R indexes [all data]	R_1 = 0.1716, wR_2 = 0.2939
Largest diff. peak/hole / e Å^{-3}	3.73/-0.55

Table 4-4: Fractional Atomic Coordinates (×10^4) and Equivalent Isotropic Displacement Parameters (Å^2×10^3) for E3. U_{eq} is defined as 1/3 of the trace of the orthogonalised U_{IJ} tensor

Atom	*x*	*y*	*z*	U(eq)
S1	8138(5)	7361.4(14)	7531.2(15)	41.3(9)
S2	3071(6)	5555.1(15)	5822.3(17)	66.6(12)
O1	9238(14)	7963(3)	7711(4)	52(2)
N2	4634(15)	6284(4)	4496(5)	38(2)
O2	5415(14)	7243(4)	7721(4)	74(3)
N3	1225(19)	5614(4)	4104(5)	46(2)
N4	1133(16)	5833(4)	3213(5)	43(2)
N1	10030(20)	6872(5)	8127(6)	50(3)
C4	6522(16)	6681(4)	5017(5)	21(2)
C6	8396(19)	6968(5)	4555(7)	32(3)
N5	675(17)	6184(4)	1369(5)	56(3)
C1	8222(18)	7207(5)	6360(5)	32(2)
C2	6440(20)	6811(5)	5916(7)	29(2)
C3	10153(19)	7513(5)	5901(6)	41(3)

C5	10221(17)	7386(4)	4972(6)	35(2)
C7	3010(20)	5843(4)	4763(6)	35(2)
C9	-1030(20)	5794(5)	1693(7)	49(3)
C8	-750(20)	5627(5)	2647(7)	55(3)
C10	-2820(20)	5618(6)	992(8)	80(4)
C12	-40(30)	6252(6)	429(7)	73(4)
C11	-2200(30)	5896(6)	201(8)	77(4)

Table 4-5: Bond Lengths for E3

Atom	Atom	Length/Å	Atom	Atom	Length/Å
S1	O2	1.437(7)	C4	C6	1.367(12)
S1	O1	1.437(7)	C6	C5	1.380(12)
S1	N1	1.616(11)	N5	C9	1.329(12)
S1	C1	1.760(8)	N5	C12	1.396(12)
S2	C7	1.676(9)	C1	C2	1.353(12)
N2	C7	1.345(11)	C1	C3	1.404(12)
N2	C4	1.434(10)	C3	C5	1.397(11)
N3	C7	1.336(11)	C9	C10	1.340(13)
N3	N4	1.390(10)	C9	C8	1.439(13)
N4	C8	1.262(11)	C10	C11	1.378(15)
C4	C2	1.358(11)	C12	C11	1.336(15)

Table 4-6: Bond Angles for E3

Atom	Atom	Atom	Angle/°	Atom	Atom	Atom	Angle/°
O2	S1	O1	118.4(4)	C2	C1	S1	120.4(7)
O2	S1	N1	106.3(6)	C3	C1	S1	118.2(7)
O1	S1	N1	108.6(5)	C1	C2	C4	120.8(9)
O2	S1	C1	106.5(4)	C5	C3	C1	118.0(9)
O1	S1	C1	107.7(4)	C6	C5	C3	118.4(9)
N1	S1	C1	109.0(5)	N3	C7	N2	115.4(8)
C7	N2	C4	131.0(7)	N3	C7	S2	118.2(8)

C7	N3	N4	120.1(9)	N2	C7	S2	126.4(7)
C8	N4	N3	116.1(8)	N5	C9	C10	107.7(10)
C2	C4	C6	119.1(9)	N5	C9	C8	121.1(9)
C2	C4	N2	123.7(8)	C10	C9	C8	131.2(11)
C6	C4	N2	117.1(7)	N4	C8	C9	122.3(10)
C5	C6	C4	122.4(9)	C11	C10	C9	109.2(11)
C9	N5	C12	108.8(9)	C11	C12	N5	107.0(10)
C2	C1	C3	121.4(9)	C10	C11	C12	107.3(10)

Table 4-7: Anisotropic Displacement Parameters ($Å^2×10^3$) for E3. The Anisotropic displacement factor exponent takes the form: $-2\pi^2[h^2a^{*2}U_{11}+2hka^*b^*U_{12}+\ldots]$.

Atom	U_{11}	U_{22}	U_{33}	U_{23}	U_{13}	U_{12}
S1	29.3(16)	71(2)	23.9(14)	-12.2(13)	2.9(10)	1.1(14)
S2	94(3)	66(3)	36.1(16)	12.6(15)	-11.2(15)	-38.5(18)
O1	69(5)	51(6)	33(4)	-24(3)	-4(3)	4(4)
N2	51(6)	43(6)	22(4)	-1(4)	10(4)	-6(4)
O2	32(5)	154(9)	38(4)	-30(4)	13(3)	-17(4)
N3	62(7)	43(7)	31(5)	6(4)	0(4)	-15(5)
N4	51(6)	51(7)	27(5)	-4(4)	-4(4)	-12(4)
N1	36(8)	84(9)	29(5)	8(4)	4(6)	-3(6)
C4	28(6)	18(6)	17(5)	-2(4)	2(4)	0(4)
C6	33(7)	47(8)	14(5)	-2(5)	-1(5)	16(5)
N5	59(7)	79(8)	27(5)	4(5)	-12(4)	-19(5)
C1	22(6)	51(8)	21(5)	0(5)	1(4)	-1(5)
C2	33(7)	29(7)	26(6)	5(5)	8(5)	-2(5)
C3	28(7)	58(9)	37(6)	-11(5)	2(5)	-6(5)
C5	25(6)	54(8)	25(5)	-1(5)	-2(4)	1(5)
C7	49(7)	26(7)	30(6)	1(4)	-2(5)	-8(5)
C9	61(8)	47(8)	37(6)	3(5)	-4(6)	-21(6)
C8	57(8)	70(9)	35(6)	2(6)	-2(5)	-24(6)
C10	69(9)	116(13)	50(8)	-4(8)	-14(7)	-40(8)
C12	77(10)	96(12)	44(8)	-7(7)	5(6)	7(8)
C11	80(11)	88(12)	53(8)	-4(7)	-34(7)	-26(8)

Table 4-8: Hydrogen Atom Coordinates (Å×10^4) and Isotropic Displacement Parameters (Å^2×10^3) for E3.

Atom	*x*	*y*	*z*	U(eq)
H2	4517	6338	3913	46
H5	2001	6365	1687	68
H8	-1991	5357	2852	66
H10	-4256	5351	1032	96
H11	-3108	5846	-383	92
H3	11610(190)	7790(40)	6320(60)	60(30)
H4	10700(200)	8100(60)	4260(80)	90(40)
H5	5470(140)	6650(30)	6250(50)	0(20)
H6	8550(150)	6920(40)	4040(50)	30(30)
H2	11230(170)	6880(40)	8010(60)	0(30)
H8	-360(170)	5340(40)	4200(50)	30(30)
H1	7500(500)	6860(110)	8710(170)	90(120)
H12	-2200(300)	6620(90)	-930(110)	240(70)

4.4.2. Crystal data of compound E8

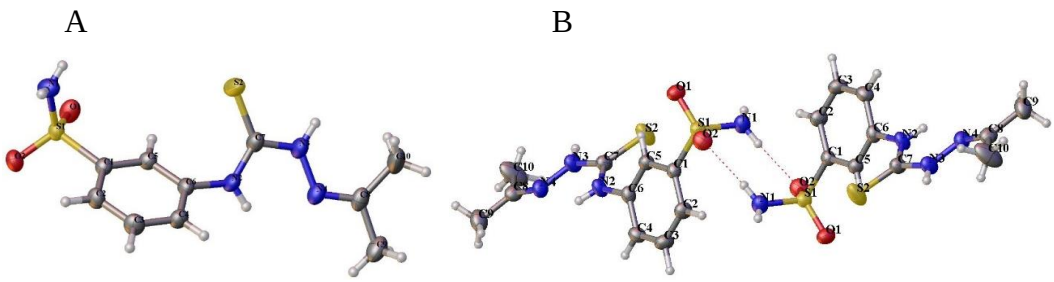

Figure 4-222: A) Crystal structure of compound E8 illustrated with thermal ellipsoids drawn at 50% probability to show the spatial arrangement of atoms. B) Molecular packing showing intermolecular hydrogen bonding.

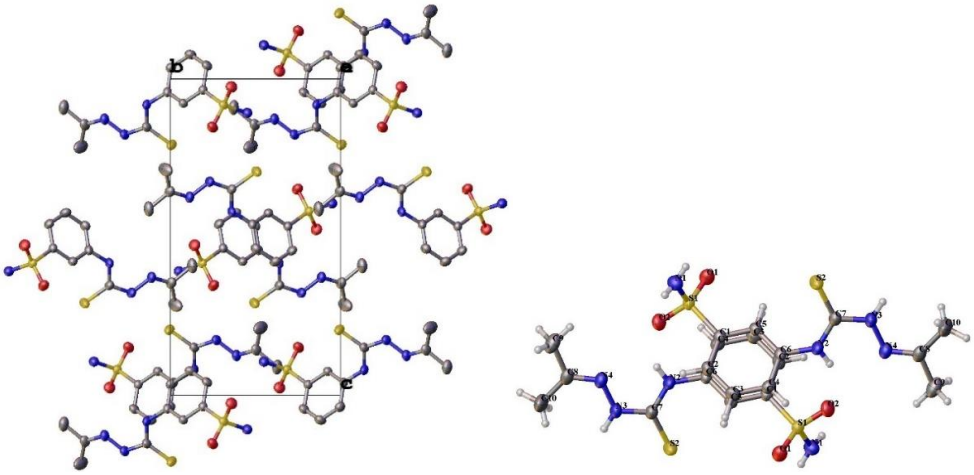

Figure 4-223: Crystal packing of compound E8 showing probable π – π interactions between the benzenesulfonamide rings.

Table 4-9: Sample and crystal data for E8

Identification code	**E8**
Empirical formula	$C_{10}H_{14}N_4O_2S_2$
Formula weight	286.37 g/mol
Temperature/K	297(2)
Crystal system	monoclinic
Space group	$P2_1/n$
a/Å	8.5768 (6)
b/Å	9.2551 (7)
c/Å	17.2143 (12)
α/°	90
β/°	91.933(2)
γ/°	90
Volume/$Å^3$	1365.68(17)
Z	4
$\rho_{calc}g/cm^3$	1.393
μ/mm^{-1}	0.390
F(000)	600
Radiation	MoKα (λ = 0.71073)
2Θ range for data collection/°	2.37 to 27.25
Index ranges	$-11 \leq h \leq 11$, $-11 \leq k \leq 11$, $-22 \leq l \leq 22$

Reflections collected	47491
Independent reflections	3042 [R_{int} = 0.0727, R_{sigma} = 0.0272]
Data/restraints/parameters	3042/0/220
Goodness-of-fit on F^2	1.043
Final R indexes [I>=2σ (I)]	R_1 = 0.0355, wR_2 = 0.0891
Final R indexes [all data]	R_1 = 0.0470, wR_2 = 0.0957
Largest diff. peak/hole / e $Å^{-3}$	0.45 /-0.34

Table 4-10: Atomic coordinates and equivalent isotropic atomic displacement parameters ($Å^2$) for E8. U(eq) is defined as 1/3 of the trace of the orthogonalized U_{ij} tensor.

Atom	x	y	z	U(eq)
S1	0.54021(5)	0.81314(5)	0.58213(2)	0.02884(13)
S2	0.11351(8)	0.50625(6)	0.70801(3)	0.05215(19)
O1	0.59976(16)	0.74690(15)	0.65220(8)	0.0404(3)
O2	0.64812(15)	0.85875(15)	0.52490(8)	0.0388(3)
N2	0.1924(2)	0.35989(17)	0.58106(9)	0.0358(4)
N4	0.09005(19)	0.11229(16)	0.62657(9)	0.0368(4)
N3	0.0792(2)	0.23003(17)	0.67542(10)	0.0388(4)
N1	0.4443(2)	0.95118(19)	0.60707(12)	0.0393(4)
C1	0.41041(19)	0.69085(18)	0.53464(10)	0.0276(3)
C5	0.3561(2)	0.57518(19)	0.57636(10)	0.0294(4)
C6	0.2495(2)	0.48150(18)	0.54105(10)	0.0298(4)
C4	0.2025(2)	0.5027(2)	0.46395(11)	0.0343(4)
C2	0.3636(2)	0.7142(2)	0.45752(11)	0.0349(4)
C8	0.0207(2)	0.9956(2)	0.64423(12)	0.0375(4)
C3	0.2602(2)	0.6179(2)	0.42284(11)	0.0383(4)
C7	0.1323(2)	0.3596(2)	0.65184(10)	0.0338(4)
C9	0.0358(3)	0.8720(3)	0.58982(17)	0.0508(6)
C10	0.9268(5)	0.9711(4)	0.71391(19)	0.0740(10)

Table 4-11: Bond lengths (Å) for E8.

Atom	Atom	Length/Å	Atom	Atom	Length/Å
S1	O1	1.4320(13)	S1	O2	1.4374(13)
S1	N1	1.5868(18)	S1	C1	1.7685(17)
S2	C7	1.6776(19)	N2	C7	1.338(2)
N2	C6	1.416(2)	N2	H7	0.80(2)

N4	C8	1.275(2)	N4	N3	1.381(2)
N3	C7	1.351(2)	N3	H8	0.85(2)
N1	H1	0.82(2)	N1	H2	0.75(3)
C1	C5	1.379(2)	C1	C2	1.391(2)
C5	C6	1.385(2)	C5	H6	0.93(2)
C6	C4	1.388(3)	C4	C3	1.381(3)
C4	H5	0.90(2)	C2	C3	1.379(3)
C2	H3	0.94(2)	C8	C10	1.485(3)
C8	C9	1.487(3)	C3	H4	0.98(2)
C9	H14	0.93(3)	C9	H12	0.91(3)
C9	H13	0.99(3)	C10	H9	0.78(4)
C10	H10	0.89(4)	C10	H11	1.01(6)

Table 4-12: Bond angles (°) for E8.

Atom	**Atom**	**Atom**	**Angle (°)**	**Atom**	**Atom**	**Atom**	**Atom**
O1	S1	O2	118.91(8)	O1	S1	C1	108.46(8)
O2	S1	C1	106.31(8)	O2	S1	N1	107.50(9)
N1	S1	C1	108.43(9)	O1	C1	N1	106.88(10)
C5	C1	S1	118.33(13)	C2	C1	S1	119.92(13)
N2	C7	S2	124.77(14)	N3	C7	S2	120.37(14)
C7	N2	C6	126.48(16)	C7	N3	N4	119.17(16)
C5	C1	C2	121.75(16)	C1	C5	C6	119.13(16)
C4	C6	C5	119.84(16)	C4	C6	N2	118.88(16)
C5	C6	N2	121.22(16)	C8	N4	N3	118.79(17)
C3	C4	C6	120.09(17)	C3	C2	C1	118.27(17)
N2	C7	N3	114.80(17)	C4	C3	C2	120.91(18)
N4	C8	C9	116.78(19)	N4	C8	C10	126.3(2)
C10	C8	C9	116.9(2)	C3	C2	H3	121.6(12)
C1	C5	H6	119.5(13)	C6	C5	H6	121.4(13)
C1	C2	H3	120.1(13)	C3	C4	H5	121.5(14)
C6	C4	H5	118.5(14)	C4	C3	H4	119.3(14)
C2	C3	H4	119.8(14)	S1	N1	H1	118.1(15)
C7	N2	H7	115.0(16)	C6	N2	H7	118.5(16)
C7	N3	H8	116.6(16)	N4	N3	H8	124.2(16)
C8	C9	H13	110.2(16)	C8	C9	H14	113.1(17)
C8	C9	H12	108.5(19)	S1	N1	H2	116.(2)
H14	C9	H13	104.(2)	H12	C9	H13	110.(2)
C8	C10	H10	112.(2)	H1	H1	H2	119.(3)
H14	C9	H12	111.(3)	C8	C10	H9	117.(3)

C8	C10	H11	107.(3)	H10	C10	H11	96.(3)
H9	C10	H10	128.(4)	H9	C10	H11	84.(4)

Table 4-13: Anisotropic atomic displacement parameters (Å^2) for E8. The anisotropic atomic displacement factor exponent takes the form: $-2\pi^2[h^2 a^{*2} U_{11} + ... + 2 h k a^* b^* U_{12}]$

Atom	U_{11}	U_{22}	U_{33}	U_{23}	U_{13}	U_{12}
S1	0.0310(2)	0.0271(2)	0.0284(2)	0.00188(17)	0.00110(16)	-0.00496(17)
S2	0.0901(5)	0.0333(3)	0.0341(3)	-0.0049(2)	0.0185(3)	-0.0162(3)
O1	0.0461(8)	0.0377(7)	0.0366(7)	0.0055(6)	-0.0098(6)	-0.0058(6)
O2	0.0340(7)	0.0417(7)	0.0410(7)	0.0017(6)	0.0082(6)	-0.0088(6)
N2	0.0518(10)	0.0234(8)	0.0327(8)	-0.0030(6)	0.0065(7)	-0.0091(7)
N4	0.0431(9)	0.0264(8)	0.0407(9)	0.0016(7)	-0.0009(7)	-0.0057(7)
N3	0.0547(10)	0.0289(8)	0.0329(9)	0.0023(7)	0.0038(8)	-0.0124(7)
N1	0.0532(11)	0.0330(9)	0.0318(9)	0.0008(7)	0.0050(8)	0.0030(8)
C1	0.0284(8)	0.0251(8)	0.0292(8)	-0.0001(7)	0.0020(6)	-0.0011(7)
C5	0.0343(9)	0.0282(9)	0.0255(8)	0.0011(7)	0.0013(7)	-0.0015(7)
C6	0.0341(9)	0.0241(8)	0.0316(9)	-0.0002(7)	0.0065(7)	-0.0023(7)
C4	0.0357(10)	0.0345(10)	0.0327(9)	-0.0042(8)	-0.0012(7)	-0.0062(8)
C2	0.0402(10)	0.0338(10)	0.0306(9)	0.0068(8)	0.0021(7)	-0.0065(8)
C8	0.0373(10)	0.0333(10)	0.0412(10)	0.0041(8)	-0.0084(8)	-0.0095(8)
C3	0.0431(11)	0.0431(11)	0.0282(9)	0.0052(8)	-0.0046(8)	-0.0040(9)
C7	0.0422(10)	0.0294(9)	0.0296(9)	0.0028(7)	-0.0015(7)	-0.0073(8)
C9	0.0494(13)	0.0325(11)	0.0702(16)	-0.0042(11)	-0.0024(12)	-0.0063(10)
C10	0.102(3)	0.0648(19)	0.0567(17)	-0.0114(14)	0.0192(16)	-0.053(2)

Table 4-14: Hydrogen atomic coordinates and isotropic atomic displacement parameters (Å2) for E8.

Atom	x	y	z	U(eq)
H8	0.038(3)	0.228(3)	0.7188(14)	0.046(6)
H6	0.390(2)	0.563(2)	0.6275(12)	0.034(5)
H3	0.403(2)	0.793(2)	0.4302(12)	0.036(5)
H5	0.134(3)	0.440(2)	0.4418(12)	0.043(6)
H7	0.191(2)	0.284(3)	0.5595(12)	0.037(6)
H1	0.400(3)	0.999(2)	0.5730(14)	0.038(6)
H4	0.227(3)	0.631(2)	0.3684(14)	0.051(6)
H2	0.410(3)	0.949(3)	0.6473(17)	0.059(8)

Atom	x	y	z	U(eq)
H9	-0.043(5)	0.005(4)	0.753(2)	0.107(14)
H14	0.092(3)	-0.105(3)	0.5462(16)	0.061(8)
H12	0.081(3)	-0.204(3)	0.6164(17)	0.078(9)
H13	-0.067(4)	-0.157(3)	0.5687(15)	0.071(8)
H10	-0.141(4)	-0.102(4)	0.7071(19)	0.093(10)
H11	-0.153(6)	0.051(6)	0.715(3)	0.149(19)

4.4.3. Crystal data of compound 4e

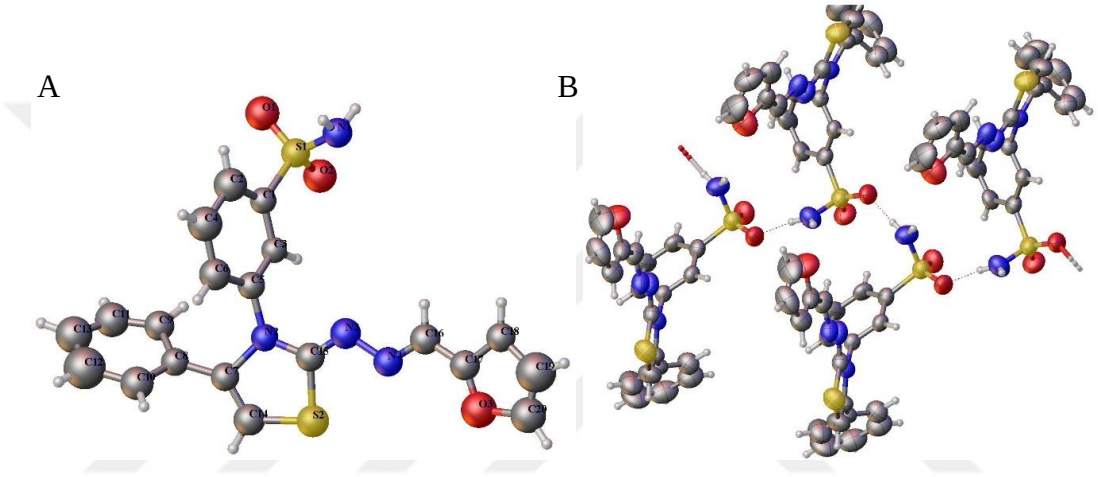

Figure 4-224: A) Crystal structure of compound 4e illustrated with thermal ellipsoids drawn at 50% probability to show the spatial arrangement of atoms. B) Molecular packing showing intermolecular hydrogen bondings.

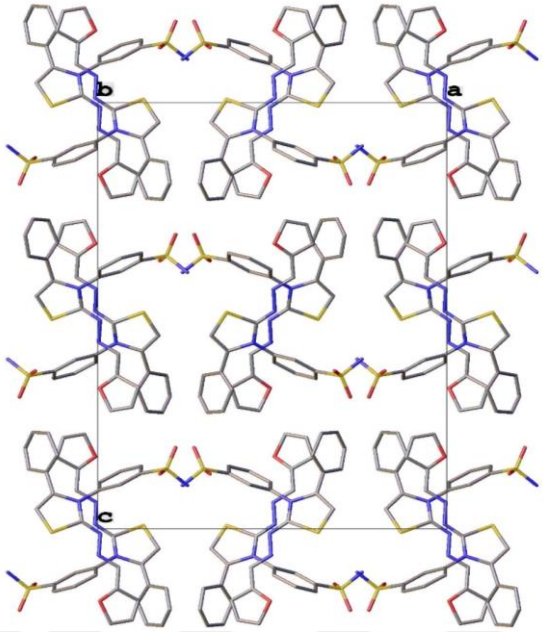

Figure 4-225: Crystal packing of compound 4e

Table 4-15: Crystal data and structure refinement for 4e.

Identification code	**4e**
Empirical formula	$C_{20}H_{16}N_4O_3S_2$
Formula weight	424.51
Temperature/K	297.31
Crystal system	orthorhombic
Space group	Pbca
a/Å	18.4103(14)
b/Å	8.8317(7)
c/Å	26.701(2)
α/°	90
β/°	90
γ/°	90
Volume/Å^3	4341.4(6)
Z	8
ρ_{calc}g/cm^3	1.2989
μ/mm^{-1}	0.273
F(000)	1762.7
Radiation	Mo Kα (λ = 0.71073)
2Θ range for data collection/°	4.42 to 50.86

Index ranges	$-22 \leq h \leq 22, -10 \leq k \leq 10, -32 \leq l \leq 32$
Reflections collected	132630
Independent reflections	4010 [R_{int} = 0.1410, R_{sigma} = 0.0456]
Data/restraints/parameters	4010/0/122
Goodness-of-fit on F^2	6.837
Final R indexes [I>=2σ (I)]	R_1 = 0.3888, wR_2 = 0.7776
Final R indexes [all data]	R_1 = 0.4456, wR_2 = 0.7917
Largest diff. peak/hole / e $Å^{-3}$	13.76/-2.82

Table 4-16: Fractional Atomic Coordinates (×10⁴) and Equivalent Isotropic Displacement Parameters (Å²×10³) for 4e. U_{eq} is defined as 1/3 of the trace of the orthogonalised U_{IJ} tensor.

Atom	*x*	*y*	*z*	U(eq)
S1	6970(3)	3555(7)	6406(3)	46(2)
S2	3693(5)	3630(9)	4920(3)	58(2)
O2	6785(11)	5080(20)	6292(7)	65(5)
N2	4466(10)	2630(20)	5640(7)	38(5)
O1	7233(11)	3250(20)	6906(8)	72(6)
N3	5074(13)	2980(30)	4892(8)	57(6)
N4	5035(11)	3330(20)	4376(8)	52(6)
C5	5054(12)	2030(30)	5914(8)	36(6)
N1	7567(12)	3090(30)	6019(10)	60(6)
C1	6237(14)	2390(30)	6300(10)	49(7)
C3	5645(11)	3010(20)	6037(8)	29(5)
C15	4546(13)	3060(30)	5173(9)	38(6)
C18	6166(16)	3020(30)	3319(11)	54(7)
C7	3729(15)	2670(30)	5828(10)	52(7)
C2	6250(18)	970(30)	6470(12)	63(8)
C8	3537(11)	2070(30)	6329(9)	35(6)
C17	5557(17)	3450(30)	3592(12)	63(8)
C4	5666(13)	-30(30)	6353(10)	51(7)
C6	5055(13)	530(30)	6089(10)	46(7)
O3	5064(18)	3780(40)	3305(12)	131(11)
C16	5603(16)	3230(30)	4100(10)	58(7)
C9	3850(14)	2800(30)	6728(9)	48(7)
C14	3255(18)	3160(30)	5464(12)	68(8)
C11	3591(17)	2310(30)	7241(13)	66(8)
C10	3034(18)	900(40)	6399(13)	71(9)

C20	5380(20)	3590(40)	2776(14)	77(9)
C13	3151(17)	1190(40)	7269(13)	72(9)
C19	5980(30)	3230(60)	2860(20)	126(15)
C12	2930(20)	470(50)	6891(16)	96(12)

Table 4-17: Bond Lengths for 4e.

Atom	Atom	Length/Å	Atom	Atom	Length/Å
S1	O2	1.42(2)	C18	C17	1.39(4)
S1	O1	1.45(2)	C18	C19	1.28(5)
S1	N1	1.56(3)	C7	C8	1.48(4)
S1	C1	1.72(3)	C7	C14	1.38(4)
S2	C15	1.78(3)	C2	C4	1.42(4)
S2	C14	1.71(3)	C8	C9	1.37(3)
N2	C5	1.41(3)	C8	C10	1.40(4)
N2	C15	1.31(3)	C17	O3	1.22(4)
N2	C7	1.45(3)	C17	C16	1.37(4)
N3	N4	1.41(3)	C4	C6	1.42(3)
N3	C15	1.23(3)	O3	C20	1.54(4)
N4	C16	1.28(3)	C9	C11	1.51(4)
C5	C3	1.43(3)	C11	C13	1.28(4)
C5	C6	1.40(3)	C10	C12	1.38(5)
C1	C3	1.41(3)	C20	C19	1.18(6)
C1	C2	1.33(4)	C13	C12	1.26(5)

Table 4-18: Angles for 4e.

Atom	Atom	Atom	Angle/°	Atom	Atom	Atom	Angle/°
O1	S1	O2	117.0(12)	C8	C7	N2	122(2)
N1	S1	O2	105.9(13)	C14	C7	N2	111(2)
N1	S1	O1	109.1(13)	C14	C7	C8	127(3)
C1	S1	O2	110.1(12)	C4	C2	C1	120(3)
C1	S1	O1	107.6(12)	C9	C8	C7	115(2)
C1	S1	N1	106.6(13)	C10	C8	C7	123(2)
C14	S2	C15	91.4(14)	C10	C8	C9	122(2)
C15	N2	C5	121.1(19)	O3	C17	C18	110(3)
C7	N2	C5	123.2(19)	C16	C17	C18	115(3)

C7	N2	C15	115(2)	C16	C17	O3	134(3)
C15	N3	N4	123(2)	C6	C4	C2	120(3)
C16	N4	N3	120(2)	C4	C6	C5	120(2)
C3	C5	N2	117.9(19)	C20	O3	C17	106(3)
C6	C5	N2	122(2)	C17	C16	N4	121(3)
C6	C5	C3	120(2)	C11	C9	C8	116(2)
C3	C1	S1	116.9(19)	C7	C14	S2	112(2)
C2	C1	S1	120(2)	C13	C11	C9	118(3)
C2	C1	C3	124(3)	C12	C10	C8	115(3)
C1	C3	C5	117(2)	C19	C20	O3	102(4)
N2	C15	S2	110.1(17)	C12	C13	C11	123(4)
N3	C15	S2	119(2)	C20	C19	C18	118(5)
N3	C15	N2	131(2)	C13	C12	C10	125(4)
C19	C18	C17	105(4)				

Table 4-19: Hydrogen Atom Coordinates (Å×10^4) and Isotropic Displacement Parameters (Å^2×10^3) for 4e.

Atom	*x*	*y*	*z*	U(eq)
H2	6637(18)	630(30)	6664(12)	75(10)
H4	5686(13)	-1040(30)	6449(10)	61(8)
H6	4656(13)	-90(30)	6032(10)	55(8)
H3	5638(11)	4030(20)	5946(8)	35(6)
H10	2790(18)	440(40)	6133(13)	86(11)
H12	2670(20)	-430(50)	6949(16)	115(14)
H13	2988(17)	890(40)	7583(13)	86(11)
H11	3746(17)	2810(30)	7528(13)	79(10)
H9	4200(14)	3550(30)	6685(9)	57(8)
H1a	7630(140)	3300(300)	5710(120)	72(8)
H1b	7550(150)	2500(300)	5740(110)	72(8)
H18	6607(16)	2670(30)	3442(11)	64(9)
H16	6050(16)	3010(30)	4244(10)	69(9)
H14	2755(18)	3230(30)	5508(12)	81(10)
H20	5150(20)	3720(40)	2468(14)	93(11)
H19	6320(30)	3090(60)	2600(20)	151(18)

4.5. Biological Activity

4.5.1. CA Inhibition assay

The carbonic anhydrase inhibitory activities of the synthesized compounds were evaluated using the stopped-flow method. **Tables 4-20** and **4-21** show the inhibition constant (K_i) for the tested compounds **E1 – E13** and **4a – 4v,** respectively, in comparison to the reference drug, AAZ.

Table 4-20: The hCAI, hCAII, hCAIX and hCAXII enzyme inhibition values of the intermediate thiosemicarbazone derivatives (E1 – E13)

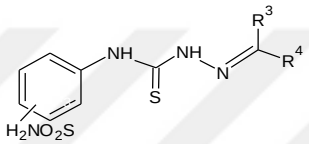

E

				K_i* (nM)			
Compound	**SO_2NH_2**	**R^3**	**R^4**	**hCAI**	**hCAII**	**hCAIX**	**hCAXII**
E1	meta	H	thiophene-2-yl-	813	48.4	95.5	90.5
E2	meta	H	5-bromothiophene-2-yl	3570	819	93.2	78.9
E3	meta	H	Pyrrole-2-yl	246	46.7	95.0	94.1
E4	meta	H	1-methylpyrrole-2-yl	236	95.3	91.8	77.7
E5	meta	H	Furan-2-yl	402	53.5	94.4	82.3
E6	para	H	Pyrrole-2-yl	65.9	19.3	77.6	235
E7	para	H	Furan-2-yl	5.24	0.92	89.8	89.4
E8	meta	CH_3	CH_3	2705	638.7	223.0	403.6
E9	meta	C_2H_5	C_2H_5	69.6	7.64	80.3	87.9
E10	para	CH_3	CH_3	62.10	7.3	111.7	92.2
E11	para	C_2H_5	C_2H_5	7.16	0.31	92.5	375
E12	para	CH_3	C_3H_7	12.4	3.29	83.4	96.8
E13	para	cyclopentylidene		2.29	0.59	75.0	91.9
AAZ	-	-	-	**250**	**12.5**	**25**	**5.7**

*The average value taken from three different tests with the stopped-flow technique. The error margin of the given values is between 5-10%.

Table 4-21: The hCAI, hCAII, hCAIX and hCAXII enzyme inhibition values of 3/4-[2-(alkylidene/arylidenehydrazinylidene)-4-(non)substitutedphenyl-1,3-thiazol-3(2*H*)-yl]benzenesulfonamide derivatives

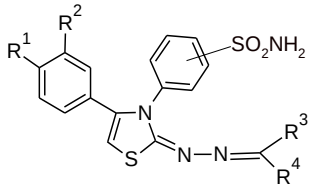

4

					***Ki** (nM)**				
Compound	**SO_2NH_2**	**R^1**	**R^2**	**R^3**	**R^4**	**hCAI**	**hCAII**	**hCAIX**	**hCAXII**
Lead	para	Br	-	C_2H_5-	C_2H_5-	783.4	3.9	13.5	2.6
4a	meta	-	-	H	thiophene-2-yl	643.3	562.9	89.2	102.4
4b	meta	-	-	H	5-bromothiophene-2-yl-	**690.8**	**>50000**	**90.1**	**79.2**
4c	meta	-	-	H	1*H*-pyrrole-2-yl	88.4	152.3	84.3	91.6
4d	meta	-	-	H	1-methyl-1*H*-pyrrole-2-yl	6701	863.8	86.6	81.5
4e	meta	-	-	H	Furan-2-yl	694.2	67.2	94.4	63.1
4f	para	-	-	H	1*H*-pyrrole-2-yl	**3370**	**5596**	**69.8**	**328**
4g	para	Br	-	H	1*H*-pyrrole-2-yl	**6873**	**5289**	**94.6**	**81.7**
4h	para	OH	-	H	1*H*-pyrrole-2-yl	**6434**	**658.7**	**1887**	**742.8**
4i	para	-	-	H	Furan-2-yl	**5950**	**2691**	**82.0**	**73.2**
4j	para	Br	-	H	Furan-2-yl	**8256**	**2943**	**87.1**	**82.9**
4k	meta	-	-	C_2H_5-	C_2H_5-	**3124**	**5255**	**93.7**	**81.8**
4l	para	Br	-	CH_3-	CH_3-	720	467	84.2	97.0
4m	para	CF_3	-	CH_3-	CH_3-	638	342	76.9	655
4n	para	OCF_3	-	CH_3-	CH_3-	826	501	89.1	208
4o	para	F	-	CH_3-	CH_3-	61.2	4.4	278.1	43.0
4p	para	-	CF_3	CH_3	CH_3	873.8	293.3	266.2	609.6
4q	para	CH_3	-	C_2H_5-	C_2H_5-	**6689**	**6286**	**89.0**	**86.7**
4r	para	F	-	C_2H_5-	C_2H_5-	**6451**	**3568**	**92.9**	**77.2**
4s	para	-	-	CH_3-	C_2H_5-	**6956**	**3919**	**81.3**	**92.2**
4t	para	-	-	cyclopentylidene		**>50000**	**>50000**	**82.5**	**76.2**
4u	para	Br	-	cyclopentylidene		**>50000**	**>50000**	**94.1**	**77.3**
4v	para	OH	-	cyclopentylidene		2794	2768	440.1	498.1
AAZ	-	-	-	-	-	**250**	**12.1**	**25.7**	**5.7**

*Average value taken from three different tests with the stopped-flow technique. The error margin of the given values is between 5-10%.

4.5.2. Cytotoxicty of 3/4-[2-(alkylidene/arylidenehydrazinylidene)-4-(non)substitutedphenyl-1,3-thiazol-3(*2H*)-yl]benzenesulfonamide derivatives (4a – 4v)

To examine the cytotoxic effects of synthesized 3/4-[2-(alkylidene/arylidenehydrazinylidene)-4-(non)substitutedphenyl-1,3-thiazol-3(2*H*)-yl]benzenesulfonamide derivatives (**4a – 4v**), endometrium (ECC-1, ATCC CRL-2923), lung (A549, ATCC CCL-185), colon (Caco-2, ATCC HTB-37; HT-29 ATCC HTB-38), breast (MCF-7, ATCC HTB-22), Glioblastoma (U118 MG, ATCC HTB-15) cancer cell lines are used and the Human Umbilical Vein Endothelial (HUVEC, ATCC PCS 100-010) cell line as a control. The results are shared in **Table 4-22**.

Table 4-22: Cytotoxic effects of 3/4-[2-(alkylidene/arylidenehydrazinylidene)-4-(non)substitutedphenyl-1,3-thiazol-3(2*H*)-yl]benzenesulfonamide derivatives (4a – 4v) on ECC-1, MCF-7, A549, HT-29, U118-MG, Caco-2 and HUVEC cell lines

	IC_{50} (µg/mL)						
Compounds	**ECC-1**	**MCF-7**	**A549**	**HT-29**	**U118-MG**	**Caco-2**	**HUVEC**
Lead compound	13.69±1.13	22.01±0.94	17.91±0.01	9.86±0.29	16.00±0.09	8.32±0.20	24.83±0.47
4a	15.97±1.66	14.88±0.35	>100	20.35±1.40	22.35±0.30	23.12±0.76	33.98±1.30
4b	8.24±0.41	11.42±0.48	19.48±0.55	15.80±0.65	17.91±0.42	2.70±0.13	16.58±0.25
4f	–	–	–	–	>100	>100	–
4g	24.74±1.56	1.98±0.06	7.61±0.17	4.84±0.34	34.16±2.27	2.20±0.08	40.87±1.25
4h	>100	>100	–	>100	–	>100	–
4i	–	–	–	–	>100	20.43±0.98	>100
4j	16.61±0.80	5.90±0.27	46.42±0.27	21.00±1.03	21.44±0.50	14.97±0.44	47.23±1.11
4k	42.99±2.96	45.22±0.94	50.25±9.56	43.31±1.50	62.63±1.63	46.32±2.06	52.03±3.21
4l	25.61±1.58	12.23±0.74	31.92±4.13	21.29±0.92	27.79±1.33	14.38±1.66	61.39±0.64
4m	60.79±2.08	44.83±0.88	>100	65.90±3.80	60.48±1.18	66.53±1.52	77.32±0.32
4n	32.77±2.02	30.34±1.31	59.53±0.58	36.10±0.90	32.77±0.85	35.25±0.64	46.21±0.25
4o	33.63±1.54	11.46±0.50	65.11±3.05	34.85±0.26	40.17±0.52	29.14±1.05	54.91±0.60
4p	52.32±2.14	30.73±1.40	57.32±2.94	58.22±0.95	55.06±1.11	41.19±2.05	58.33±1.10
4r	49.58±0.09	50.75±0.58	72.44±3.25	>100	–	47.15±2.47	59.23±2.95
4s	30.84±1.71	32.84±0.27	63.95±1.28	39.56±1.52	63.98±2.91	38.13±1.46	72.53±1.98
4t	19.04±0.70	>100	91.87±2.65	24.72±0.29	>100	32.72±0.89	61.53±0.29
4u	18.00±0.81	8.62±0.61	>100	9.81±0.40	>100	>100	>100
4v	51.74±1.25	23.08±1.49	70.59±3.50	24.75±1.11	65.48±2.45	69.36±0.81	71.64±2.12

5-FU	**8.74±0.34**	**58.46±2.33**	**18.63±2.14**	**1.99±0.15**	**>100**	**17.48±0.80**	**33.45±0.12**

Compounds that did not show any inhibition at the highest dose (100 µg/mL) are shown as **"–"** and compounds that showed less than 50% inhibition at the highest dose (100 µg/mL) are shown as " > 100 ".

4.6. Molecular Modelling Studies

To further understand the carbonic anhydrase inhibition studies and the SAR of compounds **4a – 4v**, ensemble docking was conducted with 7 and 9 available crystal structures for hCAIX and hCAXII, respectively, using the virtual screening workflow (VSW) module. VSW is a hierarchical virtual screening that docks the ligands with XP and then rescores the obtained poses with MM-GBSA. Based on the free binding energy obtained from the MM-GBSA calculations, location and the interaction of the sulfonamide group of the ligands and the similarity with the cocrystallised ligands, ligand protein interactions and complementarity, the best poses for compounds **4f**, **4i**, **4o**, **4t** and **4u** were selected and subjected to 250 ns MD simulations to determine the strength of the poses. A post-MM-GBSA free binding energy calculation was done using the trajectory file obtained during the simulation to determine the binding energy of the ligands throughout the simulation. In addition, MD simulation and post-MM-GBSA free binding energy calculation were performed on the cocrystallised ligands in hCAIX (PDB:6TL5) and hCAXII (PDB:6R6Y) to compare their binding modes and affinities with the docked pose of the selected compounds. **Figures 4-226 – 239** summarize the results of the MD simulations studies.

4.6.1. The binding pose of 3,5-diphenylbenzenesulfonamide, the cocrystallised ligand, in hCAIX (PDB:6TL5)

The binding pose of 3,5-diphenylbenzenesulfonamide in hCAIX (PDB:6TL5) reveals that the sulfonamide forms a coordination with the Zn^{2+} and two hydrogen bonds with both the backbone and sidechain of Thr199. One of the phenyls points in the direction of the hydrophobic region, while the other points in the direction of the hydrophilic region (**Figure 4-226A**).

During the 250 ns MD simulation, the coordination interaction with the Zn^{2+} was maintained. The sulfonamide continuously formed hydrogen bonds with either the backbone or the sidechain of Thr199. The hydrophobic interactions formed between

Leu198, Leu141, Val121, His94 and Trp5 continued for 45%, 20%, 25%, 25% and 20%, respectively (**Figure 4-226B & C**).

The average RMSD value of the protein Cα-atoms is 1.75 Å, while the RMSD value of the ligand fluctuated between 0.5 – 2.25 Å (**Figure 4-226D**). The average MM-GBSA binding free energy of the 6TL5 – 3,5-diphenylbenzenesulfonamide complex during the 250 ns MD simulation was −31.52 +/- 5.02 kcal/mol. The highest and lowest binding energies were − 12.72 and −44.65 kcal/mol, respectively (**Figure 4-226E**).

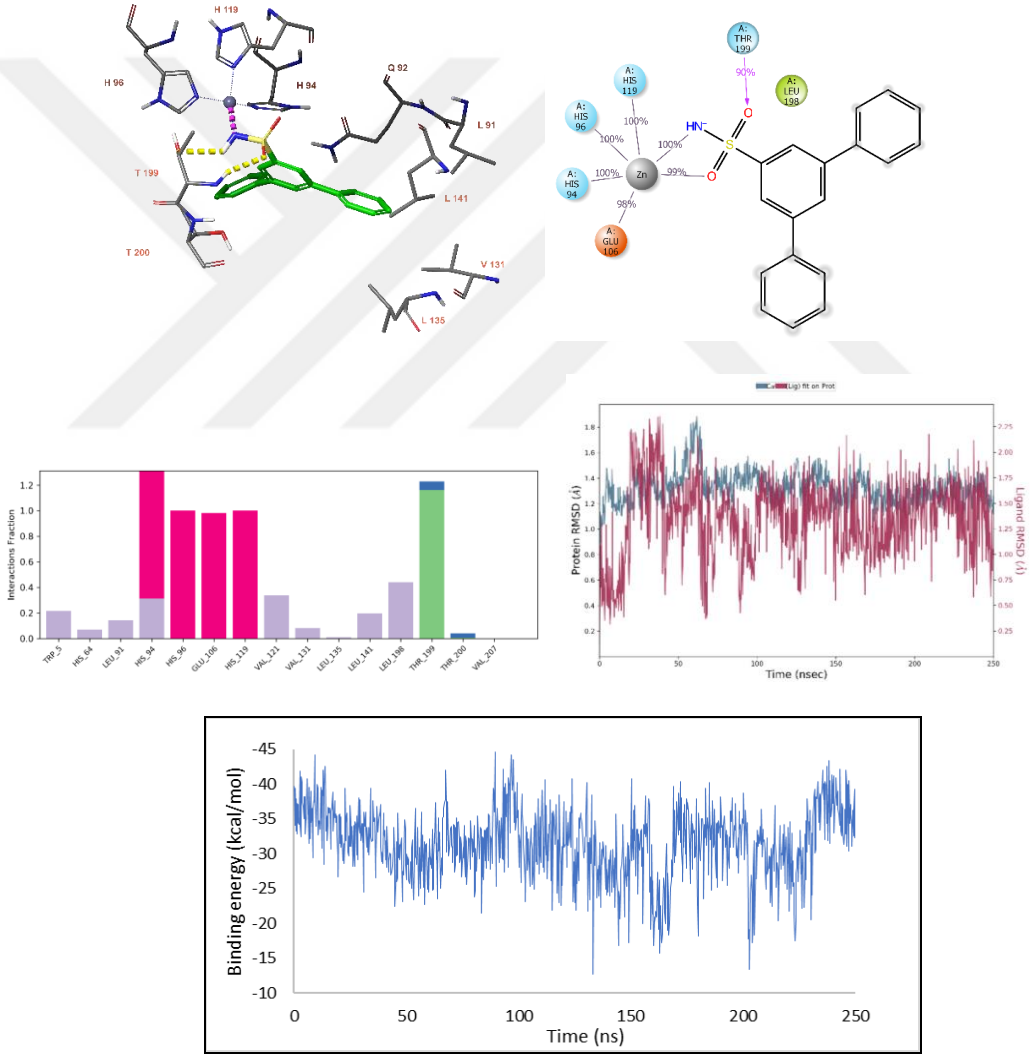

Figure 4-226: (A) The binding pose of 3,5-diphenylbenzenesulfonamide (green) in the active site of hCAIX (6TL5). The grey sphere represents the Zn^{2+}. Pink dashed lines represent metal coordination. Yellow dashed lines represent hydrogen bond. (B) Binding

interactions observed for at least 30% of the 250 ns MD simulation. Green represents hydrophobic amino acid (aa), blue represents polar aa, red represents negatively charged aa. (C) Histogram of protein-ligand contacts, with green indicating hydrogen bonds, blue indicating water-bridged hydrogen bonds, red indicating ionic bonds and grey indicating hydrophobic interactions. (D) RMSD plot of the protein Cα-atoms (blue) and ligand (red). (E) Protein-ligand interaction energy (kcal/mol) throughout the MD simulation.

4.6.2. The binding pose of 4-chloro-2-cyclohexylsulfanyl-*N*-(2-hydroxyethyl)-5-sulfamoylbenzamide, the cocrystallised ligand, in hCAXII (PDB:6R6Y)

The binding pose of 4-chloro-2-cyclohexylsulfanyl-*N*-(2-hydroxyethyl)-5-sulfamoylbenzamide, the cocrystallised molecule, in hCAXII (PDB:6R6Y) reveals that the sulfonamide forms a coordination with the Zn^{2+} and two hydrogen bonds with both the backbone and sidechain of Thr198. In addition, the ligand forms hydrogen bonds with Gln89 and Thr199. The cyclohexylsulfanyl moiety points in the direction of the hydrophobic region, while the 2-hydroxyethyl)carbamoyl moiety points in the direction of the hydrophilic region (**Figure 4-227A**).

In the 250 ns MD simulation, the coordination interaction formed with Zn^{2+} and the hydrogen bond formed with Thr199 were sustained throughout the simulation period. His91 formed a π – π stacking with benzenesulfonamide and lasted for 43% of the simulation time. The interaction with Thr199 was sustained via either a water-bridged or a direct hydrogen bond. The hydrogen bond formed with Gln was converted to a water-bridged hydrogen bond and lasted for 73% of the simulation time. In addition, new water-bridged hydrogen bonds were formed with Asn64, His66 and Pro200. These interactions lasted for 82%, 75% and 69%, respectively. The hydrophobic interactions between benzenesulfonamide and Leu197 lasted for 40% of the simulation time (**Figure 4-227B & C**).

The average RMSD value of the protein Cα-atoms is 1.7 Å, while the average RMSD value of the ligand is 1.5 Å (**Figure 4-227D**). The average MM-GBSA binding free energy of the 6R6Y – 4-chloro-2-cyclohexylsulfanyl-*N*-(2-hydroxyethyl)-5-sulfamoylbenzamide complex during the 250 ns MD simulation was −37.04 +/- 4.22 kcal/mol. The highest and lowest binding energies were −23.88 and −50.52 kcal/mol, respectively (**Figure 4-227E**).

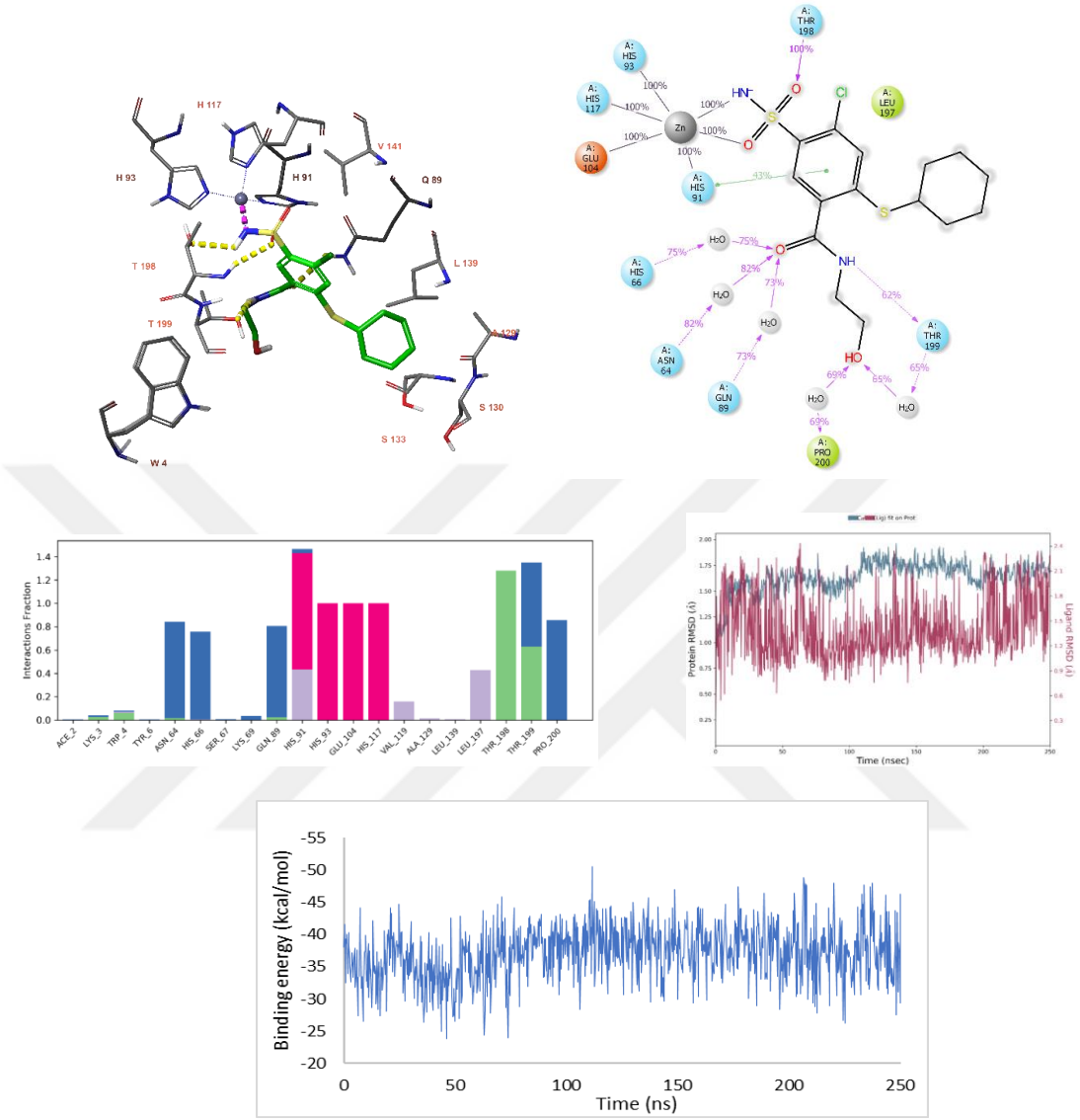

Figure 4-227: (A) The binding pose of 4-chloro-2-cyclohexylsulfanyl-*N*-(2-hydroxyethyl)-5-sulfamoylbenzamide (green) in the active site of hCAXII (6R6Y). The grey sphere represents the Zn^{2+}. Pink dashed lines represent metal coordination. Yellow dashed lines represent hydrogen bond. (B) Binding interactions observed for at least 30% of the 250 ns MD simulation. Green represents hydrophobic amino acid (aa), blue represents polar aa, red represents negatively charged aa. (C) Histogram of protein-ligand contacts, with green indicating hydrogen bonds, blue indicating water-bridged hydrogen bonds, red indicating ionic bonds and grey indicating hydrophobic interactions. (D) RMSD plot of the protein Cα-atoms (blue) and ligand (red). (E) Protein-ligand interaction energy (kcal/mol) throughout the MD simulation.

4.6.3. The docked pose of compound 4f in hCAIX (PDB: 5FL6 & 6TL5)

The docking studies of compound **4f,** the most potent hCAIX inhibitor, revealed two potential binding modes in hCAIX (PDB: 5FL6 & 6TL5). In both the poses, the deprotonated sulfonamide formed a coordination interaction with the Zn^{2+} ion, the oxygen atom formed a hydrogen bonding with the backbone of Thr200 (Thr199 for 6TL5) and the benzenesulfonamide ring formed a π – π interaction with His94. The docked pose of compound **4f** in hCAX (PDB:5FL6) revealed that the 4-phenyl ring is embedded in the hydrophobic region, facing Val130 and Ala133, whiles the 2-(((1*H*-pyrrol-2-yl)methylene)hydrazineylidene) moiety are projected towards the Trp9 (close to the hydrophilic region) where a π – π interaction is formed between Trp9 and the pyrrole ring (**Figure 4-228A**). The calculated MM-GBSA free binding energy for the pose was -34.48 kcal/mol.

During the 250 ns MD simulation, the coordination between the N^- and Zn^{2+} and the hydrogen bond between SO_2NH_2 oxygen and Thr200 were maintained throughout the simulation. The π – π stacking formed between His94 remained more than half of the simulation period. Thr201 continuously formed interactions with N_1 of the azine moiety either through a direct hydrogen bond or water-bridged hydrogen. The azine moiety moved towards the hydrophilic residues and formed new water-bridged hydrogen bonds with Asn66, His68 and Pro202 which continued for 40, 30 and 49% of the simulation time, respectively. The hydrophobic interactions between the 4-phenyl and Val130 and pyrrole and Trp9 continued for about 29 and 55% of the simulation, respectively (**Figure 4-228B & C**).

The RMSD value of the protein Cα-atoms fluctuated in the first 50 ns and then stabilized at 1.2 Å throughout. The ligand RMSD value also fluctuated in the first 50 ns and then stabilized at 2.4 Å throughout. The fluctuation was due to the rapid movement of Trp9, Asn66 and 2-(((1H-pyrrol-2-yl)methylene)hydrazineylidene) moiety (**Figure 4-228D**). The average MM-GBSA binding free energy of the 5FL6–**4f** complex during the 250 ns MD simulation was −44.20+/- 5.17 kcal/mol. The highest and lowest binding energies were −28.28 and −62.23 kcal/mol, respectively. As observed on the RSMD plot, the binding energy, though lowest, fluctuated during the first 50 ns (**Figure 4-228E).** This could be explained as the rapid movement of the 2-(((1*H*-pyrrol-2-

yl)methylene)hydrazineylidene) moiety between Trp9 and Asn66 to continuously form interactions with them.

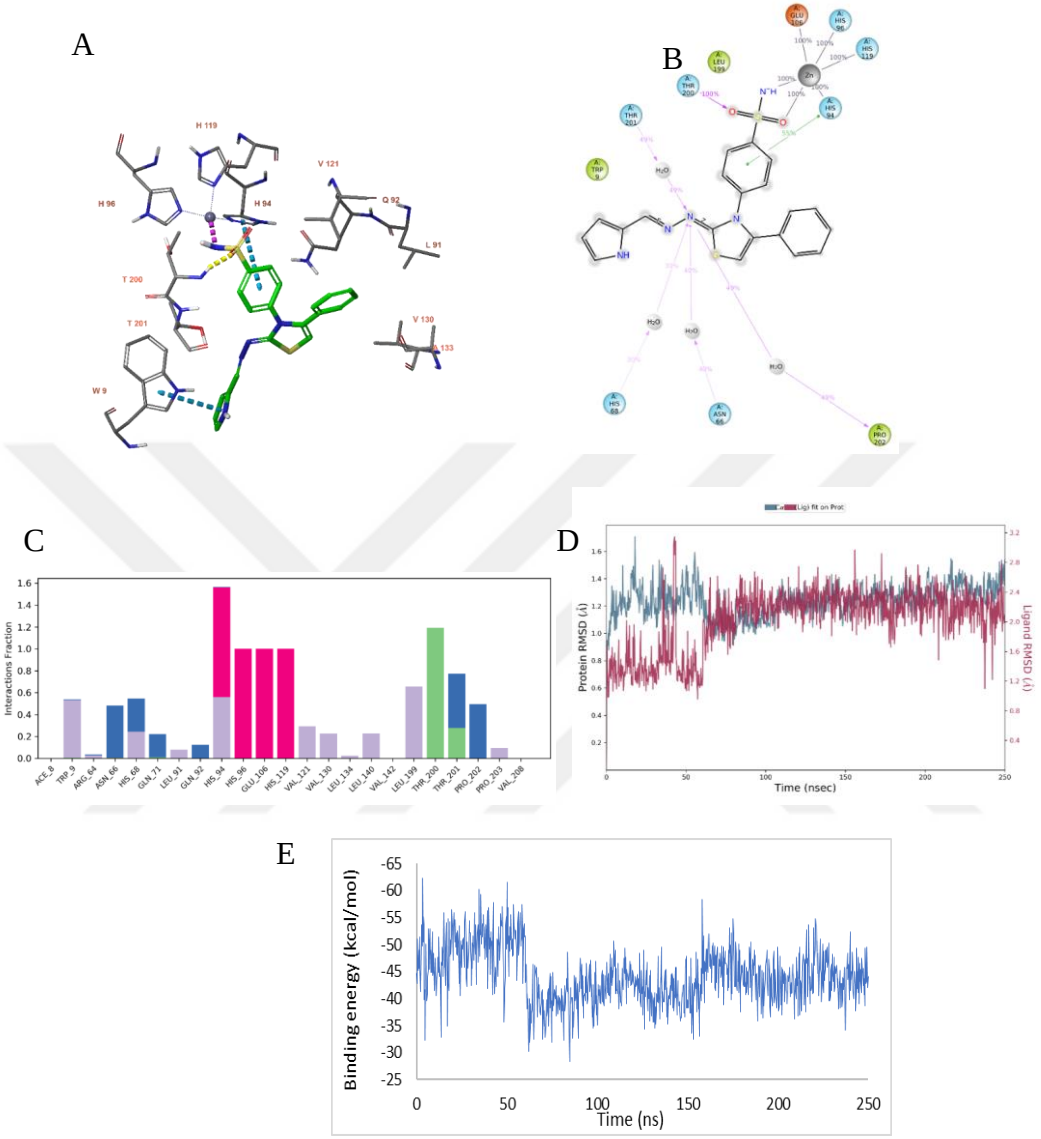

Figure 4-228: (A) The docked pose of compound 4f (green) in the active site of hCAIX (5FL6). The grey sphere represents the Zn^{2+}. Pink dashed lines represent metal coordination. Yellow dashed lines represent hydrogen bonds. Turquoise dashed lines represent π-π stacking. (B) Binding interactions observed for at least 30% of the 250 ns MD simulation. Green represents hydrophobic amino acid (aa), blue represents polar aa, red represents negatively charged aa. (C) Histogram of protein-ligand contacts, with green indicating hydrogen bonds, blue indicating water-bridged hydrogen bonds, red indicating ionic bonds and grey indicating hydrophobic interactions. (D) RMSD plot of the protein Cα-atoms (blue) and ligand (red). (E) Protein-ligand interaction energy (kcal/mol) throughout the MD simulation.

In contrast to the docking pose of compound **4f** in 5FL6, the 4-phenyl is located and well tolerated in the hydrophilic region of 6TL5, and formed a π – π stacking with His94, while the 2-(((1*H*-pyrrol-2-yl)methylene)hydrazineylidene) moiety is located in the hydrophobic region. Hydrophobic contacts are formed between the pyrrole ring and Val131 and Leu135. In addition to the hydrogen bond formed between the sulfonamide oxygen and the backbone of Thr199, the NH formed a hydrogen bond with the side chain of Thr199 (**Figure 4-229A).**

Figure 4-229B shows that the coordination between the N^- and Zn^{2+} and the hydrogen bond between SO_2NH_2 oxygen and the backbone of Thr199 were maintained throughout the simulation whiles the hydrogen bond between NH and the side chain of Thr199 was not sustained. The π – π stacking formed between 4-phenyl and His94 continued for 62% whiles the new π – π stacking formed between benzenesulfonamide and His94 continued for 83% of the simulation. Hydrophobic interactions with Leu135 and the pyrrole ring continued for %45 of the simulation (**Figure 4-229B & C**).

The average RMSD value of the protein Cα-atoms throughout the simulation is 1.4 Å. The ligand RMSD value was 0.5 Å in the first 10 ns and then rapidly shifted to 2 Å due to the movement of the 2-(((1*H*-pyrrol-2-yl)methylene)hydrazineylidene) moiety from between Leu91 and Val131 to between Val131 and Leu135. The ligand further fluctuates between 2 – 4.5 Å (**Figure 4-229D).** The average MM-GBSA binding free energy of the 6TL5–**4f** complex during the 250 ns MD simulation was −39.74+/- 5.07 kcal/mol. The highest and lowest binding energies were −23.79 and −53.25 kcal/mol, respectively (**Figure 4-229E**). In comparison to the cocrystallized ligand, which exhibited an average MM-GBSA binding free energy of -31.52+/- 5.02 kcal/mol, compound **4f** demonstrated a superior binding affinity to hCAIX (PDB: 6TL5).

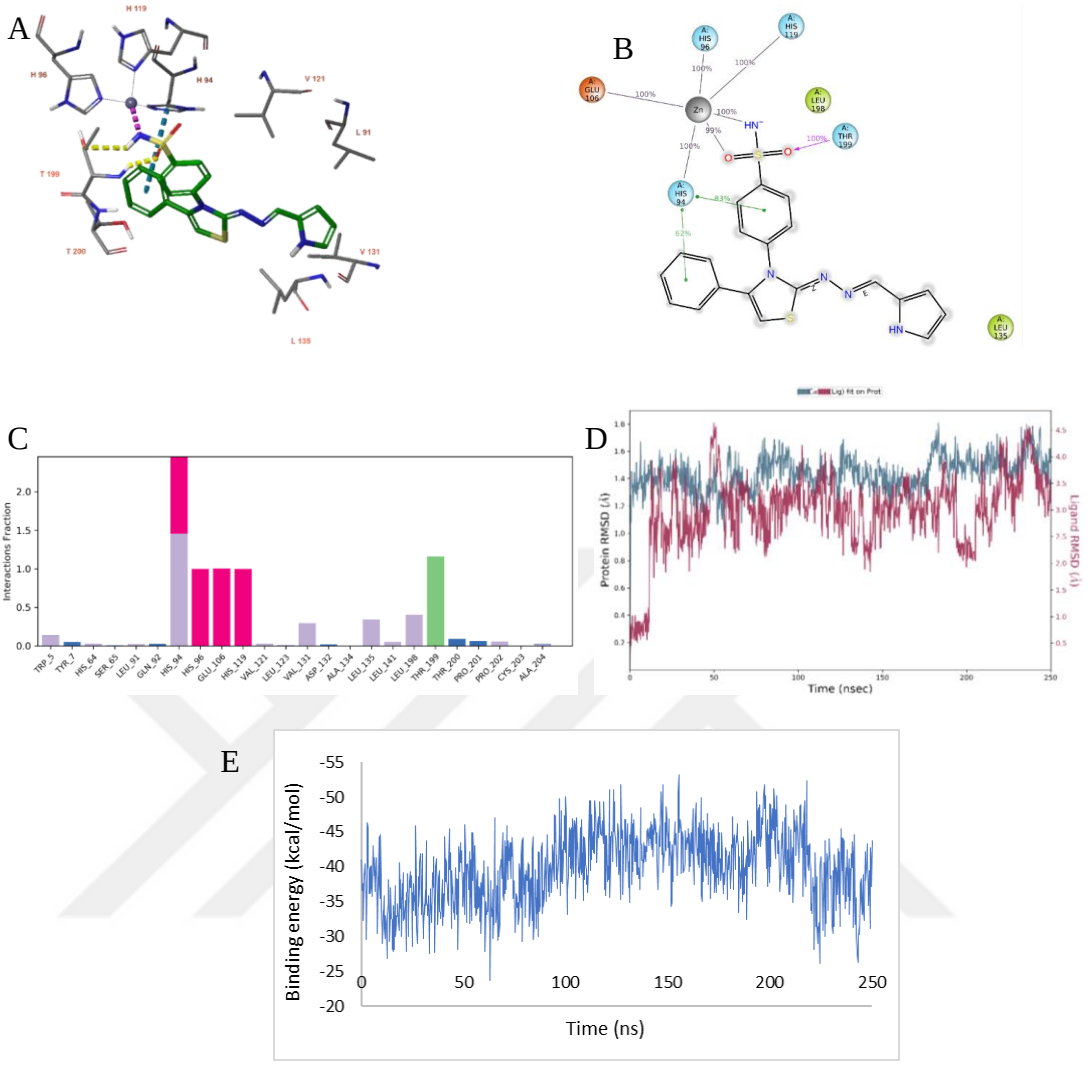

Figure 4-229: (A) The docked pose of compound 4f (green) in the active site of hCAIX (6TL5). The grey sphere represents the Zn^{2+}. Pink dashed lines represent metal coordination. Yellow dashed lines represent hydrogen bonds. Turquoise dashed lines represent π-π stacking. (B) Binding interactions observed for at least 30% of the 250 ns MD simulation. Green represents hydrophobic amino acid (aa), blue represents polar aa, and red represents negatively charged aa. (C) Histogram of protein-ligand contacts, with green indicating hydrogen bonds, blue indicating water-bridged hydrogen bonds, red indicating ionic bonds and grey indicating hydrophobic interactions. (D) RMSD plot of the protein Cα-atoms (blue) and ligand (red). (E) Protein-ligand interaction energy (kcal/mol) throughout the MD simulation.

4.6.4. The docked pose of compound 4f in hCAXII (PDB:6R6Y)

The docked pose of compound **4f** in hCAXII (PDB:6R6Y) reveals the coordination between the N^- and Zn^{2+}, the hydrogen bond between SO_2NH_2 oxygen and the backbone of Thr199, and π – π stackings formed between 4-phenyl/benzenesulfonamide and His94. The 2-(((1*H*-pyrrol-2-yl)methylene)hydrazineylidene) moiety is well tolerated in the hydrophobic region. The pyrrole aromatic carbons formed hydrophobic interactions Ala129 whereas the N_1-H formed a hydrogen bond with Thr88 (**Figure 4-230A**).

During the 250 ns MD simulation, the hydrogen bond between the oxygen of SO_2NH_2 and the backbone of Thr199, and π – π stackings between benzenesulfonamide and His94 were maintained throughout the simulation. In addition, the NH of SO_2NH_2 also formed a hydrogen bond with Thr198 which lasted for 47% of the simulation period. The π – π interaction between 4-phenyl and His94 continued for 73% of the simulation time. Hydrophobic interactions between benzenesulfonamide and Leu197 lasted for more than half of the simulation time, whereas the interaction between Leu139 and the pyrrole ring lasted for half of the simulation period (**Figure 4-230B & C**).

Although with little fluctuations, the RMSD plot reveals that the ligand is stabilized around 1.8 Å, whereas the RMSD value of the protein Cα-atoms gradually increased from 1.25 Å to 2 Å. (**Figure 4-230D**). The average MM-GBSA binding free energy of the 6R6Y– **4f** complex during the 250 ns MD simulation was −33.77+/− 4.53 kcal/mol. The highest and lowest binding energies were −18.99 and −51.90 kcal/mol, respectively (**Figure 4-230E**). In comparison to the cocrystallized ligand, which exhibited an average MM-GBSA binding free energy of -37.04+/-4.22 kcal/mol, compound **4f** demonstrates a weaker binding affinity to hCAXII (PDB: 6R6Y).

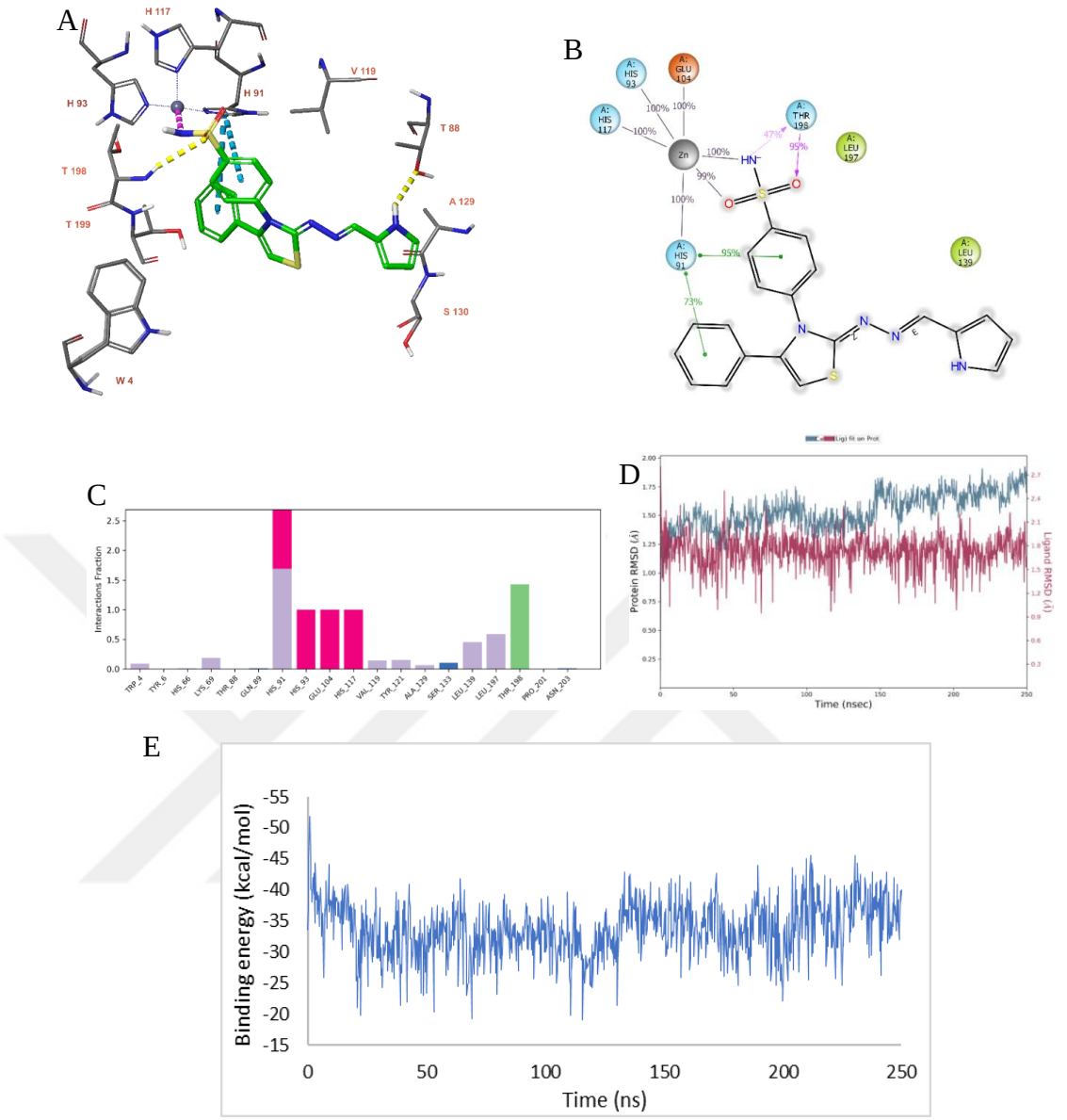

Figure 4-230: (A) The docked pose of compound 4f (green) in the active site of hCAXII (6R6Y). The grey sphere represents the Zn^{2+}. Pink dashed lines represent metal coordination. Yellow dashed lines represent hydrogen bonds. Turquoise dashed lines represent π-π stacking. (B) Binding interactions observed for at least 30% of the 250 ns MD simulation. Green represents hydrophobic amino acid (aa), blue represents polar aa, red represents negatively charged aa. (C) Histogram of protein-ligand contacts, with green indicating hydrogen bonds, blue indicating water-bridged hydrogen bonds, red indicating ionic bonds and grey indicating hydrophobic interactions. (D) RMSD plot of the protein Cα-atoms (blue) and ligand (red). (E) Protein-ligand interaction energy (kcal/mol) throughout the MD simulation.

4.6.5. The docked pose of compound 4i in hCAIX (PDB:6TL5)

The docked pose of compound **4i** in hCAIX (PDB:6TL5) depicts that the N^- and Zn^{2+} formed a coordination interaction, and SO_2NH_2 oxygen and NH formed hydrogen bonds with the backbone and the side chain of Thr199. The 2-((furan-2-ylmethylene)hydrazineylidene) moiety is located between Trp5 and the hydrophilic residues whiles the 4-phenyl pointed to the hydrophobic region. The furan formed a hydrogen bond with Trp5 (**Figure 4-231A**).

The MD simulation studies revealed that simulation the coordination between the N^- and Zn^{2+} and the hydrogen bond between SO_2NH_2 oxygen and Thr199 were maintained throughout the simulation. The new π – π stacking formed between His94 and benzenesulfonamide remained for more than half of the simulation period. The hydrogen bond formed between Trp5 and furan was lost and replaced with a π – π stacking and hydrophobic contacts that lasted for more than 30% of the simulation. The 4-phenyl ring formed hydrophobic interactions with Val121 and Val131 that did not continue up to 30% of the simulation time. The hydrophilic residues Asn62 formed either direct or water-bridged hydrogen bonds with the azine moiety for 40% and Glu67 formed water-bridged hydrogen bonds with thiazoline sulfur, azine and furan for 20% of the simulation time (**Figure 4-231B & C**).

The average RMSD value of the protein Cα-atoms throughout the simulation is 1.75 Å. The ligand RMSD value fluctuated between 0.8 – 3.2 Å. During the simulation, it is observed that 2-((furan-2-ylmethylene)hydrazineylidene) moiety frequently interacted with Trp5, Asn62, His64, Ser65 and Pro201, however, in the last 30 ns, the 2-((furan-2-ylmethylene)hydrazineylidene) moiety moved toward Pro201 and Pro201 while losing contacts with Trp5, Asn62, His64, and Ser65. This caused the increase in the ligand RMSD value from 1.6 Å to 3.2 Å (**Figure 4-231D**). This is reflected in the binding energy as it increased in the last 30 ns. The average MM-GBSA binding free energy of the 6TL5–**4i** complex during the 250 ns MD simulation was −38.13+/- 5.98 kcal/mol. The highest and lowest binding energies were −21.15 and −56.24 kcal/mol, respectively (**Figure 4-231E**). In comparison to the cocrystallized ligand, which exhibited an average MM-GBSA binding free energy of -31.52+/- 5.02 kcal/mol, compound **4i** demonstrated a superior binding affinity to hCAIX (PDB: 6TL5).

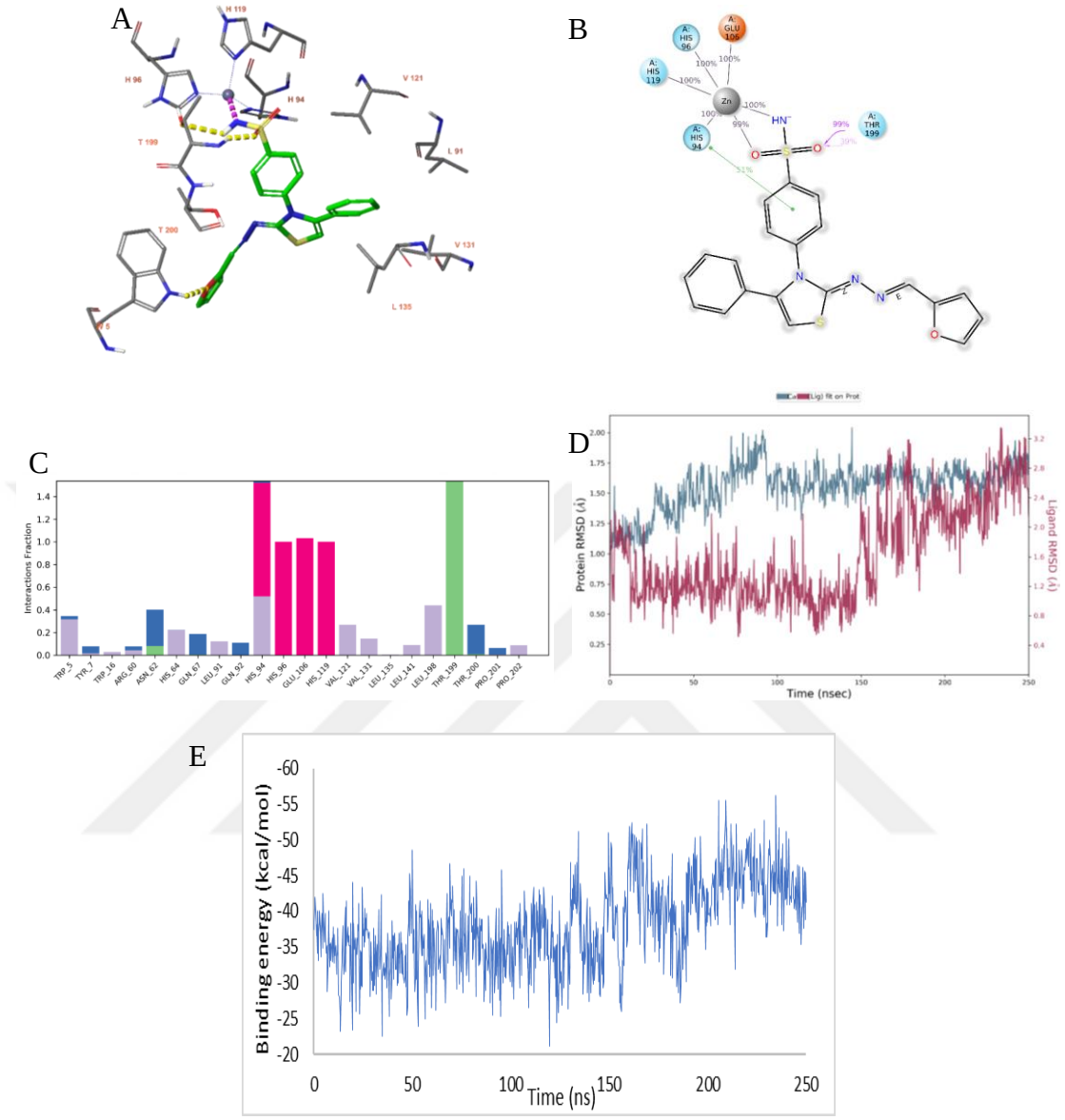

Figure 4-231: (A) The docked pose of compound 4i (green) in the active site of hCAIX (6TL5). The grey sphere represents the Zn^{2+}. Pink dashed lines represent metal coordination. Yellow dashed lines represent hydrogen bond. (B) Binding interactions observed for at least 30% of the 250 ns MD simulation. Green represents hydrophobic amino acid (aa), blue represents polar aa, red represents negatively charged aa. (C) Histogram of protein-ligand contacts, with green indicating hydrogen bonds, blue indicating water-bridged hydrogen bonds, red indicating ionic bond and grey indicating hydrophobic interactions. (D) RMSD plot of the protein Cα-atoms (blue) and ligand (red). (E) Protein-ligand interaction energy (kcal/mol) throughout the MD simulation.

4.6.6. Docked pose of compound 4i in hCAXII (PDB: 1JD0)

In hCAXII (PDB: 1JD0), compound **4i** formed a coordination interaction with Zn^{2+}, a hydrogen bond with the backbone of Thr199 and π – π stacking with His94. The 2-((furan-2-ylmethylene)hydrazineylidene) moiety is projected towards the hydrophilic residues where the furan ring formed π – π and cation – π stackings with His64. The 4-phenyl is located in the hydrophobic region and formed hydrophobic contacts with Ala131 (**Figure 4-232A**).

During the 250 ns MD simulations, the coordination interaction with the Zn and the hydrogen bond with Thr199 were sustained throughout the simulation whiles the π – π stacking with His94 did not last for more than 30% of the simulation time. The furan ring made π – π stackings with Trp5 for 26% of the simulation and a total of 40% with His64 via π – π stacking and water-bridged hydrogen bonds. 4-benzenesulfonamide ring formed hydrophobic contacts with Leu198 for 35% and the 4-phenyl ring located in the hydrophobic region made hydrophobic contacts with Val121 for more than half of the simulation. Asn62 formed water-bridged hydrogen bonds with the azine moiety and furan for 35% whereas Lys67 made cation – π interactions with the thiazoline ring for 23% (**Figure 4-232B & B**).

During the MD simulation, the furan frequently formed π – π stackings with Trp5 and His64. The trajectory has shown that the furan ring frequently made interactions with His64 and Trp5 for more than half of the simulation in the first 50 ns. However, as the 2-((furan-2-ylmethylene)hydrazineylidene) moiety moved away from Trp5 to get closer to His64, interactions with Trp5 faded out causing a rise in the binding energy from -43 to -18 kcal/mol (**Figure 4-232E**) and RMSD value of the ligand from 0.6 Å to 2.5 Å where it gets stabilized throughout the rest of the simulation (**Figure 4-232D**). The average MM-GBSA binding free energy of the 1JD0–**4i** complex during the 250 ns MD simulation was −31.08 +/- 4.19 kcal/mol. The highest and lowest binding energies were −18.52 and −43.95 kcal/mol, respectively (**Figure 4-232E**).

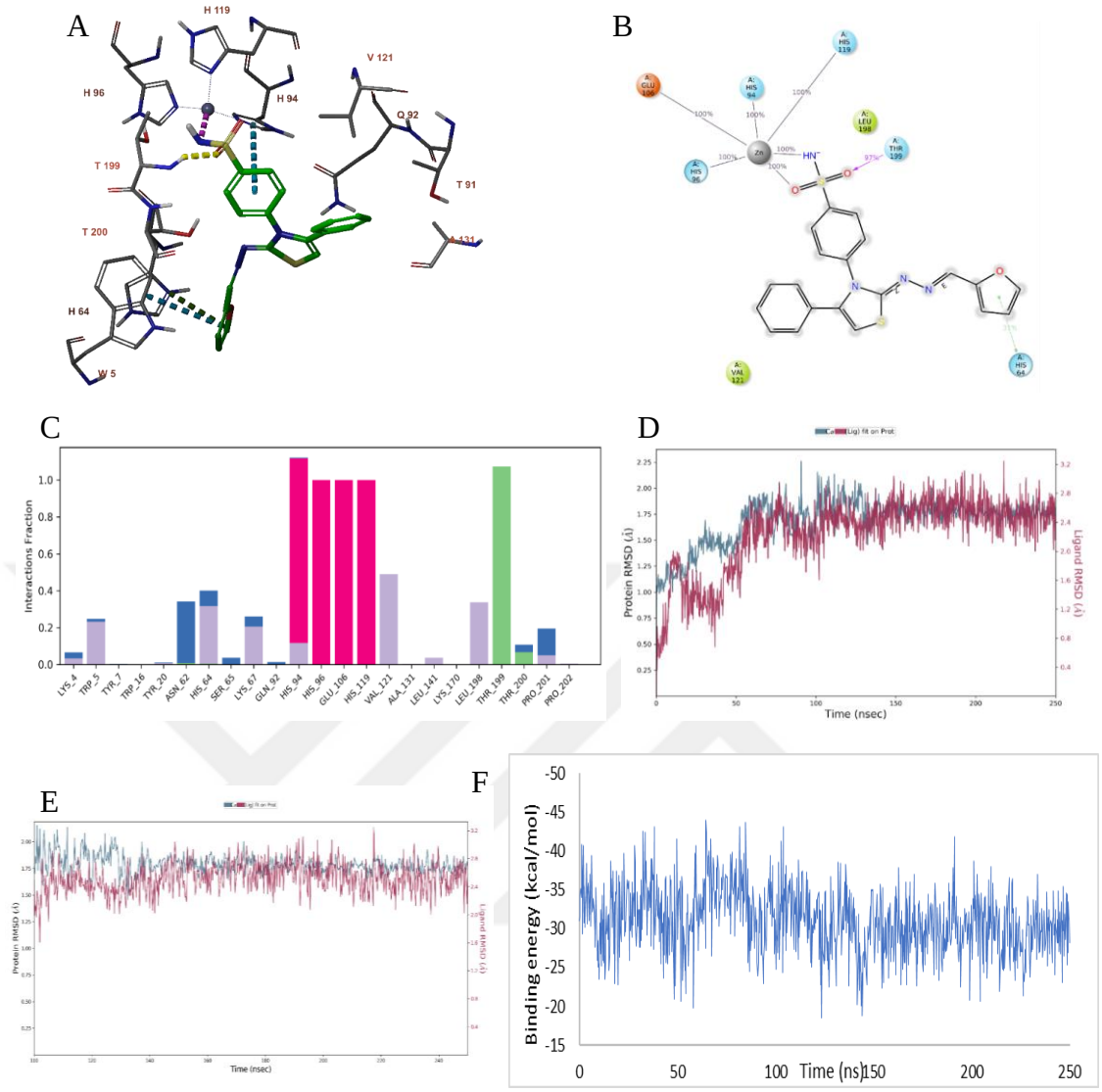

Figure 4-232: (A) The docked pose of compound 4i (green) in the active site of hCAXII (1JD0). The grey sphere represents the Zn^{2+}. Pink dashed lines represent metal coordination. Yellow dashed lines represent hydrogen bonds. Turquoise dashed lines represent π-π stacking. Green dashed lines represent cation – π interaction (B) Binding interactions observed for at least 30% of the 250 ns MD simulation. Green represents hydrophobic amino acid (aa), blue represents polar aa, red represents negatively charged aa. (C) Histogram of protein-ligand contacts, with green indicating hydrogen bonds, blue indicating water-bridged hydrogen bonds, red indicating ionic bonds and grey indicating hydrophobic interactions. (D) RMSD plot of the protein Cα-atoms (blue) and ligand (red). (E) Protein-ligand interaction energy (kcal/mol) throughout the MD simulation.

4.6.7. Docked pose of compound 4o in hCAIX (PDB: 6TL5)

In hCAIX (PDB: 6TL5), compound **4o** formed a coordination interaction with Zn^{2+}, a hydrogen bond with the backbone of Thr199 and a π – π stacking with His94. 4-(4-fluorophneyl) faced the hydrophobic region whereas the 2-(propan-2-ylidenehydrazineylidene) moiety face the hydrophilic region (**Figure 4-233A**).

During the 250 ns MD simulation, the coordination interaction with the Zn^{2+} and the hydrogen bond with Thr198 were sustained throughout the simulation. The hydrophobic contacts between Leu198 and 4-benzenesulfonamide lasted for 80%, whereas the π – π stacking with His94 lasted for 75 % of the simulation time (**Figure 4-233B & C**).

The average RMSD value of the protein Cα is 1.5 Å, whereas the RMSD value of the ligand fluctuated between 0.8 – 3.6 Å (**Figure 4-233D**). Between 107 – 116 ns,186 – 189 ns and in the last 15 ns, the high RMSD value of the ligand was due to the movement of the 4-(4-fluorophneyl) ring towards Pro202 where it made hydrophobic contacts. These interactions with Pro202 are reflected on MM-GBSA plot where the binding energy consequently decreased. The average MM-GBSA binding free energy of the 6TL5–**4o** complex during the 250 ns MD simulation was −36.35+/− 5.80 kcal/mol. The highest and lowest binding energies were −19.63 and −59.20 kcal/mol, respectively (**Figure 4-233E**). In comparison to the cocrystallized ligand, which exhibited an average MM-GBSA binding free energy of -31.52+/- 5.02 kcal/mol, compound **4o** demonstrated a superior binding affinity to hCAIX (PDB: 6TL5).

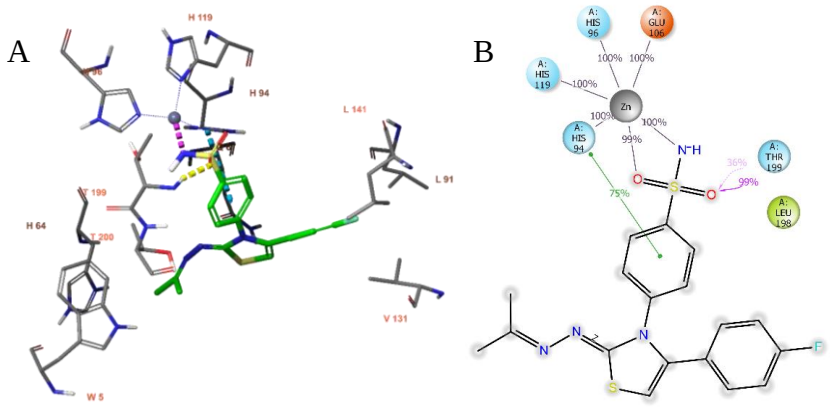

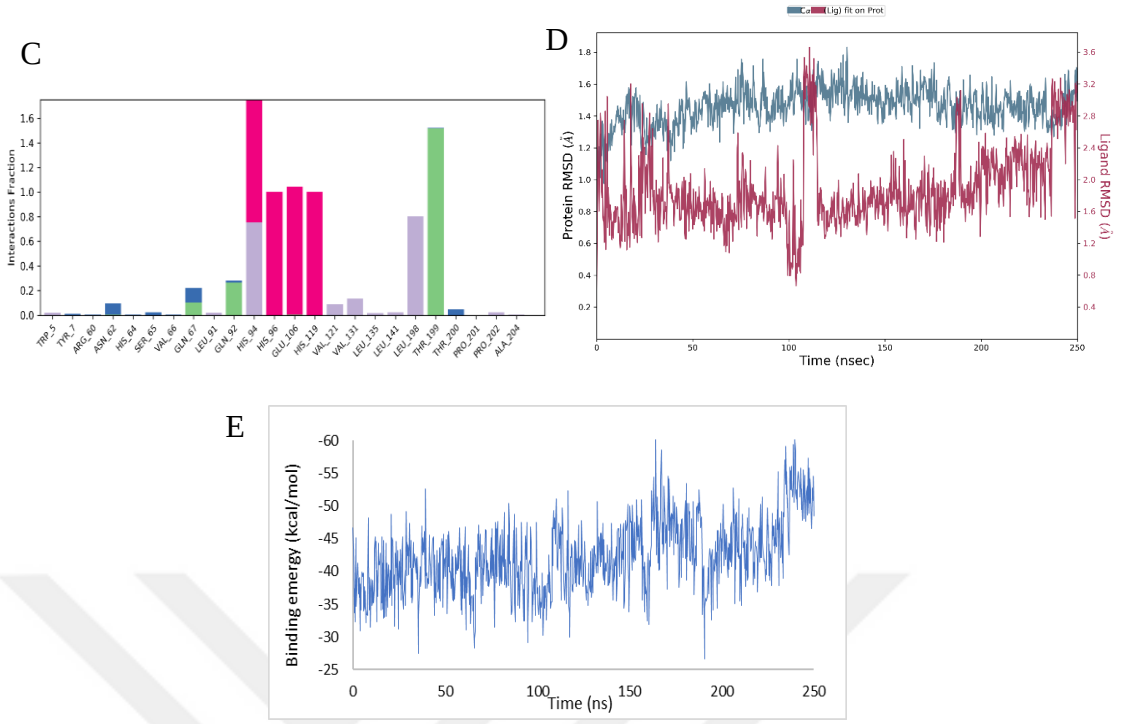

Figure 4-233: The docked pose of compound 4o (green) in the active site of hCAXI (6TL5). The grey sphere represents the Zn^{2+}. Pink dashed lines represent metal coordination. Yellow dashed lines represent hydrogen bonds. Turquoise dashed lines represent π-π stacking. (B) Binding interactions observed for at least 30% of the 250 ns MD simulation. Green represents hydrophobic amino acid (aa), blue represents polar aa, red represents negatively charged aa. (C) Histogram of protein-ligand contacts, with green indicating hydrogen bonds, blue indicating water-bridged hydrogen bonds, red indicating ionic bonds and grey indicating hydrophobic interactions. (D) RMSD plot of the protein Cα-atoms (blue) and ligand (red). (E) Protein-ligand interaction energy (kcal/mol) throughout the MD simulation.

4.6.8. Docked pose of compound 4o in hCAXII (PDB: 5LL5 & 6R6Y)

Compound **4o** was observed to have two different binding modes in hCAXII (PDB: 5LL5 and 6R6Y). In hCAXII (PDB: 5LL5), sulfonamide formed a coordination interaction with the Zn^{2+} ion and a hydrogen bond with the backbone of Thr198. The 4-benzenesulfonamide formed π – π stacking with His91. 4-(4-fluorophneyl) faced the hydrophobic region whereas the 2-(propan-2-ylidenehydrazineylidene) moiety face the hydrophilic region (**Figure 4-234A**).

The coordination interaction with the Zn^{2+}, the hydrogen bond with Thr198 and the hydrophobic contacts between Leu197 and 4-benzenesulfonamide were sustained throughout the simulation whereas the π – π stacking with His91 lasted for more than 87 % of the simulation time. The azine formed a hydrogen bond with Gln89 for 23% of the simulation (**Figure 4-234B & C)**.

The average RMSD value of the ligand was 3 Å whiles the RMSD value of the protein Cα kept rising until at 100 ns where it stabilized at 2.1 Å (**Figure 4-234E**). This was caused by the frequent movement of Trp4 until it came closer to the thiazoline ring to formed π – π stackings and hydrophobic contacts with the thiazoline and 4-(4-fluorophneyl) for total of 95% of the last 150 ns (**Figure 4-234D**). This consequently decreased the binding energy value from -35 to -55 kcal/mol. The movement of the ligand away from Trp4 increased the binding energy in the last 10 ns. The average MM-GBSA binding free energy of the 5LL5–**4o** complex during the 250 ns MD simulation was −31.11+/- 9.73 kcal/mol. The highest and lowest binding energies were −16.42 and −59.08 kcal/mol, respectively (**Figure 4-234F**).

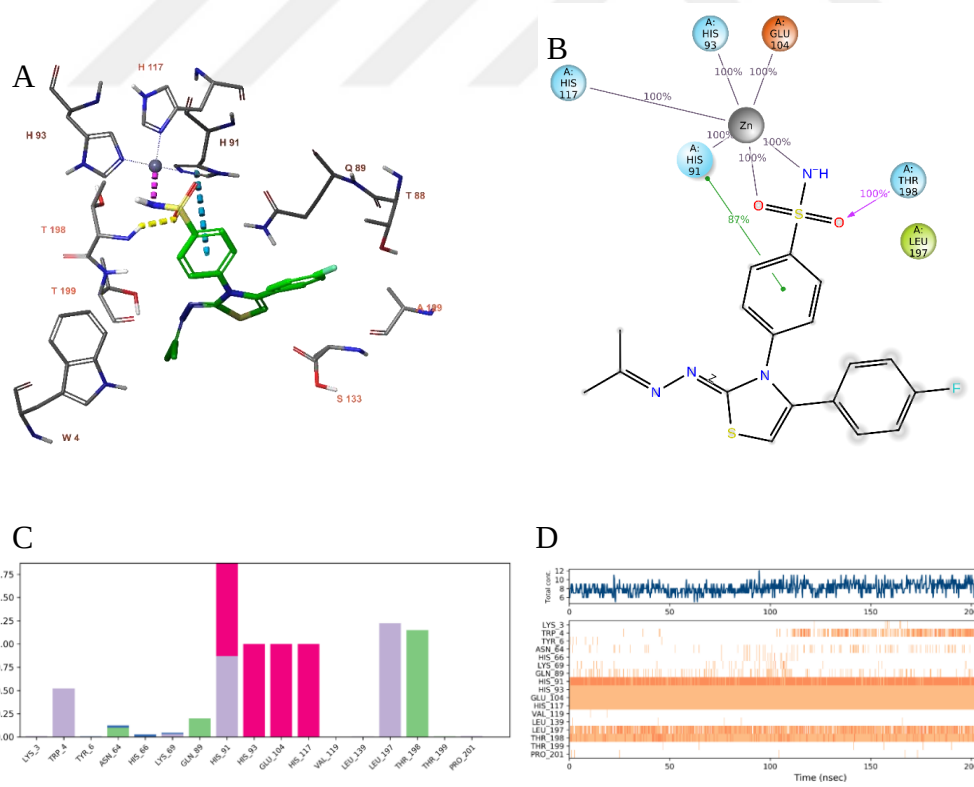

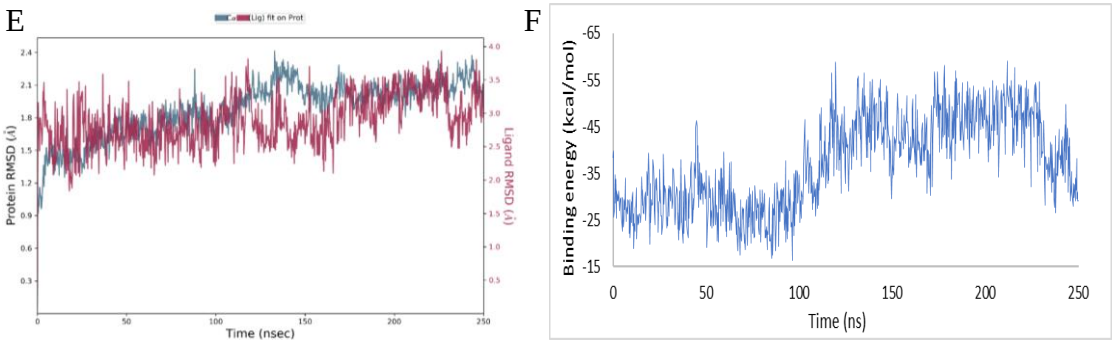

Figure 4-234: The docked pose of compound 4o (green) in the active site of hCAXII (5LL5). The grey sphere represents the Zn^{2+}. Pink dashed lines represent metal coordination. Yellow dashed lines represent hydrogen bonds. Turquoise dashed lines represent π-π stacking. (B) Binding interactions observed for at least 30% of the 250 ns MD simulation. Green represents hydrophobic amino acid (aa), blue represents polar aa, red represents negatively charged aa. (C) Histogram of protein-ligand contacts, with green indicating hydrogen bonds, blue indicating water-bridged hydrogen bonds, red indicating ionic bonds and grey indicating hydrophobic interactions. (D) A timeline representation of the interactions and contacts (0 – 250 ns). (E) RMSD plot of the protein Cα-atoms (blue) and ligand (red). (F) Protein-ligand interaction energy (kcal/mol) throughout the MD simulation.

In hCAXII (PDB: 6R6Y), the sulfonamide of compound **4o** formed a coordination interaction with the Zn^{2+} ion and hydrogen bonds with the side chain and the backbone of Thr198. The 4-(4-fluorophenyl) directed to the hydrophilic region and the 4-benzenesulfonamide formed π – π stackings with His91, whereas 2-(propan-2-ylidenehydrazineylidene) moiety faced the hydrophobic region (**Figure 4-235A)**.

The 250 ns MD simulation of **4o**-6R6Y complex revealed that sulfonamide group maintained the interactions with Zn^{2+} and Thr198 throughout the simulation. The π – π stackings between His91 and 4-(4-fluorophenyl) and 4-benzenesulfonamide were sustained for 67 and 92%, respectively. The azine formed a water-bridged hydrogen bond with Ser133 for 42% of the simulation time (**Figure 4-235B & C)**.

The average RMSD value of the protein Cα-atoms throughout the simulation was 1.75 Å. The average RMSD value of the ligand was 1.5 Å (**Figure 4-235D**). The average MM-GBSA binding free energy of the 6R6Y–**4o** complex during the 250 ns

MD simulation was −46.51+/- 8.35 kcal/mol. The highest and lowest binding energies were −24.97 and −64.68 kcal/mol, respectively (**Figure 4-235E**).

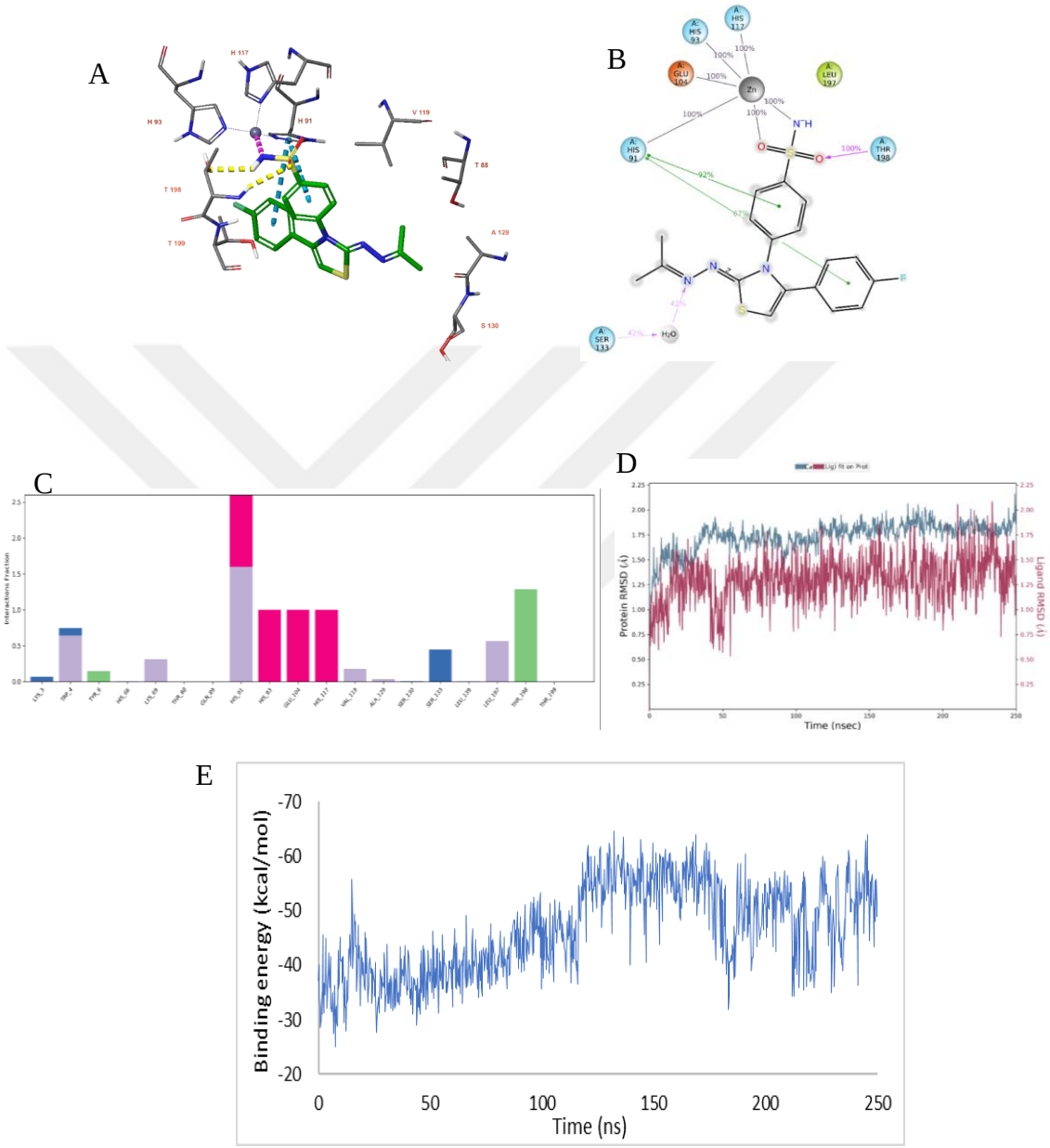

Figure 4-235: The docked pose of compound 4o (green) in the active site of hCAXII (6R6Y). The grey sphere represents the Zn^{2+}. Pink dashed lines represent metal coordination. Yellow dashed lines represent hydrogen bonds. Turquoise dashed lines represent π-π stacking. (B) Binding interactions observed for at least 30% of the 250 ns MD simulation. Green represents hydrophobic amino acid (aa), blue represents polar aa, red represents negatively charged aa. (C) Histogram of protein-ligand contacts, with green

indicating hydrogen bonds, blue indicating water-bridged hydrogen bonds, red indicating ionic bonds and grey indicating hydrophobic interactions. (D) RMSD plot of the protein Cα-atoms (blue) and ligand (red). (E) Protein-ligand interaction energy (kcal/mol) throughout the MD simulation.

4.6.9. Docked pose of compound 4t in hCAIX (PDB: 6TL5)

The sulfonamide of compound **4t** formed a coordination interaction with the Zn^{2+} ion and hydrogen bonds with the side chain and the backbone of Thr199 of hCAIX (PDB: 6TL5). The 4-phenyl directed to the hydrophilic region formed a π – π stacking with His94, whereas 4-(2-(cyclopentylidenehydrazineylidene) moiety faced the hydrophobic region forming hydrophobic contacts with Val131 and Leu131 (**Figure 4-236A**).

The contact summary of the 250 ns MD simulation revealed that sulfonamide group maintained the interactions with Zn^{2+} and Thr199 throughout the simulation. The π – π stackings between His94 and 4-benzenesulfonamide and 4-phenyl continued for 74 and 63%, respectively (**Figure 4-236B & D**).

In the RMSD plot, the high fluctuation in the 10 ns was due to the back-and-forth rapid movement of 4-(2-(cyclopentylidenehydrazineylidene) moiety between Leu91, Val131 and Pro202. This moiety further stabilized around Val131 with an average RMSD value was 1.8 Å. The average RMSD value of the protein Cα-atoms throughout the simulation is 1.4 Å (**Figure 4-236F**), however, in the last 70 ns, the RMSD value increased to 1.8 Å due to the movement of Trp5 closer to the thiazoline ring. Trp5 continuously formed π – π stacking with the thiazoline ring for about 90% of that time (**Figure 4-236C & E**), and this subsequently led to the decrease in the binding energy value from −35 to −68 kcal/mol during the last 70 ns. The average MM-GBSA binding free energy of the 6TL5–**4t** complex during the 250 ns MD simulation was −46.01+/- 8.43 kcal/mol. The highest and lowest binding energies were −27.02 and −68.10 kcal/mol, respectively (**Figure 4-236G**). In comparison to the cocrystallized ligand, which exhibited an average MM-GBSA binding free energy of -31.52+/-5.02 kcal/mol, compound **4t** demonstrated a superior binding affinity to hCAXII (PDB: 6R6Y).

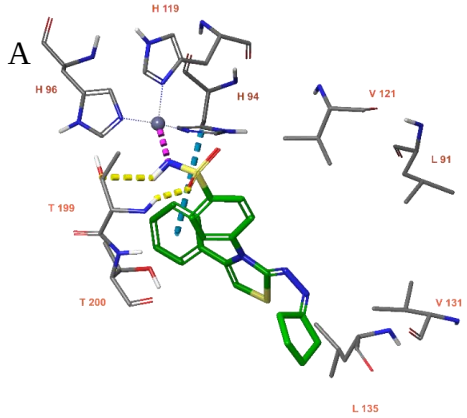
A
H 119
H 96
H 94
V 121
L 91
T 199
T 200
V 131
L 135

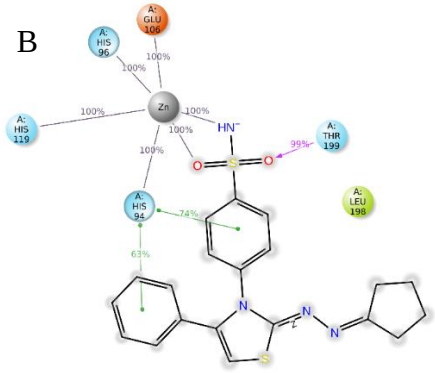
B
A: GLU 106
A: HIS 96
A: HIS 119
Zn
HN
A: THR 199
A: HIS 94
A: LEU 198
100%
99%
74%
63%

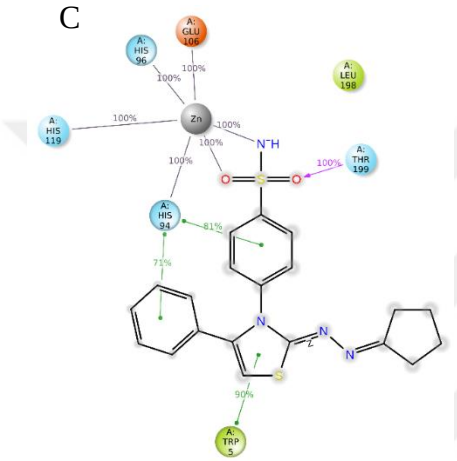
C
A: GLU 106
A: HIS 96
A: LEU 198
A: HIS 119
Zn
N-H
A: THR 199
A: HIS 94
A: TRP 5
100%
81%
75%
90%

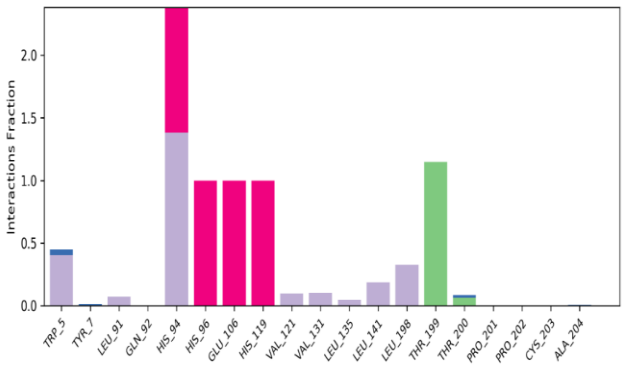
D
Interactions Fraction
2.0
1.5
1.0
0.5
0.0
TRP_5
TYR_7
LEU_91
GLN_92
HIS_94
HIS_96
GLU_106
HIS_119
VAL_121
VAL_131
LEU_135
LEU_141
LEU_198
THR_199
THR_200
PRO_201
PRO_202
CYS_203
ALA_204

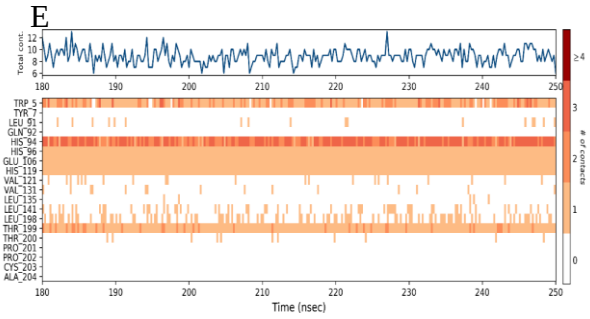
E
Total cont.
180
190
200
210
220
230
240
250
Time (nsec)

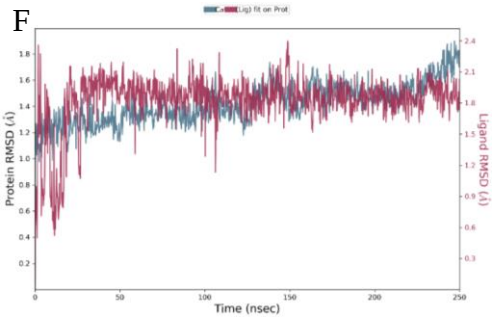
F
Protein RMSD (Å)
Ligand RMSD (Å)
Time (nsec)

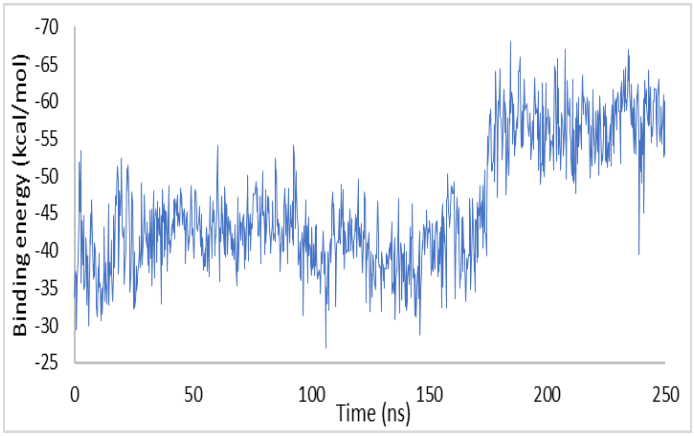
G
Binding energy (kcal/mol)
-70
-65
-60
-55
-50
-45
-40
-35
-30
-25
0
50
100
150
200
250
Time (ns)

Figure 4-236: The docked pose of compound 4t (green) in the active site of hCAIX (6TL5). The grey sphere represents the Zn^{2+}. Pink dashed lines represent metal coordination. Yellow dashed lines represent hydrogen bond. Turquoise dashed lines represent π-π stacking. (B) Binding interactions observed for at least 30% of the 250 ns MD simulation. (C) Binding interactions observed for at least 30% of the last 70 ns of the MD simulation. Green represents hydrophobic amino acid (aa), blue represents polar aa, red represents negatively charged aa. (D) Histogram of protein-ligand contacts, with green indicating hydrogen bonds, blue indicating water-bridged hydrogen bonds, red indicating ionic bond and grey indicating hydrophobic interactions. (E) A timeline representation of the interactions and contacts (180 – 250 ns). (F) RMSD plot of the protein Cα-atoms (blue) and ligand (red). (G) Protein-ligand interaction energy (kcal/mol) throughout the MD simulation.

4.6.10. Docked pose of compound 4t in hCAXII (PDB: 6R6Y)

The docked pose of compound **4t** in hCAXII (6R6Y) is comparable to that of hCAIX (6TL5), with the sulfonamide coordinated to Zn^{2+} and hydrogen bonded to Thr199, the 4-phenyl oriented to the hydrophilic region forming a π – π stacking with His91, and the 4-(2-(cyclopentylidenehydrazineylidene) moiety facing the hydrophobic region (**Figure 4-237A**).

The 250 ns MD simulation revealed that sulfonamide group maintained the interactions with Zn^{2+} and Thr198 throughout the simulation. The π – π stackings between His91 and 4-benzenesulfonamide and 4-phenyl continued for 92 and 48%, respectively. Trp5 made π – π stacking with the thiazoline ring for 30% of the simulation (**Figure 4-237B & D**).

Whiles the average RMSD value of the protein Cα-atoms throughout the simulation was 1.7 Å, it kept rising throughout the simulation. The ligand RMSD value was 1.75 Å (**Figure 4-237F).** The average MM-GBSA binding free energy of the 6R6Y–**4t** complex during the 250 ns MD simulation was −44.58+/- 7.33 kcal/mol. The highest and lowest binding energies were −27.16 and −62.23 kcal/mol, respectively (**Figure 4-237G**). As observed in the RMSD plot, the RMSD value of the protein Cα-atoms started to gradually increase after the first 90 ns. This was due to the movement

of Trp4 closer to the thiazoline and the 4-phenyl rings. Trp4 formed π – π stacking with these rings for a total of 76% of that time (**Figure 4-237C & E**), and this subsequently led to the decrease in the binding energy value from −40 to −62 kcal/mol during the last 70 ns. In comparison to the cocrystallized ligand, which exhibited an average MM-GBSA binding free energy of -37.04+/-4.22 kcal/mol, compound **4t** demonstrated a superior binding affinity to hCAXII (PDB: 6R6Y).

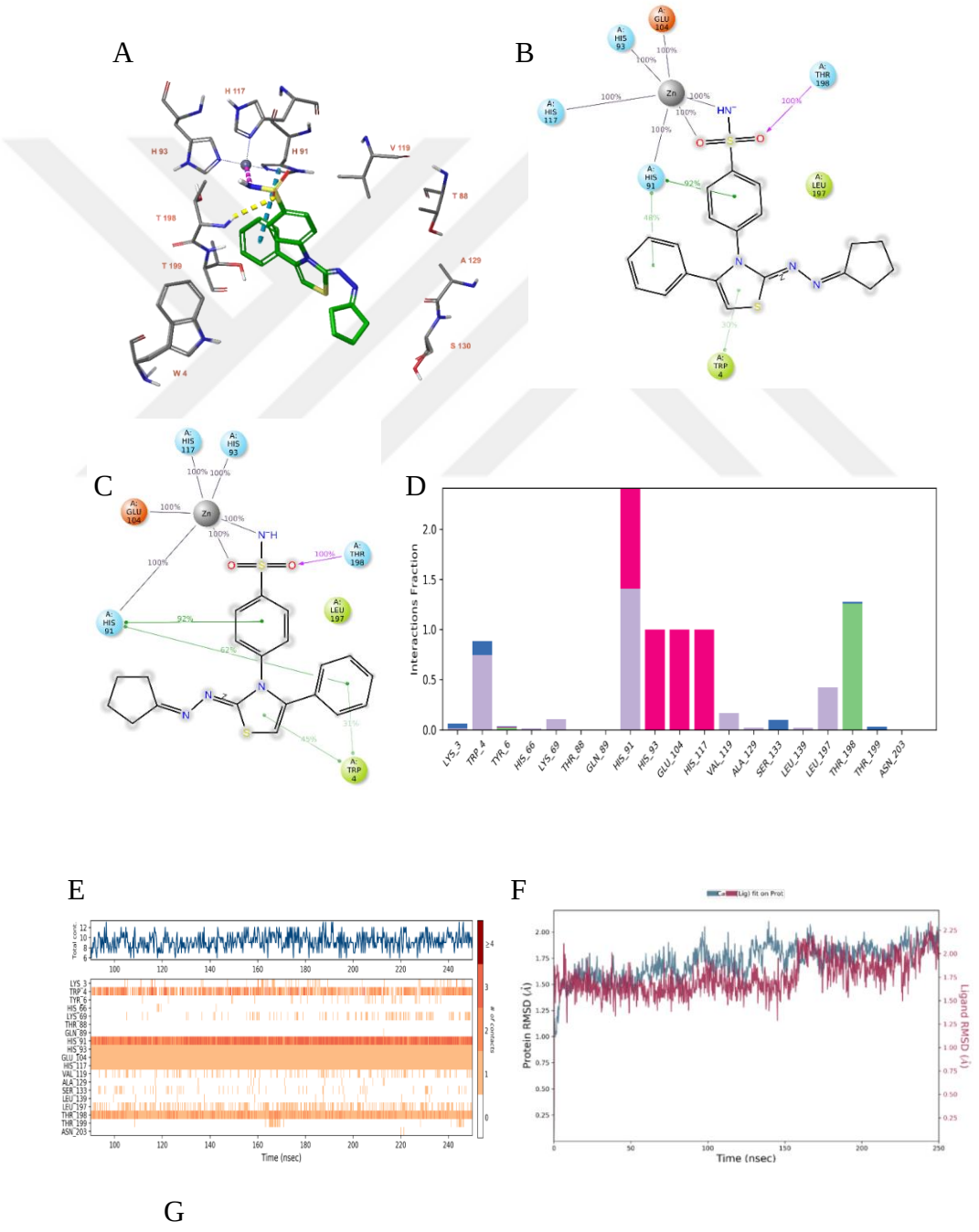

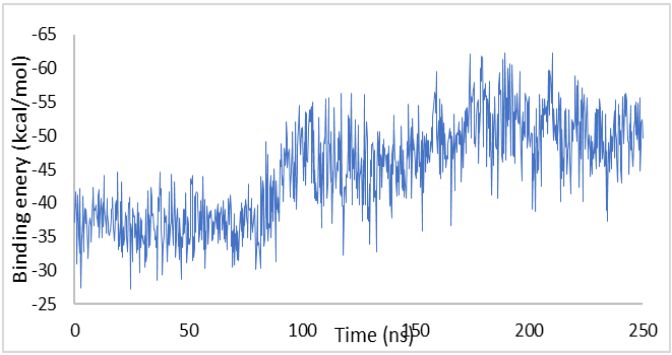

Figure 4-237: The docked pose of compound 4t (green) in the active site of hCAXII (6R6Y). The grey sphere represents the Zn^{2+}. Pink dashed lines represent metal coordination. Yellow dashed lines represent hydrogen bonds. Turquoise dashed lines represent π-π stacking. (B) Binding interactions observed for at least 30% of the 250 ns MD simulation. (C) Binding interactions observed for at least 30% of the last 50 ns of the MD simulation. Green represents hydrophobic amino acid (aa), blue represents polar aa, red represents negatively charged aa. (D) Histogram of protein-ligand contacts, with green indicating hydrogen bonds, blue indicating water-bridged hydrogen bonds, red indicating ionic bonds and grey indicating hydrophobic interactions. (E) A timeline representation of the interactions and contacts (180 – 250 ns). (F) RMSD plot of the protein Cα-atoms (blue) and ligand (red). (G) Protein-ligand interaction energy (kcal/mol) throughout the MD simulation.

4.6.11. Docked pose of compound 4u in hCAIX (PDB: 6TL5)

Contrary to the docked pose of **4t** in hCAIX (6TL5), compound **4u** had its 4-(4-bromophenyl) moiety facing the hydrophobic region and the 4-(2-(cyclopentylidenehydrazineylidene) moiety facing the hydrophilic region. As expected, the sulfonamide coordinated to Zn^{2+} and hydrogen bonded to the backbone of Thr199 (**Figure 4-238A**).

The interactions formed between the sulfonamide and Zn^{2+} and Thr199 were sustained throughout the simulation period. His94 formed a π – π stacking with 4-benzenesulfonamide which lasted for 73% of the simulation time. The 4-(4-bromophenyl) moiety was well tolerated in the hydrophobic region and formed hydrophobic interactions with Val121 and Val131. The hydrophobic interactions

between 4-benzenesulfonamide and Leu198 lasted for 70% of the simulation time (**Figure 4-238B & C**).

The RMSD value of the protein Cα-atoms fluctuated between the accepted range of 1 – 2 Å. The ligand RMSD value rapidly fluctuated between 1 – 4 Å due to large movements of the cyclopentane and 4-(4-bromophenyl) moieties (**Figure 4-238D & E**). The average MM-GBSA binding free energy of the 6TL5–**4u** complex during the 250 ns MD simulation was −44.27+/- 6.15 kcal/mol. The highest and lowest binding energies were −26.05 and −64.43 kcal/mol, respectively (**Figure 4-238F**). In comparison to the cocrystallized ligand, which exhibited an average MM-GBSA binding free energy of -31.52 +/- 5.02 kcal/mol, compound **4u** demonstrated a superior binding affinity to hCAIX (PDB: 6TL5).

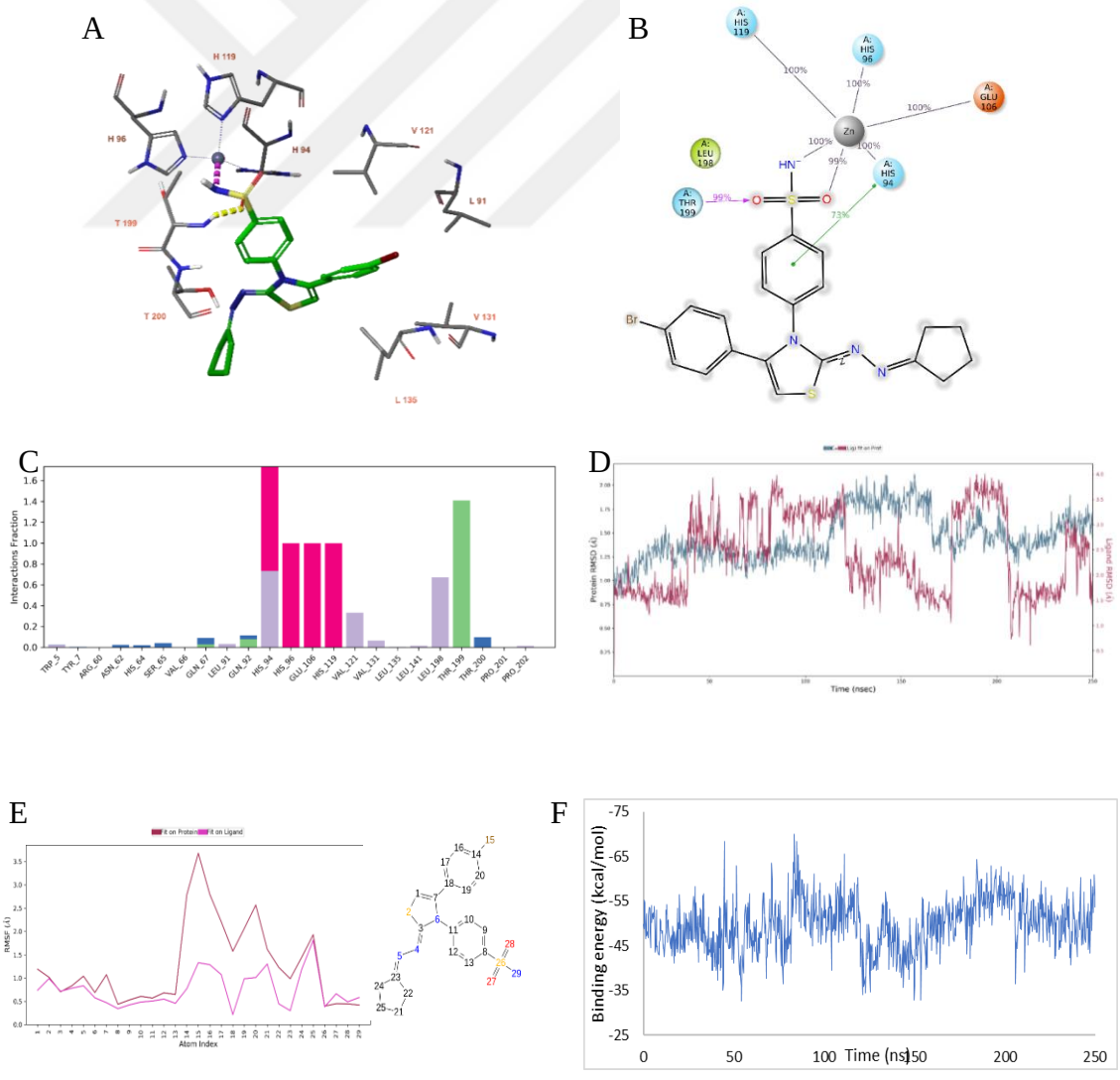

Figure 4-238: The docked pose of compound 4u (green) in the active site of hCAIX (6TL5). The grey sphere represents the Zn^{2+}. Pink dashed lines represent metal coordination. Yellow dashed lines represent hydrogen bonds. (B) Binding interactions observed for at least 30% of the 250 ns MD simulation. Green represents hydrophobic amino acid (aa), blue represents polar aa, red represents negatively charged aa. (C) Histogram of protein-ligand contacts, with green indicating hydrogen bonds, blue indicating water-bridged hydrogen bonds, red indicating ionic bonds and grey indicating hydrophobic interactions. (D) The Ligand Root Mean Square Fluctuation. (E) RMSD plot of the protein Cα-atoms (blue) and ligand (red). (F) Protein-ligand interaction energy (kcal/mol) throughout the MD simulation.

4.6.12. Docked pose of compound 4u in hCAXII (PDB: 6R6Y)

In the docked pose of compound **4u** in hCAXII (PDB: 6R6Y), the sulfonamide formed a coordination interaction with the Zn^{2+} ion and hydrogen bonds with the side chain and the backbone of Thr198. The bromine of 4-(4-bromophenyl) directed to the hydrophilic region formed a halogen bond with Tyr6, whereas 4-(2-(cyclopentylidenehydrazineylidene) moiety faced the hydrophobic region (**Figure 4-239A**).

The interactions formed between the sulfonamide and Zn^{2+} and Thr199 were sustained throughout the simulation period. His94 formed a π – π stacking with 4-benzenesulfonamide and 4-(4-bromophenyl) moieties which lasted for 90 and 54% of the simulation time, respectively. Lys69 formed cation – π interaction with 4-(4-bromophenyl) that lasted for 72% of the simulation time. The hydrophobic interactions between 4-benzenesulfonamide and Leu197 lasted for 40% of the simulation time (**Figure 4-239B & C**).

The average RMSD value of the protein Cα-atoms throughout the simulation is 1.75 Å, while the average RMSD value of the ligand was 2.4 Å (**Figure 4-239D**). The average MM-GBSA binding free energy of the 6R6Y–**4u** complex during the 250 ns MD simulation was −39.15+/- 6.24 kcal/mol. The highest and lowest binding energies were −20.40 and −55.81 kcal/mol, respectively (**Figure 4-239E**). In comparison to the cocrystallized ligand, which exhibited an average MM-GBSA binding free energy of -

37.04+/-4.22 kcal/mol, compound **4u** demonstrated a similar binding affinity to hCAXII (PDB: 6R6Y).

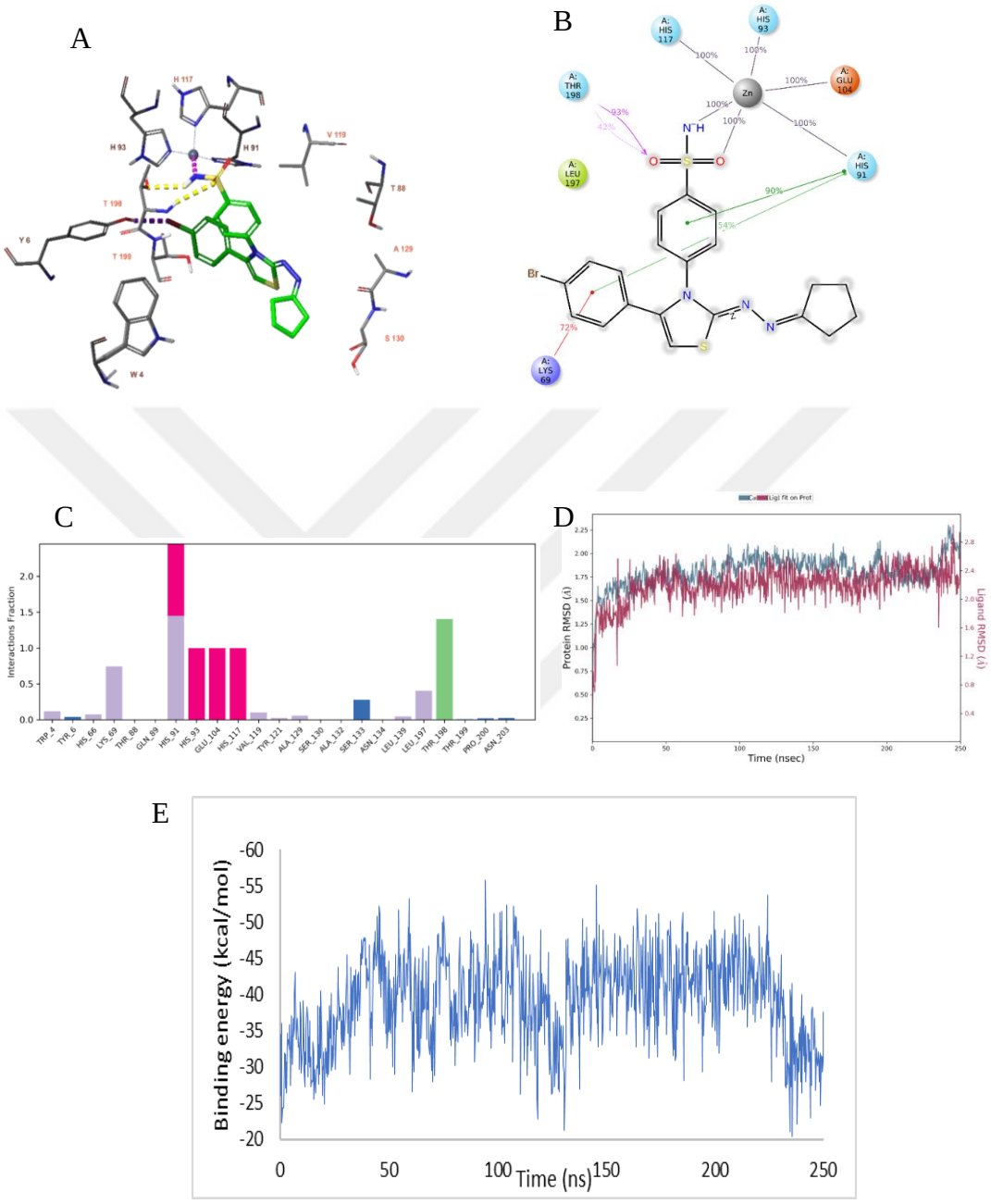

Figure 4-239: A) The docked pose of compound 4u (green) in the active site of hCAXII (6R6Y). The grey sphere represents the Zn^{2+}. Pink dashed lines represent metal coordination. Yellow dashed lines represent hydrogen bonds. Purple dashed lines represent halogen bond (B) Binding interactions observed for at least 30% of the 250 ns MD simulation. Green represents hydrophobic amino acid (aa), blue represents polar aa, red represents negatively charged aa. (C) Histogram of protein-ligand contacts, with green

indicating hydrogen bonds, blue indicating water-bridged hydrogen bonds, red indicating ionic bonds and grey indicating hydrophobic interactions. (D) RMSD plot of the protein Cα-atoms (blue) and ligand (red). (E) Protein-ligand interaction energy (kcal/mol) throughout the MD simulation.

5. DISCUSSION

5.1. Chemistry

Fifteen novel thiosemicarbazones and twenty-two 4-thiazoline-containing compounds were designed and synthesized. The starting compound for the synthesis was either 3-aminobenzenesulfonamide or 4-aminobenzenesulfonamide. Both compounds were obtained commercially. These compounds were converted to isothiocyanate derivatives (B) by treating them with thiophosgene in the presence of HCl in H_2O. In a facile reaction, the 3/4-isothiocyanatobenzenesulfonamides were treated with an equimolar amount of hydrazine monohydrate in ice to afford corresponding thiosemicarbazides (**C**).

The next reaction involves the treatment of the two **C** derivatives with various aldehydes or ketones (**D**) under reflux to obtain 13 novel thiosemicarbazones (**E**). All the aldehydes and ketones used were obtained commercially. Even though most of the reported methods in the literature include the use of acid catalysts such as sulfuric acid, pTSOH, and glacial acetic acid, the reactions proceeded smoothly without a catalyst.

The obtained **E** derivatives were eventually cyclocondensed under reflux with appropriate α-bromoacetophenone derivatives (**3**) to produce 22 novel benzenesulfonamide-containing 4-thiazoline derivatives (**4**) as depicted in the figure below. The **3** derivatives were obtained from commercial sources except for 2-bromo-1-(4-hydroxyphenyl)ethane-1-one (**3c**), which was used in the synthesis of final compounds, compounds **4h** and **4v**. Compound **3c** was prepared by refluxing 1-(4-hydroxyphenyl)ethan-1-one with $CuBr_2$ in ethylacetate to facilitate the bromination of the α-carbon. The progression of the reactions was monitored with TLC and by colour change. Purification of the compounds was done with recrystallization and preparative thin layer chromatography (TLC). The purity of the compounds was determined with TLC, elemental analysis and LC-MS. The structures of all the synthesized compounds were elucidated and confirmed with FT-IR, ^{1}H-NMR, ^{13}C-NMR, and LC-MS, and XRD analysis for compounds **E3, E10** and **4a.**

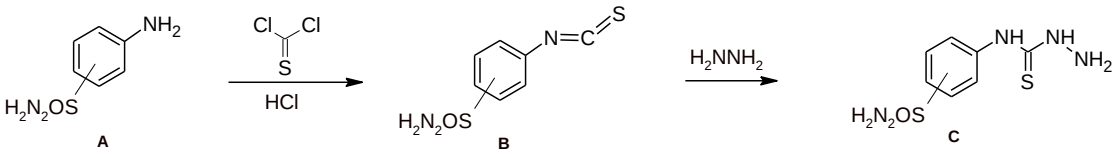

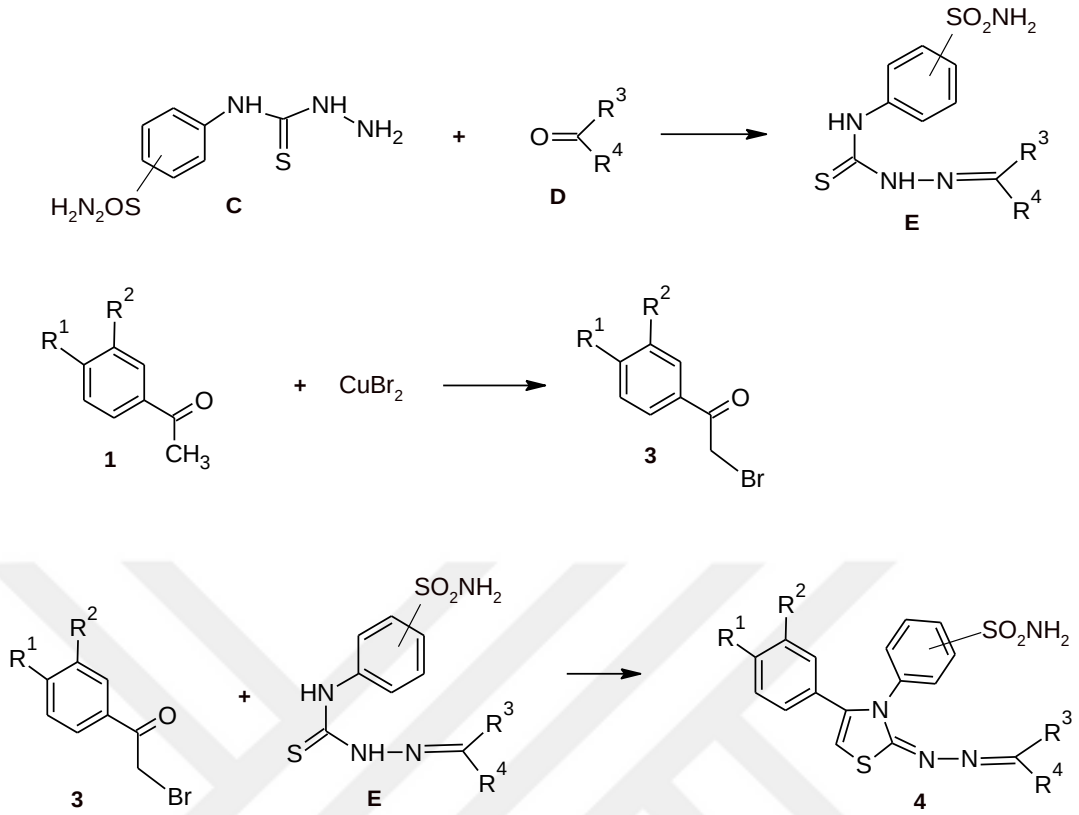

Scheme 5-1: Genera synthesis pathway of 3/4-[4-(Non)substitutedphenyl-2-(alkylidene/arylidenehydrazinylidene)-1,3-thiazol-3(2*H*)-yl]benzenesulfonamide derivatives (4a-4v) starting from 3/4-aminobenzenesulfonamide

5.1.1. 3/4-Isothiocyanatobenzenesulfonamide (B)

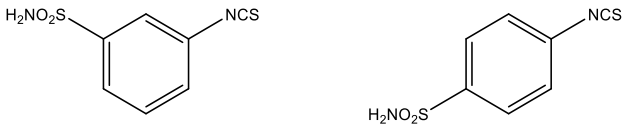

Amines or their salts readily react with thiophosgene to produce isothiocyanate. Contrary to phosgene and isocyanates, thiophosgene and isothiocyanates are stable in water, hence the reaction can proceed in an aqueous medium. An acid can be added to the amine to produce an aminium salt. This prevents the formation of symmetrical thiourea that can result from the reaction of the formed isothiocyanate with an excess of thiophosgene. The reaction proceeds smoothly and takes place in two steps: The formation of thiocarbamyl chloride and then the formation of the isothiocyanate (**Scheme 5-2**) (McKee and Bost 1946; Assony 1961; Callingham et al. 2015). Based on

this information, 3/4-aminobenzenesulfonamide was reacted with 25 mL of concentrated HCl in H_2O (100 mL) to form the anilinium salt which readily dissolves in water for sulfanilamide and not for 3-aminobenzenesulfonamide. While stirring, an equimolar amount of thiophosgene was added dropwise which turns the colour of the mixture to orange. Immediate precipitation occurs indicating the formation of isothiocyanate. The progress of the reaction was determined by TLC and the disappearance of the orange colour of thiophosgene. The precipitate was filtered, washed with plenty of water and dried to obtain 88.6 – 92.3% of the corresponding isothiocyanates.

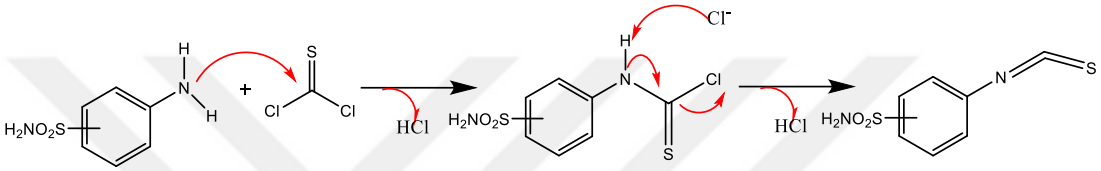

Scheme 5-2: Synthesis mechanism of 3/4-Isothiocyanatobenzenesulfonamide (B)

Table 5-1: Physical properties of 3/4-Isothiocyanatobenzenesulfonamide (B)

Compound	SO_2NH_2	Colour	Yield (%)	Reported Melting Point (ºC)	Observed Melting Point (ºC)
B1	Meta	White	88.6	128 – 130	131.3 – 132.0
B2	Para	White	92.3	212 – 214	212.7 – 213.0

IR Spectral Analysis

The formation of the isothiocyanate group was confirmed by IR analysis. The absorption band of N=C=S of 4-isothiocyanatobenzenesulfonamide was observed between 2194 and 2121 cm^{-1} as reported in the literature (Gauthier et al. 2006) and this is in correlation with observed bands for **B1** and **B2. Figures 5-1 – 3** reveal the disappearance of the aniline N-H stretch and the formation of a broad characteristic band of C=N=S at 2160 cm^{-1} with a shoulder at 2225 cm^{-1} for compound **B1** and at 2112 cm^{-1} with a shoulder at 2194 cm^{-1} for compound **B2.**

Table 5-2: IR data of 3/4-Isothiocyanatobenzenesulfonamide (B)

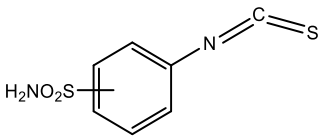

Compound	SO_2NH_2	N-H s.b.	Ar. C-H s.b.	N=C=S s.b.	Ar. C=C s.b. N-H b.b.	S=O s.b.	C-N s.b.	Ar. subs. C-H b.b..
B1	Meta	3356, 3253, 3111	3084	2225, 2160	1593, 1566, 1475	1330, 1147	1307	885, 800, 675 (meta)
B2	Para	3344, 3251, 3122	3089	2194, 2112	1581, 1485	1330,1149	1300	839 (para)

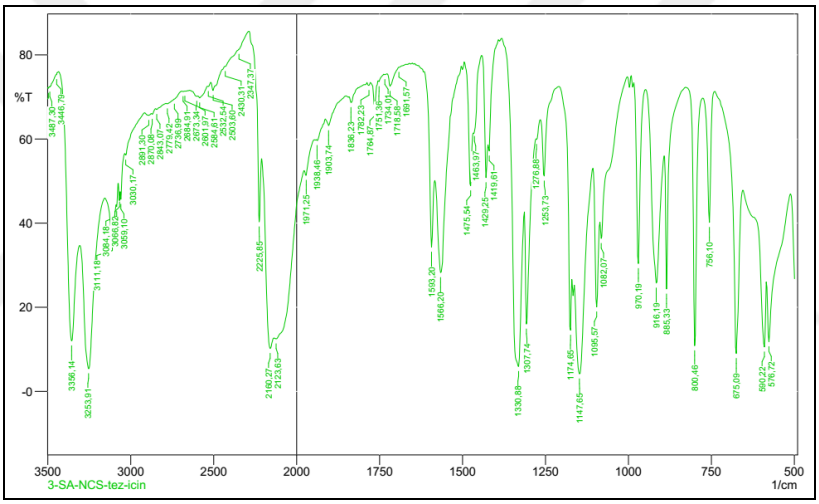

Figure 5-1: IR spectrum of compound B1

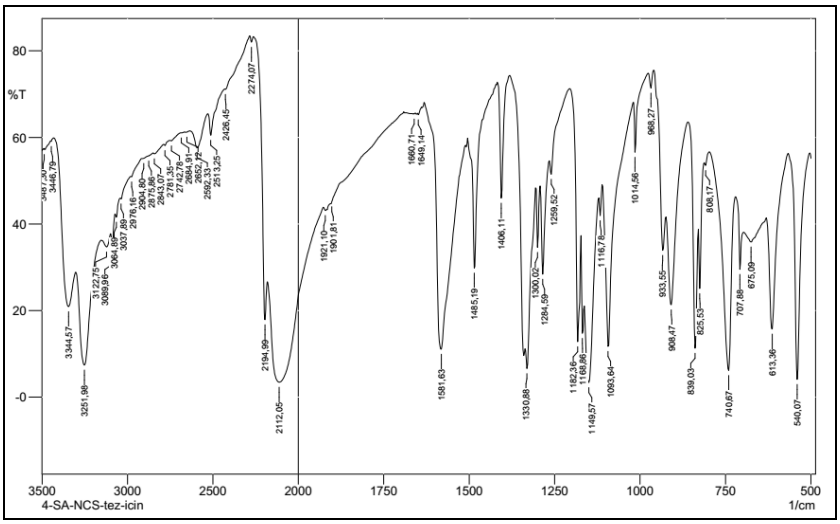

Figure 5-2: IR spectrum of compound B2

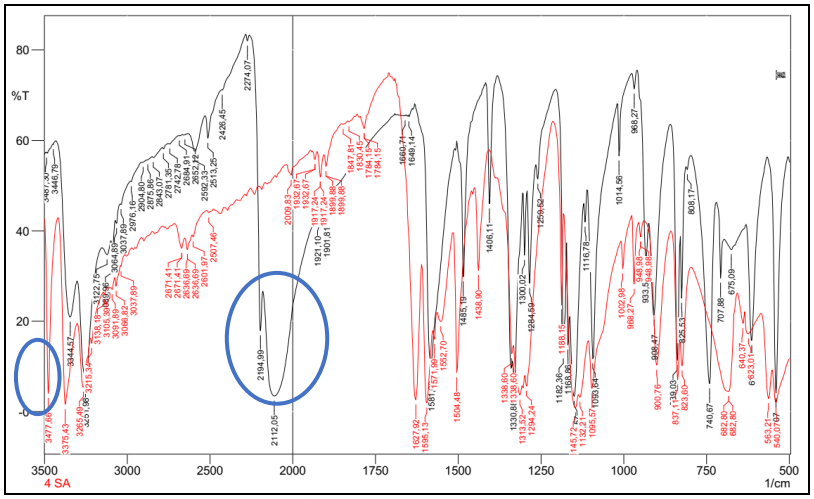

Figure 5-3: Comparative IR spectrum of compounds of A2 and B2. Red represents A2 and black represents B2.

5.1.2. *N*-(3/4-sulfamoylphenyl)hydrazinecarbothioamide (C)

Isothiocyanates are important precursors in the synthesis of nitrogen and sulfur-containing derivatives and their corresponding heterocycles due to the high electrophilicity and nucleophilicity associated with the carbon and sulfur atoms, respectively, and their continuous π electron system (El-Gaby et al. 2018). As previously mentioned, various methods have been employed in the preparation of thiosemicarbazide derivatives and one of the most facile reactions that produce high yields is the reaction of isothiocyanate derivatives with hydrazine monohydrate.

The synthesis of *N*-(3/4-sulfamoylphenyl)hydrazinecarbothioamide has been reported in previous literature (Karalı et al. 2017; Eraslan Elma 2017; Demir-Yazıcı et al. 2021). A cooled ethanolic solution of **C** derivatives is added dropwise to an equimolar amount of a cooled ethanolic solution of hydrazine monohydrate in an ice bath while vigorously stirring. The reaction is very fast and facile. The precipitate formed as soon as the addition of **C** ends is filtered out, washed with ethanol, dried and recrystallized from ethanol to give white crystals with a yield of 95 – 96 %.

The formation of thiosemicarbazides occurs via a nucleophilic addition as illustrated in **Scheme 5-3**. The withdrawal of electrons of the N from the C in the isothiocyanate group makes the carbon δ+ charged and an electrophilic centre, and the N δ- charged and a nucleophilic centre. The nucleophile hydrazine attacks the δ+

charged carbon of the isothiocyanate forming a new bond between the isothiocyanate carbon and the hydrazine nitrogen. Subsequently, the migration of a hydrazine proton to the nucleophilic nitrogen from the isothiocyanate leads to the formation of thiosemicarbazides (**Scheme 5-3**).

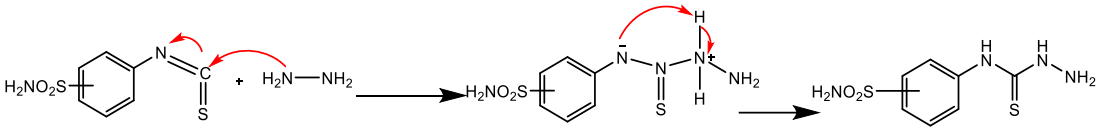

Scheme 5-3: Synthesis mechanism of *N*-(3/4-sulfamoylphenyl)hydrazinecarbothioamide (C)

Table 5-3: Physical properties of *N*-(3/4-sulfamoylphenyl)hydrazinecarbothioamide (C)

Compound	SO_2NH_2	Physical Appearance	Yield (%)	Reported Melting Point (ºC)	Observed Melting Point (ºC)
C1	Meta	Amber white powder	95	153 – 155	158.2 – 159.6
C2	Para	Amber white powder	96	212 – 214	213.4 – 214.5

IR Spectral Analysis

The disappearance of the isothiocyanate stretching band and the appearance of additional new NH stretching bands were clear manifestations of the formation of the thiosemicarbazide moiety. Another evidence of the formation of thiosemicarbazides is the formation of the C=S bond. The stretching bands of the C=S bond were observed at 1278 and 1286 cm^{-1}, for **C1** and **C2**, respectively (**Figure 5-4 & 5)**. The asymmetric and symmetric stretching bands for sulfonamide S=O were observed at 1305 and 1151 cm^{-1} for **C1** and 1136 and 1151 cm^{-1} for **C2** (**Table 5-4**). The IR values are in correlation with the reported values in the literature (Eraslan Elma 2017).

Table 5-4: IR data of *N*-(3/4-sulfamoylphenyl)hydrazinecarbothioamide (C)

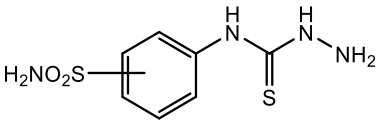

Compound	SO_2NH_2	N-H s.b.	Ar. C-H s.b.	Ar. C=C s.b. N-H b.b.	S=O s.b.	C=S s.b.	C-N s.b.	Ar. subs. C-H b.b.
C1	Meta	3323, 3303, 3255, 3223, 3159	-	1637, 1598, 1544, 1500, 1479	1336, 1151	1286	1301	896, 783, 690 (meta)
C2	Para	3363, 3321, 3264, 3211, 3203	3069, 3053	1633, 1597, 1585, 1556, 1500, 1471	1305 1151	1278	1305	841 (para

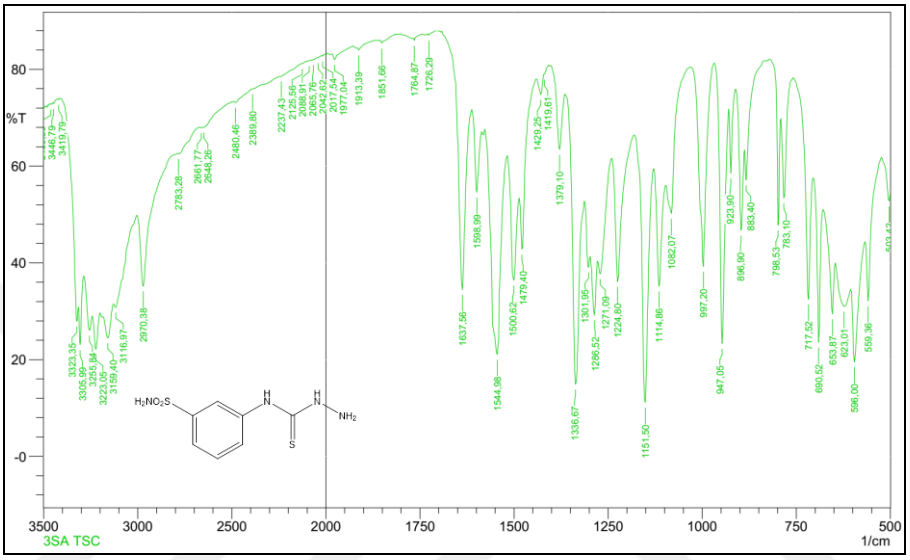

Figure 5-4: IR spectrum of compound C1

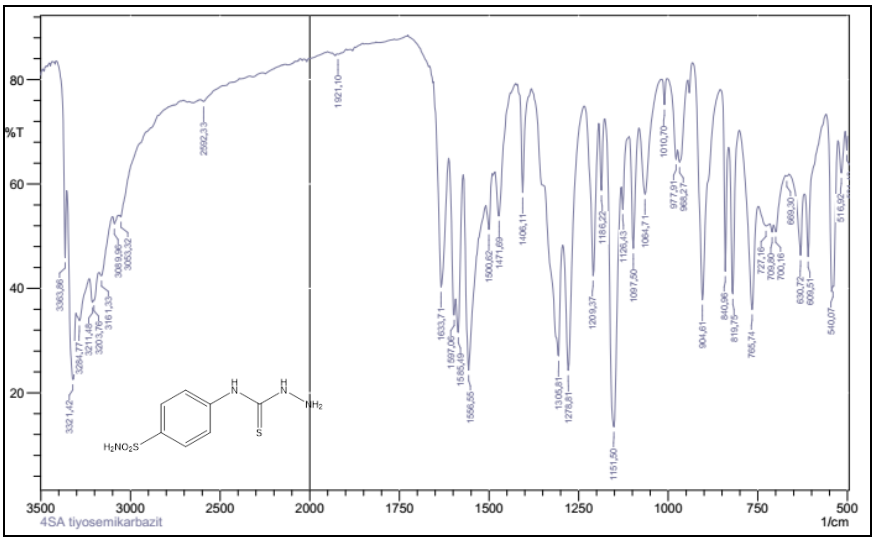

Figure 5-5: IR spectrum of compound C2

5.1.3. 2-(Alkylidene/arylidene)-*N*-(3/4-sulfamoylphenyl)hydrazine-1-carbothioamide derivatives (E)

TSC are generally prepared from the condensation of aldehydes or ketones with a thiosemicarbazide derivative in ethanol under reflux. Although this reaction may proceed without a catalyst (George et al. 2022), various studies have reported the use of different acid catalysts such as sulfuric acid, *p*-toluenesulfonic acid, glacial acetic acid and hydrochloric acid (Lima et al. 2002; Güzel et al. 2008; Karalı et al. 2017; Hałdys et al. 2020; Song et al. 2020; Shehzad et al. 2021; Gomha et al. 2021). These catalysts have reportedly improved the yield and shortened the reaction period in the synthesis of TSC.

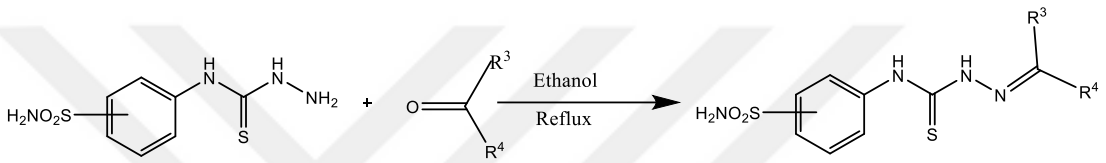

Scheme 5-4: Synthesis of 2-(Alkylidene/arylidene)-*N*-(3/4-sulfamoylphenyl)hydrazine-1-carbothioamide derivatives (E)

The TSC derivatives used in this thesis were synthesized in ethanol without a catalyst. The thiosemicarbazides (*N*-(3/4-sulfamoylphenyl)hydrazinecarbothioamide) were reacted with the equimolar molar amount of suitable aldehydes or ketones in ethanol under reflux to yield the TSCs (**Scheme 5-4**). The process of the reactions was monitored with TLC. The reaction times were between 4 – 6 hours with the aliphatic ketones having a shorter time than the aromatic aldehydes. The crude TSCs were recrystallized from ethanol. The yields were from good to excellent (48 – 92 %) with TSC having aromatic aldehyde adducts obtained in higher yields than the aliphatic ketones. The purity of the compounds was determined by TLC and elemental analysis. **Table 5-5** summarizes the physical properties of the TSC derivatives.

Table 5-5: Physical properties and elemental analysis data of 2-(Alkylidene/arylidene)-*N*-(3/4-sulfamoylphenyl)hydrazine-1-carbothioamide derivatives (E)

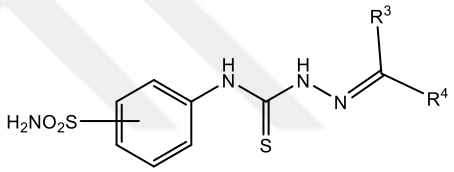

Compound	SO_2NH_2	R^3	R^4	Molecular Formula (Molecular Weight)	Colour	Yield (%)	Melting Point (°C)	Elemental Analysis (%) Calculated / Found			
								C	H	N	S
E1	meta	H	thiophene-2-yl-	$C_{12}H_{12}N_4O_2S_3$ (340.444)	Yellow	82	209.8-212.0	42.34 42.45	3.55 3.28	16.46 16.24	28.26 28.57
E2	meta	H	5-bromothiophene-2-yl	$C_{12}H_{11}BrN_4O_2S_3$ (419.340)	Greenish yellow	78	207.1-208.8	34.37 34.25	2.64 2.60	13.36 13.14	22.94 22.63
E3	meta	H	Pyrrole-2-yl	$C_{12}H_{13}N_5O_2S_2$ (323.393)	Green	80	215.9-216.5	44.57 44.32	4.05 3.85	21.66 21.43	19.83 19.58
E4	meta	H	1-methylpyrrole-2-yl	$C_{13}H_{15}N_5O_2S_2$ (337.420)	Yellow	91	201.3-202.4	46.27 46.07	4.48 4.28	20.76 20.52	19.01 18.78
E5	meta	H	Furan-2-yl	$C_{12}H_{12}N_4O_3S_2$ (324.378)	Yellow	63	201.6-202.5	44.43 44.28	3.73 3.65	17.27 16.92	19.77 19.47
E6	para	H	Pyrrole-2-yl	$C_{12}H_{13}N_5O_2S_2$ (323.393)	Green	82	228.5-229	44.57 44.36	4.05 3.82	21.66 21.34	19.83 19.48
E7	para	H	Furan-2-yl	$C_{12}H_{12}N_4O_3S_2$	Yellow	83	214.3-214.9	44.43	3.73	17.27	19.77

				(324.378)				44.14	3.38	16.96	19.43
E8	meta	CH_3	CH_3	$C_{10}H_{14}N_4O_2S_2$	White	82	184.9-187.1	41.94	4.93	19.56	22.39
				(286.373)				41.70	4.86	19.74	22.06
E9	meta	C_2H_5	C_2H_5	$C_{12}H_{18}N_4O_2S_2$	White	50	171.8-172.9	45.84	5.77	17.82	20.40
				(314.426)				45.58	5.75	17.74	20.12
E10	para	CH_3	CH_3	$C_{10}H_{14}N_4O_2S_2$	White	78	178,0-178.8	41.94	4.93	19.56	22.39
				(286.373)				41.84	4.97	19.41	22.25
E11	para	C_2H_5	C_2H_5	$C_{12}H_{18}N_4O_2S_2$	White	48	199.5-199.8	45.84	5.77	17.82	20.40
				(314.426)				45.65	5.82	17.56	20.04
E12	para	CH_3	C_3H_7	$C_{12}H_{18}N_4O_2S_2$	Amber white	49	186.6-187.1	45.84	5.77	17.82	20.40
				(314.426)				45.74	5.48	18.16	20.08
E13	para	cyclopentylidene		$C_{12}H_{16}N_4O_2S_2$	White	92	208.8-209.8	46.13	5.16	17.93	20.53
				(312.411)				46.38	5.45	17.62	20.31

The reaction of thiosemicarbazides with aldehydes or ketones is a facile Schiff base condensation. It proceeds via addition and elimination reactions (Liu et al. 2004). In the first step of the proposed reaction mechanism in **Scheme 5-5**, the basic nitrogen of thiosemicarbazide with lone pair of electrons acts as the nucleophile and attacks the δ+ charged carbonyl carbon of aldehyde/ketone. This results in the formation of a bond between the N_1 of thiosemicarbazide and the carbonyl carbon. This is followed by the transfer of the hydrogens on N_1 to the oxygen and subsequent dehydration to form the azomethine moiety (Chaaban et al. 2016; Eraslan Elma 2017; Shezi 2017).

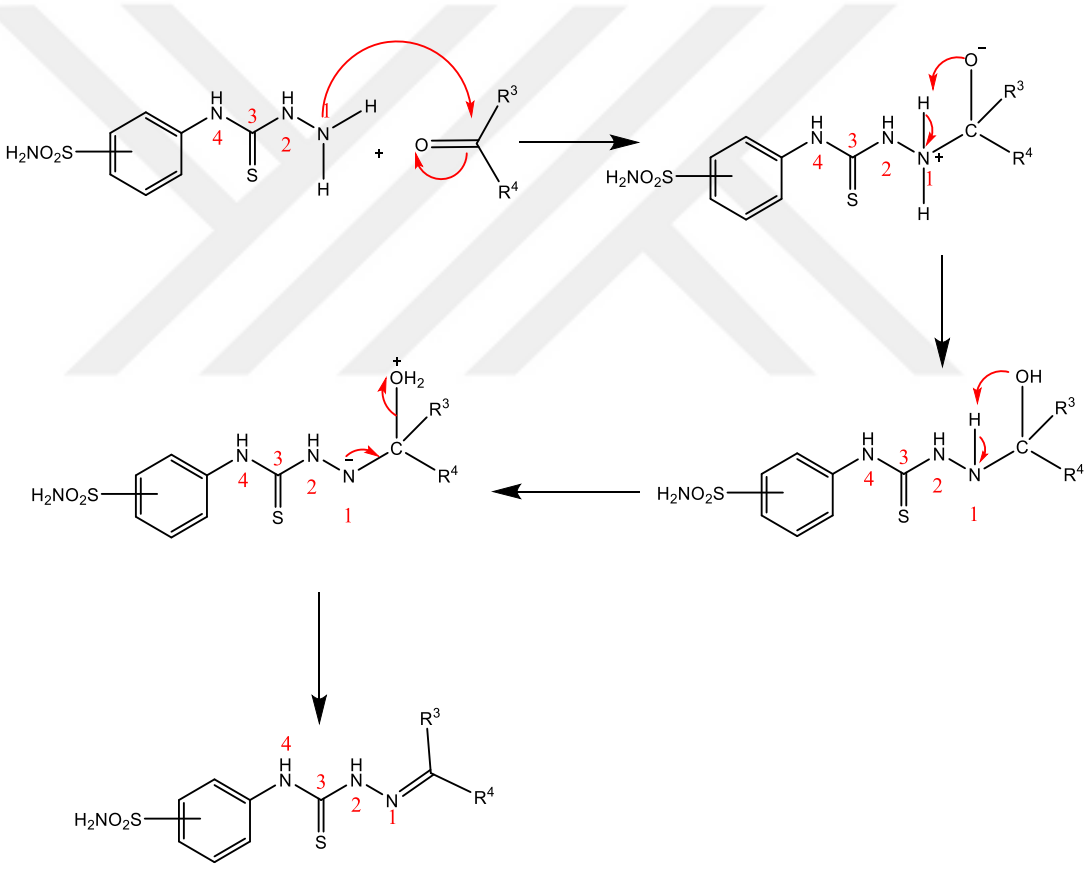

Scheme 5-5: Proposed synthesis mechanism of 2-(Alkylidene/arylidene)-*N*-(3/4-sulfamoylphenyl)hydrazine-1-carbothioamide derivatives (E)

5.1.3.1. IR Spectral Analysis

The characteristic IR bands for TSCs are the thiocarbonyl C=S, the thioamide NH, and the azomethine C= N stretching bands. The aromatic aldehydes and aliphatic

ketones generally have their carbonyl bands at 1740–1720 cm^{-1} and 1730–1700 cm^{-1}, respectively (Stuart 2004). These ketones and aldehydes used in the synthesis of TSC derivatives have their C=O stretching bands observed at 1674, 1668, 1667, 1664, 1674, 1715, 1716, 1717 and 1747 cm^{-1} for thiophene-2-carbaldehyde, 5-bromothiophene-2-carbaldehyde, pyrrole-2-carbaldehyde, 1-methylpyrrole-2-carbaldehyde, furan-2-carbaldehyde, acetone, 3-pentanone, 2-pentanone and cyclopentanone, respectively (**Figure 5-6**) (SDBS 4170, 6336, 1187, 22384, 1309, 319, 529, 2673, 7939).

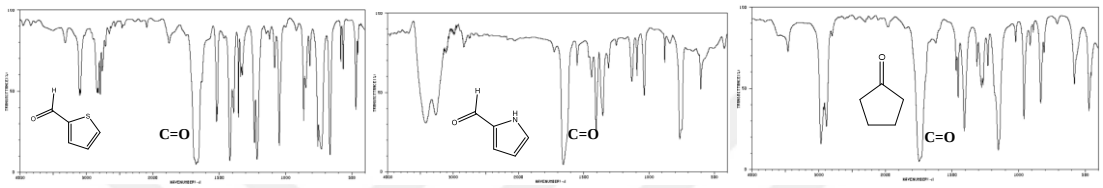

Figure 5-6: IR spectra of D1, D3 and D9 obtained from SDBS

The disappearance of the carbonyl peaks and the appearance of the azomethine peaks which are observed together with aromatic C=C stretching and N-H bending vibrations in the region 1651- 1477 cm^{-1} support the formation of the TSCs (D. M. Wiles et al.). The N-H stretching vibrations were observed between 3377 – 3134 cm^{-1}. The aromatic C-H stretching vibrations were observed between 3097 – 3001 cm^{-1}. The asymmetric and symmetric stretching vibrations of S=O were observed between 1340 – 1311 cm^{-1} and 1166 – 1149 cm^{-1}, respectively. TSC The spectral values are in line with the reported values in various literature (**Table 5-6**).

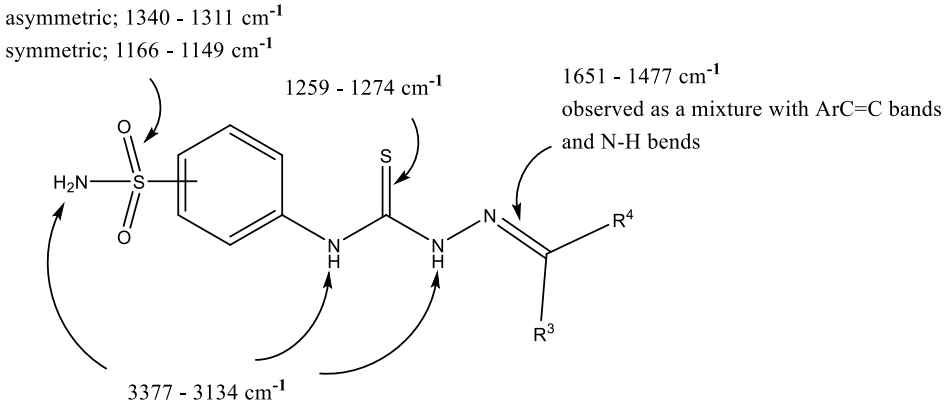

In most cases, C=N and C=C stretching vibrations are mostly coupled near 1600 cm^{-1} (Pavia et al. 2015), however, Jyothi and Farrok synthesized 2,3,4-trihydroxybenzaldehyde-4-phenylthiosemicarbazone and ascribed the highest peak in that region to C=N. They have observed C=N stretching vibrations at 1609 cm^{-1}. As previously mentioned, TSCs may undergo thione-thiol tautomerism. The observation of the C=S band between 1259 – 1274 cm^{-1} with no S-H-related intense peak between 2500 - 2800 cm^{-1} was an indication that the obtained TSCs were in their thione forms (George et al. 2022). Although the assignment of the stretching vibrations for C=S has always been controversial (D. M. Wiles and T. Suprunchuk), Jyothi and Farrok have observed the stretching vibrations for N-H and C=S of the thioamide moiety at 3400 and 1255 cm^{-1}, respectively (Jyothi and Farook 2019).

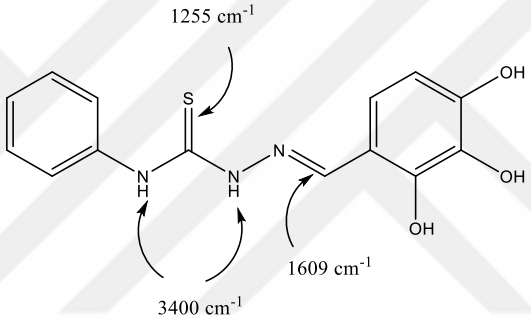

Khalaji et. al also ascribed the highest peak in that region to C=N in two of their papers describing the theoretical and spectral properties of various thiosemicarbazones. They have observed the C=N stretching vibrations for 2-(2,4-dimethoxybenzylidene)thiosemicarbazone, 2-(2,5-dimethoxybenzylidene)thiosemicarbazone, and 2-(4-isopropylbenzylidene)thiosemicarbazone at 1613, 1610 and 1590 cm^{-1}, respectively. The group also observed the stretching vibrations for N-H and C=S of the thioamide moiety between 3443 - 3139 cm^{-1} and 1230 - 1210 cm^{-1}, respectively (Khalaji et al. 2010; Khalaji et al. 2013).

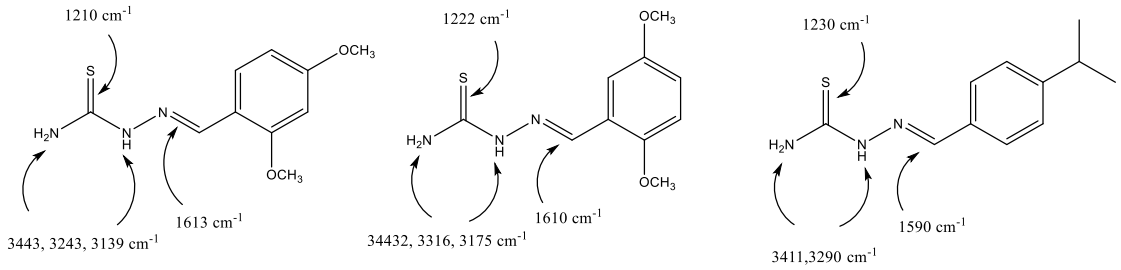

Moreover, 2-(2,4-dihydroxybenzylidene)thiosemicarbazone and 2-[(1*H*-indol-3-yl)methylene]thiosemicarbazone were synthesized and characterized by Yıldız and coworkers. The group observed NH, ArC-H, C=N, C=C, and C=S stretching vibrations at 3477 – 3175, 3042 – 3055, 1632 – 1611, 1576- 1556 and 1251 - 1239 cm^{-1}, respectively (Yıldız et al. 2009).

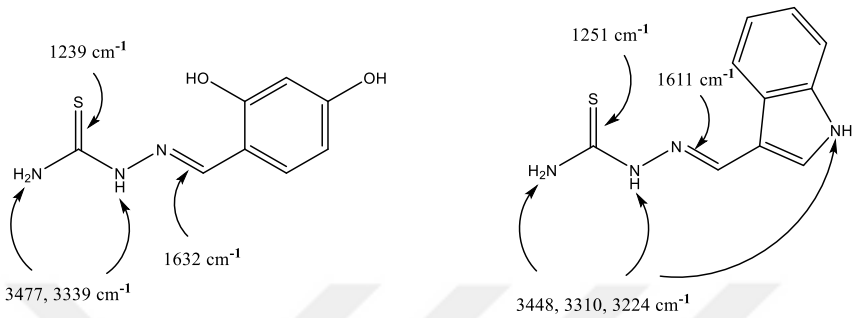

In the IR analysis of isatin-benzenesulfonamide hybrids containing TSC synthesized by Karalı et. al, while the stretching vibrations of N-H of the thioamide and SO_2NH_2 were observed between 3394 - 3115, the asymmetric and symmetric stretching vibrations for S=O were observed between 1343 – 1311 and 1161 – 1138 cm^{-1}, the C=S stretching vibrations were observed between 1224 – 1204 cm^{-1} (Karalı et al. 2017).

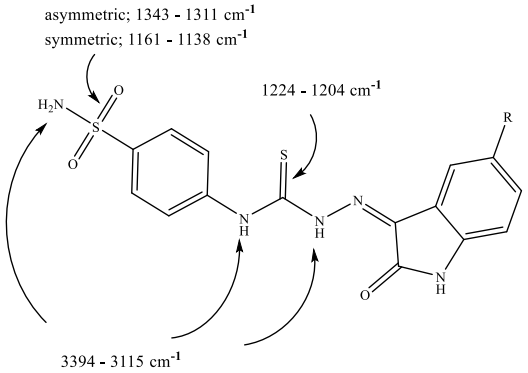

Table 5-6: IR data of 2-(Alkylidene/arylidene)-*N*-(3/4-sulfamoylphenyl)hydrazine-1-carbothioamide derivatives (E1 – E13)

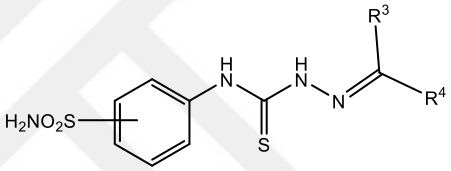

Compound	SO_2NH_2	R^3	R^4	N-H s.b.	Ar. C-H s.b. and =CH s.b	Al. C-H s.b.	Ar. C=C s.b, C=N s.b and N-H b.b	Al. C-H b.b.	S=O s.b.	C-N s.b.	C=S g.b.	Ar. subs. C-H b.b.	Others
E1	meta	H	thiophene-2-yl-	3360, 3334, 3250	3140, 3057, 3016,	--	1593, 1585, 1550, 1519, 1498	--	1330 1151	1300	1271	879, 740, 702 (meta)	
E2	meta	H	5-bromothiophene-2-yl	3334, 3307, 3273, 3255,	3155, 3076, 3022	--	1587, 1548, 1518, 1504, 1485	--	1336, 1155	1307	1265	881, 754, 704 (meta)	1080 (Ar-Br)
E3	meta	H	Pyrrole-2-yl	3375, 3294, 3255,	3124, 3088, 3055, 3005	--	1614, 1585, 1556, 1533, 1489	--	1311 1149	1300	1263	883, 748, 690 (meta)	
E4	meta	H	1-methylpyrrole-2-yl	3313, 3211	3155, 3037, 3001	2933	1616, 1585, 1552, 1527, 1510, 1485	1425, 1364	1336 1166	1303	1273	889, 773, 723 (meta)	
E5	meta	H	Furan-2-yl	3367, 3292, 3271	3147, 3045, 2976	--	1625, 1564, 1541, 1508	--	1340 1149	1288	1269	871, 758, 725 (meta)	
E6	para	H	Pyrrole-2-yl	3377, 3284, 3149, 3134	3037, 2991	--	1610, 1585, 1537, 1506	--	1328 1151	1303	1273	839 (para)	
E7	para	H	Furan-2-yl	3410, 3251, 3205	3140, 3047, 2997	--	1618, 1583, 1556, 1537, 1510	--	1334 1153	1307	1271	842 (para)	
E8	meta	CH_3	CH_3	3327, 3292	3136, 3035	2916	1651, 1600, 1585, 1519, 1483	1435, 1359	1321, 1151	1305	1259	908, 786, 702 (meta)	1820, 1751, 1705 (overtones)
E9	meta	C_2H_5	C_2H_5	3344, 3275, 3248	3089, 3062, 3045	2974, 2935, 2887, 2831	1598, 1587, 1487	1463, 1379	1321, 1163	1307	1263	900, 761, 702 (meta)	
E10	para	CH_3	CH_3	3344, 3238, 3209	3084	2960, 2931	1587, 1541, 1487	1444, 1384	1334, 1153	1307	1273	844 (para)	
E11	para	C_2H_5	C_2H_5	3290, 3246	3097	2966, 2929, 2889	1589, 1548, 1531, 1494	1433	1321 1161		1274	833 (para)	
E12	para	CH_3	C_3H_7	3360, 3240	3196, 3078	2958,	1585, 1525, 1487	1406,	1323,	1301	1261	833 (para)	

						2931, 2872, 2812		1369	1157				
E13	para	cyclopentylidene		3331, 3296, 3253	3183, 3097	2965, 2945, 2877	1585,1533, 1477	1404, 1365	1332, 1151	1303	1267	835 (para)	1649 (overtone)

5.1.3.2. ^{1}H-NMR Spectral Analysis

The ^{1}H NMR spectra of the intermediate TSC derivatives (**E1 – E13**) were recorded using TMS as the reference and DMSO-d6 as the solvent. The results are summarized in **Table 5-7**. The characteristic peaks of TSC derivatives are N_2-H (NH-N=C) and N_4-H (NHC=S) protons. These two protons are generally observed as two isolated signals since they are affected by different chemical environments. As previously established with IR studies, the presence of thione form of the TSCs is further supported by ^{1}H NMR analyses of the compounds. Thiols show variable chemical shifts between δ 1 – 4 ppm (Pavia et al. 2015). The absence of a single sharp peak related to the SH proton at around δ 3.9 ppm as assigned by Patil et al. or at δ 1.6 ppm as assigned by Suni et al. indicates the presence of the thione form of the TSCs. (Suni et al. 2006; Patil et al. 2010). In the spectra of the intermediate TSC derivatives (**E1 – E13**), while the N_2**H**-N=C protons were observed between δ 9.95 – 12.01 ppm, the N_4**H**C=S protons were observed between δ 9.48 – 10.45 ppm. This is because N_2**H**-N=C is adjacent to the imine group which causes a greater deshielding of the proton compared to the N_4**H**C=S which is adjacent to the phenyl group. In addition, N_2**H**-N=C were more downfielded than the pyrrole N_1-H in **E3** and **E8**. Comparing the chemical shifts of N_2**H**-N=C protons in TSCs with aromatic adducts (from aromatic aldehydes) (**E1 – E7**) with those containing the aliphatic adducts (from aliphatic ketones) (**E8 – E13**), it is observed that the electron-donating effect of the aliphatic groups have caused shielding of the N_2**H**-N=C protons and thus caused a more upfield shift. The aromatic rings possibly induced electron withdrawal causing a more downfield shift.

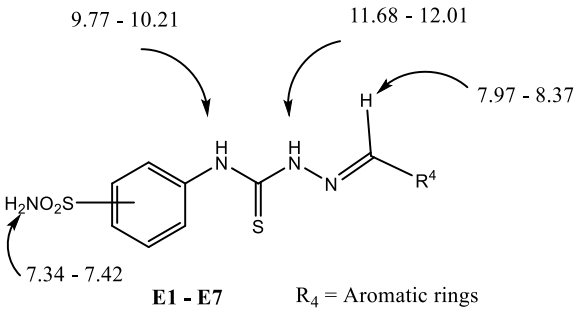

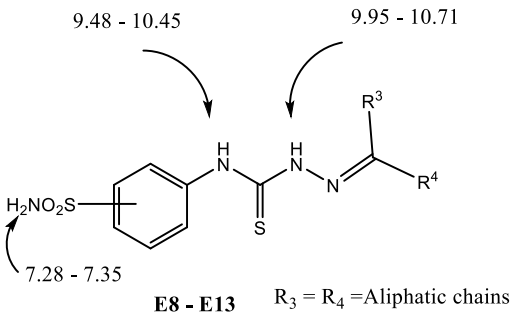

Güzel at al. analysed the ^{1}H NMR of 25 isatin-containing TSC compounds as assigned the single peaks observed between δ 12.27–12.91 ppm to N_2**H**-N=C and δ 8.93–11.17 ppm to N_4**H**C=S (Güzel et al. 2008). Soylu-Eter et al. characterized the structure of (*Z*)-*N*-(4-methoxyphenyl)-2-(1-methyl-2-oxo-5-(trifluoromethoxy)indolin-3-ylidene)hydrazine-1-carbothioamide and reported similar findings (Soylu Eter et al. 2021).

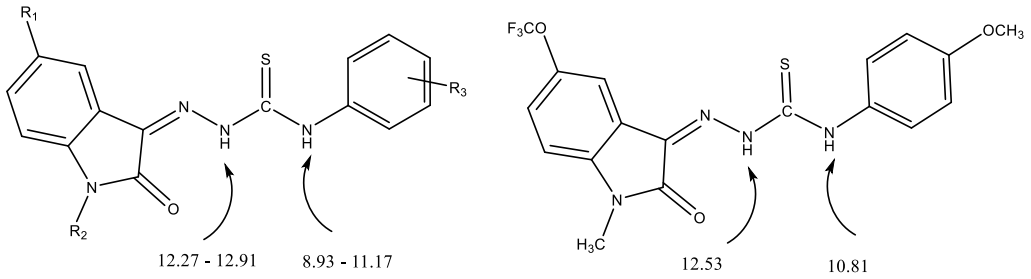

The signals related to CH=N protons in **E1 – E7** were observed between δ 7.97 – 8.37 ppm. The absence of these peaks in **E8 – E13** is an indication of the right assignment of CH=N protons. The C**H**=N, N_4**H**C=S and N_2**H**-N=C protons for several diverse TSC-containing molecules synthesized by Hussein et al. were observed between δ 8.37 – 8.73 ppm, δ 8.81 – 9.18 ppm and δ 11.40 – 11.77 ppm, respectively. (Hussein et al. 2019). Taşdemir et al. have also synthesized and characterized a series of chiral TSC derivatives. In the ^{1}H NMR spectra of the compounds, the C**H**=N, N_4**H**C=S and N_2**H**-N=C protons were observed at δ 7.98 – 8.19 ppm, δ 8.33 – 8.89 ppm and δ 11.27 – 11.87 ppm, respectively (Taşdemir et al. 2015).

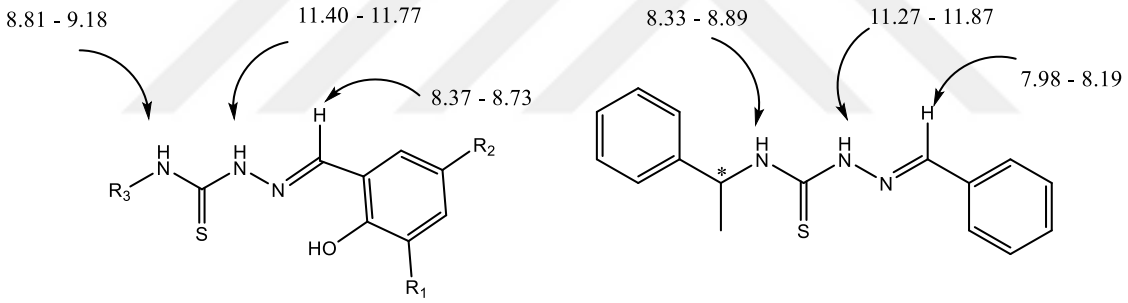

In the ^{1}H NMR spectrum of thiophene-2-carbaldehyde C_3-H, C_4-H, and C_5-H are δ, 8.03, 7.94 and 8.13 ppm, respectively. The electron-withdrawing effect of the sulfur atom deshielded the C_5-H and caused the highest downfield shift compared to the others. The C_1-CHO adjacent to C_3-H causes the downfield shift lesser than the sulfur (SDBS 4170). In the^{1}H NMR spectrum of pyrrole-2-carbaldehyde, the chemical shifts for N_1-H, C_3-H, C_4-H, and C_5-H are δ 11.41, 7.02, 6.31, and 7.23 ppm, respectively (SDBS 1187). The electron-withdrawing effect of the adjacent nitrogen deshielded the C_5-H causing the highest downfield shift. The C_1-CHO adjacent to C_3-H causes the downfield shift of the proton. The C_4-H which is more distant from both the nitrogen and C_1-CHO is the most shielded. The C_3-H, C_4-H, and C_5-H protons of furan-2-carbaldehyde, resonated at δ 7.30, 6.63 and 7.73 ppm, respectively (SDBS 1309).

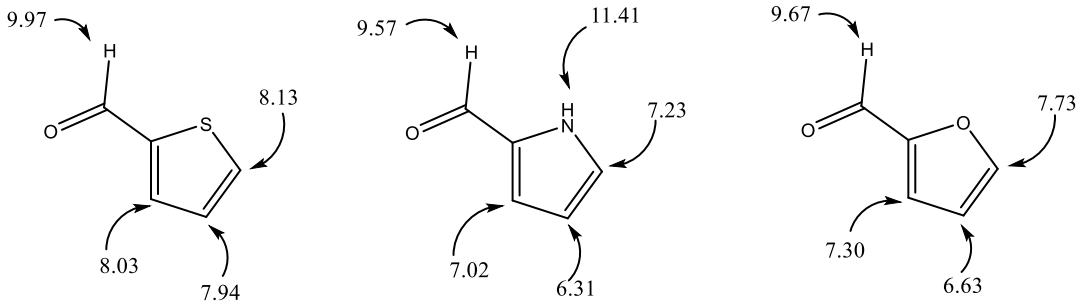

Besides, İyidoğan et al. characterized the structure of *N*-phenyl-2-(thiophen-2-ylmethylene)hydrazine-1-carbothioamide and found that the thiophene protons resonated at δ 7.54 ppm (d, *J*=3.29 Hz), δ 7.15 ppm (dd, *J*=3.73, 4.87 Hz) and δ 7.70 ppm (d, *J*=4.99 Hz) for C_3-H, C_4-H, and C_5-H, respectively (Karaküçük-İyidoğan et al. 2011). In another study, İyidoğan et al. characterized *N*-cyclohexyl-2-(furan-2-ylmethylene)hydrazine-1-carbothioamide and ascribed signal resonated at δ 6.96 ppm (d, *J*=3.40 Hz), δ 6.62 ppm (dd, *J*=3.39) and δ 7.70 ppm (d, *J*=3.52 Hz) for C_3-H, C_4-H, and C_5-H, respectively (İyidoğan et al. 2020).

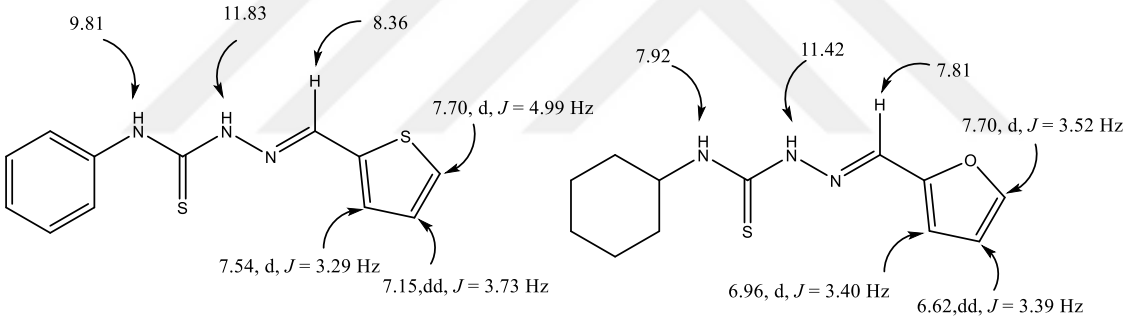

The ^{1}H NMR findings of TSC **E1 – E7** corroborate the aforementioned data. The thiophene C_3-H of **E-1** resonated between δ 7.50 – 7.58 ppm as a mixture with 3-sulfamoylphenyl C_5-H. The C_4-H observed as a doublet of a doublet at δ 7.15 (*J* = 3.7, 3.6 Hz) ppm is evidence of a thiophene proton located between two methine protons. The C_5-H was observed as a doublet at δ 7.71 (*J* = 5.0 Hz) ppm. The N_1-H, C_3-H, C_4-H, and C_5-H protons of the **E-3** pyrrole ring were observed as a singlet at δ 11.50 ppm, a multiplet at δ 6.50 – 6.51 ppm, a doublet-doublet at δ 6.16 (*J* = 3.5, 1.6 Hz) ppm, and a multiplet at δ 7.87 ppm, respectively. Similarly, the C_3-H, C_4-H, and C_5-H protons of the **E-7** furan ring were observed as a doublet at δ 7.09 (*J* = 3.5 Hz) ppm, a doublet-doublet at δ 6.67 (*J* = 4.3, 1.8 Hz) ppm, a doublet at δ 7.87 (*J* = 1.2 Hz) ppm, respectively. In addition, the absence of aldehyde protons supports the successful formation of TSCs.

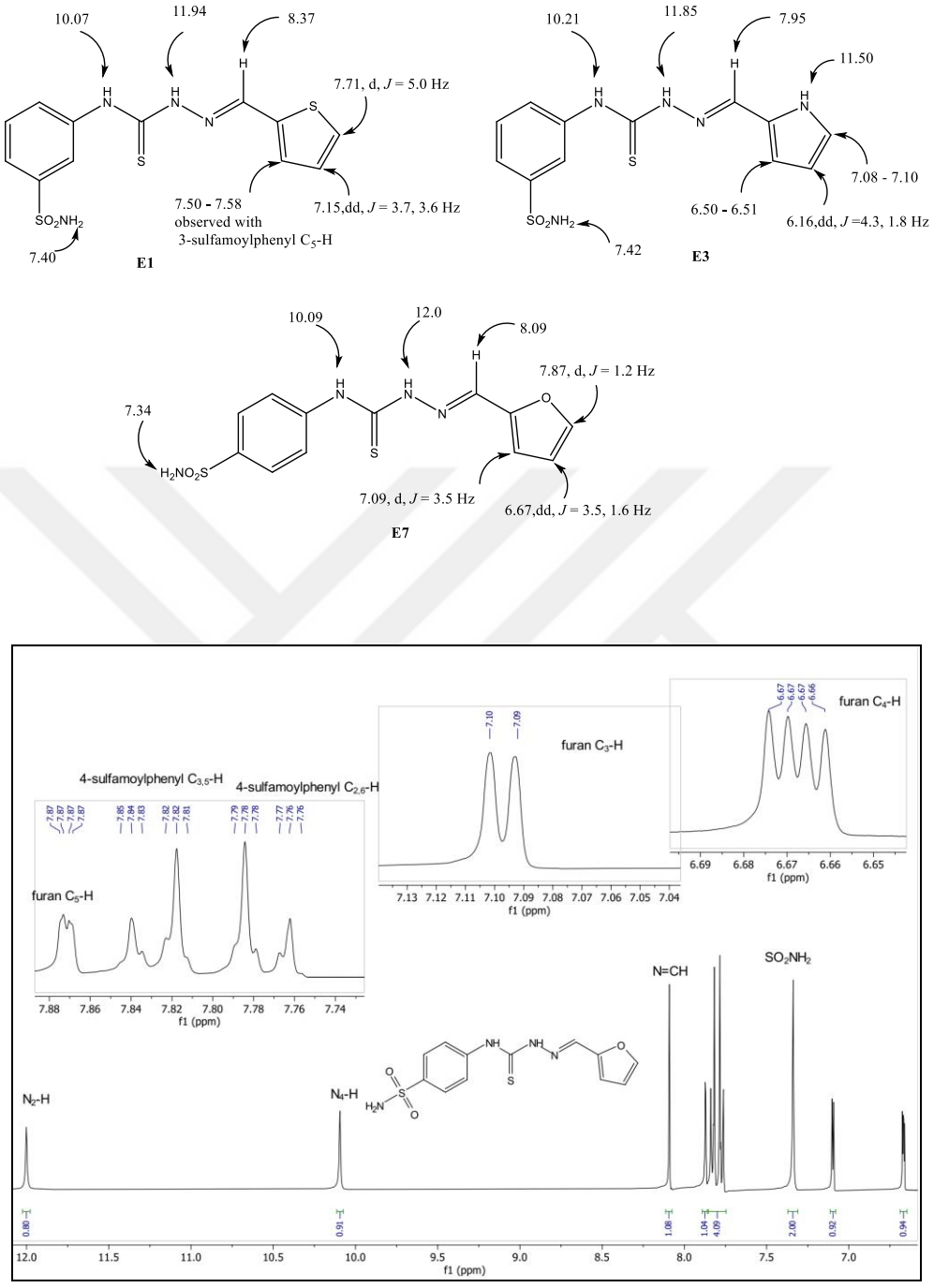

Figure 5-7: ^{1}H NMR Spectrum of compound E7.

Aliphatic methyl and methylene protons are generally observed between δ 0.7–1.3 ppm and δ 1.2–1.4 ppm, respectively. However, in TSC **E8 – E13**, the -CH_3 and -CH_2- are adjacent to C=N and the inductive electron-withdrawing effect and the anisotropic deshielding caused by the π electrons of C=N caused a downfield shift. The protons of -CH_3

and -CH_2- adjacent to C=N were observed between δ 1.94 – 2.00 ppm and δ 2.34 – 2.56 ppm, respectively. The effect of C=N decreases as the C-H gets more distant from it.

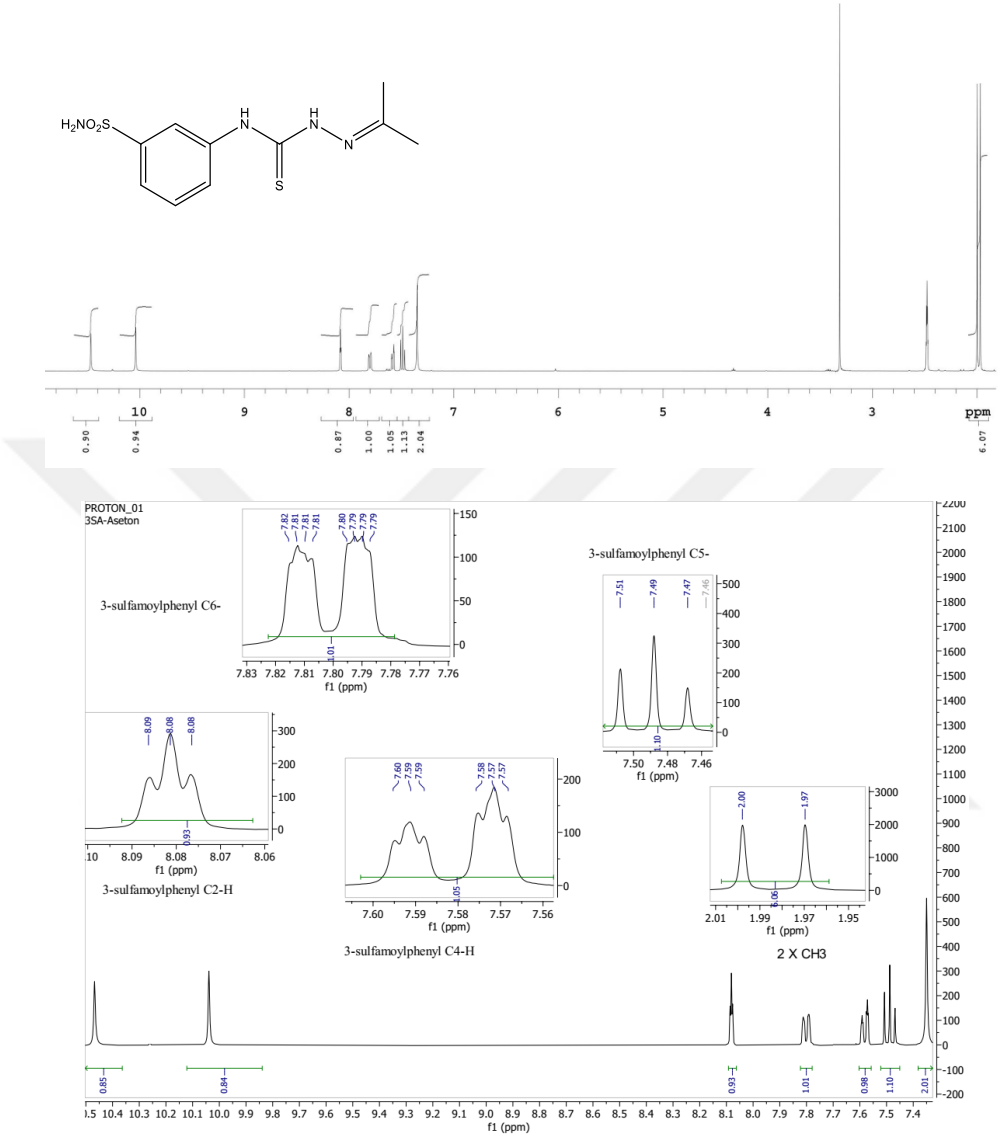

Figure 5-8: ^{1}H NMR Spectrum of compound E8.

The ^{1}H NMR findings of isatin-benzenesulfonamide hybrids containing TSC synthesized and characterized by Karalı et al. and Eraslan Elma also revealed that the N_4**H**C=S protons were resonated between δ 10.93 – 11.22 and δ 12.65 – 12.92 ppm whereas the N_2**H**-N=C protons were resonated between δ 10.98 – 11.49 and δ 12.56 – 13.07 ppm, respectively. In addition, SO_2NH_2 protons were observed between δ 7.36 – 7.60 and δ 7.43 – 7.71 ppm (Karalı et al. 2017; Eraslan Elma 2017).

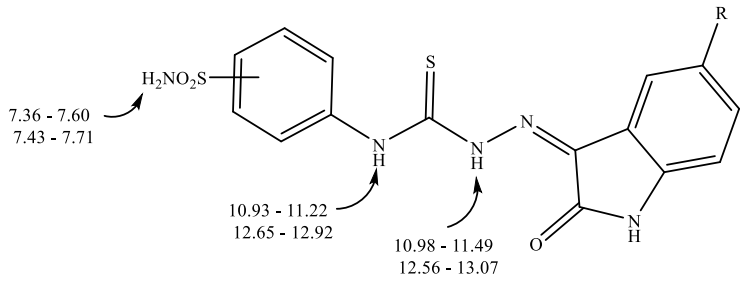

SO_2NH_2 has both inductive and mesomeric electron-withdrawing effects which cause the deshielding of aromatic protons, particularly the *ortho* protons. The thioamide of the TSC group also reduces the electron density and thus causes the deshielding of aromatic protons. Eraslan Elma has studied the effect of the sulfonamide and thiosemicarbazide groups on the chemical shifts of benzene aromatic protons present in *N*-(3-sulfamoylphenyl)hydrazinecarbothioamide (**C1**) and concluded that the SO_2NH_2 caused a downfield shift on *ortho*, *para* and *meta* protons by δ 0.58, 0.31, 0.31 ppm, respectively. While the thiosemicarbazide caused a downfield shift on *ortho* and *para* protons by δ 0.38 and 0.03 ppm, respectively, it caused an upfield shift on *meta* protons by δ 0.17 ppm. The C_2-H, C_4-H, C_5-H and C_6-H protons were observed at 8.17 (s), 7.52 (d, J = 7.1 Hz), 7.45 (dd, J = 7.8; 7.8 Hz) and 7.82 ppm (d, J = 6.8 Hz), respectively (Eraslan Elma 2017). Based on this

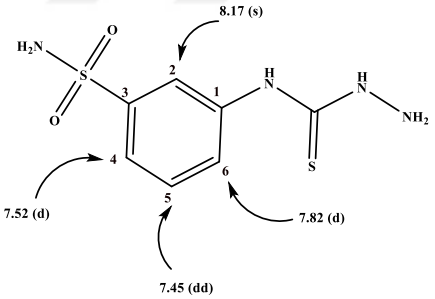

information, the protons of sulfamolyphenyl moiety of compounds **E1 – E13** were assigned. In the ^{1}H NMR spectra of compounds **E1 – E5**, **E8**, and **E9**, the C_2-H proton located in an *ortho* position to both SO_2NH_2 and thiosemicarbazide is the most deshielded proton and was observed between δ 8.03 – 8.27 ppm as a triplet (J = 1.9 – 2.0 Hz). This shows that the protons *meta*-couple with $C_{4/6}$-H. The C_4-H protons resonated between δ 7.58 – 7.65 ppm as doublet of triplets (dt) (J = 7.8 – 8.2; 1.6 – 1.8 Hz) indicating that the protons *ortho*-couple with C_5-H and *meta*-couple with $C_{2/6}$-H. The peaks of C_5-H protons were observed between δ 7.49 – 7.58 ppm as triplet by *ortho*-coupling with $C_{4/6}$-H. It is evident from this observation that the coupling constants of $C_{4/6}$-H are highly similar, resulting in a triplet instead of a doublet of doublets (dd). Although it was anticipated that the C_6-H protons would exhibit a

doublet of doublets of doublets (ddd) pattern due to the dissimilarity in coupling constants between C_2-H and C_4-H, only the first doublet was distinctly observed while the rest of the pattern was less distinguishable as in the case of compound **E8** (**Figure 5-8)**. Based on the structure of *para*-SO_2NH_2-containing molecules (**E6, E7, E10 – E13**), one would anticipate that the 4-sulfamoylphenyl-$C_{2/6}$-protons would have the same chemical shift, as well as 4-sulfamoylphenyl-$C_{3/5}$ protons, resulting in a single doublet for 4-sulfamoylphenyl-$C_{2/6}$-protons as well as sulfamoylphenyl-$C_{3/5}$ protons owing to an *ortho* splitting between the two sets of protons. However, it is observed on the spectra of these compounds that 4-sulfamoylphenyl-$C_{2/6}$-protons are not magnetically equivalent, as well as sulfamoylphenyl-$C_{3/5}$ protons. Consequently, these protons couple with each other at similar but different coupling constants, resulting in an apparent or pseudo d that looks like a ddd, however, this phenomenon is called the second-order effect and is represented as AA'BB' system. The AA'BB' splitting does not follow the n+1 rule as in first order systems and thus, will not be correct to be described as a doublet. However, in some compounds, due to a low resolution, the *J* value is not practically measurable, resulting in a dd or a d as in the case of **E12**. Analysing the ^{1}H NMR spectrum of compound **E7** in **Figure 5-7**, the doublet-triplet splitting is obvious. A similar phenomenon is observed in the ^{1}H NMR spectra of anethole and *p*-chloronitrobenzene (**Figure 5-9**) (Silverstein et al. 2005; Pavia et al. 2015).

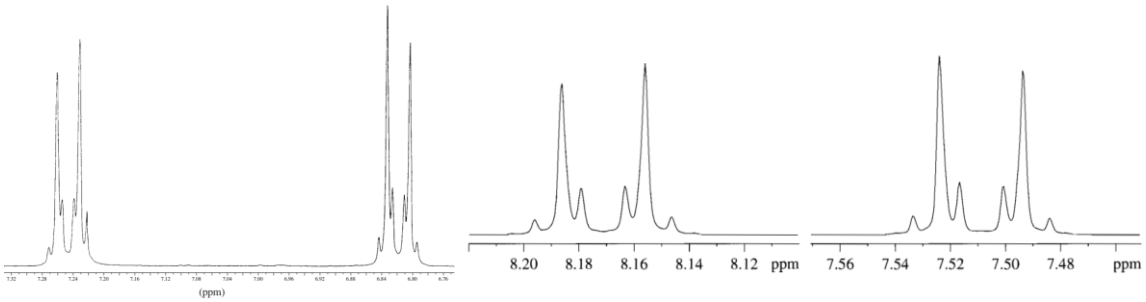

Figure 5-9: ^{1}H NMR spectrum of A) anethole (6.676 – 7.32 ppm). B) *p*-chloronitrobenzene (7.48 – 8.20 ppm)

Table 5-7: ^{1}H NMR data of 2-(Alkylidene/arylidene)-*N*-(3/4-sulfamoylphenyl)hydrazine-1-carbothioamide derivatives (E1 – E13)

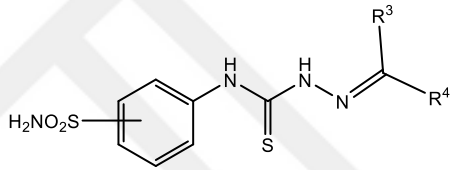

Compound	SO_2NH_2	R^3	R^4	SO_2NH_2	3/4-sulfamoylphenyl protons	N_4-H	N_2-H	R3 protons	R4 protons
E1	meta	H	thiophene-2-yl-	7.40 (2H, s)	7.50-7.58 (2H, m, 3-sulfamoylphenyl C_5-H and thiophene C_3-H); 7.64 (1H, dt, *J*=7.8, 1.7 Hz, 3-sulfamoylphenyl C_4-H), 7.82 (1H, ddd, *J*=8.1, 2.2, 1.0 Hz, 3-sulfamoylphenyl C_6-H); 8.05 (1H, t, *J*=2.0 Hz, 3-sulfamoylphenyl C_2-H)	10.07 (1H, s)	11.94 (1H, s)	8.37 (1H, s, N=CH)	7.15 (1H, dd, J=3.7, 3.6 Hz, thiophene C_4-H); 7.50-7.58 (2H, m, 3-sulfamoylphenyl C_5-H and thiophene C_3-H); 7.71 (1H, d, *J*=5.0 Hz, thiophene C_5-H)
E2	meta	H	5-bromothiophene-2-yl	7.40 (2H, s)	7.55 (1H, t, *J*=7.9 Hz, 3-sulfamoylphenyl C_5-H), 7.65 (1H, dt, *J*=7.8, 1.8 Hz, 3-sulfamoylphenyl C_4-H), 7.80 (1H, ddd, *J*=8.0, 2.2, 1.0 Hz, 3-sulfamoylphenyl C_6-H), 8.03 (1H, t, *J*=2.0 Hz, 3-sulfamoylphenyl C_2-H)	10.09 (1H, s)	12.01 (1H, s)	8.26 (1H, s, N=CH)	7.27 (1H, d, *J*=3.9 Hz, thiophene C_4-H), 7.37 (1H, d, *J*=3.9 Hz, thiophene C_3-H)
E3	meta	H	Pyrrole-2-yl	7.42 (2H, s)	7.58 (1H, t, *J*=7.9 Hz, 3-sulfamoylphenyl C_5-H), 7.65 (1H, dt, *J*=7.8, 1.8 Hz, 3-sulfamoylphenyl C_4-H), 7.92 (1H, ddd, *J*=7.9, 2.2, 1.1 Hz, 3-sulfamoylphenyl C_6-H), 8.07 (1H, t, *J*=1.9 Hz, 3-sulfamoylphenyl C_2-H)	10.21 (1H, s)	11.85 (1H, s)	7.97 (1H, s, N=CH),	6.16 (1H, dd, *J*=4.3, 1.8 Hz, pyrrole C_4-H), 6.50-6.51 (1H, m, pyrrole C_3-H), 7.08-7.10 (1H, m, pyrrole C_5-H), 11.50 (1H, s, pyrrole)
E4	meta	H	1-methylpyrrole-2-yl	7.39 (2H, s)	7.53 (1H, t, *J*=7.9 Hz, 3-sulfamoylphenyl C_5-H), 7.62 (1H, dt, *J*=7.8, 1.8 Hz, 3-sulfamoylphenyl C_4-H), 7.81 (1H, d, *J*=8.0 Hz, 3-sulfamoylphenyl C_6-H), 8.12 (1H, t, *J*=2.0 Hz, 3-sulfamoylphenyl C_2-H)	9.77 (1H, s)	11.68 (1H, s)	8.15 (1H, s, N=CH),	3.85 (3H, s, N-CH_3), 6.11 (1H, dd, *J*=3.9, 2.5 Hz, pyrrole C_4-H), 6.65 (1H, dd, *J*=3.9, 1.7 Hz, pyrrole C_3-H), 7.00 (1H, t, *J*=2.2 Hz, pyrrole C_5-H)

E5	meta	H	Furan-2-yl	7.40 (2H s)	7.54 (1H, t, *J*=7.9 Hz, 3-sulfamoylphenyl C_5-H), 7.63 (1H, dt, *J*=7.8, 1.8 Hz, 3-sulfamoylphenyl C_4-H), 7.84 (1H, ddd, *J*=8.1, 2.3, 1.1 Hz, 3-sulfamoylphenyl C_6-H), 8.05-8.12 (2H, m, 3-sulfamoylphenyl C_2-H and N=CH)	10.13 (1H, s)	11.95 (1H, s)	8.05-8.12 (2H, m, 3-sulfamoylphenyl C_2-H and N=CH),	6.67 (1H, dd, *J*=3.5, 1.8 Hz, furan C_4-H), 7.10 (1H, dd, *J*=3.4, 0.7 Hz, furan C_3-H), 7.87 (1H, dd, *J*=1.8, 0.7 Hz, furan C_5-H)
E6	para	H	Pyrrole-2-yl	7.35 (2H s)	7.82 (2H, app.d (AA'BB'), *J*=8.6 Hz, 4-sulfamoylphenyl $C_{2,6}$-H), 7.87 (2H, app.d (AA'BB'), *J*=8.6 Hz, 4-sulfamoylphenyl $C_{3,5}$-H),	10.21 (1H, s)	11.91 (1H, s)	7.97 (1H, s, N=CH),	6.14-6.17 (1H, m, pyrrole C_4-H), 6.50-6.51 (1H, m, pyrrole C_3-H), 7.09-7.11 (1H, m, pyrrole C_5-H), 11.59 (1H, s, pyrrole NH)
E7	para	H	Furan-2-yl	7.34 (2H s)	7.77 (2H, app.d (AA'BB'), *J*=8.6 Hz, 4-sulfamoylphenyl $C_{2,6}$-H), 7.83 (2H, app.d (AA'BB'), *J*=8.6 Hz, 4-sulfamoylphenyl $C_{3,5}$-H)	10.09 (1H, s)	12.00 (1H, s)	8.09 (1H, s, N=CH),	6.67 (1H, dd, *J*=3.5, 1.6 Hz, furan C_4-H), 7.09 (1H, d, *J*=3.5 Hz, furan C_3-H), 7.87 (1H, d, *J*=1.2 Hz, furan C_5-H)
E8	meta	CH_3	CH_3	7.35 (2H s)	7.49 (1H, t, *J*=8.2 Hz, 3-sulfamoylphenyl C_5-H), 7.58 (1H, dt, *J*=8.2, 1.6 Hz, 3-sulfamoylphenyl C_4-H), 7.80 (1H, d, *J*=7.8 Hz, 3-sulfamoylphenyl C_6-H), 8.08 (1H, t, *J*=1.6 Hz, 3-sulfamoylphenyl C_2-H),	10.04 (1H, s)	10.46 (1H, s)	1.97 (3H, s, -CH_3)	1.99 (3H, s, -CH_3)
E9	meta	C_2H_5	C_2H_5	7.34 (2H s)	7.52 (1H, t, *J*=8.0 Hz, 3-sulfamoylphenyl C_5-H), 7.69 (1H, dt, *J*=7.9, 1.8 Hz, 3-sulfamoylphenyl C_4-H), 7.99 (1H, ddd, *J*=8.0, 2.3, 1.1 Hz, 3-sulfamoylphenyl C_6-H), 8.27 (1H, t, *J*=2.0 Hz, 3-sulfamoylphenyl C_2-H)	9.48 (1H, s)	9.95 (1H, s)	1.12-1.19 (6H, m, 2 x CH_3), 2.56 (2H, q, *J*=7.6 Hz, -**CH_2**CH_3)	1.12-1.19 (6H, m, 2 x CH_3), 2.41 (2H, q, *J*=7.4 Hz, -**CH_2**CH_3)
E10	para	CH_3	CH_3	7.28 (2H s)	7.73 (2H, app.d (AA'BB'), *J*=8.7 Hz, 4-sulfamoylphenyl $C_{3,5}$-H), 7.83 (2H, app.d (AA'BB'), *J*=8.7 Hz, 4-sulfamoylphenyl $C_{2,6}$-H),	10.02 (1H, s)	10.52 (1H, s)	1.97, 2.00 (6H, 2s, -CH_3),	1.97, 2.00 (6H, 2s, -CH_3)
E11	para	C_2H_5	C_2H_5	7.31 (2H s)	7.76 (2H, app.d (AA'BB'), *J*=8.5 Hz, 4-sulfamoylphenyl $C_{3,5}$-H), 7.85 (2H, app.d (AA'BB'), *J*=8.6 Hz, 4-sulfamoylphenyl $C_{2,6}$-H)	9.97 (1H, s)	10.65 (1H, s)	1.0, 1.10 (6H, 2t, *J*=7.4 Hz, 2 x CH_3), 2.34, 2.45 (4H, 2q, *J*=7.4 Hz, 2 x -CH_2-),	1.0, 1.10 (6H, 2t, *J*=7.4 Hz, 2 x CH_3), 2.34, 2.45 (4H, 2q, *J*=7.4 Hz, 2 x -CH_2-)
E12	para	CH_3	C_3H_7	7.30 (2H, s)	7.76 (2H, *J*=8.6 Hz, 4-sulfamoylphenyl $C_{3,5}$-H), 7.85 (2H, *J*=8.6 Hz, 4-sulfamoylphenyl $C_{2,6}$-H),	10.45 (1H, s)	10.71 (1H, s)	1.94 (3H, d, *J*=5.1 Hz, -CH_3),	0.88-0.92 (3H, m, -CH_2CH_2**CH_3**), 1.57 (2H, sekstet, *J*=7.4 Hz, -CH_2**CH_2**CH_3), 2.24 (2H, t, *J*=7.8 Hz, -**CH_2**CH_2CH_3)

E13	para	cyclopentylidene	7.30 (2H, s)	7.74 (2H, app.d (AA'BB'), *J*=8.6 Hz, 4-sulfamoylphenyl $C_{2,6}$-H), 7.82 (2H, app.d (AA'BB'), *J*=8.6 Hz, 4-sulfamoylphenyl $C_{3,5}$-H)	10.03 (1H, s)	10.47 (1H, s).	1.71, 1.78 (4H, 2p, *J*=7.0 Hz, cyclopentane $C_{3,4}$-H), 2.39-2.49 (4H, m, cyclopentane $C_{2,5}$-H)

5.1.3.3. ^{13}C-NMR Spectral Analysis

To support the findings of ^{1}H-NMR spectroscopy and further elucidate the structures, ^{13}C NMR spectra of **E**1, **E3, E5, E8, and E10** were recorded with a 100/125 MHz NMR device, using DMSO-d6 as a solvent. The results are summarized in **Table 5-8**. The characteristic peaks in TSC derivatives are the thione and azomethine peaks which were observed between 174.1 – 176.4 ppm and 132.7 – 153.7 ppm. The fact that the C=S carbon is directly attached to sulfur and two nitrogens, is more downfielded than the C=N carbon with a single electronegative atom. The aromatic carbons of benzenesulfonamide were observed between 121.6 – 144.0 ppm. These results and interpretations are comparable with the reported findings in the literature.

Table 5-8: ^{13}C NMR data of 2-(Alkylidene/arylidene)-*N*-(3/4-sulfamoylphenyl)hydrazine-1-carbothioamide derivatives (E1 – E13)

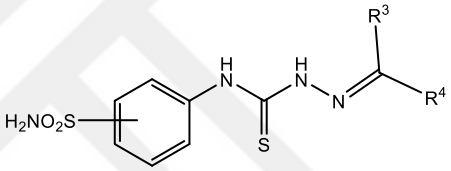

Compound	SO_2NH_2	R^3	R^4	3/4-sulfamoylphenyl	C=S	C=N	R^3	R4
E1	meta	H	thiophene-2-yl-	122.3 (3-sulfamoylphenyl C4), 122.6 (3-sulfamoylphenyl C2), 129.6 (3-sulfamoylphenyl C5), 129.0 (3-sulfamoylphenyl C6), 139.6 (3-sulfamoylphenyl C1), 144.0 (3-sulfamoylphenyl C3)	175.7	138.6 (N=CH)	--	128.0 (thiophene C4), 129.5 (thiophene C5), 131.2(thiophene C3), 138.3 (thiophene C2)
E3	meta	H	Pyrrole-2-yl	121.3 (3-sulfamoylphenyl C2), 121.5 (3-sulfamoylphenyl C4), 128.1 (3-sulfamoylphenyl C5), 127.7 (3-sulfamoylphenyl C6), 138.8 (3-sulfamoylphenyl C1), 143.5 (3-sulfamoylphenyl C3)	174.1	134.1 (N=CH)	--	108.9 (pyrrole C4), 113.3 (pyrrole C3), 121.7 (pyrrole C5), 126.7 (pyrrole C2)
E5	meta	H	Furan-2-yl	121.6 (3-sulfamoylphenyl C4), 121.7 (3-sulfamoylphenyl C2), 128.0 (3-sulfamoylphenyl C5), 128.0 (3-sulfamoylphenyl C6), 138.8 (3-sulfamoylphenyl C1), 143.4 (3-sulfamoylphenyl C3)	175.1	132.7 (N=CH)	--	111.9 (furan C4), 112.9 (furan C3), 144.70 (furan C5), 148.7 (furan C2)
E8	meta	CH_3	CH_3	121.8 (3-sulfamoylphenyl C_4), 121.9 (3-sulfamoylphenyl C_2), 128.1 (3-sulfamoylphenyl C_6), 128.3 (3-sulfamoylphenyl C_5), 139.5 (3-sulfamoylphenyl C_1), 143.8 (3-sulfamoylphenyl C_3)	176.4	153.2 (N=C)	17.9 (-CH_3)	24.9 (-CH_3)
E10	para	CH_3	CH_3	124.3 (4-sulfamoylphenyl $C_{2,6}$), 125.6 (4-sulfamoylphenyl $C_{3,5}$), 139.7 (4-sulfamoylphenyl C_4), 142.1 (4-sulfamoylphenyl C_1)	176.1	153.7 (N=C)	18.0 (-CH_3)	25.0 (-CH_3)

In the ^{13}C NMR of isatin-containing TSC derivatives, Güzel at al. observed the thione peaks between δ 176.65 – 178.06 ppm (Güzel et al. 2008). Soylu-Eter et al. assigned the signal resonated at δ 176.65 ppm to the thione of (4-methoxyphenyl)-2-(1-methyl-2-oxo-5-(trifluoromethoxy)indolin-3-ylidene)hydrazine-1-carbothioamide (Soylu Eter et al. 2021).

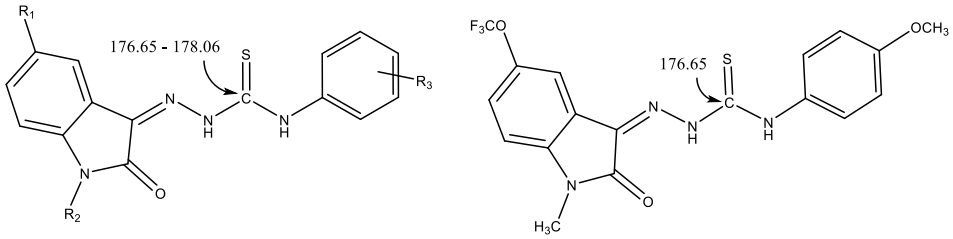

In addition, Hussein et al. observed C=S peaks between δ 176.3 – 177.7 ppm while the C=N peaks appeared between δ 147.8 – 155.6 ppm (Hussein et al. 2019).

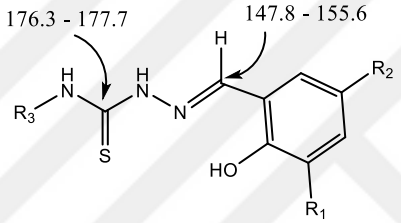

In the ^{13}C NMR spectrum of thiophene-2-carbaldehyde, C1, C_2, C_3, C_5, and C_4 carbons are resonated at δ 182.97,144.02, 136.44, 135.11 and 128.41 ppm, respectively. The electron-withdrawing effects of -CHO and sulfur caused the highest downfield of C_2, followed by C_3. The C_4 is the least deshielded due to the farther distance away from -CHO and sulfur atom (SDBS 4170). In the ^{13}C NMR spectrum of pyrrole-2-carbaldehyde, the chemical shifts for C1, C_2, C_5, C_3, and C_4 are δ 179.54, 132.91, 127.28, 122.11 and 111.34 ppm, respectively (SDBS 1187). The C1, C_2, C_5, C_3, and C_4 carbons of furan-2-carbaldehyde, resonated at δ 177.93, 153.06, 148.31, 121.55 and 112.76 ppm, respectively (SDBS 1309).

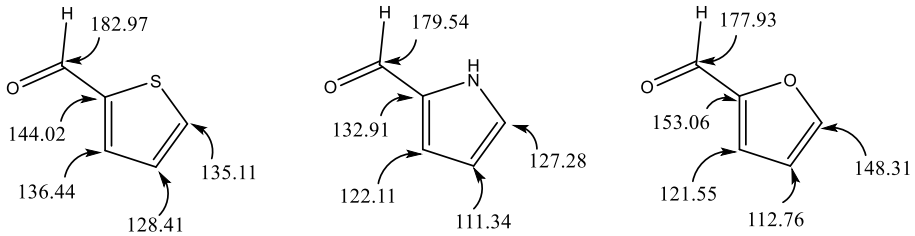

Peaks observed between δ 176.1 - 176.9 ppm were assigned to C=S and those observed between δ 132.4 – 138.3 ppm were assigned to C=N of various TSCs. (Karaküçük-İyidoğan et al. 2011). Similarly, Taşdemir et al. observed the C=S peaks of various chiral

TSCs between δ 175.71 – 177.22 ppm and the C=N peaks between δ 143.68 – 144 pm (Taşdemir et al. 2015). The team, in another study, ascribed peaks between δ 174.22 – 176.21 to C=S whereas peaks between δ 137.28 – 140.65 ppm were ascribed to C=N. In the ^{13}C NMR of *N*-cyclohexyl-2-(furan-2-ylmethylene)hydrazine-1-carbothioamide, İyidoğan et al. assigned peaks resonated at 149.2, 134.2, 118.0 and 112.3 ppm to C_2, C_5, C_3, and C_4 carbons of furan, respectively (İyidoğan et al. 2020).

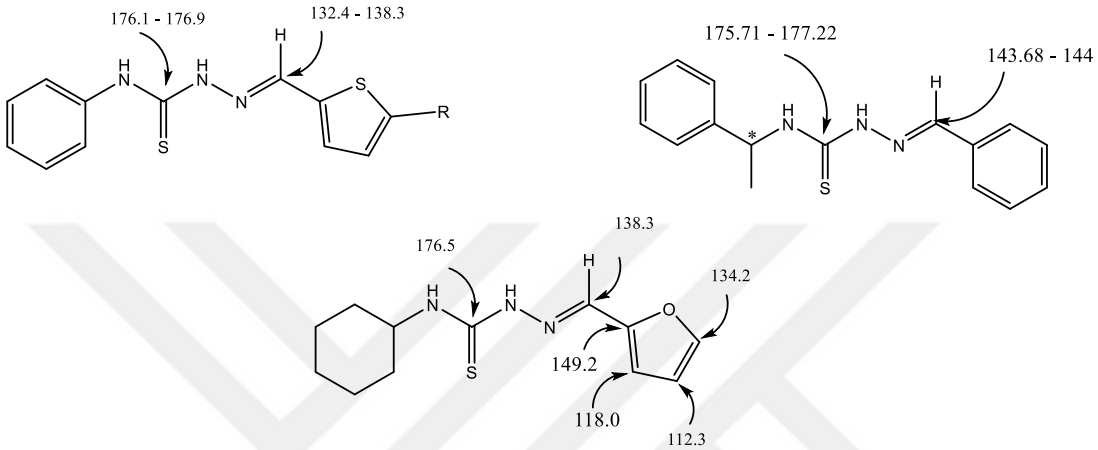

In the characterization of 2-(2-oxoindolin-3-ylidene)-*N*-(4-sulfamoylphenyl)hydrazine-1-carbothioamide, Karalı et al. and assigned the peaks resonated at 177.09 ppm to C=S, 143.34 ppm to 4-sulfamoylphenyl C_1, 142.14 ppm to 4-sulfamoylphenyl C_4, 126.67 ppm to 4-sulfamoylphenyl $C_{3,5}$ and 125.98 ppm to 4-sulfamoylphenyl $C_{2,6}$.

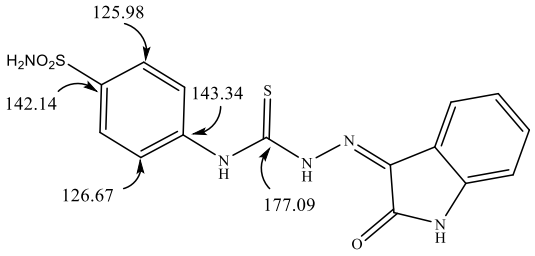

The effects of the sulfonamide and thiosemicarbazide groups on the chemical shifts of benzene aromatic carbons present in *N*-(3-sulfamoylphenyl)hydrazinecarbothioamide (**C1**) were studied by Eraslan Elma. The effect of SO_2NH_2 on *ipso*, *ortho*, *meta* and *para* carbons were found to be 15.30, -2.96, 0.38 and 3.24, respectively. The effect of thiosemicarbazide on *ipso*, *ortho*, *meta* and *para* carbons were found to be 9.22, -4.24, 0.42 and -2.45, respectively.

These theoretical values showed a correlation with the experimental values (Eraslan Elma 2017).

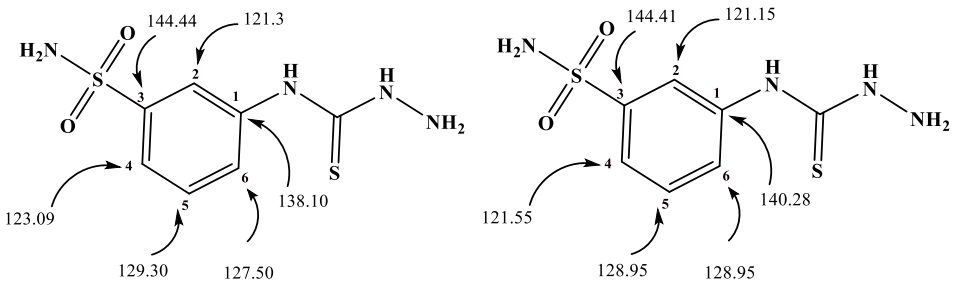

Based on the above information, Eraslan Elma characterized the structures of 2-(5-substituted-2-oxoindolin-3-ylidene)-*N*-(3-sulfamoylphenyl)hydrazine-1-carbothioamide derivatives and assigned the peaks observed between 176.54 – 177.35 ppm to C=S, 144.31 – 145.14 ppm to C_3, 138.73 – 139.63 ppm to C_1, 128.96 – 129.87 ppm to C_5, 128.84 – 129.80 to C_6, 123.05 – 124.05 ppm to C_4 and 122.47 – 123.56 ppm to C_2.

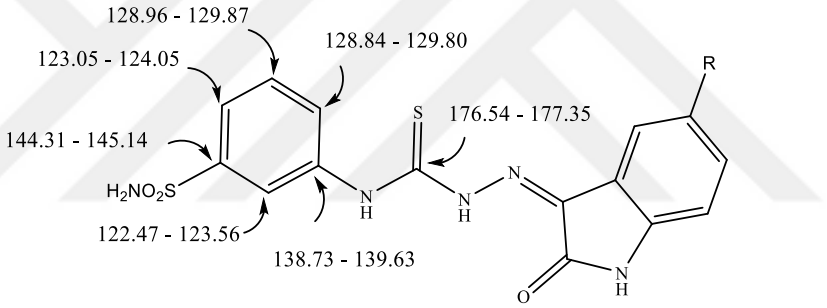

In the ^{13}C NMR of compounds **E1, E3, E5, E8** and **E10**, the absence of aldehyde or ketone-related peaks, the appearance of CH=N and C=S peaks between 132.7 – 153.7 ppm and 174.1 – 176.4 ppm, respectively, substantiates the formation of TSCs. In the ^{13}C NMR spectrum of compound **E1,** the C=S and CH=N peaks were observed at 175.7 and 138.6 ppm, respectively. The peaks related to C_2, C_3, C_5 and C_4 of the thiophene ring were observed in decreasing order at 138.3, 131.2, 129.5 and 128.0 ppm. The peaks related to C_3, C_1, C_6, C_5, C_2 and C_4 of 3-sulfamoylphenyl were observed at 144.4, 139.6, 129.0, 128.6, 122.6 and 122.3 ppm, respectively (**Figure 5-10**).

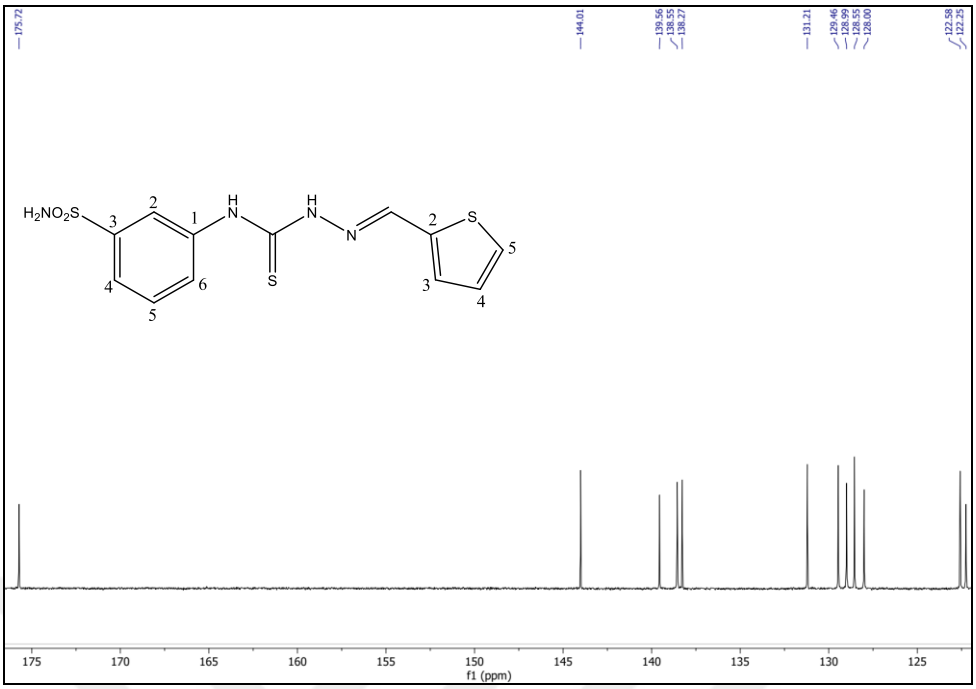

Figure 5-10: ^{13}C NMR spectrum of E1 (122 – 176 ppm)

To support the ^{1}H NMR and decoupled ^{13}C NMR findings, HSQC (Heteronuclear Single Quantum Correlation), a 2D NMR analysis for compounds **E**1, **E3, E5, E8, and E10** was carried out. In the HSQC spectrum of compound **E1**, the thiophene C_4-H, and C_5-H proton signals resonated at δ 7.15 and 7.71 ppm, respectively, correlated with thiophene C_4, and C_5 carbon signals resonated at 128.0 and 129.5 ppm, respectively. Proton signals corresponding to the 3-sulfamoylphenyl C_2-H, C_4-H and C_6-H also correlated with respective C_2, C_4 and C_6 carbon signals. Proton signals corresponding to two protons originating from 3-sulfamoylphenyl C_5-H and thiophene C_3-H protons that were evaluated as multiplets in the δ 7.50 – 7.58 ppm range correlated with 3-sulfamoylphenyl C_5 and thiophene C_3 at δ 128.6 and 131.2 ppm, respectively. The absence of the signals related to SO_2NH_2, N_2-H and N_4-H protons, and 3-sulfamoylphenyl C_1, C_3, thiophene C_1 and C=S carbons confirms the accuracy of the findings (**Figure 5-11**).

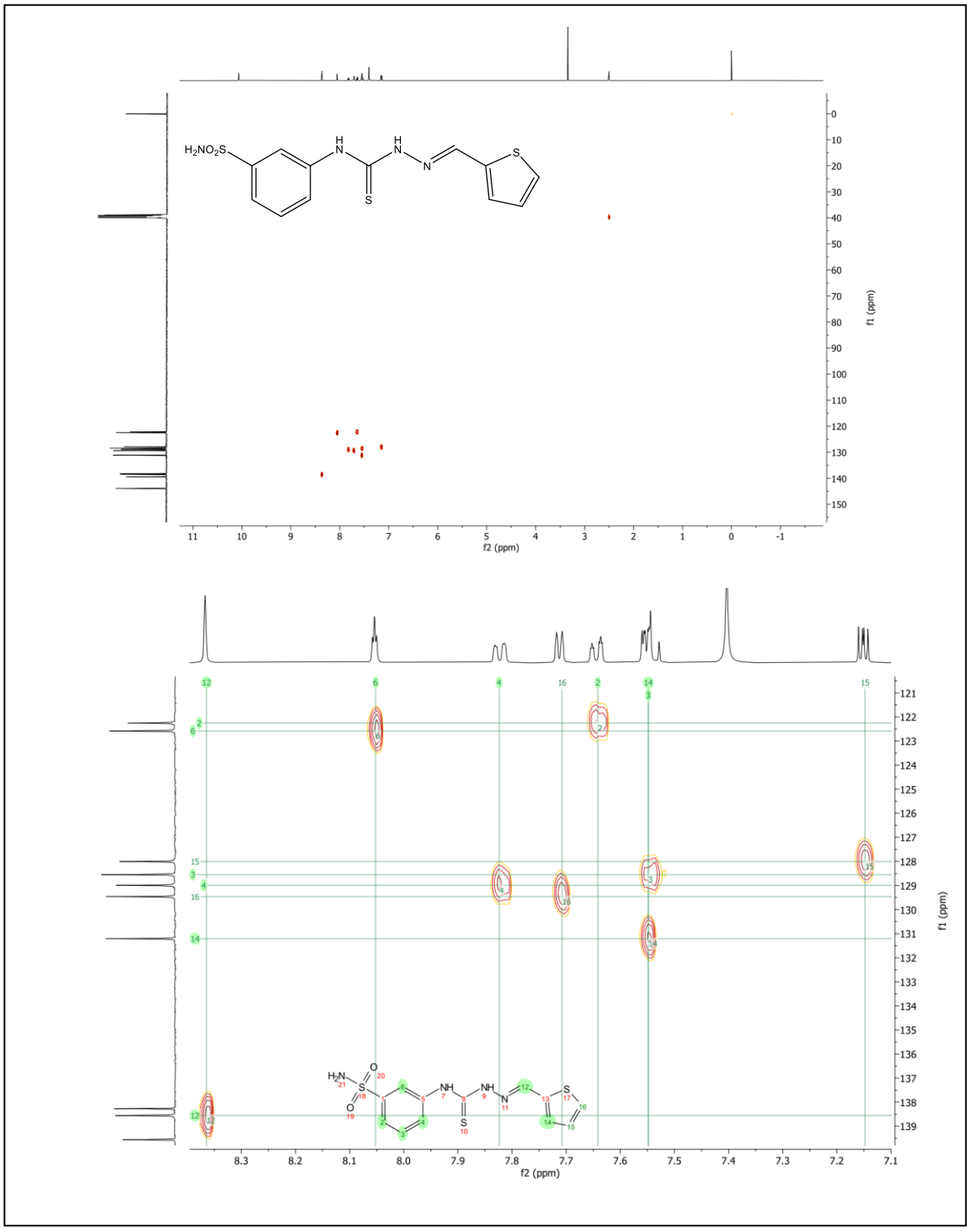

Figure 5-11: HSQC spectrum of compound E1

5.1.3.4. Mass Spectral Analysis

To confirm the purity and molecular weight of all the synthesized thiosemicarbazone intermediates (**E1 – E13**), mass spectra were obtained by electrospray ionization method

(ESI) using Agilent Infinity 1260 II LC-MS device. ESI is one of the most applied techniques for studying the molecular weight of organic compounds and biomolecules (Pavia et al. 2015). It is conducted either in a positive or negative mode. In the positive ion mode, ESI generates abundant molecular ions $[M+H]^+$ or protonated molecular ions from a basic sample with little fragmentation. The charges of the ions produced in ESI do not always correspond to the sample's charge state. The charge transferred to the sample molecules is caused by a combination of charge concentration in the droplets during aerosol evaporation and electrochemical processes caused by the capillary's electrostatic potential. Negative ions or deprotonated molecular ions $[M-H]^-$ may also be formed in ESI by the loss of protons from acidic samples to basic species in solution. This is called the negative ion mode. Positive ion mode may produce molecular ions as their Na^+, NH_4^+ and Li^+ adducts whereas the negative ion mode may produce in the form of chlorine adduct ions (Snyder 1995). Dimers of samples may also be observed as $[2M+H]^+$ or $[2M+Na]^+$ especially if a high concentration of the sample is used (Pramanik et al. 2002).

The m/z values of $[M-H]^-$ molecular ion peaks for compounds **E1 – E13** were obtained as the base peak (except for compounds **E3** and **E6**) and were in accordance with the expected molecular weights. The bromine atom has ^{79}Br and ^{81}Br isotopes with relative abundances of 100% and 98%, respectively. Compound **E2** having one bromine atom showed two molecular ion peaks with m/z values of $[M-H]^-$ and $[M-H]^-+2$ with a relative ratio of approximately 1:1 (**Figure 5-12**).

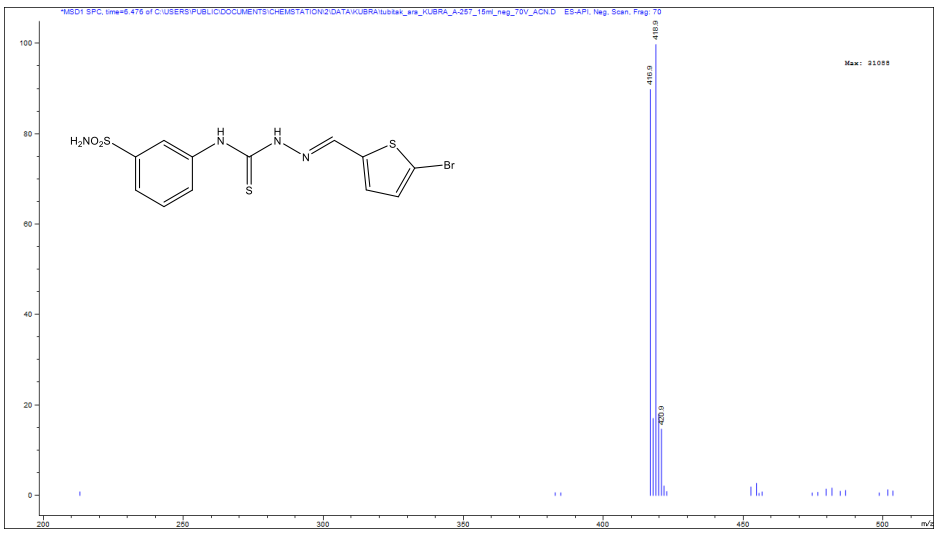

Figure 5-12: Mass spectrum of compound E2

In addition to the molecular ion peaks of compounds **E3** and **E6**, peaks related to $[2M+H]^-$, $[2M+Na]^-$ and $[2M+HCl]^-$ dimers were observed. These peaks were consecutively observed for compound **E6** as m/z 645, 667 and 681, respectively. The $[2M+H]^-$ peak had the highest relative abundance in both of these compounds (**Figure 5-13**).

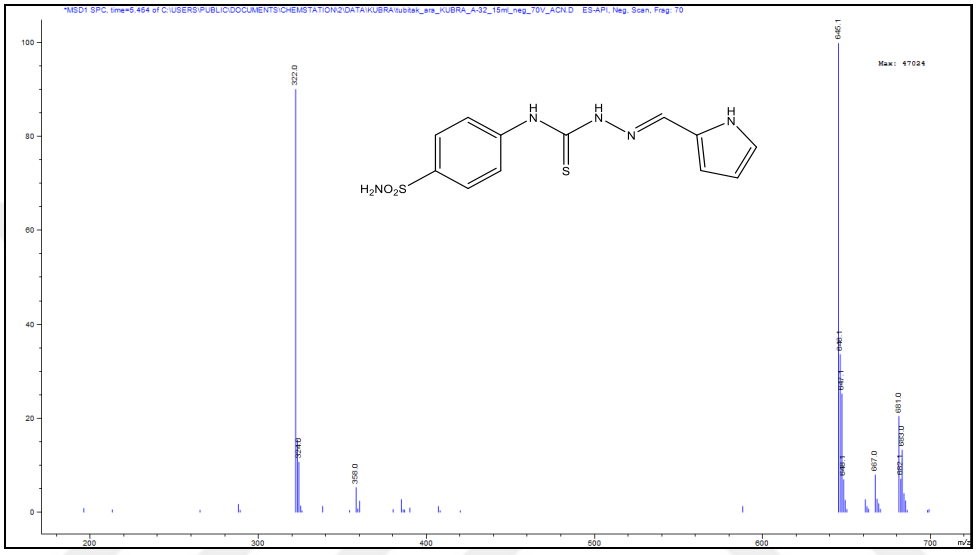

Figure 5-13: Mass spectrum of compound E6

In compounds **E8** and **E9**, the molecular ion peaks were visible with the chlorine adduct ions as $[M-H+Cl]^-$. In addition, a fragment ion peak was observed for both of these compounds as $[M-H]^- - 34$ as a loss of sulfur atom (**Figure 5-14**). The proposed mechanism for this fragmentation is depicted in **Figure 5-15** as reported in the literature (Karaküçük-İyidoğan et al. 2011; Stariat et al. 2013).

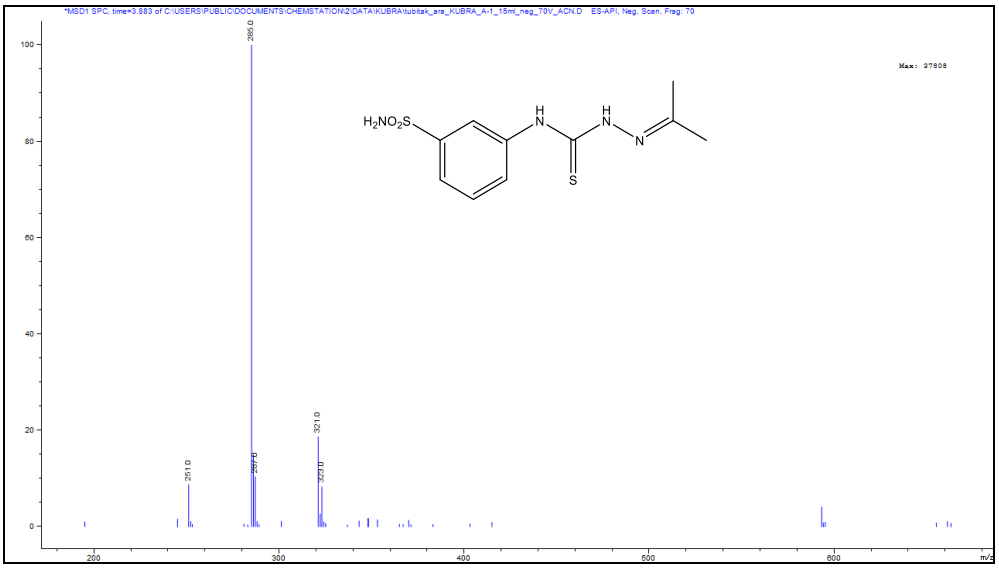

Figure 5-14: Mass spectrum of compound E8

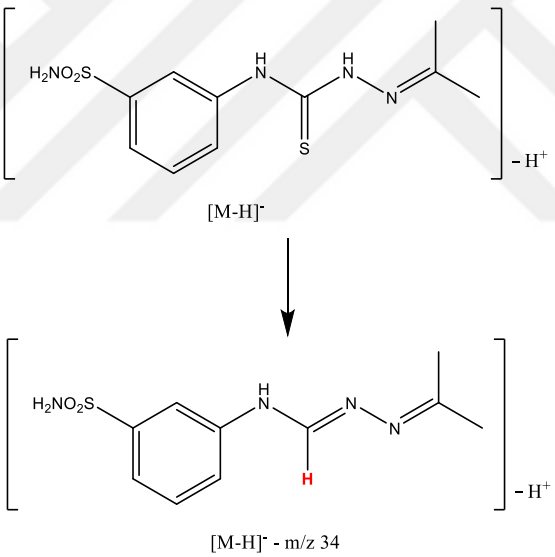

Figure 5-15: Desulfurization pathways of compound E8

The $[M-H]^-$ was observed as the base peak in compounds **E1**, **E2**, **E4**, **E5**, **E7**, **E10** – **E13**. Peaks related to the chlorine adduct, $[M-H+Cl]^-$ and the dimer $[2M+Na]^-$ were observed in these compounds. **Figure 5-16** shows the mass spectrum of compound **E13**.

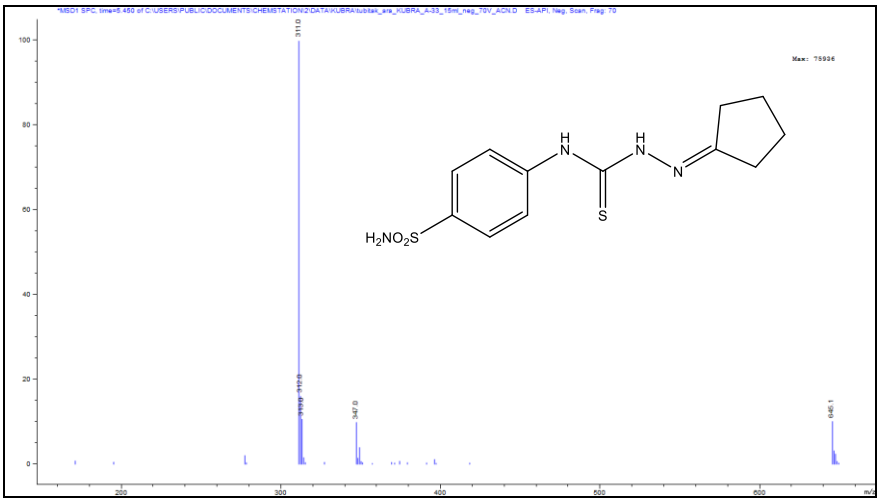

Figure 5-16: Mass spectrum of compound E13

5.1.4. 3/4-[4-(Non)substitutedphenyl-2-(alkylidene/arylidenehydrazinylidene)-1,3-thiazol-3(2*H*)-yl]benzenesulfonamide derivatives (4a-4v)

Hanstzch cyclocondensation reaction of various thioamide, thiourea, thiosemicarbazide and TSC derivatives with α-haloketones is the most employed method in thiazole synthesis. TSC derivatives cyclised with α-haloketones in methanol, ethanol or propanol to yield 4-thiazoline derivatives. During this reaction, sodium acetate can be used to neutralise the HBr acid produced which might lead to the formation of the salt product of the obtained thiazolines. Due to hydrazo/azine tautomerism observed in these compounds, the generated C=N bond could be exocyclic forming 4-thiazolines or endocyclic forming thiazoles (Pereira et al. 2019; Nechak et al. 2019). However, endocyclic is common when the N_4 of TSC is non-substituted.

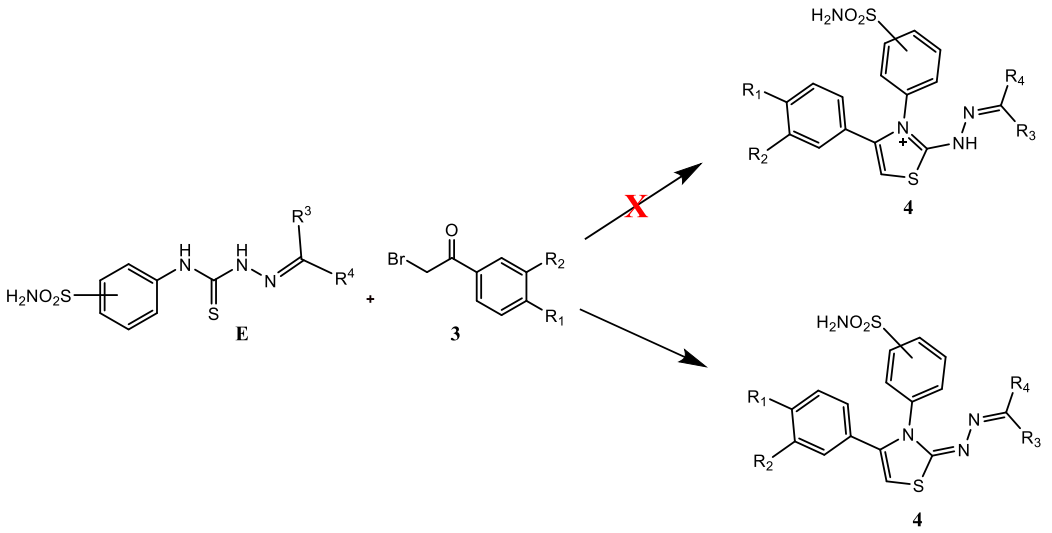

Scheme 5-6: Synthesis of 3/4-[4-(Non)substitutedphenyl-2-(alkylidene/arylidenehydrazinylidene)-1,3-thiazol-3(*2H*)-yl]benzenesulfonamide derivatives (4a-4v) showing possible hydrazo/azine tautomerism

The designed benzenesulfonamide-thiazoline hybrids (**4a – 4v**) were successfully synthesized by Hanstzch cyclocondensation reaction of various TSC derivatives (**E – E13**) and 4/3-(non)substituted-α-bromoacetophenones (**3a – 3f**) with various yields of 30 – 99% (**Scheme 5-6**). Equimolar amounts of suitable **E** and **3** derivatives were refluxed in chloroform-ethanol (2:1) for 2.5 – 6 hours. The progress of the reactions was followed by a change of colour and TLC. The obtained crude products were purified by recrystallisation from ethanol or preparative TLC. The purity of the compounds was determined by TLC, elemental analysis and LC-MS methods. Elucidation of the structures was carried out with IR, ^{1}H NMR and ^{13}C NMR. Elemental analysis and physical properties of the compounds are given in **Table 5-9**.

A possible mechanism for the cyclization of TSCs and 4/3-(non)substituted-α-bromoacetophenones is proposed in **Scheme 5-7**. The reaction involves three steps: nucleophilic substitution S_N2 on the α-carbon, cyclization, and dehydration. In the first step, thione – thiol tautomerism occurs, followed by the nucleophilic attack of the thiol sulfur of the TSC on the electrophilic α-carbon of the aromatic ketone, forming a covalent bond and removal of HBr. The new intermediate formed undergoes an intramolecular nucleophilic attack of the N_4 on the carbonyl carbon to form a thiazolidine intermediate which subsequently undergoes dehydration to afford the **4** derivatives (Nechak et al. 2019; Ngoc Toan and Dinh Thanh 2021).

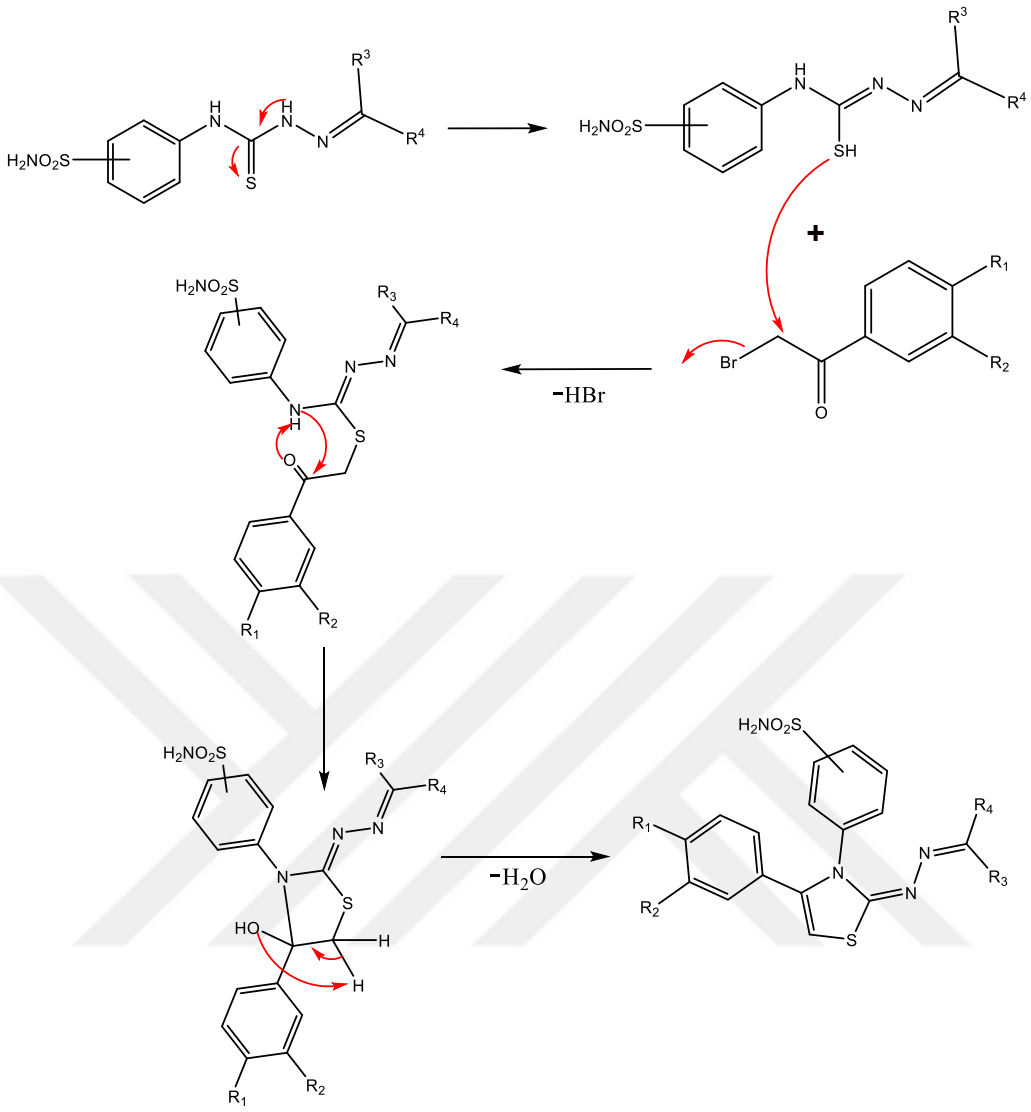

Scheme 5-7: Proposed synthesis mechanism of 3/4-[4-(Non)substitutedphenyl-2-(alkylidene/arylidenehydrazinylidene)-1,3-thiazol-3(*2H*)-yl]benzenesulfonamide derivatives (4a-4v)

The thione – thiol tautomerism preferentially occurs between thione and N_2. Tautomerism between thione and N_4 is not preferred and does not lead to product formation (**Scheme 5-8**) (Özbey et al. 2003; Ngoc Toan and Dinh Thanh 2021).

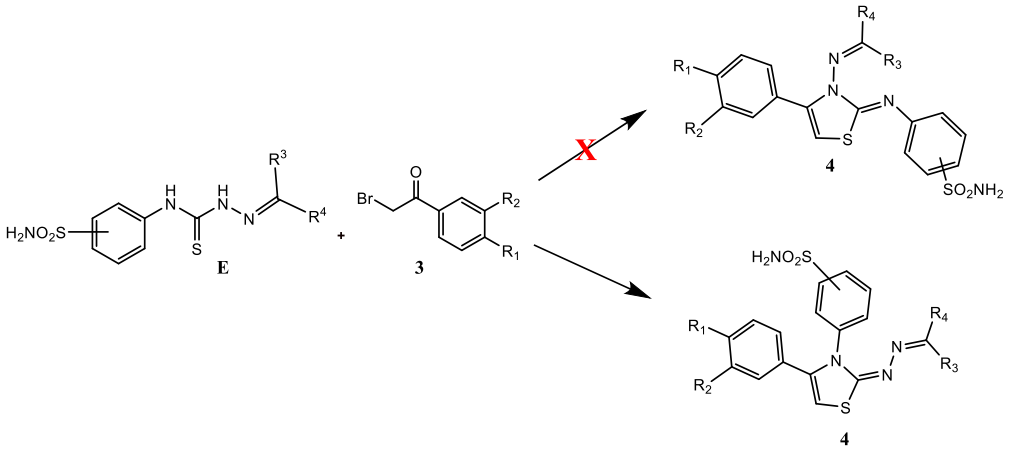

Scheme 5-8: Synthesis of 3/4-[4-(Non)substitutedphenyl-2-(alkylidene/arylidenehydrazinylidene)-1,3-thiazol-3(*2H*)-yl]benzenesulfonamide derivatives (4a-4v) proceeding through thione – thiol tautomerism between thione and N_2

Table 5-9: Elemental analysis data and physical properties of 3/4-[4-(Non)substitutedphenyl-2-(alkylidene/arylidenehydrazinylidene)-1,3-thiazol-3(*2H*)-yl]benzenesulfonamide derivatives (4a-4v)

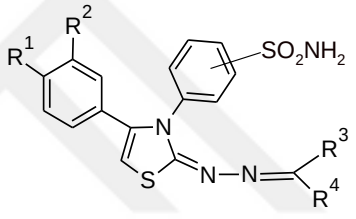

4

Compound	SO_2NH_2	R_1	R_2	R_3	R_4	Molecular Formula (Molecular Weight)	Colour	Yield (%)	Melting Point (°C)	Elemental Analysis (%) Calculated / Found			
										C	H	N	S
4a	meta	-	-	H	thiophene-2-yl	$C_{20}H_{16}N_4O_2S_3$ (440.561)	Yellow	94	271.7-273.0	54.52 54.81	3.66 3.35	12.72 13.12	21.83 21.57
4b	meta	-	-	H	5-bromothiophene-2-yl-	$C_{20}H_{15}BrN_4O_2S_3$ (519.457)	Dark orange	63	251.0-251.8	46.24 45.96	2.91 2.77	10.79 10.77	18.52 18.21
4c	meta	-	-	H	1*H*-pyrrole-2-yl	$C_{20}H_{17}N_5O_2S_2$ (423.511)	Dark green	56	245.2-246.4	56.72 56.50	4.05 3.72	16.54 16.10	15.14 15.61
4d	meta	-	-	H	1-methyl-1*H*-pyrrole-2-yl	$C_{21}H_{19}N_5O_2S_2$ (437.537)	Dark green	61	247.0-249.9	57.65 57.53	4.38 4.04	16.01 15.86	14.66 14.46
4e	meta	-	-	H	Furan-2-yl	$C_{20}H_{16}N_4O_3S_2$ (424.496)	Yellow	98	237.4 (decomposition)	56.59 56.60	3.80 3.49	13.20 13.37	15.11 14.78
4f	para	-	-	H	1*H*-pyrrole-2-yl	$C_{20}H_{17}N_5O_2S_2$	Dark	94	249.9-251.5	56.72	4.05	16.54	15.14

						(423.51)	green			56.35	3.88	16.21	14.87
4g	para	Br	-	H	1*H*-pyrrole-2-yl	$C_{20}H_{16}BrN_5O_2S_2$ (502.41)	Dark green	58	238.4-239.5	47.81 47.57	3.21 2.95	13.94 13.62	12.76 12.48
4h	para	OH	-	H	1*H*-pyrrole-2-yl	$C_{20}H_{17}N_5O_3S_2$ (439.51)	Dark green	85	290,3-290.6	54.65 54.48	3.90 4.23	15.93 15.72	14.59 14.33
4i	para	-	-	H	Furan-2-yl	$C_{20}H_{16}N_4O_3S_2$ (424.50)	Yellow	65	263.2-264.4	56.59 56.44	3.80 3.63	13.30 12.95	15.11 15.36
4j	para	Br	-	H	Furan-2-yl	$C_{20}H_{15}BrN_4O_3S_2$ (503.39)	Yellow	74	233.5 – 235.8	47.72 47.54	3.00 2.65	11.13 11.51	12.74 12.47
4k	meta	-	-	C_2H_5-	C_2H_5-	$C_{20}H_{22}N_4O_2S_2$ (414.54)	Brown	45	217.0 – 218.1	57.95 57.64	5.35 5.04	13.52 13.14	15.47 15.32
4l	para	Br	-	CH_3-	CH_3-	$C_{18}H_{17}BrN_4O_2S_2$ (465.39)	Orange	71	176.1 – 177.1	46.4546.17	3.68 3.37	12.04 11.76	13.78 13.42
4m	para	CF_3	-	CH_3-	CH_3-	$C_{19}H_{17}F_3N_4O_2S_2$ (454.49)	Yellow	41	163.3 – 165.1	50.21 50.48	3.77 4.15	12.33 12.62	14.11 14.44
4n	para	OCF_3	-	CH_3-	CH_3-	$C_{19}H_{17}F_3N_4O_3S_2$ .CH_3CH_2OH (516.55)	Yellow	43	150.8 – 151.3	48.83 48.47	4.49 4.26	10.85 10.51	12.41 12.05
4o	para	F	-	CH_3-	CH_3-	$C_{18}H_{17}FN_4O_2S_2$ (404.48)	Brown	66	226.9 – 228.0	53.45 53.22	4.24 4.01	13.85 13.48	15.85 15.54
4p	para	-	CF_3	CH_3	CH_3	$C_{19}H_{17}F_3N_4O_2S_2$ (454.489)	Yellow	30	178.0 – 178.8	50.21 49.85	3.77 3.50	12.33 12.60	14.11 13.80
4q	para	CH_3	-	C_2H_5-	C_2H_5-	$C_{21}H_{24}N_4O_2S_2$ (428.57)	Brown	50	209.9 – 210.6	58.85 58.58	5.64 5.77	13.07 12.86	14.96 14.67
4r	para	F	-	C_2H_5-	C_2H_5-	$C_{20}H_{21}FN_4O_2S_2$ (432.53)	Yellow	30	231.2 – 231.8	55.54 55.31	4.89 4.60	12.95 12.63	14.83 14.54
4s	para	-	-	CH_3-	C_3H_7-	$C_{20}H_{22}N_4O_2S_2$ .CH_3CH_2OH	Orange	75	150.0 – 152.1	57.37 57.22	6.13 5.87	12.16 11.85	13.92 13.56

					(460.61)							
4t	para	-	-	cyclopentylidene	$C_{20}H_{20}N_4O_2S_2$ (412.53)	Ivory	80	260.9 – 262.4	58.23 58.49	4.89 5.25	13.58 13.14	15.55 15.26
4u	para	Br	-	cyclopentylidene	$C_{20}H_{19}BrN_4O_2S_2$ .CH_3CH_2OH (537.49)	Amber White	99	234.7 – 238	49.16 48.87	4.69 4.36	10.42 10.03	11.93 11.57
4v	para	OH	-	cyclopentylidene	$C_{20}H_{20}N_4O_3S_2$ (428.53)	Yellow	82	206 – 207.9	56.06 56.26	4.70 4.66	13.07 12.88	14.97 14.64

5.1.4.1. IR Spectral Analysis

The thiocarbonyl, N_2 and N_4 are involved in the cyclocondensation process forming a new azomethine and a tertiary amine present in the thiazole (N_3). In the IR spectra, N-H stretching vibrations related to NHs present in the TSC moiety and the C=S disappeared confirming the cyclization and the formation of the thiazoline ring (**Figure 5-17**). The N-H stretching bands related to the sulfonamide were observed between 3477 – 3122 cm^{-1}. The aromatic C-H stretching vibrations were observed between 3196 – 3032 cm^{-1}. The asymmetric and symmetric stretching vibrations of S=O were observed between 1355 – 1323 cm^{-1} and 1174 – 1149 cm^{-1}, respectively. The C=N and C=C stretchings, and N-H bending vibrations were observed in the region 1660 – 1449 cm^{-1} (**Figure 5-17**).

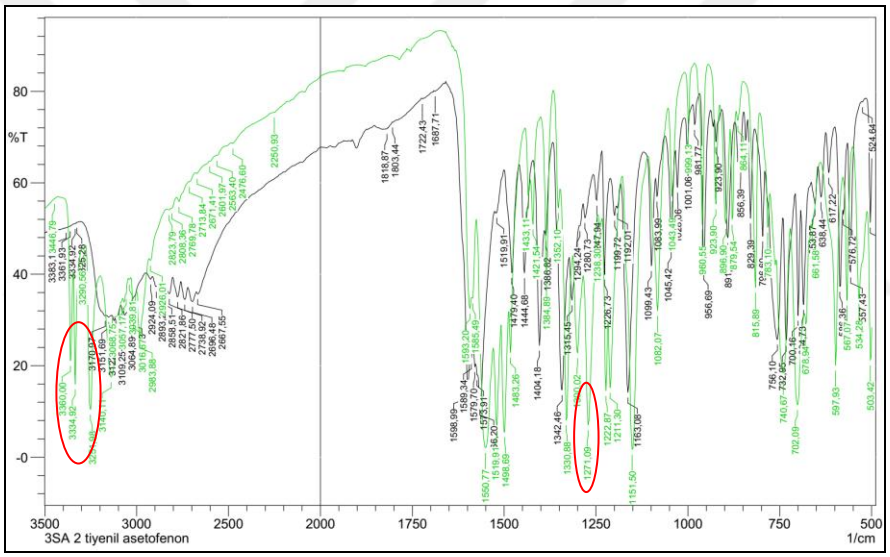

Figure 5-17: Comparative IR spectrum of compounds of E1 and 4a. Green represents E1 and black represents 4a.

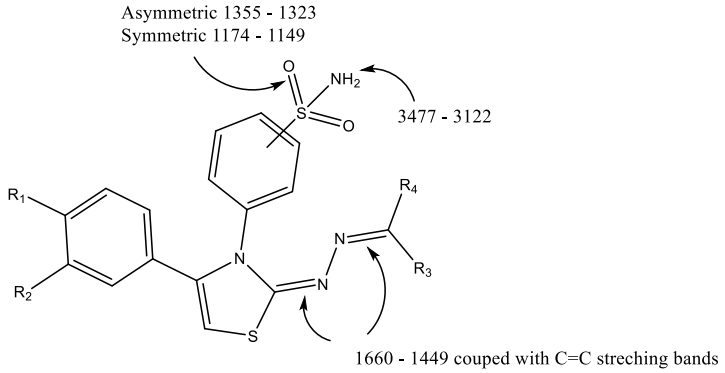

Özbey et al observed the C=N stretching bands of 3-(3-benzyl-2-((4-methylbenzylidene)hydrazineylidene)-2,3-dihydrothiazol-4-yl)-2*H*-chromen-2-one at 1556 cm $^{-1}$. In the IR analysis of a series of 1-(5-(((-4-(4-bromophenyl)-3-substituedlthiazol-2(3*H*)-ylidene)hydrazineylidene)methyl)-2-methyl-1*H*-pyrrol-3-yl)ethan-1-one, Hassan et al. observed the C=N stretching bands between 1599 – 1640 cm $^{-1}$. Mamidala et al. also analyzed the IR spectra of 4-thiazoline-coumarin hybrids and observed the C=N stretching bands between 1601–1613 cm $^{-1}$.

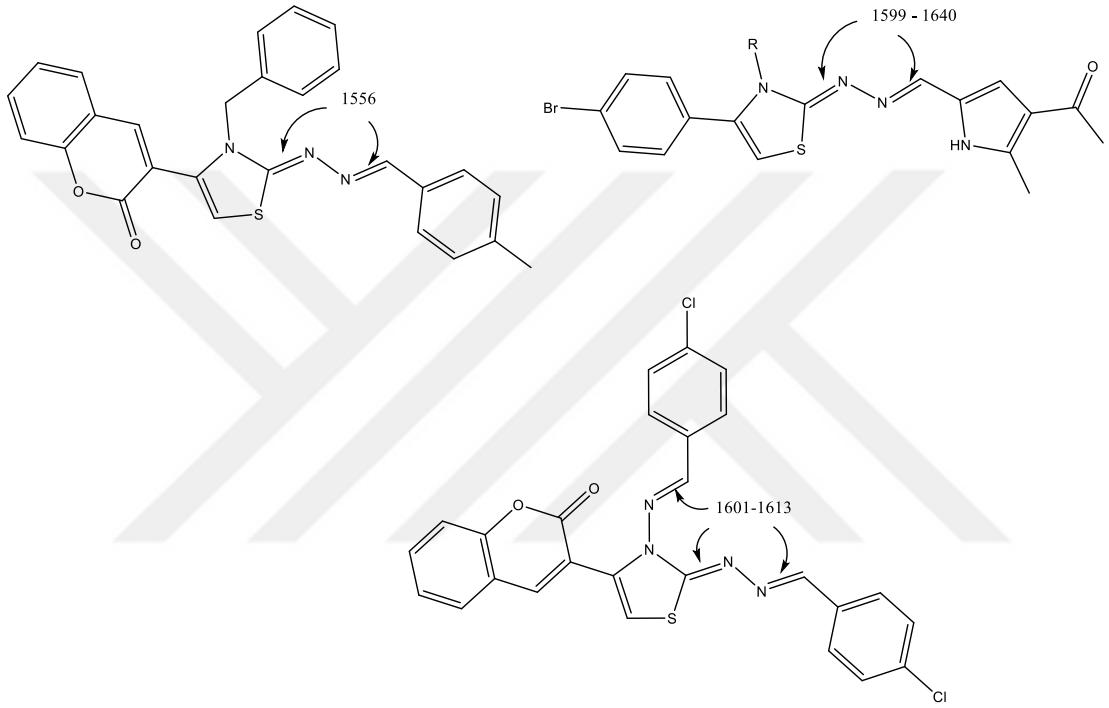

In the IR characterization of novel 4-thiazoline-containing compounds, Shehzad et al. observed the C=N stretching bands between 1567 – 1614 cm $^{-1}$. In another study conducted on different novel compounds, the team observed the C=N stretching bands between 1558 – 1748 cm $^{-1}$.

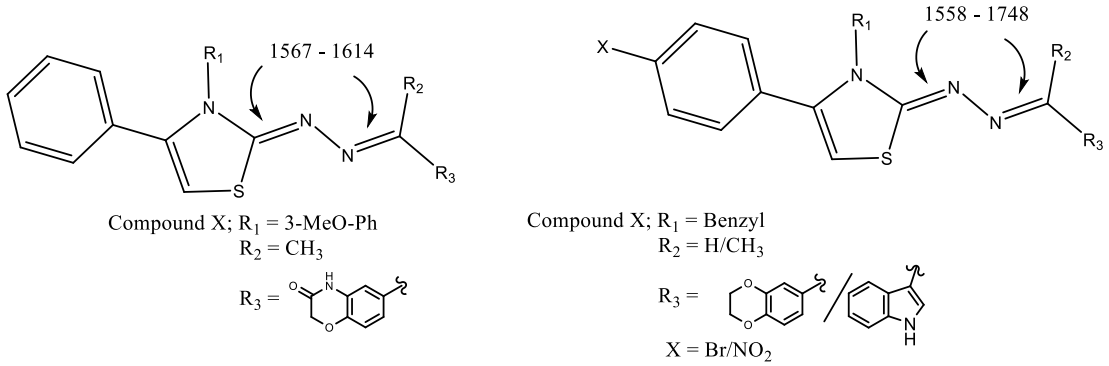

Compound X; R_1 = 3-MeO-Ph
R_2 = CH_3
R_3 =

Compound X; R_1 = Benzyl
R_2 = H/CH_3
R_3 =
X = Br/NO_2

Table 5-10: IR data of 3/4-[4-(Non)substitutedphenyl-2-(alkylidene/arylidenehydrazinylidene)-1,3-thiazol-3(*2H*)-yl]benzenesulfonamide derivatives (4a-4v)

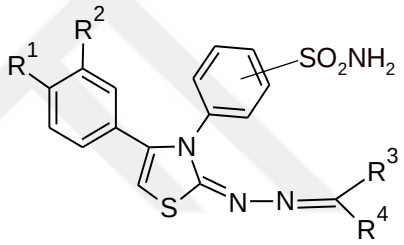

4

Compound	SO_2NH_2	R^1	R^2	R^3	R^4	N-H s.b.	Ar. C-H s.b. and =CH s.b	Al. C-H s.b.	Ar. C=C s.b, C=N s.b and N-H b.b	Al. C-H b.b.	S=O s.b.	C-N s.b.	Ar. subs. C-H b.b.	Others
4a	meta	-	-	H	thiophene-2-yl	3170, 3122	3064, 3047	--	1598, 1589, 1579, 1573, 1566	--	1342, 1163	1315	732, 684 (mono), 891, 756, 700 (meta)	
4b	meta	-	-	H	5-bromothiophene-2-yl-	3402, 3387	3174, 3109, 3064	--	1598, 1591, 1579, 1566	--	1344, 1163	1315	732, 686, (mono), 893, 752, 700 (meta)	1080 (Ar-Br)
4c	meta	-	-	H	1*H*-pyrrole-2-yl	3464, 3421, 3365	3132, 3089, 3059	--	1612, 1602, 1593, 1583	--	1323, 1149	1305	744, 688 (mono), 881, 752, 700 (meta)	
4d	meta	-	-	H	1-methyl-1*H*-pyrrole-2-yl	3255	3130, 3099,	2949,2856	1602, 1589, 1560	1425, 1364	1346, 1161	1307	756, 696 (mono), 864,	

							3064						773, 696 (meta)	
4e	meta	-	-	H	Furan-2-yl	3263, 3226	3151, 3136, 3099, 3064	--	1595, 1579, 1558, 1525	--	1350, 1168	1330	748, 688 (mono), 885, 759, 700 (meta)	
4f	para	-	-	H	1*H*-pyrrole-2-yl	3444, 3321, 3265	3124, 3084, 3032	--	1610, 1585, 1566, 1550, 1535	--	1325, 1155	1317	750, 702 (mono), 829 (para)	
4g	para	Br	-	H	1*H*-pyrrole-2-yl	3444, 3352, 3234	3120, 3169, 3030	--	1633, 1597, 1581, 1552, 1517	--	1334, 1163	1312	856 (para)	1080 (Ar-Br)
4h	para	OH	-	H	1*H*-pyrrole-2-yl	3371, 3286	3176, 3118, 3093, 3059	--	1606, 1585, 1568, 1541, 1508	--	1354, 1166	1300	873, 833 (para)	3479 (OH)
4i	para	-	-	H	Furan-2-yl	3340, 3257	3097, 3057, 3039	--	1616, 1598, 1566, 1548, 1516	--	1346, 1166	1321	769, 698 (mono), 862 (para)	
4j	para	Br	-	H	Furan-2-yl	3458, 3336	3143, 3109, 3095, 3068	--	1624, 1591, 1573, 1546	--	1354, 1168	1325	839, 819 (para)	1072 (Ar-Br)
4k	meta	-	-	C_2H_5-	C_2H_5-	3313, 3261	3072	2991, 2978, 2937,	1639, 1589, 1588, 1527, 1479	1442, 1427	1352, 1163	1309	746, 686 (mono) 877, 758, 698 (meta)	

								2873, 2806						
4l	para	Br	-	CH_3-	CH_3-	3425, 3385	3196, 3116, 3057	2926, 2889	1595, 1585,1575, 1550, 1489	1435	1355, 1170	1290	813, 800 (para)	1074 (Ar-Br)
4m	para	CF_3	-	CH_3-	CH_3-	3402, 3371	3188, 3120, 3062	2933	1620, 1600, 1583, 1558, 1492	1436, 1409	1325, 1174	1290	856, 827 (para)	1357, 1138, 1116 (C-F)
4n	para	OCF_3	-	CH_3-	CH_3-	3292, 3234	3107, 3022, 2976	2877, 2773, 2721	1598, 1585, 2568, 1504, 1492	1435, 1404	1342, 1168	1313	827 (para)	
4o	para	F	-	CH_3-	CH_3-	3477, 3417	3148, 3113, 3047	2789, 2727	1633, 1598, 1583, 1560, 1504, 1490	1435, 1404	1340, 1165	-	839, 829 (para)	1228 (Ar-F)
4p	para	-	CF_3	CH_3	CH_3	3323, 3251	3105, 3076	-	1629, 1600, 1585, 1562, 1494	1433	1346, 1168	1311	867, 756, 698 (meta), 800 (para)	1327, 1161, 1138 (C-F)
4q	para	CH_3	-	C_2H_5-	C_2H_5-	3429, 3419	3165, 3116, 3039	2983, 2968, 2937, 2875	1620, 1602, 1573, 1508, 1489	1411, 1404	1354, 1170	1317	815, 814 (para)	
4r	para	F	-	C_2H_5-	C_2H_5-	3429, 3305	3140, 3101,	2978, 2945,	1589, 1575, 1556, 1516,	1398	1342, 1172	1313	864, 825 (para)	1222 (Ar-F)

							3062	2883,	1500, 1489					
4s	para	-	-	CH_3-	C_3H_7-	3302, 3257	3105, 3024	2960, 2927, 2870, 2709	1579, 1564, 1529, 1492	1444, 1406	1342, 1170	1309	765, 694 (mono), 829 (para)	
4t	para	-	-	cyclopentylidene		3369, 3296	3064, 3039	2966, 2926, 2887, 2677	1660, 1633, 1577, 1562, 1492	1444, 1408	1346, 1172	1307	763, 696 (mono), 840 (para)	
4u	para	Br	-	cyclopentylidene		3417, 3379	3182, 3103, 3055	2972, 2945, 2885	1645, 1606, 1683, 1548, 1487	1413, 1398	1355, 1172	1296	819, 802 (para)	1070 (Ar-Br)
4v	para	OH	-	cyclopentylidene		3373, 3269	3190, 3116, 3068	2970, 2872, 2725	1651, 1604, 1585, 1575, 1508	1438, 1404	1340, 1166	1307	837, 829 (para)	3464 (OH)

5.1.4.2. ^{1}H-NMR Spectral Analysis

The TSC N_2 and N_4 protons were observed between δ 9.48 – 12.01 ppm. The analyses of ^{1}H NMR spectra of **4** derivatives highlight the disappearance of signals related to these protons and the formation of a new signal located between δ 6.54 – 7.01 ppm which is related to the C_5-H proton of the thiazoline ring, and these findings support the cyclization of TSCs. Similar to the intermediates, the SO_2NH_2 protons were observed between δ 7.37 – 7.55 ppm, whereas the N=C-H protons were observed between δ 7.49 – 8.35 ppm. The findings of ^{1}H NMR spectra of compounds **4a – 4v** are summarized in **Table 5-11**.

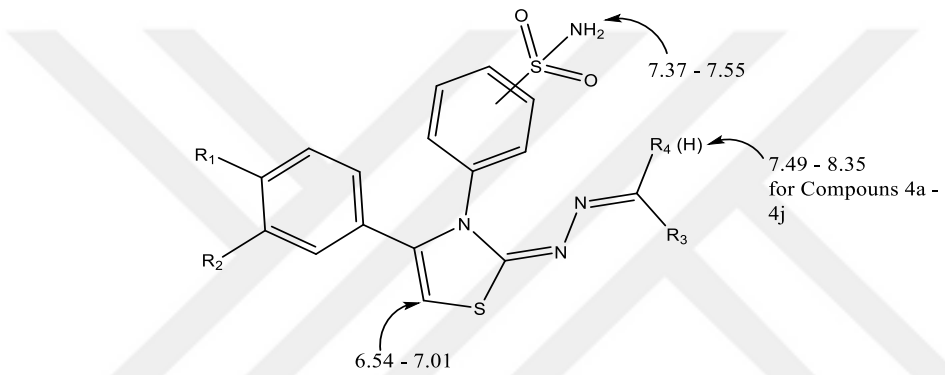

Turan-Zitouni et al. characterized the structure of 4-thiazoline-containing tetralin derivatives and observed the C_5-H proton of the thiazoline between δ 7.0 –7.19 ppm as singlets (Turan-Zitouni et al. 2018). In the ^{1}H NMR of 3-(3-benzyl-2-((4-methylbenzylidene)hydrazineylidene)-2,3-dihydrothiazol-4-yl)-2*H*-chromen-2-one, Özbey et al. ascribed the singlet signal at δ 6.23 ppm to the thiazoline C_5-H proton and the singlet at δ 7.72 ppm to the N=C-H proton (Özbey et al. 2003).

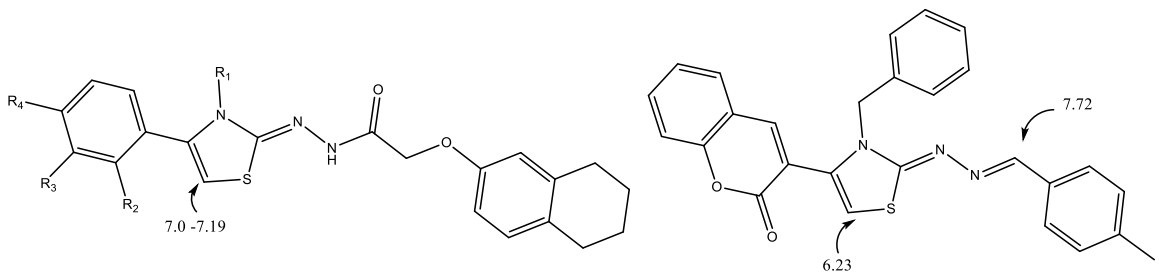

Hassan et al. characterized a series of 1-(5-(((-4-(4-bromophenyl)-3-substituedlthiazol-2(3*H*)-ylidene)hydrazineylidene)methyl)-2-methyl-1*H*-pyrrol-3-yl)ethan-1-one and observed the characteristic thiazoline C_5-H protons between δ 6.72 –

7.64 ppm and the N=C-H protons between δ 7.57 – 8.43 ppm (Hassan 2007). Recently, Mamidala et al. characterized 4-thiazoline-coumarin hybrids and observed the characteristic thiazoline C_5-H protons between δ 6.62–7.08 ppm and the N=C-H protons between δ 8.37 – 10.25 ppm (Mamidala et al. 2021)

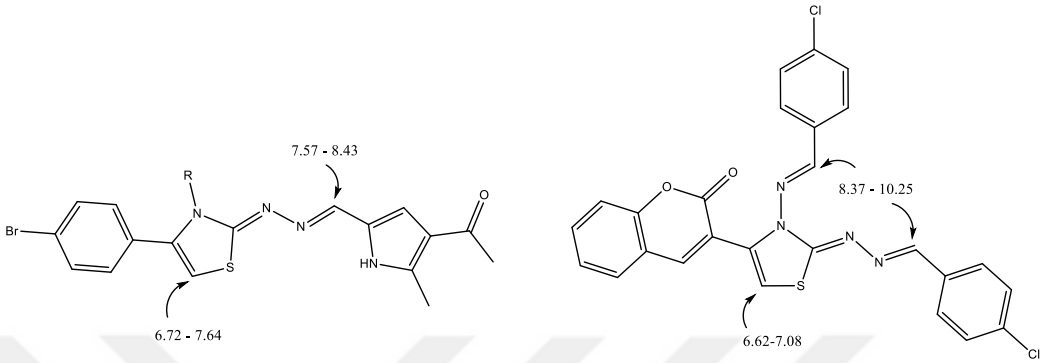

D'Ascenzio et al. characterised the structure of (*E*)-4-(4-fluorophenyl)-2-(2-(3-methylcyclopentylidene)hydrazineyl)thiazole and observed the 4-(4-fluorophenyl) $C_{2,6}$-H between 7.70 – 7.72 ppm as dd (J_{HH} = 8.6 Hz, J_{HF} = 5.0 Hz) and 4-(4-fluorophenyl) $C_{3,5}$-H protons between 7.18 – 7.20 ppm as dd (J_{HF} = 8.5 Hz, J_{HH} = 8.5 Hz). The characteristic thiazoline C_5-H proton was observed at 6.63 ppm (D'Ascenzio et al. 2014).

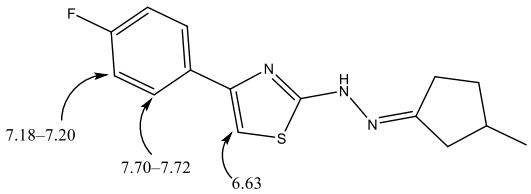

Similar to the findings of D'Ascenzio et al., the 4-(4-fluorophenyl) $C_{2,6}$-H protons are more deshielded than the 4-fluorophenyl $C_{3,5}$-H protons in compounds **4o** and **4r** containing the 4-(4-fluorophenyl) moiety. This can be attributed to the resonance effect of the fluorine atom, which, despite being highly electronegative, donates lone pair electrons, increasing the electron density of the *ortho* carbon and causing a shielding effect on the 4-(4-fluorophenyl) $C_{3,5}$-H protons. In addition, fluorine, having a spin quantum number of ½, behaves like protons and couples with adjacent protons in ^{1}H-NMR, resulting in a splitting of the *ortho* and *meta* protons with coupling constants of approximately 8.9 Hz and 5.8 Hz, respectively (Pavia et al. 2015).

In the spectrum of compound **4o**, the thiazoline C_5-H proton was observed at δ 6.69 ppm. The SO_2NH_2 protons were observed between δ 7.22 – 7.46 ppm as a broad peak beneath the peaks of 4-benzenesulfonamide $C_{3,5}$-H protons, which were observed as an apparent or pseudo doublet (AA'BB') with a coupling constant of *J*=8.6 Hz. The 4-benzenesulfonamide $C_{2,6}$-H protons were similarly observed at δ 7.77 ppm with a coupling constant of *J*=8.6 Hz. The 4-(4-fluorophenyl) $C_{3,5}$-H protons located *ortho* to both 4-F and 4-(4-fluorophenyl) $C_{2,6}$-H protons experienced an AA'BB'X splitting that looks like an apparent or a pseudo triplet (or triplet of triplets) with a coupling constant of *J*=8.6 Hz at δ 7.11 ppm. The observed triplet splitting is surprising, as one would expect two large splittings causing a doublet-doublet, as reported by D'Ascenzio et al. However, the coupling constants J_{23} and J_{3F} are coincidentally similar, which resulted in a large triplet splitting. The 4-(4-fluorophenyl) $C_{2,6}$-H protons were observed between δ 7.23 ppm as an apparent doublet of doublets (AA'BB'X) with coupling constants of *J*= 8.6, 5.2 Hz. The two aliphatic methyl protons were observed at δ 1.88 and δ 2.01 ppm (**Figure 5-18**).

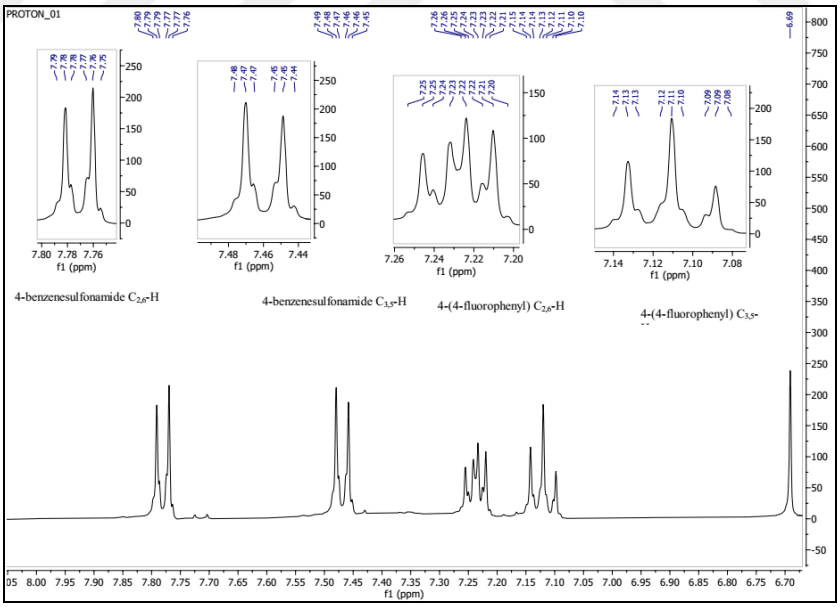

Figure 5-18: ^{1}H-NMR spectrum of compound 4o (6.7 – 8 ppm)

Similar to the spectrum of compound **4o**, spectrum, the thiazoline C_5-H proton of compound **4r** was observed at δ 6.59 ppm. The SO_2NH_2 was observed at 7.40 – 7.43

ppm as a broad peak coupled with 4-benzenesulfonamide $C_{3,5}$-H protons, which was observed at δ 7.42 ppm as a pseudo doublet (AA'BB') with a coupling constant of J=8.6 Hz. The 4-benzenesulfonamide $C_{2,6}$-H protons were observed at 7.74 ppm as a pseudo doublet (AA'BB') with a coupling constant of J=8.6 Hz. The 4-(4-fluorophenyl) $C_{3,5}$-H protons positioned in an *ortho* position to both 4-F and 4-(4-fluorophenyl) $C_{2,6}$-H protons experienced an AA'BB'X splitting (pseudo triplet) with a coupling constant of J=9.0 Hz. The 4-(4-fluorophenyl) $C_{2,6}$-H protons were observed at δ 7.22 ppm as a pseudo doublet of doublets (AA'BB'X) with J=8.3, 5.2 Hz (**Figure 5-19**).

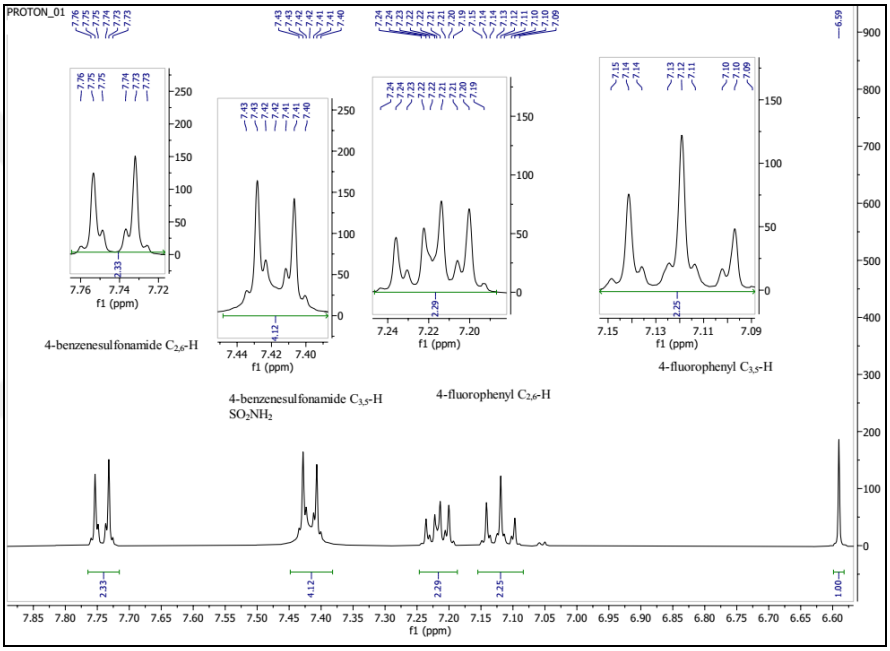

Figure 5-19: ^{1}H-NMR spectrum of compound 4r (6.6 – 7.85 ppm)

The aliphatic protons were observed as expected. The CH_2 protons overlapped as multiplets. One of the CH_3 protons was observed as a triplet whereas the other one was observed as triplet-doublet due to a second-order effect (**Figure 5-20**).

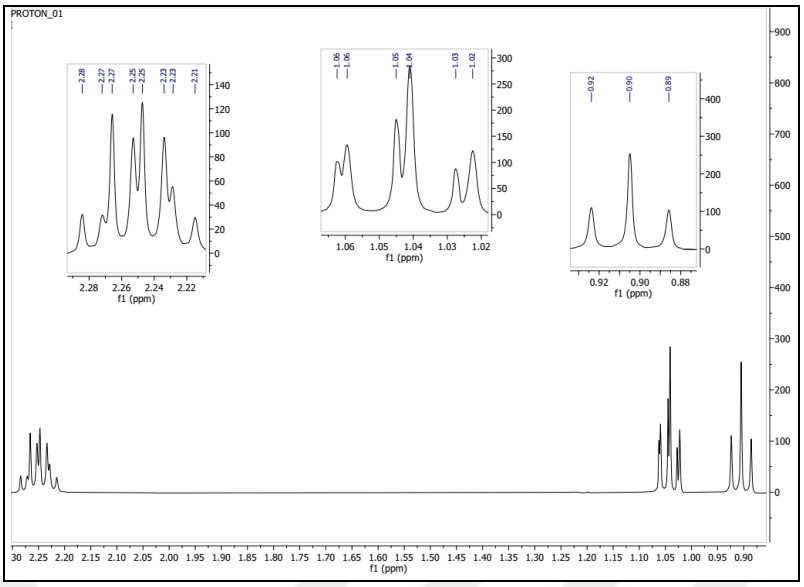

Figure 5-20: ^{1}H-NMR spectrum of compound 4r (0.9 – 2.3 ppm)

In the ^{1}H NMR spectral analysis of compounds **4g, 4j, 4l** and **4u** containing the 4-(4-bromophenyl) moiety, the Br atom reduces the electron density of the ortho carbon via inductive effect resulting in the deshielding of $C_{3,5}$-H protons, while subtly increasing the electron density of the meta carbon via resonance effect. In the ^{1}H NMR spectrum of compound **4j**, 4-(4-bromophenyl) $C_{2,6}$-H protons were observed at 7.14 ppm as AA'BB' with a *J* value of 8.6 Hz. The 4-(4-bromophenyl) $C_{3,5}$-H protons overlapped with 4-benzenesulfonamide $C_{3,5}$-H and SO_2NH_2 protons between 7.47 – 7.52 ppm. (**Figure 5-21**).

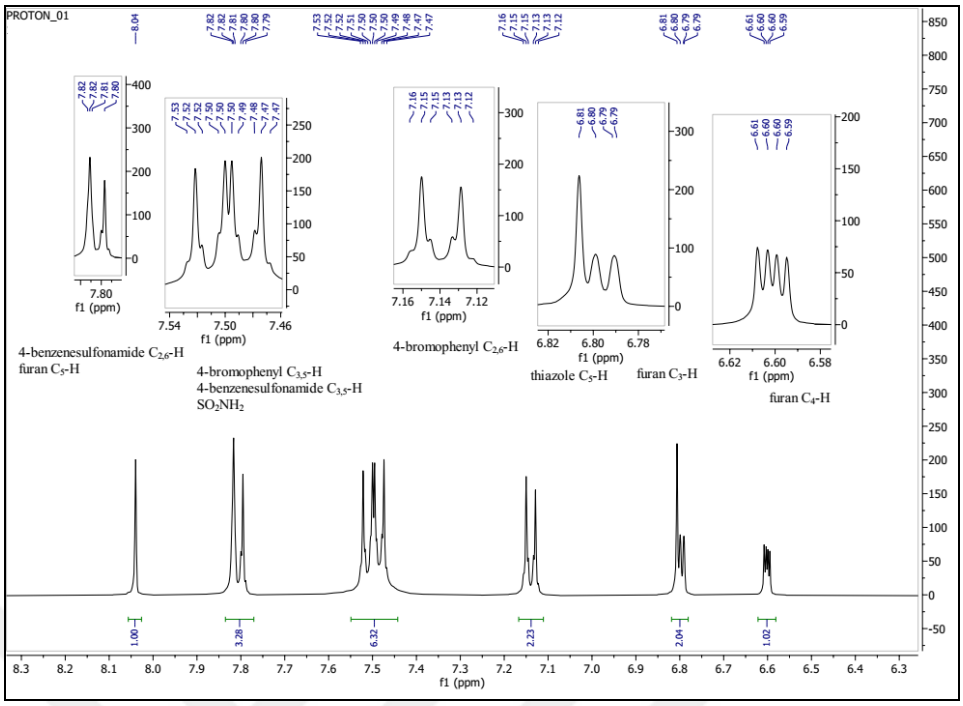

Figure 5-21: ^{1}H-NMR spectrum of compound 4j (6.3 – 8.3 ppm)

The ^{1}H-NMR spectra of compounds **4a – 4f, 4i, 4k, 4s** and **4t** followed a general pattern for the 4-(non-substituted)phenyl protons. The phenyl $C_{2,6}$-H protons resonated between δ 7.12 – 7.21 ppm as doublet-doublet with *ortho* coupling constants of J = 8.0 – 7.8 Hz and a *meta* coupling constant of J = 1.7 – 1.8 Hz save for compounds **4f, 4i, 4s** and **4t** which were observed as multiplets. The $C_{3,4,5}$-H protons were observed together between δ 7.24 – 7.31 ppm as multiplets.

In the ^{1}H NMR spectral analysis of compounds **4h** and **4v** containing the 4-(4-hydroxyphenyl) moiety, the OH proton for **4h** was observed at δ 3.42 ppm as a broad singlet, coupled with ethanol whereas the OH proton for **4v** was not observed. The -CH_3 protons on the 4-phenyl ring of compound **4q** were observed in the expected region of δ 2.23 ppm.

Table 5-11: ^{1}H NMR data of 3/4-[4-(Non)substitutedphenyl-2-(alkylidene/arylidenehydrazinylidene)-1,3-thiazol-3(*2H*)-yl]benzenesulfonamide derivatives (4a-4v)

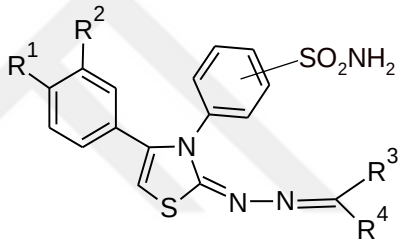

4

Compound	SO_2NH_2	R1	R2	R^3	R^4	SO_2NH_2	3/4- benzenesulfonamide protons	4-phenyl	R^3 protons	R^4 protons	Thiazole C_5-H
4a	meta	-	-	H	thiophene-2-yl	7.46 (2H, broad s, -SO_2NH_2)	7.49 (1H, ddd, *J*=7.9, 2.0, 1.1 Hz, benzenesulfonamide C_4-H), 7.56 (1H, t, *J*=7.8 Hz, benzenesulfonamide C_5-H), 7.71-7.81 (2H, m, benzenesulfonamide $C_{2,6}$-H)	7.19 (2H, dd, *J*=7.8, 1.9 Hz, phenyl $C_{2,6}$-H), 7.24-7.30 (3H, m, phenyl $C_{3,4,5}$-H)	8.35 (1H, s, N=CH)	7.10 (1H, dd, *J*=5.1, 3.5 Hz, thiophene C_4-H), 7.34 (1H, dd, 7.60 (1H, dt, *J*=5.0, 1.0 Hz, thiophene C_5-H), *J*=3.6, 1.2 Hz, thiophene C_3-H)	6.73
4b	meta	-	-	H	5-bromothiophene-2-yl-	7.46 (2H, broad s, -SO_2NH_2)	7.48 (1H, ddd, *J*=7.9, 2.1, 1.2 Hz, 3-benzenesulfonamide C_4-H), 7.56 (1H, t, *J*=8.1 Hz, 3-benzenesulfonamide C_5-H), 7.68-7.83 (2H, m, 3-benzenesulfonamide $C_{2,6}$-H)	7.18 (2H, dd, *J*=7.9, 1.8 Hz, phenyl $C_{2,6}$-H), 7.25-7.28 (3H, m, phenyl $C_{3,4,5}$-H)	8.25 (1H, s, N=CH)	7.14 (1H, d, *J*=4.2 Hz, 5-bromothiophene C_4-H), 7.22 (1H, d, *J*=3.9 Hz, 5-bromothiophene C_3-H),	6.73
4c	meta	-	-	H	1*H*-pyrrole-2-yl	7.49 (2H, broad s, -SO_2NH_2)	7.56 (1H, d, *J*=8.3 Hz, benzenesulfonamide C_4-H), 7.61 (1H, t, *J*=7.8 Hz, benzenesulfonamide C_5-H), 7.81 (1H, dt, *J*=7.7, 1.5 Hz, benzenesulfonamide C_6-H), 7.89 (1H, s, benzenesulfonamide C_2-H)	7.19 (2H, dd, *J*=8., 1.7 Hz, phenyl $C_{2,6}$-H), 7.25-7.31 (3H, m, phenyl $C_{3,4,5}$-H)	8.07 (1H, s, N=CH)	6.15 (1H, dt, *J*=3.6, 2.4 Hz, pyrrole C_4-H), 6.45-6.53 (1H, m, pyrrole C_3-H), 6.98 (1H, d, *J*=1.5 Hz, pyrrole C_5-H), 11.39 (1H, s, pyrrole NH)	6.91

4d	meta	-	-	H	1-methyl-1*H*-pyrrole-2-yl	7.48 (2H, broad s, -SO_2NH_2)	7.53 (1H, dt, *J*=7.9, 2.1 Hz, benzenesulfonamide C_4-H), 7.59 (1H, t, *J*=7.9 Hz, benzenesulfonamide C_5-H), 7.78 (1H, dt, *J*=7.8, 1.8 Hz, benzenesulfonamide C_6-H), 7.83 (1H, t, *J*=1.9 Hz, benzenesulfonamide C_2-H)	7.19 (2H, dd, *J*=7.9, 1.8 Hz, phenyl $C_{2,6}$-H), 7.24-7.29 (3H, m, phenyl $C_{3,4,5}$-H)	8.13 (1H, s, N=CH)	3.88 (3H, s, N-CH_3), 6.09 (1H, dd, *J*=3.8, 2.6 Hz, pyrrole C_4-H), 6.48 (1H, dd, *J*=3.8, 1.7 Hz, pyrrole C_3-H), 6.99 (1H, t, *J*=2.1 Hz, pyrrole C_5-H)	6.78
4e	meta	-	-	H	Furan-2-yl	7.46 (2H, broad s, -SO_2NH_2)	7.49 (1H, ddd, *J*=7.9, 2.2, 1.2 Hz, benzenesulfonamide C_4-H), 7.56 (1H, t, *J*=7.8 Hz, benzenesulfonamide C_5-H), 7.76 (1H, dt, *J*=7.8, 1.5 Hz, benzenesulfonamide C_6-H), 7.78 (1H, t, *J*=1.9 Hz, benzenesulfonamide C_2-H),	7.19 (2H, dd, *J*=7.8, 1.8 Hz, phenyl $C_{2,6}$-H), 7.25-7.30 (3H, m, phenyl $C_{3,4,5}$-H)	8.04 (1H, s, N=CH)	6.61 (1H, dd, *J*=3.4, 1.8 Hz, furan C_4-H), 6.81 (1H, d, *J*=2.7 Hz, furan C_3-H), 7.82 (1H, d, *J*=1.3 Hz, furan C_5-H)	6.75
4f	para	-	-	H	1*H*-pyrrole-2-yl	7.50 (2H, broad s, -SO_2NH_2)	7.57 (2H, d, *J*=8.2 Hz, 4-benzenesulfonamide $C_{3,5}$-H), 7.82 (2H, d, *J*=8.6 Hz, 4-benzenesulfonamide $C_{2,6}$-H), .	7.19-7.21 (2H, m, phenyl $C_{2,6}$-H), 7.27-7.29 (3H, m, phenyl $C_{3,5}$-H)	8.06 (1H, s, N=CH)	6.14 (1H, d, *J*=3.1 Hz, pyrrole C_4-H), 6.48 (1H, s, pyrrole C_3-H), 6.97 (1H, s, pyrrole C_5-H), 11.38 (1H, s, pyrrole)	6.89
4g	para	Br	-	H	1*H*-pyrrole-2-yl	7.55 (2H, broad s, -SO_2NH_2)	7.63 (2H, app.d (AA'BB'), *J*=8.6 Hz, 4-benzenesulfonamide $C_{3,5}$-H), 7.93 (2H, app.d (AA'BB'), *J*=8.6 Hz, 4-benzenesulfonamide $C_{2,6}$-H)	7.21 (2H, app.d (AA'BB'), *J*=8.2 Hz, 4-bromophenyl $C_{2,6}$-H), 7.52 (2H, app.d (AA'BB'), *J*=8.2 Hz, 4-bromophenyl $C_{3,5}$-H)	7.49 (1H, s, N=CH)	6.11 (1H, q, *J*=3.1 Hz, pyrrole C_4-H), 6.52 (1H, t, *J*=1.6 Hz, pyrrole C_3-H), 6.89 (1H, broad s, pyrrole C_5-H), 10.79 (1H, s, pyrrole)	6.85
4h	para	OH	-	H	1*H*-pyrrole-2-yl	7.53 (2H, broad s, -SO_2NH_2)	7.59 (2H, d, *J*=8.5 Hz, 4-benzenesulfonamide $C_{3,5}$-H), 7.86 (2H, d, *J*=8.5 Hz, 4-benzenesulfonamide $C_{2,6}$-H)	3.42 (broad singlet, OH, coupled with ethanol), 6.64 (2H, d, *J*=8.7 Hz, 4-hydroxyphenyl $C_{3,5}$-H), 6.99-7.01 (3H, m, pyrrole C_5-H and 4-hydroxyphenyl $C_{2,6}$-H)	8.08 (1H, s, N=CH),	6.15-6.17 (1H, m, pyrrole C_4-H), 6.51 (1H, broad singlet, pyrrole C_3-H), 6.99-7.01 (3H, m, pyrrole C_5-H and 4-hydroxyphenyl $C_{2,6}$-H), 11.41 (1H, s, pyrrole NH)	6.81

4i	para	-	-	H	Furan-2-yl	7.48 (4H, d, *J*=8.6 Hz, 4-benzenesulfonamide $C_{3,5}$-H and -SO_2NH_2)	7.48 (4H, app.d (AA'BB'), *J*=8.6 Hz, 4-benzenesulfonamide $C_{3,5}$-H and -SO_2NH_2), 7.77 (2H, app.d (AA'BB'), *J*=8.6 Hz, 4-benzenesulfonamide $C_{2,6}$-H)	7.18-7.20 (2H, m, phenyl $C_{2,6}$-H), 7.25-7.28 (3H, m, phenyl $C_{3,4,5}$-H)	8.02 (1H, s, N=CH)	6.60 (1H, dd, *J*=3.1, 1.6 Hz, furan C_4-H), 6.77 (1H, d, *J*=3.1 Hz, furan C_3-H), 7.81 (1H, d, *J*=1.6 Hz, furan C_5-H)	6.68
4j	para	Br	-	H	Furan-2-yl	7.47-7.52 (6H, m, 4-bromophenyl $C_{3,5}$-H, 4-benzenesulfonamide $C_{3,5}$-H and -SO_2NH_2)	7.47-7.52 (6H, m, 4-bromophenyl $C_{3,5}$-H, 4-benzenesulfonamide $C_{3,5}$-H and -SO_2NH_2), 7.81 (3H, d, *J*=8.6 Hz, 4-benzenesulfonamide $C_{2,6}$-H and furan C_5-H)	7.14 (2H, app.d (AA'BB'), *J*=8.6 Hz, 4-bromophenyl $C_{2,6}$-H), 7.47-7.52 (6H, m, 4-bromophenyl $C_{3,5}$-H, 4-benzenesulfonamide $C_{3,5}$-H and -SO_2NH_2)	8.04 (1H, s, N=CH)	6.60 (1H, dd, *J*=3.1, 1.6 Hz, furan C_4-H), 6.80 (1H, d, *J*=3.1 Hz, furan C_3-H), 7.81 (3H, d, *J*=8.6 Hz, 4-benzenesulfonamide $C_{2,6}$-H and furan C_5-H)	6.81
4k	meta	-	-	C_2H_5-	C_2H_5-	7.37-7.44 (3H, m, -SO_2NH_2 and 3-benzenesulfonamide C_6-H)	7.37-7.44 (3H, m, -SO_2NH_2 and 3-benzenesulfonamide C_6-H), 7.51 (1H, t, *J*=7.9 Hz, 3-benzenesulfonamide C_5-H), 7.71 (1H, d, *J*=7.9 Hz, 3-benzenesulfonamide C_4-H), 7.80 (1H, s, 3-benzenesulfonamide C_2-H)	7.12-7.21 (2H, m, phenyl $C_{2,6}$-H), 7.26 (3H, dd, *J*=5.0, 2.0 Hz, phenyl $C_{3,4,5}$-H),	0.90 (3H, t, *J*=7.6 Hz, -CH_3), , 2.23-2.31 (4H, m, 2 x CH_2)	1.06 (3H, t, *J*=7.5 Hz, -CH_3) , 2.23-2.31 (4H, m, 2 x CH_2)	6.64
4l	para	Br	-	CH_3-	CH_3-	7.38-7.50 (6H, m, 4-bromophenyl $C_{3,5}$-H and 4-benzenesulfonamide $C_{3,5}$-H and -SO_2NH_2)	7.38-7.50 (6H, m, 4-bromophenyl $C_{3,5}$-H and 4-benzenesulfonamide $C_{3,5}$-H and -SO_2NH_2), 7.76 (2H, app.d (AA'BB'), *J*=8.6 Hz, 4-benzenesulfonamide $C_{2,6}$-H)	7.11 (2H, app.d (AA'BB'), *J*=8.6 Hz, 4-bromophenyl $C_{2,6}$-H), 7.38-7.50 (6H, m, 4-bromophenyl $C_{3,5}$-H and 4-benzenesulfonamide $C_{3,5}$-H and -SO_2NH_2)	1.84 (3H, s, -CH_3)	1.94 (3H, s, -CH_3)	7.03
4m	para	CF_3	-	CH_3-	CH_3-	7.43 (2H, broad s, -SO_2NH_2)	7.46 (2H, d, *J*=8.6 Hz, 4-benzenesulfonamide $C_{3,5}$-H), 7.77 (2H, d, *J*=8.6 Hz, 4-benzenesulfonamide $C_{2,6}$-H)	7.39 (2H, d, *J*=8.2 Hz, 4-trifluoromethylphenyl $C_{2,6}$-H), 7.65 (2H, d, *J*=8.2 Hz, 4-trifluoromethylphenyl $C_{3,5}$-H)	1.84 (3H, s, -CH_3),	1.94 (3H, s, -CH_3)	6.81
4n	para	OCF_3	-	CH_3-	CH_3-	7.45 (2H, d, *J*=8.2 Hz, 4-benzenesulfon	7.45 (2H, app.d (AA'BB'), *J*=8.2 Hz, 4-benzenesulfonamide $C_{3,5}$-H and -SO_2NH_2), 7.76 (2H, app.d	7.27-7.31 (4H, m, 4-trifluoromethoxyphenyl $C_{2,3,5,6}$-H)	1.84 (3H, s, -CH_3)	1.95 (3H, s, -CH_3)	6.71

						amide $C_{3,5}$-H and -SO_2NH_2)	(AA'BB'), *J*=8.2 Hz, 4-benzenesulfonamide $C_{2,6}$-H)				
4o	para	F	-	CH_3-	CH_3-	7.22 – 7.46 (2H)	7.46 (2H, app.d (AA'BB'), *J*=8.6 Hz, 4-benzenesulfonamide $C_{3,5}$-H), 7.77 (2H, app.d (AA'BB'), *J*=8.6 Hz, 4-benzenesulfonamide $C_{2,6}$-H)	7.11 (2H, app.t (AA'BB'X), *J*=8.6 Hz, 4-fluorophenyl $C_{3,5}$-H), 7.23 (2H, app.dd (AA'BB'X), *J*=8.6, 5.5 Hz, 4-fluorophenyl $C_{2,6}$-H)	1.88 (3H, s, CH_3)	2.01 (3H, s, CH_3)	6.69
4p	para	-	CF_3	CH_3	CH_3	7.39-7.48 (6H, m, -SO_2NH_2 and 4-benzenesulfonamide $C_{3,5}$-H and 3-trifluorophenyl $C_{5,6}$-H)	7.39-7.48 (6H, m, -SO_2NH_2 and 4-benzenesulfonamide $C_{3,5}$-H and 3-trifluorophenyl $C_{5,6}$-H), 7.73 (2H, d, *J*=8.6 Hz, 4-benzenesulfonamide $C_{2,6}$-H)	7.39-7.48 (6H, m, -SO_2NH_2 and 4-benzenesulfonamide $C_{3,5}$-H and 3-trifluorophenyl $C_{5,6}$-H), 7.52 (1H, s, 3-trifluorophenyl C_2-H), 7.61 (1H, d, *J*=7.8 Hz, 3-trifluorophenyl C_4-H)	1.80 (3H, s, -CH_3)	1.90 (3H, s, -CH_3)	6.77
4q	para	CH_3	-	C_2H_5-	C_2H_5-	7.40-7.43 (4H, m, 4-benzenesulfonamide $C_{3,5}$-H, app.d (AA'BB') *J*=8.6 Hz and -SO_2NH_2)	7.40-7.43 (4H, m, 4-benzenesulfonamide $C_{3,5}$-H, app.d (AA'BB'), *J*=8.6 Hz and -SO_2NH_2), 7.75 (2H, app.d (AA'BB'), *J*=8.6 Hz, 4-benzenesulfonamide $C_{2,6}$-H)	2.23 (3H, s, 4-methylphenyl -CH_3), 7.03-7.08 (4H, m, 4-methylphenyl $C_{2,3,5,6}$-H)	0.91 (3H, t, *J*=7.4 Hz, -CH_3), 2.26 (4H, m, 2 x CH_2)	1.04 (3H, t, *J*=7.4 Hz, -CH_3), 2.26 (4H, 2 x CH_2)	6.54
4r	para	F	-	C_2H_5-	C_2H_5-	7.40-7.43 (4H, m, 4-benzenesulfonamide $C_{3,5}$-H, app.d (AA'BB'), *J*=8.6 Hz and -SO_2NH_2)	7.40-7.43 (4H, m, 4-benzenesulfonamide $C_{3,5}$-H, app.d (AA'BB'), *J*=8.6 Hz and -SO_2NH_2), 7.74 (2H, app.d (AA'BB'), *J*=8.6 Hz, 4-benzenesulfonamide $C_{2,6}$-H)	7.12 (2H, app.t (AA'BB'X), *J*=9.0 Hz, 4-fluorophenyl $C_{3,5}$-H), 7.22 (2H, app.dd (AA'BB'X), *J*=8.3, 5.2 Hz, 4-fluorophenyl $C_{2,6}$-H)	0.91 (3H, t, *J*=7.4 Hz, -CH_3), 2.25 (4H, qd, *J*=7.4, 1.9 Hz, 2 x CH_2)	1.04 (3H, td, *J*=7.4, 1.6 Hz, -CH_3), 2.25 (4H, qd, *J*=7.4, 1.9 Hz, 2 x CH_2)	6.59
4s	para	-	-	CH_3-	C_3H_7-	7.40-7.53 (4H, m, 4-benzenesulfonamide $C_{3,5}$-H, AA'BB'	7.40-7.53 (4H, m, 4-benzenesulfonamide $C_{3,5}$-H, app.d (AA'BB'), *J*=8.6 and -SO_2NH_2), 7.74 (2H, app.d (AA'BB'), *J*=8.6 Hz, 4-	7.15-7.17 (2H, m, phenyl $C_{2,6}$-H), 7.25 – 7.28 (3H, phenyl $C_{3,4,5}$-H)	1.82 (3H, s, pentan-2-ylidene C_1-H)	0.89 (3H, t, *J*=7.4 Hz, pentan-2-ylidene C_5-H), 1.52 (2H, sextet, *J*=7.4 Hz, pentan-2-ylidene C_4-H), 2.21 (2H, t,	6.63

						J=8.6, 2.4, 1.9 and -SO_2NH_2)	benzenesulfonamide $C_{2,6}$-H)			*J*=7.8 Hz, pentan-2-ylidene C_3-H)	
4t	para	-	-	cyclopentylidene		7.44 (4H, d, *J*=8.6 Hz, 4-benzenesulfonamide $C_{3,5}$-H and -SO_2NH_2)	7.44 (4H, d, *J*=8.6 Hz, 4-benzenesulfonamide $C_{3,5}$-H and -SO_2NH_2), 7.74 (2H, app.d (AA'BB'), *J*=8.6 Hz, 4-benzenesulfonamide $C_{2,6}$-H)	7.15-7.17 (2H, m, phenyl $C_{2,6}$-H), 7.25 (3H, m, phenyl $C_{3,4,5}$-H)	1.63-1.69 (4H, m, cyclopentylidene $C_{3,4}$-H), 2.27 (2H, t, *J*=6.6 Hz, cyclopentylidene $C_{2/5}$-H), 2.37 (2H, t, *J*=7.0 Hz, cyclopentylidene $C_{2/5}$-H)		6.66
4u	para	Br	-	cyclopentylidene		7.43 (4H, d, *J*=7.0 Hz, 4-bromophenyl $C_{3,5}$-H and -SO_2NH_2)	7.48 (2H, app.d (AA'BB'), *J*=8.6 Hz, 4-benzenesulfonamide $C_{3,5}$-H), 7.75 (2H, app.d (AA'BB'), *J*=8.6 Hz, 4-benzenesulfonamide $C_{2,6}$-H)	7.11 (2H, app.d (AA'BB'), *J*=8.5 Hz, 4-bromophenyl $C_{2,6}$-H), 7.43 (4H, app.d (AA'BB'), *J*=8.5 Hz, 4-bromophenyl $C_{3,5}$-H and -SO_2NH_2)	1.62-1.68 (4H, m, cyclopentylidene $C_{3,4}$-H), 2.25 (2H, t, *J*=7.0 Hz, cyclopentylidene $C_{2/5}$-H), 2.36 (2H, t, *J*=6.6 Hz, cyclopentylidene $C_{2/5}$-H)		6.69
4v	para	OH	-	cyclopentylidene		7.45 (4H, d, *J*=8.5 Hz, 4-benzenesulfonamide $C_{3,5}$-H and -SO_2NH_2)	7.45 (4H, d, *J*=8.7 Hz, 4-benzenesulfonamide $C_{3,5}$-H and -SO_2NH_2), 7.78 (2H, app.d (AA'BB'), *J*=8.7 Hz, 4-benzenesulfonamide $C_{2,6}$-H)	6.64 (2H, app.d (AA'BB'), *J*=8.7 Hz, 4-hydroxyphenyl $C_{3,5}$-H), 6.96 (2H, app.d (AA'BB'), *J*=8.7 Hz, 4-hydroxyphenyl $C_{2,6}$-H)	1.66-1.71 (4H, m, cyclopentylidene $C_{3,4}$-H), 2.30 (2H, t, *J*=6.7 Hz, cyclopentylidene $C_{2/5}$-H), 2.42 (2H, t, *J*=6.7 Hz, cyclopentylidene $C_{2/5}$-H)		6.57

5.1.4.3. ^{13}C-NMR Spectral Analysis

The ^{13}C NMR analyses of the compounds were conducted with Bruker Advance Neo (500 Hz) and Varian Mercury (Agilent) (400 MHz) using DMSO-d_6 as solvent. Similar to H, the ^{13}C atom has a spin quantum number of ½ and therefore can couple with protons. The coupling between ^{13}C and H causes multiplets to overlap, making it challenging to interpret the spectrum efficiently. For this reason, the interactions between protons and ^{13}C are all obliterated, showing the carbon peaks as singlets. This is called proton decoupling. On the other hand, the interaction between a fluorine atom with a spin quantum number of ½ and ^{13}C is not obliterated and is observed in the spectra of compounds containing fluorine.

To further substantiate the characterization of the compounds, APT and HSQC analyses on some compounds were conducted. The disappearance of signals related to C=S and the formation of a new peak located between δ 101.9 – 105.3 ppm which is related to the C_5 of the thiazoline ring confirms the cyclization of TSCs. The thiazoline C_4 and C_2 were observed between δ 140.4 – 145.4 ppm and δ 165.8 – 177.3 ppm, respectively. The N=C carbon peaks for compounds **4a – 4j** were observed between δ 141.2 – 146.8 ppm whereas the N=C carbon peaks for compounds **4k – 4v** were more downfielded to the region between δ 162.4 – 176.5 ppm. The shielding of N=C in compounds **4a – 4j** was due to the attachment of the proton as R^3. The results of the ^{13}C NMR analyses summarized in **Table 5-13** are consistent with the findings in the literature.

In the ^{13}C NMR of 3-(3-benzyl-2-((4-methylbenzylidene)hydrazineylidene)-2,3-dihydrothiazol-4-yl)-2*H*-chromen-2-one, Özbey et al. ascribed the peaks at δ 116.65, 151.95 and 159.33 ppm to the thiazoline C_5, N=C and the thiazoline C_2, respectively (Özbey et al. 2003). Ngoc Toan and Dinh Thanh characterized a series of 4-thiazoline–coumarin hybrid compounds with D-glucose/D-galactose and ascribed the carbon peaks between δ 101.5 – 101.6 ppm to thiazoline C_5 and δ 155.6 – 157.9 ppm to C=N (Ngoc Toan and Dinh Thanh 2021).

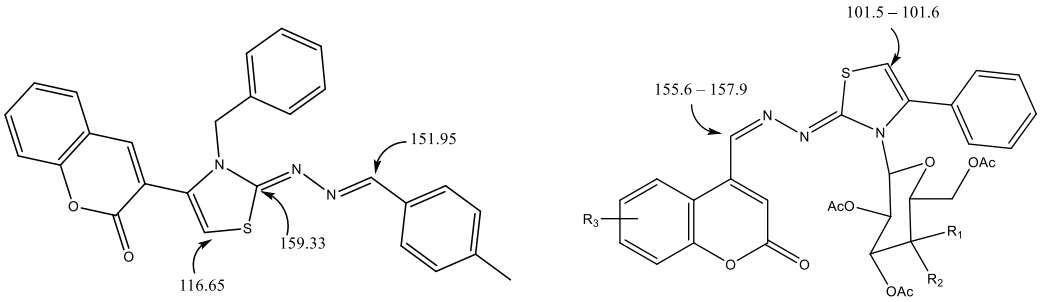

In the structural elucidation of 6,8-dichloro-3-(3-((4-chlorobenzylidene)amino)-2-((4-chlorobenzylidene)hydrazineylidene)-2,3-dihydrothiazol-4-yl)-2*H*-chromen-2-one, Mamidala et al. observed the characteristic thiazoline C_5 and C_2 at δ 105.25 and 168.05 ppm and the two N=C carbons at δ 144.14 and 151.27 ppm (Mamidala et al. 2021)

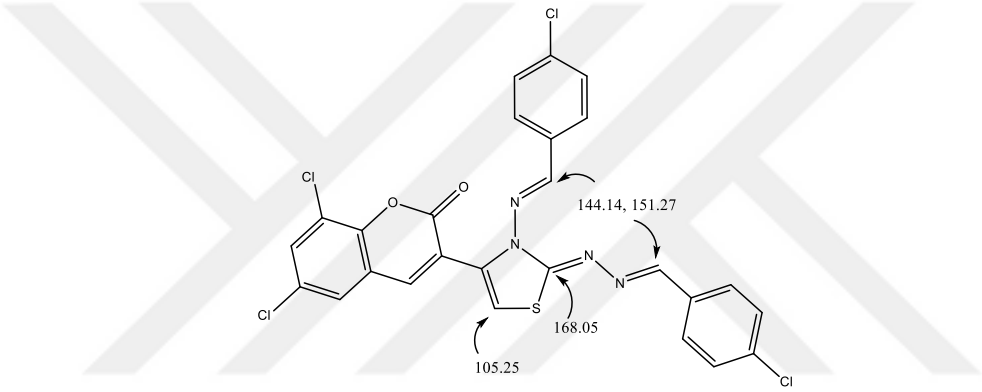

In the ^{13}C NMR of compound **4a,** the thiophene C_2, C_3, and C_4 signals were observed at δ 139.5, 130.6, and 127.9 ppm, respectively. The C_5 signal was observed together with the signals of 4-phenyl $C_{2\text{-}6}$ at δ 128.4, 128.5, 128.7, 128.8 ppm. The phenyl C_1 and 3-benzenesulfonamide C_5 peaks were observed at δ 129.8, 129.9 ppm. The phenyl C_1 is the most deshielded carbon because it is quatenary carbon and experienced a steric shift. The thiazoline C_2, C_4, and C_5 signals were seen at δ 169.0, 145.0 and 103.1, respectively. The peaks related to C_1, C_3, C_4, and $C_{2/6}$ of 3-sulfamoylphenyl were observed at δ 139.3, 137.1, 132.1 and 125.5/125.9 ppm, respectively.

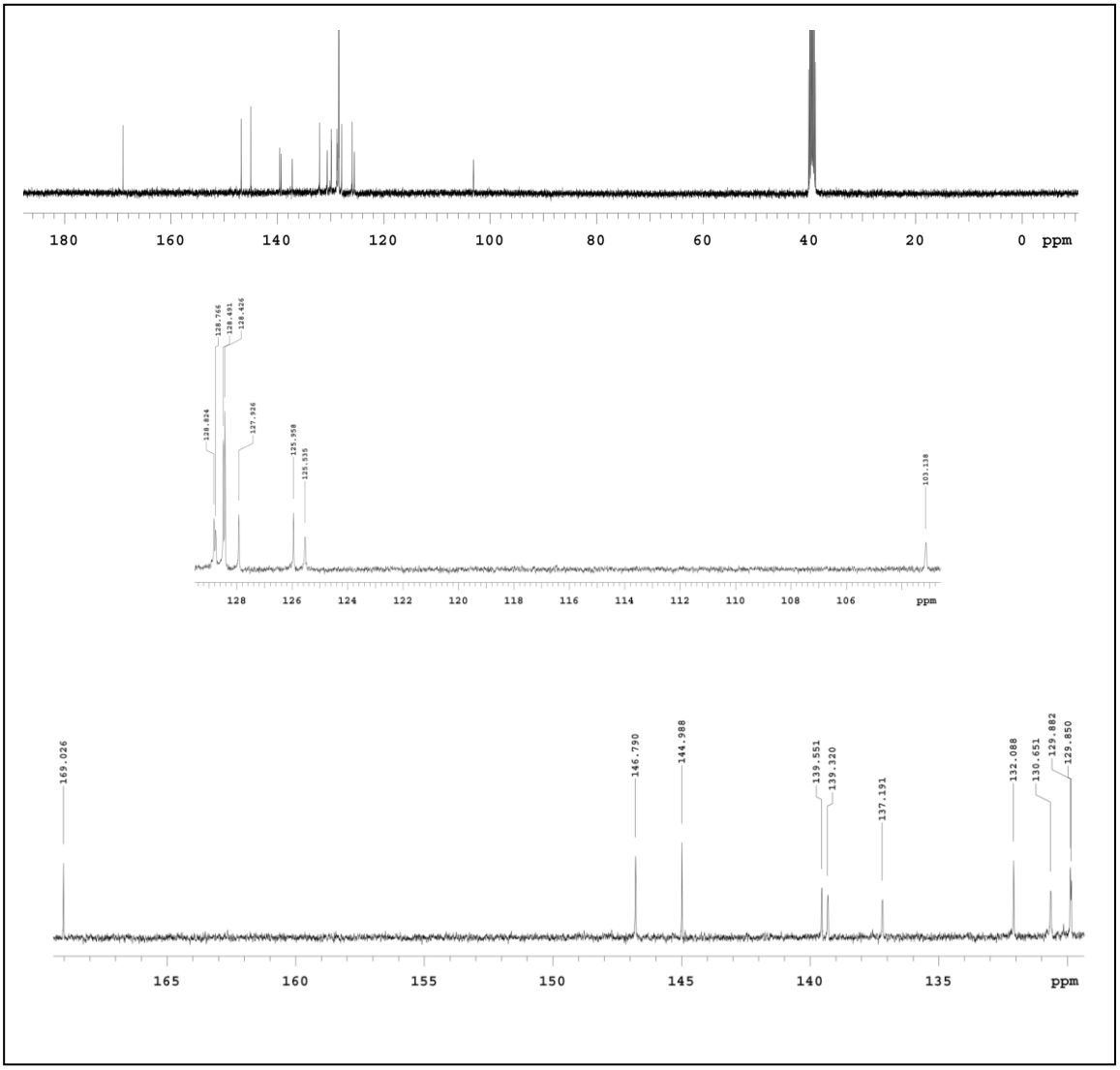

Figure 5-22: ^{13}C NMR spectrum of compound 4a

To support the ^{1}H NMR and decoupled ^{13}C NMR findings, compounds **4a, 4b, 4c, 4e, 4f, 4i, 4j, 4l, 4m, 4n, 4s a**nd **4u** were further analysed with HSQC. In this spectrum of compound **4a**, the quaternary carbons did not appear, which supports the assignment of peaks. The thiazoline C_5-H proton at δ 6.73 ppm correlated with the thiazoline C_5 peak at δ 103.1 ppm, whereas the N=CH proton signal at δ 8.35 ppm correlated with the N=C carbon signal at 146.8 ppm. The thiophene C_4-H peaks observed at δ 7.10 ppm correlated with δ 127.9 ppm, showing that this signal belongs to thiophene C_4. The thiophene C_3-H proton signal resonated at δ 7.34 ppm as a dd, correlated with the thiophene C_3 carbon signal at δ 130.6 ppm. The thiophene C_5-H proton observed at δ 7.60 ppm as a dt correlated with carbon signals at δ 128.4, 128.5, 128.8, 128.8 ppm. The rest of these carbon signals correlated with 4-phenyl C_2-

$_6$-H protons observed between δ 7.19 – 7.30 ppm. The 3-benzenesulfonamide $C_{2,6}$ carbon signals at δ 125.5 and 125.9 ppm correlated with the multiplets of 3-benzenesulfonamide $C_{2,6}$-H protons at δ 7.71-7.81 ppm. Proton signal of 3-sulfamoylphenyl C_5-H at δ 7.56 ppm correlated with 3-sulfamoylphenyl C_5 and phenyl C_1 at δ 129.8 and δ 129.9 ppm, whereas the signal of 3-sulfamoylphenyl C_4-H at δ 7.49 ppm as ddd correlated with 3-sulfamoylphenyl C_4 at δ 132.1 ppm.

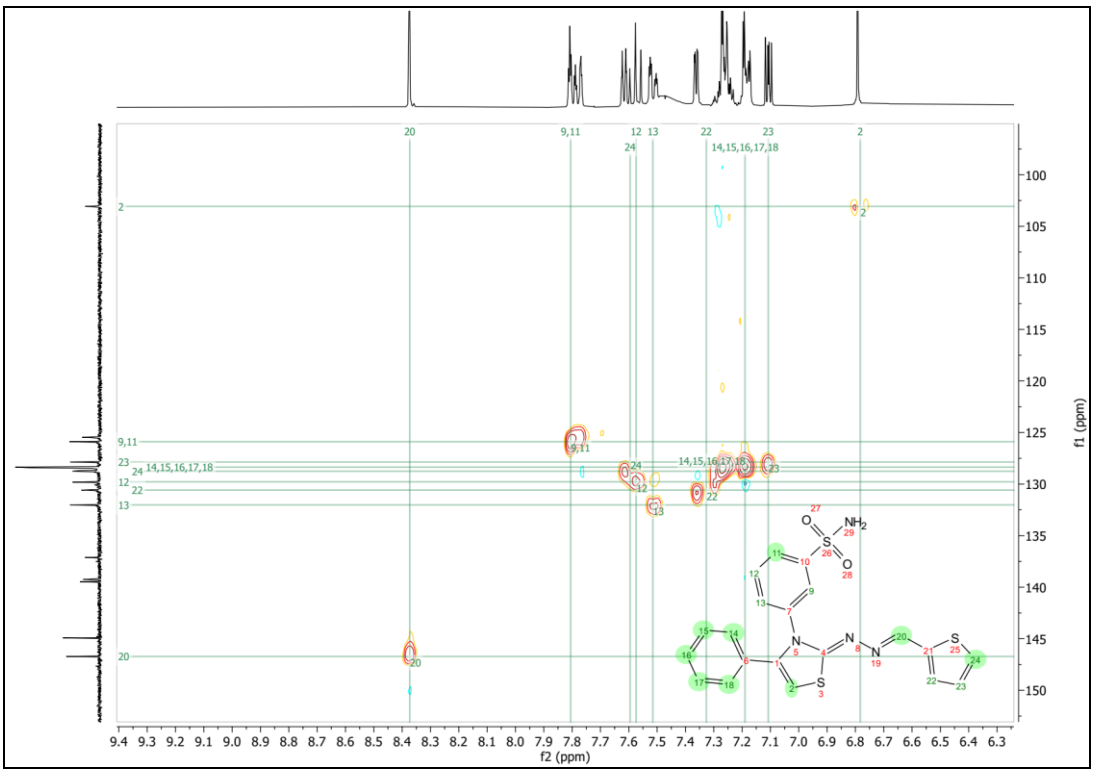

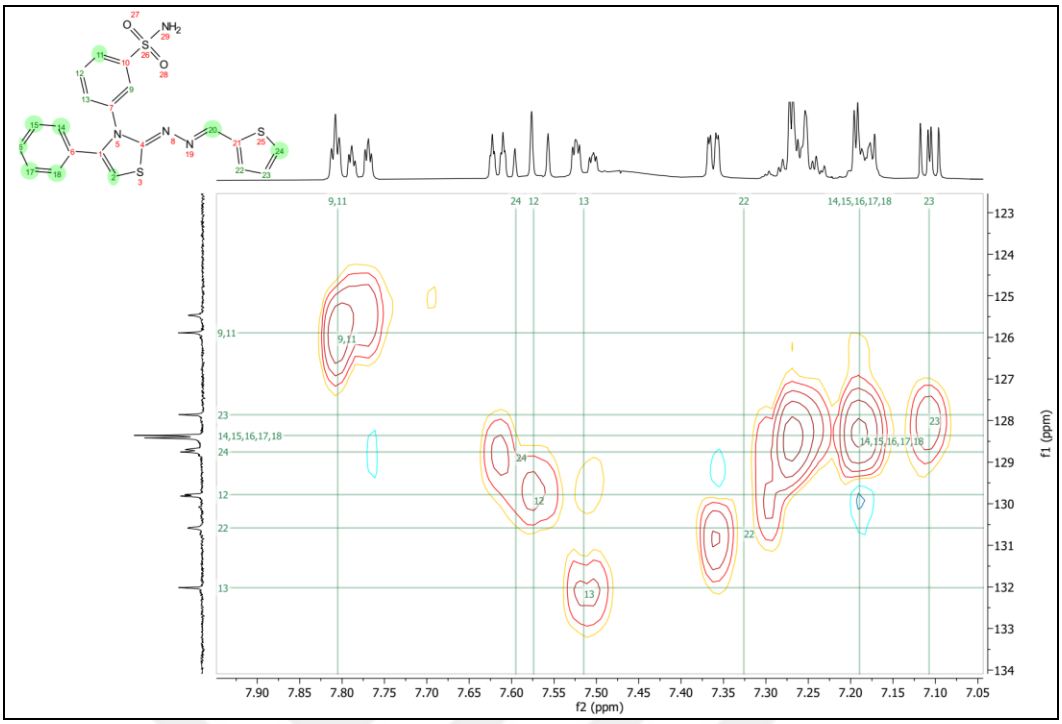

Figure 5-23: HSQC spectrum of compound 4a

The attached proton test (APT) is useful in distinguishing quaternary and secondary carbons from primary and tertiary ones. In an APT spectrum, quaternary (C) and methylene CH_2 carbons are obtained as positive signals, whereas methine CH and methyl CH_3 are obtained as negative signals. Compounds **4b, 4h, 4p** and **4v** were analysed with APT technique. Analysing the structure of compound **4b**, seven quaternary carbons and 13 methine carbons are present. In the APT spectrum of compound **4b**, 7 peaks are observed in the positive region corresponding to the quaternary carbons. However, in the negative region, 10 peaks are observed instead of 13. This is because the 4-phenyl C_2 and C_6 and the 4-phenyl C_3 and C_5 are equivalent carbons. The 4-phenyl C_1 overlapped with one of these pairs forming the tallest peak of three carbons at δ 128.9 ppm. The height of peaks does not necessarily give the integrals of peaks on ^{13}C NMR, albeit it gives a rough estimation of the number of carbons when compared to other equivalent CH_x carbons, where X is the number of hydrogens. The addition of a 5-Br to the thiophene rings marks the only difference between compounds **4a** and **4b**. The ^{13}C NMR of these two compounds showed a similar trend, with the exception of the presence of a quaternary peak at 114 ppm, which is an indication of the presence of the 5-Br-thiophene C5.

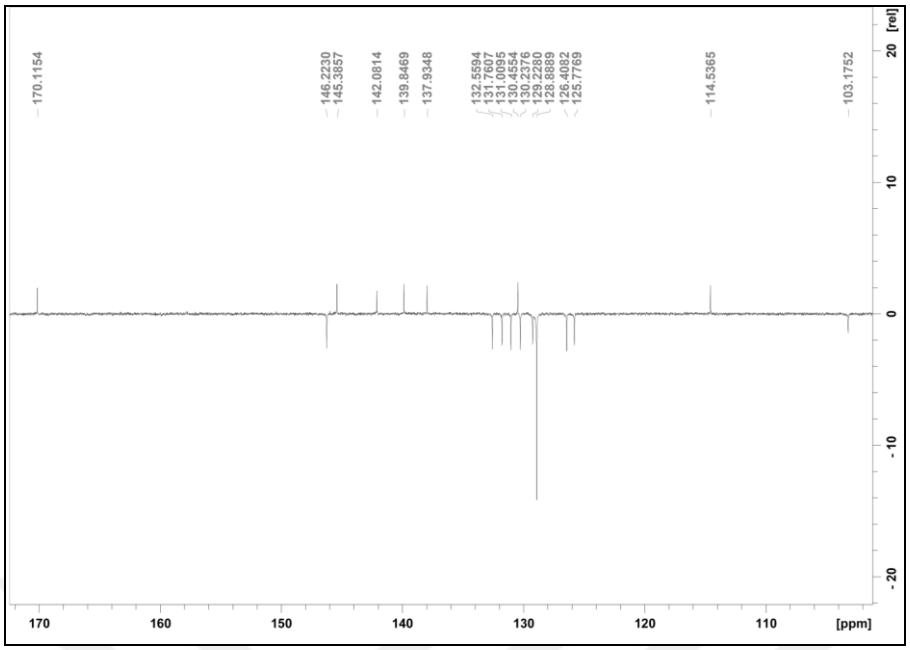

Figure 5-24: APT spectrum of compound 4b

As previously mentioned, the fluorine atom interacts with the ^{13}C nuclei causing a splitting in the ^{13}C NMR spectra. The chemical shits and the ^{13}C – F couplings constants of fluorobenzene are given in **Table 5-12** (Pavia et al. 2015)

Table 5-12: Chemical shifts and the ^{13}C – F couplings constants of fluorobenzene

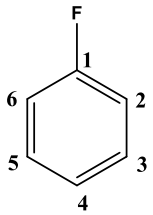

Carbon Atoms	Chemical Shift (ppm)	Splitting	Coupling constant (Hz)
C1	162.9	doublet	245
C2	115.3	doublet	20.7
C3	129.9	doublet	8.5
C4	124.0	doublet	2.5

In the ^{13}C NMR characterisation of (*E*)-4-(4-fluorophenyl)-2-(2-(3-methylcyclopentylidene)hydrazineyl)thiazole, D'Ascenzio et al. observed the 4-(4-fluorophenyl)-$C_{2,6}$ carbons at δ 127.84 ppm, 4-(4-fluorophenyl)-$C_{3,5}$ carbons at δ 116.5 ppm, 4-(4-fluorophenyl)-C_1 carbon at δ 123.98 ppm and 4-(4-fluorophenyl)-C_4 carbon at δ 163.84 ppm (D'Ascenzio et al. 2014).

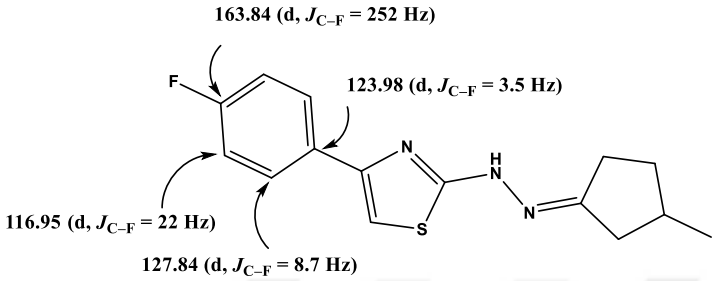

In the ^{13}C NMR of compound **4o** containing the 4-(4-fluorophenyl) moiety the 4-fluorophenyl $C_{2,6}$ carbons are more deshielded than the 4-fluorophenyl $C_{3,5}$ carbons. The 4-fluorophenyl $C_{3,5}$ carbons in an *ortho* position to the F were observed as a doublet at δ 115.4 ppm with a *J* value of 21.9 Hz, whereas the 4-fluorophenyl $C_{2,6}$ carbons in a *meta* position to the F were observed as a doublet at δ 130.5 ppm with a *J* value of 11.6 Hz. The 4-fluorophenyl C_1 carbon in a *para* position to the F was observed at δ 126.8 ppm and did not interact with F. The 4-fluorophenyl C_4 carbon directly attached to the fluorine was the most deshielded due to the direct inductive electron withdrawal of the F atom. It was observed at δ 161.9 ppm with a *J* value of 245.1 Hz. The 4-benzenesulfonamide $C_{2,6}$ carbons were observed at δ 126.1 ppm, whereas the 4-benzenesulfonamide $C_{3,5}$ carbons were observed at 128.8 ppm. The 4-benzenesulfonamide C_4 and C_1 were observed at δ 137.9 and 139.9 ppm, respectively. The thiazoline C5, C4 and C2 were observed at δ 102.6, 143.0, and 165.9 ppm, respectively, whereas the C=N carbon peak was observed at δ 163.7 ppm. The methyl carbons are more downfielded to δ 18.6 and 24.0 ppm due to their attachment to the C=N.

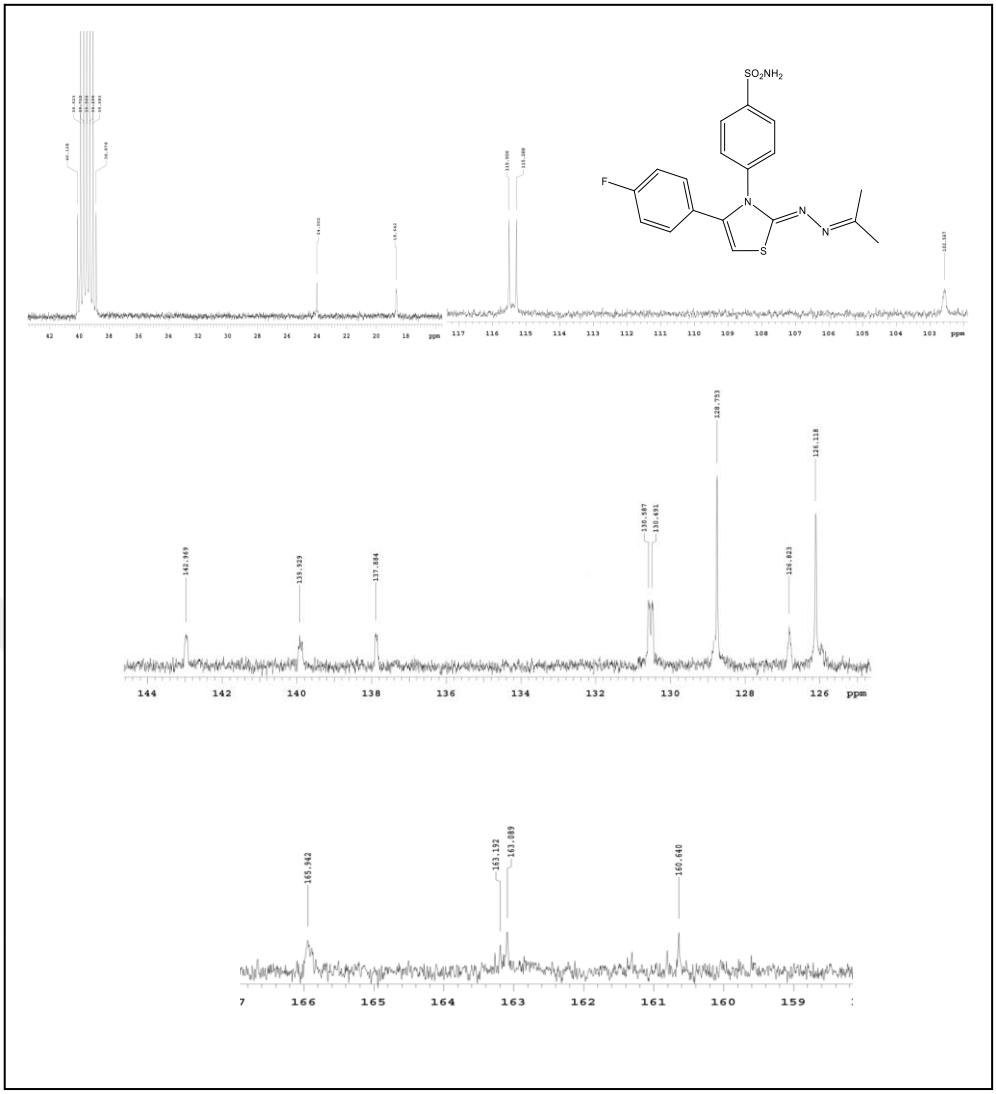

Figure 5-25: ^{13}C-NMR spectrum of compound 4o

In the spectrum of compound **4m,** the -CF_3 carbon is splitted into a tripet with a coupling constant of *J*=270.0 Hz. Although one would anticipate a 1:3:3:1 quartet splitting pattern due to the three neighbouring fluorines as per n +1 rule. However, quaternary carbons lack the Overhauser enhancement from proton decoupling and fluorinated carbons exhibit low signal intensities, which may cause the lost of one the peaks in the noise. The 4-trifluoromethylphenyl-$C_{3,5}$ carbons were observed at δ 125.9 ppm, while the trifluoromethylphenyl-$C_{2,6}$ carbons were observed in the same region with 4-benzenesulfonamide-$C_{3,5}$ at δ 129.1, 129.2, 129.6 ppm. The trifluoromethylphenyl-C_1 and trifluoromethylphenyl-C_4 carbons were observed at 135.0 and 128.9 ppm, respectively.

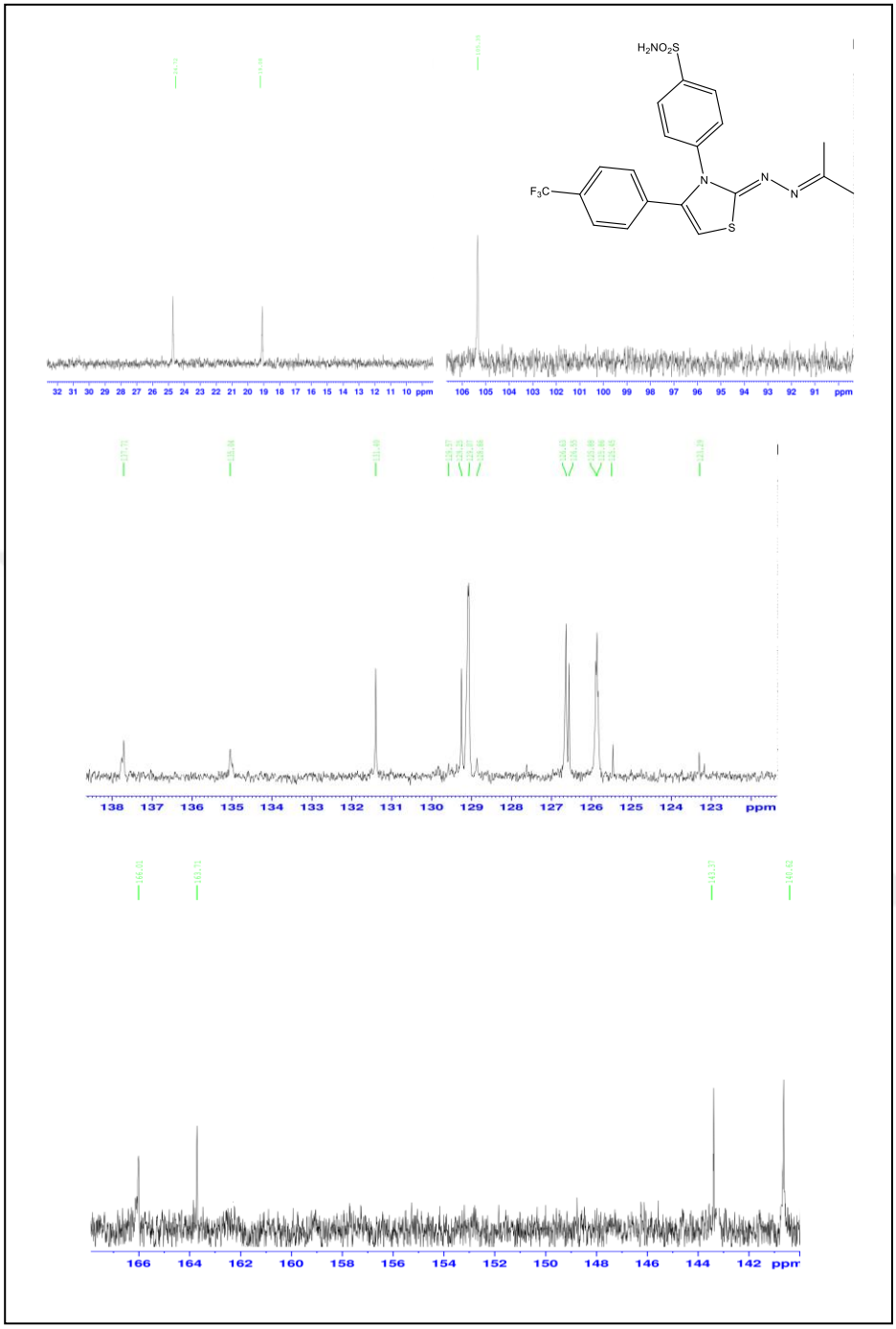

Figure 5-26: ^{13}C-NMR spectrum of compound 4m

In the HSQC spectrum of compound **4m**, the absence of the quatenary carbons supports the assignment of peaks in ^{1}H NMR and ^{13}C NMR spectra. The thiazoline C_5-H proton at δ 6.81 ppm correlated with the thiazoline C_5 peak at δ 105.3 ppm. The two CH_3 protons at δ 1.84 and 1.94 ppm correlated with the two CH_3 carbons observed at δ 19.1 and 24.7 ppm. 4-trifluoromethylphenyl $C_{3,5}$ protons observed δ 7.65 ppm correlated with at 4-

trifluoromethylphenyl $C_{3,5}$ carbons at δ 125.9 ppm, while the 4-trifluoromethylphenyl $C_{2,6}$ protons observed δ 7.39 ppm correlated with at 4-trifluoromethylphenyl $C_{2,6}$ carbons, which overlapped with 4-benzenesulfonamide $C_{3,5}$ carbons observed between δ 128.9 – 129.6 ppm. The 4-benzenesulfonamide $C_{3,5}$ carbons between δ 128.9 – 129.6 ppm also correlated with-benzenesulfonamide $C_{3,5}$ protons observed at δ 7.46 ppm, while the 4-benzenesulfonamide $C_{2,6}$ carbons observed at δ 126.5, 126.6 ppm correlated with 4-benzenesulfonamide $C_{2,6}$ protons observed at δ 7.77 ppm.

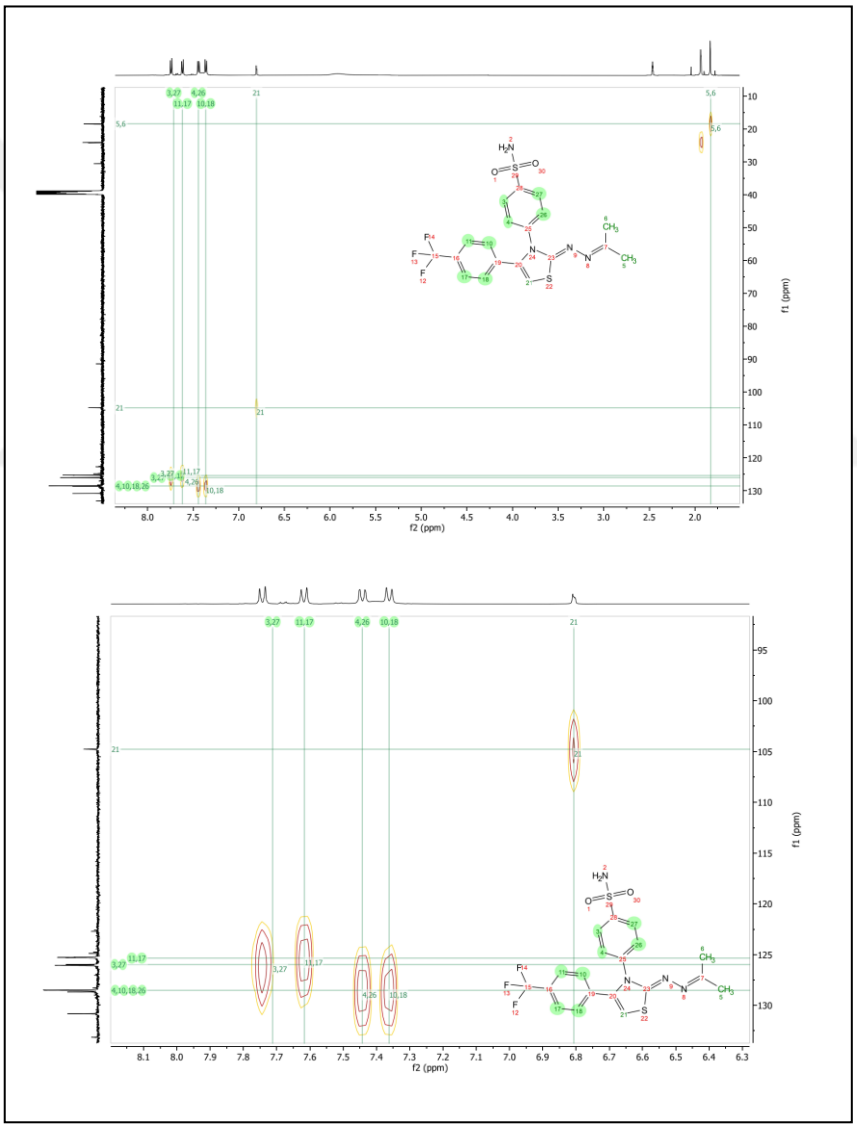

Figure 5-27: HSQC spectrum of compound 4m

Table 5-13: ^{13}C NMR data of 3/4-[4-(Non)substitutedphenyl-2-(alkylidene/arylidenehydrazinylidene)-1,3-thiazol-3(*2H*)-yl]benzenesulfonamide derivatives (4a-4v)

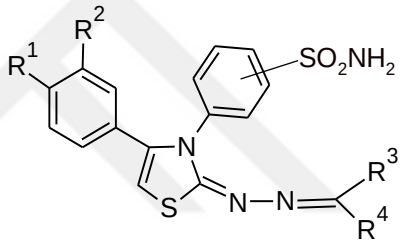

4

Compound	SO_2NH_2	R^1	R^2	R^3	R^4	3/4-benzenesulfonamide	4-phenyl	4-thiazoline	-N=C-	R^3	R^4	
4a	meta	-	-	H	thiophene-2-yl	125.5, 125.9 (3-benzenesulfonamide $C_{2,6}$), 129.8, 129.9 (phenyl C_1/ 3-benzenesulfonamide C_5), 132.1 (3-benzenesulfonamide C_4), 137.1 (3-benzenesulfonamide C_3), 139.3 (3-benzenesulfonamide C_1)	128.4, 128.5, 128.7, 128.8 (phenyl C2,3,4,5,6 / thiophene C5), 129.8, 129.9 (phenyl C1/ 3-benzenesulfonamide C5)	103.1 (thiazole C5), 145.0 (thiazole C4), 169.0 (thiazole C2)	146.8 (N=CH)	--	127.9 (thiophene C4), 128.4, 128.5, 128.7, 128.8 (phenyl C2,3,4,5,6 / thiophene C5), 130.6 (thiophene C3), 139.5 (thiophene C2)	Decoupled, HSQC
4b	meta	-	-	H	5-bromothiophene-2-yl-	125.8, 126.4 (3-benzenesulfonamide $C_{2,6}$), 130.2 (3-benzenesulfonamide C_5), 132.5 (3-benzenesulfonamide C_4), 138.0 (3-benzenesulfonamide C_3), 139.8 (3-benzenesulfonamide C_1)	128.9, 129.2 (phenyl $C_{2,3,4,5,6}$), 130.4 (phenyl C_1)	103.2 (thiazole C5), 145.4 (thiazole C4), 170.1 (thiazole C2)	146.2 (N=CH)	--	114.5 (5-bromothiophene C5), 131.0 (5-bromothiophene C4), 131.8 (5-bromothiophene C3), 142.0 (5-bromothiophene C2)	APT, HSQC

4c	meta	-	-	H	1*H*-pyrrole-2-yl	125.4, 126.3 (3-benzenesulfonamide C2,6), 128.3 (3-benzenesulfonamide C5), 129.0 (3-benzenesulfonamide C4), 136.0 (3-benzenesulfonamide C3)	127.8, 127.9, 128.0 (phenyl C2,3,4,5,6), 129.5 (phenyl C1)	103.3 (thiazole C5), 144.0 (thiazole C4), 166.6 (thiazole C2)	144.5 (N=CH)	--	109.0 (pyrrole C4), 113.2 (pyrrole C3), 122.4 (pyrrole C5), 131.5 (pyrrole C2)	Decoupled, HSQC
4d	meta	-	-	H	1-methyl-1*H*-pyrrole-2-yl	125.3, 126.9 (3-benzenesulfonamide C2,6), 129.2 (3-benzenesulfonamide C5), 129.5 (3-benzenesulfonamide C4 / phenyl C1), 137.0 (3-benzenesulfonamide C3)	127.7, 127.8, 128.1 (phenyl C2,3,4,5,6), 129.5 (3-benzenesulfonamide C4 / phenyl C1),	101.9 (thiazole C5), 144.3 (thiazole C4), 167.0 (thiazole C2)	144.5 (N=CH)	--	35.9 (CH_3), 107.6 (pyrrole C4), 114.8 (pyrrole C3), 124.6 (pyrrole C5)	Decoupled
4e	meta	-	-	H	Furan-2-yl	125.5 (3-benzenesulfonamide C6), 126.0 (furan C5, 3-benzenesulfonamide C2), 129.8 (3-benzenesulfonamide C5), 132.1 (3-benzenesulfonamide C4), 139.5 (3-benzenesulfonamide C3), 145.0 (3-benzenesulfonamide C1)	128.4, 128.5, 128.8 (phenyl C2,3,4,5,6), 137.1 (phenyl C1),	103.1 (thiazole C5), 145.2 (thiazole C4), 169.3 (thiazole C2)	141.7 (N=CH)	--	112.2 (furan C4), 114.1 (furan C3), 149.6 (furan C2), 126.0 (furan C5, 3-benzenesulfonamide C2)	Decoupled, HSQC
4f	para	-	-	H	1*H*-pyrrole-2-yl	127.1, 127.6 (4-benzenesulfonamide C2,6), 129.8 (4-benzenesulfonamide C3/5), 139.4 (4-	128.9, 129.0, 129.1, 129.5 (phenyl C2,3,4,5,6), 136.5 (phenyl C1)	104.7 (thiazole C5), 144.1 (thiazole C4), 167.6 (thiazole C2)	145.1 (N=CH)	--	110.1 (pyrrole C4), 114.4 (pyrrole C3), 123.6 (pyrrole C5), 130.2 (pyrrole C2)	Decoupled, HSQC

						benzenesulfonamide C4), 140.2 (4-benzenesulfonamide C1)						
4g	para	Br	-	H	1*H*-pyrrole-2-yl	126.7 (4-benzenesulfonamide C2,6), 129.2 (4-benzenesulfonamide C3/5), 137.6 (4-benzenesulfonamide C4), 139.8 (4-benzenesulfonamide C1)	122.1 (4-bromophenyl C4 / pyrrole C5), 129.3 (4-bromophenyl C1), 130.2 (4-bromophenyl C2,6), 131.4 (4-bromophenyl C3,5)	103.3 (thiazole C5), 140.4 (thiazole C4), 168.3 (thiazole C2)	143.8 (N=CH)	--	109.5 (pyrrole C4), 113.7 (pyrrole C3), 122.1 (4-bromophenyl C4 / pyrrole C5)	Decoupled
4h	para	OH	-	H	1*H*-pyrrole-2-yl	127.2 (4-benzenesulfonamide $C_{2,6}$), 129.9 (4-benzenesulfonamide $C_{3,5}$), 139.2 (4-benzenesulfonamide C_4), 140.8 (4-benzenesulfonamide C_1)	115.7 (4-hydroxyphenyl $C_{3,5}$), 120.6 (4-hydroxyphenyl C_1), 130.4, 130.8 (4-hydroxyphenyl $C_{2,6}$), 158.5 (4-hydroxyphenyl C_4)	103.3 (thiazole C5), 144.6 (thiazole C4), 167.7 (thiazole C2)	144.9 (N=CH)	--	110.1 (pyrrole C4), 114.5 (pyrrole C3), 123.7 (pyrrole C5)	APT
4i	para	-	-	H	Furan-2-yl	125.7, 125.8 (4-benzenesulfonamide C2,6), 128.6, 128.7 (4-benzenesulfonamide C3/5), 138.5 (4-benzenesulfonamide C4), 139.6 (4-benzenesulfonamide C1),	127.7 (phenyl C2,6), 127.8, 127.9, 128.0 (phenyl C3,4,5), 129.8 (phenyl C1)	102.1 (thiazole C5), 142.5 (thiazole C4), 168.6 (thiazole C2)	141.2 (N=CH)	--	111.8 (furan C4), 112.9 (furan C3), 144.3 (furan C5), 149.4 (furan C2)	Decoupled, HSQC

4j	para	Br	-	H	Furan-2-yl	126.8, 127.0 (4-benzenesulfonamide C2,6), 129.8, 129.9 (4-benzenesulfonamide C3/5), 138.6 (4-benzenesulfonamide C4), 140.0 (4-benzenesulfonamide C1)	122.7 (4-bromophenyl C4), 128.4 (4-bromophenyl C1), 130.9 (4-bromophenyl C2,6), 131.9, 132.0 (4-bromophenyl C3,5)	104.3 (thiazole C5), 143.9 (thiazole C4), 169.5 (thiazole C2)	142.4 (N=CH)	--	112.7 (furan C4), 114.6 (furan C3), 147.62 (furan C5), 150.1 (furan C2)	Decoupled, HSQC
4k	meta	-	-	C_2H_5-	C_2H_5-	124.5, 125.6 (3-benzenesulfonamide C2,6), 130.4 (3-benzenesulfonamide C5), 131.3 (3-benzenesulfonamide C4), 138.0 (3-benzenesulfonamide C3), 138.8 (3-benzenesulfonamide C1)	128.0, 128.4, 128.5 (phenyl C2,3,4,5,6), 129.2 (phenyl C1),	102.3 (thiazole C5), 144,6 (thiazole C4), 169.4 (thiazole C2)	166.3 (N=C)	10.4 (CH_3), 23.9 (-CH_2-)	10.8 (CH_3), 28.4 (-CH_2-)	Decoupled,
4l	para	Br	-	CH_3-	CH_3-	126.2 (4-benzenesulfonamide C2,6), 128.7 (4-benzenesulfonamide C3/5), 137.7 (4-benzenesulfonamide C4), 140.1 (4-benzenesulfonamide C1)	121.9 (4-bromophenyl C4), 129.7 (4-bromophenyl C1), 130.1 (4-bromophenyl C2,6), 131.4 (4-bromophenyl C3,5)	103.3 (thiazole C5), 142.8 (thiazole C4), 165.8 (thiazole C2)	162.4 (N=C)	18.7 (CH_3)	24.1 (CH_3)	Decoupled, HSQC
4m	para	CF_3	-	CH_3-	CH_3-	126.5, 126.6 (4-benzenesulfonamide C2,6), 128.9, 129.1, 129.2, 129.6 (4-trifluoromethylphenyl C2,4,6 / 4-	125.4 (t, distinguishable), *J*=270.0 Hz, CF_3), 125.9, 125.9 (4-trifluoromethylphenyl C3,5), 128.9, 129.1, 129.2, 129.6 (4-trifluoromethylphenyl	105.3 (thiazole C5), 143.4 (thiazole C4), 166.0 (thiazole C2)	163.7 (N=C)	19.1 (CH_3)	24.7 (CH_3)	Decoupled, HSQC

						benzenesulfonamide C3,5), 131.4 (4-trifluoromethylphenyl C4), 137.7 (4-benzenesulfonamide C4), 140.6 (4-benzenesulfonamide C1)	C2,4,6 / 4-benzenesulfonamide C3,5), 135.0 (4-trifluoromethylphenyl C1)					
4n	para	OCF_3	-	CH_3-	CH_3-	126.6 (4-benzenesulfonamide C2,6), 129.2 (4-benzenesulfonamide C3,5), 137.9 (4-benzenesulfonamide C4), 140.5 (4-benzenesulfonamide C1)	119.4 (OCF_3, non-distinguishable), 121.4 (4-trifluoromethoxyphenyl C3,5), 130.6 (4-trifluoromethoxyphenyl C2,6), 132.7 (4-trifluoromethoxyphenyl C1), 148.6 (4-trifluoromethoxyphenyl C4)	104.0 (thiazole C5), 143.3 (thiazole C4), 166.3 (thiazole C2)	163.0 (N=C),	19.14 (CH_3)	24.6 (CH_3)	Decoupled, HSQC
4o	para	F	-	CH_3-	CH_3-	126.1 (4-benzenesulfonamide C2,6), 128.8 (4-benzenesulfonamide C3,5), 137.9 (4-benzenesulfonamide C4), 139.9 (4-benzenesulfonamide C1)	115.4 (d, *J*=21.9 Hz, 4-fluorophenyl C3,5), 126.8 (4-fluorophenyl C1), 130.5 (d, *J*=11.6 Hz, 4-fluorophenyl C2,6), 161.9 (d, *J*=245.1 Hz, 4-fluorophenyl C4)	102.6 (thiazole C5), 143.0 (thiazole C4), 165.9 (thiazole C2)	163.7 (N=C)	18.6 (CH_3)	24.0 (CH_3)	Decoupled
4q	para	CH_3	-	C_2H_5-	C_2H_5-	126.4, 126.6 (4-benzenesulfonamide C2,6), 129.1, 129.4 (4-benzenesulfonamide C3,5),	21.2 (4-methylphenyl CH_3), 128.4, 129.5 (4-methylphenyl C2,3,5,6), 130.3 (4-methylphenyl C1), 138.6 (4-	102.6 (thiazole C5), 143.2 (thiazole C4), 169.9 (thiazole C2)	164.6 (N=C)	10.9 (CH_3), 24.4 (-CH_2-)	11.2 (CH_3), 28.8 (-CH_2-)	Decoupled,

						139.4 (4-benzenesulfonamide C4), 141.0 (4-benzenesulfonamide C1)	methylphenyl C4)					
4r	para	F	-	C_2H_5-	C_2H_5-	125.9 (4-benzenesulfonamide C2,6), 128.7 (4-benzenesulfonamide C3,5), 137.6 (4-benzenesulfonamide C4), 140.4 (4-benzenesulfonamide C1)	115.5 (d, *J*=22.7 Hz, 4-fluorophenyl C3/5), 127.2 (4-fluorophenyl C1), 130.3 (d, *J*=8.3 Hz, 4-fluorophenyl C2/6), 161.7 (d, *J*=259.1 Hz, 4-fluorophenyl C4)	102.5 (thiazole C5), 142.5 (thiazole C4), 168.3 (thiazole C2)	166.1 (N=C)	10.8 (CH_3), 23.8 (-CH_2-),	10.6 (CH_3), 28.4 (-CH_2-)	Decoupled
4s	para	-	-	CH_3-	C_3H_7-	126.0, 126.2 (4-benzenesulfonamide C2/6), 128.7, 128.8 (4-benzenesulfonamide C3/5), 139.1 (4-benzenesulfonamide C4), 140.0 (4-benzenesulfonamide C1)	128.1, 128.2 (phenyl C2/6), 128.5 (phenyl C3,4,5), 130.3 (phenyl C1)	103.0 (thiazole C5), 143.0 (thiazole C4), 166.6 (thiazole C2)	165.3 (N=C)	17.4 (pentan-2-ylidene C1),	13.6 (pentan-2-ylidene C5), 19.9 (pentan-2-ylidene C4), 33.9 (pentan-2-ylidene C3)	Decoupled, HSQC
4t	para	-	-	cyclopentylidene		126.1 (4-benzenesulfonamide C2,6), 128.2, 128.4, 128.7 (phenyl C2,3,4,5,6 and 4-benzenesulfonamide C3,5), 139.1 (4-benzenesulfonamide C4), 140.0 (4-benzenesulfonamide C1),	128.2, 128.4, 128.7 (phenyl C2,3,4,5,6 and 4-benzenesulfonamide C3,5), 130.1 (phenyl C1)	102.8 (thiazole C5), 142.9 (thiazole C4), 174.9 (thiazole C2)	165.9 (N=C)	24.0, 24.4 (cyclopentylidene C3,4), 30.3, 32.4 (cyclopentylidene C2,5)		Decoupled
4u	para	Br	-	cyclopentylidene		126.1 (4-benzenesulfonamide C2,6),	121.9 (4-bromophenyl C4), (4-bromophenyl C1), 130.1 (4-bromophenyl	103.4 (thiazole C5), 142.8 (thiazole C4),	165.5 (N=C)	24.0, 24.4 (cyclopentylidene C3,4), 30.2 (cyclopentylidene C2,5)		Decoupled, HSQC

					128.6 (4-benzenesulfonamide C3,5), 129.6 137.7 (4-benzenesulfonamide C4), 139.9 (4-benzenesulfonamide C1)	C2,6), 131.4 (4-bromophenyl C3,5)	174.6 (thiazole C2)			
4v	para	OH	-	cyclopentylidene	126.6 (4-benzenesulfonamide $C_{2,6}$), 129.3 (4-benzenesulfonamide $C_{3,5}$), 140.0 (4-benzenesulfonamide C_4), 140.4 (4-benzenesulfonamide C_1),	115.7 (4-hydroxyphenyl $C_{3,5}$), 121.3 (4-hydroxyphenyl C_1), 130.3 (4-hydroxyphenyl $C_{2,6}$), 158.2 (4-hydroxyphenyl C_4)	101.5 (thiazole C5), 143.5 (thiazole C4), 175.4 (thiazole C2).	166.7 (N=C)	24.5, 24.9 (cyclopentylidene C3,4), 30.8, 32.9 (cyclopentylidene C2,5)	APT

5.1.4.4. Mass Spectral Analysis

The mass spectra of compounds **4a** – **4o**, **4q**, **4s** – **4v** were obtained using the electrospray ionization method in LC/MS-MS. Ion peaks were detected using positive ionization mode. The purities of the compounds were determined with LC/MS-MS which revealed little to no contaminants. The $[M+H]^+$, $[M+2H]^+$ and $[M+3H]^+$ peaks for each compound were observed without fragments. The $[M+H]^+$ was obtained as the base peak. Compounds **4b**, **4g**, **4h**, **4l** and **4u** having a single bromine atom each showed two molecular ion peaks as $[M+H]^+$ and $[M+H]^+$+2. The ratio of the relative abundance of the isotopic peaks is almost 1:1. In addition, $[M+2H]^+$, and $[M+2H]^+$+2 were observed (**Figure 5-28**).

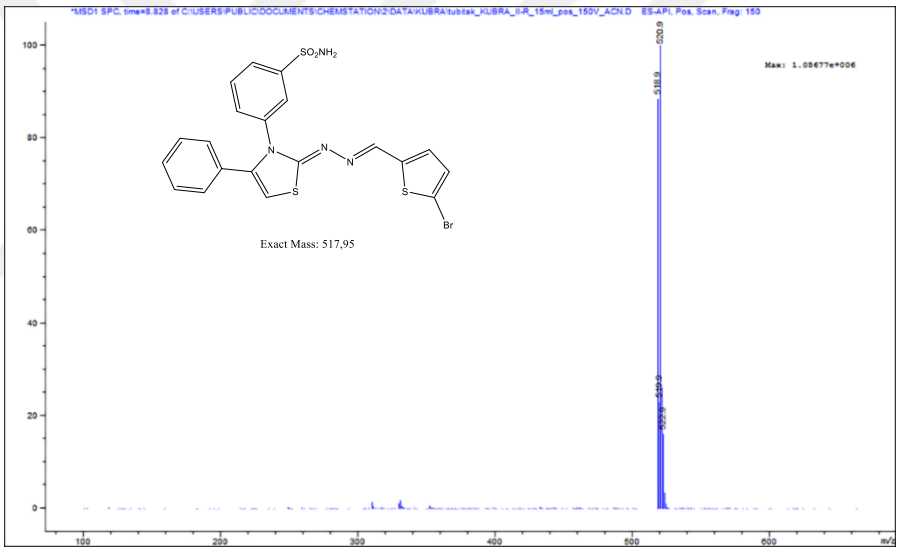

Figure 5-28: Mass spectrum of compound 4b

Similar to compound **4b**, compound **4g** having a single bromine also showed peaks related to $[M+H]^+$, $[M+H]^+$+2, $[M+2H]^+$, and $[M+2H]^+$+2 as observed in **Figure 5-29**.

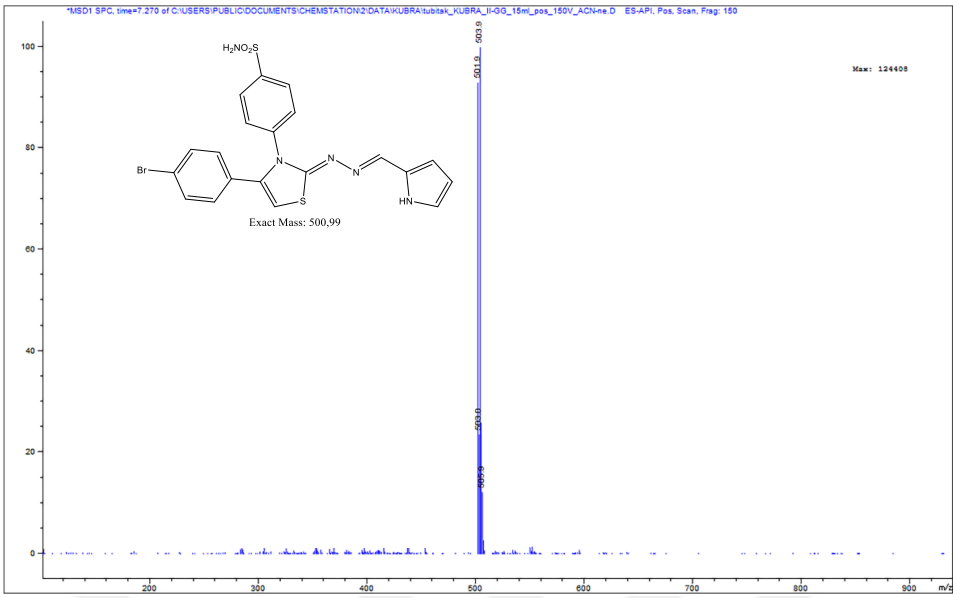

Figure 5-29: Mass spectrum of compound 4g

5.2. Single X-ray Diffraction Analyses

Crystal data and structure refinement parameters of compounds **E3**, **E8** and **4e** were presented in **Table 4-2, 8 & 14**, respectively. The molecules were crystallised in a monoclinic system with a P2 1/C space group. The crystal structures were determined by direct method and refined to have the final R indices of 0.17, 0.05 and 0.45 for **E3, E8** and **4e**, respectively. Each cell unit contains a single compound (Z=1) for **E3** and four molecules (Z=4) for **E8** and **4e**.

Compound **E3** demonstrates a trans (*E*) configuration which is supported by the torsion angle measured between N3 – N4 – C8 – C9 was -177º. If the configuration was *Z*, the torsion angle would have been close to zero. Subhashree et al. analysed the crystal structure of (*E*)-2-(2-hydroxy-5-methoxybenzylidene)hydrazine-1-carbothioamide and calculated the torsion angle as -178.9 (2) (Subhashree et al. 2017). **Tables 4-4 & 5** show the bond lengths and angles between the atoms of compound **E3**. The bond length of S2 – C7 calculated as 1.676 (9) Å, is shorter than the bond length of S1 – C1 calculated as 1.760 (8), confirming that the S2 – C7 bond is an sp2 hybridised and the TSCs were formed in the thione form. The C=N N4 – C8 bond length was calculated as 1.262 (11) Å, which is shorter than the bond lengths of sp3 N3 – C7, N2 – C7 and N2 – C4, which were found to be 1.336(11), 1.345(11) and 1.434(10) Å, respectively. The bond angles of N2 – C7 – S2, N3 – C7 – N2, and C7 – N3 – N4 were

obtained as 126.4(7), 115.4(8), and 120.1(9)º, respectively. Similar characteristic bond lengths and angles of various TSC derivatives have been reported in the literature (Yıldız et al. 2009; Rana et al. 2011; Anderson et al. 2016; Kılıç-Cıkla et al. 2016; Subhashree et al. 2017). While the bond lengths of N5 – C12, N5 – C9, C9 – C10, C10 – C11, and C11 – C12 of the furan moiety were obtained as 1.396(12), 1.329(12), 1.340(13), 1.378(15), and 1.336(15) Å, respectively, the bond angles of C9 – N5 – C12, N5 – C9 – C10 and C11 – C12 – N5 were obtained as 108.8(9), 107.7(10) and 107.0(10)º, respectively. The values are in agreement from the values obtained in the crystal studies of 2-chloro-1-(1*H*-pyrrol-2-yl)ethan-1-one (Domagała et al. 2022). The S1 – N1, S1 – O1 and S1 – C1 bond lengths of the sulfonamide group were obtained as 1.616(11), 1.437(7) and 1.760(8), respectively. In addition, the bond angles of O1 – S1 – N1, O1 – S1 – O2 and O2 – S1 – C1 were found as 108.6(5), 118.4(4), and 106.5(4), respectively. These findings are in alignment with the reported data from the literature (Haramura et al. 2003; Ceylan et al. 2015)

In structure **E8**, similar bond lengths and angles were obtained, however, the fact that both R^3 and R^4 are both methyls, no geometric isomerism is observed. The intermolecular hydrogen bondings observed between the sulfonamide groups and the π – π interactions between benzenesulfonamide rings sandwiched to each other stabilised the molecular structure, as shown in the intermolecular packing and crystal packing in **Figures 4-222 & 223.**

In structure **4e**, similar bond lengths and angles were obtained for benzenesulfonamide moiety. The geometric configuration for the C=N attached to the thiazoline ring is confirmed to *Z*, whereas the one closer to the furan ring is *E*. The thiazoline ring, the azine –C=N–N=C– and the furan ring are in the same plane. The benzenesulfonamide and the 4-phenyl rings are orthogonal to the thiazoline ring. The bond length and angles were provided in **Table 4-16 & 17**. The C=N (N3 – C15 and N4 – C16) bond lengths obtained as 1.23(3) and 1.28(3) Å are shorter than the single N2 – C5 bond which is 1.41(3). The bond length for the thiazoline C7 – C14, C7 – N2, C15 – N2, S2 – C14 and S2 – C15 obtained as 1.38(4), 1.45(3), 1.31(3), 1.71(3), and 1.78(3) Å, respectively, and the bond angles for C14 – S2 – C15, S2 – C15 – N2 and C7 – N2 – C15 as 91.4(14), 110.1(17) and 115(2)º are in accordance with the literature (Özbey et al. 2003; Ahmad et al. 2014; Pervez et al. 2015). The bond lengths of O3 – C17, O3 –

C20, C17 – C18, C18 – C19 and C19 – C20 of the furan ring were calculated as 1.22(4), 1.54(4), 1.39(4), 1.28(5), and 1.18(6), respectively, whereas the bond angles of C17 – O3 – C20, O3 – C17 – C18 and O3 – C20 – C19 were calculated as 106(3), 110(3) and 102(4)^{o}, respectively. The structure is stabilized by intermolecular hydrogen bonds formed between the sulfonamide groups (**Figure 4-224**).

5.3. Biological Activity

5.3.1. CA inhibition assay for 2-(alkylidene/arylidene)-*N*-(3/4-sulfamoylphenyl)hydrazine-1-carbothioamide derivatives (E)

The TSC intermediates (**E1 – E13**) which are novel compounds were also assayed for their carbonic anhydrase inhibition using the stopped-flow method. The compounds were tested against the cytosolic hCAI/II and the tumour-associated hCAIX/XII isoenzymes and the results were given in **Table 4-20**. Most of the compounds showed nanomolar inhibition against the isoenzymes and demonstrated a better inhibition than the reference compound, acetazolamide, against the cytosolic hCAI/II isoenzymes. Besides, the compounds, generally, were not selective towards the tumour-associated hCAIX/XII over the cytosolic hCAI/II isoenzymes. Compound **E13** recorded the highest inhibition against hCAI and hCAIX with K_i values of 2.29 nM and 75.0 nM, respectively. Compounds **E11** and **E4** have the highest inhibition against hCAII and hCAXII with K_i values of 0.31 nM and 77.7 nM, respectively. From **Table 4-20**, it could be inferred that the *para* position of the sulfonamide groups favours the inhibitory activity against all the isoenzymes and the *meta* position favours selectivity towards hCAIX/XII over hCAI/II isoenzymes. Compound **E2** with a *meta* SO_2NH_2 and R^4 as 5-bromothiophene-2-yl showed the highest selectivity towards hCAIX over hCAI and hCAII with selectivity indexes of 38.3 and 8.8, respectively. Again, compound **E2** demonstrated selectivity indexes for hCAI / hCAXII and hCAII / hCAXII as 45.2 and 10.4, respectively. Compound **E8** with *meta* SO_2NH_2 and R^3= R^4 (CH_3) showed the lowest inhibition against hCAIX and hCAXII but also showed selectivity towards hCAIX and hCAXII over hCAI and hCAII. The change of *meta* SO_2NH_2 to *para* SO_2NH_2 (**E10**) enhanced inhibition against all the enzymes and drastically reduced selectivity towards hCAIX and hCAXII.

Table 5-14: Selectivity ratios for the inhibition of hCAIX and hCAXII over hCAI and hCAII for E1 – E13

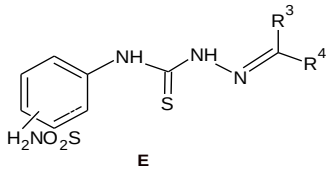

E

				K_i (nM) Selectivity Ratio			
Compound	**SO_2NH_2**	**R^3**	**R^4**	**hCA I / hCA IX**	**hCA II / hCA IX**	**hCA I / hCA XII**	**hCA II / hCA XII**
E1	meta	H	thiophene-2-yl-	8.5	0.5	9.0	0.5
E2	meta	H	5-bromothiophene-2-yl	38.3	8.8	45.2	10.4
E3	meta	H	Pyrrole-2-yl	2.6	0.5	2.6	0.5
E4	meta	H	1-methylpyrrole-2-yl	2.6	1.0	3.0	1.2
E5	meta	H	Furan-2-yl	4.3	0.6	4.9	0.7
E6	para	H	Pyrrole-2-yl	0.8	0.2	0.3	0.1
E7	para	H	Furan-2-yl	0.1	0.0	0.1	0.0
E8	meta	CH_3	CH_3	12.1	2.9	6.7	1.6
E9	meta	C_2H_5	C_2H_5	0.9	0.1	0.8	0.1
E10	para	CH_3	CH_3	0.6	0.1	0.7	0.1
E11	para	C_2H_5	C_2H_5	0.1	0.0	0.0	0.0
E12	para	CH_3	C_3H_7	0.1	0.0	0.1	0.0
E13	para	cyclopentylidene		2.29	0.0	0.0	0.0
Acetazolamide	-	-	-	10.0	0.5	43.9	2.2

5.3.2. CA inhibition assay for 3/4-[4-(non)substitutedphenyl-2-(alkylidene/arylidenehydrazinylidene)-1,3-thiazol-3(2*H*)-yl]benzenesulfonamide derivatives (4a – 4v)

Compounds **4a – 4v** were evaluated for their inhibitory activity against the off-target cytosolic hCAI and hCAII and the cancer-associated hCAIX and hCAXII using the stopped-flow CO_2 hydrase assay. The *K*i values of the compounds against these isozymes and standard drug acetazolamide are summarized in **Table 4-21**. Compared to compounds **E1 – E13**, it is interesting that the application of the dual tail approach has significantly enhanced selectivity towards the tumour-associated hCAIX and hCAXII over the ubiquitous hCAI and hCAII except compounds **4d**, **4e**, and **4q**. The position of the SO_2NH_2 and the nature of R^1 – R^4 affect the activity.

Comparing the impact of the position of the SO_2NH_2 group, it is observed that the *para* position of the SO_2NH_2 group generally improved both activity and selectivity towards hCAIX and hCAXII over hCAI and hCAII. Shifting the SO_2NH_2 (**4d**) from *meta* to *para* - SO_2NH_2 (**4f**) improved the activity against hCAIX from 84.3 to 69.8 nM and improved the selectivity over hCAI and hCAII to 43 and 80 folds, respectively. While the inhibition potency of compound **4f** against hCAXII decreased by 3.6 times, the selectivity over hCAI and hCAII increased to 10 and 17 folds, respectively. Again, the shift of *meta* SO_2NH_2 (**4e**) to *para* SO_2NH_2 (**4i**) has improved the inhibition potency against hCAIX from 94.4 to 82.0 nM with selectivity indexes of 72.6 and 32.8 for hCAI/hCAIX and hCAII/hCAIX, respectively. On the other hand, compound **4i** expressing a lesser inhibition potency than **4e** against hCAXII showed a higher selectivity to hCAXII over hCAI and hCAII with selectivity indexes of 81.3 and 36.8 for hCAI/hCAXII and hCAII/hCAXII, respectively. From these findings, it could be predicted that while para SO_2NH_2 slightly reduces potency against hCAXII, it slightly improves potency against hCAIX and generally improves selectivity over the ubiquitous hCAI and hCAII.

Comparing compounds **4f** and **4g**, **4i** and **4j**, and **4t** and **4u**, the *para* substitution of Br on the phenyl ring did not have any parallel effect on the inhibitory activity against hCAIX and hCAXII. However, comparing the **lead compound** with compound **4q**, the replacement of Br with CH_3 reduced the inhibition potency against hCAIX by 6.6 times, but the selectivity over hCAI and hCAII increased by 1.3 and 235 times, respectively. On the other hand, the activity against hCAXII was reduced by 33 times and the selectivity over hCAI was reduced by approximately 4 times, whereas the selectivity over hCAII was increased by 48 times. Also, the replacement of Br with F reduced the activity of compound **4r** against hCAIX by 6 times but increased the selectivity over hCAI and hCAII by 69 times and 38 times, respectively. Meanwhile, the activity against hCAXII and the selectivity over hCAI were reduced by 48 and 3.6 times, respectively, but the selectivity was increased by 30.8 times. The para substitution of OH on the phenyl ring significantly reduced both the activity against hCAIX and hCAXII and the selectivity over hCAI and hCAII in **4h** and **4v**. Comparing compounds **4l** – **4o**, replacement of Br with F reduced the activity of compound **4o** thrice against hCAIX and led to the loss of selectivity over hCAI and hCAII, however, activity against hCAXII against increased 2.3-fold but no significant improvement on

selectivity. While the replacement of Br with CF_3 slightly improved the activity of compound **4m** against hCAIX and reduced the selectivity over hCAI and hCAII, it notably reduced its activity against hCAXII by 6.6 times with a complete loss of selectivity over hCAI and hCAII. A decrease in activity against both hCAIX and hCAXII was observed with the replacement of Br with OCF_3, however, selectivity towards hCAIX over hCAI and hCAII slightly improved whiles selectivity towards hCAXII over hCAI and hCAII decreased twice.

Comparison of the effect of R^3 and R^4 on the activity shows that replacing the diethyl group of the **lead compound** with 1*H*-pyrrole-2-yl reduced the potency of **4g** against hCAIX by 7 times but the selectivity indexes for hCAI/hCAIX increased from 58 to 72.7 and for hCAII/hCAIX from 0.3 to 55.9. On the other hand, the potency against hCAXII was reduced by 31.4 times, but the selectivity index for hCAI/hCAXII decreased from 301 to 84.1 and the selectivity index for hCAII/hCAXII increased from 1.5 to 64.7. Similar observations were made with compound **4j**. Replacing the diethyl group with 2-furyl reduced the potency of **4j** against hCAIX by 6.5 times but the selectivity indexes for hCAI/hCAIX increased from 58 to 94.8 and for hCAII/hCAIX from 0.3 to 33.8. On the other hand, the potency against hCAXII was reduced by 32 times, but the selectivity index for hCAI/hCAXII decreased from 301.3 to 99.6 and the selectivity index for hCAII/hCAXII increased from 1.5 to 35.5. Therefore, it could be deduced that R^3 and R^4 being aromatic reduces activity against hCAIX and hCAXII, however, while it significantly increased the selectivity towards hCAIX over hCAI and hCAII, and the selectivity towards hCAXII over hCAII, it reduced the selectivity towards hCAXII over hCAI. Substitution of the diethyl group with dimethyl reduced the activity of compound **4l** against hCAIX and hCAXII by 6.2 and 37.3 times, respectively, and decreased the selectivity indexes for hCAI/hCAIX from 58 to 8.6 and for hCAI/hCAXII from 301.3 to 7.4. Meanwhile, the selectivity indexes for hCAII/hCAIX increased from 0.3 to 5.5 and 1.5 to 4.8 for hCAII/hCAXII. The replacement of diethyl with cyclopentyl reduced the activity of compound **4u** against both hCAIX and hCAXII by 7 and 30 times, respectively, however, the selectivity over hCAI and hCAII was enhanced the most with selectivity indexes for hCAI/hCAIX and hCAII/hCAIX as 531.4 and for hCAI/hCAXII and hCAII/hCAXII as 646.8. It could be derived from these findings that the replacement of the diethyl group in the lead

compound with aromatic rings improved the selectivity, whereas the replacement with a similar aliphatic group, but less flexible significantly increased the selectivity.

Table 5-15: Selectivity ratios for the inhibition of hCAIX and hCAXII over hCAI and hCAII for 4a – 4v

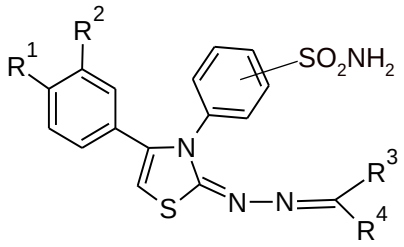

4

Compound	SO_2NH_2	R_1	R_2	R_3	R_4	K_i (nM) Selectivity Ratio			
						hCAI/ hCAIX	**hCAII/ hCAIX**	**hCAI/ hCAXII**	**hCAII/ hCAXII**
Lead	para	Br	-	C_2H_5-	C_2H_5-	58.0	0.3	301.3	1.5
4a	meta	-	-	H	thiophene-2-yl	7.2	6.3	6.3	5.5
4b	meta	-	-	H	5-bromothiophene-2-yl-	7.7	554.9	8.7	631.3
4c	meta	-	-	H	1*H*-pyrrole-2-yl	1.0	1.8	1.0	1.7
4d	meta	-	-	H	1-methyl-1*H*-pyrrole-2-yl	77.4	10.0	82.2	10.6
4e	meta	-	-	H	Furan-2-yl	7.4	0.7	11.0	1.1
4f	para	-	-	H	1*H*-pyrrole-2-yl	48.3	80.2	10.3	17.1
4g	para	Br	-	H	1*H*-pyrrole-2-yl	72.7	55.9	84.1	64.7
4h	para	OH	-	H	1*H*-pyrrole-2-yl	3.4	0.3	8.7	0.9
4i	para	-	-	H	Furan-2-yl	72.6	32.8	81.3	36.8
4j	para	Br	-	H	Furan-2-yl	94.8	33.8	99.6	35.5
4k	meta	-	-	C_2H_5-	C_2H_5-	33.3	56.1	38.2	64.2
4l	para	Br	-	CH_3-	CH_3-	8.6	5.5	7.4	4.8
4m	para	CF_3	-	CH_3-	CH_3-	8.3	4.4	1.0	0.5
4n	para	OCF_3	-	CH_3-	CH_3-	9.3	5.6	4.0	2.4
4o	para	F	-	CH_3-	CH_3-	0.2	0.0	1.4	0.1
4p	para	-	CF_3	CH_3	CH_3	3.3	1.1	1.4	0.5
4q	para	CH_3	-	C_2H_5-	C_2H_5-	75.2	70.6	77.2	72.5
4r	para	F	-	C_2H_5-	C_2H_5-	69.4	38.4	83.6	46.2

4s	para	-	-	CH_3-	C_3H_7-	85.6	48.2	75.4	42.5
4t	para	-	-	cyclopentylidene		606.1	606.1	656.2	656.2
4u	para	Br	-	cyclopentylidene		531.3	531.3	646.8	646.8
4v	para	OH	-	cyclopentylidene		6.3	6.3	5.6	5.6
Acetazolamide	-	-	-	-	-	10	0.5	43.9	2.2

5.3.3. Cytotoxicity of 3/4-[4-(Non)substitutedphenyl-2-(alkylidene/arylidenehydrazinylidene)-1,3-thiazol-3(2*H*)-yl]benzenesulfonamide derivatives (4a – 4v)

Some of the synthesized compounds from 3/4-[2-(alkylidene/arylidenehydrazinylidene)-4-(non)substitutedphenyl-1,3-thiazol-3(2*H*)-yl]benzenesulfonamide derivatives that showed selectivity towards the tumour-associated hCAIX and hCAXII over hCAI and hCAII were selected to be tested for their anticancer activity against a series of cancer cell lines. Several studies have reported the upregulation of hCAIX and hCAXII in these cancer cells except for Caco-2 (Ivanov et al. 2001; Pijnenborg et al. 2007; Dubois et al. 2009; Svastova et al. 2012; Kumar et al. 2013; Tafreshi et al. 2014; Klier et al. 2016; Imbrasaitė et al. 2019; Lin et al. 2021; Matulienė et al. 2022). The results of the anticancer test were summarized in **Table 4-22**. Among the selected compounds, compound **4g** was found to be the most potent with a wide range of anticancer activity against the cancer cell lines, showing a mean IC_{50} value of 12.59 µg/mL. It inhibited MCF-7, A549, HT-29 and Caco-2 with IC_{50} values of 1.98, 7.61, 4.84 and 2.20 µg/mL, respectively. Compounds **4f** and **4h** were inactive against the cell lines. Compound **4i** has moderate activity against Caco-2 with an IC_{50} value of 20.43 µg/mL, but it is inactive against the other cell lines.

Compound **4b** showed the highest potency against ECC-1 with an IC_{50} value of 8.24 µg/mL and a selectivity index of 2.01. Compound **4u** with an IC_{50} value of 18.00 µg/mL showed the highest selectivity over HUVEC with a selectivity index of >5.56. Compounds **4f**, **4h** and **4i** were not active against ECC-1 (**Table 5-16**).

Table 5-16: Cytotoxicity on endometrium cancer cell line (ECC-1)

Compound	ECC-1	HUVEC
4a	15.97±1.66	33.98±1.30
4b	8.24±0.41	16.58±0.25

4f	–	–
4g	24.74±1.56	40.87±1.25
4h	>100	–
4i	–	>100
4j	16.61±0.80	47.23±1.11
4k	42.99±2.96	52.03±3.21
4l	25.61±1.58	61.39±0.64
4m	60.79±2.08	77.32±0.32
4n	32.77±2.02	46.21±0.25
4o	33.63±1.54	54.91±0.60
4p	52.32±2.14	58.33±1.10
4r	49.58±0.09	59.23±2.95
4s	30.84±1.71	72.53±1.98
4t	19.04±0.70	61.53±0.29
4u	18.00±0.81	>100
4v	51.74±1.25	71.64±2.12
5-FU	**8.74±0.34**	**33.45±0.12**

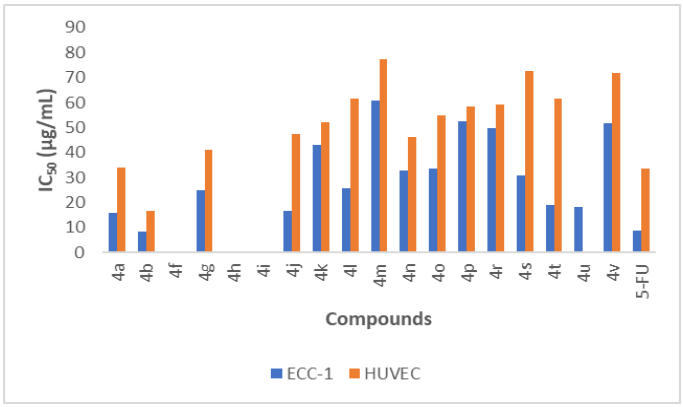

Compound **4g** with an IC_{50} value of 1.98 µg/mL and a selectivity index of 20.64 showed the highest selectivity and the best cytotoxic activity against the breast cancer cell line, MCF-7. All the compounds, with the exception of compounds **4f**, **4h**, **4i**, **4r**, and **4t**, demonstrated more cytotoxicity than the reference drug, **5-FU**. Compound **4g** showed enhanced activity against MCF-7 by 11 and 33 times compared to the **lead compound** and **5-FU**, respectively **(Table 5-17).**

Table 5-17: Cytotoxicity on breast cancer cell line (MCF-7)

Compounds	MCF-7	HUVEC
4a	14.88±0.35	33.98±1.30
4b	11.42±0.48	16.58±0.25
4f	–	–
4g	1.98±0.06	40.87±1.25
4h	>100	–
4i	–	>100
4j	5.90±0.27	47.23±1.11
4k	45.22±0.94	52.03±3.21
4l	12.23±0.74	61.39±0.64
4m	44.83±0.88	77.32±0.32
4n	30.34±1.31	46.21±0.25

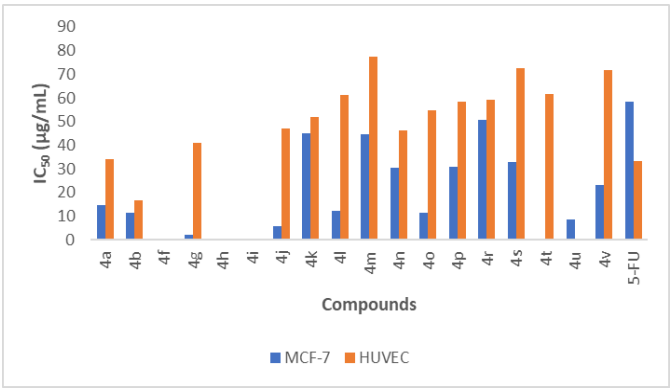

4o	11.46±0.50	54.91±0.60
4p	30.73±1.40	58.33±1.10
4r	50.75±0.58	59.23±2.95
4s	32.84±0.27	72.53±1.98
4t	>100	61.53±0.29
4u	8.62±0.61	>100
4v	23.08±1.49	71.64±2.12
5-FU	**58.46±2.33**	**33.45±0.12**

Table 5-18 shows the cytotoxicity against the lung cancer cell line, A549. Compound **4g** with an IC_{50} value of 7.61 µg/mL and a selectivity index of 5.37 showed enhanced activity twice against A549 compared to the **lead compound** and **5-FU**. Compounds **4a**, **4f**, **4h**, **4i**, **4m**, and **4u** did not show cytotoxic activity against A549.

Table 5-18: Cytotoxicity on lung cancer cell line (A549)

Compound	A549	HUVEC
4a	>100	33.98±1.30
4b	19.48±0.55	16.58±0.25
4f	–	–
4g	7.61±0.17	40.87±1.25
4h	–	–
4i	–	>100
4j	46,42±0,27	47,23±1,11
4k	50,25±9,56	52,03±3,21
4l	31,92±4,13	61,39±0,64
4m	>100	77.32±0.32
4n	59.53±0.58	46.21±0.25
4o	65.11±3.05	54.91±0.60
4p	57.32±2.94	58.33±1.10
4r	72.44±3.25	59.23±2.95
4s	63.95±1.28	72.53±1.98
4t	91.87±2.65	61.53±0.29
4u	>100	>100
4v	70.59±3.50	71.64±2.12
5-FU	**18.63±2.14**	**33.45±0.12**

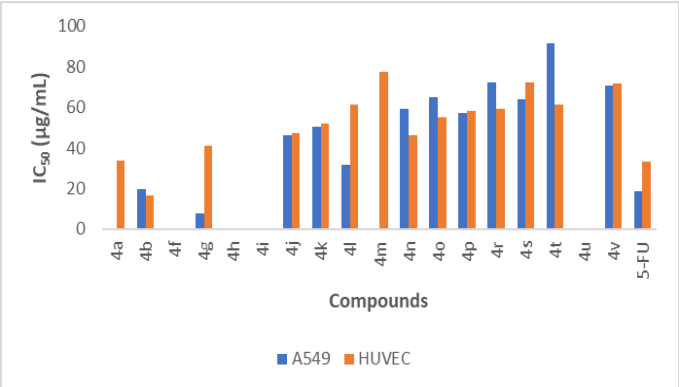

In the cytotoxicity test against the colon cancer cell lines, HT-29 and Caco-2, compound **4g** demonstrated the lowest IC_{50} value of 4.84 and 2.20 µg/mL and a selectivity index of 8.44 and 18.58, respectively. Compound **4g** exhibited a better cytotoxic profile and selectivity than the **lead compound** against HT-29 and Caco-2. Compared to 5-FU, compound **4g** showed a slightly lower activity against HT-29 and improved activity against Caco-2 by 7.8 times. Compound **4i** which is inactive against HT-29 and the normal cell, HUVEC, showed moderate cytotoxicity against Caco-2 with an IC_{50} value of 20.43 µg/mL. Compound **4u** which is inactive against Caco-2 and the normal cell, HUVEC, showed promising cytotoxicity against HT-29 with an IC_{50} value of 9.81 µg/mL (**Table 5-19**).

Table 5-19: Cytotoxicity on colon cancer cell lines (HT-29 and Caco-2)

Compound	HT-29	Caco-2	HUVEC
4a	20.35±1.40	23.12±0.76	33.98±1.30
4b	15.80±0.65	2.70±0.13	16.58±0.25
4f	–	>100	–
4g	4.84±0.34	2.20±0.08	40.87±1.25
4h	>100	>100	–
4i	–	20.43±0.98	>100
4j	21.00±1.03	14.97±0.44	47.23±1.11
4k	43.31±1.50	46.32±2.06	52.03±3.21
4l	21.29±0.92	14.38±1.66	61.39±0.64
4m	65.90±3.80	66.53±1.52	77.32±0.32
4n	36.10±0.90	35.25±0.64	46.21±0.25
4o	34.85±0.26	29.14±1.05	54.91±0.60
4p	58.22±0.95	41.19±2.05	58.33±1.10
4r	>100	47.15±2.47	59.23±2.95
4s	39.56±1.52	38.13±1.46	72.53±1.98
4t	24.72±0.29	32.72±0.89	61.53±0.29
4u	9.81±0.40	>100	>100
4v	24.75±1.11	69.36±0.81	71.64±2.12
5-FU	**1.99±0.15**	**17.48±0.80**	**33.45±0.12**

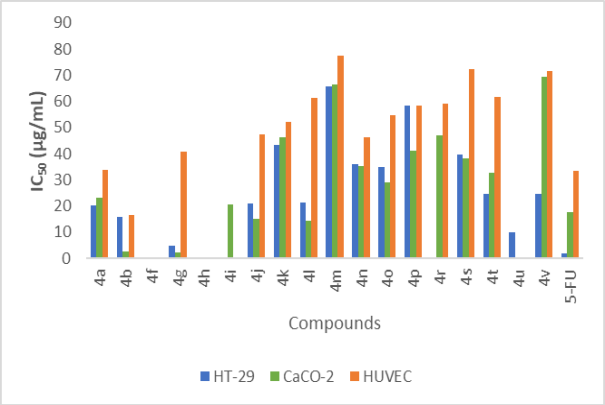

The most potent molecule against glioblastoma cell lines (U118-MG), the most aggressive type of brain cancer, was compound **4b**, according to **Table 5-20**, however, it did not exhibit selectivity over HUVEC. The reference drug, 5-FU was inactive against U118-MG. Compounds **4j** and **4l** with IC_{50} values of 21.44 and 27.79 µg/mL, respectively, exhibited the highest selectivity index of 2.20.

Table 5-20: Cytotoxicity on glioblastoma cancer cell line (U118-MG)

Compound	U118-MG	HUVEC
4a	22.35±0.30	33.98±1.30
4b	17.91±0.42	16.58±0.25
4f	>100	–
4g	34.16±2.27	40.87±1.25
4h	–	–
4i	>100	>100
4j	21.44±0.50	47.23±1.11
4k	62.63±1.63	52.03±3.21
4l	27.79±1.33	61.39±0.64
4m	60.48±1.18	77.32±0.32
4n	32.77±0.85	46.21±0.25
4o	40.17±0.52	54.91±0.60
4p	55.06±1.11	58.33±1.10
4r	–	59.23±2.95
4s	63.98±2.91	72.53±1.98
4t	>100	61.53±0.29
4u	>100	>100
4v	65.48±2.45	71.64±2.12
5-FU	**>100**	**33.45±0.12**

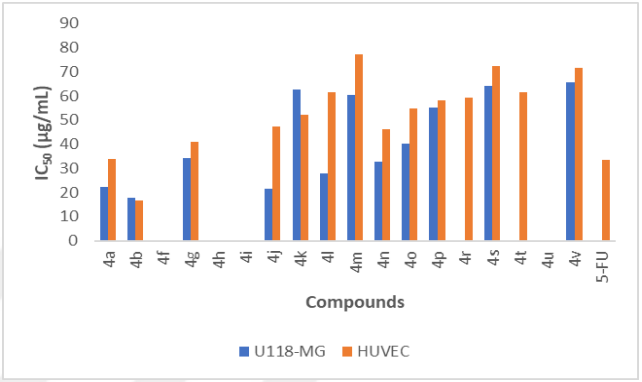

In a nutshell, compound **4f** having the lowest *K*i value against hCAIX demonstrated poor activity against the cancer cell lines and compound **4o** having the lowest *K*i value against hCAXII did not show the best anticancer activity among the tested compounds. This shows that instead of hCAIX and hCAXII, these compounds may exert their anticancer properties through other mechanisms.

5.4. In silico ADME prediction

Table 4-2 provided the predicted ADME properties of compounds **4a – 4v**. The recommended values were obtained from QikProp 4.4 user manual (Schrödinger 2015). The presence of hydrogen bond donors (HBDs) and acceptors (HBAs) is an important property in determining the ability of the compound to interact with the target protein. Compounds with higher HBDs and HBAs may have better pharmacological activity. All the compounds have the recommended number of both HBDs and HBAs. The QPlogPo/w explains the partition coefficient between octanol and water, which is a crucial factor in defining the lipophilicity of a compound. Compounds with ideal lipophilicity typically have superior absorption properties. The QPlogPo/w values of the

compounds are within the accepted range with values less than 5. The QPlogS represents the aqueous solubility of the compounds. Aqueous solubility is an essential parameter in defining the ability of a compound to dissolve and reach the bloodstream, and compounds having higher aqueous solubility may demonstrate superior absorption properties. Except for compounds **4b**, **4m**, **4n**, **4p**, and **4u**, which may have a low solubility owing to the presence of halogens, the QPlogS values are within the accepted range. The QPPCaco parameter describes the ability of the compounds to penetrate the gut-blood barrier, which is important in defining the permeability of the compound to the intestinal barrier. The values are within the recommended range with compounds **4a**, **4b**, and **4k** having higher permeability values. QPlogBB describes the ability of the compounds to penetrate the blood-brain. This parameter is important in assessing whether the compounds will have therapeutic or toxic effects on the central nervous system. The QPlogKhsa describes the binding affinity of the compound to human serum albumin (HSA), which is essential for determining the ability of the compound to be well distributed in the bloodstream and eventually reach the site of action. Compounds with higher binding affinity to HSA may have lower concentrations in systemic circulation. The values are within the recommended range. The (Percent) Human Oral Absorption describes the absorption properties of orally taken drugs. The compounds generally demonstrated good absorption properties. The PSA which is the polar surface area is important for ideal absorption and distribution. The PSA values for the compounds are within the accepted range. The compounds obey Lipinski's RO5, except for compounds **4b**, **4g** and **4j**, which have MW of more than 500 g/mol.

5.5. Molecular modelling studies

In addition to the coordination interaction between the sulfonamide group and Zn^{2+} ion, the reference drug, AAZ, forms a hydrogen bond with the backbone of Thr199 with its sulfonamide group. Also, the thiadiazol ring of AAZ forms $\pi - \pi$ interaction with His94. Due to the small size of AAZ, it does not form interactions with the hydrophilic or the hydrophobic halves of the active site (See **Figure 4-1B**).

Although the active sites of these four hCA isozymes are at least 34% identical, there are significant differences exist that potentially affect ligand-binding interactions. In hCAI, the substitution of Thr200 with His200 hinders the formation of hydrogen bonds with the sulfonamide group of ligands, preventing them from approaching the

Zn^{2+} ion and establishing coordination interactions. Besides, the applied docking protocol did not produce any docked pose of the compounds with any of the hCAI crystal structures, which could explain their low activity against hCAI. In hCAII, the hydrophobic half contains a relatively bulky Phe131 instead of small-sized Val131 in hCAIX and Ala131 in hCAXII. Consequently, the docked pose obtained for compound **4f** in the active site of hCAIX (PDB: 5FL6 & 6TL5) as depicted in **Figures 228-A** and **229-A**, and hCAXII (PDB: 6R6Y) as depicted in **Figure 4-230A** may not be achieved in hCAII due to a possible clash with Phe131.

The introduction of an OH group in compounds **4h** and **4v** resulted in a significant decrease in inhibitory activity against both hCAIX and hCAXII. Most of the ligands demonstrated two binding modes; either the 4-phenyl part faced the hydrophobic region and the alkylidene/arylidenehydrazinylidene moiety faced the hydrophilic region or vice versa. In both these possible binding modes in hCAIX obtained from XP docking, the OH group clashes with Leu91 (PDB: 3IAI) and Tyr7 (PDB: 6TL5) (**Figure 5-30**). This could be the underlying reason for the reduced activity against these enzymes.

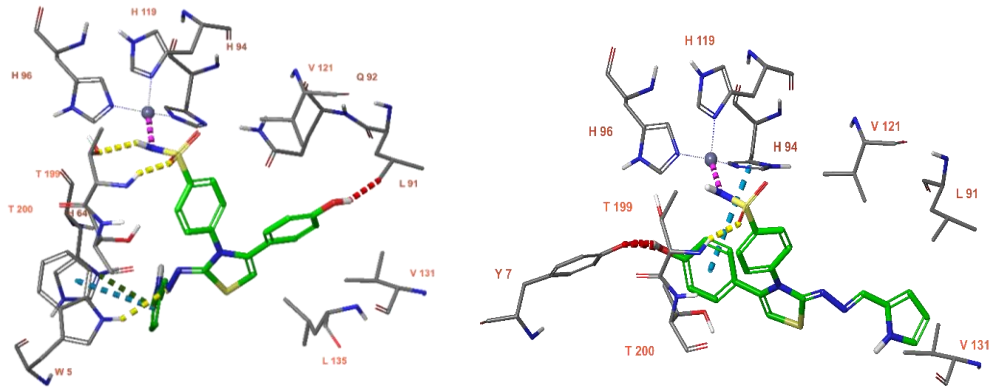

Figure 5-30: Docked pose of compound 4h in A) hCAIX (PDB: 3IAI). B) hCAIX (PDB: 6TL5)

The docked pose of compound **4o** in hCAXI and hCAXII (**Figure 4-233, 234 & 235**) demonstrated that the size/length of the 2-(propan-2-ylidenehydrazineylidene) moiety was not enough to form interaction or clashes with the diverse amino acid

residues present in the binding pocket and hence did not show selectivity against the isoenzymes.

Advanced molecular modelling studies were conducted after the preliminary SP docking studies conducted on the compounds did not establish a linear correlation with the CA inhibition data. These studies include reverse ensemble docking with XP scoring function, rescoring with MM-GBSA, 250 ns MD simulations on selected compounds (**4f**, **4i**, **4o**, **4t** and **4u)** and then MM-GBSA binding free energy calculation of these compounds during the MD simulation. **Table 5-21** summarizes the result of the molecular modelling studies conducted on compounds **4f**, **4i**, **4o**, **4t** and **4u**. Although these molecular modelling studies provided insight into the probable binding modes of the ligands, their interactions with the protein, and their selectivity profile, they were not able to establish a clear relationship with the CA inhibition data.

Table 5-21: Summary of molecular modelling studies compounds 4f, 4i, 4o, 4t and 4u

Compounds	hCAIX inhibition (*K*i=nM)	Preliminary SP docking Score in hCAIX (PDB: 3IAI) (kcal/mol)	XP docking Score in hCAIX (PDB) (kcal/mol)	Pre-MM-GBSA (kcal/mol)	Post-MM-GBSA (kcal/mol)	hCAXII inhibition (*K*i=nM)	Preliminary SP docking Score in hCAXII (PDB: 1JD0) (kcal/mol)	XP docking Score in hCAXII (PDB) (kcal/mol)	Pre-MM-GBSA (kcal/mol)	Post-MM-GBSA (kcal/mol)
4f	69.8	-7.49	-7.45 (5FL6)	-34.48	-44.20	328	-6.48	-8.71 (6R6Y)	-29.08	-33.77
			-8.04 (6TL5)	-34.04	-39.74					
4i	82.0	-7.24	-7.94 (6TL5)	-40.20	-38.13	73.2	-6.86	-7.00 (1JD0)	-38.86	-31.08
4o	278.1	-7.28	-6.48 (6TL5)	-21.43	-36.35	43.0	-6.22	-6.74 (5LL5)	-29.32	-37.11
								-7.84 (6R6Y)	-25.48	-46.51
4t	82.5	-7.38	-8.34 (6TL5)	-33.08	-46.00	76.2	-6.52	-7.98 (6R6Y)	-26.16	-44.58
4u	94.1	-5.48	-7.74 (6TL5)	-38.06	-44.27	77.3	-6.02	-8.20 (6R6Y)	-28.22	-39.145

BIBLIOGRAPHY

Abaza, M. and Luqmani, Y. A. (2013). The influence of pH and hypoxia on tumor metastasis. *Expert Review of Anticancer Therapy*, ***13*****(10)**, 1229–1242.

Abbate, F., Casini, A., Owa, T., Scozzafava, A. and Supuran, C. T. (2004). Carbonic anhydrase inhibitors: E7070, a sulfonamide anticancer agent, potently inhibits cytosolic isozymes I and II, and transmembrane, tumor-associated isozyme IX. *Bioorganic and Medicinal Chemistry Letters*, ***14*****(1)**, 217–223.

Abdel-Aziz, A. A.-M., El-Azab, A. S., Abu El-Enin, M. A., Almehizia, A. A., Supuran, C. T. and Nocentini, A. (2018). Synthesis of novel isoindoline-1,3-dione-based oximes and benzenesulfonamide hydrazones as selective inhibitors of the tumor-associated carbonic anhydrase IX. *Bioorganic Chemistry*, ***80***, 706–713.

Abdel-Aziz, A. A.-M., El-Azab, A. S., Bua, S., Nocentini, A., Abu El-Enin, M. A., Alanazi, M. M., et al. (2019). Design, synthesis, and carbonic anhydrase inhibition activity of benzenesulfonamide-linked novel pyrazoline derivatives. *Bioorganic Chemistry*, ***87***, 425–431.

Ahinko, M., Niinivehmas, S., Jokinen, E. and Pentikäinen, O. T. (2019). Suitability of MMGBSA for the selection of correct ligand binding modes from docking results. *Chemical Biology & Drug Design*, ***93*****(4)**, 522–538.

Ahmad, M., Pervez, H., Ben Hadda, T., Toupet, L. and Naseer, M. M. (2014). Synthesis and solid state self-assembly of an isatin–thiazoline hybrid driven by three self-complementary dimeric motifs. *Tetrahedron Letters*, ***55*****(39)**, 5400–5403.

Akdemir, A., Güzel-Akdemir, O., Scozzafava, A., Capasso, C. and Supuran, C. T. (2013). Inhibition of tumor-associated human carbonic anhydrase isozymes IX and XII by a new class of substituted-phenylacetamido aromatic sulfonamides. *Bioorganic & Medicinal Chemistry*, ***21*****(17)**, 5228–5232.

Akdemir, A., Monte, C. de, Carradori, S. and Supuran, C. T. (2015). Computational investigation of the selectivity of salen and tetrahydrosalen compounds towards the tumor-associated hCA XII isozyme. *Journal of Enzyme İnhibition and Medicinal Chemistry*, ***30*****(1)**, 114–118.

Alaei, L., Khodarahmi, R., Sheikh-Hasani, V., Sheibani, N. and Moosavi-Movahedi, A. A. (2018). Mechanistic investigation of sulfonamide ligands as human carbonic anhydrase II inhibitors. *International Journal of Biological Macromolecules*, ***120*****(Pt A)**, 1198–1207.

Aldera, A. P. and Govender, D. (2021). Carbonic anhydrase IX: A regulator of pH and participant in carcinogenesis. *Journal of Clinical Pathology*, **74**, 350–354

Alonso, H., Bliznyuk, A. A. and Gready, J. E. (2006). Combining docking and molecular dynamic simulations in drug design. *Medicinal Research Reviews*, ***26*****(5)**, 531–568.

Alterio, V., Hilvo, M., Di Fiore, A., Supuran, C. T., Pan, P., Parkkila, S., et al. (2009). Crystal structure of the catalytic domain of the tumor-associated human carbonic anhydrase IX. *Proceedings of the National Academy of Sciences of the United States of America*, ***106*****(38)**, 16233–16238.

Altıntop, M. D., Kaplancıklı, Z. A., Ciftçi, G. A. and Demirel, R. (2014). Synthesis and biological evaluation of thiazoline derivatives as new antimicrobial and anticancer agents. *European Journal of Medicinal Chemistry*, ***74***, 264–277.

Al-Wahaibi, L. H., Youssif, B. G. M., Taher, E. S., Abdelazeem, A. H., Abdelhamid, A. A. and Marzouk, A. A. (2021). Design, Synthesis, Biological Evaluation, and Computational Studies of Novel Tri-Aryl Imidazole-Benzene Sulfonamide Hybrids as Promising Selective Carbonic Anhydrase IX and XII Inhibitors. *Molecules (Basel, Switzerland)*, ***26*****(16)**.

Aly, A. A., Mohamed, A. H., and Ramadan, M. (2020). Synthesis and colon anticancer activity of some novel thiazole/-2-quinolone derivatives. *Journal of Molecular Structure*, ***1207***, 127798.

Amariucai-Mantu, D., Mangalagiu, V., Bejan, I., Aricu, A. and Mangalagiu, I. I. (2022). Hybrid Azine Derivatives: A Useful Approach for Antimicrobial Therapy. *Pharmaceutics*, ***14*****(10)**, 2026.

Amnerkar, N. D, and Bhusari, K. P. (2011). Synthesis of some thiazolyl aminobenzothiazole derivatives as potential antibacterial, antifungal and anthelmintic agents. *Journal of Enzyme İnhibition and Medicinal Chemistry*, ***26*****(1)**, 22–28.

Anderson, B., Jasinski, J., Freedman, M., Millikan, S., O'Rourke, K. and Smolenski, V. (2016). Synthesis, Crystal Structural Investigations, and DFT Calculations of Novel Thiosemicarbazones. *Crystals*, ***6*****(2)**, 17.

Anderson, N. M. and Simon, M. C. (2020). The tumor microenvironment. *Current Biology : CB*, ***30*****(16)**, R921-R925.

Andreucci, E., Peppicelli, S., Carta, F., Brisotto, G., Biscontin, E., Ruzzolini, J., et al. (2017). Carbonic anhydrase IX inhibition affects viability of cancer cells adapted to extracellular acidosis. *Journal of Molecular Medicine (Berlin, Germany)*, ***95*****(12)**, 1341–1353.

Andreucci, E., Peppicelli, S., Ruzzolini, J., Bianchini, F., Biagioni, A., Papucci, L., et al. (2020). The acidic tumor microenvironment drives a stem-like phenotype in melanoma cells. *Journal of Molecular Medicine*, ***98*****(10)**, 1431–1446.

Aridoss, G., Amirthaganesan, S., Kim, M. S., Kim, J. T. and Jeong, Y. T. (2009). Synthesis, spectral and biological evaluation of some new thiazolidinones and thiazoles based on t-3-alkyl-r-2,c-6-diarylpiperidin-4-ones. *European Journal of Medicinal Chemistry*, ***44*****(10)**, 4199–4210.

Aspatwar, A., Tolvanen, M. E. E., Ortutay, C. and Parkkila, S. (2014). Carbonic anhydrase related proteins: Molecular biology and evolution. In S. C. Frost & R. McKenna (Eds.), *Carbonic Anhydrase: Mechanism, Regulation, Links to Disease, and Industrial Applications*. Springer Netherlands; **(75)** 135–156.

Assony, S. J. (1961). The chemistry of isothiocyanates. In N. Kharasch (Ed.), *Organic sulfur compounds*. Symposium Publications Division, Pergamon Press; 326–338

Autenrieth, W. and Koburger, J. (1903). Ueber die Einwirkung aromatischer Amine auf Aethylendisulfochlorid und über Vinylsulfonderivate. *Berichte Der Deutschen Chemischen Gesellschaft*, ***36*(3)**, 3626–3634.

Ayati, A., Emami, S., Moghimi, S. and Foroumadi, A. (2019). Thiazole in the targeted anticancer drug discovery. *Future Medicinal Chemistry*, ***11*(15)**, 1929–1952.

Baranauskienė, L. and Matulis, D. (2019). Overview of Human Carbonic Anhydrases. In D. Matulis (Ed.), *Carbonic Anhydrase as Drug Target*. Springer International Publishing; 3–14

Baronas, D., Dudutienė, V., Paketurytė, V., Kairys, V., Smirnov, A., Juozapaitienė, V., et al. (2021). Structure and mechanism of secondary sulfonamide binding to carbonic anhydrases. *European Biophysics Journal*, ***50*(7)**, 993–1011.

Bartosová, M., Parkkila, S., Pohlodek, K., Karttunen, T. J., Galbavý, S., Mucha, V., et al. (2002). Expression of carbonic anhydrase IX in breast is associated with malignant tissues and is related to overexpression of c-erbB2. *The Journal of Pathology*, ***197*(3)**, 314–321.

Bauer, D. J. (1965). Clinical experience with the antiviral drug marboran (1-methylisatin 3-thiosemicarbazone). *Annals of the New York Academy of Sciences*, ***130*(1)**, 110–117.

Becker, B. (1955). The Mechanism of the Fall in Intraocular Pressure Induced by the Carbonic Anhydrase Inhibitor, Diamox *American Journal of Ophthalmology*, ***39*(2)**, 177–184.

Becker, H. M. and Deitmer, J. W. (2020). Transport Metabolons and Acid/Base Balance in Tumor Cells. *Cancers*, ***12*(4)**, 899.

Becker, H. M. and Deitmer, J. W. (2021). Proton Transport in Cancer Cells: The Role of Carbonic Anhydrases. *International Journal of Molecular Sciences*, ***22*****(6)**, 3171.

Belskaya, N. P., Kostova, I. and Fan, Z. (2020). Thiazole cores as organic fluorophore units: Synthesis and fluorescence. *Targets in Heterocyclic Systems*, ***23***, 116.

Belyaev, E. S., Shkirdova, A. O., Kozhemyakin, G. L., Tyurin, V. S., Emets, V. V., Grinberg, V. A., et al. (2021). Azines of porphyrinoids. Does azine provide conjugation between chromophores? *Dyes and Pigments*, ***191***, 109354.

Benej, M., Pastorekova, S. and Pastorek, J. (2014). Carbonic anhydrase IX: Regulation and role in cancer. In S. C. Frost & R. McKenna (Eds.), *Carbonic Anhydrase: Mechanism, Regulation, Links to Disease, and Industrial Applications*. Springer Netherlands: **(75)**, 199–219

Bennett, J. E., Kontis, V., Mathers, C. D., Guillot, M., Rehm, J., Chalkidou, K., et al. (2020). Ncd Countdown 2030: Pathways to achieving Sustainable Development Goal target 3.4. *The Lancet*, ***396*****(10255)**, 918–934.

Bharti, N., Husain, K., Gonzalez Garza, M., Cruz-Vega, D. E., Castro-Garza, J., Mata-Cardenas, B. D., et al. (2002). Synthesis and in vitro antiprotozoal activity of 5-nitrothiophene-2-carboxaldehyde thiosemicarbazone derivatives. *Bioorganic & Medicinal Chemistry Letters*, ***12*****(23)**, 3475–3478.

Bikobo, D. S. N., Vodnar, D. C., Stana, A., Tiperciuc, B., Nastasă, C., Douchet, M. and Oniga, O. (2017). Synthesis of 2-phenylamino-thiazole derivatives as antimicrobial agents. *Journal of Saudi Chemical Society*, ***21*****(7)**, 861–868.

Birbrair, A. (Ed.). (2020). *Advances in experimental medicine and biology: v.* ***1234***. *Tumor microenvironment: Non-hematopoietic cells*. Springer.

Blaszczak, W. and Swietach, P. (2021). What do cellular responses to acidity tell us about cancer? *Cancer and Metastasis Reviews*, ***40*****(4)**, 1159–1176.

Bogdanov, A., Bogdanov, A., Chubenko, V., Volkov, N., Moiseenko, F., and Moiseyenko, V. (2022). Tumor acidity: From hallmark of cancer to target of treatment. *Frontiers in Oncology*, ***12***, 979154.

Bonardi, A., Bua, S., Combs, J., Lomelino, C., Andring, J., Osman, S. M., et al. (2022). The three-tails approach as a new strategy to improve selectivity of action of sulphonamide inhibitors against tumour-associated carbonic anhydrase IX and XII. *Journal of Enzyme İnhibition and Medicinal Chemistry*, ***37*****(1)**, 930–939. 6

Bonardi, A., Nocentini, A., Bua, S., Combs, J., Lomelino, C., Andring, J., et al. (2020). Sulfonamide Inhibitors of Human Carbonic Anhydrases Designed through a Three-Tails Approach: Improving Ligand/Isoform Matching and Selectivity of Action. *Journal of Medicinal Chemistry*, ***63*****(13)**, 7422–7444.

Bondock, S., Gieman, H. and El-Shafei, A. (2016). Selective synthesis, structural studies and antitumor evaluation of some novel unsymmetrical 1-hetaryl-4-(2-chloroquinolin-3-yl)azines. *Journal of Saudi Chemical Society*, ***20*****(6)**, 695–702.

Borcea, A.-M., Ionuț, I., Crișan, O. and Oniga, O. (2021). An Overview of the Synthesis and Antimicrobial, Antiprotozoal, and Antitumor Activity of Thiazole and Bisthiazole Derivatives. *Molecules (Basel, Switzerland)*, ***26*****(3)**, 624.

Brahimi-Horn, M. C., Chiche, J. and Pouysségur, J. (2007). Hypoxia and cancer. *Journal of Molecular Medicine (Berlin, Germany)*, ***85*****(12)**, 1301–1307.

Brahimi-Horn, M. C. and Pouysségur, J. (2007). Oxygen, a source of life and stress. *FEBS Letters*, ***581*****(19)**, 3582–3591.

Bramley, S. E., Dupplin, V., Goberdhan, D. G. C. and Meakins, G. D. (1987). The Hantzsch thiazole synthesis under acidic conditions: Change of regioselectivity. *Journal of the Chemical Society, Perkin Transactions* ***1*****(0)**, 639.

B-Rao, C., Subramanian, J. and Sharma, S. D. (2009). Managing protein flexibility in docking and its applications. *Drug Discovery Today*, ***14*****(7-8)**, 394–400.

Bray, F., Laversanne, M., Weiderpass, E. and Soerjomataram, I. (2021). The ever-increasing importance of cancer as a leading cause of premature death worldwide. *Cancer*, ***127*(16)**, 3029–3030.

Briganti, F., Mangani, S., Orioli, P., Scozzafava, A., Vernaglione, G. and Supuran, C. T. (1997). Carbonic anhydrase activators: X-ray crystallographic and spectroscopic investigations for the interaction of isozymes I and II with histamine. *Biochemistry*, ***36*(34)**, 10384–10392.

British Columbia Cancer Agency, Welichem Biotech Inc. and Canadian Cancer Society. (2022, June 23). *An Open-label, Multi-center, Phase 1b Study to Investigate the Safety and Tolerability of SLC-0111 (WBI-5111) in Combination With Gemcitabine in Metastatic Pancreatic Ductal Adenocarcinoma Subjects Positive for Carbonic Anhydrase IX: NCT03450018, H17-02841*. https://clinicaltrials.gov/ct2/show/NCT03450018

Buttke, T. M., McCubrey, J. A. and Owen, T. C. (1993). Use of an aqueous soluble tetrazolium/formazan assay to measure viability and proliferation of lymphokine-dependent cell lines. *Journal of Immunological Methods*, ***157*(1-2)**, 233–240.

Callingham, M., Blum, F. and Pavé, G. (2015). One-Step Synthesis of 2-Chloropyrimidin-4-ol Derivatives: An Unusual Reactivity of Thiophosgene. *Organic Letters*, ***17*(19)**, 4930–4932.

Campos, N. S. P. de, Souza, B. S., Da Silva, G. C. P., Porto, V. A., Chalbatani, G. M., Lagreca, G., et al. (2022). Carbonic Anhydrase IX: A Renewed Target for Cancer Immunotherapy. *Cancers*, ***14*(6)**, 1392.

Cancer Tomorrow. (2022, March 29). https://gco.iarc.fr/tomorrow/en/dataviz/isotype

Čapkauskaitė, E., Zubrienė, A., Paketurytė, V., Timm, D. D., Tumkevičius, S. and Matulis, D. (2018). Thiazole-substituted benzenesulfonamides as inhibitors of 12 human carbonic anhydrases. *Bioorganic Chemistry*, ***77***, 534–541.

Cardoso, M. V. O., Oliveira Filho, G. B., Siqueira, L. R. P., Espíndola, J. W. P., Silva, E. B. D., Mendes, A. P. O., et al. (2019). 2-(phenylthio)ethylidene derivatives as anti-Trypanosoma cruzi compounds: Structural design, synthesis and antiparasitic activity. *European Journal of Medicinal Chemistry*, ***180***, 191–203.

Carta, F., Supuran, C. T. and Scozzafava, A. (2014). Sulfonamides and their isosters as carbonic anhydrase inhibitors. *Future Medicinal Chemistry*, ***6*****(10)**, 1149–1165.

Ceylan, Ü., Durgun, M., Türkmen, H., Yalçın, Ş. P., Kilic, A. and Özdemir, N. (2015). Theoretical and experimental investigation of 4-[(2-hydroxy-3-methylbenzylidene)amino]benzenesulfonamide: Structural and spectroscopic properties, NBO, NLO and NPA analysis. *Journal of Molecular Structure*, ***1089,*** 222–232.

Chaaban, I., El Khawass, E. S. M., Mahran, M. A., Abd El Razik, H. A. and El Salamouni, N. S. (2016). Unexpected products from the reaction of different compounds with hydrazine hydrate or aryl thiosemicarbazides. *Journal of Saudi Chemical Society*, ***20*****(5)**, 547–552.

Chegwidden, W. R. (2021). The Carbonic Anhydrases in Health and Disease. In W. R. Chegwidden and N. D. Carter (Eds.), *The Carbonic Anhydrases: Current and Emerging Therapeutic Targets*. Springer International Publishing; (**75**) 1–12.

Chen, K.-T. and Seimbille, Y. (2022). New Developments in Carbonic Anhydrase IX-Targeted Fluorescence and Nuclear Imaging Agents. *International Journal of Molecular Sciences*, ***23*****(11)**, 6125.

Chen, Z., Ai, L., Mboge, M. Y., Tu, C., McKenna, R., Brown, K. D., et al. (2018). Differential expression and function of CAIX and CAXII in breast cancer: A comparison between tumorgraft models and cells. *Plos One*, ***13*****(7)**, e0199476.

Cheng, F., Li, W., Liu, G. and Tang, Y. (2013). In silico ADMET prediction: Recent advances, current challenges and future trends. *Current Topics in Medicinal Chemistry*, ***13*****(11)**, 1273–1289.

Chiche, J., Ilc, K., Laferrière, J., Trottier, E., Dayan, F., Mazure, N. M., et al. (2009). Hypoxia-inducible carbonic anhydrase IX and XII promote tumor cell growth by counteracting acidosis through the regulation of the intracellular pH. *Cancer Research*, ***69*(1)**, 358–368.

Choschzick, M., Oosterwijk, E., Müller, V., Woelber, L., Simon, R., Moch, H. et al. (2011). Overexpression of carbonic anhydrase IX (CAIX) is an independent unfavorable prognostic marker in endometrioid ovarian cancer. *Virchows Archiv*, ***459*(2)**, 193–200.

Churchill-Davidson, I., Foster, C. A. and Thomlinson, R. H. (1958). High-pressure oxygen and radiotherapy. *Medical World*, ***88*(2)**, 125–128.

Claussen, H., Buning, C., Rarey, M. and Lengauer, T. (2001). Flexe: Efficient molecular docking considering protein structure variations. *Journal of Molecular Biology*, ***308*(2)**, 377–395.

Collaborative Medicinal Development Pty Limited. (2019, February 21). *A Phase 1 Dose-finding and Pharmacokinetic Study of DpC, Administered Orally to Patients With Advanced Solid Tumors: NCT02688101, CMD-2015-001*. https://clinicaltrials.gov/ct2/show/NCT02688101

Cremlyn, R. J. W. (2007). *Chlorosulfonic acid: A versatile reagent*. Royal Society of Chemistry.

Wiles, D. M., Gingras, B. A. and Suprunchuk, T. (1967). The C=S stretching vibration in the infrared spectra of some thiosemicarbazones. *Canadian Journal of Chemistry*, ***45*(5)**.

Wiles, D. M. and Suprunchuk, T. (1968). The infrared absorption spectra of thiosemicarbazide and related compounds: NH_2 and NH vibrations. *Canadian Journal of Chemistry*, ***47***, *1087*

D'Ambrosio, K., Simone, G. de and Supuran, C. T. (2015). Human Carbonic Anhydrases: Catalytic Properties, Structural Features, and Tissue Distribution.

In C. T. Supuran and G. de Simone (Eds.), *Carbonic anhydrases as biocatalysts: From theory to medical and industrial applications.* Elsevier; 17–30.

D'Ambrosio, K., Di Fiore, A., Buonanno, M., Monti, S. M. and Simone, G. de. (2019). Chapter 7 - η- and θ-carbonic anhydrases. In C. T. Supuran and A. Nocentini (Eds.), *Carbonic anhydrases: Biochemistry and pharmacology of an evergreen pharmaceutical target*. Elsevier; 139–148.

D'Ascenzio, M., Carradori, S., Secci, D., Mannina, L., Sobolev, A. P., Monte, C. de, et al. (2014). Identification of the stereochemical requirements in the 4-aryl-2-cycloalkylidenhydrazinylthiazole scaffold for the design of selective human monoamine oxidase B inhibitors. *Bioorganic & Medicinal Chemistry*, ***22*****(10)**, 2887–2895.

Davenport, H. W. (1984). The early days of research on carbonic anhydrase. *Annals of the New York Academy of Sciences*, ***429***, 4–9.

DeBerardinis, R. J. and Chandel, N. S. (2016). Fundamentals of cancer metabolism. *Science Advances*, ***2*****(5)**, e1600200.

Debnath, S. and Mondal, S. (2018). Sultams: Recent Syntheses and Applications. *European Journal of Organic Chemistry*, ***2018*****(8)**, 933–956.

Demir-Yazıcı, K., Apaydın, Ç. B., Soylu-Eter, Ö., Özsoy, N. and Karalı, N. (2021). Synthesis, molecular modeling and cholinesterase inhibitory effects of 2-indolinone-based hydrazinecarbothioamides. *Future Medicinal Chemistry*, ***13*****(24)**, 2133–2151.

Demir-Yazıcı, K., Bua, S., Akgüneş, N. M., Akdemir, A., Supuran, C. T. and Güzel-Akdemir, Ö. (2019). Indole-Based Hydrazones Containing A Sulfonamide Moiety as Selective Inhibitors of Tumor-Associated Human Carbonic Anhydrase Isoforms IX and XII. *International Journal of Molecular Sciences*, ***20*****(9)**.

Demir-Yazıcı, K., Güzel-Akdemir, Ö., Angeli, A., Supuran, C. T. and Akdemir, A. (2020). Novel Indole-Based Hydrazones as Potent Inhibitors of the α-class Carbonic Anhydrase from Pathogenic Bacterium Vibrio cholerae. *International Journal of Molecular Sciences*, ***21*(9)**.

DeRuiter, J. (Ed.). (2005). *Principles of drug action*. https://scholar.google.com/citations?user=4pylmdcaaaaj&hl=en&oi=sra

Di Fiore, A., Pedone, C., D'Ambrosio, K., Scozzafava, A [Andrea], Simone, G. de and Supuran, C. T [Claudiu T.] (2006). Carbonic anhydrase inhibitors: Valdecoxib binds to a different active site region of the human isoform II as compared to the structurally related cyclooxygenase II "selective" inhibitor celecoxib. *Bioorganic & Medicinal Chemistry Letters*, *16*(2), 437–442.

Diao, Y., Lu, W., Jin, H., Zhu, J., Le Han, Xu, M., et al. (2012). Discovery of diverse human dihydroorotate dehydrogenase inhibitors as immunosuppressive agents by structure-based virtual screening. *Journal of Medicinal Chemistry*, ***55*(19)**, 8341–8349.

Diori Karidio, I. and Sanlier, S. H. (2021). Reviewing cancer's biology: An eclectic approach. *Journal of the Egyptian National Cancer Institute*, *33*(1), 32.

Distinto, S., Meleddu, R., Ortuso, F., Cottiglia, F., Deplano, S., Sequeira, L., et al. (2019). Exploring new structural features of the 4-(3-methyl-4-aryl-2,3-dihydro-1,3-thiazol-2-ylidene)aminobenzenesulphonamide scaffold for the inhibition of human carbonic anhydrases. *Journal of Enzyme İnhibition and Medicinal Chemistry*, ***34*(1)**, 1526–1533.

Domagała, M., Dubis, A. T., Wojtulewski, S., Zabel, M. and Pfitzner, A. (2022). Hydrogen Bonding in Crystals of Pyrrol-2-yl Chloromethyl Ketone Derivatives and Methyl Pyrrole-2-Carboxylate. *Crystals*, ***12*(11)**, 1523.

Dos Santos Silva, T. D., Bomfim, L. M., da Cruz Rodrigues, A. C. B., Dias, R. B., Sales, C. B. S., Rocha, C. A. G., et al. (2017). Anti-liver cancer activity in vitro

and in vivo induced by 2-pyridyl 2,3-thiazole derivatives. *Toxicology and Applied Pharmacology*, ***329***, 212–223.

Dubois, L., Lieuwes, N. G., Maresca, A., Thiry, A., Supuran, C. T., Scozzafava, A., et al. (2009). Imaging of CA IX with fluorescent labelled sulfonamides distinguishes hypoxic and (re)-oxygenated cells in a xenograft tumour model. *Radiotherapy and Oncology : Journal of the European Society for Therapeutic Radiology and Oncology*, ***92*****(3)**, 423–428.

Durrant, J. D. and McCammon, J. A. (2011). Molecular dynamics simulations and drug discovery. *BMC Biology*, ***9*****(1)**, 71.

Dvorak, H. F. (1986). Tumors: Wounds that do not heal. Similarities between tumor stroma generation and wound healing. *The New England Journal of Medicine*, ***315*****(26)**, 1650–1659.

Eales, K. L., Hollinshead, K. E. R. and Tennant, D. A. (2016). Hypoxia and metabolic adaptation of cancer cells. *Oncogenesis*, ***5*****(1)**, e190.

Eicher, T., Hauptmann, S. and Speicher, A. (2003). *The chemistry of heterocycles: Structure, reactions, syntheses, and applications* (2nd completely rev. and enl. ed. Translated by Hans Suschitzky and Judith Suschitzky). Wiley-VCH.

Eldehna, W. M., Abo-Ashour, M. F., Nocentini, A., El-Haggar, R. S., Bua, S., Bonardi, A., et al. (2019). Enhancement of the tail hydrophobic interactions within the carbonic anhydrase IX active site via structural extension: Design and synthesis of novel N-substituted isatins-SLC-0111 hybrids as carbonic anhydrase inhibitors and antitumor agents. *European Journal of Medicinal Chemistry*, ***162***, 147–160.

El-Gaby, M. S. A., Ghorab, M. M., Ismail, Z. H., Abdel-Gawad, S. M. and Aly, H. M. (2018). Synthesis, structural characterization and anticancer evaluation of pyrazole derivatives. *Medicinal Chemistry Research*, ***27*****(1)**, 72–79.

El-Haggar, R., Hammad, S. F., Alsantali, R. I., Alrooqi, M. M., El Hassab, M. A., Masurier, N. et al. (2022). 3-Substituted-2,3-Dihydrothiazole as a promising scaffold to design EGFR inhibitors. *Bioorganic Chemistry*, ***129***, 106172.

Eraslan Elma, P. (2017). *1H-indole-2,3-dione 3-thiosemicarbazone derivatives carrying 3-sulfamoylphenyl moiety: Synthesis, structure determination, molecular modeling and biological activity evaluation* [Ph.D]. Istanbul University, Istanbul.

Ertas, M., Sahin, Z., Berk, B., Yurttas, L., Biltekin, S. N. and Demirayak, S. (2018). Pyridine-substituted thiazolylphenol derivatives: Synthesis, modeling studies, aromatase inhibition, and antiproliferative activity evaluation. *Archiv Der Pharmazie*, ***351*****(3-4)**, e1700272.

Ferguson, P. J., Phillips, J. R., Selner, M. and Cass, C. E. (1984). Differential activity of vincristine and vinblastine against cultured cells. *Cancer Research*, ***44*****(8)**, 3307–3312.

Ferreira, L. G., Dos Santos, R. N., Oliva, G. and Andricopulo, A. D. (2015). Molecular docking and structure-based drug design strategies. *Molecules (Basel, Switzerland)*, ***20*****(7)**, 13384–13421.

Fidler, I. J. (2002). The organ microenvironment and cancer metastasis. *Differentiation; Research in Biological Diversity*, ***70*****(9-10)**, 498–505.

Fidler, I. J. (2003). The pathogenesis of cancer metastasis: The 'seed and soil' hypothesis revisited. *Nature Reviews Cancer*, ***3*****(6)**, 453–458.

Finkelmeier, F., Canli, Ö., Peiffer, K.-H., Walter, D., Tal, A., Koch, C., et al. (2018). Circulating hypoxia marker carbonic anhydrase IX (CA9) in patients with hepatocellular carcinoma and patients with cirrhosis. *PloS One*, ***13*****(7)**, e0200855.

Fukumura, D. and Jain, R. K. (2007). Tumor microvasculature and microenvironment: Targets for anti-angiogenesis and normalization. *Microvascular Research*, ***74*****(2-3)**, 72–84.

Ganga, M. and Sankaran, K. R. (2020). Synthesis, spectral characterization, DFT, molecular docking and biological evaluation of some newly synthesized asymmetrical azines of 3,5-dimethoxy-4-hydroxy benzaldehyde. *Chemical Data Collections*, ***28***, 100475.

Gauthier, M. P., Michaux, C., Rolin, S., Vastersaegher, C., Leval, X. de, Julémont, F., Pochet, L., et al. (2006). Synthesis, molecular modelling and enzymatic evaluation of (+/-)3,5-diphenyl-2-thioxoimidazolidin-4-ones as new potential cyclooxygenase inhibitors. *Bioorganic & Medicinal Chemistry*, ***14*****(4)**, 918–927.

Gazieva, G. A. and Kravchenko, A. N. (2012). Thiosemicarbazides in the synthesis of five- and six-membered heterocyclic compounds. *Russian Chemical Reviews*, ***81*****(6)**, 494–523.

George, J., Lekha, V. S., G, R. N., Mary, Y. S., Al-Otaibi, J. S. and K, R. (2022). Synthesis, crystal structure and anti-tumour activity studies of 4-Tertiarybutylcyclohexanonethiosemicarbazone. *Journal of Molecular Structure*, ***1265***, 133490.

Gerweck, L. E., Vijayappa, S. and Kozin, S. (2006). Tumor pH controls the in vivo efficacy of weak acid and base chemotherapeutics. *Molecular Cancer Therapeutics*, ***5*****(5)**, 1275–1279.

Ghorab, M. M., Alsaid, M. S., Al-Dosary, M. S., Nissan, Y. M. and Attia, S. M. (2016). Design, synthesis and anticancer activity of some novel thioureido-benzenesulfonamides incorporated biologically active moieties. *Chemistry Central Journal*, ***10*****(1)**, 19.

Giovannuzzi, S., D'Ambrosio, M., Luceri, C., Osman, S. M., Pallecchi, M., Bartolucci, G., et al. (2021). Aromatic Sulfonamides including a Sulfonic Acid Tail_ New Membrane Impermeant Carbonic Anhydrase Inhibitors for Targeting

Selectively the Cancer-Associated Isoforms. *International Journal of Molecular Sciences*, ***23*****(1)**.

Gomha, S. M., Abdelhady, H. A., Hassain, D. Z. H., Abdelmonsef, A. H., El-Naggar, M., Elaasser, M. M., et al. (2021). Thiazole-Based Thiosemicarbazones: Synthesis, Cytotoxicity Evaluation and Molecular Docking Study. *Drug Design, Development and Therapy*, ***15***, 659–677.

Gondi, G., Mysliwietz, J., Hulikova, A., Jen, J. P., Swietach, P., Kremmer, E., et al. (2013). Antitumor Efficacy of a Monoclonal Antibody That Inhibits the Activity of Cancer-Associated Carbonic Anhydrase XII. *Cancer Research*, ***73*****(21)**, 6494–6503.

Gopinath, P. and Kathiravan, M. K. (2022). Molecular insights of oxadiazole benzene sulfonamides as human carbonic anhydrase IX inhibitors: Combined molecular docking, molecular dynamics, and 3D QSAR studies. *Journal of the Indian Chemical Society*, ***99*****(2)**, 100339.

Graham, K. and Unger, E. (2018). Overcoming tumor hypoxia as a barrier to radiotherapy, chemotherapy and immunotherapy in cancer treatment. *International Journal of Nanomedicine*, ***13***, 6049–6058.

Graves, A. P., Shivakumar, D. M., Boyce, S. E., Jacobson, M. P., Case, D. A. and Shoichet, B. K. (2008). Rescoring docking hit lists for model cavity sites: Predictions and experimental testing. *Journal of Molecular Biology*, ***377*****(3)**, 914–934.

Green, S. L., Freiberg, R. A. and Giaccia, A. J. (2001). P21(Cip1) and p27(Kip1) regulate cell cycle reentry after hypoxic stress but are not necessary for hypoxia-induced arrest. *Molecular and Cellular Biology*, ***21*****(4)**, 1196–1206.

Greenidge, P. A., Kramer, C., Mozziconacci, J.-C. and Sherman, W. (2014). Improving docking results via reranking of ensembles of ligand poses in multiple X-ray protein conformations with MM-GBSA. *Journal of Chemical Information and Modeling*, ***54*****(10)**, 2697–2717.

Greenidge, P. A., Kramer, C., Mozziconacci, J.-C. and Wolf, R. M. (2013). Mm/gbsa binding energy prediction on the PDBbind data set: Successes, failures, and directions for further improvement. *Journal of Chemical Information and Modeling*, ***53*****(1)**, 201–209.

Grincevičienė, Š., Vaitkienė, D., Kanopienė, D., Vansevičiūtė, R., Tykvart, J., Sukovas, A., et al. (2022). Factors, associated with elevated concentration of soluble carbonic anhydrase IX in plasma of women with cervical dysplasia. *Scientific Reports*, ***12*****(1)**, 15397.

Gupta, R. R., Kumar, M. and Gupta, V. (1999). *Heterocyclic Chemistry: Volume II: Five-Membered Heterocycles*. Springer Berlin / Heidelberg.

Gürsoy, A. and Karalı, N. (2003). Synthesis, characterization and primary antituberculosis activity evaluation of 4-(3-coumarinyl)-3-benzyl-4-thiazolin-2-one benzylidenehydrazones. *Turkish Journal of Chemistry*, ***27***.

Güzel, O., Karali, N. and Salman, A. (2008). Synthesis and antituberculosis activity of 5-methyl/trifluoromethoxy-1H-indole-2,3-dione 3-thiosemicarbazone derivatives. *Bioorganic & Medicinal Chemistry*, ***16*****(19)**, 8976–8987.

Güzel-Akdemir, Ö., Akdemir, A., Karalı, N. and Supuran, C. T. (2015). Discovery of novel isatin-based sulfonamides with potent and selective inhibition of the tumor-associated carbonic anhydrase isoforms IX and XII. *Organic & Biomolecular Chemistry*, ***13*****(23)**, 6493–6499.

Haapasalo, J., Nordfors, K., Haapasalo, H. and Parkkila, S. (2020). The Expression of Carbonic Anhydrases II, IX and XII in Brain Tumors. *Cancers*, ***12*****(7)**, 1723.

Hałdys, K., Goldeman, W., Jewgiński, M., Wolińska, E., Anger, N., Rossowska, J., et al. (2018). Inhibitory properties of aromatic thiosemicarbazones on mushroom tyrosinase: Synthesis, kinetic studies, molecular docking and effectiveness in melanogenesis inhibition. *Bioorganic Chemistry*, ***81***, 577–586.

Hałdys, K., Goldeman, W., Jewgiński, M., Wolińska, E. Anger-Góra, N., Rossowska, J., et al. (2020). Halogenated aromatic thiosemicarbazones as potent inhibitors of tyrosinase and melanogenesis. *Bioorganic Chemistry*, ***94***, 103419.

Halloum, I., Viljoen, A., Khanna, V., Craig, D., Bouchier, C., Brosch, R., et al. (2017). Resistance to Thiacetazone Derivatives Active against Mycobacterium abscessus Involves Mutations in the MmpL5 Transcriptional Repressor MAB_4384. *Antimicrobial Agents and Chemotherapy*, ***61*****(4)**.

Hanahan, D. (2022). Hallmarks of Cancer: New Dimensions. *Cancer Discovery*, ***12*****(1)**, 31–46.

Hanahan, D. and Weinberg, R. A. (2011). Hallmarks of cancer: The next generation. *Cell*, ***144*****(5)**, 646–674.

Haramura, M., Tanaka, A., Akimoto, T. and Hirayama, N. (2003). Crystal Structure of Dichlorphenamide. *Analytical Sciences: X-Ray Structure Analysis Online*, ***19***, X35-X36.

Harris, A. L. (2002). Hypoxia--a key regulatory factor in tumour growth. *Nature Reviews Cancer*, ***2*****(1)**, 38–47.

Hass, R., Ohe, J. von der and Ungefroren, H. (2020). Impact of the Tumor Microenvironment on Tumor Heterogeneity and Consequences for Cancer Cell Plasticity and Stemness. *Cancers*, ***12*****(12)**.

Hassan, S. Y. (2007). Synthesis of some thiazolyl and thiadiazolyl derivatives of substituted furan and pyrrole. *Journal of Heterocyclic Chemistry*, ***44*****(1)**, 21–27.

Hassanpour, S. H. and Dehghani, M. (2017). Review of cancer from perspective of molecular. *Journal of Cancer Research and Practice*, ***4*****(4)**, 127–129.

Henriques, O. M. (1928). Die bindungsweise des kohlendioxyds im blute. *Biochem. Z*, ***200*****(1)**, 24.

Hiepp, L., Mayr, D., Gärtner, K., Schmoeckel, E., Klauschen, F., Burges, A., et al. (2022). Carbonic anhydrase XII as biomarker and therapeutic target in ovarian carcinomas. *Plos One*, ***17*(7)**, e0271630.

Hou, T., Wang, J., Li, Y. and Wang, W. (2011). Assessing the performance of the molecular mechanics/Poisson Boltzmann surface area and molecular mechanics/generalized Born surface area methods. II. The accuracy of ranking poses generated from docking. *Journal of Computational Chemistry*, ***32*(5)**, 866–877.

Hu, C.-J., Wang, L.-Y., Chodosh, L. A., Keith, B. and Simon, M. C. (2003). Differential roles of hypoxia-inducible factor 1alpha (HIF-1alpha) and HIF-2alpha in hypoxic gene regulation. *Molecular and Cellular Biology*, ***23*(24)**, 9361–9374.

Huang, S.-Y. and Zou, X. (2007). Ensemble docking of multiple protein structures: Considering protein structural variations in molecular docking. *Proteins: Structure, Function, and Genetics*, ***66*(2)**, 399–421.

Huber, A. R., Tan, D., Sun, J., Dean, D., Wu, T. and Zhou, Z. (2015). High expression of carbonic anhydrase IX is significantly associated with glandular lesions in gastroesophageal junction and with tumorigenesis markers BMI1, MCM4 and MCM7. *BMC Gastroenterology*, ***15*(1)**, 80.

Hussein, M. A., Iqbal, M. A., Umar, M. I., Haque, R. A. and Guan, T. S. (2019). Synthesis, structural elucidation and cytotoxicity of new thiosemicarbazone derivatives. *Arabian Journal of Chemistry*, ***12*(8)**, 3183–3192.

Hynninen, P., Vaskivuo, L., Saarnio, J., Haapasalo, H., Kivelä, J., Pastoreková, S., et al. (2006). Expression of transmembrane carbonic anhydrases IX and XII in ovarian tumours. *Histopathology*, ***49*(6)**, 594–602.

Hyuga, S., Wada, H., Eguchi, H., Otsuru, T., Iwgami, Y., Yamada, D., et al. (2017). Expression of carbonic anhydrase IX is associated with poor prognosis through regulation of the epithelial-mesenchymal transition in hepatocellular carcinoma. *International Journal of Oncology*, ***51*(4)**, 1179–1190.

Ibrahim-Hashim, A., Cornnell, H. H., Abrahams, D., Lloyd, M., Bui, M., Gillies, R. J., et al. (2012). Systemic buffers inhibit carcinogenesis in TRAMP mice. *The Journal of Urology*, ***188*(2)**, 624–631.

Ibrahim-Hashim, A., Wojtkowiak, J. W., Lourdes Coelho Ribeiro, M. de, Estrella, V., Bailey, K. M., Cornnell, H. H., et al. (2011). Free Base Lysine Increases Survival and Reduces Metastasis in Prostate Cancer Model. *Journal of Cancer Science & Therapy*, *Suppl* ***1*(4)**.

Ibrar, A., Zaib, S., Khan, I., Jabeen, F., Iqbal, J. and Saeed, A. (2015). Facile and expedient access to bis-coumarin–iminothiazole hybrids by molecular hybridization approach: Synthesis, molecular modelling and assessment of alkaline phosphatase inhibition, anticancer and antileishmanial potential. *RSC Advances*, ***5*(109)**, 89919–89931.

Nascimento, I.J., de Aquino, T.M. and da Silva-Júnior, E.F. (2022). The New Era of Drug Discovery: The Power of Computer-aided DrugDesign (CADD). *Letters in Drug Design & Discovery*, ***19*(11)**, 951–955.

Imbrasaitė, A., Stravinskienė, D. and Žvirblienė, A. (2019). Detection of Carbonic Anhydrases. In D. Matulis (Ed.), *Carbonic Anhydrase as Drug Target*. Springer International Publishing; 323–333.

Imtaiyaz Hassan, M., Shajee, B., Waheed, A., Ahmad, F. and Sly, W. S. (2013). Structure, function and applications of carbonic anhydrase isozymes. *Bioorganic & Medicinal Chemistry*, ***21*(6)**, 1570–1582.

Ismail, Z. H., Ghorab, M. M., Mohamed, E. M. A., Aly, H. M. and El-Gaby, M. S. A. (2008). Antitumor Activity of Some Novel 1,2,5-Thiadiazole Derivatives. *Phosphorus, Sulfur, and Silicon and the Related Elements*, ***183*(10)**, 2541–2554.

Ivanov, S., Liao, S.-Y., Ivanova, A., Danilkovitch-Miagkova, A., Tarasova, N., Weirich, G., et al. (2001). Expression of Hypoxia-Inducible Cell-Surface Transmembrane Carbonic Anhydrases in Human Cancer. *The American Journal of Pathology*, ***158*(3)**, 905–919.

İyidoğan, A., Oruç-Emre, E. E. and Çakir, Ü. (2020). One pot synthesis and spectral characterization of 5-Substitutedfuran-2-carbaldehyde N4-cyclohexyl thiosemicarbazones and their Ni(II) complexes. *Turkish Journal of Analytical Chemistry*, ***2*****(2)**, 81–86.

Jähde, E., Glüsenkamp, K. H., Klünder, I., Hülser, D. F., Tietze, L. F. and Rajewsky, M. F. (1989). Hydrogen ion-mediated enhancement of cytotoxicity of bis-chloroethylating drugs in rat mammary carcinoma cells in vitro. *Cancer Research*, ***49*****(11)**, 2965–2972.

Janczewski, Ł., Kręgiel, D. and Kolesińska, B. (2021). Synthesis of Isothiocyanates Using DMT/NMM/TsO- as a New Desulfurization Reagent. *Molecules (Basel, Switzerland)*, ***26*****(9)**.

Jiang, Y., Wang, C. and Zhou, S. (2020). Targeting tumor microenvironment in ovarian cancer: Premise and promise. *Biochimica Et Biophysica Acta. Reviews on Cancer*, ***1873*****(2)**, 188361.

Joshi, S. D., Kumar, S. R. P., Patil, S., Vijayakumar, M., Kulkarni, V. H., Nadagouda, M. N., et al. (2019). Chemical synthesis, molecular modeling and pharmacophore mapping of new pyrrole derivatives as inhibitors of InhA enzyme and Mycobacterium tuberculosis growth. *Medicinal Chemistry Research*, ***28*****(11)**, 1838–1863.

Joule, J. A. and Mills, K. (2010). *Heterocyclic Chemistry, Fifth Edition*. Wiley.

Jyothi, N. R. and Farook, N. A. M. (2019). Synthesis and Characterization of Newly Synthesized Thiosemicarbazone Ligands with IR, NMR and Mass Spectral Techniques. *Oriental Journal of Chemistry*, ***35*****(1)**, 43–47.

Kang, H. J., Kim, I. H., Sung, C. O., Shim, J. H. and Yu, E. (2015). Expression of carbonic anhydrase 9 is a novel prognostic marker in resectable hepatocellular carcinoma. *Virchows Archiv*, ***466*****(4)**, 403–413.

Karaküçük-İyidoğan, A., Taşdemir, D., Oruç-Emre, E. E. and Balzarini, J. (2011). Novel platinum(II) and palladium(II) complexes of thiosemicarbazones derived from 5-substitutedthiophene-2-carboxaldehydes and their antiviral and cytotoxic activities. *European Journal of Medicinal Chemistry*, ***46*****(11)**, 5616–5624.

Karalı, N., Akdemir, A., Göktaş, F., Eraslan Elma, P., Angeli, A., Kızılırmak, M., et al. (2017). Novel sulfonamide-containing 2-indolinones that selectively inhibit tumor-associated alpha carbonic anhydrases. *Bioorganic & Medicinal Chemistry*, ***25*****(14)**, 3714–3718.

Katritzky, A. R. (Ed.). (2008). *Comprehensive heterocyclic chemistry III*. Elsevier.

Kaur, N. (2022). *Lawesson's Reagent in Heterocycle Synthesis: Thiazole Synthesis*.

Kazokaitė, J., Becker, H. M., Barker, H. R., Aspatwar, A., Parkkila, S., Dubois, L. J., et al. (2019). Efficacy of Novel CA IX Inhibitors in Biological Models. In D. Matulis (Ed.), *Carbonic Anhydrase as Drug Target;* 265–287.

Kazokaitė, J., Niemans, R., Dudutienė, V., Becker, H. M., Leitāns, J., Zubrienė, A., et al. (2018). Novel fluorinated carbonic anhydrase IX inhibitors reduce hypoxia-induced acidification and clonogenic survival of cancer cells. *Oncotarget*, ***9*****(42)**, 26800–26816.

Kciuk, M., Gielecińska, A., Mujwar, S., Mojzych, M., Marciniak, B., Drozda, R., et al. (2022). Targeting carbonic anhydrase IX and XII isoforms with small molecule inhibitors and monoclonal antibodies. *Journal of Enzyme İnhibition and Medicinal Chemistry*, ***37*****(1)**, 1278–1298.

Keilin, D. and Mann, T. (1939). Carbonic Anhydrase. *Nature*, ***144*****(3644)**, 442–443.

Khalaji, A. D., Grivani, G., Akerdi, S. J., Gotoh, K., Ishida, H. and Mighani, H. (2010). Synthesis, spectroscopic characterization, crystal structures, and theoretical studies of (E)-2-(2,4-dimethoxybenzylidene)thiosemicarbazone and (E)-2-(2,5-dimethoxybenzylidene)thiosemicarbazone. *Structural Chemistry*, ***21*****(5)**, 995–1003.

Khalaji, A. D., Mehrani, S., Eigner, V. and Dusek, M. (2013). Synthesis, experimental and theoretical studies on its crystal structure and FT-IR spectrum of new thiosemicarbazone compound E-2-(4-isopropylbenzylidene)thiosemicarbazone. *Journal of Molecular Structure*, ***1047***, 87–94.

Kılıç-Cıkla, I., Güveli, Ş., Yavuz, M., Bal-Demirci, T. and Ülküseven, B. (2016). 5-Methyl-2-hydroxy-acetophenone-thiosemicarbazone and its nickel(II) complex: Crystallographic, spectroscopic (IR, NMR and UV) and DFT studies. *Polyhedron*, ***105***, 104–114.

Kim, D. S., Jeong, Y. M., Park, I. K., Hahn, H. G., Lee, H. K., Kwon, S. B., et al. (2007). A new 2-imino-1,3-thiazoline derivative, KHG22394, inhibits melanin synthesis in mouse B16 melanoma cells. *Biological & Pharmaceutical Bulletin*, ***30*****(1)**, 180–183.

Kim, J. Y., Shin, H. J., Kim, T. H., Cho, K. H., Shin, K. H., Kim, B. K., et al. (2006). Tumor-associated carbonic anhydrases are linked to metastases in primary cervical cancer. *Journal of Cancer Research and Clinical Oncology*, ***132*****(5)**, 302–308.

Kim, S.-H., Turnbull, J. and Guimond, S. (2011). Extracellular matrix and cell signalling: The dynamic cooperation of integrin, proteoglycan and growth factor.

Kim, S. and Yi, K. Y. (1985). Di-2-Pyridyl thionocarbonate. A new reagent for the preparation of isothiocyanates and carbodiimides. *Tetrahedron Letters*, ***26*****(13)**, 1661–1664.

Klier, M., Jamali, S., Ames, S., Schneider, H.-P., Becker, H. M. and Deitmer, J. W. (2016). Catalytic activity of human carbonic anhydrase isoform IX is displayed both extra- and intracellularly. *The FEBS Journal*, ***283*****(1)**, 191–200.

Kocarnik, J. M., Compton, K., Dean, F. E., Fu, W., Gaw, B. L., Harvey, J. D., et al. (2022). Cancer Incidence, Mortality, Years of Life Lost, Years Lived With Disability, and Disability-Adjusted Life Years for 29 Cancer Groups From 2010

to 2019: A Systematic Analysis for the Global Burden of Disease Study 2019. *JAMA Oncology*, ***8*(3)**, 420–444.

Koch, S., Mayer, F., Honecker, F., Schittenhelm, M. and Bokemeyer, C. (2003). Efficacy of cytotoxic agents used in the treatment of testicular germ cell tumours under normoxic and hypoxic conditions in vitro. *British Journal of Cancer*, ***89*(11)**, 2133–2139.

Korkeila, E., Talvinen, K., Jaakkola, P. M., Minn, H., Syrjänen, K., Sundström, J. and Pyrhönen, S. (2009). Expression of carbonic anhydrase IX suggests poor outcome in rectal cancer. *British Journal of Cancer*, ***100*(6)**, 874–880.

Koshland, D. E. (1995). The Key–Lock Theory and the Induced Fit Theory. *Angewandte Chemie International Edition in English*, ***33*(2324)**, 2375–2378.

Kouatly, O., Geronikaki, A., Kamoutsis, C., Hadjipavlou-Litina, D. and Eleftheriou, P. (2009). Adamantane derivatives of thiazolyl-N-substituted amide, as possible non-steroidal anti-inflammatory agents. *European Journal of Medicinal Chemistry*, ***44*(3)**, 1198–1204.

Krebs, H. A. (1948). Inhibition of carbonic anhydrase by sulphonamides. *Biochemical Journal*, *43*(4), 525–528.

Krock, B. L., Skuli, N. and Simon, M. C. (2011). Hypoxia-induced angiogenesis: Good and evil. *Genes & Cancer*, ***2*(12)**, 1117–1133.

Kryshchyshyn, A., Kaminskyy, D., Karpenko, O., Gzella, A., Grellier, P. and Lesyk, R. (2019). Thiazolidinone/thiazole based hybrids - New class of antitrypanosomal agents. *European Journal of Medicinal Chemistry*, ***174***, 292–308.

Kumar, K., Wigfield, S., Gee, H. E., Devlin, C. M., Singleton, D., Li, J. L., et al. (2013). Dichloroacetate reverses the hypoxic adaptation to bevacizumab and enhances its antitumor effects in mouse xenografts. *Journal of Molecular Medicine*, ***91*(6)**, 749–758. 2

L. C. King and G. K. Ostrum (1964). Selective Bromination with Copper(II) Bromide1. *Journal of Organic Chemistry*.

Laconi, E. (2007). The evolving concept of tumor microenvironments. *BioEssays : News and Reviews in Molecular, Cellular and Developmental Biology*, ***29*****(8)**, 738–744.

Lau, J., Lin, K. S. and Bénard, F. (2017). Past, Present, and Future: Development of Theranostic Agents Targeting Carbonic Anhydrase IX. *Theranostics*, ***7*****(17)**, 4322–4339.

Lee, S.-H. and Griffiths, J. R. (2020). How and Why Are Cancers Acidic? Carbonic Anhydrase IX and the Homeostatic Control of Tumour Extracellular pH. *Cancers*, ***12*****(6)**, 1616.

Lendahl, U., Lee, K. L., Yang, H. and Poellinger, L. (2009). Generating specificity and diversity in the transcriptional response to hypoxia. *Nature Reviews. Genetics*, ***10*****(12)**, 821–832.

Lewis, M. and Glaser, R. (2002). The azine bridge as a conjugation stopper: An NMR spectroscopic study of electron delocalization in acetophenone azines. *The Journal of Organic Chemistry*, ***67*****(5)**, 1441–1447.

Li, A. P. (2001). Screening for human ADME/Tox drug properties in drug discovery. *Drug Discovery Today*, ***6*****(7)**, 357–366.

Lima, G. M. de, Neto, J. L., Beraldo, H., Siebald, H. and Duncalf, D. J. (2002). Structural and spectral studies of thiosemicarbazones derived from 2-acetylthiophene. *Journal of Molecular Structure*, ***604*****(2-3)**, 287–291.

Lin, H.-Y. (2019). *The use of computer-aided drug design in small molecule drug discovery: The use of computer-aided drug design in small molecule drug discovery* [Ph.D Thesis, The University of Sydney, Australia].

Lin, K. Y., Hin Lam, C., Lin, X. H., Hsu, J. I., Fan, S. Y., Gupta, N. K., et al. (2021). Improved Stabilities of Labeling Probes for the Selective Modification of

Endogenous Proteins in Living Cells and In Vivo. *Chemistry – an Asian Journal*, ***16*****(8)**, 937–948.

Lin, X., Dorr, H. and Nuss, J. M. (2000). Utilization of Fukuyama's sulfonamide protecting group for the synthesis of N-substituted α-amino acids and derivatives. *Tetrahedron Letters*, ***41*****(18)**, 3309–3313.

Lin, Y., Liang, X., Zhang, X., Ni, Y., Zhou, X. and Zhao, X. (2022). Metabolic cross-talk between ovarian cancer and the tumor microenvironment-providing potential targets for cancer therapy. *Frontiers in Bioscience (Landmark Edition)*, ***27*****(4)**, 139.

Lionta, E., Spyrou, G., Vassilatis, D. K. and Cournia, Z. (2014). Structure-based virtual screening for drug discovery: Principles, applications and recent advances. *Current Topics in Medicinal Chemistry*, ***14*****(16)**, 1923–1938.

Lipinski, C. A., Lombardo, F., Dominy, B. W. and Feeney, P. J. (1997). Experimental and computational approaches to estimate solubility and permeability in drug discovery and development settings. *Advanced Drug Delivery Reviews*, ***23*****(1-3)**, 3–25.

Liu, X., Shi, D., Zhou, S., Liu, H., Liu, H. and Yao, X. (2018). Molecular dynamics simulations and novel drug discovery. *Expert Opinion on Drug Discovery*, ***13*****(1)**, 23–37.

Liu, Y., Ren, J. and Jin, G.-Y. (2004). A Facile and Rapid Method for the Synthesis of Novel Pyrazolyl Thiosemicarbazones. *ChemInform*, ***35*****(1)**.

Loncaster, J. A., Harris, A. L., Davidson, S. E., Logue, J. P., Hunter, R. D., Wycoff, C. C., et al. (2001). Carbonic Anhydrase (CA IX) Expression, a Potential New Intrinsic Marker of Hypoxia: Correlations with Tumor Oxygen Measurements and Prognosis in Locally Advanced Carcinoma of the Cervix. *Cancer Research*, ***61*****(17)**, 6394–6399.

Lou, Y., McDonald, P. C., Oloumi, A., Chia, S., Ostlund, C., Ahmadi, A., et al. (2011). Targeting tumor hypoxia: Suppression of breast tumor growth and metastasis by novel carbonic anhydrase IX inhibitors. *Cancer Research*, ***71*****(9)**, 3364–3376.

Luo, N. (2022). Editorial: Tumor microenvironment in cancer hallmarks and therapeutics. *Frontiers in Molecular Biosciences*, ***9***, 1019830.

Macalino, S. J. Y., Gosu, V., Hong, S. and Choi, S. (2015). Role of computer-aided drug design in modern drug discovery. *Archives of Pharmacal Research*, ***38*****(9)**, 1686–1701.

Maffucci, I., Hu, X., Fumagalli, V. and Contini, A. (2018). An Efficient Implementation of the Nwat-MMGBSA Method to Rescore Docking Results in Medium-Throughput Virtual Screenings. *Frontiers in Chemistry*, ***6***, 43.

Maghraby, M. T.-E., Abou-Ghadir, O. M. F., Abdel-Moty, S. G., Ali, A. Y. and Salem, O. I. A. (2020). Novel class of benzimidazole-thiazole hybrids: The privileged scaffolds of potent anti-inflammatory activity with dual inhibition of cyclooxygenase and 15-lipoxygenase enzymes. *Bioorganic & Medicinal Chemistry*, *28*(7), 115403.

Mahon, B. P., Pinard, M. A. and McKenna, R. (2015). Targeting Carbonic Anhydrase IX Activity and Expression. *Molecules (Basel, Switzerland)*, ***20*****(2)**, 2323–2348.

Mahoney, B. P., Raghunand, N., Baggett, B. and Gillies, R. J. (2003). Tumor acidity, ion trapping and chemotherapeutics. *Biochemical Pharmacology*, ***66*****(7)**, 1207–1218.

Maltepe, E., Keith, B., Arsham, A. M., Brorson, J. R. and Simon, M. C. (2000). The role of ARNT2 in tumor angiogenesis and the neural response to hypoxia. *Biochemical and Biophysical Research Communications*, ***273*****(1)**, 231–238.

Mamidala, S., Peddi, S. R., Aravilli, R. K., Jilloju, P. C., Manga, V. and Vedula, R. R. (2021). Microwave irradiated one pot, three component synthesis of a new series

of hybrid coumarin based thiazoles: Antibacterial evaluation and molecular docking studies. *Journal of Molecular Structure*, ***1225***, 129114.

Mamo, M., Ye, I. C., DiGiacomo, J. W., Park, J. Y., Downs, B. and Gilkes, D. M. (2020). Hypoxia Alters the Response to Anti-EGFR Therapy by Regulating EGFR Expression and Downstream Signaling in a DNA Methylation-Specific and HIF-Dependent Manner. *Cancer Research*, ***80*(22)**, 4998–5010.

Mann, T., and Keilin, D. (1940). Sulphanilamide as a Specific Inhibitor of Carbonic Anhydrase. *Nature*, ***146*(3692)**, 164–165.

Mansoori, B., Mohammadi, A., Davudian, S., Shirjang, S. and Baradaran, B. (2017). The Different Mechanisms of Cancer Drug Resistance: A Brief Review. *Advanced Pharmaceutical Bulletin*, ***7*(3)**, 339–348.

Maren, T. H. (1995). The Development of Topical Carbonic Anhydrase Inhibitors. *Journal of Glaucoma*, ***4*(1)**, 49.

Masini, E., Carta, F., Scozzafava, A. and Supuran, C. T. (2013). Antiglaucoma carbonic anhydrase inhibitors: A patent review. *Expert Opinion on Therapeutic Patents*, ***23*(6)**, 705–716.

Matolay, O., Beke, L., Gyurkovics, A., Francz, M., Varjasi, G., Rejtő, L., et al. (2019). Quantitative Analysis of Carbonic Anhydrase IX Uncovers Hypoxia-Related Functional Differences in Classical Hodgkin Lymphoma Subtypes. *International Journal of Molecular Sciences*, ***20*(14)**, 3463.

Matulienė, J., Žvinys, G., Petrauskas, V., Kvietkauskaitė, A., Zakšauskas, A., Shubin, K., et al. (2022). Picomolar fluorescent probes for compound affinity determination to carbonic anhydrase IX expressed in live cancer cells. *Scientific Reports*, ***12*(1)**, 17644.

Mays, J. R., Weller Roska, R. L., Sarfaraz, S., Mukhtar, H. and Rajski, S. R. (2008). Identification, synthesis, and enzymology of non-natural glucosinolate

chemopreventive candidates. *Chembiochem: A European Journal of Chemical Biology*, ***9*(5)**, 729–747.

Mboge, M. Y., Chen, Z., Wolff, A., Mathias, J. V., Tu, C., Brown, K. D., et al. (2018). Selective inhibition of carbonic anhydrase IX over carbonic anhydrase XII in breast cancer cells using benzene sulfonamides: Disconnect between activity and growth inhibition. *PloS One*, ***13*(11)**, e0207417.

McDonald, P. C., Chafe, S. C., Supuran, C. T., and Dedhar, S. (2022). Cancer therapeutic targeting of hypoxia induced carbonic anhydrase IX: From bench to bedside. *Cancers*, ***14*(14)**.

McDonald, P. C., Chia, S., Bedard, P. L., Chu, Q., Lyle, M., Tang, L., et al. (2020). A Phase 1 Study of SLC-0111, a novel inhibitor of carbonic anhydrase IX, in patients with advanced solid tumors. *American Journal of Clinical Oncology*, ***43*(7)**, 484–490.

McIntyre, A., Patiar, S., Wigfield, S., Li, J. L., Ledaki, I., Turley, H., et al. (2012). Carbonic anhydrase IX promotes tumour growth and necrosis in vivo and inhibition enhances anti-VEGF therapy. *Clinical Cancer Research: An Official Journal of the American Association for Cancer Research*, ***18*(11)**, 3100–3111.

McKee, R. L., and Bost, R. W. (1946). Para-Substituted phenyl isothiocyanates and some related thioureas. *Journal of the American Chemical Society*, ***68*(12)**, 2506.

McLoughlin, C., Clyburne, J. A. C., and Weinberg, N. (2007). Azines: Conjugation stoppers or conjugation switches. *Journal of Materials Chemistry*, ***17*(40)**, 4304.

Méhes, G., Matolay, O., Beke, L., Czenke, M., Jóna, Á., Miltényi, Z., et al. (2019). Hypoxia-related carbonic anhydrase IX expression is associated with unfavourable response to first-line therapy in classical Hodgkin's lymphoma. *Histopathology*, ***74*(5)**, 699–708.

Meldrum, N. U., and Roughton, F. J. (1933). Carbonic anhydrase. Its preparation and properties. *The Journal of Physiology*, ***80*(2)**, 113–142.

Meldrum N. U. (1932). Some properties of carbonic anhydrase, the CO_2 enzyme present in blood. *J. Physiol.*, ***75***, 15–16.

Meleddu, R., Distinto, S., Cottiglia, F., Angius, R., Caboni, P., Angeli, A., et al. (2020). New Dihydrothiazole Benzensulfonamides: Looking for Selectivity toward Carbonic Anhydrase Isoforms I, II, IX, and XII. *ACS Medicinal Chemistry Letters*, ***11*****(5)**, 852–856.

Meleddu, R., Distinto, S., Cottiglia, F., Angius, R., Gaspari, M., Taverna, D., et al. (2018). Tuning the Dual Inhibition of Carbonic Anhydrase and Cyclooxygenase by Dihydrothiazole Benzensulfonamides. *ACS Medicinal Chemistry Letters*, ***9*****(10)**, 1045–1050.

Meleddu, R., Maccioni, E., Distinto, S., Bianco, G., Melis, C., Alcaro, S., et al. (2015). New 4-(3-cyclohexyl-4-aryl-2,3-dihydro-1,3-thiazol-2-ylidene)aminobenzene-1-sulfonamides, synthesis and inhibitory activity toward carbonic anhydrase I, II, IX, XII. *Bioorganic & Medicinal Chemistry Letters*, ***25*****(16)**, 3281–3284.

Metwally, M. A., Bondock, S., El-Azap, H. and Kandeel, E.-E. M. (2011). Thiosemicarbazides: synthesis and reactions. *Journal of Sulfur Chemistry*, ***32*****(5)**, 489–519.

Moeker, J., Peat, T. S., Bornaghi, L. F., Vullo, D., Supuran, C. T. and Poulsen, S.-A. (2014). Cyclic secondary sulfonamides: Unusually good inhibitors of cancer-related carbonic anhydrase enzymes. *Journal of Medicinal Chemistry*, ***57*****(8)**, 3522–3531.

Mustafa, S., Nair, V., Chittoor, J. and Krishnapillai, S. (2004). Synthesis of 1, 2, 4-Triazoles and Thiazoles from Thiosemicarbazide and its Derivatives. *Mini-Reviews in Organic Chemistry*, ***1*****(4)**, 375–385.

Najmanovich, R., Kuttner, J., Sobolev, V. and Edelman, M. (2000). Side-chain flexibility in proteins upon ligand binding. *Proteins: Structure, Function, and Genetics*, ***39*****(3)**, 261–268.

Nakao, M., Ishii, G., Nagai, K., Kawase, A., Kenmotsu, H., Kon-No, H., et al. (2009). Prognostic significance of carbonic anhydrase IX expression by cancer-associated fibroblasts in lung adenocarcinoma. *Cancer*, ***115*****(12)**, 2732–2743.

Narasimhamurthy, K. H., Sajith, A. M., Joy, M. N. and Rangappa, K. S. (2020). An Overview of Recent Developments in the Synthesis of Substituted Thiazoles. *ChemistrySelect*, ***5*****(19)**, 5629–5656.

Nechak, R., Achouche Bouzroura, S., Benmalek, Y., Boufroua, N., Nedjar Kolli, B., Poulain Martini, S., et al. (2019). Synthesis, identification and antimicrobial activity of substituted thiazolines and 1,3,4-thiadiazines from dehydroacetic acid. *Synthetic Communications*, ***49*****(15)**, 1895–1905.

Neri, D. and Supuran, C. T. (2011). Interfering with pH regulation in tumours as a therapeutic strategy. *Nature Reviews. Drug Discovery*, ***10*****(10)**, 767–777.

Netti, P. A., Berk, D. A., Swartz, M. A., Grodzinsky, A. J. and Jain, R. K. (2000). Role of extracellular matrix assembly in interstitial transport in solid tumors. *Cancer Research*, ***60*****(9)**, 2497–2503.

Newell, K., Franchi, A., Pouysségur, J. and Tannock, I. (1993). Studies with glycolysis-deficient cells suggest that production of lactic acid is not the only cause of tumor acidity. *Proceedings of the National Academy of Sciences of the United States of America.*

Ngoc Toan, V. and Dinh Thanh, N. (2021). Novel thiazoline–coumarin hybrid compounds containing sugar moieties: Synthesis, biological evaluation and molecular docking study as antiproliferative agents. *New Journal of Chemistry*, ***45*****(24)**, 10636–10653.

Nocentini, A., Donald, W. A. and Supuran, C. T. (2019). Human carbonic anhydrases. In C. T. Supuran & A. Nocentini (Eds.), *Carbonic anhydrases: Biochemistry and pharmacology of an evergreen pharmaceutical target*; 151–185.

Nocentini, A., Supuran, C. T. and Capasso, C. (2021). An overview on the recently discovered iota-carbonic anhydrases. *Journal of Enzyme İnhibition and Medicinal Chemistry*, ***36*****(1)**, 1988–1995.

Omar, K., Geronikaki, A., Zoumpoulakis, P., Camoutsis, C., Soković, M., Cirić, A., et al. (2010). Novel 4-thiazolidinone derivatives as potential antifungal and antibacterial drugs. *Bioorganic & Medicinal Chemistry*, ***18*****(1)**, 426–432.

Ondriskova, E., Debreova, M. and Pastorekova, S. (2015). Tumor-Associated Carbonic Anhydrases IX and XII. In C. T. Supuran and G. de Simone (Eds.), *Carbonic anhydrases as biocatalysts: From theory to medical and industrial applications;* 169–205.

Ong, C. H. C., Lee, D. Y., Lee, B., Li, H., Lim, J. C. T., Lim, J. X., et al. (2022). Hypoxia-regulated carbonic anhydrase IX (CAIX) protein is an independent prognostic indicator in triple negative breast cancer. *Breast Cancer Research*, ***24*****(1)**, 38.

Osguthorpe, D. J., Sherman, W. and Hagler, A. T. (2012). Generation of receptor structural ensembles for virtual screening using binding site shape analysis and clustering. *Chemical Biology & Drug Design*, ***80*****(2)**, 182–193.

Othman, E. M., Fayed, E. A., Husseiny, E. M. and Abulkhair, H. S. (2022). The effect of novel synthetic semicarbazone- and thiosemicarbazone-linked 1,2,3-triazoles on the apoptotic markers, VEGFR-2, and cell cycle of myeloid leukemia. *Bioorganic Chemistry*, ***127***, 105968.

Owa, T., Yoshino, H., Okauchi, T., Yoshimatsu, K., Ozawa, Y., Sugi, N. H., et al. (1999). Discovery of novel antitumor sulfonamides targeting G1 phase of the cell cycle. *Journal of Medicinal Chemistry*, ***42*****(19)**, 3789–3799.

Ozmen Ozgun, D., Gul, H. I., Yamali, C., Sakagami, H., Gulcin, I., Sukuroglu, M., et al. (2019). Synthesis and bioactivities of pyrazoline benzensulfonamides as carbonic anhydrase and acetylcholinesterase inhibitors with low cytotoxicity. *Bioorganic Chemistry*, ***84***, 511–517.

Özbey, S., Karalı, N. and Gürsoy, A. (2003). Synthesis of 4-(3-coumarinyl)-3-benzyl-4-thiazolin-2-one 4-methylbenzylidenehydrazone and determination of the isomeric structure by X-ray analysis. *Zeitschrift Für Kristallographie - Crystalline Materials*, ***218*****(12)**, 819–822.

Pacchiano, F., Carta, F., McDonald, P. C., Lou, Y., Vullo, D., Scozzafava, A., et al. (2011). Ureido-substituted benzenesulfonamides potently inhibit carbonic anhydrase IX and show antimetastatic activity in a model of breast cancer metastasis. *Journal of Medicinal Chemistry*, ***54*****(6)**, 1896–1902.

Paget, S. (1889). The distribution of secondary growths in cancer of the breast. *The Lancet*, ***133*****(3421)**, 571–573.

Park, K. and Cho, A. E. (2017). Using reverse docking to identify potential targets for ginsenosides. *Journal of Ginseng Research*, ***41*****(4)**, 534–539.

Parker, E. N., Song, J., Kishore Kumar, G. D., Odutola, S. O., Chavarria, G. E., Charlton-Sevcik, A. K., et al. (2015). Synthesis and biochemical evaluation of benzoylbenzophenone thiosemicarbazone analogues as potent and selective inhibitors of cathepsin L. *Bioorganic & Medicinal Chemistry*, ***23*****(21)**, 6974–6992.

Parkkila, S. (2021). Carbonic Anhydrase Isozymes as Diagnostic Biomarkers and Therapeutic Targets. In W. R. Chegwidden and N. D. Carter (Eds.), *The Carbonic Anhydrases: Current and Emerging Therapeutic Targets*; **75**, 3–36.

Parks, S. K., Chiche, J. and Pouyssegur, J. (2011). Ph control mechanisms of tumor survival and growth. *Journal of Cellular Physiology*, ***226*****(2)**, 299–308.

Parmakhtiar, B., Burger, R. A., Kim, J. H. and Fruehauf, J. P. (2019). Hıf Inactivation of p53 in Ovarian Cancer Can Be Reversed by Topotecan, Restoring Cisplatin and Paclitaxel Sensitivity. *Molecular Cancer Research : MCR*, ***17*****(8)**, 1675–1686.

Pastorekova, S. and Gillies, R. J. (2019). The role of carbonic anhydrase IX in cancer development: Links to hypoxia, acidosis, and beyond. *Cancer Metastasis Reviews*, ***38*****(1-2)**, 65–77.

Patard, J.-J., Fergelot, P., Karakiewicz, P. I., Klatte, T., Trinh, Q. D., Rioux-Leclercq, N., Said, J. W., Belldegrun, A. S. and Pantuck, A. J. (2008). Low CAIX expression and absence of VHL gene mutation are associated with tumor aggressiveness and poor survival of clear cell renal cell carcinoma. *International Journal of Cancer*, ***123*****(2)**, 395–400.

Patil, S. A., Naik, V. H., Kulkarni, A. D., Kamble, U., Bagihalli, G. B. and Badami, P. S. (2010). DNA cleavage, in vitro antimicrobial and electrochemical studies of Co(II), Ni(II), and Cu(II) complexes with m -substituted thiosemicarbazide Schiff bases. *Journal of Coordination Chemistry*, ***63*****(4)**, 688–699.

Patskovsky, Y. V., Negrebetskaya, E. N., Chernomaz, A. A., Voloshchuk, T. P., Rubashevsky, E. L., Kitam, O. E., et al. (1996). Aromatic thiosemicarbazones, their antiviral action and interferon. 1. The decreasing of adenovirus type 1 resistance against interferon by methisazone in vitro. *Biopolymers and Cell*, ***12*****(2)**, 74–83.

Pavia, D. L., Lampman, G. M., Kriz, G. S. and Vyvyan, J. R. (2015). *Introduction to spectroscopy* (Fifth edition). Cengage Learning.

Pereira, P. S., Lima, M. d. C. A. de, Neto, P. P. M., Oliveira-Tintino, Cícera Datiane de Morais, Tintino, S. R., et al. (2019). Thiazolidinedione and thiazole derivatives potentiate norfloxacin activity against NorA efflux pump over expression in Staphylococcus aureus 1199B strains. *Bioorganic & Medicinal Chemistry*, ***27*****(17)**, 3797–3804.

Pervez, H., Ahmad, M., Hadda, T. B., Toupet, L. and Naseer, M. M. (2015). Synthesis and fluorine-mediated interactions in methanol-encapsulated solid state self-assembly of an isatin-thiazoline hybrid. *Journal of Molecular Structure*, ***1098***, 124–129.

Pfeiffer, W.-D., Ahlers, K. D., Saghyan, A. S., Villinger, A. and Langer, P. (2014). Unexpected Ring Enlargement of 2-Hydrazono-2,3-dihydro-1,3-thiazoles to 1,3,4-Thiadiazines. *Helvetica Chimica Acta*, ***97*(1)**, 76–87.

Phiromphu, N., Suramitr, S., Chotima, R., Boonseng, B., Songsasen, A. and Piyasaengthong, A. (2021). Azine-hydrazone Tautomerism of Thiazolylazo Pyridine Compound: Synthesis, Structural Determination, and Biological Activities. *Journal of Molecular Structure*, ***1230***, 129658.

Picón-Ferrer, I., Hueso-Ureña, F., Illán-Cabeza, N. A., Jiménez-Pulido, S. B., Martínez-Martos, J. M., Ramírez-Expósito, M. J., et al. (2009). Chloro-fac-tricarbonylrhenium(I) complexes of asymmetric azines derived from 6-acetyl-1,3,7-trimethylpteridine-2,4(1H,3H)-dione with hydrazine and aromatic aldehydes: Preparation, structural characterization and biological activity against several human tumor cell lines. *Journal of Inorganic Biochemistry*, ***103*(1)**, 94–100

Pijnenborg, J. M. A., Wijnakker, M., Hagelstein, J., Delvoux, B. and Groothuis, P. G. (2007). Hypoxia contributes to development of recurrent endometrial carcinoma. *International Journal of Gynecological Cancer: Official Journal of the International Gynecological Cancer Society*, ***17*(4)**, 897–904.

Pillai, S. R., Damaghi, M., Marunaka, Y., Spugnini, E. P., Fais, S. and Gillies, R. J. (2019). Causes, consequences, and therapy of tumors acidosis. *Cancer and Metastasis Reviews*, ***38*(1-2)**, 205–222.

Pinzi, L. and Rastelli, G. (2019). Molecular Docking: Shifting Paradigms in Drug Discovery. *International Journal of Molecular Sciences*, ***20*(18)**.

Posner, G. H., Cho, C. G., Green, J. V., Zhang, Y. and Talalay, P. (1994). Design and synthesis of bifunctional isothiocyanate analogs of sulforaphane: Correlation between structure and potency as inducers of anticarcinogenic detoxication enzymes. *Journal of Medicinal Chemistry*, ***37*(1)**, 170–176.

Potter, C. P. S. and Harris, A. L. (2003). Diagnostic, prognostic and therapeutic implications of carbonic anhydrases in cancer. *British Journal of Cancer*, ***89*(1)**, 2–7.

Pramanik, B. N., Ganguly, A. K. and Gross, M. L. (2002). *Applied electrospray mass spectroscopy*. *Practical spectroscopy: v.* ***32*.** Marcel Dekker.

Psurski, M., Janczewski, Ł., Świtalska, M., Gajda, A., Goszczyński, T. M., Oleksyszyn, J., et al. (2017). Novel phosphonate analogs of sulforaphane: Synthesis, in vitro and in vivo anticancer activity. *European Journal of Medicinal Chemistry*, ***132***, 63–80.

Qayed, W. S., Hassan, M. A., El-Sayed, W. M., Rogério A Silva, J. and Aboul-Fadl, T. (2022). Novel Azine Linked Hybrids of 2-Indolinone and Thiazolodinone Scaffolds as CDK2 Inhibitors with Potential Anticancer Activity: In Silico Design, Synthesis, Biological, Molecular Dynamics and Binding Free Energy Studies. *Bioorganic Chemistry*, ***126***, 105884.

Queen, A., Bhutto, H. N., Yousuf, M., Syed, M. A. and Hassan, M. I. (2022). Carbonic anhydrase IX: A tumor acidification switch in heterogeneity and chemokine regulation. *Seminars in Cancer Biology.*

Raghunand, N., Mahoney, B. P. and Gillies, R. J. (2003). Tumor acidity, ion trapping and chemotherapeutics. *Biochemical Pharmacology*, ***66*(7)**, 1219–1229.

Rana, A., Parekh, N., Dabhi, H., Bhoi, D. and Kumari, N. (2011). Synthesis, Crystal Structural Characterization and Biological Properties of Thiosemicarbazones of Schiff Bases Derived from 4-Acyl-2-pyrazoline-5-one. *E-Journal of Chemistry*, ***8*(4)**, 1820–1831.

Rani, S., Roy, S., Singh, M. and Kaithwas, G. (2022). Regulation of Transactivation at C-TAD Domain of HIF-1α by Factor-Inhibiting HIF-1α (FIH-1): A Potential Target for Therapeutic Intervention in Cancer. *Oxidative Medicine and Cellular Longevity*, ***2022***, 2407223.

Rastelli, G., Del Rio, A., Degliesposti, G. and Sgobba, M. (2010). Fast and accurate predictions of binding free energies using MM-PBSA and MM-GBSA. *Journal of Computational Chemistry*, ***31*****(4)**, 797–810.

Raveesha, R., Anusuya, A. M., Raghu, A. V., Yogesh Kumar, K., Dileep Kumar, M. G., Benaka Prasad, S. B., et al. (2022). Synthesis and characterization of novel thiazole derivatives as potential anticancer agents: Molecular docking and DFT studies. *Computational Toxicology*, ***21***, 100202.

Ricci-Lopez, J., Aguila, S. A., Gilson, M. K. and Brizuela, C. A. (2021). Improving Structure-Based Virtual Screening with Ensemble Docking and Machine Learning. *Journal of Chemical Information and Modeling*, ***61*****(11)**, 5362–5376.

Robey, I. F., Baggett, B. K., Kirkpatrick, N. D., Roe, D. J., Dosescu, J., Sloane, B. F., et al. (2009). Bicarbonate increases tumor pH and inhibits spontaneous metastases. *Cancer Research*, ***69*****(6)**, 2260–2268.

Rosenman, K. (1978). Benefits of saccharin: A review. *Environmental Research*, ***15*****(1)**, 70–81.

Rueda, M., Bottegoni, G. and Abagyan, R. (2010). Recipes for the selection of experimental protein conformations for virtual screening. *Journal of Chemical Information and Modeling*, ***50*****(1)**, 186–193.

Sahakyan, H. (2021). Improving virtual screening results with MM/GBSA and MM/PBSA rescoring. *Journal of Computer-Aided Molecular Design*, ***35*****(6)**, 731–736.

Said, M. A., Eldehna, W. M., Nocentini, A., Bonardi, A., Fahim, S. H., Bua, S., et al. (2020). Synthesis, biological and molecular dynamics investigations with a series of triazolopyrimidine/triazole-based benzenesulfonamides as novel carbonic anhydrase inhibitors. *European Journal of Medicinal Chemistry*, ***185***, 111843.

Sansone, P., Piazzi, G., Paterini, P., Strillacci, A., Ceccarelli, C., Minni, F., et al. (2009). Cyclooxygenase-2 or carbonic anhydrase-IX up-regulation promotes invasive potential and hypoxia survival in colorectal cancer cells. *Journal of Cellular and Molecular Medicine*, ***13*****(9B)**, 3876–3887.

Santhosh, L., Durgamma, S., Shekharappa and Sureshbabu, V. V. (2018). Staudinger/aza-Wittig reaction to access Nβ-protected amino alkyl isothiocyanates. *Organic & Biomolecular Chemistry*, ***16*****(26)**, 4874–4880.

Santos, I. C. and Brodbelt, J. S. (2021). Structural Characterization of Carbonic Anhydrase-Arylsulfonamide Complexes Using Ultraviolet Photodissociation Mass Spectrometry. *Journal of the American Society for Mass Spectrometry*, ***32*****(6)**, 1370–1379.

Santos, L. H. S., Ferreira, R. S. and Caffarena, E. R. (2019). Integrating Molecular Docking and Molecular Dynamics Simulations. In W. Filgueira de Azevedo (Ed.), *Springer protocols: Docking screens for drug discovery*; **2053**, 13–34.

Schrödinger. (2015). *QikProp* (4.4th ed.). Schrödinger.

Scozzafava, A., Menabuoni, L., Mincione, F., Briganti, F., Mincione, G. and Supuran, C. T. (1999). Carbonic anhydrase inhibitors. Synthesis of water-soluble, topically effective, intraocular pressure-lowering aromatic/heterocyclic sulfonamides containing cationic or anionic moieties: Is the tail more important than the ring? *Journal of Medicinal Chemistry*, ***42*****(14)**, 2641–2650.

Search of: indisulam - List Results - ClinicalTrials.gov. (2022, November 5). https://clinicaltrials.gov/ct2/results?cond=indisulam&term=&cntry=&state=&city=&dist=

Sefika Feyza, M., Selin, S. and Saliha Ece, A. (2022). Fundamentals of Molecular Docking and Comparative Analysis of Protein–Small-Molecule Docking Approaches. In *Biomedical Engineering: Vol. 0. Molecular Docking - Recent Advances [Working Title]* (Vol. 0).

Selvendiran, K., Bratasz, A., Kuppusamy, M. L., Tazi, M. F., Rivera, B. K. and Kuppusamy, P. (2009). Hypoxia induces chemoresistance in ovarian cancer cells by activation of signal transducer and activator of transcription 3. *International Journal of Cancer*, ***125*****(9)**, 2198–2204.

Semenza, G. L. (2007). Hypoxia-inducible factor 1 (HIF-1) pathway. *Science's STKE : Signal Transduction Knowledge Environment*, ***2007*****(407)**.

Sevinçli, Z. Ş., Cantürk, Z., Dikmen, M. and Karalı, N. L. (2020). Anticancer and antituberculosis effects of 5-fluoro1H-indole-2,3-dione 3-thiosemicarbazones. *İstanbul Journal of Pharmacy*, ***50*****(3)**.

Sevinçli, Z. Ş., Duran, G. N., Özbil, M. and Karalı, N. (2020). Synthesis, molecular modeling and antiviral activity of novel 5-fluoro-1H-indole-2,3-dione 3-thiosemicarbazones. *Bioorganic Chemistry*, ***104***, 104202.

Sezer, C. (1996). *Bazı 2-sübstitüe 4[(4-sübstitüe pirol-1-il) fenil] tiyazol türevlerinin sentezi* [Master's Thesis]. Anadolu University, Eskişehir.

Sharma, M., Astekar, M., Soi, S., Manjunatha, B. S., Shetty, D. C. and Radhakrishnan, R. (2015). Ph Gradient Reversal: An Emerging Hallmark of Cancers. *Recent Patents on Anti-Cancer Drug Discovery*, ***10*****(3)**, 244–258.

Sharma, P. C., Bansal, K. K., Sharma, A., Sharma, D. and Deep, A. (2020). Thiazole-containing compounds as therapeutic targets for cancer therapy. *European Journal of Medicinal Chemistry*, ***188***, 112016.

Shehzad, M. T., Imran, A., Hameed, A., Rashida, M. A., Bibi, M., Uroos, M., et al. (2021). Exploring synthetic and therapeutic prospects of new thiazoline derivatives as aldose reductase (ALR2) inhibitors. *RSC Advances*, ***11*****(28)**, 17259–17282.

Shehzad, M. T., Khan, A., Islam, M., Halim, S. A., Khiat, M., Anwar, M. U., et al. (2020). Synthesis, characterization and molecular docking of some novel hydrazonothiazolines as urease inhibitors. *Bioorganic Chemistry*, ***94***, 103404.

Sheldrick, G. M. and Schneider, T. R. (1997). Shelxl: High-resolution refinement. *Methods in Enzymology*, ***277***, 319–343.

Shezi, S. (2017). *Synthesis, characterisation and antibacterial activity of substituted 2-quinoline thiosemicarbazones* [Master's Thesis]. University of KwaZulu-Natal, Durban, South Africa.

Siegel, R. L., Miller, K. D., Fuchs, H. E. and Jemal, A. (2022). Cancer statistics, 2022. *CA: A Cancer Journal for Clinicians*, ***72*****(1)**, 7–33.

Silverstein, R. M., Webster, F. X. and Kiemle, D. J. (2005). *Spectrometric identification of organic compounds* (7th ed. / Robert M. Silverstein, Francis X. Webster, David J. Kiemle). John Wiley & Sons.

Silvia Bua. (2019). *Hybrid Pharmacores as Carbonic Anhydrase Inhibitors* [Doctoral Thesis]. Università degli Studi di Firenze, Florence, Italy.

Singh, A., Malhotra, D., Singh, K., Chadha, R. and Bedi, P. M. S. (2022). Thiazole derivatives in medicinal chemistry: Recent advancements in synthetic strategies, structure activity relationship and pharmacological outcomes. *Journal of Molecular Structure*, ***1266***, 133479.

SitaRam, Celik, G., Khloya, P., Vullo, D., Supuran, C. T. and Sharma, P. K. (2014). Benzenesulfonamide bearing 1,2,4-triazole scaffolds as potent inhibitors of tumor associated carbonic anhydrase isoforms hCA IX and hCA XII. *Bioorganic & Medicinal Chemistry*, ***22*****(6)**, 1873–1882.

Snyder, A. P. (1995). *Biochemical and biotechnological applications of electrospray ionization mass spectrometry*. *ACS symposium series, 0097-6156: Vol. 619*.

Solomon, S. and Mulugeta, W. (2019). Diagnosis and Risk Factors of Advantage Cancers in Ethiopia. *Journal of Cancer Prevention*, ***24*****(3)**, 163–172.

Song, J., Pan, R., Li, G., Su, W., Song, X., Li, J. and Liu, S. (2020). Synthesis and anticancer activities of thiosemicarbazones derivatives of thiochromanones and related scaffolds. *Medicinal Chemistry Research*, ***29*****(4)**, 630–642.

Soylu Eter, Ö., Atioğlu, Z., Akkurt, M., Ersanlı, C. and Karalı, N. (2021). Molecular and crystal structure of 1-methyl 5-trifluoromethoxy-1H-indole-2,3-dione 3-[4-(4-methoxyphenyl)thiosemicarbazone]. *İstanbul Journal of Pharmacy*, ***51*(1)**, 59–66.

SR Pattan, NS Dighe, SA Nirmal, AN Merekar, RB Laware, HV Shinde et al. (2009). Synthesis and biological evaluation of some substituted amino thiazole derivatives. *Asian Journal of Research in Chemistry*, *2*(2), 196–201.

Stadie, W. C. and O'Brien, H. (1933). The catalysis of the hydration of carbon dioxide and dehydration of carbonic acid by an enzyme isolated from red blood cells. *Journal of Biological Chemistry*, ***103*(2)**, 521–529.

Stanzione, F., Giangreco, I. and Cole, J. C. (2021). Chapter Four - Use of molecular docking computational tools in drug discovery. In D. R. Witty & B. Cox (Eds.), *Progress in Medicinal Chemistry*; **60**, 273–343.

Stariat, J., Kovaříková, P., Kučera, R., Klimeš, J., Kalinowski, D. S., Des Richardson, R., et al. (2013). Identification of in vitro metabolites of the novel anti-tumor thiosemicarbazone, DpC, using ultra-high performance liquid chromatography-quadrupole-time-of-flight mass spectrometry. *Analytical and Bioanalytical Chemistry*, ***405*(5)**, 1651–1661.

Stewart, B. W., Wild, C. and Weiderpass, E. (Eds.). (2020). *World cancer report: Cancer research for cancer prevention*. IARC Press. https://publications.iarc.fr/586

Stillebroer, A. B., Mulders, P. F. A., Boerman, O. C., Oyen, W. J. G. and Oosterwijk, E. (2010). Carbonic anhydrase IX in renal cell carcinoma: İmplications for prognosis, diagnosis, and therapy. *European Urology*, ***58*(1)**, 75–83.

Stromgaard, K., Krogsgaard-Larsen, P. and Madsen, U. (2016). *Textbook of Drug Design and Discovery, Fifth Edition* (5th ed.). Chapman and Hall/CRC.

Stuart, B. (2004). *Infrared spectroscopy: Fundamentals and applications. Analytical techniques in the sciences*. Wiley.

Study of COTI-2 as Monotherapy or Combination Therapy for the Treatment of Malignancies - Full Text View - ClinicalTrials.gov. (2023, February 15). https://www.clinicaltrials.gov/ct2/show/NCT02433626

A Study of SLC-0111 and Gemcitabine for Metastatic Pancreatic Ductal Cancer in Subjects Positive for CAIX - Full Text View - ClinicalTrials.gov. (2022, November 5). https://clinicaltrials.gov/ct2/show/NCT03450018?cond=SLC-0111&draw=2&rank=1

Subhashree, G. R., Haribabu, J., Saranya, S., Yuvaraj, P., Anantha Krishnan, D., Karvembu, R. and Gayathri, D. (2017). In vitro antioxidant, antiinflammatory and in silico molecular docking studies of thiosemicarbazones. *Journal of Molecular Structure*, ***1145***, 160–169.

Suh, J., Yum, E. K., Cheon, H. G. and Cho, Y. S. (2012). Synthesis and biological evaluation of N-aryl-4-aryl-1,3-thiazole-2-amine derivatives as direct 5-lipoxygenase inhibitors. *Chemical Biology & Drug Design*, ***80*****(1)**, 89–98.

Sung, H., Ferlay, J., Siegel, R. L., Laversanne, M., Soerjomataram, I., Jemal, A. and Bray, F. (2021). Global Cancer Statistics 2020: Globocan Estimates of Incidence and Mortality Worldwide for 36 Cancers in 185 Countries. *CA: A Cancer Journal for Clinicians*, ***71*****(3)**, 209–249.

Suni, V., Prathapachandra Kurup, M. R. and Nethaji, M. (2006). Structural and spectral perspectives of a novel thiosemicarbazone synthesized from di-2-pyridyl ketone and 4-phenyl-3-thiosemicarbazide. *Spectrochimica Acta Part a: Molecular and Biomolecular Spectroscopy*, ***63*****(1)**, 174–181.

Supuran, C. T. and Mugelli, A. (2019). Polypharmacology of carbonic anhydrase inhibitors. *Pharmadvances*, ***01*****(00)**.

Supuran, C. T. (2008). Carbonic anhydrases: Novel therapeutic applications for inhibitors and activators. *Nature Reviews Drug Discovery*, ***7*****(2)**, 168–181.

Supuran, C. T. (2010). Carbonic anhydrase inhibitors. *Bioorganic & Medicinal Chemistry Letters*, ***20*****(12)**, 3467–3474.

Supuran, C. T. (2016a). How many carbonic anhydrase inhibition mechanisms exist? *Journal of Enzyme İnhibition and Medicinal Chemistry*, ***31*****(3)**, 345–360. 1

Supuran, C. T. (2016b). Structure and function of carbonic anhydrases. *Biochemical Journal*, ***473*****(14)**, 2023–2032.

Supuran, C. T. (2017a). Advances in structure-based drug discovery of carbonic anhydrase inhibitors. *Expert Opinion on Drug Discovery*, ***12*****(1)**, 61–88.

Supuran, C. T. (2017b). Carbonic Anhydrase Inhibition and the Management of Hypoxic Tumors. *Metabolites*, ***7*****(3)**.

Supuran, C. T. and Simone, G. de. (2015). Carbonic Anhydrases: An Overview. In C. T. Supuran & G. de Simone (Eds.), *Carbonic anhydrases as biocatalysts: From theory to medical and industrial applications* Elsevier; 3–13.

Svastova, E., Witarski, W., Csaderova, L., Kosik, I., Skvarkova, L., Hulikova, A., et al. (2012). Carbonic anhydrase IX interacts with bicarbonate transporters in lamellipodia and increases cell migration via its catalytic domain. *The Journal of Biological Chemistry*, ***287*****(5)**, 3392–3402.

Swayampakula, M., Venkateswaran, G., McDonald, P. C. and Dedhar, S. (2021). Carbonic Anhydrase IX Interactome and the Regulation of Cancer Progression. In W. R. Chegwidden & N. D. Carter (Eds.), *The Carbonic Anhydrases: Current and Emerging Therapeutic Targets*; **75**, 179–204.

Swietach, P. (2019). What is pH regulation, and why do cancer cells need it? *Cancer and Metastasis Reviews*, ***38*****(1-2)**, 5–15.

Syrjänen, L., Luukkaala, T., Leppilampi, M., Kallioinen, M., Pastorekova, S., Pastorek, J., et al. (2014). Expression of cancer-related carbonic anhydrases IX and XII in normal skin and skin neoplasms. *APMIS*, ***122*(9)**, 880–889.

Tafreshi, N. K., Lloyd, M. C., Bui, M. M., Gillies, R. J. and Morse, D. L. (2014). Carbonic anhydrase IX as an imaging and therapeutic target for tumors and metastases. In S. C. Frost & R. McKenna (Eds.), *Carbonic Anhydrase: Mechanism, Regulation, Links to Disease, and Industrial Applications*; **75**, 221–254.

Takacova, M., Bullova, P., Simko, V., Skvarkova, L., Poturnajova, M., Feketeova, L., et al. (2014). Expression pattern of carbonic anhydrase IX in Medullary thyroid carcinoma supports a role for RET-mediated activation of the HIF pathway. *The American Journal of Pathology*, ***184*(4)**, 953–965.

Tanpure, R. P., Ren, B., Peat, T. S., Bornaghi, L. F., Vullo, D., Supuran, C. T., et al. (2015). Carbonic anhydrase inhibitors with dual-tail moieties to match the hydrophobic and hydrophilic halves of the carbonic anhydrase active site. *Journal of Medicinal Chemistry*, ***58*(3)**, 1494–1501.

Tars, K. and Matulis, D. (2019). X-Ray Crystallographic Structures of High-Affinity and High-Selectivity Inhibitor Complexes with CA IX That Plays a Special Role in Cancer. In D. Matulis (Ed.), *Carbonic Anhydrase as Drug Target*; 203–213.

Taşdemir, D., Karaküçük-İyidoğan, A., Ulaşli, M., Taşkin-Tok, T., Oruç-Emre, E. E. and Bayram, H. (2015). Synthesis, molecular modeling, and biological evaluation of novel chiral thiosemicarbazone derivatives as potent anticancer agents. *Chirality*, ***27*(2)**, 177–188.

Thomlinson, R. H. and Gray, L. H. (1955). The histological structure of some human lung cancers and the possible implications for radiotherapy. *British Journal of Cancer*, ***9*(4)**, 539–549.

Tian, S., Sun, H., Pan, P., Li, D., Zhen, X., Li, Y. and Hou, T. (2014). Assessing an ensemble docking-based virtual screening strategy for kinase targets by

considering protein flexibility. *Journal of Chemical Information and Modeling*, ***54*(10)**, 2664–2679.

Tišler, M. (1956). Syntheses in the 4-Substituted Thiosemicarbazide Series. *Croatica Chemica Acta*, ***28*(3)**, 147–154.

Tonissen, K. F. and Poulsen, S.-A. (2021). Carbonic anhydrase XII inhibition overcomes P-glycoprotein-mediated drug resistance- a potential new combination therapy in cancer. *Cancer Drug Resistance (Alhambra, Calif.)*, ***4*(2)**, 343–355.

Totrov, M. and Abagyan, R. (2008). Flexible ligand docking to multiple receptor conformations: A practical alternative. *Current Opinion in Structural Biology*, ***18*(2)**, 178–184.

Turan-Zitouni, G., Yurttaş, L., Tabbi, A., Akalın Çiftçi, G., Temel, H. E. and Kaplancıklı, Z. A. (2018). New Thiazoline-Tetralin Derivatives and Biological Activity Evaluation. *Molecules (Basel, Switzerland)*, ***23*(1)**.

Uslu, A. (2016). *Synthesis of 1,3-thiazolidin-4-one derivatives* [Master's Thesis]. Dokuz Eylül Üniversity, Izmir.

van Slyke, D. D. and Hawkins, J. A. (1930). Studies of gas and electrolyte equilibria in blood. *Journal of Biological Chemistry*, ***87*(2)**, 265–279.

Vander Heiden, M. G., Cantley, L. C. and Thompson, C. B. (2009). Understanding the Warburg effect: The metabolic requirements of cell proliferation. *Science (New York, N.Y.)*, ***324*(5930)**, 1029–1033.

Vleugel, M. M., Greijer, A. E., Shvarts, A., van der Groep, P., van Berkel, M., Aarbodem, Y., et al. (2005). Differential prognostic impact of hypoxia induced and diffuse HIF-1alpha expression in invasive breast cancer. *Journal of Clinical Pathology*, ***58*(2)**, 172–177.

Volarath, P., Harrison, R. W. and Weber, I. T. (2007). Structure based drug design for HIV protease: From molecular modeling to cheminformatics. *Current Topics in Medicinal Chemistry*, ***7*(10)**, 1030–1038.

Waheed, A. and Sly, W. S. (2017). Carbonic anhydrase XII functions in health and disease. *Gene*, ***623***, 33–40.

Wan, Y., Fang, G., Chen, H., Deng, X. and Tang, Z. (2021). Sulfonamide derivatives as potential anti-cancer agents and their SARs elucidation. *European Journal of Medicinal Chemistry*, ***226***, 113837.

Wang, D., Zhao, C., Xu, F., Zhang, A., Jin, M., Zhang, K., et al. (2021). Cisplatin-resistant NSCLC cells induced by hypoxia transmit resistance to sensitive cells through exosomal PKM2. *Theranostics*, ***11*(6)**, 2860–2875.

Wang, E., Sun, H., Wang, J., Wang, Z., Liu, H., Zhang, J. Z. H. et al. (2019). End-Point Binding Free Energy Calculation with MM/PBSA and MM/GBSA: Strategies and Applications in Drug Design. *Chemical Reviews*, ***119*(16)**, 9478–9508.

Wang, L., Guo, C., Li, X., Yu, X., Li, X., Xu, K., et al. (2019). Design, synthesis and biological evaluation of bromophenol-thiazolylhydrazone hybrids inhibiting the interaction of translation initiation factors eIF4E/eIF4G as multifunctional agents for cancer treatment. *European Journal of Medicinal Chemistry*, ***177***, 153–170.

Wang, Y. (2021). Rapid Identification of Potential Inhibitors of Bruton's Tyrosine Kinase (BTK) by Structure-based Virtual Screening. In *ACM Digital Library, 2021 11th International Conference on Bioscience, Biochemistry and Bioinformatics*. Association for Computing Machinery¸33–36

Wang, Y., Xing, J., Xu, Y., Zhou, N., Peng, J., Xiong, Z., et al. (2015). In silico ADME/T modelling for rational drug design. *Quarterly Reviews of Biophysics*, ***48*(4)**, 488–515.

Warburg, O. (1956). On the origin of cancer cells. *Science (New York, N.Y.)*, ***123*****(3191)**, 309–314.

Watson, P. H., Chia, S. K., Wykoff, C. C., Han, C., Leek, R. D., Sly, W. S., et al. (2003). Carbonic anhydrase XII is a marker of good prognosis in invasive breast carcinoma. *British Journal of Cancer*, ***88*****(7)**, 1065–1070.

Weber, C. E. and Kuo, P. C. (2012). The tumor microenvironment. *Surgical Oncology*, ***21*****(3)**, 172–177.

Wei, R., Liu, S., Zhang, S., Min, L. and Zhu, S. (2020). Cellular and Extracellular Components in Tumor Microenvironment and Their Application in Early Diagnosis of Cancers. *Analytical Cellular Pathology (Amsterdam)*, *2020*, 6283796.

White, K. A., Grillo-Hill, B. K. and Barber, D. L. (2017). Cancer cell behaviors mediated by dysregulated pH dynamics at a glance. *Journal of Cell Science*, ***130*****(4)**, 663–669.

Wilden, J. D. (2010). The Sulfonamide Motif as a Synthetic Tool. *Journal of Chemical Research*, ***34*****(10)**, 541–548.

Winum, J. Y. (2014). Classical sulfonamides and their bioisosters as carbonic anhydrase inhibitors. In C. T. Supuran & C. Capasso (Eds.), *Targeting carbonic anhydrases: Claudiu T. Supuran, University of Florence, Italy, Clemente Capasso, Italian National Research Council*; **14**, 18–33.

Winum, J. Y., Temperini, C., El Cheikh, K., Innocenti, A., Vullo, D., Ciattini, S., et al. (2006). Carbonic anhydrase inhibitors: Clash with Ala65 as a means for designing inhibitors with low affinity for the ubiquitous isozyme II, exemplified by the crystal structure of the topiramate sulfamide analogue. *Journal of Medicinal Chemistry*, ***49*****(24)**, 7024–7031.

World Health Organization. (2020). *WHO report on cancer: setting priorities, investing wisely and providing care for all*. https://www.who.int/publications/i/item/9789240001299

Wright, S. W. and Hallstrom, K. N. (2006). A convenient preparation of heteroaryl sulfonamides and sulfonyl fluorides from heteroaryl thiols. *The Journal of Organic Chemistry*, ***71*****(3)**, 1080–1084.

Wu, T. and Dai, Y. (2017). Tumor microenvironment and therapeutic response. *Cancer Letters*, ***387***, 61–68.

Wykoff, C. C., Beasley, N. J. P., Watson, P. H., Turner, K. J., Pastorek, J., Sibtain, A., et al. (2000). Hypoxia-inducible Expression of Tumor-associated Carbonic Anhydrases. *Cancer Research*, ***60*****(24)**, 7075–7083.

Xu, S., Rouzer, C. A. and Marnett, L. J. (2014). Oxicams, a class of nonsteroidal anti-inflammatory drugs and beyond. *IUBMB Life*, ***66*****(12)**, 803–811.

Xu, Y. S., Chigan, J. Z., Li, J. Q., Ding, H. H., Sun, L. Y., Liu, L., et al. (2022). Hydroxamate and thiosemicarbazone: Two highly promising scaffolds for the development of SARS-CoV-2 antivirals. *Bioorganic Chemistry*, ***124***, 105799.

Y. Mboge, M., McKenna, R. and C. Frost, S. (2016). Advances in Anti-Cancer Drug Development Targeting Carbonic Anhydrase IX and XII. In Atta-ur-Rahman & K. Zaman (Eds.), *Topics in Anti-Cancer Research;* 3–42.

Yamagata, M., Hasuda, K., Stamato, T. and Tannock, I. F. (1998). The contribution of lactic acid to acidification of tumours: Studies of variant cells lacking lactate dehydrogenase. *British Journal of Cancer*, ***77*****(11)**, 1726–1731.

Yıldız, M., Ünver, H., Erdener, D., Kiraz, A. and İskeleli, N. O. (2009). Synthesis, spectroscopic studies and crystal structure of (E)-2-(2,4-dihydroxybenzylidene)thiosemicarbazone and (E)-2-[(1H-indol-3-yl)methylene]thiosemicarbazone. *Journal of Molecular Structure*, ***919*****(1-3)**, 227–234.

Yoo, C. W., Nam, B. H., Kim, J. Y., Shin, H. J., Lim, H., Lee, S., et al. (2010). Carbonic anhydrase XII expression is associated with histologic grade of cervical cancer and superior radiotherapy outcome. *Radiation Oncology (London, England)*, ***5***, 101.

Zamanova, S., Shabana, A. M., Mondal, U. K. and Ilies, M. A. (2019). Carbonic anhydrases as disease markers. *Expert Opinion on Therapeutic Patents*, ***29*(7)**, 509–533.

Zhang, X., Perez-Sanchez, H. and Lightstone, F. C. (2017). A Comprehensive Docking and MM/GBSA Rescoring Study of Ligand Recognition upon Binding Antithrombin. *Current Topics in Medicinal Chemistry*, ***17*(14)**, 1631–1639.

Zhang, X., Wong, S. E., and Lightstone, F. C. (2014). Toward fully automated high performance computing drug discovery: A massively parallel virtual screening pipeline for docking and molecular mechanics/generalized Born surface area rescoring to improve enrichment. *Journal of Chemical Information and Modeling*, ***54*(1)**, 324–337

PLAGIARISM REPORT

STUDIES ON NOVEL 4-THIAZOLINE-CONTAINING BENZENESULFONAMIDE DERIVATIVES TARGETING THE TUMOUR-ASSOCIATED HUMAN CARBONIC ANHYDRASE IX AND XII ENZYMES FOR CANCER THERAPY

ORİJİNALLİK RAPORU

%7	%3	%5	%2
BENZERLİK ENDEKSİ	İNTERNET KAYNAKLARI	YAYINLAR	ÖĞRENCİ ÖDEVLERİ

BİRİNCİL KAYNAKLAR

1	Muhammed Trawally, Kübra Demir-Yazıcı, Serap İpek Dingis-Birgül, Kerem Kaya, Atilla Akdemir, Özlen Güzel-Akdemir. "Dithiocarbamates and dithiocarbonates containing 6-nitrosaccharin scaffold: Synthesis, antimycobacterial activity and in silico target prediction using ensemble docking-based reverse virtual screening", Journal of Molecular Structure, 2022 Yayın	%2
2	Submitted to Indian Institute of Technology, Madras Öğrenci Ödevi	%1
3	theses.gla.ac.uk İnternet Kaynağı	%1
4	Muhammed Trawally, Kübra Demir-Yazıcı, Serap İpek Dingiş-Birgül, Kerem Kaya, Atilla Akdemir, Özlen Güzel-Akdemir. "Mandelic	<%1